Vol. 45 - N. 1 SUPPLEMENT

Bollettino di Geofisica
teorica ed applicata

An International Journal of Earth Sciences

Guest Editors: G. Bertotti, S. Buiter, P. Ruffo and G. Schreurs

From Mountains to Sedimentary Basins:
Modelling and Testing Geological Processes

Extended Abstracts of the
GeoMod2004 International Conference

Emmetten – Lake Lucerne
Switzerland
9-11 June 2004

Istituto Nazionale di Oceanografia
e di Geofisica Sperimentale

ISSN 0006-6729

Responsibility for all statements made in B.G.T.A. lies with the authors

Cover design and typesetting: Nino Bon Studio Grafico – Trieste
Printing: Stella Artigrafiche – Trieste
Authorized by the Tribunale di Trieste, n. 242, September 17, 1960

INTERNATIONAL CONFERENCE

From Mountains to Sedimentary Basins:
Modelling and Testing Geological Processes

9-11 June 2004
Emmetten – Lake Lucerne
Switzerland

EXTENDED ABSTRACTS

SPONSORS

ENI E&P Division

EAGE-SEG Italian Section

Vrije Universiteit Amsterdam

University of Bern

Dalhousie University, Halifax, Canada

IASPEI - International Association of Seismology and Physics of the Earth's Interior

IFP - Institut Français du Pétrole

ISES - Netherlands Research Centre for Integrated Solid Earth Sciences

Max und Elsa Beer-Brawand-Fonds (Bern, Switzerland)

SANW - Swiss Academy of Sciences

SNF - Swiss National Science Foundation

SCIENTIFIC COMMITTEE

ATILLA AYDIN - Stanford University, USA
JEAN BRAUN - ANU, Canberra, Australia
JEAN-PIERRE BRUN - Géosciences Rennes, France
ROGER BUCK - Lamont-Doherty, Palisades, USA
BERNARD COLLETTA - IFP, Rueil Malmaison, France
STEPHAN DUPPENBECKER - BP Exploration, Sunbury-on-Thames, UK
CLAUDIO FACCENNA - Università Roma Tre, Italy
ONNO ONCKEN - GFZ, Potsdam, Germany
ADRIAN PFIFFNER - University of Bern, Switzerland

ORGANIZING COMMITTEE

GIOVANNI BERTOTTI - Vrije Universiteit Amsterdam, The Netherlands
SUSANNE BUITER - Dalhousie University, Halifax, Canada
PAOLO RUFFO - Eni E&P Division, Milan, Italy
GUIDO SCHREURS - University of Bern, Switzerland

CONFERENCE SECRETARIAT

ANGELA MARCHETTO - EAGE-SEG Italian Section

CONTENTS

Session 1 - Surface Processes

Session 2 - Orogenesis

Session 3 - Sedimentary Basins

Session 4 - Fractures, Faults and Fluid Flow

Session 5 - Methods and Techniques

Session 1

SURFACE PROCESSES

LANDSCAPE, STRUCTURE AND NEOTECTONICS IN THE SWISS AND FRENCH PREALPES KLIPPEN BELT

1-01

C. Bonnet(*), J. Mosar(*)

(*) Département de Géosciences - Géologie & Paléontologie, Ch. Du Musée 6, CH - 1700 Fribourg, Switzerland. E-mail: Cécile.Bonnet@unifr.ch Jon.Mosar@unifr.ch

Summary

We present first results from a study on morphotectonics, tectonic processes and landscape evolution in the Préalpes klippen belt in Switzerland and France. We further present how analogue modelling experiments of erosion can help understand the morphotectonic evolution.

Abstract text

The challenge of this project is to qualitatively and quantitatively address the recent, post-emplacement, tectonic deformation in the Préalpes Klippen and its foreland and link it to the morphotectonic evolution. The main objective is to establish a link between the neotectonic and morphotectonic evolution and the physical processes shaping the Préalpes. To date studies on neo- or morphotectonics in the Préalpes are very rare.

The Préalpes klippen are formed by a series of nappes of which the most important are the Préalpes Médianes. This nappe detached from its Briançonnais homeland during its incorporation into the orogenic wedge and was subsequently emplaced towards the N-NW onto the foreland during and after the Early Oligocene. Most tectonic and all of its very low-grade metamorphic features were acquired during the incorporation into the Alpine accretionary wedge between 45 and 27Ma. Some out-of-sequence thrusting to the N and to the W-NW (Préalpes and underlying Subalpine Flysch), brittle faults cutting the whole nappe structure, and a high structural relief in the Préalpes to the N and S of Lake Léman, have been linked to events post-dating the emplacement of the Préalpes onto the Alpine foreland.

Former studies have shown that 3 brittle deformation events occur between the main emplacement and the post-emplacement tectonics in the Préalpes:

1) Deformation during pre- to syn-emplacement on the Oligocene Molasse foreland led to the formation of thrusts and tear-faults. Fault/striae sets show a NW-SE compression and a horizontal NE-SW extension consistent with thrusting and strike-slip movement
2) In the E Chablais Préalpes, large-scale strike-slip faults crosscut the folds and thrusts, postdating the Oligocene emplacement of the Préalpes klippen (ex. NW-SE sinistral Tanay-Tombeau des Allemands accident).
3) A third generation of brittle faults can be seen in the Quaternary cover in front of the Préalpes in the Chablais area. The main fault described in the Quaternary sediments (Bouchillon-Evian accident) strikes NW-SE and has a normal NE-downward offset. This fault has supposedly been active into the present.

Despite many studies, we are today still lacking a clear understanding of the Préalpes tectonic evolution post-dating the nappe emplacement (post-Early Oligocene, 30 Ma). For instance the evolution of the brittle faulting and of the geomorphic history are very poorly known and constrained and it is the aim of this project to gain new insight into these recent processes.

We will show initial results from a pilot study in theVanil Noir area south of Fribourg in the Swiss Préalpes. The Préalpes Médianes are in this area formed by large-scale fault-related folds. Important changes in the topography are related to the anticlinal and synclinal tectonic structures and the depth of the basal detachment, but also to the position of the thick limestone of Late Jurassic age which are very resistant to erosion and form distinct morphological features. In addition the area is dissected with numerous brittle faults that have a good expression in the massif limestone layers, but are difficult to trace in the softer levels of interlayered marls and argillites such as in the Middle Jurassic and the Cretaceous. We undertook a systematic investigation of the brittle faults in the area using orthophotographies combined with digital elevation models. This made it possible to make a fracture/fault map. The most striking feature is the persistence and the extent (often in the km range)

of many of the observed faults. These faults have orientations coincident with the major morphological features such as crests and valleys, which indicates the intricate relationship between structure and morphological evolution.
Many of the faults seen in the orthophotograpies can be directly identified and observed in the field. It was possible in many occurrences to measure displacements on these faults and from there on calculate paleo-stress tensors. We compared these measurements with directional measurements of other faults and also observations on relative chronology from fractures and veins to establish a tectonic sequence for the development of the brittle structures in the Vanil Noir area.
A similar approach was used in the Chablais Préalpes along the Tanay-Tombeau des Allemands sinistral strike slip zone that cut the whole nappe structure. The fault/striae analysis shows N-S compression and E-W extension acting upon two main fault surfaces oriented NW-SE and NE-SW, respectively. This fault has an important impact on the regional morphological development and it is speculated that it may extend into the Molasse substratum and the Lake Léman.
All our investigations are centralized in a GIS system that incorporates the both field observations and remote sensing information.
In addition our study includes analogue modelling which will help us better understand the effects of fluvial and glacial erosion and the shaping of landscapes. We will present the experimental setup. During the analogue experiments different materials and experimental layouts are exposed to a rainfall simulator (sprinklers) that causes erosion to occur in the experimental setup. We will show first results from our modelling and applications to the Préalpes area.

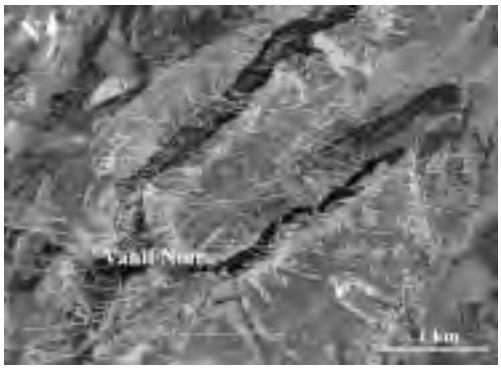

Fig.1 - Interpreted lineament map of the Vanil Noir area, south of Fribourg (Switzerland), overlain on the regional orthophotographies. Observed lineaments are interpreted as brittle faults. The general fold axes direction is NE-SW.

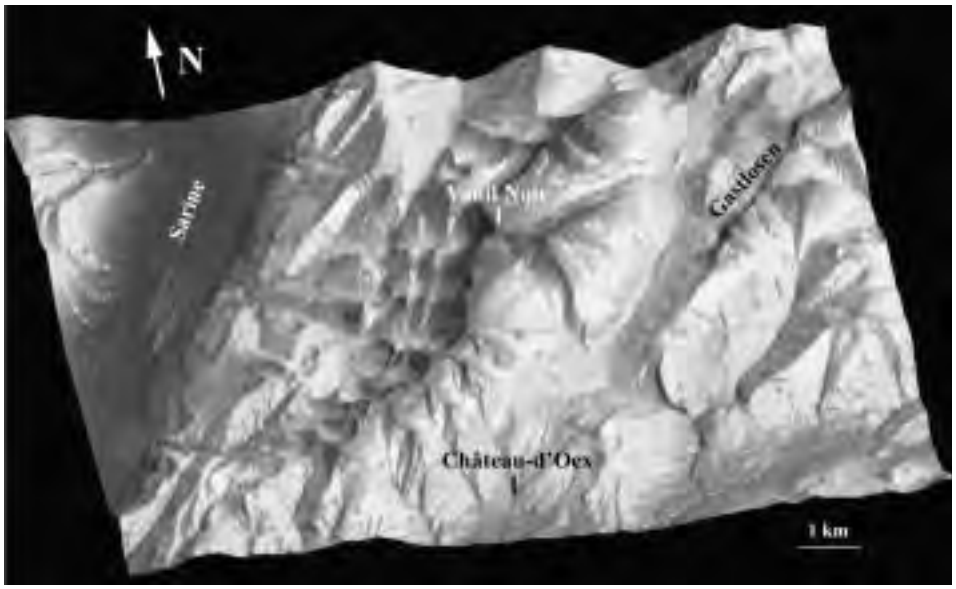

Fig.2 - Digital Elevation Model of the Vanil Noir area south of Fribourg (Switzerland). The DEM clearly shows the major morphological structures and includes the same area as the fracture map of figure 1.

MORPHOLOGY AND STRUCTURE OF ACTIVE THRUST FAULT SURFACE RUPTURES: ANALOGUE MODELING 1-02

C. Bonnet(*), J. Malavieille (**), S. Dominguez(**), H. Philip(**)

(*) Département de Géosciences, Géologie et Paléontologie – Université de Pérolles - 1700 FRIBOURG (Suisse)

(**) Dynamique de la Lithosphère – Université Montpellier II – CC60 - 34095 MONTPELLIER Cedex 5 (France)

Summary

Earthquakes surface ruptures are often complex and segmented. They give only a rough idea about seismic focal mechanism, fault plane geometry and slip at depth. Surface deformation caused by active thrust is frequently distributed not only on the fault plane but also in extrados structures affecting the hangingwall, folding or segments of hidden rupture developed far from the major fault. Estimates of the total rupture length must account for most of these deformations. The main processes and parameters that control the variability of rupture's morphology associated with thrust faulting, are studied using sandbox models. Results of modeling are compared to natural examples.

Abstract text

To model surface deformation caused by active thrust, we used an experimental set-up composed of three rigid blocks limited by two faults dipping 30° (F30) and 45° (F45) respectively (Fig.1). The blocks simulate relative basement rocks in nature, they are covered by layers of different granular materials simulating the most surficial sediments and/or soil layers affected by surface ruptures. Due to shortening, the basement faults will induce deformation and fault propagation in the analogue material. The deformations studied in moels are compared to deformations developed during an unique seismic event or a recurrence of several earthquakes, assuming that associated erosion and deposition of sediments is negligible. Various geometrical and mechanical boundary conditions have been tested. We describe here the most significant results issued from 40 experiments performed for the study. The experiments have been together compared at equal shortening values.

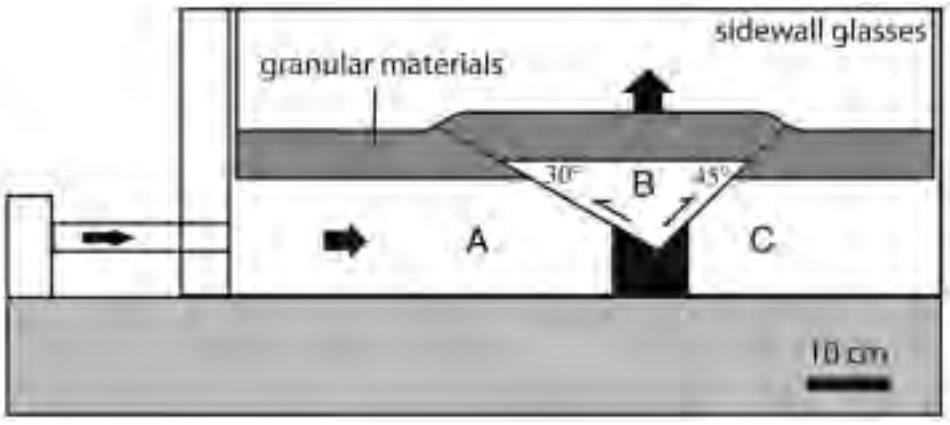

Figure 1 - Sketch of the experimental device.

Influence of fault plane geometry and dip on kinematics: The reference experiment is composed by an homogeneous 6 cm-thick sand-cake in which F45 propagates accross the sand towards the surface remaining at the same dip, trapping hangingwall material under the fault plane. F30 flattens rapidly and reaches the surface horizontally. Higher is the basal fault dip and more simple and linear are the ruptures. Conversely, for low-dip fault planes, the rupture is complex, zones of relay appear and a lot of thrust slices develop. Extrados deformation is due to the convex curvature of fault displaced layers. It is recognizable by the presence of tension gashes and/or normal faults on the hangingwall. The

intrados deformation is due to the topography flexure at the thrust front after the rigid tilting of a part of material. It is caracterized by surficial backthrusts formation (Fig. 2). When the fault remains at high dip to the surface, hangingwall material is trapped under the fault plane and hangingwall extrados deformation appears belatedly among the thrust front. On the other hand, when the fault flattens, extrados normal faults are diffusively distributed on the hangingwall surface and sometimes join the basal rigid blocks (Fig.2). There is no extrados deformation when the hangingwall is folded.
When changing the rheology of model materials, different behaviours occur. For example, high cohesion silica powder in the upper half part of the sand-cake will develop tensions gashes in the fault hangingwall, whereas coarser granular materials (as round rice or semolina) induce diffuse deformation and folding of the hangingwall. The deformation is more diffuse when the granular material is coarser. In the semolina (mean diameter about 1mm), deformation zone is more localized than in the round rice. A décollement layer (glass beads) in the footwall is activated only if placed among the surface. Inside a multilayered stratificate of silicium powder/glass beads analog to interbedded limestones and clays, the fault generated by F30 follows a flat décollement in the glass beads level and merges at the surface inducing frontal imbrication of thrust slices (Fig. 2).

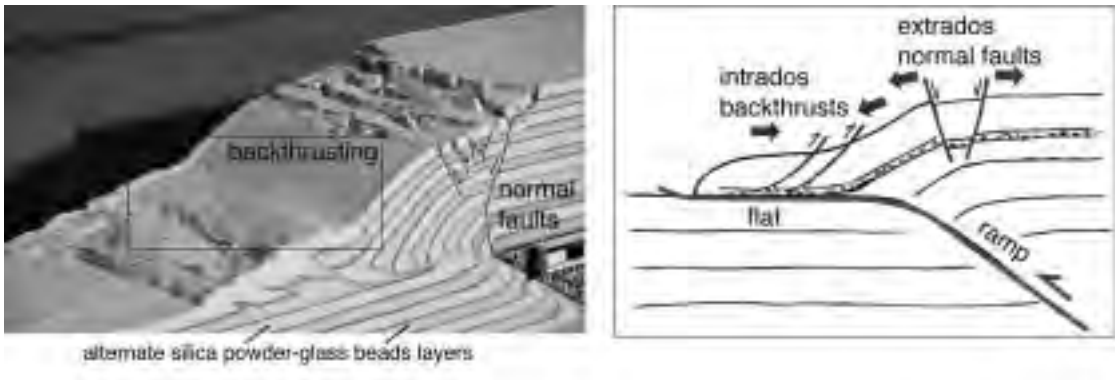

Figure 2 - The dip change of the main thrust plane, from the ramp to a horizontal flat, produces extrados deformations (normal faults) and intrados deformations (backthrusts).

The topography plays an important role in the distribution of deformation close to the surface. If the sandcake is thicker (preexisting topography) above the uplifted basement block (Fig. 3), the faults above F30 and F45 develop a flat geometry beneath the relief boundaries. The main effect of the sand relief is to disturb the local stress field at the vicinity of the basement faults. This perturbation occurs only if the relief is significantly larger than the uplifted basement block. Above F30, a glass beads level placed at shallow depth in the sandcake is activated as a décollement and successive thrust slices are created in the thrust front (Fig. 3, detail a). Above F45, an out of sequence thrust fault cuts later the footwall, merging in the middle of the slope (Fig. 3, detail b)
The Spitak (Armenia) earthquake (7 december 1988, M=6,9) shows good illustrations of the effect of the rheology of the shallow sediments on the surface rupture. It occurred in the North of Armenia where continental collision between the Arabian block and the Russian plateform induces a N/S striking compressive tectonics. The rupture linked to the earthquake appears complex. The surface expression of the fault is characterized by segmentation (Philip et al., 1992). Each segment of the rupture presents an important morphological variability, caused by the behaviour of the heterogeneous surficial formations. The experiments described in figure 4 can be compared to geological observations. When the structure is simple (basement directly covered by a soil), the scarps are simple too. The fault plane that reaches the surface becomes more vertical, and tension gashes appear on the hangingwall, parallely to the main rupture (Fig. 4A). This develops a weakness responsible for the collapse of the hangingwall front. The scarps present a large variability of morphologies when some quaternary sediments (for example poorly cemented conglomerates simulated by round rice) are located between the basement and the soil, where the fault flattens (Fig. 4B). The sediments have a

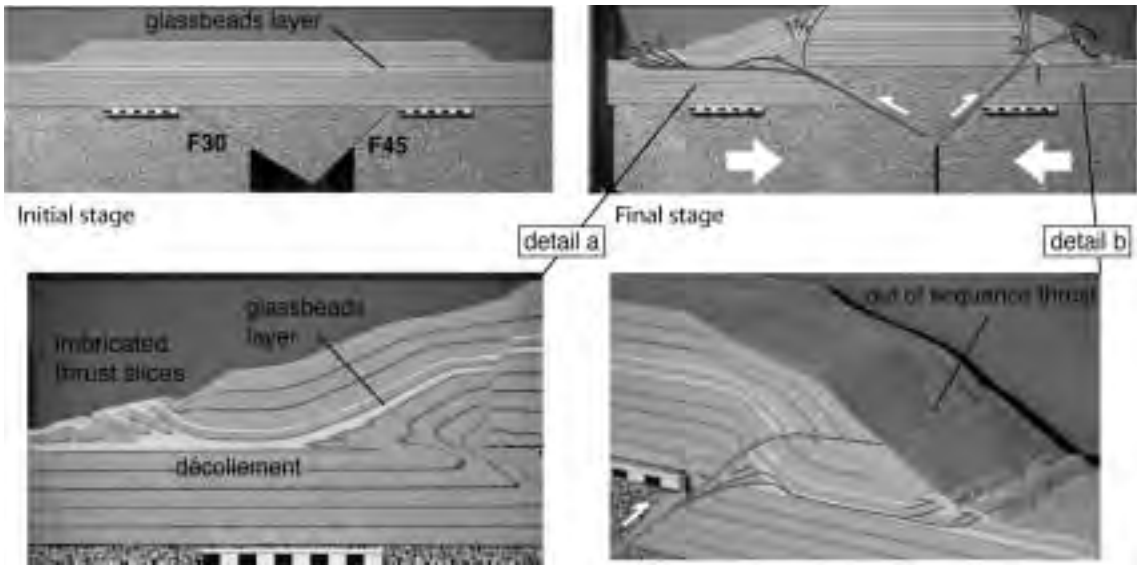

Figure 3 - Two stages of a model showing the effect of a preexisting topography. Above F30 (detail a), a glass beads level is activated as a décollement and successive thrust slices are created in the thrust front. Above F45 (detail b), an out of sequence thrust fault cuts later the footwall.

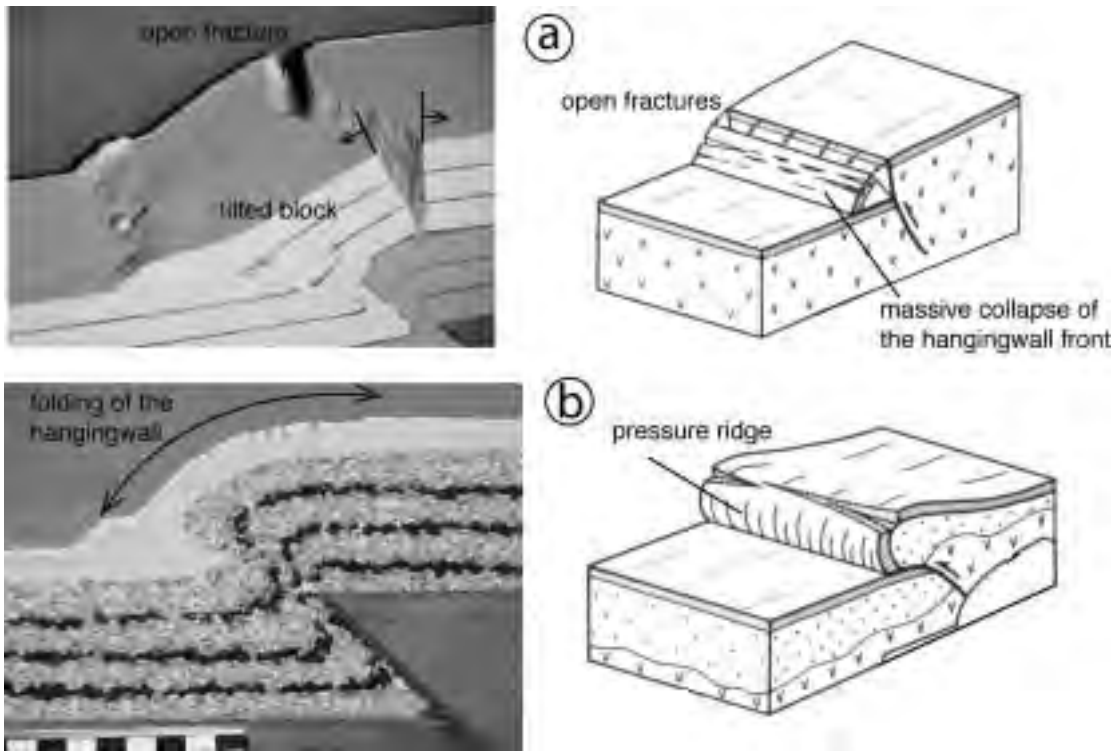

Figure 4 - Examples of deformation observed in two layered models simulating different behaviours of shallow sedimentary sequences. a) A highly cohesive upper layer induces tilting of the hangingwall block and fracture opening. b) Poorly cemented conglomerates are simulated by round rice covered by silica powder modeling high cohesion soils. Diffuse deformation in soft sediments induces folding of the hangingwall and distributed open fractures on the fault scarp anticline. Both sketches illustrate a similar situation along segments of the Spitak rupture.

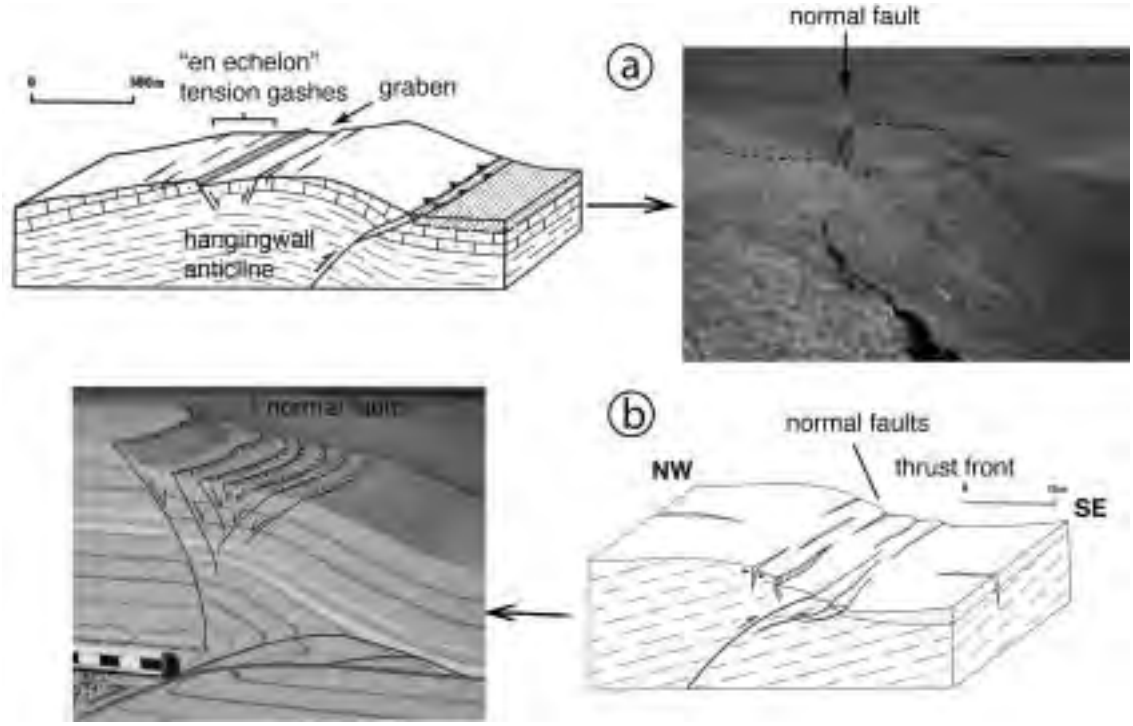

Figure 5 - Two main types of structures develop in the hangingwall of El Asnam fault: - a) Wide grabens located on the crest of the fault relief. - b) Small scale normal faults caused by the dip change of the fault in the footwall.

less cohesive behaviour than the relative basement inducing folding of the hangingwall. Such thrust fold may be broken at the hinge (Fig. 4B).

Paradoxical normal faults induced by large earthquakes are often observed in convergent settings (eg. Avouac et al., 1992). Collision between African and Eurasian plates induces a NNW/SSE compressional tectonic setting responsible for associated thrust faults and strike-slip faults. The El Asnam earthquake (10 october 1980, M=7.3), produced a complex 40 km long surface rupture. The fault is segmented and the main mechanism corresponds to a NW/SE thrust fault combined with a left-lateral strike-slip motion (Philip et Meghraoui, 1983). All along the main fault zone, numerous normal faults and tensile fractures have been observed and described as structures which accomodates the deformation close to the ground surface. As on the experiments of figure 5, two main types of structures develop: - a) Wide grabens located on the crest of the fault relief (Fig. 5a). They can be interpreted as extrados deformation in the hangingwall anticline fold. - b) Small scale normal faults caused by the fault geometry in the footwall (Fig. 5b). They develop above the break point where the fault ramp joins the flat.

To conclude, the deformation caused at shallow depth and on the ground surface by large magnitude earthquakes is strongly dependant of the geometry of the main fault and of the mechanical behaviour of shallow crossed terranes in the upper part of the brittle upper crust. Our experiments show a strong influence of fault plane geometry on seismically induced deformations and structures. The dip change of the major thrust plane, from the ramp to a horizontal flat, produces extrados deformations (tensile fractures in cohesive materials and/or development of paradoxical normal faults), intrados deformations (backthrusts) and gravity induced collapse structures. The rheology of crossed shallow formations determine the style of surface ruptures. The deformation is more diffuse when the granular material is coarser. Weak layers (glass beads) in the footwall are activated as décollements only if placed among the surface, often allowing the development of imbricated thrust slices. Topographic changes (changes induced by faulting and addition of a preexisting topography) influence the local stress field and consequently the fault propagates to the surface close to the relief slope rupture. In the same way, a preexisting relief above the main fault favors décollement activation.

REFERENCES

- Avouac, J.-P., Meyer, B., Tapponier, P., 1992. On the growth of normal faults and the existence of flats and ramps along the El Asnam active fold and thrust system. Tectonics, 11, n°1, 1-11.
- Philip, H., Rogozhin, E., Cisternas, A., Bousquet, J.-C., Borisov, B., Karakhanian, A., 1992. The Armenian earthquake of 1988 December 7: faulting and folding, neotectonics and palaeosismicity. Geophys. J. Int., 110, 141-158.
- Philip, H. et Meghraoui, M., 1983. Structural analysis and interpretation of the surface deformations of the El Asnam earthquake of October 10, 1980. Tectonics, 2, 17-49.

RELATIONSHIPS BETWEEN UPLIFT, EROSION AND SEDIMENT FLUX: INSIGHTS FROM EXPERIMENTAL MODELING 1-03

S. Bonnet, A. Crave, J. Babault

Geosciences Rennes, Univ. Rennes1, UMR CNRS 6118, Campus de Beaulieu, 35042 RENNES Cedex France

Introduction

Erosion is now considered as main agent in geodynamics and it is proposed for example that erosional unloading may influence the geometry and evolution of mountains belts (Horton et al., 1999; Beaumont et al., 2001; Schlunegger and Simpson, 2002). As erosion shaped the landscapes, geomorphological studies are at the heart of our understanding of long-term erosion. However, documenting the evolution of landscape is not straightforward so numerical modeling has been extensively developed in recent years. Numerical models of relief development are based on intuitive assumptions that are very difficult to verify from the study of natural systems. Experimental modeling has then been developed to provide physical tests for numerical models. We present here the different experimental models of relief development and we illustrate their use for numerical and geological purposes.

Experimental reliefs

Experimental modeling in Geomorphology is not as developed as in Tectonics and the definition of experimental procedures is still in progress. The first attempts have been made by the development of a Rainfall Erosion Facility (REF) at the Colorado State University by Stanley Schumm and his team at the end of the 70' (see a review in Schumm et al., 1987). It consists in large flume (18 x 10 m) where a mixture of sand, clay and silt is eroded by an artificial rainfall. It produces large experimental drainage basins and important results have been obtained concerning their dynamics (modes of drainage network growth, response to base-level lowering,...). This device is still used today (e. g. Pelletier, 2003) but each experience is highly time-consuming (an experience needs for example the preparation of 300,000 Kg of material). It limits the possibility to perform numerous runs and to test the senibiltiy to parameters. Only recently a device has been developed to produce Digital Elevation Models (DEMs) of experiments to follow quantitatively the relief development.

Three devices have been developed in recent times. They all concern models with smaller size than the experiments described above. The main differences between them concern (i) the development or not of a device to apply an uplift or a base level variation to the models during their erosion, (ii) the use of a device to digitize the reliefs and the accuracy of topographic data.

The experimental device developed at the University of Minnesota by Hasbargen and Paola (2000) consists of an oval tank ~1 m in diameter and 1 m deep with a single outlet dammed by a motor-controlled gate. The tank is filled with a mix of silica silt, kaolinite and water (D_{50} 0.045mm). An artificial rainfall is produced by sprinkles located at the top of the tank (droplet size <0.2 mm). During an experiment, the motor drops the outlet of the tank so it lowers the base-level for erosion. It forms experimental drainage networks whose evolution is monitored by video and by the output eroded flux (the weight of eroded products recorded at the outlet). A second device is developed by Hancock and Willgoose (2001) at the University of Newcastle, Australia. It consists of a 1.5 x 1.5 m box with a

single outlet, that is filled with ash flow (D_{50} 0.016 mm). It is set within a rainfall simulator where sprinklers produce an artificial rainfall (droplet size ~0.1 mm). The relief evolution is recorded by cameras and DEMs are produced by photogrammetry. Finally, an experimental device is developed at Géosciences Rennes since 1997 (Crave et al., 2000; Bonnet and Crave, 2003; Lague et al., 2003). It differs from the other by devices to uplift the models during their erosion and to produce rapidly high-resolution DEMs of experiments during their run.

Design and procedure

The experimental device developed at Géosciences Rennes consists in a rainfall simulator where a fog is produced using industrial sprinklers that deliver a high pressure water/air mixture (droplet size ~0.1 mm). This device allows to produce rainfall rates ranking from 50 to 200 mm/h. The eroded material (150 Kg for an experiment) is a paste made by mixing granular silica (D_{50} 0.01 mm) with water. This material is used because of its high angle of rest which allows the development of topographic incisions. Its resistance to erosion can be lowered by the adjunction of different proportions of rounded grains of silica. However, technical problems of grain segragation during mixing limit this possibility today. The silica paste is introduced in a box ("erosion box") with an internal size of 40 x 60 cm and a depth of 50 cm. Its base can be moved upward or downward within the box, and its movements are driven by a screw and a computer-controlled stepping motor. During an experiment, the base moves upward at a constant rate and it pushes the silica paste outside the top of the erosion box at a rate defined as the uplift rate (1 to 100 mm/h). The uplifted silica paste is therefore eroded by running water at its surface (Figure 1). Note that the droplet size is small enough to avoid any splash dispersion at the surface of the models so the only erosion process acting on the topographies is runoff. During an experimental run we regularly stop the uplift and rainfall devices to construct 0.5 mm square-grid DEMs of experiments (Figure 1). We digitize the topography at different time-steps, usually from 30 to 60 min of erosion. Topographic informations are derived from optical stereo data acquired with the Advanced TOpometric Sensor (ATOS) developed by the gOm company.

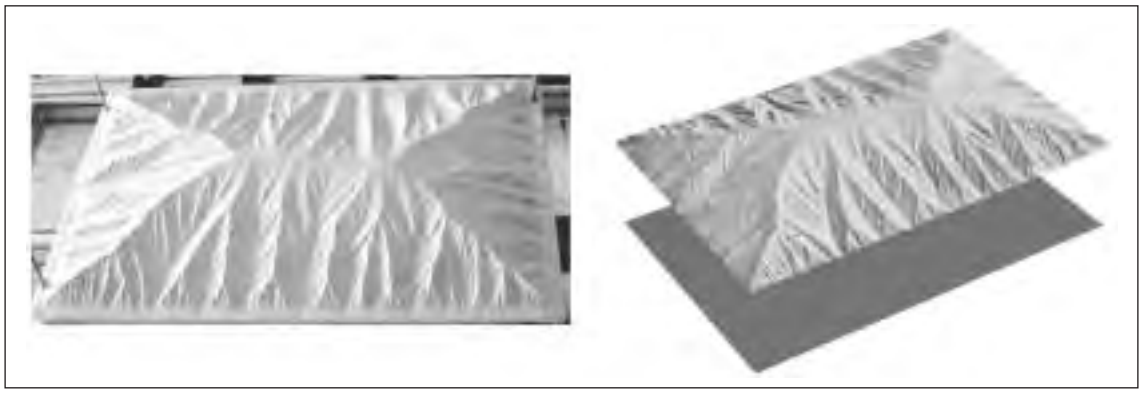

Figure 1 - Photograph and Digital Elevation Model (0.5 mm square-grid) of an experiment (size is 600 x 400 mm).

Scaling and objectives of experiments

Contrary to experiments in Tectonics (Davy and Cobbold, 1991), scaling of experimental models in Geomorphology is not performed so they are not analog models. A perfect scaling of laboratory-scale reliefs is nearly impossible as natural large-scale conditions cannot be downscaled in the laboratory without scale distortions (Crave et al., 2000; Hasbargen and Paola, 2000; Lague et al., 2003). That is why all the recent experimental models were initially developed to provide physical tests for numerical landscape evolution models (SIBERIA model: Willgoose et al. 1991; EROS model: Crave and Davy, 2001). As we explain below, these experimental models are also usefull to test the methods of landscape analysis and the conceptual models of relief behaviour.

Dynamics of experimental reliefs

Relief development under constant uplift and rainfall rates

Experiments begin with the erosion box filled with silica paste up to the top of the erosion box so that the first stages of evolution correspond to a plateau uplift. Figure 2 shows the evolution of mean and maximum elevation of a topography that evolves under constant uplift and rainfall rates. The evolution of such an experiment typically involves a growth phase and a steady-state phase. During the growth phase, some topographic incisions form along the four borders of the model. As uplift continues, they grow and propagate inward up to complete dissection of the plateau. This phase is characterized by an increase in both the mean and maximum elevations. After the growth phase, the mean and maximum elevations remain stable with time (Fig. 1) even if local geometry evolves. A constant mean elevation with time is a criterion used to define a statistical steady-state of the topography (Hack, 1960). This criterion does not imply that the geometry of the topography is stable at the local scale (Hasbargen and Paola, 2000) but only that the output sediment flux equals the input uplift flux. This last point is demonstrated by the sediment flux monitiring in the exepriments of Paola and Hasbargen (2000).

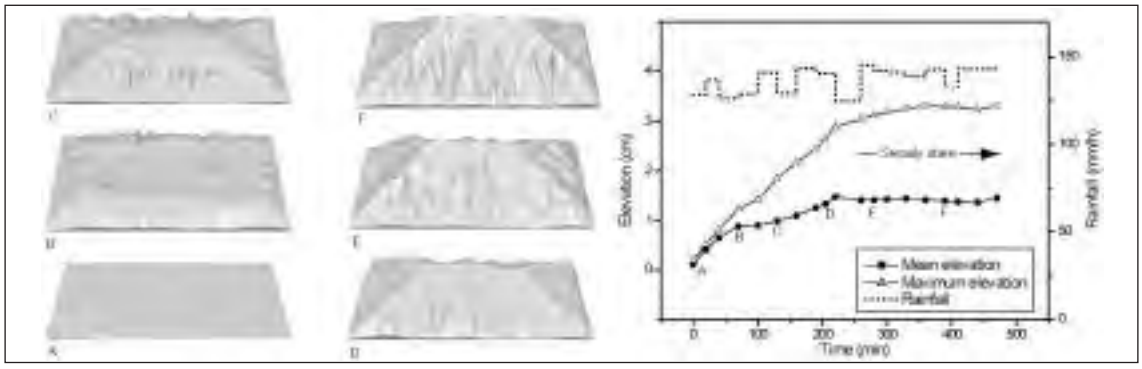

Figure 2 - Evolution of mean and maximal elevation of an experiment up to steady-state, calculated from high-resolution DEMs taken at different time intervals (pixel size 1 mm). A-F are 3D views of DEMs (A-D: growth phase; E-F: steady state). Uplift rate is 15 mm/h and mean rainfall rate is 137 ± 7 mm/h.

Relief geometry: inluence of uplift and rainfal rates

The influence of the uplift rate on the steady-state topographies of experimental models was has been studied by Lague et al. (2003). They demonstrate that the mean elevation of models at steady-state increases with the uplift rate following a threshold-linear relationship. This result agrees with the existence of linear relationships between denudation rate and relief (Ahnert, 1970) or between denudation rate and mean elevation (Pinet and Souriau, 1988).

On the opposite, Bonnet and Crave (2003) and Crave et al (2004) show that the mean elevation of models at steady-state decreases with the rainfall rate (Figure 3). The nature of this relationship is not well-defined today, mainly because of the low range of rainfall capacities of the device used.

The external forcing and the dynamic states of topographies are well-known and the acquisition of high-resolution DEMs allows the measurement of local erosion rates from topographic records. It is then possible to derive an erosion law of the experimental models. Lague et al. (2003) shown that the local erosion rate of experiments linearly correlates with the local topographic slope. It implies that the timescale to reach steady-state does not depend on the uplift rate. These results has been successfully used to test the EROS numerical landscape evolution model (Crave and Davy, 2001).

Figure 3 - Examples of small-scale (14 x 20 cm) experiments at steady-state with the same uplift rate (15 mm/h) but under high (left: 165 mm/h) and low (right: 100 mm/h) rainfall rates.

Case studies

Climatic versus tectonic uplift of topography

Numerical models of landscape evolution incorporate both uplift rate and erosion efficiency to simulate landscape dynamics (e. g. Howard, 1994; Crave and Davy, 2001). Then, the surface uplift of a topography could result either from an increasing tectonic uplift rate or from decreasing erosion efficiency. These models correlate the erosion efficiency with the water flux and thus with climate through rainfall. It assumes a potential link between surface uplift dynamics and climate. We developed an experimental study of the rainfall influence on relief dynamics (Bonnet and Crave, 2003; Crave et al., 2004) in order to test the theoretical approach based on intuitive assumptions on geomorphological processes. We verify that the surface uplift of a topography results from an increase of the applied uplift rate of from a decrease of the rainfall rate (Bonnet and Crave, 2003). We show that the climatically and tectonically induced surface uplift of a topography differs by their pattern of denudation so it is theoretically possible to determinate the cause of a surface uplift by looking at the output sediment flux, as recorded in sedimentary basins.

High-elevation erosional surfaces and the recent uplift of mountain belts

High-elevation erosional surfaces in mountain belts (Pyrenees, Rockies,...) are often interpreted as remnants of an initial peneplain of low elevation that is recently uplifted, but often "without any reference to when crustal thickening and other tectonic processes occured" (Molnar and England, 1990). The interpretation of such surfaces is at the heart of the debate between late Cenozoic uplift of mountain ranges and global climate change. A review of the geological evolution of these mountain belts show that these erosional surfaces form at the end of their evolution, in association with continental aggradation within their foreland basins. We develop an experimental approach of erosion and sedimentation interactions by using the device described above, in association with a device that allows the eroded products to deposit at the foot of the uplifted relief (Figure 4). We demonstrate that peneplanation of a landscape can occur even in the existence of an active uplift when sediment aggradation suddently occured at its foothill as for exemple when foreland basin sedimentation classically changes from marine to continental molasses.. These erosional surfaces primarly from at high-elevation so no post-tectonic phase of mountain uplift is necessary to account from their elevation.

Figure 4 - Photograph of experiment of erosion of an uplifted relief associated with the foothill deposition of the eroded products.

Conclusion and development needs

Experimental modeling in Geomorphology is developed to provide physical tests of numerical simulations of landscape evolution. Presently, one main limitation concerns the nature of the erosional processes that act on the reliefs. The future challenge is to develop a new methodology for the study of coupled erosional processes, a necessary condition for a better understanding of interactions between hillsope and rivers.

REFERENCES

• Ahnert (1970), Geol. Soc. Am. Bull., 91, 2-4.
• Babault et al. (2004), Geology, submitted.
• Beaumont et al. (2001), Nature, 414, 738-742.
• Bonnet and Crave (2003), Geology, 31, 123-126.
• Crave et al. (2000), Physics Chem. Earth, 25, 549-553.
• Crave and Davy (2001), Computer & Geosciences, 27, 815-827.
• Crave et al. (2004), J. Geophys. Res., submitted.
• Davy and Cobbold (1991), Tectonophysics, 188, 1-25.
• Hack (1960), Am. J. Sci., 258, 80-97.
• Lague et al. (2003), J. Geophys. Res., 108.
• Hancock and Willgosse (2001), Earth Surf. Process. Landforms, 26, 475-490.
• Horton et al. (1999), Tectonics, 18, 1292-1304.
• Howard (1994), J. Geophys. Res., 30, 13971-13986.
• Hasbargen and Paola (2000), Geology, 28, 1067-1070.
• Peizhen et al. (2001), Nature, 891_897.
• Pelletier (2003), Geomorphology, 183-196.
• Pinet and Souriau (1988), Tectonics, 7, 563-582.
• Schlunegger and Simpson (2002) Geology, 30, 907-910.
• Schumm et al (1987)
• Willgoose et al. (1991) Earth Surf. Process. Landforms, 16, 237-254.

RECENT ADVANCES AND CURRENT PROBLEMS IN MODELLING SURFACE PROCESSES AND THEIR INTERACTION WITH TECTONICS AND CRUSTAL DEFORMATION

1-04

Jean Braun

Research School of Earth Sciences, The Australian National University, Canberra, Australia
Email: Jean.Braun@anu.edu.au - Ph: +61-2-6125-5512 - Fax: +61-2-6125-5443

Introduction

Understanding the complex interactions between the solid Earth and the overlying hydrosphere has become one of the main research areas in the field of geodynamics. Along the Earth's surface, material is eroded away, transported and deposited by a wide range of fluvial, glacial, hillslope and aeolian processes. Because the Earth's upper surface is characterized by a very large density gradient (between the solid Earth and the overlying atmosphere), these mass movements lead to substantial horizontal gradients in gravitational potential energy which, in turn, can cause or prevent deformation of the Earth's crust. On the other hand, erosional and transport processes are, for the most part, caused by topographic gradients along the Earth's surface, which are created by deformation of the crust under the action of deep-seated tectonic forces. It is thus clear that these interactions have the potential to lead to complex feedbacks between the various parts of the system (the Earth's hydrosphere, lithosphere and mantle). Furthermore, because most of the interactions between the various components of the system (such as the relationship between climate and erosion, between surface slope and the rate of mass transport by surface processes or between lateral density gradients and lithospheric deformation) are strongly non-linear, the system is likely to behave as a so-called 'complex system' whose behaviour cannot be approximated by the linear combination of the behaviour of its components.

Recent advances in computer power have made it possible to model surface processes such as erosion, transport and deposition of material at the Earth's surface with reasonable resolution. This increase in computer power has transformed the field of geomorphology from descriptive to quantitative. Researchers have become empowered with novel techniques to test the concepts that had been developed, mostly through observation, over the previous decades. Unfortunately, because of the inherent difficulty in measuring directly the efficiency of natural processes beyond the human scale,

a quantitative understanding of erosional processes over geological time and spatial scales remains poorly defined. Many questions are still unanswered: Is channel incision the limiting process for fluvial erosion in high-relief tectonically active areas? How important are other processes such as landsliding and/or the transport and removal of debris from river channels? What is the exact nature of the relationship between slope, local discharge and the rate of bedrock channel incision? What is the dominant process causing erosion beneath glaciers and ice sheets? Numerical modelling has provided new tools to integrate the geological record and provide partial answers to many of these questions but it is still limited by the spatial and temporal resolution of current models which prevent an integration of processes from the human to the geological scale.
In this paper, I propose to review the recent advances in understanding erosional processes brought by numerical modelling as well as the limitations of the current landscape evolution models (LEMs). I will then review the various numerical methods that have been used to investigate the coupling between tectonic and erosion and, using arbitrarily chosen examples, I will highlight some of the results obtained so far. I will then focus on defining the many outstanding problems in terms of the current limitations of the existing methods and of our understanding of the system. The main purpose of this presentation will be to stimulate discussion among the workshop participants on several topics: (a) under which conditions can we clearly define and measure the efficiency of the coupling between tectonics, surface processes and climate and (b) can we design/find a natural experiment where the feedbacks between the various components of the system are clearly evidenced.

Brief review of numerical models of surface processes

Most numerical models of surface processes in tectonically active regions assume that the dominant mechanism is bedrock channel incision which, in turn, causes landsliding of valley walls [1, 2, 3]. Transport within the channel is then required to bring material out of the valley system. Many representations of these coupled processes have been proposed [4, 5, 6]. Channel incision is commonly thought to be proportional to local slope and discharge. The exact nature of the relationship between incision, slope and drainage area is not fully understood but is likely to be non-linear [6]. Few attempts have also been made at studying bedrock channel incision and the development of fluvial networks by analog modelling [7]. Hillslope processes (such as landsliding, soil creep or surface transport) are commonly represented by a simple linear diffusion law relating surface curvature to erosion/deposition rate [8]. Limitations of this linear representation have been demonstrated and more complex relationships between transport and local slope have been proposed and investigated [9].
The climatic conditions currently experienced by the planet are not characteristic of the conditions experienced by most active mountain belts over the last 3 Myr. Since the onset of Quaternary cyclic glaciations, high altitude regions have been covered by ice more often than not. This implies that the dominant erosional process in active mountain belts may not be fluvial erosion and transport but glacial erosion. Sliding ice is very efficient at eroding bedrock. Frozen ice protects it. Thus, for glacial erosion to be efficient requires that the climate be sufficiently cold to promote the formation of relatively extensive ice caps and glaciers but not too cold to completely freeze the ice to the bedrock. These conditions have been met relatively frequently in mountainous regions during the most recent glaciations as proven by the presence of well defined glacial landforms such as deeply incised U-shaped valleys and steep-walled cirques. Glacial erosion is though to be proportional to the sliding velocity of ice [10]. Several attempts have been made at modelling glacial erosion, at the scale of a single valley [11] or at the scale of an orogen [12].
Fluvial and glacial erosion processes are thought to result from the physical interaction between water (ice) and rock. It is clear, however, that chemical weathering also plays an important, but commonly poorly constrained role in removing and transporting material at the earth surface. This is particularly true in karsts landscapes. Recent work has demonstrated that, in these environments, surface erosion is proportional to discharge (and thus drainage area) but relatively insensitive to local slope [13]. Finally little has been done to improve our understanding of and/or quantify the role of wind-driven (aeolian) erosion in natural systems, especially on geological time scales and at the scale of orogenic processes.

Coupling erosion and tectonics

Tectonic models

The simplest model assumes that, in compressional orogens, the Earth's crust behaves like a Coulomb material that is at critical taper [14] and deformation is caused by shortening of a relatively weak plate against a stronger one. This leads to a simple relationship between surface slope, the dip of the detachment underlying the orogen (commonly assumed to be along the crust-mantle boundary), the frictional strength of the deforming crust and that of the detachment. The model can be generalized to a doubly-vergent critical taper [15, 16] where deformation is driven by a subduction-like process beneath a crustal layer of relatively uniform strength. Numerically this process has been commonly represented by the imposition of a velocity discontinuity (or strain singularity) at the base of the deforming crustal layer [16, 17, 18, 19]. These tectonic models are two-dimensional but are able to incorporate the complex vertical rheological layering of the crust (and lithospere). Other models have been developed to study tectonic processes in the horizontal plane by integrating/averaging the vertical component of deformation. These so-called 'thin sheet models' of the Earth's lithosphere have been widely used to consider tectonic processes at the continental scale [20, 21, 22, 19]. Apart from a few exceptions, limitations imposed by computational issues have so far prevented modelers to study the deformation of the Earth's crust in three dimensions. Recent advances in computing power will soon allow us to overcome this limitation.

Coupled tectonic-erosion models

2D vertical tectonic models can be coupled to surface processes in two ways: either by assuming that erosion can be modeled by a simple one-dimensional representation of surface processes [18, 23, 24] or by using the deformation of the surface predicted by the tectonic model to drive tectonic uplift of a two-dimensional LEM, the results of which are averaged along the direction perpendicular to the direction of tectonic transport and fed back into the tectonic model [25].

Thin sheet models are, in principle, better suited to be coupled to planform LEMs [26, 27] but are inherently limited by the assumption of small horizontal gradients in crustal thickness, and hence, surface topography. Coupling 3D tectonic models to LEMs is clearly the only approach garanteed to provide us with a realistic representation of the system that will lead to an in-depth understanding of its complex interactions.

Another important component of the interaction between tectonics and surface processes is the potential that horizontal tectonic transport has to perturb the efficiency of surface processes through drainage re-organization. The effect has been demonstrated to be important [28] but certainly requires much more attention.

Finally it is worth noting that modelling the coupling between tectonic and surface processes has not been limited to numerical representations of the system. Analog models of crustal deformation have been coupled to simple physical representation of surface erosion [29] but also, and more recently, to numerical models of surface processes [30].

Using numerical models to improve our understanding of the coupling

To better understand the nature of the feedbacks between the various components of the system requires a quantitative assessment of the efficiency of each of the proposed physical processes. This is commonly summarized as the need to determine the time scales over which each of the processes operates. To determine the rate of tectonic or erosional processes, one commonly relies on some sort of chronometry based on the cooling of rocks as they travel towards the surface of the Earth. Many studies have used thermochronological datasets to obtain information about the rate of tectonic processes [31, 32]; more recently, the advent of low-temperature systems such fission track and (U-Th)/He dating in apatite has led some to use thermochronological data to infer quantitative constraints on the rate of landform evolution [33, 34, 35]. To properly extract from thermochronological data information about the rate of tectonic and geomorphic processes, requires however much caution as these processes perturb themselves the temperature of the crust. For example, it has been shown that the relationship between age and elevation contains information on both the mean rate of exhumation driven by large-scale tectonic uplift as well as information on the rate of landform evolution [36, 37]. Recently LEMs have been coupled to a three-dimensional model of heat transport in the crust that

includes the effects of heat loss through a high-relief upper surface to demonstrate the importance of advective and conductive heat transport in the setting of thermochronological systems in actively deforming mountain belts and other high-relief environments [38].

Discussion

Soon 3D tectonic models will become available at a spatial resolution that will permit to couple them to LEMs. This development will create the opportunity to provide new quantitative constraints on the coupling between erosion and tectonics. In particular, we will be able to better investigate the effect of horizontal tectonic advection on landform evolution, the effect of erosional unloading on the development of brittle structures in the uppermost crust, the effect that erosion might have on the dynamics of continental collision at the lithospheric scale, in small obliquely convergent orogens but also in large-scale orogens where strong gradients in system behaviour exist in all three dimensions. It is equally important, however, that we design appropriate experiments that favour the expression of the dynamical behaviour of the system, especially the strength of the coupling between its various components. Ultimately, this work will then motivate us to create new, more direct methods to question, analyze and understand the natural system.

REFERENCES

[1] Hovius, N., Stark, C. P., and Allen, P. A. Geology 25 (3), 231–234 (1997).
[2] Hovius, N., Stark, C. P., Hao-Tsu, C., and Jium-Chuan, L. J. Geol. 108, 73–89 (2000).
[3] Whipple, K. X. and Tucker, G. J. Geophys. Res. 107, 10.1029/2000JB000,044 (2002).
[4] Howard, A. D. Water Resour. Res. 30(7), 2261–2285 (1994).
[5] Kooi, H. and Beaumont, C. J. Geophys. Res. 99, 12,191–12,209 (1994).
[6] Whipple, K. X., Kirby, E., and Tucker, G. J. Geophys. Res. 104, 17,661–17,674 (1999).
[7] Lague, D., Crave, A., and Davy, P. J. Geophys. Res. 108, 10.1029/2002JB001785 (2003).
[8] Anhert, F. In L'Evolution des versants, Macar, P., editor, 22–41 (Universit´e de Li`ege, Belgium, 1967).
[9] Braun, J., Heimsath, A. J., and Chappell, J. Geology 29, 683–686 (2001).
[10] Hallett, B. J. Glaciol. 89, 39–50 (1979).
[11] Harbor, J. Geol. Soc. Am. Bull. 104, 1364–1375 (1992).
[12] Tomkin, J. Landforming processes in glaciated orogens: a numerical study. PhD thesis, The Australian National Unversity, Canberra, ACT, Australia, dec (2000).
[13] Kauffman, G. and Braun, J. Terra Nova 36, 1381–1391 (2001).
[14] Dahlen, F. A. J. Geophys. Res. 89, 10,125–10,133 (1984).
[15] Koons, P. O. Geology 18, 679–682 (1990).
[16] Willett, S., Beaumont, C., and Fullsack, P. Geology 21, 371–374 (1993).
[17] Beaumont, C., Fullsack, P., and Hamilton, J. Tectonophysics 232, 119–132 (1994). [18] Batt, G. E. and Braun, J. Geophys. J. Int. 128, 364–382 (1997).
[19] Ellis, S. Geology 24, 699–702 (1996).
[20] Vilotte, J.-P., Daignières, M., and Madariaga, R. J. Geophys. Res. 87, 10,709–10,728 (1982).
[21] England, P. and McKenzie, D. Geophys. J. Roy. Astr. S. 70, 295–321 (1982).
[22] England, P. and Houseman, G. A. J. Geophys. Res. 94, 17,561–17,579 (1989).
[23] Willett, S. D. J. Geophys. Res. 104, 28,957–28,981 (1999).
[24] Hilley, G. and Strecker, M. J. Geophys. Res. (in press).
[25] Beaumont, C., Fullsack, P., and Hamilton, J. In Thrust Tectonics, McClay, K. R., editor, 1–18 (Chapman and Hall, New York, 1992).
[26] Ellis, S. Continental convergence: length scales, aspect ratios, and styles of crustal deformation. PhD thesis, Dalhousie University, Halifax, N.S., Canada, (1995).
[27] Braun, J. and Shaw, R. D. In Continental Reactivation and Reworking, Miller, J., Holdsworth, R., Buick, I., and Hand, M., editors, 165–193 (Geological Society, Special Publication 184, London, 2001).
[28] Willett, S. D., Slingerland, R., and Hovius, N. Am. J. Sci. 301, 455–485 (2001).
[29] Chemenda, A. I., Mattauer, M., Malavieille, J., and Bokun, A. N. Earth Planet. Sc. Lett. 132, 225–232 (1995).
[30] Persson, K., Garcia-Castellanos, D., and Sokoutis, D. J. Geophys. Res. 109, 10.1029/2002JB002274 (2004).
[31] McDougall, I. and Harrison, T. M. Geochronology and Thermochronology by the 40Ar/39Ar Method. Oxford University Press, New York, first edition, (1988).
[32] Batt, G. E., Braun, J., Kohn, B. P., and McDougall, I. Geol. Soc. Am. Bull. 112(2), 250–266 (2000).
[33] van der Beek, P. and Braun, J. Basin Res. 10, 49–68 (1998).
[34] van der Beek, P. and Bishop, P. J. Geophys. Res. 1108, 2309, 10.1029/2002JB002125 (2003).
[35] Tomkin, J., Brandon, M., Pazzaglia, F., Barbour, J., and WIllett, S. J. Geophys. Res. 108, 2308, doi:10.1029/2001JB000862 (2003).
[36] Braun, J. Earth Planet. Sc. Lett. 200, 331–343 (2002).
[37] Braun, J. Terra Nova 14, 210–214 (2002).
[38] Braun, J. and van der Beek, P. J. Geophys. Res. (in press).

COMPLEX FAULTING SEQUENCES CONTROLLED BY DYNAMIC TOPOGRAPHY IN 3D EXPERIMENTAL DEFORMATION OF DOUBLY-VERGENT COULOMB WEDGES

1-05

M. Del Castello(*), K.R. McClay(**), G.A. Pini(***)

(*) CNR–ISMAR, Sezione di Geologia Marina, Via Gobetti, 101, 40129, Bologna, Italy.

(**) Fault Dynamics Research Group, Geology Department, Royal Holloway University of London, Egham, Surrey, TW20 0EX, UK.

(***) Dipartimento di Scienze della Terra e Geologico-Ambientali, Via Zamboni, 67, 40126, Bologna, Italy.

Summary

In this paper, sandbox modelling was used to investigate the dynamic effect of localised syn-tectonic erosion and/or sedimentation on the deformation mechanics of accretionary systems. High obliquity was chosen as the main boundary condition to analyse 3D strain partitioning of a doubly-vergent Coulomb wedge, for the particular case in which a subduction polarity reversal event affected wedge development. In the experiments, the first phase of shortening (P1) produces a pre-existing topography affecting wedge development during second phase (P2). The elevation potential can be varied in the models via sequential events of syn-tectonic denudation and/or sedimentation, performed on distinct sectors of the deforming wedge. Experimental results suggest that the parallelism between the imbricates at the thrust front and the strike-slip fault at the rear of the prism predicted by theoretical models is valid only at steady-state, when failure conditions exist everywhere at the basal décollement. Before this stage, different velocity fields characterise mass transfer in distinct sectors, leading to unexpected wedge behaviour during which superficial extension or compression, both located in the axial zone, predate the full-development of a strike-slip fault.

Abstract text

The effect of the third dimension on the evolution of orogenic systems as well as other geological settings is one of the most challenging tasks faced by Earth scientists. 2D steady-state models are often used in order to unravel the complexity of rock deformation processes, although space and time are undoubtedly of primary importance in deciphering natural systems. In fact, mountain ranges arrangement may vary considerably as their dynamic balance is continuously modified. Among the variables that influence the 2D development and geometry of structures along convergent margins, the following have been suggested to be the most important ones: 1) convergence rate normal to the margin, 2) thickness and rheology of the sediments entering the subduction zone, 3) syn-tectonic sedimentation and erosion, 4) frictional resistance at the base of the deforming wedge. When the framework is extended to the 3D, additional quantities must be taken into account; these are: 5) obliquity of subduction, 6) slip vectors, 7) degree of strike-slip partitioning, 8) lateral variations of wedge topography and surface processes, 9) lateral variations of thickness and rheology of the lithosphere, 10) time and space evolution of major troughs or foreland basins, which, in turn, might alter the lateral lithostatic overburden in front of the deforming margin.

Mechanical and kinematic control exerted on fold and thrust belts evolution by pure frictional rheology along potential failure surfaces has been widely applied to model compressional systems in nature. The idea that a thrust system can resemble a wedge of non-cohesive material tapering in front of an advancing bulldozer blade makes scaled sandbox modeling one of the most powerful and commonly used technique in order to unravel the behavior of a pile of sediments (or rocks) subjected to shortening. In this study, simple analogue modeling technique was used to analyze the three-dimensional response of an accreting system to localized events of syn-tectonic denudation and sedimentation. The models reflect the idea that elevation potential as well as flexure might not be constant along the wedge strike and, in principle, erosional and re-sedimentation processes may strongly change in time and space (Fig.1). In other words, the way in which the accreting system redistributes its mass balance can be a key control on wedge dynamics.

It must be underscored that denudation and sedimentation were not mass-balanced during experimental procedure. Modeling of surface processes has only recently been the focus of great

attention by geologists and is still far to be resolved. In any case, scaling these processes is hardly achievable in analogue models, due to the limitations of this simple experimental methodology. Despite this simplification, the models described here are an excellent opportunity for further discussion and modeling prospects. An unexpected wedge response to shortening was revealed during lab work in terms of strike-slip partitioning and confirmed the overall complexity of deformation. Animations of model runs allowed continuous recording of multistage faulting sequences, comprising extension, compression and wrenching, all belonging to a single, unchanging stress configuration.

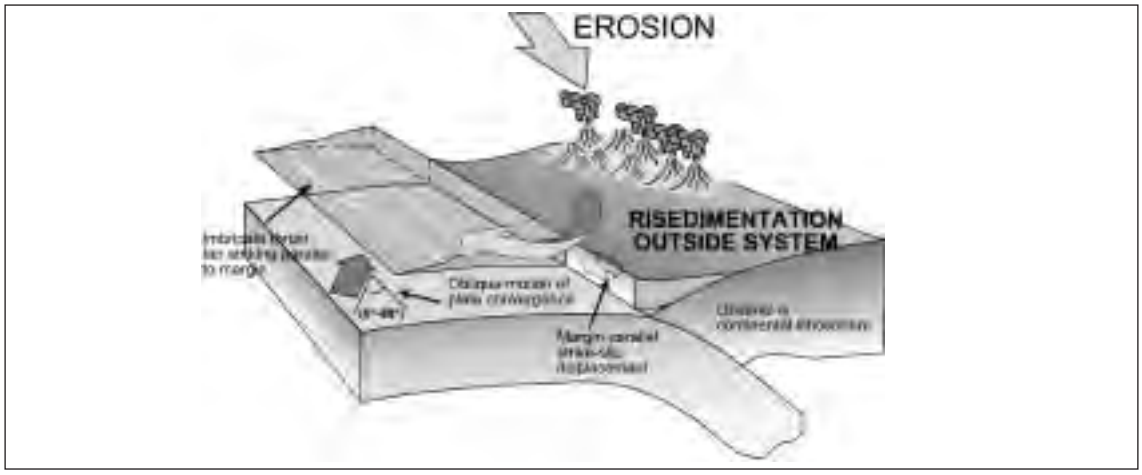

Fig.1: The concept of strain partitioning, illustrating margin parallel thrusts with slip vectors aligned normal to the trench along with a component of strike-parallel displacement by strike-slip faulting. Note the possible uneven mass redistribution due to surface processes.

Syn-tectonic sedimentation

These experiments were intended to study the effect of a pre-existing, asymmetric overload in the down going section. The overload was reproduced by a syn-tectonic wedge of sand, which was carefully sieved in the P2 prowedge region. This covered half of the total down going area (Fig.2a). This was done before the beginning of P2 (or just after the switch in subduction direction). The sand wedge was layered trying to simulate a three dimensional sedimentary body, with radially decreasing

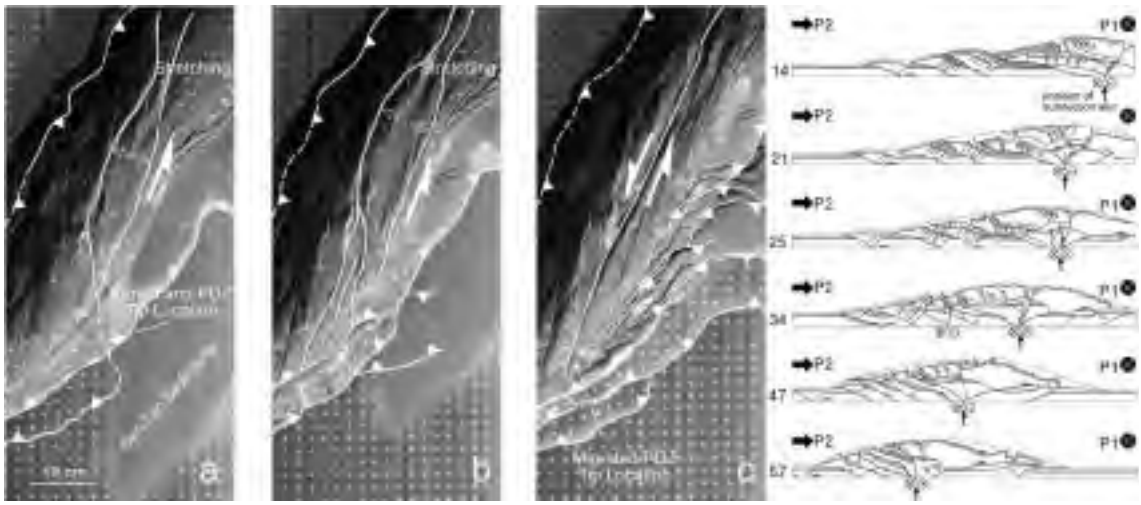

Fig.2: a) asymmetric overload controls along-strike propagation of the new forethrust in the prowedge region; b) stretching in the axial zone persists up to final basal décollement yielding; c) along-strike strike-slip fault propagating throughout the axial zone. Sequential sectioning of this experiment (sections are from right to left in figure 2c). Symbol at the subduction slot position indicates sinistral wrenching. P1 subduction vector is out from the page. Shaded parts of the wedge indicate syn-tectonic sediments.

thickness and a maximum overload close to the P1 retrowedge toe that nearly doubled the incoming section. Prowedge kinematics showed to be strongly affected by the presence of the syn-tectonic sediments. The first forward thrust that formed broke through the undeformed sand-pack (Fig.2a). It was continuous along strike and seemed not further affected by the presence of the syn-tectonic sand wedge, which was imposed in the system immediately after its nucleation. Conversely, the subsequent unit was strongly discontinuous. In fact, it showed a tip point located at the boundary with the syn-tectonic sand wedge, where dislocation dramatically died out (Fig.2a). The forethrust tip absorbed differential deformation across at the transition in sand thickness and forced the rotation of a complex deformation zone, showing stretching in the axial zone (Fig.2a). The dilatational domain persisted in the area and stretching increased in magnitude, while rupturing propagated along the basal décollement (Fig.2b), until the formation of the first continuous forethrust (Fig.2c). This was the turning point, when a discrete, through going wrench fault developed in the axial zone and eventually paralleled the subduction slot.

Serial cross-sections performed at the end of the model run reveals the complex faulting pattern within the wedge (Fig.2). In this experiment, the wedge internal architecture is characterised by high along-strike variability, resulted from the complex wedge growth history. The wide prowedge is made by very long imbricates that are affected by strong back thrusting (sections 14 and 21). A thicker down going section due to the presence of syn-tectonic sediments produces an anomalously wide first thrust unit, but their average length is quickly regained as the syn-tectonic wedge pinches out. Along strike transition from imbricate thrusting to out-of-sequence reactivation is evident (a truncated duplex is nicely evident in section 47). A general “reflection” of faults dipping can be observed in almost all the sections, with a distinct “neutral” surface dividing deeper sectors, where thrusting and back thrusting dominate, from shallower ones where extension is still clearly detectable (sections 25, 34, 47) also at considerable distance from the main wrench fault.

Syn-tectonic denudation

A further step in the analysis of three dimensional wedge mechanics was to include asymmetric erosion. After the end of P1, a metal scraper was used to lower down the axial zone of about 30% of its original height. Denudation affected half the original axial zone length (Fig.3). This was repeatedly carried out every 5 cm of shortening, for a total of 8 events, each lowering the axial zone to the same initial height. In the experiment shown,no sand was removed from the system. After each scraping off event, the removed material was only let slide down the wedge slope, by turn on each side of the

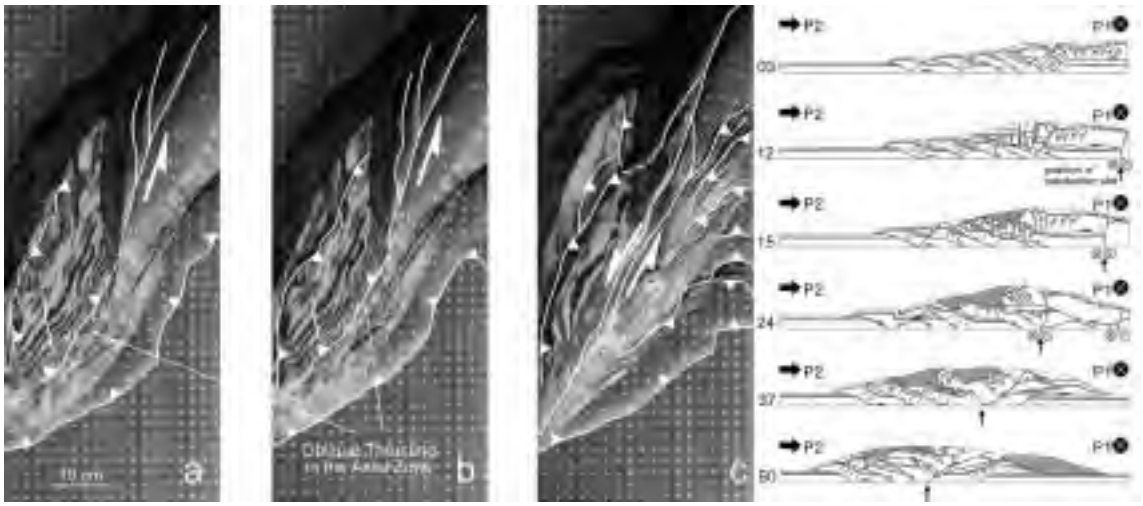

Fig.3: a) PDZ propagates towards the eroded sector in the form of an oblique-reverse fault; b) as long as the axial zone is eroded reverse faulting is favoured, uplifting the unstable low topography; c) dip-slip thrusting along the retrothrust is still dominant with respect to strike-slip parallel to the margin. Sequential sectioning for this experiment, (sections are from right to left in figure 3c). Symbol at the subduction slot position indicates sinistral wrenching. P1 subduction vector is out from the page. Shaded parts of the wedge indicate eroded sediments.

deforming wedge. Thus, the mass balance was respected. Prowedge region displayed a uniform behavior in this case. Forethrust did not show any fault trace termination. They nucleated at a constant pace, constantly building forward the prowedge region (Fig.3). Nevertheless, a mechanical linkage between prowedge and the rest of the deforming wedge was always present. The only anomaly observed, in an otherwise smooth response to shortening, was detected between 15% and 20% of shortening, when deformation in the prowedge apparently partitioned between dip-slip in correspondence to the outermost deformation front and reverse oblique motion at the transition with the axial zone (Fig.3a and b). During sequential denudation events, a fully developed sinistral strike-slip faulting was evident only in the non-eroded sector (Fig.3a and b). Perhaps, it was connected to the previously mentioned reverse oblique segment in the eroded region. However, pure strike-slip kinematics cannot be assumed for the whole wrench deformation zone. Only towards the end of the experiment (Fig.3c), when denudation no longer occurred, a widespread wrench system can be observed in plan view, suggesting that also syn-tectonic erosion is a key factor in controlling total strike-slip partitioning.

The strong effect exerted by asymmetric denudation on strain partitioning is even more evident observing fault architecture in cross section. The wedge displays a wide prowedge region made up by long thrust unit (sections 3 and 12). Although less developed than the case with syn-tectonic sediments, back thrusting is again present and strike-slip movement at shallow levels progressively increases as the axial zone is approached (sections 15 and 24). Out-of-sequence thrusting in the inner prowedge region is favoured by syn-tectonic denudation. In the eroded sector, continued retrothrust activity causes uplift, faulting and dismembering of the first thrust unit accreted in the prowedge region during earliest stages of shortening (section 37). As a result, the prowedge region drastically narrows. Strike-slip motion is distributed over a wide area in the axial zone. However, wrenching tends to fade out entering the eroded sector, and the steeply dipping fault required by kinematic models is replaced by a low angle retrothrust accommodating dip-slip motion (sections 37 and 50).

Conclusions

- Experimental observations indicate a continuous mechanical feedback between prowedge region basal décollement and retrothrust in determining how three-dimensional deformation is partitioned within the wedge. Both timing and mode of retrothrust activation are crucial factors in influencing critical wedge mechanics as a whole.
- Although total strike-slip partitioning has been confirmed in the 30° obliquity unidirectional subduction experiment, this is not a requirement for highly oblique convergent setting where potential décollement surfaces are kept within the frictional stability field.
- High level of shear resistance on the prowedge basal décollement might be able to control localization of compressive stress surpluses in the axial zone, thus suppressing margin-parallel wrench faulting for a significant time interval.
- Evolving topography and basal shear resistance with respect to a fixed basal/internal coefficients of friction ratio offers a wide spectrum of faulting development for a stress configuration that remains fixed with time.
- If differences of velocity exist, then the wedge response to shortening will be highly uneven and, consequently, mass transfer modes will cause wedge behavior to depart from theoretical predictions. When strain along the retrothrust is non-coaxial either with strain in the prowedge region or with that along the potential strike-slip fault, a temporary tensile stress couple may develop, leading to transient margin-parallel extension of the axial zone.
- Vertical strain partitioning has been observed in the 3D models sections.

EVALUATION OF RECENT COLLISION-RELATED TECTONIC PUSH IN THE EASTERN MEDITERRANEAN-CAUCASUS ZONE: FEM MODELLING APPROACH

1-06

Marek Jarosiński

Polish Geological Institute, Rakowiecka 4, Warsaw, Poland

Abstract

The recent geodynamics of Central Europe is investigated using the FEM modelling approach. The elastic, plane model combines in one system faults as contact elements, tectonic blocks with various elastic property and thickness, topography-related stresses and tectonic forces exerted to the boundary segments. In order to reproduce a complex stress pattern in the investigated area, a precise adjustment of boundary conditions and model properties were necessary. The use of stress regimes and fault activity as additional model constraints, allowed for better balancing of tectonic forces. In the course of modelling, the diversity of tectonic push in the Mediterranean-Caucasus collision zone and ridge push at the North Sea passive margin segment were evaluated.

Introduction

The paper aims to examine, to what extent the complex stress pattern in the plate interior of Central Europe can be explained by fare field tectonic stresses, including stresses produced by local gravity potential energy. Taking advantage of the high stress heterogeneity in this area the attempt was done to evaluate the diversity of tectonic forces along the collision zone with Africa and the North Sea passive margin. The model bridges the gap between the plate-scale models, with their unsatisfactory fit between modelled stress directions and data [Grünthal & Stromeyer, 1992; Gölke & Coblentz, 1996; Loohuis et al., 2001], and local scale models, with their very direct relation between the loads and stresses [Bada, et al., 1998].

The modelled area is limited to the central and eastern Europe (Fig. 1), which comprises a complex structural junction. The area is divided by the Alpine-Carpathian suture in the foreland (the North European part of the plate) and the hinterland (the South European part of the plate). The North European plate embraces the East European Craton (EEC) and the Paleozoic platform consists of Avalonia and Armorica types of terranes accreted in Caledonian and Variscan époques, respectively. The hinterland plate comprises an array of terranes amalgamated in Tertiary period, in the course of the Alpine collision.

The prominent feature of the examined area is the heterogeneity of the recent stress field both in terms of horizontal stress (S_{Hmax}) direction and also in stress regime conditions. In the vast area of the EEC, the Alps, the Carpathians and their foreland, the Pannonian region and the Dinarides, the axes of horizontal compression deviate significantly from a general NW-SE trend, characteristic for Western Europe and a large part of Scandinavia [Reinecker et al., 2003, Gerner et al, 1999, Jarosiñski, 1999]. Looking at the map of the S_{Hmax} trajectories, generally two large-scale bows originated in the Dinarides can be defined. The Northern one passes through the Alcapa – the Ma≥opolska Massif – the margin of EEC to eastern Scandinavia, and the southern one, striking through the Pannonian basin – the Moesian and Scytian platform – the Black Sea to the Pontides (fig. 2). The Aegean extensional province is located in the centre of the southern bow. Reproducing this general stress pattern was the first principal condition of proper solution of the model. However, local stress features were also taken into account.

The general collisional setting of Africa with Eurasia is determined by the northward advance of the African plate with slight left lateral rotation. This rotation is expressed by the changing velocity of the convergence from 6 mm/yr in the western part of Mediterranean to 9 mm/yr in the eastern part and (farther) up to 25 mm/yr for the Arabian plate rotation [Minster & Jordan, 1978]. Within the Mediterranean collision zone several segments characterized by individual geodynamic behaviour are differentiated: the Ionian Sea, the Greek segment of the Hellenides, the Aegean Sea, the Marmara Sea, the Black Sea and the Caucasus segments. In result of modelling, tectonic pressure on each segment has been evaluated.

Model construction

The FEM model, built in ANSYS code, comprised of 3963 triangular, plain, solid elements with mid-nodes (fig. 1). In the central part, the nominal size of the element fringe was 50 km, while for peripheral areas, a coarse mesh with 100 - 200 km size of element was applied. Elastic and isotropic elements were used, with material properties characterized by constant Poisson's ratio and optionally, constant or variable Young modulus (E) and thickness. Within every singular tectonic unit, material properties were kept constant. The model also comprised contact elements that reproduced 16 regional dislocations. Each dislocation was built of several straight linear segments, comprising several contact elements. Faults accommodated only planar strike-slip offset. The mechanical properties of faults were defined by friction coefficient, which values were declared separately for each fault segment. Due to frictional slip on dislocations, solutions of the model were not linear. The energy was preserved in the model - the friction motion along faults effected only in deformation but not in energy dissipation by heating.

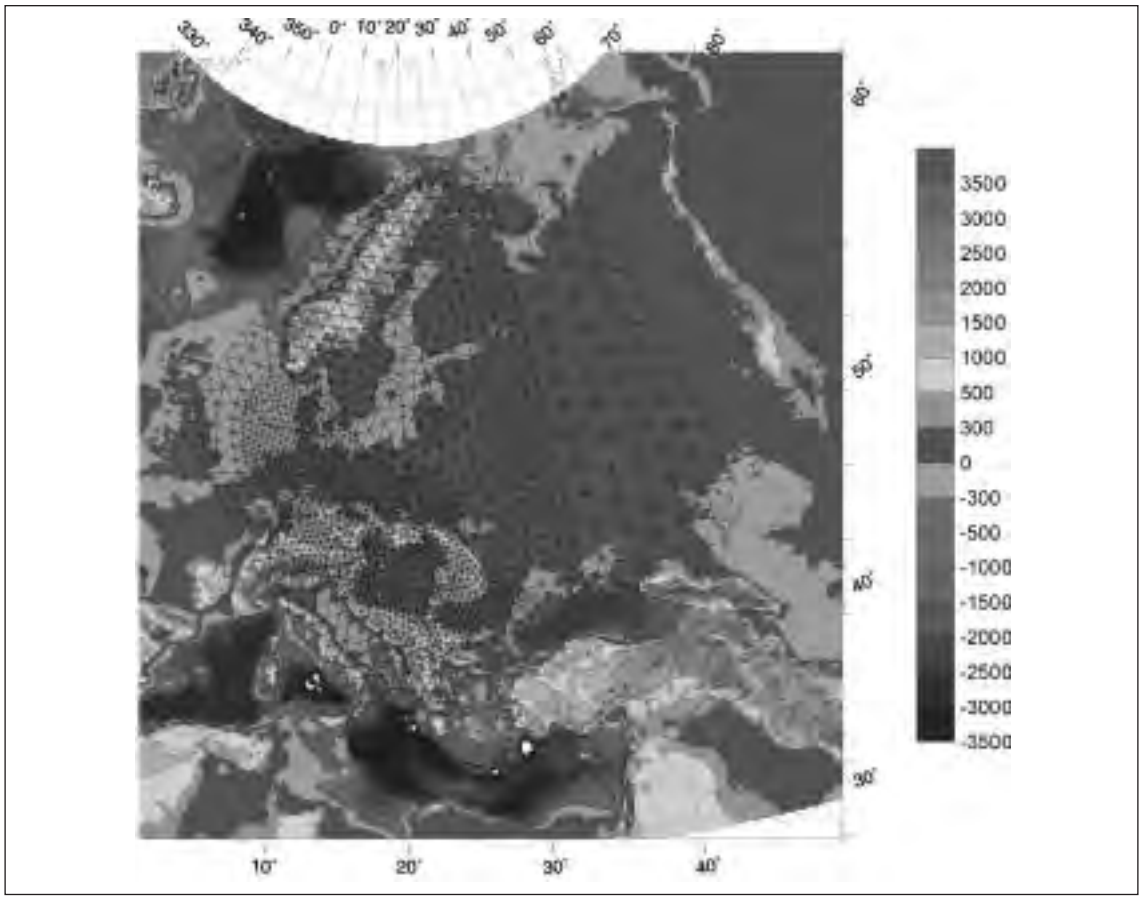

Fig. 1 – The mesh of FEM model, showing its location at the background of topographic map of Europe.

Boundary loads, treated as model variables, were imposed in three different ways (1) as constant pressure on the boundary segment, (2) linearly changing pressure along segment, and (3) forces exerted to the nodes where tectonic push or pull is not perpendicular to the boundary. The circumference of the model was divided into fourteen boundary segments. Detailed segmentation of the boundary allowed for accurate analysis of altering boundary loads that were required to balance the external forces with the internal stress pattern. Geodynamical significance of the boundary segments is crucial for consistency of the model and validity of its results. Based on geological and geophysical data 24 tectono-mechanical units were differentiated. Models were optionally constructed with constant or variable material properties among tectonic units. Introducing several main fault

zones allowed for inferences of the critical friction coefficients that prevented reactivation of passive faults or permitted motion on active ones.
Stresses due to topography were computed following the concept of gravity potential energy elaborated by Coblentz et al. [1994]. However, this correction was implemented in a different way. In the first step, the potential energy for each element was computed from the average altitude of the element, relative to the reference sea level. This energy was applied as a pressure on the fringes of each triangle element. Positive gravity potential energy in elevated areas was reproduced by pressure directed outwards from the element, negative energy in marine basins was applied as a pressure directed inwards the element. The pressure was averaged over the thickness of a given tectonic unit.

Modelling procedure

Forward modelling with trials-and-error(s) routine was used to obtain the best fit of computed stress directions to the measured S_{Hmax}. The only constant attribute of the model was its geometry - boundary, areas, fault zones and esh. The other features, such as loads on the boundary, pressure on the elements (representing topography-related stresses), material properties and friction coefficients were variables. In the first run of the mechanically uniform model, the ridge push exerted to the NW margin of the model and free boundary in the Aegean region were the only predefined boundary loads. Subsequently, the boundary loads were successively adjusted in the course of interaction with topography-related stresses, faults and taking into account stress regimes. To examine the influence of different factors on S_{Hmax} distribution, four sets of models were designed: (1) Pure geometry models (constant material property, no faults, no topography); (2) Topography including models (no faults) and faults including models (no topography); (3) Faults and topography including models (constant material property); (4) Models with faults, topography and variable material properties. For each set of models several arrays of boundary forces were tested.

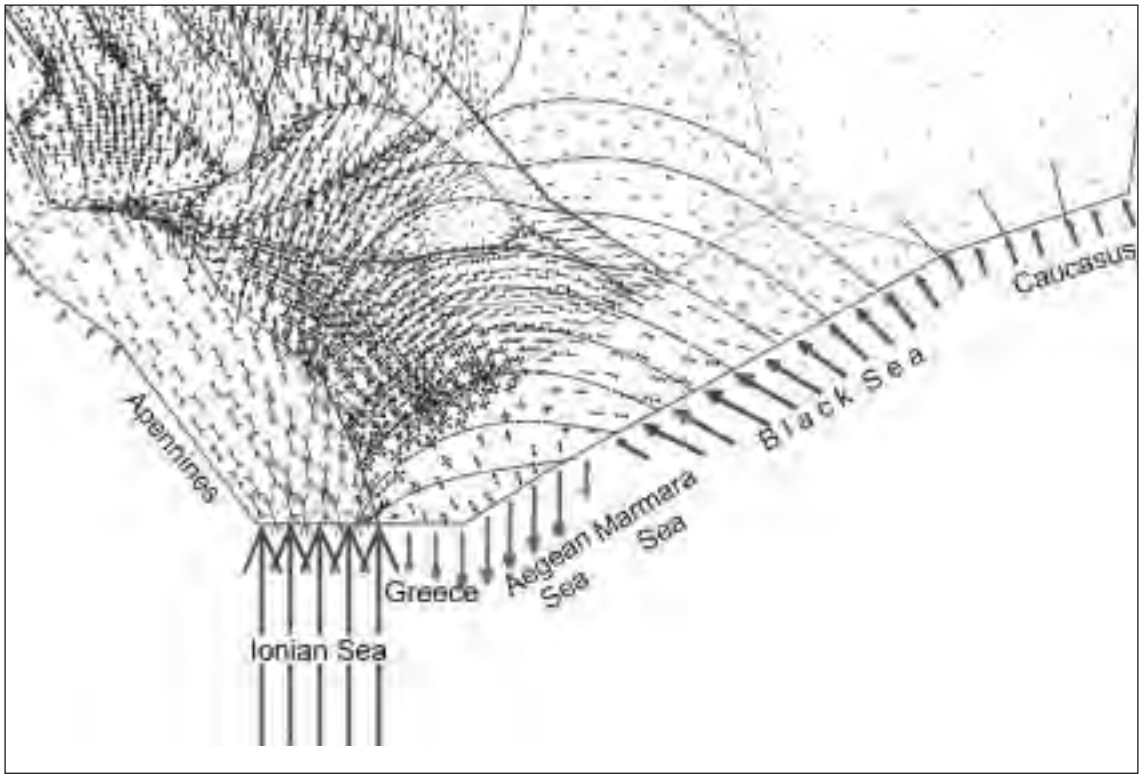

Fig. 2 – Southern part of the model shows modeled stress directions (arrows) with comparison to stress trajectories (dashed lines) based on data. Boundary loads on south segment are marked with arrows, which lengths are proportional to tectonic pressure.

Results of modelling

The results of the modelling characterise the configuration of tectonic forces in the collision zone with Africa and also the tectonic push of the Mid-Atlantic ridge, exerted to the continental margin, normalized to the sea level. The main findings, concerning the southern part of the model are as follow:

- A complex stress pattern in the questioned area can be reproduced, using a relatively narrow range of boundary loads when taking into account stress regimes and fault reactivation constraints.
- The Apennine side of Adria indenter was approximated by a free boundary or loaded with minor compression up to 0.5 x 10^{12} N/m. This implies that push from the Apennines is not an important factor for stress distribution in Central Europe.
- The stress field in Central Europe remains under the dominant influence of Adria push, which is transmitted through the narrow corridor of the Ionian Sea, where tectonic pressure was estimated on 8 x 10^{12} – 9 x 10^{12} N/m. The lack of subduction zone at this short fragment of the collision zone with Africa may be accounted for by enormous stress concentration. Compression exerted at the Pannonian region is caused by a combination of dextral motion along Dinaric suture and the left lateral rotation of Adria. This rotation is a by-product of eccentricity between northward push at Ionian segment and resistance against this push in the Alps.
- Extension in the Aegean segment was evaluated on -2.1 x 10^{12} N/m, with systematic decay in the Greece segment.
- The Marmara Sea segment is transitional from the Aegean extensional segment to the Black Sea compressive segment.
- Obliquity of tectonic push at the Black Sea segment is necessary to balance the model. It is most probably caused by the westward escape of the Anatolian block. For this segment tectonic push changes from 2.4 x 10^{12} N/m in the western end, to 1.0 x 10^{12} N/m in the eastern end. This difference may be explained by stronger rheology and higher efficiency of stress transmission in the western part of the Black Sea than in the eastern one, as postulated by Cloetingh et al. [2003].
- Tectonic push in a range 1.0 x 10^{12} N/m is transmitted from the Caucasus segment to the EEC. The reason for this relatively small push is probably the strain accommodation within still active orogen.
- Ridge push on the NW passive margin of Europe changes in a range 0.95 x 10^{12} - 1.5 x 10^{12} N/m. It is comparable to the magnitude calculated by other authors [Gölke & Coblentz, 1996; Andeweg, 2002], when considering counteraction of continental margin extension in a range of 1.0 x 10^{12} N/m.
- Average differential stresses within mechanically heterogeneous lithosphere, produced by above boundary tectonic forces and topography-related loads were estimated on: 0-10 MPa for the highest orogen chains like Eastern and Southern Carpathians and the Alps, 20-50 MPa for the Pannonian region and 40-70 MPa for southernmost Adria and Dinarides.

REFERENCES

- Andeweg, B., 2002. Cenozoic tectonic evolution of the Iberian Peninsula: causes and effects of changing stress fields. Netherlands Research School of Sedimentary Geology, Amsterdam, publication 20020101.
- Bada, G., Cloetigh, S., Gerner, P., Horváth, F., 1998. Sources of recent tectonic stress in the Pannonian region: inferences from finite element modeling. Geophys. J. Int., 134, 87-101
- Cloetingh, S., Spadini, G., Van Wees, J.D., Beekman, F., 2003. Thermo-mechanical modeling of Black Sea Basin (de)formation. Sediment. Geol. 156, 169-184.
- Coblentz, D.D., R.M. Richardson and M. Sandiford , 1994. On the gravitational potential of the Earth's lithosphere. Tectonics, 13 (1994), pp. 929–945.
- Gerner, P., Bada, G., Dövenyi, P., Müller, B., Oncescu, M., Cloetingh S., and Horváth F., 1999, Recent tectonic stress and crustal deformation in and around the Pannonian Basin: data and models. In: B. Durand, L. Jolivet, F. Horváth and M. Seranne, Editors, The Mediterranean Basins: Tertiary Extension within the Alpine Orogen Geological Society, Special Publication No. 156, pp. 269–294.
- Gölke, M., Coblentz, D., 1996. Origins of the European regional stress field. Tectonophysics, 266, pp. 11–24.
- Grünthal, G., Stromeyer, D., 1992. The recent crustal stress field in central Europe: trajectories and finite element modeling. J. Geophys. Res. 97: 11805–11820.
- Jarosiński M., 1999. Badania współczesnych naprezeń skorupy ziemskiej w glebokich otworach wiertniczych w Polsce metoda analizy struktur zniszczeniowych breakouts. Instrukcje i Metody Badań Geologicznych PIG, z. 56: 1-147.
- Loohuis, J.J.P., Wortel, M.J.R., Meijer, P.T., 2001. A first order stress model for the Eurasian plate with an assessment of the role of the Alpine collision zone, xx in preparation.
- Reinecker, J., Heidbach, O., Mueller, B., 2003. The 2003 release of the World Stress Map (available online at www.world-stress-map.org).

EROSION AND EXHUMATION IN ACCRETIONARY OROGENS: EXPERIMENTAL AND GEOLOGICAL APPROACHES 1-07

E. Konstantinovskaia[1], J. Malavieille[2]

[1] *Geological Institute Russian Academy of Sciences, 7, Pyzhevsky per., 119 017 Moscow, Russia. E-mail: konst@ginras.ru*

[2] *Laboratoire Dynamique de la Lithosphere, UMR 5573, cc 60, Universite Montpellier 2, place E. Bataillon, 34095 Montpellier, cedex 5, France. E-mail: malavie@dstu.univ-montp2.fr*

The role of erosion on exhumation and deformation history of accretionary orogens is studied by experimental and geological approaches. The fault propagation, kinematics and rates of exhumation in an eroded thrust wedge are analysed by analogue modeling, testing different parameters (friction, rheologic layering, sediment input/output ratio). A model coulomb wedge is submitted to an uniform erosion, maintaining a constant slope during shortening. A different way of fault propagation is observed in the eroded thrust wedges with low and high basal friction. The diversity of exhumation mode in the eroded thrust wedges is controlled by the mode of fault propagation. The uplift of material is realized along a series of vertical and sub-vertical thrusts in the middle part of the eroded thrust wedge with low basal friction. The material is exhumed along a bunch of inclined (20-50º) thrusts in the rear of the eroded thrust wedge with high basal friction. The zone of maximum exhumation is generally localized in the middle part of the eroded thrust wedge and migrated toward the backstop with continuous shortening. The vertical exhumation rate increases with time and the later accreted material particles are faster transferred to the main exhumation zone if compare to the early accreted particles. The exhumation is realized two times faster in the wedges with a half of thickness if compare to the full thickness wedges. The total eroded material at the end of convergence constitutes 36-50% of initial model area for the thrust wedges with low basal friction and 20-40% for the thrust wedges with high basal friction. The extent of basal underplating increases with total shortening. The area of basal underplated material constitutes up to 30% and to 40% of the eroded thrust wedge area for the models with low and high basal friction, respectively. Our results are compared to different present-day active and ancient convergent orogens (Himalaya, Taiwan, Southern Alps of New Zealand, Cascadia orogen).

Keywords: thrust wedge, experimental modeling, erosion, exhumation, Himalaya, Taiwan, Southern Alps of New Zealand, Cascadia orogen

UNDERSTANDING AND ANALYZING LITHOSTRATIGRAPHIC VARIABILITY TO FORECAST RESERVOIR POTENTIAL 1-08

M. Perlmutter

Chevron Texaco, Exploration Technology Company, Bellaire, Texas, U.S.A. 77401

Summary

The phase relationships of precession-scale sediment yield cycles and glacioeustatic cycles can cause predictable differences in the marine stratigraphy of the Northern and Southern Hemispheres. Specific differences are dependent on location within each hemisphere, are evident in the variations in lithology, bed thickness and distribution, and can impact how reservoirs are forecast. Stratigraphic variability can be analyzed using lacunarity analysis.

Abstract

At precession-scale (~20 kyr), Northern and Southern Hemisphere insolation cycles are 10,000 years out of phase. Consequently, similar climatic successions in opposite hemisphere, and associated sediment yield cycles can also be 10,000 years out of phase, as well. Prior to the Plio-Pleistocene, the common glacial condition was a unipolar icecap. Under this condition, precession-scale eustasy will

tend to track the insolation cycle of the glaciated hemisphere. The result is that similar climatic successions in opposite hemispheres will have sediment yield cycles with distinctly different phase relationships to glacioeustasy. Such differences would not exist in an ice-free world.

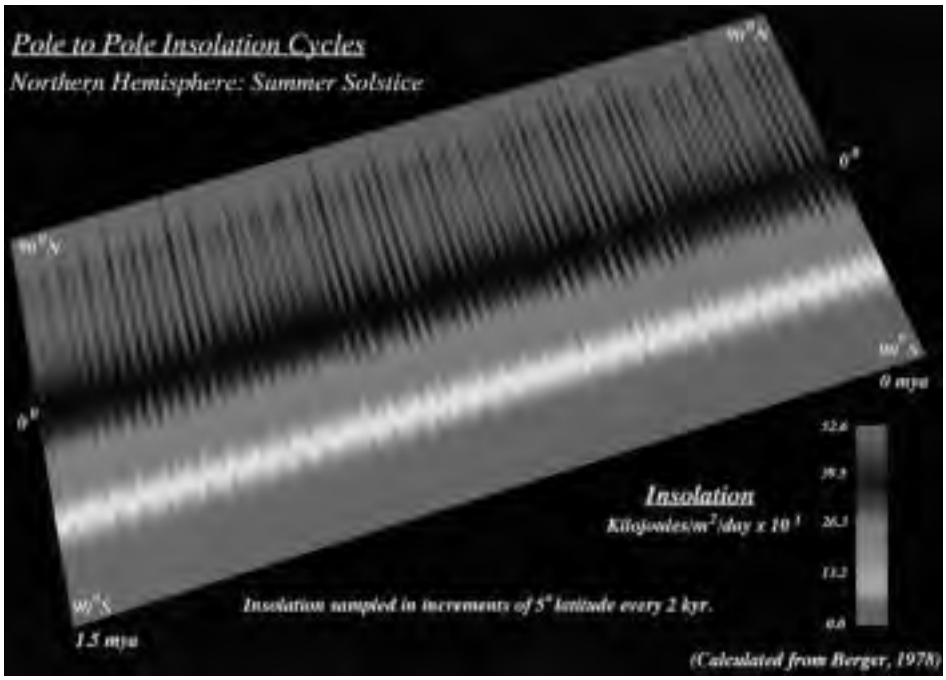

Figure 1. Insolation cycles. The vertical axis is latitude. The horizontal axis is time. Color indicates insolation. The greatest changes in insolation, up to 30%, occur at the highest climate cycle frequency, precession (Perlmutter and Plotnick, 2003).

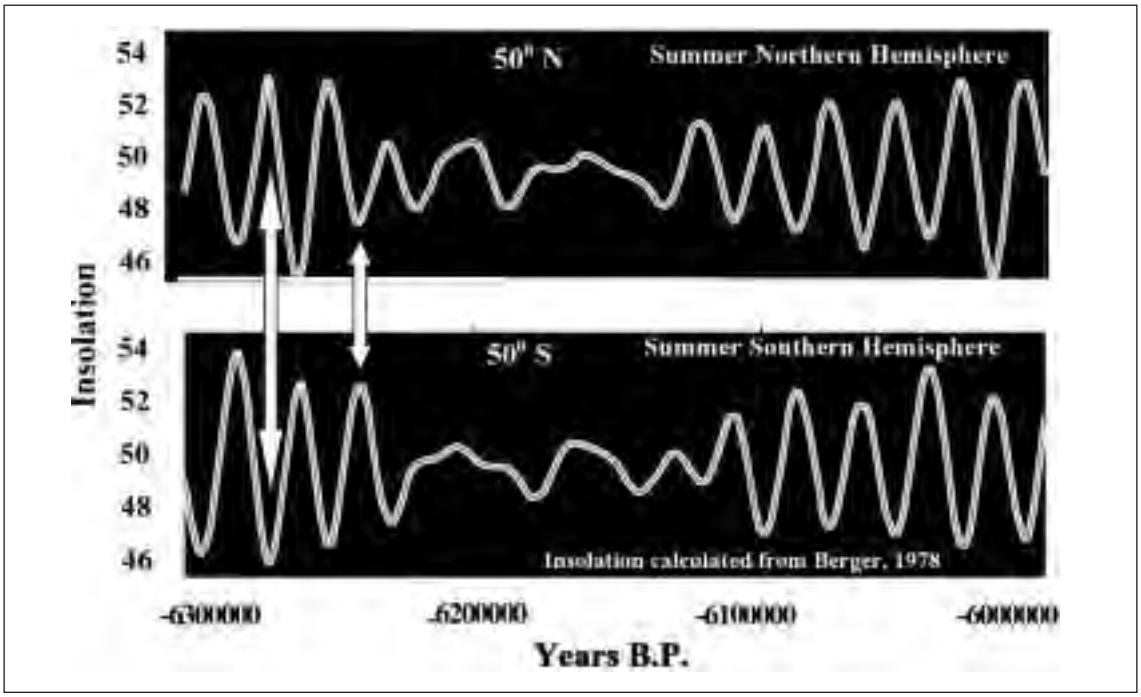

Figure 2. Insolation cycles plotted at 50° N and S showing antipodal behavior at the scale of precession (Perlmutter and Plotnick, 2003 a). Regional climates and associated sediment yields in opposite hemispheres are about 10,000 yrs. out of phase, as well. Prior to the Plio-Pleistocene, only the Southern Hemisphere controlled sea level.

By taking into account a priori the impact of the interaction of sediment yield and sea level, exploration areas that are prone to the development of sand-rich submarine fans can be evaluated and high graded. Understanding the inherent stratigraphic variability of a system will help improve stratigraphic models and interpretation, and reduce the uncertainty associated with exploration analyses.

The distribution, clustering and cyclicity of stratigraphic patterns in both computer models and the real world data can be evaluated using lacunarity. Lacunarity is a multi-scaled statistical measure of translational invariance; the extent to which a pattern differs from location to location, and through time. Lacunarity analysis has been used to examine stratigraphic models designed to display phase relationships of yield and sea level, and the distribution of sand beds determined from SP (Spontaneous Potential) logs from the Taylorsville basin, Virginia and from GR (Gamma Ray) logs in the Gulf of Mexico. This work has indicated that lacunarity can distinguish different distribution patterns of sand and shale intervals, and their cyclicity, within a chronostratigraphic framework.

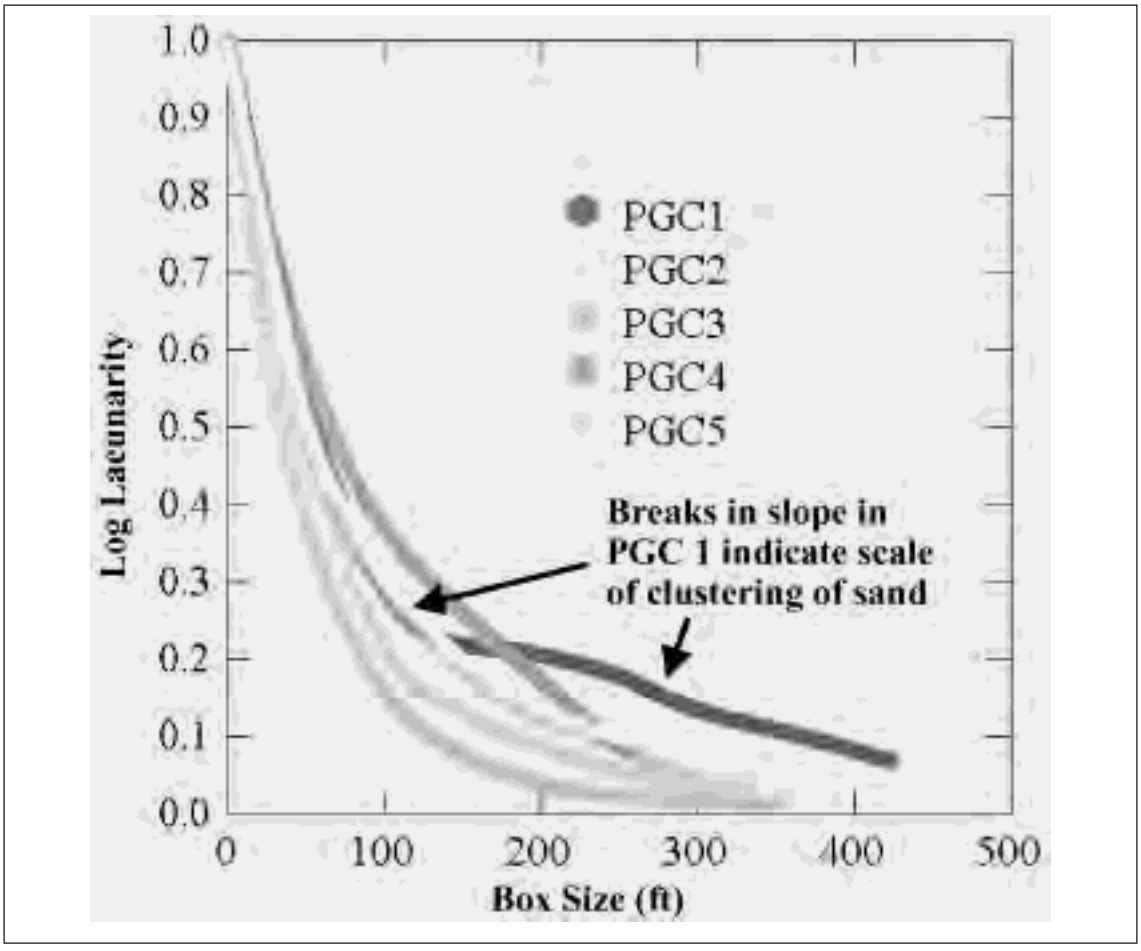

Figure 3. Lacunarity analysis of sand bed distributions in lowstand prograding complexes (PGC) from the Eugene Island area, Gulf of Mexico (Perlmutter and Plotnick, 2003 b). The analysis is from well OCS-8435. The concave shape of the curves for PGC 2 -5 (pre-glaciation) indicate a random distribution of sand beds. The breaks in slope of PGC 1 (post-glaciation) indicate sand beds distribution is non-random and has two scales of clustering.

REFERENCES

- Perlmutter, M.A. R.E. Plotnick, 2003, Predictable Differences in the Marine Stratigraphy of the Northern and Southern Hemisphere and the Impact on Reservoir Distribution, 2002 Proceedings of the Gulf Coast SEPM Annual Meeting, pp. 231- 256.
- Perlmutter, M.A., R.E. Plotnick, 2003, Hemispheric Asymmetry of the Stratigraphic Record: Conceptual Proof of a Unipolar Icecap, B. Cecil (ed.), The Impact of Climate on Stratigraphy, SEPM Spec. Pub. #77, pp. 51-66.

NUMERICAL MODELLING OF DYNAMIC INTERACTIONS BETWEEN EROSION, DEPOSITION AND 3-D (THIN PLATE) DEFORMATION 1-09

G.D.H. Simpson

Geological Institute, ETH Zurich, CH-8092 Switzerland. <guy.simpson@erdw.ethz.ch>

Summary

This work summarises a few results of a new mathematical model developed to investigate interactions between erosion, deposition and dynamic 3-D deformation within fold-belt settings. The model consists of a thin elastic-plastic (von Mises) plate overlying an inviscous substrate. The model can be compressed from the side and responds by the development of folds. The surface topography is advected along with the deforming plate and changes due to fluvial and hillslope sediment transport. This mass redistribution creates loads on the underlying plate that can influence subsequent deformation, erosion and deposition. Results of the model indicate that the complex load distribution related to the 3-D nature of erosion and deposition (including river valleys and ranges) can cause 3-D deformation, even when imposed convergence is purely 2-D. The nature of this deformation and the conditions for its formation are briefly discussed. This study shows that that sediment-routing systems developing in fold-and-thrust belt settings must be viewed as reflecting two-way coupling between surface processes and the deforming substrate and not just in terms of interactions between local base-level variations and the rates of fluvial incision and aggradation.

Abstract text

It is becoming increasingly recognized that surface processes such as erosion and deposition have an important influence on deformation associated with the formation of mountain belts. Nevertheless, much of our understanding regarding how erosion and deposition influence deformation comes from numerically modelling two-dimensional (2-D) vertical sections (e.g., plane strain) through the crust coupled to 1-D eroding surface profiles (e.g., see Beaumont et al., 2000 and references therein). This approach provides information on the spatial distribution of displacements in a vertical plane and estimation of the (mean) surface topography. The 2-D models do not, however, provide any information on how the 3-D deformation field and landscape morphology including river valleys and ridges evolve and interact with one another. Does erosion and deposition continue to have an important influence on deformation in 3-D given that erosion in 3-D is typically highly localized in narrow valleys? Can the 3-D nature of erosion and/or deposition induce 3-D deformation even when regional compression is purely two-dimensional? How are the drainage network, surface topography and location of depo-centers influenced by the 3-D-nature of deformation? These are some of the questions which have motivated the development of the model discussed within this study.

The aim of this extended abstract is to discuss some results of a new model developed to investigate fully dynamic coupling between erosion, deposition and (quasi) 3-D deformation (Figure 1). A more detailed description of the model and results is given by Simpson (2004a, 2004b, 2004c). The mechanical part of the model consists of a thin elastic-plastic plate overlying an inviscous substrate. The plate can be compressed from the side and responds by the dynamic development of folds. The surface topography is advected along with the deforming plate and changes in response to coupled fluvial and hillslope sediment transport. This mass redistribution creates loads on the plate that can influence subsequent deformation. Note that vertical deformation can result from both a flexural-isostatic response to erosion and/or deposition (i.e., passive response) and internal deformation (i.e., dynamic response).

The model developed is intended to be applicable to relatively small scale (<200 km) fold belts developing on the margins of compressive orogens. This scale is small enough such that individual folds can be resolved and also small enough such that the crustal strength (due to elasticity) must be considered finite (i.e., isostacy is not locally compensated). Thus, the influence of surface processes on deformation is not obvious from the outset. The simple one-layer rheological stratification of the model is intended to represent the elasto-plastic upper crust (or some other competent unit) overlying a very weak lower crust (or other weak horizon such as evaporites) which is completely decoupled from the mantle (or underlying units).

As an example of a model application, the remainder of this abstract will be concerned with the issue of whether erosion and deposition can induce three-dimensional deformation, even when the applied convergence is purely two-dimensional. One argument against this possibility is that the high frequency loads related, for example, to erosion of closely-spaced river valleys would be effectively filtered out due to the elastic strength of the crust. Thus, the three-dimensional effects related to surface processes would not be experienced by the deforming crust. Some field studies appear to confirm this view (e.g., Gilchrist et al., 1994; Leonard, 2002). However, a counter argument is that the crust may be deforming plastically in which case even relatively high frequency loads may induce local deformation. This type of behaviour is characteristic of critical wedges where small perturbations to the equilibrium taper (caused, for example, by erosion) induce internal deformation to restore criticality (Davis et al., 1983). Once again, some studies provide evidence in support of this possibility (Norris and Cooper, 1997; Parvis et al., 1997; Simpson, 2004b). The fact that both scenarios are possible reflects the importance of stress levels (and therefore rheological behaviour) in determining how strongly surface processes influence deformation.

As a preliminary investigation of whether erosion and deposition can induce three-dimensional deformation, a number of simple experiments have been performed where relatively small-scale localized erosion is imposed quasi-kinematically. The initial model setup consists of a 100 x 100 km

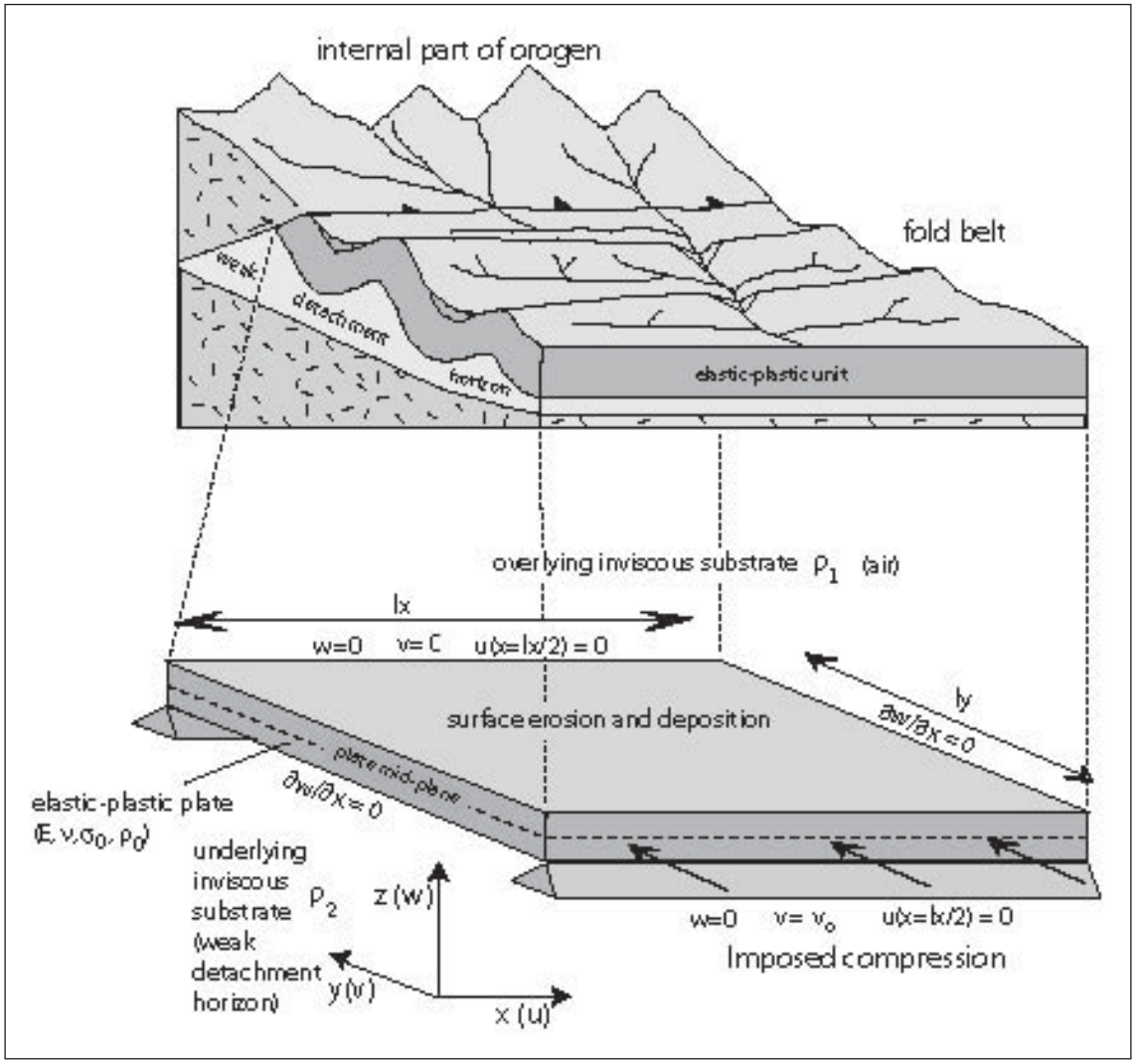

Figure 1. Schematic diagram showing geological setting (a) and corresponding mathematical model (b) described within this study.

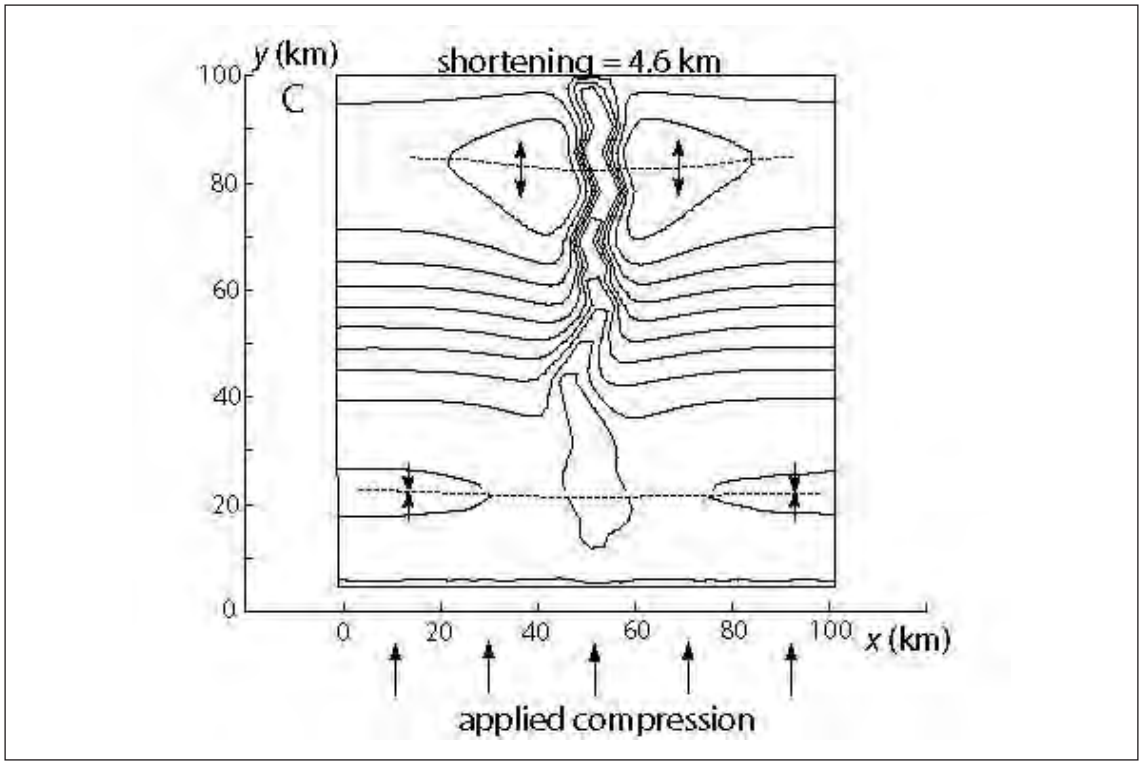

Figure 2. Surface topography resulting from interaction between folding and river incision. Note that the river intersects the axial culmination of an anticline. This associated is due to river incision amplifying deformation.

spatial domain that has a constant regional slope of 1% which is compressed along the lower boundary at a constant rate perpendicular to the regional slope while the upper boundary is blocked in this direction. Lateral boundaries are free to deform. A single localized river is initiated on the sloping surface by specifying a fixed discharge inlet at the approximate center of the upper boundary. The discharge is then free to flow down the surface and incise a river by transporting sediment. Simulations indicate that when the plate buckles, the resulting folds, rather than being cylindrical, are doubly plunging with culminations coinciding with the river (Figure 2). This leads to the remarkable situation whereby the river interests the fold structures at their highest structural and topographic position. Interestingly, this strange association between transverse rivers and fold structures is commonly observed in fold belts but is often ignored. The modeling indicates that these structures form as a result of river-enhanced deformation. It is important to note that deformation in the absence of river incision is characterized by development of cylindrical structures that are initiated after significantly greater amounts of shortening than in the presence of incision. Moreover, if river incision occurs in crust not subject to regional deformation, the response induced by erosion is flexural-isostatic in origin and probably too small to be observed in nature. Thus, whether rivers exert an influence on local deformation depends critically on the timing between river incision and regional deformation. This point may explain why some observations indicate that river incision has had very little influence on deformation (Gilchrist et al., 1994) whereas other observations show that rivers have had an important influence (e.g., Norris and Cooper, 1997; Pavlis et al., 1997).

That localized river incision can have a significant influence on 3-D deformation raises the question of how this effect is manifested in a deforming zone subject to fully 3-D erosion and deposition. Once again, to investigate this problem a number of simulations have been performed. As in the previous example, the initial setup consists of a uniformly sloping ramp which is compressed along the lower boundary perpendicular to the regional slope. However, the surface is now subjected to 3-D erosion and deposition. Results indicate that the ability of surface processes to influence three-dimensional deformation depends on the relative timing between mass transport and deformation and on the

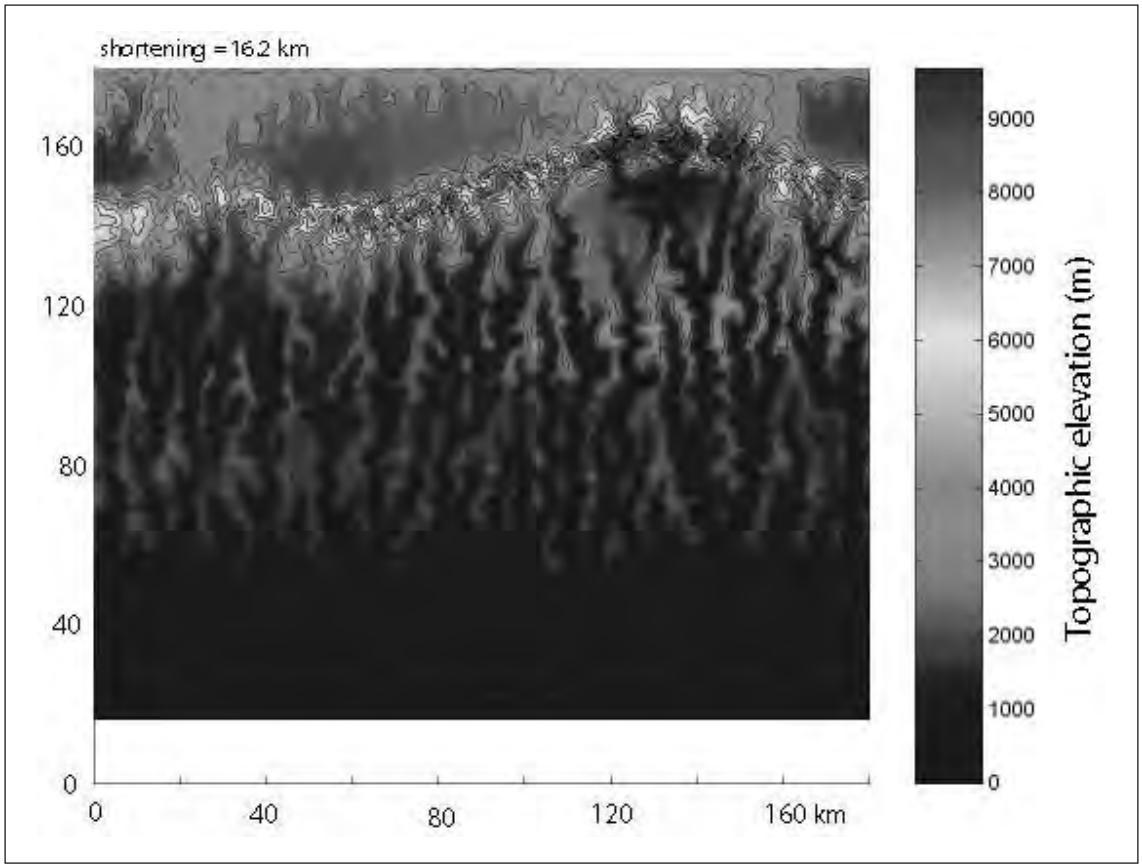

Figure 3. Topography formed as a result of interaction between erosion, deposition and 3-D deformation. Note the close spatial correlation between the largest river catchment and the highest topography which results from erosion-amplified deformation. Note also that only one fold is well developed, which is because efficient erosion tends to localized all deformation on a single structure.

amount of material eroded and/or deposited (which determines the magnitude of the load). When the initial topography is regionally flat, deformation remains cylindrical since loads created by surface processes are mainly imposed after deformation. For intermediate slopes, deformation and surface processes interact in a complex manner giving rive to 3-D en-echelon structures which evolve in a transient manner. When the initial topography is relatively steep, deformation becomes dramatically amplified and localized by erosion. This both stabilizes deformation and leads to interesting features where the largest rivers coincide with the greatest structural amplitude and the highest topography.
The modeling summarized here indicates that under some circumstances one can anticipate major two-way interaction between erosion, deposition and three-dimensional deformation. These interactions are most important when (1) the timing of mass transport coincides with the time when the crust is deforming plastically in response to regional compression, and (2) the drainage pattern is such that mass can be efficiency transported away from regions undergoing tectonic uplift and that the pattern of mass transfer is oblique to deformation. This is best achieved with a transverse drainage pattern. The result of efficient erosion and deposition is to amplify and localize deformation. The fact that these effects occur at relatively small scales reflects the importance of plastic deformation. The origin of these effects lies mainly in the ability of erosion and deposition to decrease the influence of gravity during deformation, by unloading anticlines and loading synclines. In addition, mass redistribution resulting from erosion and deposition that occurs prior to buckling tends to have the same effect as an initial imperfection, which also tends to reduce the amount of loading required to initiate buckling. Effects due to changes in the plate thickness are of secondary importance except for advanced stages of convergence (and erosion) when they may begin to dominate.

Most previous studies that have investigated interactions between surface processes and 3-D deformation have adopted kinematic tectonic models (arguing that explaining the geometry of natural orogens is more important than predicting the internal deformation field) and then use surface process models to determine mass redistribution from which a vertical flexural-isostatic component is determined (e.g., Johnson and Beaumont, 1995; Garcia-Castellanos et al., 1997; Garcia-Castellanos, 2002). However, as the current dynamic model illustrates, although surface processes do induce a vertical flexural component of deformation, by far the greatest influence arises from the way in which surface processes modify the dynamic deformation instabilities (in this case, folding) leading to major changes to pattern of deformation and the overall geometry of the orogen. This point indicates that fully dynamic modeling of three-dimensional interactions between surface processes and deformation is necessary to understand the morphology and evolution of topography and the pattern of deformation itself in natural orogens.

REFERENCES

- Beaumont et al, (2000), in Geomorphology and Global Tectonics, pp. 1-31.
- Davis et al. (1983), J. Geophys. Res., 89, 1153-1172.
- Garcia-Castellanos et al. (1997) , Computers and Geosciences, 23, 993-1003.
- Garcia-Castellanos (2002), Basin Research, 14, 89-104.
- Gilchrist et al. (1994), Geology, v. 22, p. 963–966.
- Johnson and Beaumont (1995), in Stratigraphic Evolution of Foreland Basins, 3-24.
- Leonard (2002), Geology, 30, 595–598.
- Norris and Cooper (1997), Journal of Structural Geology, v. 19, p. 1323–1342.
- Pavlis et al. (1997), Tectonics, v. 16, p. 810–822.
- Simpson (2004a), Journal of Geophysical Research, Earth Surface (in press).
- Simpson (2004b), Geology, (in press).
- Simpson (2004c), Journal of Geophysical Research, Earth Surface (in review).

THE IMPACT OF CURVILINEAR HINGE SECTORS ON GROWTH STRATA PATTERNS IN CONTRACTIONAL FAULT-BEND AND FAULT-PROPAGATION FOLDING

1-10

S. Tavani, F. Storti, F. Salvini

Dipartimento di Scienze Geologiche, Università "Roma Tre", Largo S.L. Murialdo 1, I-00146 Roma, Italy

Summary

In this contribution we illustrate results of analytical models specifically designed for simulating the evolution of curvilinear fault-bend and fault-propagation anticlines in sedimentary environments. Curvilinerar fold geometries were simulated by using circular-hinge sectors between constantly-dipping rock panels. Model evolution highlighted the development of growth stratal geometries, in both the fold kinematics, when sintectonic sedimentation occurred. Our results have a first order impact on the currently available templates of growth strata patterns to infer fault-fold kinematic.

Abstract text

Growth strata geometry have been recognised as a valuable tool for inferring folding mechanism at shallow structural levels (Medwedeff, 1989; Suppe et al., 1992; Poblet et al., 1997; Storti and Poblet, 1997; Hardy and Ford, 1997; Allmendinger, 1998). Syntectonic sediments, in fact, passively record the progressive geometric evolution of their substratum (pre-growth strata). Wedge-like geometries (growth wedges), develop in thrust-related folds involving limb rotation (e.g. Riba, 1976; Hardy and Poblet, 1994). Conversely, folds developed by kink-band migration, are characterised by growth strata patterns consisting of uniformly dipping rock panels (e.g. Suppe et al., 1992). Several works based on kink-style fold geometry, showed that growth wedges are expected in decollement folding (e.g. Storti and Poblet, 1997) and in trishear fault-propagation folding (e.g. Allmendinger, 1998), whereas fault-

bend and fault-propagation folding produce growth strata patterns consisting of flat lying panels and growth triangles (e.g. Suppe et al., 1992; Storti and Poblet, 1997).
We implemented curvilinear geometries in the classical kink-style models of fault-bend and fault-propagation folding, to provide additional kinematic pathways for these folding mechanisms (Fig. 1). Our geometrical solutions produce remarkable differences with respect to the kink-style models, including the development of curvilinear anticlines above staircase fault geometries and the occurrence of limb rotation in fault-bend folding and in fault-propagation folding.

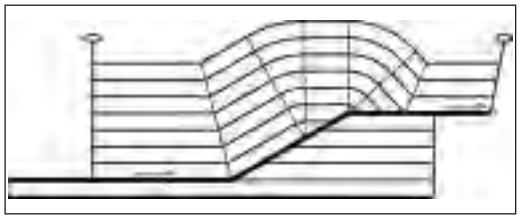

Fig. 1 – Geometry of a curvilinear fault-bend anticline

As a consequence, development of growth wedges is predicted for both folding mechanisms. Application of model results for a growth fault-bend anticline is shown in Figure 2.

The occurrence of growth wedges in constant thickness fault-bend and fault-propagation folding, invalidates the univocal correlation between growth wedges occurrence and décollement folding as the folding mechanism.

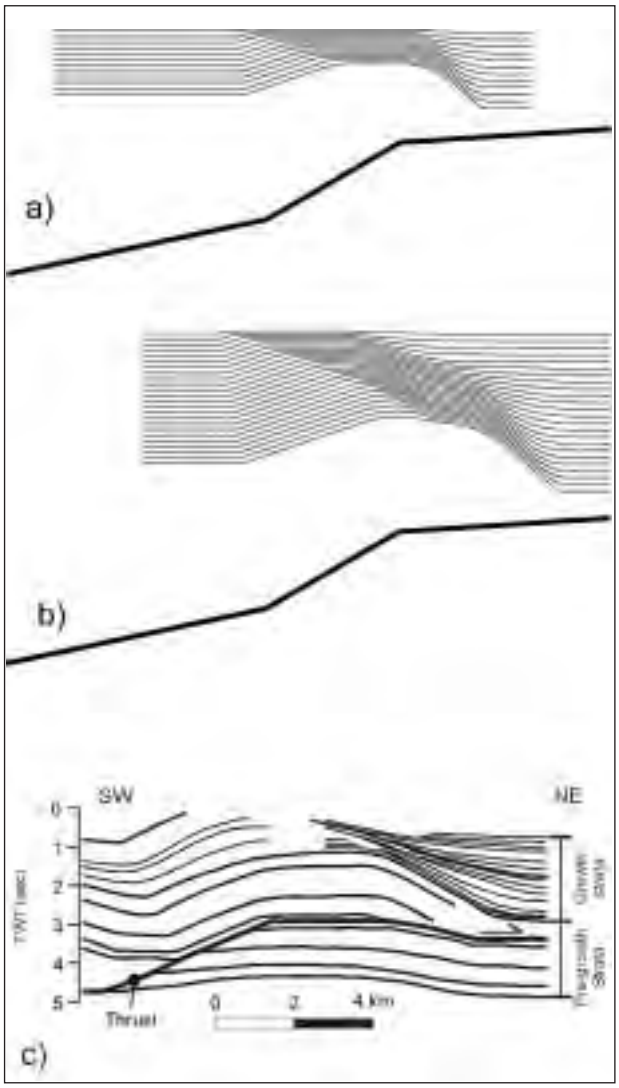

Fig. 2 – Growth strata patterns predicted for a curvilinear fault bend anticline during Step I (a) and Step II (b), and comparison with a natural example (after Medwedeff, 1989)

REFERENCES

- Allmendinger, R.W. (1998), Tectonics, 17, 640-656
- Hardy, S., Ford, M., (1997), Tectonics, 16, 841-854
- Hardy, S., Poblet, J., (1994), Geology, 22, 371-374
- Medwedeff, D., (1989), American Association Petroleum Geology Bulletin, 73, 54-67
- Poblet, J., McClay, K., Storti, F., Munoz, J.A., (1997), Journal of Structural Geology, 19, 369-381
- Riba, O. (1976), Sedimentary Geology, 15, 213-233
- Storti, F., Poblet, J., (1997), Tectonophysics, 282, 353-373.
- Suppe, J., Chou, G.T., Hook, S.C., (1992), In: McClay, K.R. (Ed.), Thrust Tectonics. Chapman and Hall, London, pp. 105-121.

MODELING INTERACTIONS BETWEEN EROSION AND TECTONICS IN THREE-DIMENSIONS – EXAMPLES FROM NEW ZEALAND AND TAIWAN

1-11

P. Upton(*), P.O. Koons(*), K. Mueller(**), Y. Chen(***)

(*) Department of Earth Sciences, University of Maine, Orono ME 04473, USA
(**) Department of Geological Sciences, University of Colorado, Boulder CO 80309, USA
(***) Department of Geology, National Taiwan University, Taipei, Taiwan, R.O.C.

Summary

Distribution of strain within the lithosphere depends on the interplay between far-field velocities and rheological structure and can also be influenced by interactions between surface processes and tectonics. A full treatment of the complexity of these interactions requires consideration of the deformation in three-dimensions. In many cases partitioning of the three velocity components reveal the sensitivity of the lithospheric deformation to variations in boundary conditions and rheological structure. New Zealand and Taiwan are regions of highly three-dimensional active deformation and rapid erosion rates and are ideally suited for predicting the three-dimensional interplay between tectonic driving forces, focused erosion and rheological structure.

Introduction

The sensitivity of the Earth to three-dimensional deformation is evidenced worldwide in the many plate boundaries that are aligned obliquely to the relative plate motion vector responsible for their deformation. Partitioning of strain is observed in subduction zones, collisional belts and extensional systems. Partitioning of the horizontal components of strain as well as how strain is partitioned vertically throughout the lithosphere depends on a mix of far field velocities and rheological structure (e.g., Koons et al., 2002, 2003, Upton et al., 2003). Considerable research over the past decade has focused on the complex interaction between surface processes and shortening in active contractional mountain belts (e.g. Koons, 1990, Willet et al., 1993; Willet, Beaumont et al., 1992,). Evidence suggests that focused erosion strongly influences the position of deformational fronts, the localization of new or reactivated faults and temporal variations in crustal rheology due to perturbation of thermal structure (e.g., Koons et al. 2002, 2003). As erosional signals are also often oblique to the direction of plate motion or to the plate boundary itself, they contribute to the three-dimensionality of the deforming system. Three-dimensional geodynamic modeling enables the rheological structure and erosional forcing of compressive orogens to be assessed using observations of orientations and strain patterns to condition mechanical models. We can then field test predictions derived from these models. New Zealand and Taiwan contain mountain belts that have both been densely instrumented and are ideally suited to studies of this kind. Data required for this modeling includes dense geodetic and seismograph networks, measurements of modern heat flow and high resolution thermochronologic history, river gauging data or dam infilling to define rates of erosion in river networks, and rock strength data.

We present three-dimensional models designed to investigate rheological structure and the interaction of surface processes with active Quaternary strain fields in two regions of active deformation and high erosion rates, New Zealand and Taiwan. We integrate field observations, geophysical data and measured rates to test conceptual models of the development of the two orogens. Our New Zealand models focus on the Alpine Fault and how the thermal structure and rheology have evolved as a result of concentrated erosion along this oblique plate boundary. For Taiwan we consider the effect of higher erosion rates on uplift rates and deformation style of a localized region centered over the leading edge of the orogen. The processes we address in Taiwan are of particular interest because they appear to occur over shorter spatial and temporal scales than have previously been documented.

Modeling technique

Models were developed using the numerical code FLAC^{3D}, in which results are based upon fully three-dimensional solutions for the governing force and velocity equations using a modified Lagrangian technique that allows large strains, spatially and temporally varied erosion and also permits analysis of non-linearities that arise in solution of the equations [ITASCA, Cundall and Board, 1988].

Materials are represented by polyhedral elements within a three-dimensional grid that uses an explicit, time-marching solution scheme and a form of dynamic relaxation. Each element behaves according to a prescribed linear or nonlinear stress/strain law in response to applied forces or boundary restraints. The constitutive relationships used in the models include elastic, non-associated elastic-plastic (Vermeer and de Borst, 1984) and creep or viscous flow laws. Non-associated elastic-plastic rheologies include the Mohr-Coulomb and Von Mises criteria.

New Zealand

The Southern Alps of New Zealand have formed in the last 5 Ma as a result of oblique compression between the Pacific and Australian plates. The Alpine Fault represents the boundary between the two plates and the Alpine Fault region is subjected to extremely high rates of erosion (Whitehouse, 1987). Fig. 1 shows geodynamic models that illustrate how thermal weakening as a result of the high erosion rates controls strain partitioning within the Alpine Fault Zone (Koons et al., 2003). Weakening of the upper crust by thermal thinning forces oblique slip to be concentrated onto a single oblique structure rather than the more typical partitioning observed in other oblique orogens (Fig. 1, Koons et al. 2003). Measured stretching lineations and other indicators of orogenic kinematics closely match those predicted by the geodynamic models (Fig. 1B, Koons et al. 2003).

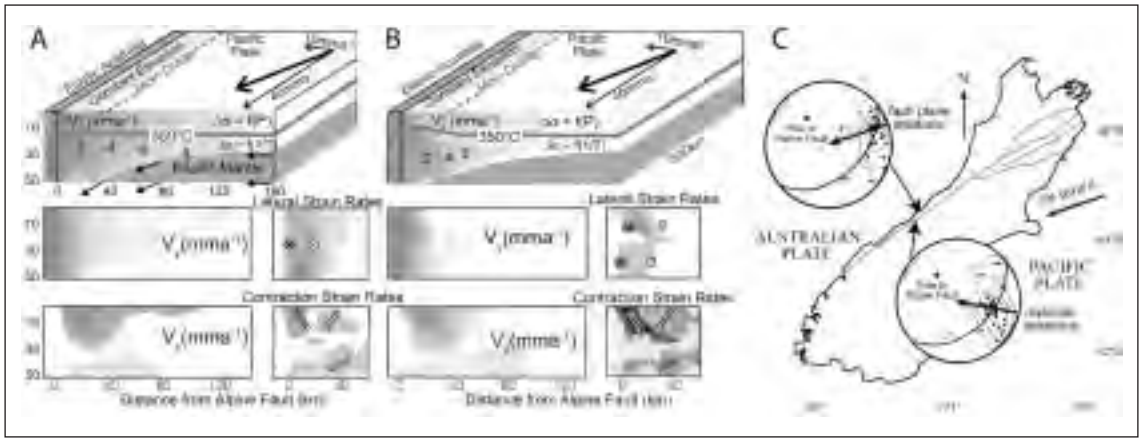

Figure 1: Model of oblique compression for a two-layered crust. A) Rheologic layering is approximately horizontal. Velocity parallel to the plate boundary (Vy) and vertical velocity (Vz) are shown along with contours of lateral strain (dark = high) and convergent strain rates (represented as rotation rates in the x-z plate about the y-axes). Strain partitioning occurs such that the orogen-parallel velocity is taken up on a vertical fault and exhumation occurs along a dipping fault. B) Results for an evolved model that includes thermal weakening associated with rapid exhumation of material along the western side of the orogen. Both lateral and convergent strains are concentrated along a single, east-dipping structure through the upper brittle crust while at depth the two components remain spatially separated. C) South Island. Measurements of fault plane striations in basal gouge and stretching lineations within mylonites are plotted on equal-area stereoplots. Stretching lineations reflect convergent movement at depth along the dipping structure while fault plane striations reflect exhumation and transcurrent movement occurring on the single dipping structure in the upper crust. Modified from Koons et al., (2003).

Taiwan

The Taiwanese orogen has developed as a result of oblique convergence between the Luzon Arc of the Philippine Sea Plate and the Eurasian Plate over the last ~5 Ma. The present day rate of convergence is 82 mm/yr based on recent GPS measurements (Yu et al., 1997). Convergence is accommodated largely within Taiwan as the rate decreases from >50 mm/yr on the East Coast to nearly zero in the Coastal Plain (Yu et al., 1997). Collision of the Luzon Arc initially occurred near the northern end of the Island and the point of collision between the Arc and the passive margin has since migrated southward with time (Suppe, 1984).

Taiwan is characterized by NNE-striking thrust sheets or terranes aligned parallel to the Eurasian passive margin that expose more greatly exhumed rocks towards the core of the orogen. The Hsuehshan Belt and Western Backbone Range expose predominantly unmetamorphosed to mildly

metamorphosed clastic sediments and comprise Taiwan's Slate Belt (Tillman and Byrne, 1995; Fisher et al., 2002). These rocks separate unmetamorphosed rocks of the thin-skinned foothills belt to the west from high-grade rocks of the Tananao complex further east. Pre-Tertiary continental crust of Eurasian affinity has been exhumed on the eastern side of the orogen where it is now exposed in the Eastern Backbone Range (Tillman and Byrne, 1995; Pulver et al., 2002). The Luzon Arc, now sutured to Taiwan and exposed in the Coastal Mountains, acts as a backstop to the wedge. The active deformation front of the western edge of the orogen is defined by non metamorphosed Oligocene to Pliocene passive margin sediments overlain by Pleistocene synorogenic conglomerates in the Western Foothills which have been shortened across a 30-km wide belt of active thrust sheets and fault-related folds (e.g., Suppe, 1976; Suppe, 1980; Hung, 1999). The mechanics of mountain building in the Taiwanese orogen are subject to debate. Two significantly different models are proposed; a detachment model where the mountains are formed above a main detachment zone as an accretionary wedge (e.g., Supp,e 1984, Carena et al., 2002) and a lithospheric model which proposes collision of the two plates down to at least 60 km with extrusion of previously subducted material (e.g., Wu et al., 1997, Lin, 2002).

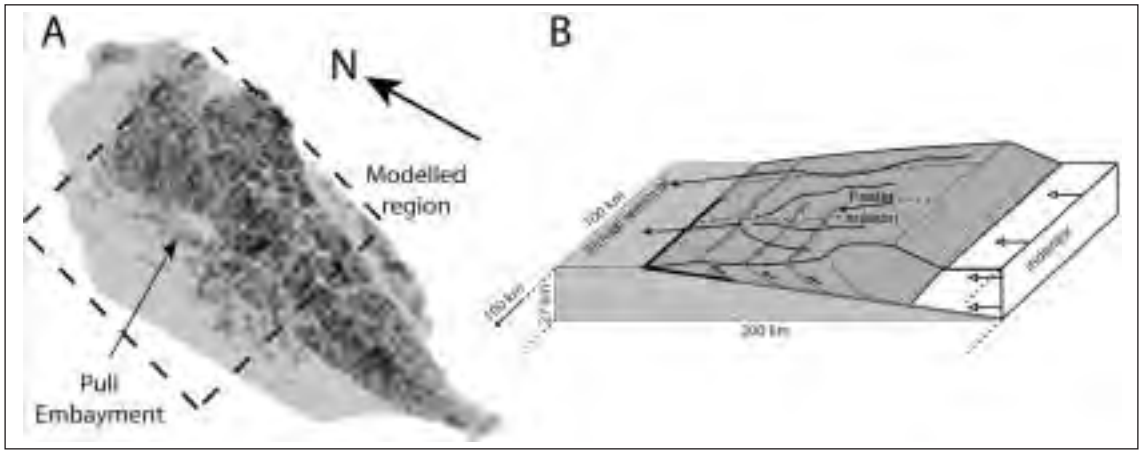

Figure 2: A: Oblique view of the Taiwan mountain belt. The frontal portion of the orogen contains the Puli Embayment, a region that at 1000m average elevation, is ~1500 meters lower than adjacent portions of the belt to the north and south that lie at ~2500 meters. Although the thrust front at the southern edge of the embayment is clearly affected by the Peikang High, a buried Miocene extensional horst (that acts as an indentor in the foreland), the Puli region itself is marked by north to south trending thrusts that extend across the region of lower topography (suggesting the depression is not structural in origin). Note the active frontal thrust sheets in the southwestern part of the Island that limit the location of catchment basins and river networks in the Puli embayment. B: Block model consisting of a wedge of sediment (ϕ = 35°) above a weak dipping décollement (ϕ = 14°), which separates the wedge from the underlying basement material of the Eurasian plate. The sedimentary wedge is bounded to the east by the indenter. Deformation in this model is concentrated along the décollement and within the sedimentary wedge and is a result of an imposed velocity condition. Focused erosion is imposed within the Puli Embayment.

We ran a series of models, based on the detachment model of the Taiwainese orogen, aimed at testing whether enhanced exhumation within a region with dimensions 50 km x 50 km would led to a focusing of uplift and deformation into that region. The model geometry is shown in Fig 2B. Our block model consists of a decollement dipping into the Central Ranges of Taiwan. A wedge of stronger material acts as an backstop. The orogen is modeled as a pressure dependent Mohr-Coulomb material with a friction angle of 35°. The decollement is made considerably weaker with a friction angle of 14°. We varied the rate of exhumation relative to the velocity of incoming material and compared the dynamics of the system with uniform exhumation to those of a system with higher rates of exhumation concentrated in one region.

Our results show a marked response to an increase in the amount of exhumation in a part of the orogen (Fig. 3,4). With uniform exhumation, the fold and thrust belt propagates forward as is common in many thin-skinned compressive belts. Deformation initially occurs next to the indentor, however, as the orogen begins to grow with increasing displacement, the active front of the orogen begins to

deform previously undeformed material of the foreland basin. Some displacement is still occurring on faults in the hinterland of the belt, however the highest strain rates occur in the foreland region. If higher erosion rates are simulated at scales similar to the Puli Embayment, a response is quickly observed. Both the vertical and horizontal velocity components abruptly step hindward to a location beneath the region of low elevation, which results in strain being concentrated in the region undergoing the highest amount of exhumation.

Summary

The nature of deformation patterns through the lithosphere reflect the influence of far- field velocities and rheological structure. In actively deforming regions, far-field velocities can be measured but the rheological profile of the lithosphere is more difficult to determine. Geodynamic modeling allows us to test models of rheological structure and its influence of lithospheric deformation. In New Zealand, we show that high erosion rates led to temporal variation in crustal rheology as a result of perturbation of thermal structure, resulting in a change in the nature of partitioning of oblique motion with time. We also ran a series of models aimed at testing whether enhanced exhumation in a region similar to the Puli Embayment in Taiwan could lead to focusing of uplift and deformation into that region. Our results showed that with uniform exhumation, the fold and thrust belt propagates forward with the highest strain rates occurring in the foreland region. Where higher erosion rates are simulated, both vertical and horizontal velocity components abruptly step hindward, resulting in strain being concentrated in the region of highest exhumation.

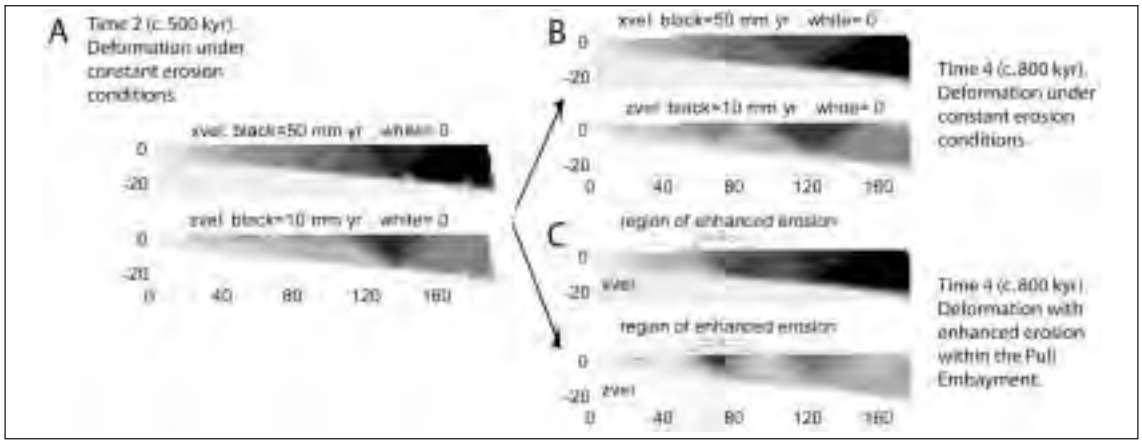

Figure 3: A: After c. 250 kyr of deformation, the horizontal velocity component has moved into the foreland while the majority of the vertical component of deformation remains focused around the Central Ranges. A small amount of vertical displacement is occurring outboard. B: After c. 880 kyr of deformation. With continuing deformation the outboard wedge increases in overall elevation. In the model with focused erosion, deformation increasingly moves into the region of the Puli Embayment.

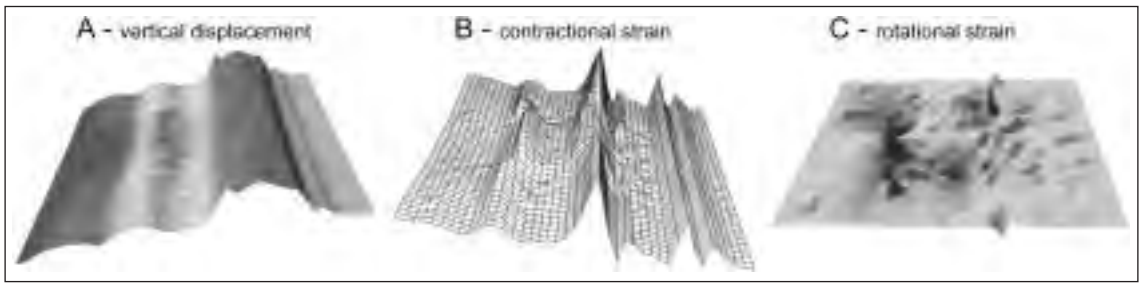

Figure 4: Model with focused erosion within the Puli Embayment. A: block diagram showing the vertical displacement over the whole model. B: Contractional strain (calculated from displacements). The pattern of contractional strain is perturbed by increased erosion, concentrating this component of strain at the western edge of the region subjected to focused erosion.. C: Rotational strain, sinistral is negative, dextral is positive. Rotational strain occurs on the edges of the region of higher erosion. Transfer strike-slip faulting would be expected in these regions.

REFERENCES

- Beaumont et al. (1992), in Thrust Tectonics, p. 1-18
- Carena et al. (2002), Geology, 30, 935-938
- Cundall and Board (1988), Proc of the 6th Int Conf on Num Methods in Geomechanics, vol. 2, 101-108
- Fisher et al. (2002), GSA Special Paper 358, 93-106
- Hung et al. (1999), Terrestrial, Atmospheric, and Oceanic Sciences, 10 (3), 543-568
- Koons (1990), Geology, 18, 679-682
- Koons et al. (2002), American Journal of Science, 302, 749-773
- Koons et al. (2003), Geology, 31, 3-6
- Lin (2002), Terra Nova, 14, 281-287
- Pulver et al (2002), GSA Special Paper 358, p. 107-120
- Suppe (1980), Petroleum Geology of Taiwan, 17, 1-16
- Suppe (1984), Memoir of the Geological Society of China 6, 21-33
- Tillman and Byrne (1995), Tectonics, 14, 322-341
- Upton et al. (2003), Tectonics, 22, 1068, doi:10.1029/2002 TC 001431
- Vermeer and de Borst (1984), Heron, 29, 1-64
- Whitehouse (1987), in International geomorphology, p. 897-924
- Willett et al. (1993), Geology, v. 21, 371-374
- Wu et al. (1997), Tectonophysics, 274, 191-220
- Yu eta al. (1997), Tectonophysics, 274, 41-59

Session 2

OROGENESIS

WHAT CONTROLS THE MODES OF TECTONIC SHORTENING IN CENTRAL ANDES? 2-01

A. Babeyko, S. Sobolev

GeoForschungsZentrum-Potsdam – 14473 POTSDAM Germany

Summary

The two main segments of the central Andean plateau, Altiplano and Puna, demonstrate different styles and magnitude of tectonic shortening. We show that different shortening modes - pure and simple shear accompanied by thin or thick skin tectonics - might be controlled by the two parameters: (i) strength of the foreland uppermost crust and (ii) thermal state of the Brazilian shield which indents the plateau from the east.

Introduction

The Altiplano-Puna plateau of the Central Andes is the second greatest plateau in the world after Tibet with average elevation of about 4 km and area of more than 500,000 km^2 (Isacks, 1988). The plateau is a product of crustal shortening of the weak western edge of South America between the subducting Nasca plate at the west and indenting Brazilian shield at the east (for reviews see, e.g., Isacks, 1988; Allmendinger et al., 1997; Lamb et al., 1997).

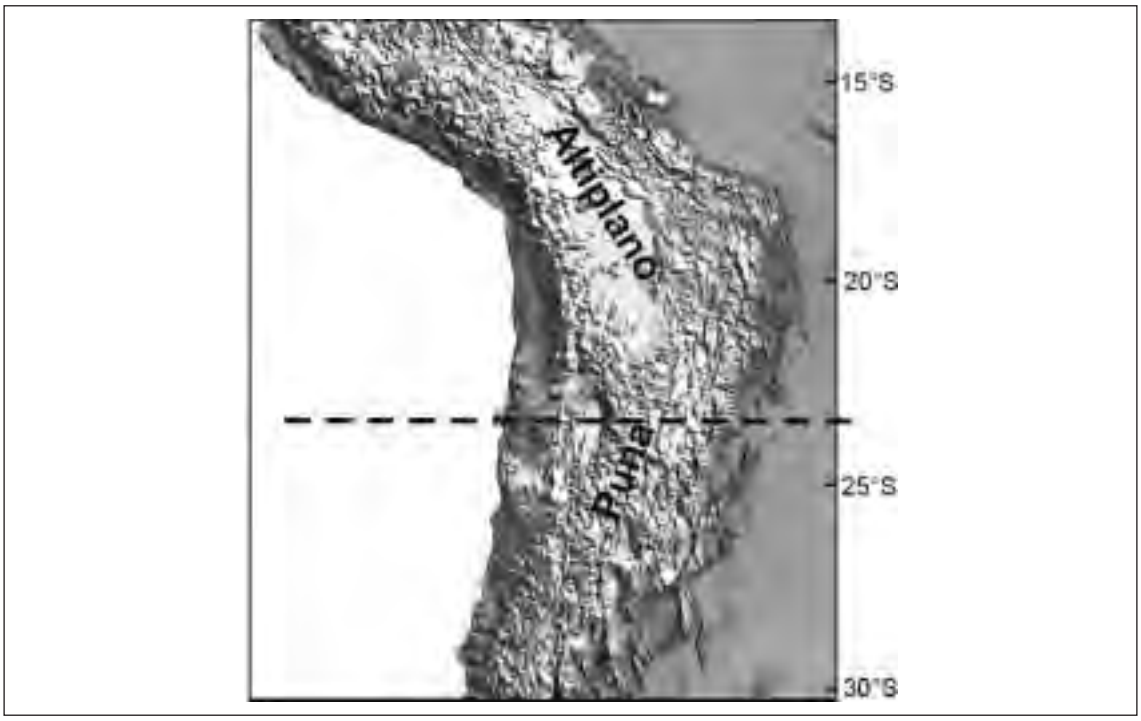

Figure 1. Relief map of the central Andean plateaus. Dashed line divides the northern and southern segments, which differ in the style and magnitude of shortening.

Along the strike, the Central Andean plateau could be subdivided into two distinct segments with different magnitude and style of shortening (Figure 1). The boundary between these segments lies at 23-24°S. North of 23°S, in the Altiplano segment, tectonic shortening occurred in two different stages with only limited time overlap in between. According to Allmendinger and Gubbels (1996), the earlier, pure-shear stage of shortening, was followed since late Miocene by a simple-shear stage (in pure-shear, upper and lower crustal shortening occur in the same vertical column of rocks, instead, in simple-shear, the loci of upper and lower crustal deformation are separated laterally). The latter stage is characterized by migration of surface deformation into the foreland by formation of a broad thin-

skinned Subandean thrust belt and simultaneous increase of the plateau uplift rate (Gregory-Wodzicki, 1996).
In contrast to the Altiplano, the Puna lacks a thin-skinned foreland thrust belt. Instead, foreland structures, which belong to the Santa Barbara System, demonstrate a thick-skin tectonics with much less overall shortening. Comparing the Altiplano and Puna, Allmendinger and Gubbels (1996) noted that the most obvious reason for the observed differences in shortening style from north to south is the presence of a thick layer of Paleozoic sediments in Bolivia and its virtual absence farther south. In addition, some geophysical data (Whitman et al. 1996) imply that the leading part of the Brazilian shield south of 24°S might be considerably hotter and, hence, rheologically weaker than its northern part.
The above remarks give an idea, that the two important parameters, namely, the strength of the foreland uppermost crust as well as the thermal state of the indenting shield, might control the general shortening mode of the system.

Model

As a numerical tool we use 2-D parallel thermo-mechanical finite element code. Our code combines explicit lagrangian finite element FLAC algorithm (Polyakov et al., 1993; Cundall and Board, 1988) with marker technique of particle-in-cell method (Sulsky et al., 1995; Moresi et al., 2001). Markers track not only material properties but also full strain and stress tensors. This minimizes numerical diffusion related to remeshing. The explicit lagrangian time-marching algorithm allows for strongly non-linear rheologies. We employ both Maxwell visco-elastic rheology with stress-dependent viscosity as well as Mohr-Coloumb elasto-plasticity with softening. For more details and benchmarking see Babeyko et al. (2002).

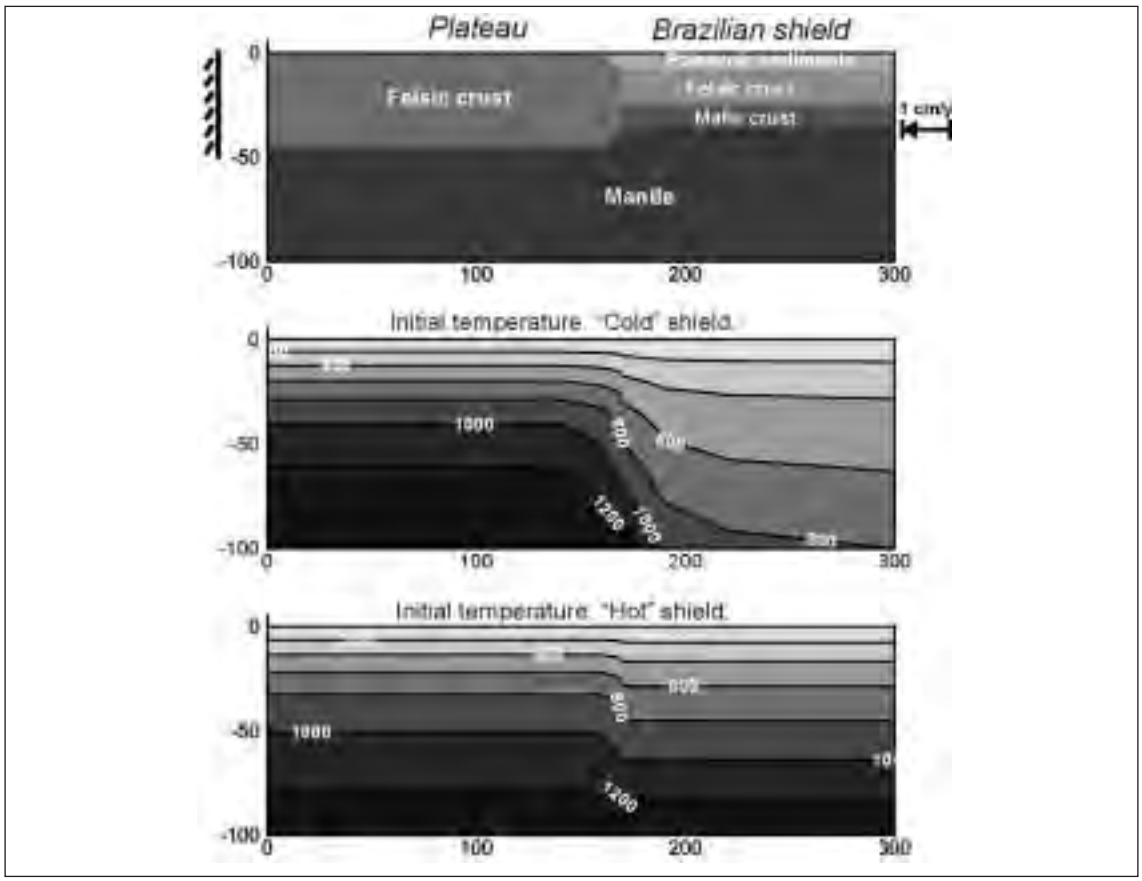

Figure 2. Model setup. Shown are initial geometry and the two contrasting temperature distributions corresponding to "cold" and "hot" indenting shield.

The model setup is presented in Figure 2. Since we do not intend to model the whole cenozoic history of the orogen, but instead, only the late Miocene transition from pure- into simple-shear mode, our starting model has already pre-thickened crust under the plateau (left side of the model). The crust of the colder Brazilian shield has normal thickness and contains the 8km-thick sedimentary layer. Two contrasting temperature setups reflect the cases of a "cold" (stiffer) and a "hot" (weaker) indenting shield.

Creep law parameters for the felsic crust and sedimentary layer are as for the wet quartzite by Gleason and Tullis (1995), for the mafic crust – as for Pikwitonei granulite by Wilks and Carter (1990), and for the mantle peridotite – as for dry olivine by Hirth and Kohlstedt (1996). Initial cohesion and friction angle are 20 MPa and 30º, respectively. All the layers are subjected to plastic and viscous softening. As a normal softening we employ ten-folds decrease of the friction angle (or viscosity) as accumulated strain increases from 50 to 150%. In addition, the foreland sediments may be initially weak (cohesion down to 1 MPa, friction angle down to 3º) or experience much more aggressive softening (10-times friction angle drop already at 2% strain). These cases are referred below as cases with "weak sediments" in opposite to models with "strong sediments", which imply no special softening in the sedimentary layer.

The whole system is driven by constant shortening of 1 cm/year applied to the right side of the model box. Left side is fixed in its upper 60 km. Below that depth material is free to flow out of the box. Lower side of the model box is also opened. These boundary conditions simulate east-west indenting of the thermally activated plateau lithosphere by the colder Brazilian shield.

Results

In general, results of all the model runs could be classified in terms of the three end-member modes presented on Figure 3. In the case of the cold shield and strong sediments (Fig. 3a) the system clearly demonstrates pure-shear behavior. The plateau, rheologically the weakest part of the system because of the initial thermal softening, is being shortened more or less homogeneously. No deformation takes place on the indenting shield.

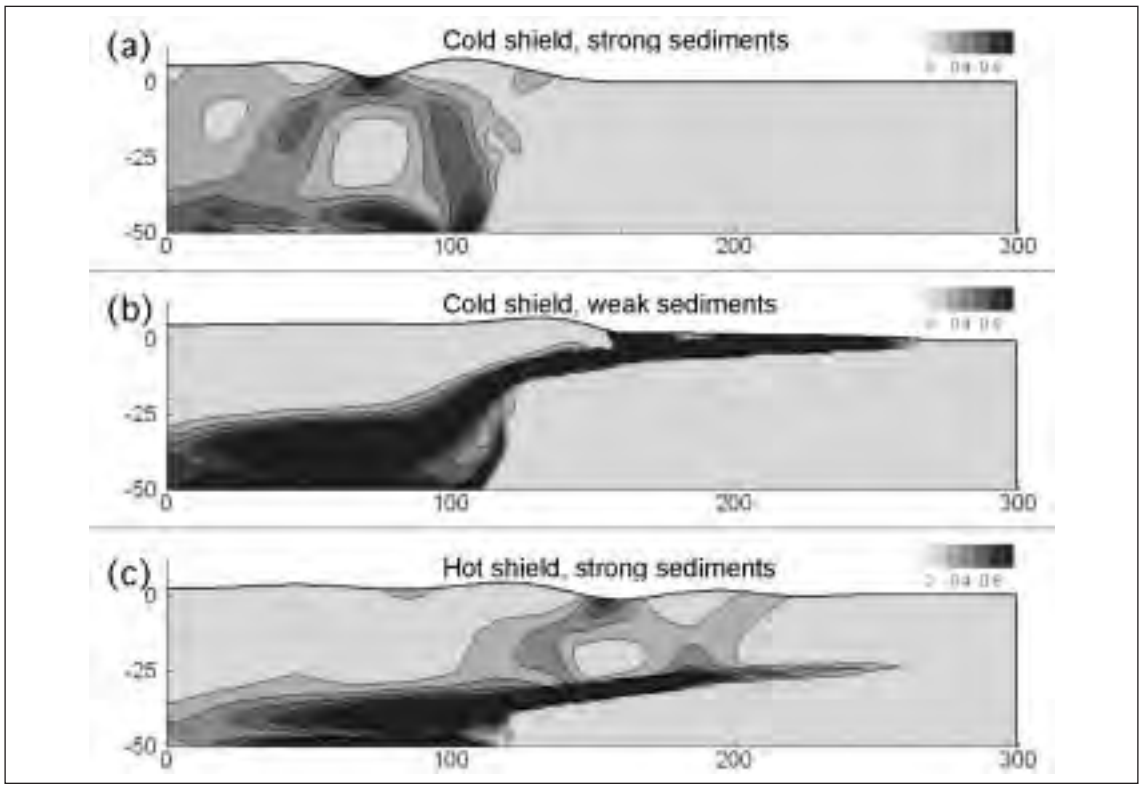

Figure 3. Accumulated strain after 50-80 km of shortening for the three end-member modes.

In contrast, the model with very weak sediments on the cold shield (Fig. 3b) demonstrates prominent simple-shear mode of shortening. Here cohesion in the sedimentary layer was set to 1 MPa and friction angle to 3 degrees. Shield underthrusting is accompanied by rapidly east-propagating thin-skin thrust zone. Shallow dipping decollement located at 8 to 12-14 km depth is in good agreement with observations (Allmendinger and Gubbels, 1996).

The third end-member corresponds to the strong sedimentary layer and hot shield (Fig. 3c). Here foreland deformation could be characterized as a thick-skin with deep decollement at about 25 km (Puna foreland). Note, that the foreland deforms despite of absence of weak sedimentary layer – the crust of the hot shield is weak enough by itself.

These three models are the end-member models corresponding to boundary values of the input parameters. Of course, there are a lot of intermediate scenarios demonstrating interplay and superposition of the pure- and simple-shear modes. Which mode takes over, depends on the strength of the sedimentary layer and, to a less extent, on the thermal weakness of the shield.

Our modelling supports the idea of Allmendinger and Gubbels (1996) that the thick layer of Paleozoic sediments at the Bolivian foreland might be responsible for simple-shear mode of shortening north of 23°S. In order to switch the system from pure- into simple-shear mode (which took place in Altiplano in late Miocene), the uppermost crust of the foreland should become considerably weaker than the neighbour crust of the plateau. Modelling shows that the effective friction angle in sediments must drop below 10 degrees, i.e., more that 3 times relative to its normal value. However, the question - what was the physical nature of the weakening remains open. At least we may consider two hypotheses. The first idea was suggested by Cobbold and Castro (1997). They argued that rapid hydrocarbon generation leads to pore fluid pressure increase, which, in turns, reduces frictional resistance to deformation. Another triggering event might be the uplift of the Eastern Cordillera and establishment of the topographic barrier, which changed the local climate into less arid (O. Oncken, pers. communication). Increased precipitation rate at the eastern flanks of the plateau combined with the absolute plateau uplift might produce a pore pressure wave towards the foreland.

South of 24°S, in Puna, absence of weak sediments on the foreland precludes shallow shield underthrusting and formation of a wide foreland trust belt. However, the observed deformation does not correspond to the pure-shear end-member as well. The foreland of the Puna is thick-skinned deformed – a pattern, similar to what is shown on Figure 3c for the case of the hot shield. Thus, our modelling supports the idea that the Brazilian shield in Puna is probably hotter than in Altiplano (Whitman et al., 1996, based on observations of the seismic Q-factor).

REFERENCES

- Allmendinger and Gubbels (1996), Tectonophysics, 259, 1-13.
- Allmendinger et al. (1997), Annu. Rev. Earth Planet. Sci., 25, 139-174.
- Babeyko et al. (2002), Earth. Planet. Sci. Lett., 199, 373-388.
- Cobbold and Castro (1997), VI Simposio Bolivariano, Resumenes, Asoc. Colomb. Geol. Geofis. Petrol., Bogota, p. 9.
- Cundall and Board (1988), In: 6th Interna-tional Conference in Numerical Methods in Geomechanics (ed. Swoboda, G.), A. A. Balkema, Brookfield, Vt., 2101-2108.
- Gleason and Tullis (1995), Tectonophysics, 247, 1-23.
- Gregory-Wodzicki (2000), Geol. Soc. Amer. Bulletin, 112, 1091-1105.
- Hirth and Kohlstedt (1996), Earth Planet. Sci. Lett., 144, 93-108.
- Isacks (1988), J. Geophys. Res., 93, 3211-3231.
- Lamb et al. (1997), In: Orogeny Through Time (eds. Burg J.-P. and Ford M.), Geol. Soc. Spec. Publ., 121, 237–264.
- Moresi et al. (2001), In: Proceedings of the Fifth International Workshop on Bifurcation and Localization in Geomechanics (eds. Mühlhaus H. et al.), Balkema, Rotterdam, ISBN 90265 18234, 345–355.
- Poliakov et al. (1993), in: Flow and Creep in the Solar System: Observations, Modelling and Theory (eds. Stone D.B. and Runcorn S.K.), Kluwer Academic Publishers, 175-195.
- Sulsky et al. (1995), Comput. Phys. Commun., 87, 236–252.
- Whitman et al. (1996), Tectonophysics, 259, 29-40.
- Wilks and Carter (1990), Tectonophysics, 182, 57-77.

COMBINING TECTONIC SHORTENING AND SURFACE EROSION 2-02

A. Babeyko, T. Vietor, S. Sobolev
GeoForschungsZentrum-Potsdam – 14473 POTSDAM Germany

Summary

In a series of numerical experiments we show how shortening tectonics and erosion may interplay at plateau margins. Surface erosion strongly affects structural style and localization of deformation. At low erosion rates deformation pattern is controlled by the strength of the foreland uppermost crust. Strong foreland "locks" the deformation inside the plateau. In contrast, soft foreland sediments switch the deformation into the external parts of the orogen and promote the formation of a wide foreland thrust belt. High fluvial erosion rates tend to localize the shortening along single, steep thrust at the base of the plateau margin. Accomodation of the tectonic shortening by this single fault might be very effective, especially in the case of strong foreland.

Introduction

Erosion rates and exhumation depth differ strongly along the strike of the Andean Orogen. In the semi-arid regions south of the Santa Cruz elbow not more than less than 5 km of rock have been removed in the Eastern Cordillera since 30 Ma (Ege, 2004). In contrast, along the northeastern humid flank of the Eastern Cordillera in the La Paz area up to 8 km of overburden have been removed since about 10 Ma (Benjamin, 1986, Masek et al., 1994). Both areas show significant difference in structural style, for example the Subandean is a lot wider in the dryer southern region than in the northern one. Even stronger precipitation and deeper exhumation with higher rates are observed in the Himalayas that border the Tibet plateau. Here, exhumation of mid-crustal rocks at the plateau edge has started in the lower Miocene (White et al. 2002). In this preliminary study we test end-member models and point out some similarities with the Andean and Tibetan plateau flanks.

Model

As a numerical tool we use 2D parallel thermo-mechanical finite element code. Our code combines the explicit lagrangian finite element FLAC algorithm (Polyakov et al., 1993; Cundall and Board, 1988) with the marker technique of the particle-in-cell method (Sulsky et al., 1995; Moresi et al., 2001). Markers track not only material properties but also full strain and stress tensors. This minimizes numerical diffusion related to remeshing. The explicit lagrangian time-marching algorithm allows for strongly non-linear rheologies. We employ both Maxwell visco-elastic rheology with stress-dependent viscosity as well as Mohr-Coloumb elasto-plasticity with softening. For more details and benchmarking see Babeyko et al. (2002).

The starting configuration includes a plateau, composed of felsic, pre-heated and pre-thickened crust, and a colder, and hence, stiffer foreland composed of three crustal layers: sediments, a felsic layer, and a mafic layer (Figure 1). Creep law parameters for the felsic crust and sedimentary layer are as for the wet quartzite by Gleason and Tullis (1995), for the mafic crust – as for Pikwitonei granulite by Wilks and Carter (1990), and for the mantle peridotite – as for dry olivine by Hirth and Kohlstedt (1996). Cohesion and friction angle are 20 MPa and 30º, respectively. In some models, the sedimentary sequence on the foreland is subjected to very intense plastic softening (drop of the internal friction angle ten-times at 2% of plastic strain). These cases are referred below as cases with "weak sediments" in opposite to models with "strong sediments", which imply no special softening in the sedimentary layer. To account for the viscous softening in dislocation creep, viscosity is decreased ten times as strain increases from 50% to 150%.

Kinematic boundary conditions that push the foreland towards the plateau at 1cm/yr drive the experiments.

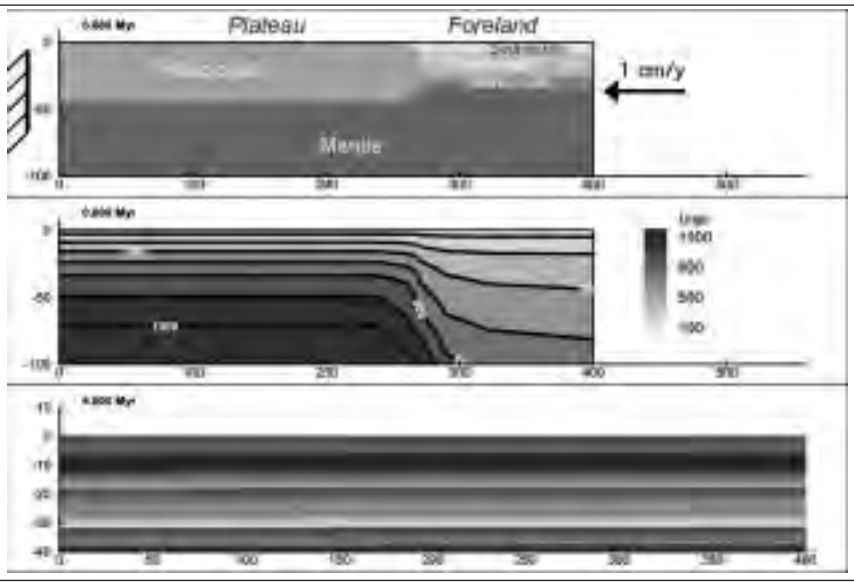

Figure 1. Model setup. Shown are initial geometry, temperature as well as initial distribution of layered material markers for the upper 40 km of the model. Later on, these marker layers will illustrate deformation pattern and efficiency of erosion.

Erosion is driven in two different ways by the local slope (Willett, 1999).

(1) An algorithm that simulates fluvial erosion calculates the erosion rate by:
$dh/dt = K_f * dy/dx * |x-x_r|$
here dy/dx is local slope, |x-xr| - absolute distance from the drainage divide, K_f - erosion coefficient. We employ two values of the K_f: 10^{-13} referenced as "high" and 10^{-12} referenced as "low".

(2) Landsliding erosion rates are:
$dh/dt = K_l * d^2y/dx^2$
K_l also takes two values: 10^{-5} referenced as "high" and 10^{-6} as "low".

Results

As a reference model we use the case with low overall erosion and strong sediments. Figure 2 shows the result of the experiment after 100 km of shortening. The initially thermally weakened plateau region localizes the deformation. Exhumation is very low and the plateau thickens throughout the entire test.

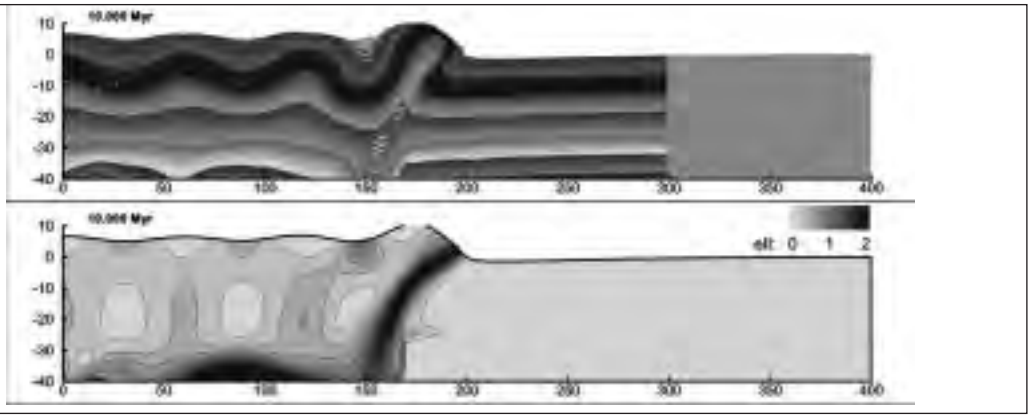

Figure 2. Case with low overall erosion and strong foreland sediments. Shown are the distortion of initial marker field, which illustrates erosion efficiency, and the second invariant of strain tensor. Note the vertical exaggeration that gives the thrust zone a steeper appearance.

Switching on both erosion mechanisms leads to an extremely deep exhumation (Figure 3). Deformation becomes effectively localized on a single shear zone. The plateau is not thickened in this experiment, which illustrates the high efficiency of the exhumation.

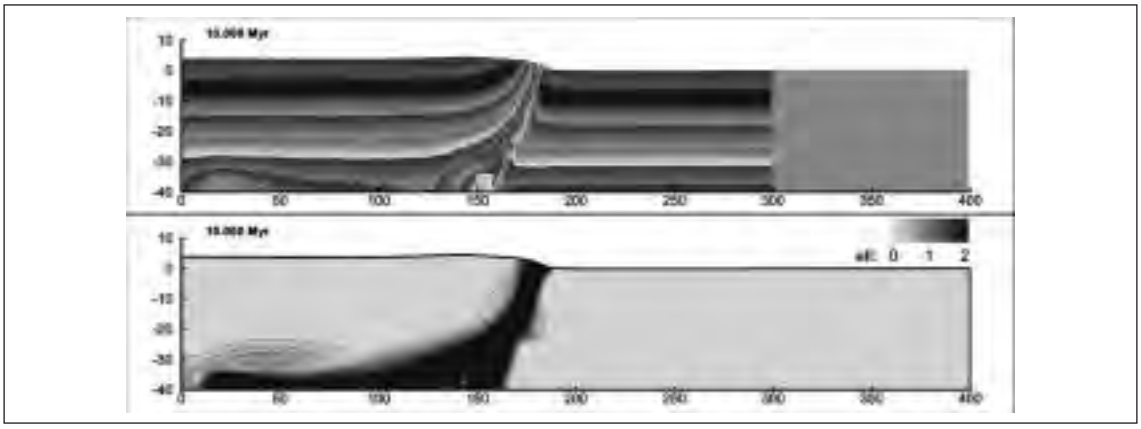

Figure 3. Fluvial erosion – high, landsliding erosions – high, sediments – strong.

In the next run we switch-off the effect of fluvial erosion (Figure 4). The landsliding unloads the hanging walls of the thrusts at the steepest surface slope. The steepest landscape always appears near the top of the plateau rim; hence the unloading favors thrusting towards the plateau.

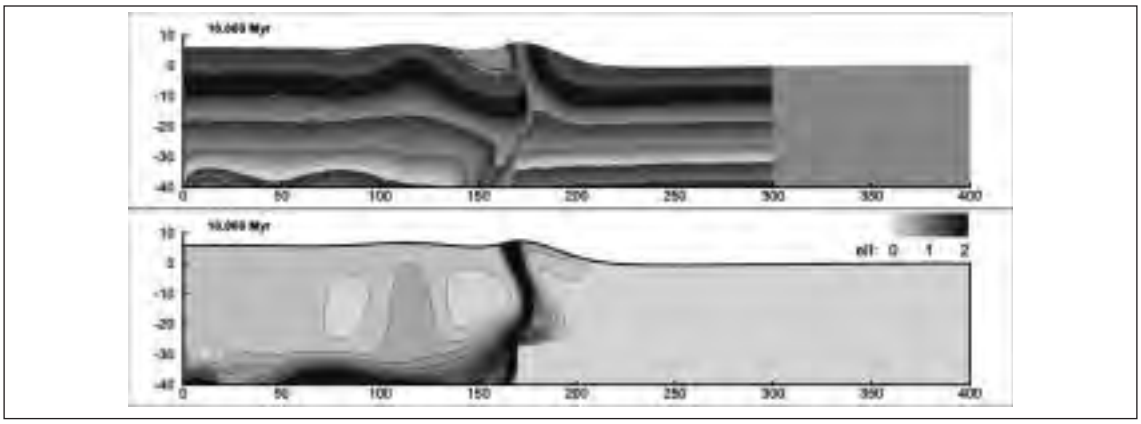

Figure 4. Fluvial erosion – low, landsliding erosions – high, sediments – strong.

The introduction of weak foreland sediments (Figure 5) enables a long low-angle overthrust, which is additionally favored by exhumation of its hanging wall, which unloads the thrust.

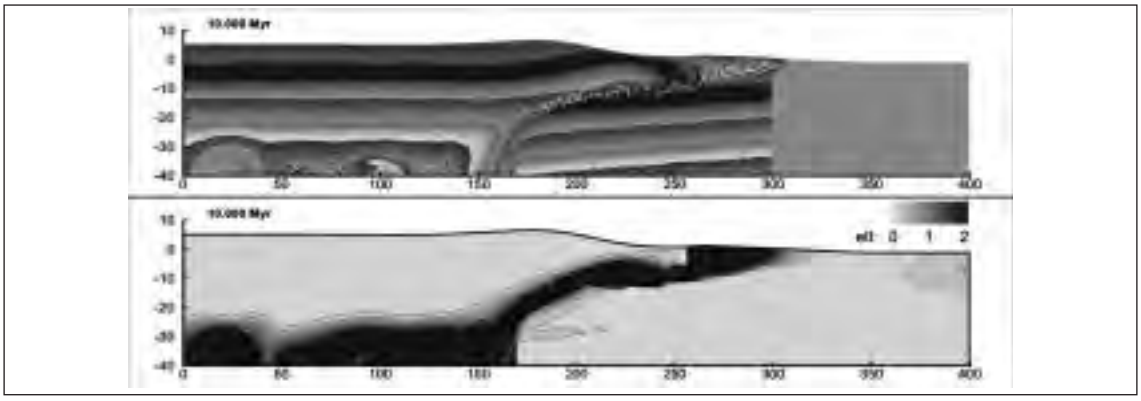

Figure 5. Fluvial erosion – low, landsliding erosions – high, sediments – weak.

Switching-on of the high fluvial erosion combined with soft sediments again suppresses long overthrusting (Figure 6). In this experiment a single fault facilitated by erosion effectively accomodates tectonic shortening. The evolving anticline is rapidly eroded and deeply exhumed. Again, as in case 2, plateau loses a lot of material by surface erosion and there is no apparent thickening of the plateau.

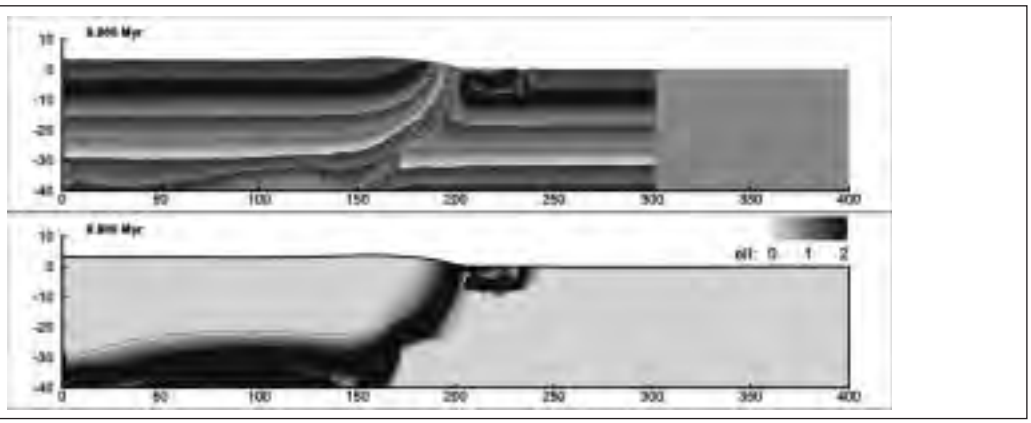

Figure 6. Fluvial erosion – high, landsliding erosions – high, sediments – weak.

Results of our model runs imply that the Andes can be considered to have a rather weak foreland which consequently leads to the formation of a wide thrust belt in the Subandean range. However, north of the Santa Cruz elbow, increased fluvial erosion may help to inhibit the formation of a wide thin-skin thrust belt. Along the Himalayas the precipitation rates are locally even higher than north of the Santa Cruz elbow. However, only mid-crustal levels are exhumed. The discrepancy to our model, which exhume lower crust as well, may be due to the fluvial erosion law we use, that erodes most efficiently at the base of the slopes. In contrast, FT-ages along the Himalaya slope are generally youngest between 2000 and 4000 m.

REFERENCES

- Babeyko et al. (2002), Earth. Planet. Sci. Lett., 199, 373-388.
- Benjamin (1986), M.S. Thesis, Dartmouth Coll., Hanover.
- Cundall and Board (1988), In: 6th Interna-tional Conference in Numerical Methods in Geomechanics (ed. Swoboda, G.), A. A. Balkema, Brookfield, Vt., 2101-2108.
- Ege, H. (2004), PhD Thesis, Freie Univ. Berlin.
- Gleason and Tullis (1995), Tectonophysics, 247, 1-23.
- Hirth and Kohlstedt (1996), Earth Planet. Sci. Lett., 144, 93-108.
- Masek et al. (1994), Journal of Geophys. Res., 99, B7, 13942-19956.
- Moresi et al. (2001), In: Proceedings of the Fifth International Workshop on Bifurcation and Localization in Geomechanics (ed. Mühlhaus et al.), Balkema, Rotterdam, ISBN 90265 18234, 345–355.
- Poliakov et al. (1993), in: Flow and Creep in the Solar System: Observations, Modelling and Theory, eds. Stone, D.B. and Runcorn, S.K., Kluwer Academic Publishers, p. 175-195.
- Sulsky et al. (1995), Comput. Phys. Commun., 87, 236–252.
- White et al. (2002), Earth Planet. Sci. Lett., 195, 29-44.
- Wilks and Carter (1990), Tectonophysics, 182, 57-77.
- Willett (1999), J. Geophys. Res., 104, 28957-28981.

EFFECT OF HORMUZ SALT ON DEFORMATION STYLE OF ZAGROS FOLD-THRUST BELT 2-03

A. Bahroudi [1,2], H.A. Koyi [1]

[1] *Hans Ramberg Tectonic Laboratory, department of Earth Sciences, Uppsala University, Villavägen 16, SE-752 36 Uppsala, Sweden*

[2] *Research Institute for Earth Sciences, Geological Survey of Iran, Azadi Sq. Meraj Avn., P.O. Box 13185-1494, Tehran, Iran*

Summary

Scaled analogue models were used to study the effect of Hormuz salt on the thin-skinned shortening in the Zagros fold-and-thrust belt (ZFTB) where Phanerozoic sedimentary cover has been shortened partly above the Hormuz salt lying on the Precambrian crystalline basement, behaving as a basal viscous decollement. The models consisted of sand layers that partly overlay a viscous layer of silicone and were shortened from one-end. Model results display how deflection zones, different topographic wedges and differential sedimentation develop and strain partitioning occurs along the ZFTB. Model results suggest the formation of a gentle taper above a viscous decollement and a relatively steeper taper above a frictional decollement. Whereas, model results display the steepest topographic wedge formed where the viscous substrate had pinched out transitionally perpendicular to the shortening direction.

Geology of the Zagros fold- thrust belt (ZFTB)

The Zagros mountains interpolate the Alpine-Himalayean orogenic chain for 2000 km between the central Iran plateau in the north, the Taurus in Turkey to the northwest the Oman Fault in the southeast (Stöcklin, 1968b; Falcon, 1967; Beydoun et al., 1992; Talbot & Alavi, 1996) resulted from the closure of the Neo-Tethys ocean due to convergence between the Arabian and Iranian plates. (Sengör & Kidd, 1979; Berberian & King, 1981; Snyder & Barazangi, 1986; Beydoun et al., 1992; Talbot & Alavi, 1996).

Across the belt, the ZFTB is divided into three different tectonic units; the Zagros Imbricate Zone, the Zagros Simply Folded Belt and the Zagros Foredeep (Fig. 1; Stöcklin, 1968b; Falcon, 1967, 1974; Berberian, 1995). On the basis of litho-facies in cover sequences and the structural style along the belt, the ZFTB is divided into several domains; the Lorestan, the Izeh, the Dezful embayment, the Fars Platform, the Mangrak-Kazerun, and Laristan domains (Fig.1; Talbot & Alavi, 1996). However, the boundary between the Simply Folded Belt and the foredeep is characterised by the MFF forms a distinct topographic step (in cross section). The MFF trends NW parallel to general trend of the

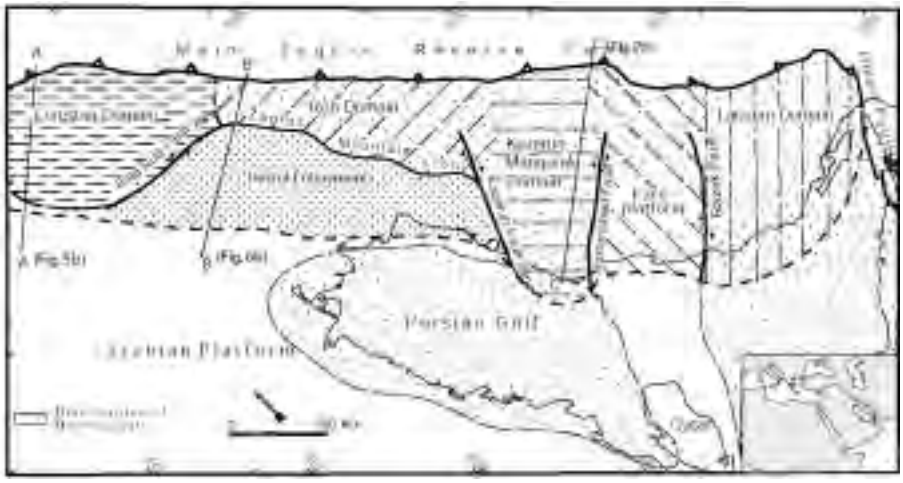

Fig.1. Distribution of the Hormuz salt and major structural domains including the Laristan, the Fars platform, Kazerun-Mangarak, the Izeh, the Lorestan and the Dezful embayment, and main faults, the Razak Fault; Nezamabad Fault; Kazerun Fault; Bala Rud Fault; along the Zagros belt.

Zagros belt and delimits the distribution of linear, tight and asymmetric folds to the south. The MFF is proposed dip-slip fault with several hundred meters of uplift in the northern part (hanging wall) and subsidence in southern part (Berberian, 1995).
The sedimentary cover (10-14 km thick) of the Zagros contains several evaporitic units with temporal and spatial variations. Among these units, the Neo-Proterozoic Hormuz salt overlying the crystalline basement is the most important unit and has controlled the deformation style of the south-eastern Zagros (see Talbot & Alavi, 1996). The distribution of emergent and buried salt diapirs shows that most of the extruded diapirs are located within three domains (the Izeh, Kazerun-Mangarak, and Laristan domains) in the Zagros simply folded belt (Fig. 1).

Fig.2. Schematic illustration of initial configuration of the ductile (SGM 36) and brittle (sand) decollements in the models showing the shortening direction and the different domains A to E.

Models consisted of layered sand simulating the sedimentary overburden in the ZFTB, resting on a viscous substrate which had a geographically uneven distribution (Fig.2). The distribution of the viscous layer, which simulated Hormuz salt, was such that in some parts of the models, the sand layer was resting directly on the rigid substrate. In this study, the viscous substrate did not change only along strike, but also across it. In our models, we have simplified the distribution pattern of Hormuz salt, so that the boundary between frictional and viscous decollements separating different domains (as A to E comparable to their prototypes) is parallel to the shortening direction.
Loose sand (2cm thick) and the PDMS (SGM-36) were used to simulate a frictional cover (Weijermars et al., 1993; Cotton & Koyi, 2000; Bonini, 2001) and a basal viscous decollement (0.5 cm and 1.5 cm thick) respectively (Weijermars et al., 1993; Cotton & Koyi, 2000; Bonini, 2001). Models were shortened at a uniform rate of 1.15 cm/h up to 30% during 15.6 hr.
In this study, scaled analogue models were used to investigate the effect of spatial distribution of the Hormuz salt on variations in structural styles in the ZFTB. Different parts of the shortened model were compared to corresponding parts within the belt in plan view and cross sections.

Model Results

In plan view, development of deflection zones in the deformation front coincided to the initial boundaries between the viscous and frictional decollements, clearly reflected differential propagation of deformation due to variation in basal decollement (Fig. 3). During Shortening, the deformation front propagated faster and further than above the viscous decollement (Fig. 4) domains C and partly D). In domains B and D where the viscous decollement changed to a frictional one perpendicular to the shortening direction, width of the deformation zone is less than in domain A which is entirely shortened above a frictional decollement (Fig.5, 6). Both the cover and decollement were shortened and thickened in these domains. However, the presence of the viscous decollement in domains B and D led to easier and more intensive deformation of the overlying cover than that above the frictional decollement. This resulted in accommodation of larger deformation against the frontal ramp where large amount of displacement took place. As a result, the overburden units were shortened more above the thickened viscous layer and the deformation front did not propagate as far as in domains C and E which were floored entirely by a viscous layer (Fig.4).
In the ZFTB, distribution of the Hormuz salt also changes both parallel and perpendicular to the general direction of the regional shortening (Figs.1, 2). North of the Dezful embayment (simulated by domain B in the model) the boundary between the viscous and frictional decollements is roughly perpendicular to the NE shortening. This has led to development of a significant morpho-tectonic feature, the Mountain Front Fault, which separates the Izeh zone, having intense deformation, from the Dezful embayment with significantly less deformation (Fig.6).
Differential propagation of deformation front in the models led to formation of four dominant

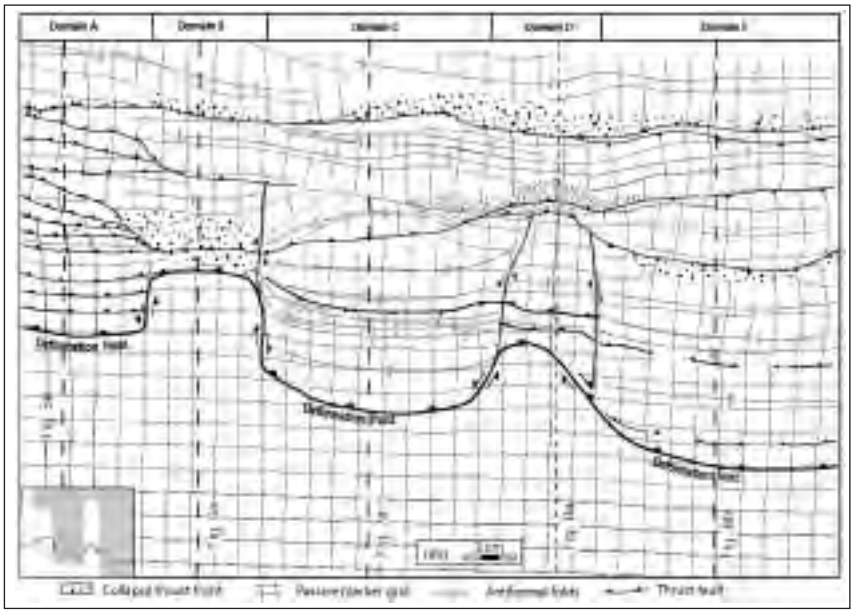

Fig.3. Top view of the model after 30% of bulk shortening, showing formation of different deflection zones across the deformation front propagating above the viscous and frictional substrates. Note that differential propagation of the deformation front in different domains of the model resulted in variation in structural style. The inset is a top view showing the initial distribution of the viscous layer (grey area) and the deformation front at 30% bulk shortening.

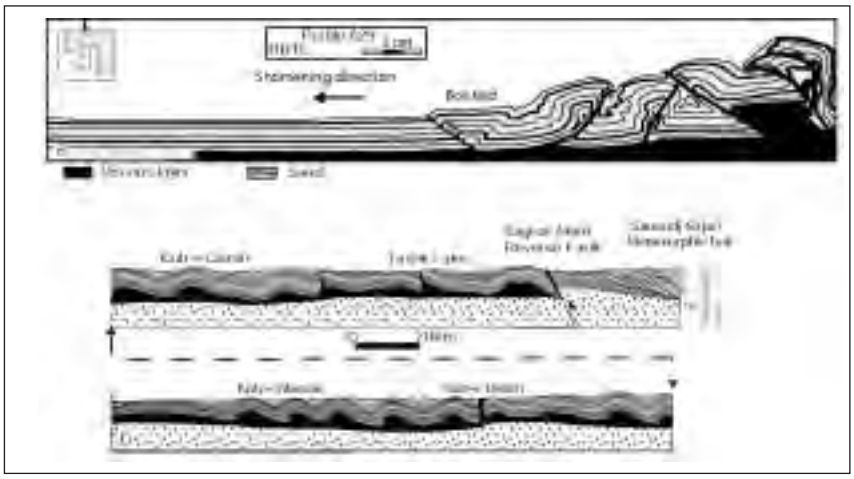

Fig.4. a) Line drawing of a profile along domain C (see Fig. 4 for location) parallel to shortening direction showing a low angle, wide taper with thrust faults including fore- and back-thrusts and fault-related folds above the viscous substrate. Note pronounced thickening of the ductile substrate, partly forward flow and its injection along some of the fault planes (Inset is a top view showing location of the cross section) and b) geological cross section of the Laristan domain across the south-eastern Zagros belt (see Fig. 1 for location) showing a wide folded zone consisting of the salt-cored anticlines (redrawn from N.I.O.C., 1976).

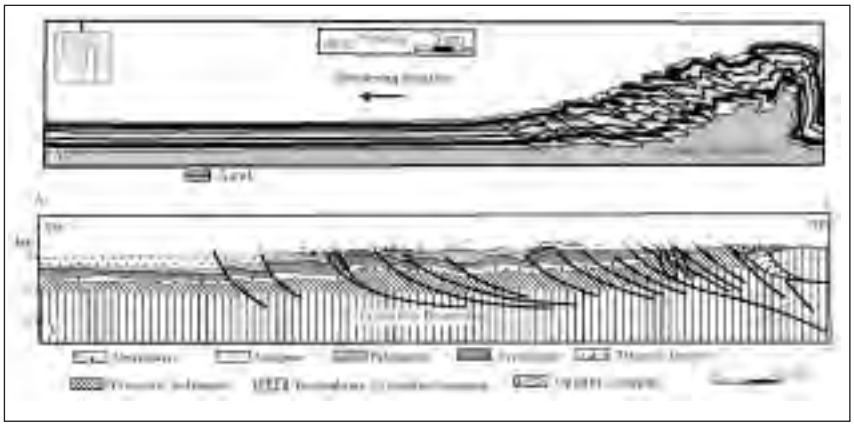

Fig.5. a) Line drawing of a profile along domain A parallel to the shortening direction (see Fig. 4 for location) showing a steep taper of an imbricate stack of closely spaced thrust faults formed above a frictional decollement (Inset is a top view showing the location of the cross section) and b) geological cross section of the Lorestan domain (see Fig. 1 for location) showing an imbricate stack in the cover and basal units (redrawn from Spaargaren, 1987).

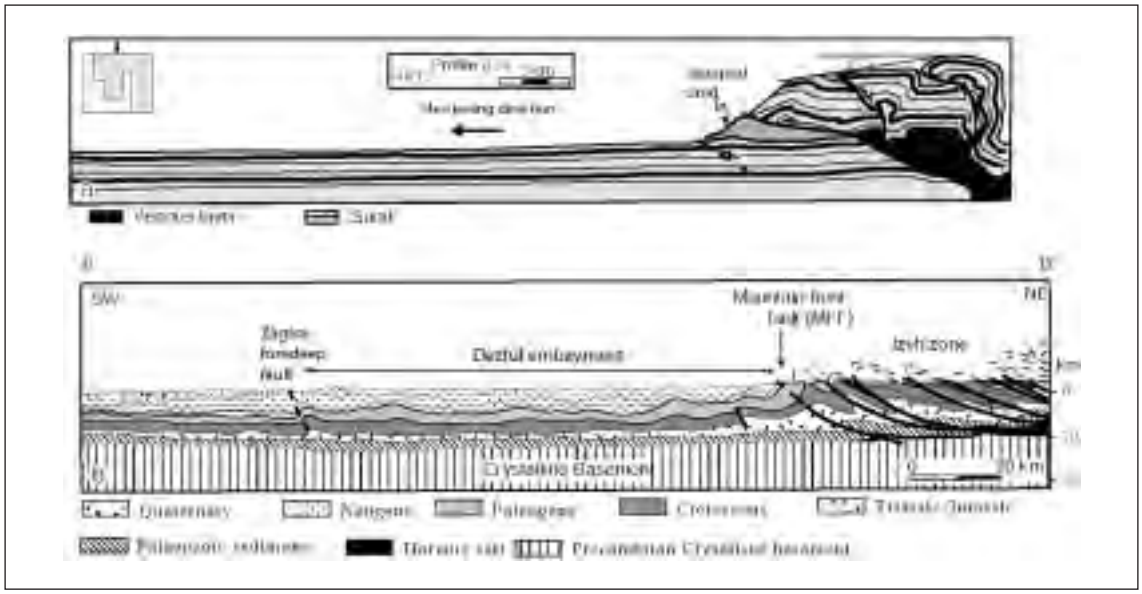

Fig.6. a) Line drawing of a profile along domain B (see Fig. 4 for location) parallel to the shortening direction showing narrow taper with some thrust faults above the viscous substrate which abruptly changes into a frictional substrate. Note the pronounced thickening of the viscous material against the footwall ramp at the boundary between the viscous-frictional decollements. In this part of the model, slumped sand was run over by hanging wall of the frontal fault (Inset is a top view showing the location of the cross section) and b) geological cross section of the Izeh domain and the Dezful embayment across the Zagros belt (see Fig. 1 for location) showing a narrow imbricate stack formed behind the MFF which separates the Dezful embayment, with low deformation, from the highly deformed Izeh domain (redrawn from Spaargaren, 1987).

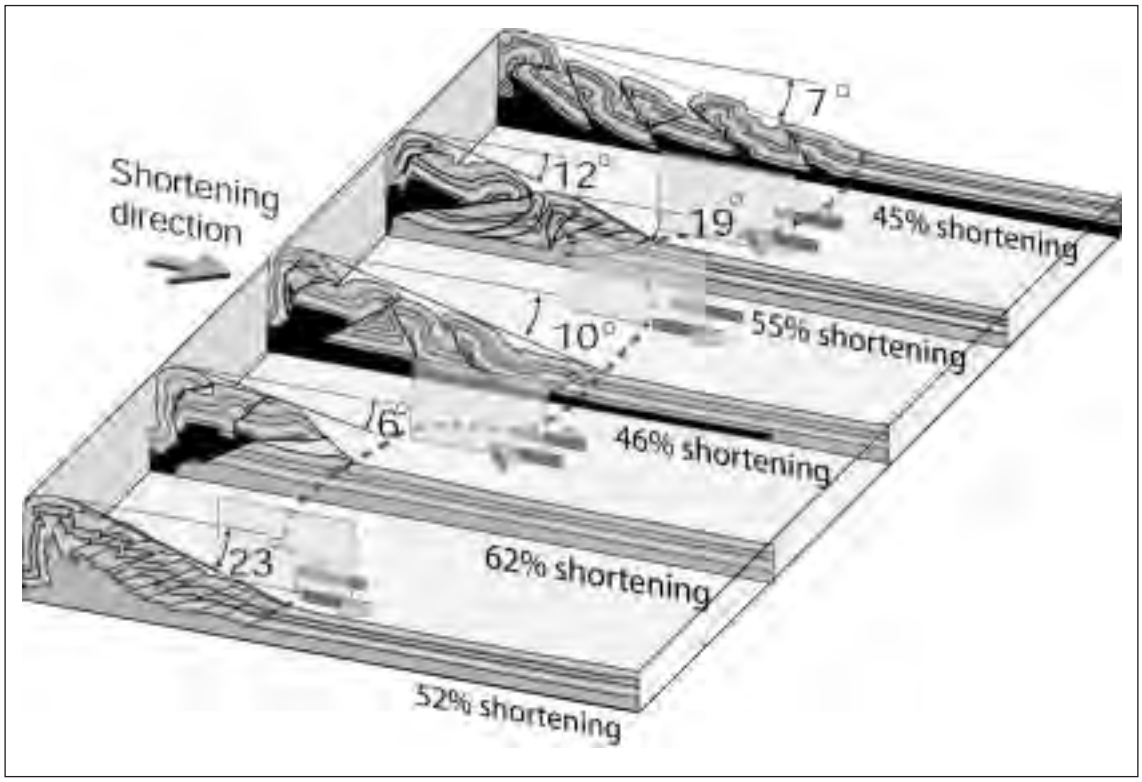

Fig.7. Diagram of Serial sections cut parallel to shortening direction illustrating the 3D variation in amount of the shortening, topographic tapers, development of deflection zones in different parts of the model.

deflection zones (with a general trend parallel to the initial boundary between the viscous and frictional decollements) offsetting left- or right-laterally the deformation front (Fig.7). In the ZFTB, some strike-slip faults, for example the Kazerun Fault, the Bala Rud Fault have been described and attributed to reactivated basement faults by previous workers (Fig.1). We use model results to argue that even if some of these faults are basement related, their surface expression is amplified by the differential propagation of the deformation front above different decollements. However, based on model results and in the lack of subsurface data about those faults, we present some alternatives for their nature (Fig.7).

Differential propagation of the deformation between the domains from the early stages of shortening led to strain partitioning and changes in deformation style in different parts of the model (Fig.7). With progressive shortening, the deformation continuously propagated in the C and E domains. The deformation propagated further at the beginning of the shortening in domains B and D (which were partly floored by a viscous layer), but it did not propagated beyond the viscous decollement into the area underlain by the frictional decollement directly where the deformation front reached this area. The forward advance of the deformation front ceased for considerable amount of shortening (about 20% of bulk shortening).

Sedimentary facies changes reported in the vicinity of the MFF indicate that the location of this fault has remained stationary since the late Eocene and its forward advance must have slowed down during a considerable amount of the shortening in the ZFTB (Fig.6). This suggests that main part of the shortening must have been accommodated within the area located NE of the Mountain Front Fault. The variation in decollement along the shortening direction led to the formation of a different topographic slope in domain B and to some extent in domain D where the viscous substrate successively tapered to a frictional decollement.

The viscous/frictional boundary in domain B acted as a frontal ramp against which a high uplifted area formed (Fig.6). Although, there is no large subsidence in front of this uplifted area underlain by the frictional decollement, such an abrupt step across the deformation front is likely to induce subsidence in a natural example. The Dezful embayment (simulated by B domain) in the ZFTB is interpreted to represent such a subsidence where thick sediments have accumulated.

Based on model results, we infer that a frontal ramp (the Mountain Front Fault) in the ZFTB and subsidence in the Dezful embayment (acting as a foreland) formed in late Eocene (e.g. Berberian, 1995; Motiei, 1995). The Dezful embayment was a sedimentary basin with pronounced subsidence where thick late Eocene-recent deposits were formed. Erosion of the uplifted domains, particularly in the Izeh domain to the northeast, provided more sediment, while, on the SW side, clastic material from the Arabian shield was transported into the embayment (e.g. Motiei, 1993). This process resulted in formation of the thickest sedimentary sequence of the ZFTB in the Dezful embayment. More subsidence increased burial depth of the source rocks in this area. As a result, organic material matured faster than those in the other domains. This can probably explain the huge accumulation of hydrocarbons in the Dezful embayment.

REFERENCES

- Berberian, M., (1995), Tectonophysics, 241, 193-224.
- Berbrian, M., King, G. C. P., (1981), Canadian Journal of Earth Sciences, 18, 210-265.
- Beydoun et al., (1992), American Association of Petroleum Geologists Bulletin Memoir, 55, 307-336.
- Bonini, M., (2001), Journal of Geophysical Research, 106, 2291-2311.
- Cotton, J. T., Koyi, H.A., (2000) Geological Society of America Bulletin, 112, 351-363.
- Falcon, N.L., (1967) Advancement Science, 24, 1-12.
- Falcon, N.l., (1974), Geological society of London, Special Publication, 4, 199-211.
- Motiei, M., (1993), Geological Survey of Iran (in persian), Tehran, 536.
- Motiei, H. (1995), Petroleum Geology of Zagros. Geological Survey of Iran (in persian), 589.
- Sengör, A.M.C., Kidd, W.S.F., (1979), Tectonophysics, 55, 361-376.
- Snyder, D.B., Barazangi, M., (1986), Tectonophysics, 5, 361-373.
- Stöcklin, J., (1968), Bulletin of American Association Petroleum geologists, 52, 1229-1258.
- Talbot, C. J., Alavi, M., (1996) Geological Society of London Special Publication, 100, 89-109.
- Weijermars, R. Jackson, M. P. A., Vedeville, B. C., (1993), Tectonophysics, 217, 143-174.

SUBDUCTION AND PLATE MOTION IN LABORATORY 2-04

Nicolas Bellahsen, Claudio Faccenna, Francesca Funiciello
Dip. di Scienze Geologiche, Università degli Studi "Roma Tre", Rome, Italy

We have performed 3-D laboratory experiments to test the influence of factors controlling plate and trench motion of a subducting plate. The systematic study has been carried out widely changing geometrical (plate and mantle thickness, plate width) and rheological (plate viscosity and density) parameters of the system and testing the relative influence on the kinematics of subduction. We scaled down our experiments to natural gravity field using silicone putty and honey to simulate the viscous behavior of slab and mantle, respectively.
Our models can be divided in two classes typified by a different style of subduction: a "retreating" style of subduction characterized by the backward motion of the trench and the slow advancing motion of the plate, and an "advancing" style, where trench is stationary or advance towards the upper plate and the plate move in faster way. In general terms, the two behaviors depend upon the distribution of the forces active into the system.

COMPRESSIVE DEFORMATIONS OF HOT ANALOGUE LITHOSPHERES AND POSSIBLE APPLICATIONS TO PRECAMBRIAN TECTONICS 2-05

F. Cagnard, J.P. Brun, D. Gapais
Géosciences Rennes, UMR 6118 CNRS, Université de Rennes 1, 35042 Rennes cedex, France

Introduction

Many Archean and Paleoproterozoic compressive zones show peculiar features that are difficult to interpret in terms of collision between resistant plates. These are in particular (1) evidence for rather early HT metamorphic conditions and partial melting at relatively shallow crustal levels, typically of the order of 25-30 km or less, (2) the occurrence of large domains marked by monotonous metamorphic conditions, which suggest locally rather flat isograds, at low angle to the Earth surface, (3) rare evidence for major strain localisation along crustal-scale thrusts or extensional detachements, and (4) large domains of rather distributed deformations that can involve substantial components of vertical stretching. In addition, ancient compressive deformations are often marked by extensive diapirism, as exemplified within Archean greenstone belts (Bouhallier et al. (1995), Chardon et al. (1996), Schwerdtner and Lumbers. (1980)). These features suggest weak lithospheres, and are consistently frequent within juvenile crust where high geotherms can be expected (Cheng et al. (2002)).
We present analogue experiments that provide some constraints to discuss deformation processes within hot and weak lithospheres. Models focus on end-member situations, with a thin brittle upper crust, a thick low-viscosity ductile crust, and a ductile lithospheric mantle.

Experimental setting

Experiments were performed using a rectangular box, with three fixed walls and a mobile wall attached to a piston driven by a stepper motor (Fig. 1a). Two thin plates, fixed to the mobile wall, slide along the lateral walls during the experiment. This arrangement creates a velocity discontinuity at model boundaries, in order to force strain localisation away from the mobile wall.

Model lithospheres are initially 40x30x3 cm. They are made of three layers, from top to bottom: a relatively thin (0.5 cm) brittle layer (upper crust) made of light sand, a thick (1 cm) low-viscosity layer of silicone putty (weak ductile crust), and a silicone layer (1.5 cm) modelling a ductile lithospheric mantle. The lithosphere model floats on a mixture of water and glycol, adjusted in density with sodium polytungstate and representing the asthenosphere (Fig. 1a).

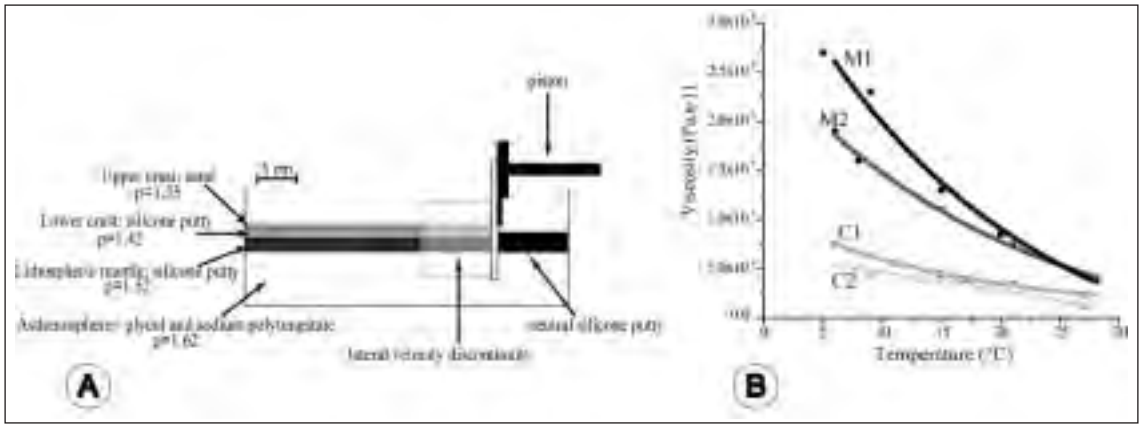

Fig. 1- (a) Sketch of experimental setting. (b) Viscosities of silicones used versus temperature. M1, M2 are silicone putties used for the lithospheric mantle and C1, C2 for the ductile crust.

The sand used has a Mohr-Coulomb behaviour, with an internal friction angle of about 30°. Silicone putties are Newtonian. Average densities within the model lithosphere are around 1.35, 1.42 and 1.52 Kg/m3 for the upper crust, lower crust and upper mantle, respectively. The density of the underlying model asthenosphere is of about 1.62 Kg/m^3.

In all experiments, models were shortened up to 50%. At the end of experiments, the model is wetted and frozen. After solidification, sections are cut within the model. In order to image the strain pattern, each model layer is constituted of several sub-layers of different colours, but comparable rheology.

A series of five experiments was performed in order to examine changes in strain patterns according to (1) the brittle-ductile coupling, and (2) the viscosity contrast between mantle and lower crust. Changes in the brittle-ductile coupling are obtained by changing the overall strain rate. On the other hand, effects of the viscosity contrast between ductile layers can be examined by performing experiments at different temperatures (Fig. 1b). Explored strain rates are 0.5, 1 and 5 cm/hour, for temperatures of 18°, 25° and 30°C. At low temperature, the differently coloured silicone layers used to build the model induce slight differences in viscosities within the mantle (M1 and M2) and the crust (C1 and C2) (Fig. 1b). However, these viscosity variations become negligible for the temperature range we used (Fig. 1b).

Main structural features

Figure 2 shows four successive surface views of one experiment, where structures with clear kinematics are underlined. Main features are (1) a localisation of curved thrusts that propagate from the lateral velocity discontinuity, (2) local along-strike changes in thrust vergencies, (3) development of narrow thrust-bounded synforms, and (4) an overall increase in the complexity of the anastomosed pattern of deformation zones.

Figure 3 shows an example of cross section within the central part of one model after 50% shortening. Within the brittle upper crust, strain localisation observed on surface views is expressed by undeformed domains surrounding a zone of intense deformation. The latter is characterized by a stack of several superposed “pop-down” structures bounded by conjugate thrusts that are often rather shallowly dipping. In most experiments, the overall geometry of the pop-down stack resembles that of a Christmas tree suggesting progressive burial of successive pop-downs with alternating asymmetry. Consistently, one dominant fault with alternating vergency often bounds the successive pop-downs (Fig. 3a).

Below undeformed or moderately deformed upper-crustal domains, a distributed thickening affects both the lithospheric mantle and the ductile crust, and the overall envelopes of the Moho and the base of the lithosphere remain flat. Below the pop-down stack, the amount of thickening is moderate, and minor vertical thinning was even observed in one experiment.

Figure 3b shows strain trajectories deduced from attitudes of the axial trace of minor folds along layer

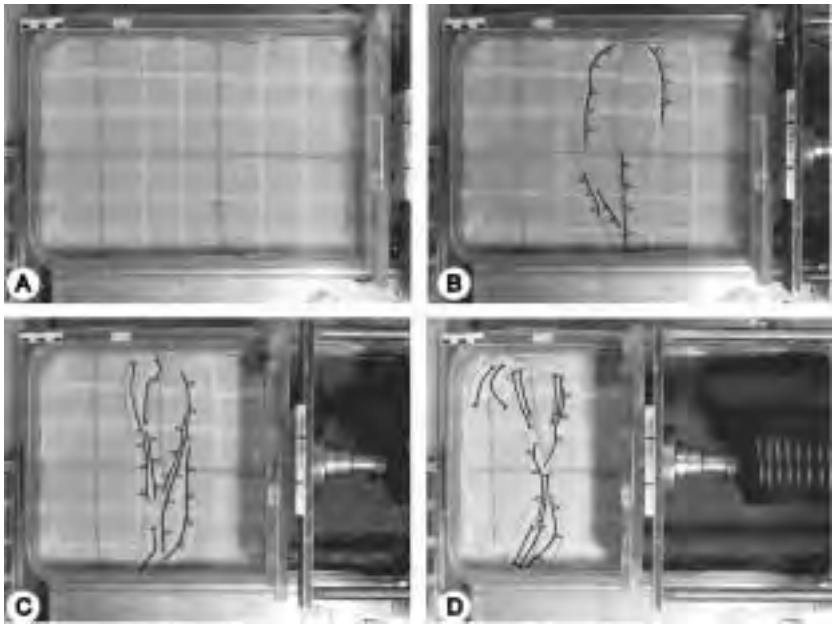

Fig. 2 - Examples of surface views of an experiment at 0% (a), 10% (b), 30% (c), 50% (d) shortening.

interfaces. Trajectories have sub-vertical attitudes, especially in the mantle and, more generally, within the ductile crust away from the stack of pop-downs. Trajectories thus emphasize that distributed horizontal shortening is accompanied by bulk vertical stretching. At the vicinity of the pop-down stack, trajectories flatten and converge toward the stack.

Effects of strain rate and viscosity contrasts

Figure 4 shows synthetic views of representative cross-sections for the five experiments. The main differences between models reflect a decrease in strain localisation with increasing strain rate and (or) decreasing temperature. With decreasing strain localisation, the number of zones where faults develop

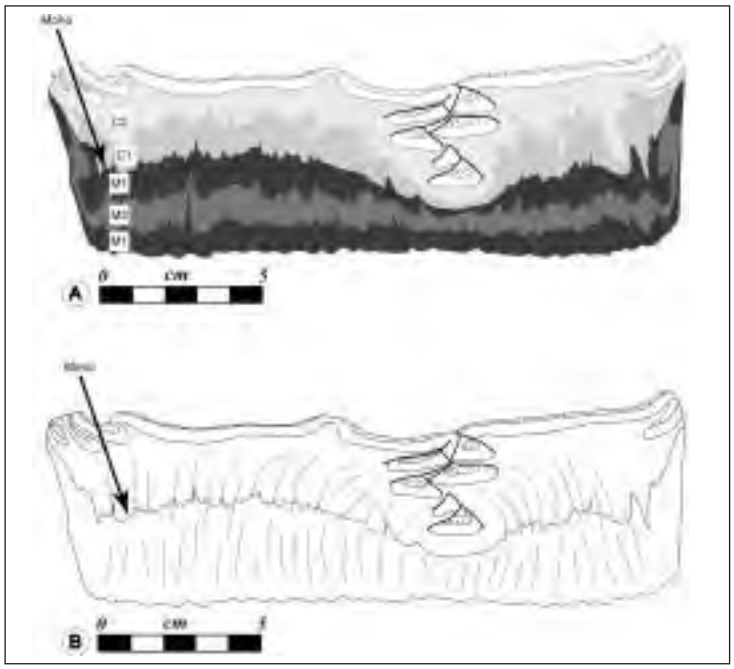

Fig. 3- (a) Example of cross-section in the central part of a model. M1, M2: coloured markers within the mantle and C1, C2: same within the ductile crust. White and dotted layers are markers within the brittle crust.
(b) Sketch of strain trajectories.

in the upper crust increases and the amount of pop-down burial decreases. The final Moho geometry is dependant on strain localisation in the brittle crust as long wavelength folding is directly related to zone of pop downs.
The increase in strain distribution with increasing strain rate or decreasing temperature reflects an overall increase of the strength of the ductile lithosphere. With decreasing temperature, the viscosity of silicones used for the mantle increases more than that of those used for the crust (Fig. 1b). This suggests that the decrease in strain localisation observed with decreasing temperature might mainly result from an increase in model mantle strength.

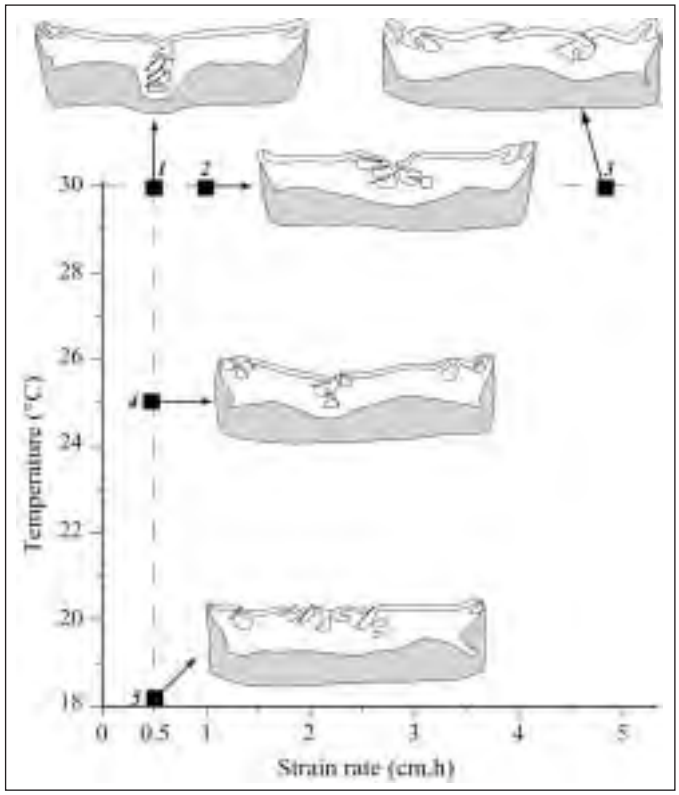

Fig. 4- Synthesis results showing variations of overall cross-section patterns according to bulk strain rate and temperature. White and grey layers are crust and lithospheric mantle, respectively.

Discussion

Several features observed in the above experiments can be compared with some specificities attached to ancient deformation zones. First, the distributed shortening of the ductile layers, associated with steeply dipping foliations is consistent with patterns observed in various Archean and Paleoproterozoic areas (e.g. Finnish Svecofenides, Ehlers et al. (1993); Dharwar craton, Bouhallier et al. (1995)). In models, the propagation of thrusts remains very limited in space, localized around pop downs. The fact that they do not seem to enhance shear localisation within the ductile crust further suggests that individual thrusts are short-lived structures. These features remind us that localised crustal shear zones leading to a regional-scale piling up of various metamorphic units is not a major characteristic of many ancient deformation zones. Furthermore, the large model domains of relatively homogeneous ductile deformation, with flat layer envelopes, are consistent with the occurrence of natural metamorphic patterns suggesting locally flat-lying isograds.
Patterns of stacked pop-downs imply that relative vertical motions are locally important. The fact that their development is here due to surface forces, and not to body forces (lack of reverse density gradients), raises the question of the primary cause of gravitational instabilities like greenstone sagductions: tectonics or gravity? Clearly, the finite pop-down patterns observed in models cannot model realistic natural structures, because thermal effects are not considered in experiments. Nevertheless, they underline that superposition of basement rocks over their sedimentary cover, a feature that occurs in ancient belts, could be the result of burial of upper-crustal fragments, and not necessarily a proof of large-scale thrust-and-nappe tectonics.

REFERENCES

- Bouhallier H. et al. (1995), Earth and Planetary Science Letters, 135, 57-75
- Chardon D. et al. (1996), Journal of Structural Geology, 18, n°8, 991-1004
- Cheng L.Z. et al. (2002), Journal of Gedynamics, 34, 11-30
- Elhers C. et al. (1993), Precambrian Research, 64, 295-309
- Schwerdtner W. M. and Lumbers S. B. (1980), Geological Association Canada Special Paper, 20, 149-180

THREE-DIMENSIONAL STRAIN PARTITIONING IN ANALOGUE VERSUS NUMERICAL MODELS OF CONVERGENT OROGENS

2-06

A.R. Cruden, M.B. Nasseri, R. Pysklywec

Dept. Of Geology, University of Toronto, 22 Russell St., Toronto, Ontario M5S 3B1, Canada
cruden@geology.utoronto.ca

Summary

The post-accretionary deformation of wide, hot orogens (e.g., Superior, Grenville, Variscan, Cordilleran, Tibetan) is characterised by pure-shear or transpressional shortening of relatively weak lithosphere (the orogen) between converging stronger blocks (the vise). In such vise models, the orogenic crust is weakened due to the properties of inherited accreted material or thermal/magmatic softening, and deformation is effectively decoupled from mantle dynamics (Ellis et al. 1998; Burg et al. 2002). The structural and topographic development of the resulting orogen depends on the vertical and lateral rheological structure of the lithosphere, the initial and final widths of the weak zone, erosion and 3D effects (e.g., lateral extrusion). We report on a series of analogue vise models and compare the resulting 3D strain fields and surface topographies to equivalent 2D numerical experiments.

Abstract

Three-dimensional strain partitioning has long been recognised as a key phenomenon in the kinematic and dynamic evolution of convergent orogens (e.g. Oldow et al. 1989; Vauchez & Nicolas 1991). A classic example is the partitioning between orogen-parallel strike-slip fault systems and ductile thickening in the Alpine-Himalayan chain (e.g., Tapponnier et al. 1982; Davy & Cobbold 1988). Recent studies have documented decoupling between upper crustal and mid- to lower-crustal deformation in convergent magmatic arc, collisional orogen and post-orogenic collapse settings (e.g., Axen et al. 1998; Garde et al. 2002; Klepies et al 2004). A common expression of such decoupling is the observation of vertical orogen sub-parallel transpression zones, upright folding and cleavage development in the upper crust versus subhorizontal fabric development and lateral flow in the mid- to lower crust, as documented by both field and seismic reflection studies in Archean to Mesozoic orogens (e.g., Collins & Vernon 1991; Jackson & Cruden 1995; Hajnal et al. 1996; Axen et al. 1998). The purpose of this contribution is to investigate the roles of orogen parallel flow and rheological stratification on the resulting vertical and lateral development of structures in convergent settings. We describe a series of 3D analogue model experiments and complementary 2D numerical models that investigate the structural and topographic response of a model orogenic lithosphere as it is compressed between converging blocks of significantly stronger lithosphere. The analogue experiments are designed to allow flow of orogenic material orthogonal to the compression direction. Comparison of these experiments with 2D numerical models, together with detailed structural and topographic data from the model surface and serial sectioning allows us to evaluate the significance of such orogen parallel flow. In this presentation, we will highlight the influence of relative variations in the strength and density of the ductile crust, which dictate the degree of coupling within the crust and body forces, respectively.

Model Set Up

Scaling and the general construction of the laboratory experiments (Fig. 1) follows the approach for analogue modelling of lithospheric deformation at 1g described by Davy and Cobbold (1988). In the models, a rheologically stratified (frictional/viscous) weak orogenic lithosphere floats isostatically on a viscous asthenosphere and is squeezed between converging strong lithospheric blocks (= jaws of the vise). The strength contrast between the vise jaws and orogen is achieved by varying the thickness of the brittle model crust (comprised of layers of quartz sand and Z-lights ceramic microspheres) and the relative viscosity of the ductile model crust and lithospheric mantle (comprised of PDMS-plasticene-Z-lights mixtures and bouncing putty) (Fig. 1). Ductile lower crust and mantle in the weak lithosphere is free to flow laterally because the margins of the model orogen are unconfined and rest on a

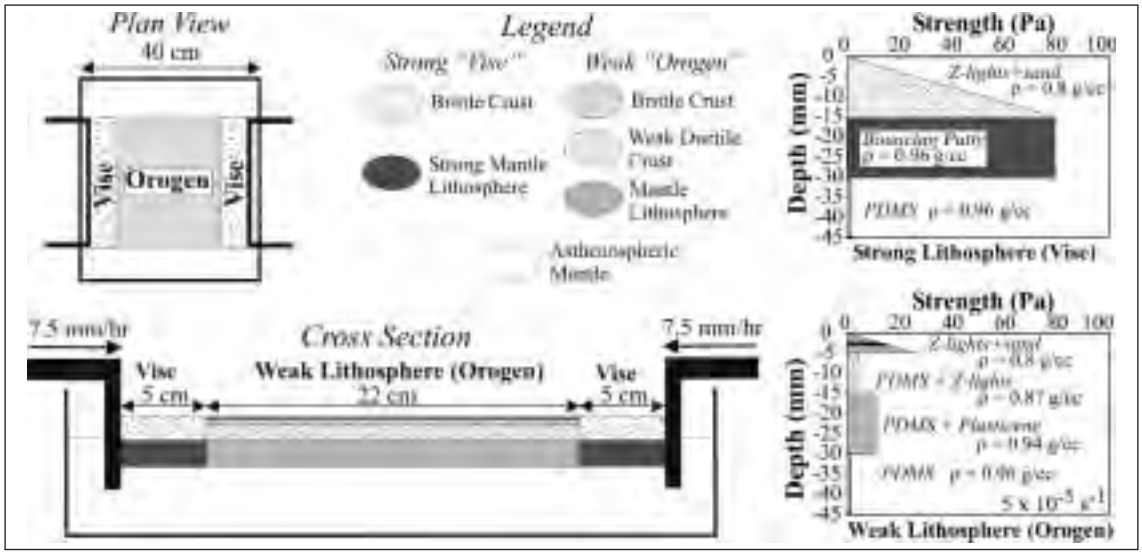

Fig. 1. Set up for both the 3D analogue and 2D numerical vise models employed in this study.

reserviour of asthenopheric mantle (PDMS). 3D strain fields in the models are determined by continuous photography of surface marker grids and serial sectioning after experiments. Surface topography is quantified at regular intervals with a precision of 0.1 mm by laser profilometry, using a laser tringulation device mounted on an X-Y gantry system. Numerical models employed arbitrary Eulerian-Lagrangian finite element techniques (Fullsack 1995). Material properties, dimensions and shortening rates in the numerical models were defined to be equivalent to those in the laboratory experiments.

Results

Firstly, we compare the results between an equivalent analogue and numerical experiment. Secondly, we contrast first order differences in behaviour between laboratory models run with a weak non-buoyant versus a buoyant even weaker lower crust. The former would correspond to an orogenic crust that is weak either due to the nature of inherited material or high heat flow, and the latter to orogenic crust weakened by partial melting or intrusion of voluminous mid-crustal granites.
Figure 2 compares the cross sectional geometries of a laboratory and numerical vise model with non-buoyant lower crust after ~50% shortening. The first-order characteristics of each model are similar, although in detail the analogue experiment developed shorter wavelength, larger amplitude folds in

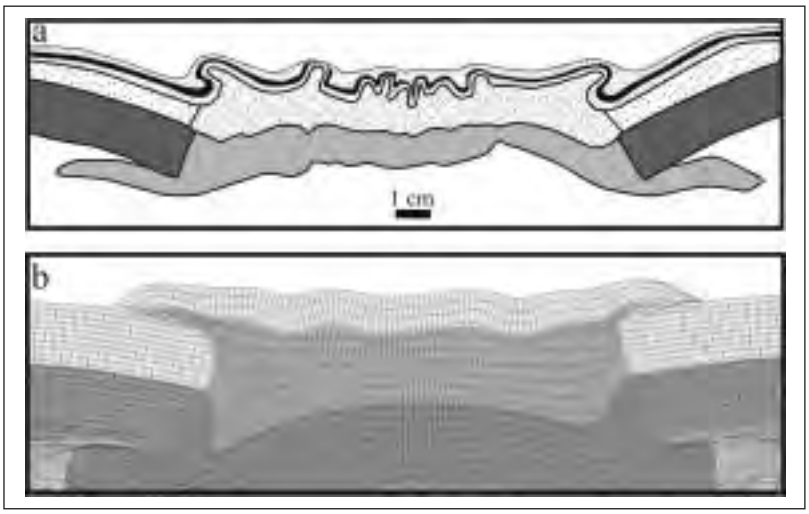

Fig. 2. Cross-section through central part of analogue vise model (a) and equivalent numerical experiment (b), after ~50% shortening. See Fig. 3a for a view of the top surface of this model.

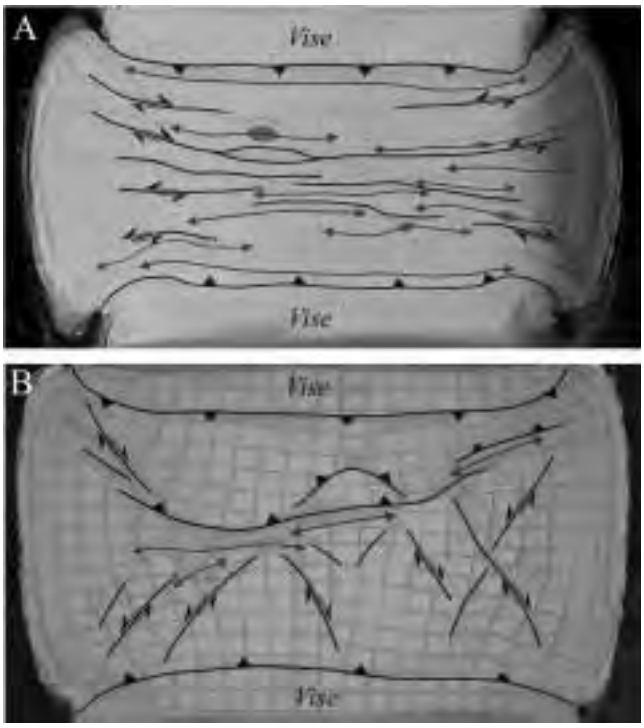

Fig. 3. Surface deformation features developed in vise models with a non-buoyant weak lower crust (a) and a buoyant weaker lower crust (b) after ~50% shortening. The cross section in Fig. 2a was cut thought the central part of (a), parallel to the shortening direction. Grey lines with arrows indicate the axial traces of doubly plunging anticlines. Grey ellipses are domes cored by ductile crust. Black lines are the traces of thrust faults (barbed) and transpressional shear zones (horizontal kinematics indicated).

the upper crust and a lower degree of thrusting of the weak crust over the strong crust. Obvious effects due to lateral flow of lower crustal material are the lower degree of thickening observed in the ductile crust as well as a suppression in the amount of relief generated in the analogue model compared to the numerical experiment. In the analogue models, the cross-sectional area of lower crust decreases with time, indicating bulk vertical flattening strain and orogen parallel extension, which is decoupled from upright folding and thickening at and above the brittle-ductile interface.

The influence of orogen parallel lower crustal flow in the analogue models is also clearly illustrated when the cross-sectional structure is compared to the surface strain field (Fig. 3). In vise models with a non-buoyant weak lower crust, strain localisation in the frictional upper crust results in development of curvilinear shear zones, whose kinematics change along strike as the flow direction in the ductile crust reverses. In nature, such zones would contain structures characteristic of transpression, although the tectonic boundary conditions have no oblique component of convergence. Note also in this model shear zones form parallel to the axial traces of upright doubling plunging folds. Local amplification of these folds (due to air bubbles?) results in domes cored by ductile crust (Fig. 3a).

Vise models with a buoyant weaker lower crust (weaker by a factor of 0.86) develop markedly different surface deformation fields (Fig. 3b) and cross-sectional geometries. In these models, upper-crustal deformation is characterised by conjugate systems of strike-slip faults, which accommodate orogen parallel extension, and the development of one major orogen-sub parallel thrust-syncline-anticline structure, which accommodates the bulk of horizontal shortening and vertical thickening strain. Decoupling of lower- from upper-crustal deformation is more pronounced in models with non-buoyant lower crust, as evidenced by a lack of buckle folds at the brittle-ductile interface, and the confinement of shear zones to the upper crust.. The differences in structural style compared to models with non-buoyant lower crust are attributed to the “water bed” effect of the buoyant, weak lower crust (e.g., Bailey 2001).

Implications

3D analogue models highlight the profound effect that syn-convergent orogen parallel flow can have on the development of structures at different levels of the crust (Fig. 4). Upper crustal deformation is characterised by the development of orogen parallel upright folds and vertical curvilinear transpression zones, whose kinematics are governed by the polarity of lower crustal flow, rather than the tectonic boundary conditions. Upper crustal deformation is decoupled from lower crustal strain, which is characterised by vertical flattening and orogen parallel stretching. The boundary between

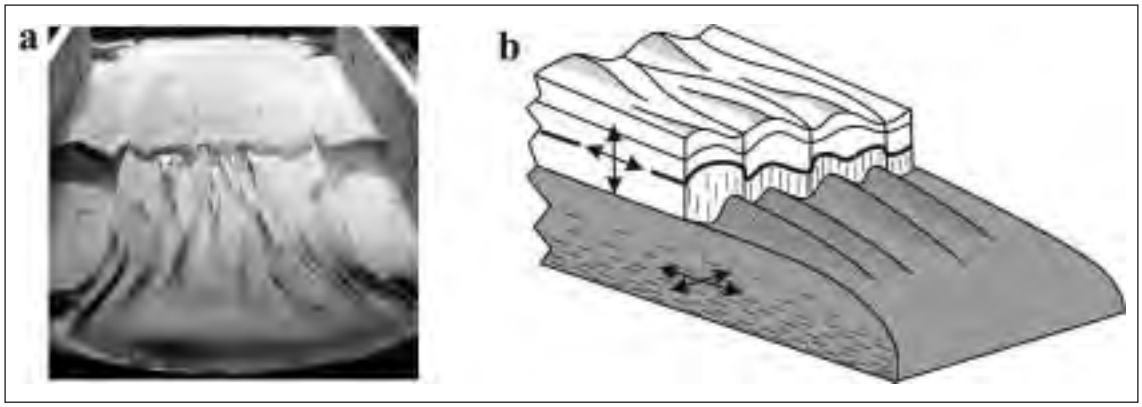

Fig. 4. (a) Oblique view of vise model with non-buoyant lower crust after ~50% shortening. The brittle upper curst has been removed by vacuum on one half of the model, revealing the 3D structure of the brittle-ductile crust interface. (b) Interpretation sketch summarising the different structural characteristics developed in the upper (white) and lower crust (grey) of the vise models.

these deformation regimes is transitional and occurs below the brittle-ductile interface in the models (Fig. 4). Different upper crustal deformation styles are developed in models with non-buoyant versus buoyant lower crust. Comparison between 3D analogue and 2D numerical experiments shows that orogen-parallel flow results in the suppression of surface relief and the net amount of crustal thickening. In nature, this may result in the development of lower pressure metamorphic assemblages in orogens that have undergone lower- crustal flow.

Simple vise models provide insight into how different strain regimes can develop at different levels of the crust, in response to boundary conditions and rheological structure. The experiments also illustrate how in some cases interpretation of local structures in the field (e.g., transpressive shear zones, deep crustal extensional fabrics) might lead to erroneous inferences about paleo-tectonic boundary conditions (e.g., oblique convergence; post-orogenic collapse).

REFERENCES

- Axen, G.J., Selverstone, J., Byrne, T., & Fletcher, J.M. 1998. If the strong crust leads, will the weak crust follow? GSA Today, 8, 1-8.
- Bailey, R.C. 2001. Dynamical analysis of continental overflow. Journal of Geodynamics, vol.31, 293-310.
- Burg, J.-P., Sokoutis, D. & Bonini, M. 2002. Model-inspired interpretation of seismic structures in the Central Alps: Crustal wedging and buckling at mature stage of collision. Geology 30, 643-646.
- Collins, W.J. & Vernon, R.H. 1991. Orogeny associated with anticlockwise P-T-t paths: evidence from low-P, high-T metamorphic terranes in the Arunta Inlier, central Australia. Geology, 19, 835-838.
- Davy, P. & Cobbold, P. 1988. Indentation tectonics in nature and experiment, 1. Experiments scaled for gravity. Bulletin of the Geological Institute, University of Uppsala, New Series, 14, 129-141.
- Ellis, S., Beaumont, C., Jamieson, R.A., & Quinlan, G. 1998. Continental collision including a weak zone: The vise model and its application to the Newfoundland Appalachians. Canadian-Journal-of-Earth-Sciences, 5, 1323-1346.
- Fullsack, P. 1995. An arbitrary Lagrangian-Eulerian formation for creeping flows and its application in tectonic models. Geophysical Journal International, 120, 1-23.
- Garde, A., Chadwick, B., Grocott, J., Hamilton, M.A., McCaffrey, K.J.W., & Swager, C.P. 2002. Mid-crustal partitioning and attachment during oblique convergence in an arc system, Paleoproterozoic Ketilidian orogen, southern Greenland. Journal of the Geological Society, London, 159, 247-261.
- Hajnal, Z., Lucas, S.B., White, D.J., Lewry, J., Bezdan, S., Stauffer, M.R. & Thomas, M.D. 1996. Seismic reflection images of strike-slip faults and linked detachments in the Trans-Hudson Orogen, Tectonics, 15, 427-439.
- Jackson, S. & Cruden, A.R. 1995. Formation of the Abitibi greenstone belt by arc-trench migration. Geology, 23, 471-474.
- Klepeis, K.A., Clarke, G.L., Gehrels, G. & Vervoort, J. 2004. Processes controlling vertical coupling and decoupling between the upper and lower crust of orogens: results from Fiordland, New Zealand. Journal of Structural Geology, 26, 765-791.
- Oldow, J.S., Bally, A.W., Avé Lallemant, H.G., and Leeman, W.P. 1989, Transpression, orogenic float, and lithospheric balance: Geology, v. 18, p. 991-994.
- Tapponnier, P., Peltzer, G., La Dain, A.Y., Armijo, R. & Cobbold, P. 1982. Propagating extrusion tectonics in Asia: New insights from simple experiments with plasticene. Geology, 10, 611-616.
- Vauchez, A. & Nicolas, A. 1991. Mountain building: strike-parallel motion and mantle anisotropy. Tectonophysics, 185, 183-201.

2.5 D THIN-SHELL GRAVITATIONAL MODELING IN THE WESTERN/CENTRAL ALPS: COMPARISON WITH SEISMOTECTONIC SYNTHESIS 2-07

B. Delacou, C. Sue, J.D. Champagnac, M. Burkhard, C. Allanic(*), N. Béthoux(**)

(*) Institut de Géologie, Université de Neuchâtel – 11, rue Argand - Case Postale 2 - 2007 Neuchâtel - SUISSE

(**) UMR Géosciences Azur - 250, rue Albert Einstein Sophia Antipolis - 06560 Valbonne - FRANCE

Summary

The strain and stress field of the western/central alpine arc is examined by the way of 2.5D. finite element modelling and through comparisons with a recent seismotectonic synthesis (Delacou et al., in press). Models with fixed boundary forces are tested with different crustal geometries to infer the response of buoyancy forces (gravitational potential anomalies). The contrasted tectonics, characterized by an overall orogen-perpendicular extension in the high topographic core of the belt and local compressive/transpressive in external zones appears to be ongoing a gravitational effect, in response to crustal heterogeneities. Apulian rotation, tested in our models, have a minor effect on the current strain/stress field of the alpine realm. Nevertheless, it could help to explain the orogen-parallel dextral mode of faulting observed all along external zones from the northern Valais to the Argentera external crystalline massif. In a context of an ongoing convergence between African and European plates, our results rise up the issue of the consequences of this convergence in the alpine realm. Our interpretation is that no collision processes are currently observed in the alpine belt, and that buoyancy-driven stresses are governing a predominant part of the present-day geodynamics of the western/central Alps.

Abstract text

The strain and stress states of the alpine realm are defined through the analysis of a 389 focal mechanisms database and the characterization of two parameters (Fig. 1): the direction of deformation (P- and T- seismotectonic axes) and the orientation of inverted stress axes ($\sigma1$, $\sigma2$, $\sigma3$) obtained from inversion of focal plane solutions.

The directional information is visualized (Fig. 1) through the projection of the P- and T-axes onto the horizontal plane, and the vectorial interpolation of these directions between focal mechanisms locations. On figure 1, P-axes trajectories are visualized in compressional to transpressional areas while T-axes are represented in extensional to transtensional areas (see B. Delacou et al. for details). The resulting P- and T-axis trajectories map reveals a globally orogen-perpendicular extension prevailing in internal zones, with T-axes striking N-S in the Valais to E-W behind the Pelvoux massif and SW-NE behind the Argentera massif. In external zones, P-axes trajectories define a large scale fan pattern convergent toward the Pô plain, swinging of 120° from a NNW direction in eastern Switzerland to NW in front of the Belledonne massif, and SW in front of the Digne nappe.

Stress inversion methods have been applied to subsets of the focal mechanisms data base to constrain the present day stress field of the alpine arc. For the details of the analysis and calculations, see (Delacou et al., submitted). The result of the inversion (Fig. 1) reveals a generalized extensive stress field in the core of the belt, with $\sigma3$ radial to the structural grain of the alpine arc, contrasting with localized zones of transpression in external zones, with radial fan-shapped $\sigma1$ converging toward the Pô plain. Strike-slip faulting occurs everywhere in the belt but is especially abundant in external zones.

The close correlation which can be seen between areas of high crustal thicknesses (correlated with high average topography) and the generalized alpine extensional tectonics leads to propose a geodynamic model where the current alpine regime is controlled, at least partly, by internal gravitational body forces. In this model, gravitational potential anomalies (GPA) driven by crustal thickness heterogeneities between internal and external zones, will induce extension in high internal zones. In response to this extensive tectonics, external areas will undergo compression/transpression in an attempt to equilibrate crustal thicknesses. This kind of model will induce radial extensive stress axes in high elevation internal zones and radial compressive stress axes in low elevation external zones.

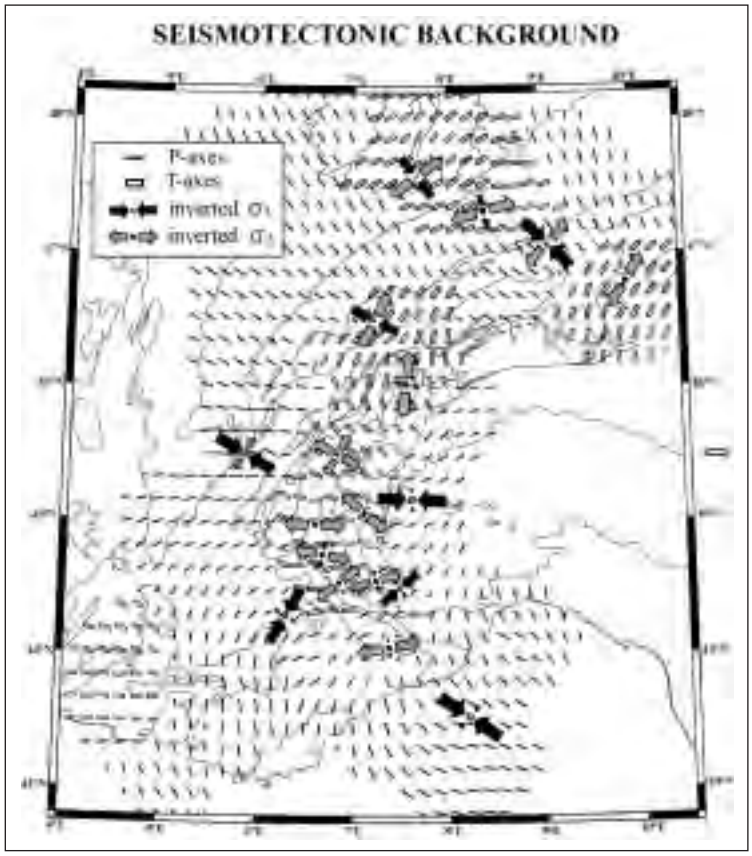

Figure 1: Strain /Stress regime infered from the analysis of a 389 focal mechanism database (Delacou et al., in press).

The 2.5D thin-shell finite element code SHELLS is used to model the stress and strain field of the western/central alpine arc. A detailed description of the method is given in (Bird, 1989; Kong and Bird, 1995; Bird, 1999). Basically, this code solves stress equilibrium and conservation of mass with presumed rheologies and densities. The models are built with a 3D structure of topography and crust/lithosphere
thicknesses and solve the momentum equation in a vertically integrated form (2D approximation), resulting in a "2.5D finite element method". This thin-shell approximation leads to solve only horizontal components of the momentum equation (the vertical one being replaced by the isostatic approximation) and no vertical shear traction is considered on vertical planes (flexural strength is ignored). The rheologies are presumed anelastic, with thermally activated nonlinear dislocation creep in the lower crust and mantle and Mohr-Coulomb frictional plasticity in the shallow parts of crust and upper mantle. A given initial surface heat flow and assumption of steady state thermal conduction are used to compute the 3D temperature model with constant but distinct heat productivity and conductivity for crust and mantle.
The models presented in this study include 295 cells used in the finite element technique. The boundaries of the models have been designed to reflect the limits of the western/central Alps, as well as the limits of our seismotectonic study. Toward the north, it has been fixed at the external limit of the Molasse Basin, toward the northwest and west to the Jura and subalpine chains external limits, toward the southwest to the lower Rhone valley, toward the south to the Ligurian margin and toward the southeast to the Pô plain. At the eastern limit of the model, an arbitrary north-south running boundary has been fixed, with free tangential sliding behaviour, limiting our study area to the western/central Alps.

3 different types of model have been computed and compared to the seismotectonic regime:

- *fixed boundaries/isostatic model*: As a first step, a simple 3D model has been constructed with the assumption of isostatic equilibrium (model A, Fig.2). The calculated stress field is characterized by

radial fan-shaped extension in the regions of high topography in the core of the belt and by radial fan-shaped compression in external zones. This pattern corresponds to GPA equilibration between regions of positive GPA in the inner areas, where high topography is correlated with high crustal thicknesses (according to the isostatic equilibrium assumption) and regions of "normal" GPA (near zero) in external zones, with little topography and the Moho close to a normal position (around 30 km). This configuration results in an extensive stress state in the core of the belt, that tends to reduce overthickened crustal material, and in a compressive stress state in external regions in response to the extension of the inner areas.

- *fixed boundaries/realistic crustal model*: To infer a more realistic 3D crustal structure, we have constructed a model (model B, Fig.2) with a Moho geometry interpreted from wide angle seismic experiments (Waldhauser et al., 1998). This result in a more complicated 3D geometry than in model A in which the highest topography is not directly overlying its crustal root. The resulting stress field appears to be more complicated than in model A. However, the general trend, that is to say inner extension vs. external compression is still present (like in model A), but regional variations can be observed.

- *rotational models*: Rotation has been supposed to play an important role in the dynamic of the western/central Alps, since at least Oligo-Miocene times (*e.g*. Collombet et al., 2002). Concerning the stress field (model C, Fig.2), the results of the rotation models appears to be not much different from the fixed models at the large scale, as radial extension is still recognized in internal zones and radial fan shaped compression characterize the external zones (at least in the northwestern part). Differences from fixed models can be seen in regional reorientation of stress axis: in the southwestern Alps, in the eastern boundary (where rotation induce frontal compression south of the alpine belt) and near the Pô plain boundary.

In conclusion, 2.5D numerical modeling, and the comparisons with large-scale seismotectonic analysis, has shown the major role of body forces in the current stress field of the western alpine arc. Actually, the balance of GPA is shown to be a very good candidate to explain the radial contrasted stress field in the western/central Alps (extensive in the core of the belt, locally compressive at the periphery). The role of rotative boundary forces is less obvious, as only regional stress reorientations appear in our models. Nevertheless, rotation models seem suitable to explain the overall dextral strike-

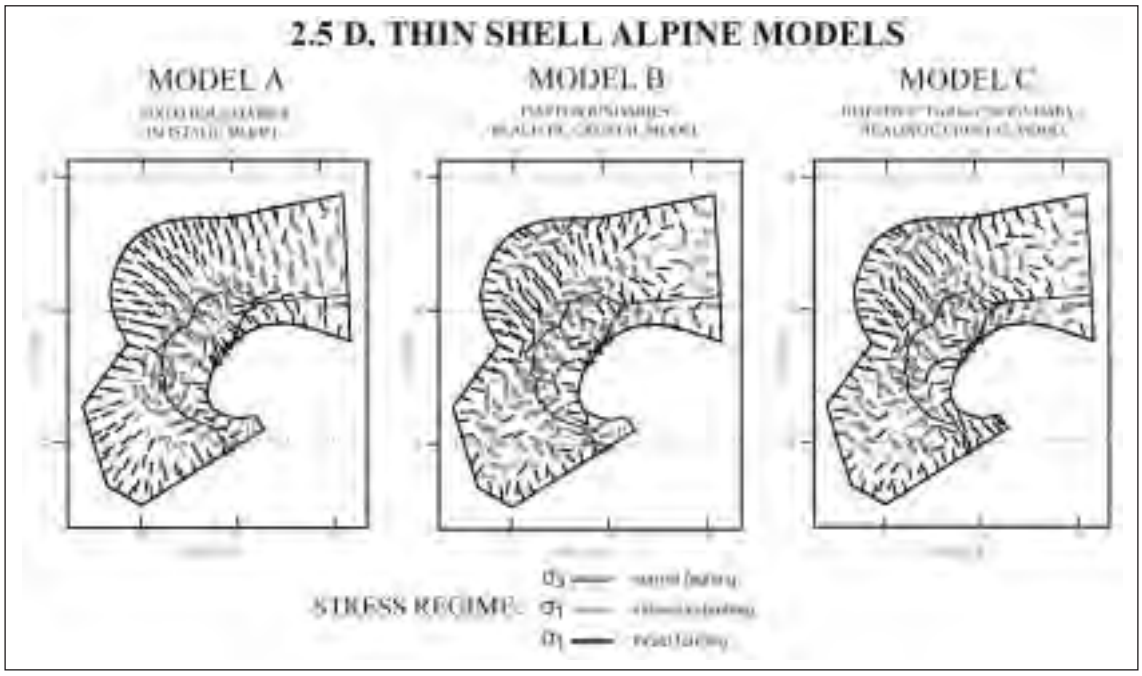

Figure 2: Modelled stress regime of the alpine arc. See the agreement with the seismotectonic regime (Figure 1).

slip mode of faulting following the external zones (*i.e*. northern-Valais/Mont Blanc/Belledonne/ Durance dextral lineaments). This study rises up the issue of the consequences of the still ongoing Europe/Africa convergence in the alpine geodynamics and more generally in the western European one. This convergence, estimated from 3 to 8 mm/year in a N to NW direction at the longitude of the Alps (see Nocquet, 2002 for a complete revision) could be consumed in different geodynamic areas between European and African stable continents, such as the maghrebian belts (as observed with the Ml 6.7 compressive earthquake that occurred the 21 mai 2003 in offshore Algeria), the Apennines, the Dinarides, the calabrian subduction, etc. In our study, no direct
effects of this convergence are useful to explain the stress field of the western/central Alps, as it is mostly controlled by internal body forces. Thus, the Adriatic micro-plate seems to be decoupled from the African plate, and the interpretation of an Apulian's African promontory should be revised considering the current geodynamics of the Alps.

REFERENCES

- Bird P. (1989). New finite element techniques for modeling deformation histories of continents with stratified temperature-dependent rheology. J. Geophys. Res., 94(B4), 3967-3990.
- Bird P. (1999). Thin-plate and thin-shell finite-element programs for forward dynamic modeling of plate deformation and faulting. Comput. Geosci., 25, 383-394.
- Collombet M., Thomas J. C., Chauvin A., Tricart P., Bouillin J. P. and Gratier. J. P. (2002). Counterclockwise rotation of the western Alps since the Oligocene: New insights from paleomagnetic data. Tectonics, 21, 352-366.
- Delacou B., Sue C., Champagnac J. D. and Burkhard M. (in press). Present-day geodynamics in the bend of the western and central Alps as constrained by earthquake analysis. Geophys. J. Int.
- Kong X. and Bird P. (1995). SHELLS: A thin-shell program for modeling neotectonics of regional or global lithosphere with faults. J. Geophys. Res., 100(B11), 22129-22131.
- Nocquet J.-M. (2002). Mesure de la déformation crustale en Europe occidentale par Géodésie spatiale. Thèse de doctorat, Université de Nice, 307pp.

SOME KEY INGREDIENTS FOR SIMULATION OF OROGENIC PROCESSES AT GEOLOGICAL AND SEISMIC TIMESCALES

2-08

S. Ellis(*), G. Schreurs(**), B. Stöckhert(***)

(*) Institute of Geological and Nuclear Sciences, PO Box 30-368, Lower Hutt, New Zealand
s.ellis@gns.cri.nz
(**) Institute of Geological Sciences, University of Bern, Switzerland
(***) Institute of Geology, Mineralogy, and Geophysics, Ruhr University, Bochum, Germany

Summary

Considerable insight has been gained by using analogue and numerical models to simulate processes at convergent margins. Here, we would like to review two of the key "ingredients" that must be considered when conducting these simulations: (1) the ability of the earth's crust to localize deformation; and (2) the interplay between deformation at different timescales.

1. Localization within crustal materials

Some model studies have suggested that continental plate boundary deformation occurs by broad-wavelength, diffuse deformation (although it is still "localized" at scales of 100-1000 km) while others have suggested that localization at smaller length-scales, along faults and ductile shear zones, plays a key role to orogenic development. These two views may be compatible if we consider them at different timescales; for example, individual faults may be active on timescales of 100,000 years but over longer timescales there may be a progression in fault activity over different parts of the system. In certain cases, though, localization at short length-scales may completely control the subsequent deformation of the orogen.

Localization effects within the crust can be broadly categorised in terms of *inherited*, *imposed*, and *dynamic* **[1]**. *Inherited* localization results from previous deformation. An example is the Tertiary

deformation of the European Alps, which shows strong localization due to strength and material contrasts inherited from the previous extensional and subduction-accretion phases **[2][3]**. In addition, crust can undergo *imposed* localization due to localized boundary conditions applied around it. Imposed localization in some cases may be controlled by subduction of underlying mantle lithosphere along a shear zone (e.g., **[4], [5]**), but erosion may also impose localization on the crust, due to the thermal weakening that accompanies it and the reduction in topographic load (e.g., **[6]**). At shorter timescales, imposed localization can also occur due to a stress transfer between upper crustal faults and mid- and lower-crustal ductile shear zones (e.g., **[1], [7]**).
Dynamic localization is perhaps the most difficult to understand and to model. It results from the inherent properties of the material, and may interact with inherited and imposed localization to various degrees.

Frictional (upper crust) localization

Brittle upper crust can clearly localize dynamically by development of faults. The similarity between features seen in sandbox experiments and real structural examples is due in part to the fact that sand is a elasto-frictional, dilatant material, with dynamic localization properties similar to those of brittle crust **[8]**. In the sandbox experiments, the "faults" are dilational shear zones that broaden to a width of about 1-2mm. In nature, faults consist of zones 1-100m thick showing significant fluid-alteration as documented by presence of clay-rich gouge and cataclasite.
Most sandbox experiments of frictional thin-skinned compression show interactions between dynamic and imposed localization, because they are conducted with very strong boundary conditions applied to the edges (e.g., **[9], [10], [11]**). These strong boundary conditions control the overall form of the deformation that develops, but frictional localization controls some of the details such as episodic thrusting or accretion.
Until recently, many numerical model experiments of collision zones did not include frictional localization and softening with increasing strain (e.g., **[12]**). Gross features were similar to the sandbox experiments, provided strong boundary conditions (e.g., assumed mantle lithosphere shear zones, or embedded faults) were included. However, the necessity for modelling softening and localization to match analogue experiments is apparent (e.g., Figure 1). Frictional localization can be introduced in numerical models by an explicit strain-softening parameter (e.g., **[6], [13], [5]**) or by

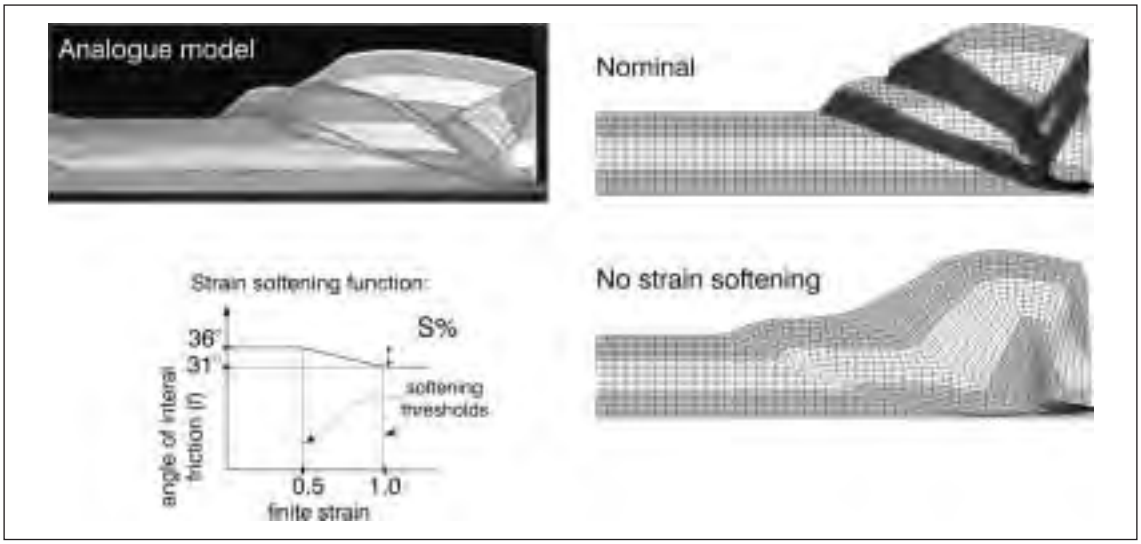

Figure 1. An illustration of the importance of frictional strain softening to thrust wedge development, using a comparison between analogue and numerical models (modified from [11]). Panel at upper left shows tomographic scan of sandbox experiment, sand layer thickness initially 3cm, where right-hand wall has advanced inwards 8 cm. Panels at right show numerical model results (scaled) for same relative amount of convergence. In the top right model, sand is represented by a frictional, strain-softening rheology as shown in graph below. The lower right panel shows the same model but without frictional strain softening. The overall geometry remains similar to the analogue experiment, but localization details are lost.

inherent frictional localization in elasto-plastic strain hardening/softening dilatant materials (e.g., **[14], [15]**). In either case, there is a competition between the dynamic frictional localization and other (imposed, inherited) effects. Which wins out depends on the relative strength of forces operating within the crust (e.g., see **[13]**).
Many major faults seen at the surface can be traced into the mid- and lower-crust by seismic imaging (e.g., **[16]**). Studies of exhumed deep extensions of faults show mylonite zones indicating localization of ductile strain accompanied by grain size reduction. For the Alpine Fault of New Zealand, strain estimates suggest deformation is localised within a 1-2 km wide shear zone down to depths of 25-30 km **[17]**. In this case, it appears that the ductile shear zone is intimately linked to the overlying brittle fault. This may be due to effects of rapid erosion, but also to imposed localization of lower crust from elastic loading by the fault, a topic we explore in section 2.

Ductile (lower crust) localization

Dynamic ductile localization of mid and lower crust can result from shear heating feedbacks, fluid release, grain-size reduction along shear zones, the formation of low-viscosity melts and other related effects (e.g., **[18], [15], [1], [19]**). It is difficult to model dynamic ductile localization effects in analogue experiments, especially since the most commonly used material representing viscous flow is a linear viscous polymer. More realistic representations of ductile localization in analogue models represents a major challenge for the future.
Erosion (a form of imposed localization that acts primarily on the lower crust) can be a very important control on gross features that develop in a collisional orogen. The feedback between erosion and tectonics has been explored in many numerical models **[20][21][22][23]** and analogue models **[24][25]**. Once considerable material has been uplifted along a fault, the fault and its extension into the lower crust can become a major, crustal-scale feature that controls subsequent development of the orogenic wedge. Asymmetric erosion may help to explain the development of long-lasting faults in some regions (e.g., the Alpine Fault of New Zealand) while other faults only remain active for shorter periods of time **[26]**. Because some of this feedback is due to thermal advection, it is quite hard to model in analogue experiments.
In summary, many factors can lead to localization in collisional orogens over geological timescales. A future challenge for modellers is to accurately represent these processes, to determine which of these are important for a particular geological setting, and how they interact.

2. Reconciling deformation at short (seismic) and long (geological) timescales

At timescales of the seismic cycle (1-1000 years), the effect of elastic loading and unloading of the crust becomes an important ingredient that must be incorporated in models of collision. Surface deformation over these time intervals is often modelled using elastic dislocation theory, which approximates the earth as an elastic half-space with embedded faults, and creeping patches at depth that load the faults over the interseismic period (e.g., **[27]**). Although dislocation models are overly simplistic, they do seem to produce a good, though non-unique, solution by inverting observed coseismic and interseismic surface deformation to obtain slip at depth. The supposition has been that, in the short-term, most of the crust loads and unloads elastically, and that faults are loaded from below by ductile creep along localized shear zones. The only permanent deformation predicted in this case is due to the cumulative motion along the fault and associated erosion and sedimentation (e.g., **[28]**). However, the detection of post-seismic creep after major earthquakes suggests that other, inelastic processes may also contribute (see summary in **[29]**).
Several numerical model groups have begun to investigate the integrated effect of many seismic cycles to produce permanent deformation. These models include embedded faults (contact surfaces), lower crustal shear zones, erosion and sedimentation effects, and long-term tectonic boundary conditions operating on the system. In some cases this has successfully reconciled long- and short-term deformation rates across collisional orogens (e.g., **[30], [31]**). These types of models also highlight the link between upper and lower crustal localization on short timescales.
A particular question that may be asked is: does the lower crustal shear zone drive faulting (by loading the fault over the interseismic period), or is it the other way around? (e.g., **[32]**). The answer may depend on how long-lived the fault has been **[26]**. A possible progression from the shortest (fault)

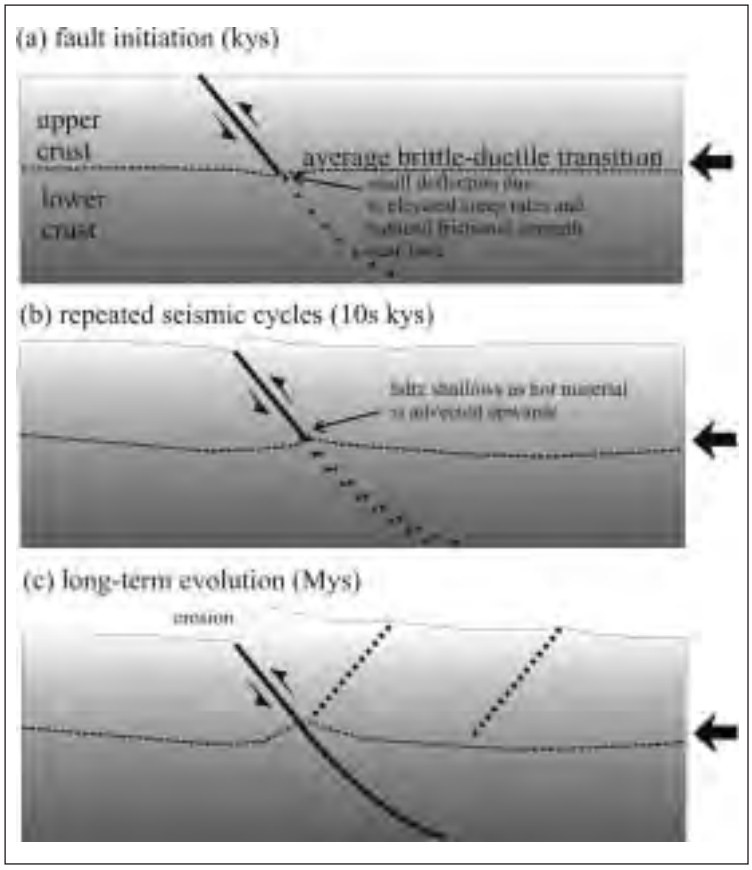

Figure 2. Schematic illustration showing effect of localization in frictional upper crust on ductile lower crust, with repeated activation of an upper crustal fault (solid line). (a) During fault initiation, stress transfer from upper crust imposes localization on the lower crust. (b) With repeated seismic cycles dynamic localization in ductile crust may occur, and stress transfer occurs in both directions. (c) On geological timescales, imposed localization from erosion causes advection of hot material towards surface and further localizes lower crust. A through-going fault/shear zone develops. Secondary faults (dashed lines) may be initiated, as topographic forces broaden the collision zone.

timescale to geological timescales is illustrated schematically in Figure 2. It can be shown that a sudden slip event along a fault in the brittle crust can load the mid-crust elastically, and that this elastic stress may then be relieved by post-seismic ductile creep **[7]**. Even when ductile crust has not dynamically softened, this imposed stress is enough to focus ductile deformation in a thin shear zone extending below the fault (Figure 2a). However, with repeated motion along the fault, dynamic softening due to shear heating, fluid release, and grain-size effects in the lower crust may enhance lower crustal localization (Figure 2b). This will further localize overall crustal deformation, and on long timescales (Figure 2c) with additional enhancement by erosion and thermal weakening, the entire crust may become localized along one major fault underlain by a weak ductile mylonite zone.

Some aspects of this process can be illustrated using numerical models that incorporate full elasto-visco-plastic behaviour over a seismic cycle (Figure 3). Figure 3 shows a model of a 30 km-thick crust with Coulomb frictional yield strength, linear elastic behaviour, and thermally-activated power-law creep properties of wet quartz, where the geothermal gradient is assumed to be 20ºC/km. A contact surface representing a dipping 30º reverse fault is imposed, with friction coefficient $\mu = 0.1$. Initially, a setup phase is run where the crustal layer is compressed from the right-hand side at 1 cm/yr. During this phase, the model determines by itself which parts of the fault creep and which parts are locked, according to the ambient strength of surrounding crust, which decreases with increasing depth. As a result, at the end of this period, a steady-state stress field is generated (Figure 3a) in which most stress has accumulated in the strong, upper, frictional crust. Figure 3a shows how the presence of a weak, creeping fault can perturb differential stress away from the normal "Christmas tree" strength profile. The fault surface is then locked for 500 years. The elastic stresses that had previously built up around the fault are relieved by ductile creeping in the mid- and lower-crust, in a lobe of enhanced strain-rate extending from the fault surface (Figure 3b). Figure 3b illustrates how imposed localization resulting from a creeping, upper crustal fault, can cause localization in the ductile lower crust, with background strain-rates enhanced by a factor of ca. 10.

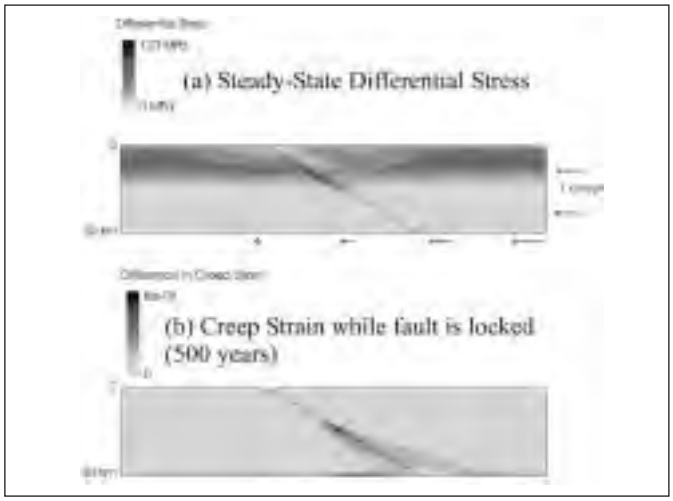

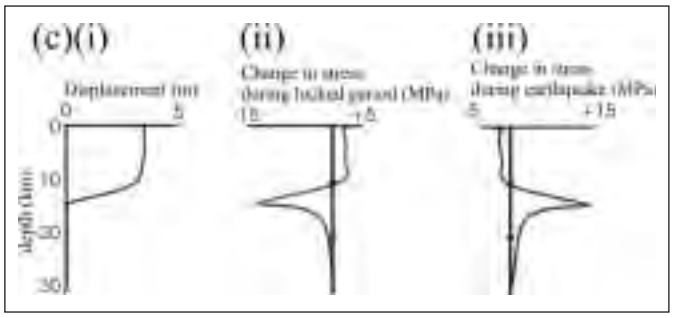

Figure 3 (a) Differential stress after 1 My in a model compressed from the side at 1 cm/yr, with a shallow dipping reverse fault with a reduced frictional strength. (b) Creep strain during a subsequent step in which the fault surface is locked. (c) (i) Plot of slip along the fault during subsequent ("earthquake") phase (ii) stress change during interseismic (locked) phase (iii) stress change during "earthquake" phase. Note that dynamic stresses are not included in the model.

After the 500 year locked period, the fault is released (coefficient of friction back to 0.1) for a short time, to represent an earthquake. Figure 3c plots fault displacement with depth, change in differential stress during the previous locked phase, and change of differential stress during the earthquake phase. Displacement along the fault naturally falls away between 10 and 15km depth, due to the increasing weakness of surrounding ductile crust. The middle panel shows the stress accumulated along the fault during the locked (interseismic) interval, with positive stress (as expected) in the upper, frictional part, and negative stress due to stress release by ductile creeping (cf. Figure 3b) in the mid-crust. The fact that the stress change during the interseismic period is negative in the mid-crust suggests that, in the absence of dynamic lower crustal localization, the lower crust does not load the upper crustal fault significantly cf. ambient (background) stressing rates. The right-hand panel shows how the stress change from the interseismic period is balanced by a release of stress along the upper part of the fault during the "earthquake", while the fall-off in slip with depth creates a positive stress in the mid-crust, which will be relieved during the following interseismic period.

What happens after multiple seismic cycles, if dynamic localization is induced in the mid and lower crust? Figure 4 shows results for a similar model to that of Figure 3, but where the area immediately around the fault has been thermally weakened by shear heating. In this case, slip falls off at shallower depths of 10-12 km (left-hand panel). The weak ductile shear zone transfers stress to the lower end of the frictional fault during the interseismic (locked) period (middle panel). This suggests that a ductile shear zone is capable of loading a fault, provided it has been weakened during dynamic localization. The question of which controls deformation – the fault or the ductile shear zone- therefore depends on the degree of weakening and localization that has taken place along both. The inversion of observed interseismic surface deformation by models including creeping patches at depth, which are assumed to load the fault, may be an over-simplification of the true process, which Figures 3 and 4 suggest is a complex mix of loading, stress transferral, and stress relaxation between upper and lower crust.

This topic remains a major challenge to modellers, and further experiments are needed to understand the relationship between the seismic cycle and deformation at geological timescales in the crust.

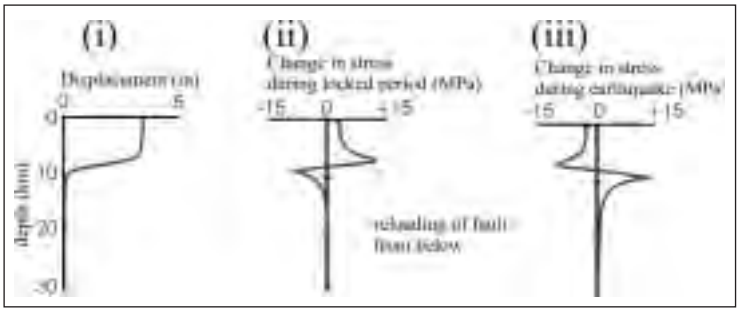

Figure 4. (i) Plot of slip along the fault during "earthquake")phase for model with thermal weakening along ductile shear zone beneath fault (ii) stress change during interseismic (locked) phase (iii) stress change during "earthquake" phase.

Other ingredients not covered here

The topics covered above are by no means an exhaustive list of ingredients that need to be considered when modelling collisional settings. For example, another key factor is the role of fluid pressure variations in the mid- and lower crust (e.g., **[33], [34]**). In particular, the buildup of overpressured fluids may act to enhance localization in compressional settings **[35]**. We have also ignored the link in deformation between crust, lower lithosphere, and asthenospheric flow, and the possibility of changes in material behaviour due to metamorphism, fluids, and generation of melts.

Nevertheless, we feel that the topics outlined here- the interactions between different forms of localization at long (geological) and short (seismic/interseismic) timescales- are important areas of research for future models, and will increase our understanding of collisional processes.

REFERENCES

[1] Montesi, L., and Zuber, M., JGR 107, B3, 10.1029/2001JB000465, 2002;
[2] Pfiffner, A., Ellis, S., and Beaumont, C, Tectonics, v. 19, 1065-1094, 2000;
[3] Buiter, S., and Pfiffner, A., Tectonics, 22, 1057, 10.1029/2002TC001417, 2003;
[4] Beaumont, C., Ellis, S., Hamilton, J., and Fullsack, P., Geology, 24, 675-678, 1996;
[5] Gerbault, M., Henrys, S., and Davey, F, JGR, 108, B7, 2341, 10.1029/2001JB001716, 2003;
[6] Ellis, S., Wissing, S., and Pfiffner, O.A., Int. J. Earth Sciences (Geol Rundsch), v. 90, 168-180, 2000;
[7] Ellis, S., and Stöckhert, B., JGR, in press, 2004;
[8] Lohrmann, J., Kukowski, N., Adam, J., Oncken, O., JSG, 25, 1691-1711, 2003;
[9] Malavieille, J., Bull. Soc. Geol. Fr., 26, 129-138, 1984;
[10] Kukowski, N., Malavieille, J., Gutscher, M.-A., Lallemand, S.E. & T.J. Reston. Marine Geology, Vol. 187/3-4, 1-13, 2002;
[11] Ellis, S., Schreurs, G., and Panien, M., JSG, in press, 2004;
[12] Willett, S. D., Beaumont, C. and Fullsack, P., Geology, v. 21, 371-374, 1993;
[13] Huismans, R., and Beaumont, C., JGR, 108, 2496, 2003;
[14] Hobbs, B., Mülhaus, H., and Ord, A, in Rheology and Tectonics, GSA Spec Pub 54, 143-165, 1990;
[15] Regenauer-Lieb, K., and Yuen, D., Earth Sci Rev, 63, 295-349, 2003;
[16] Davey, F., and 6 co-authors, NZJGG, 38, 601-604, 1995;
[17] Norris, R., and Cooper, A., JSG, 25, 2141-2157, 2003;
[18] Braun, J., and 6 others, JGR, 104, B11, 25167-25181, 1999;
[19] Beaumont C, Jamieson RA, Nguyen MH, Lee B, Nature, 414 (6865), 738-742,2001;
[20] Koons, P., Geology, 18, 679-682, 1990;
[21] Beaumont, C., Fullsack, P., and Hamilton, in Thrust Tectonics, pp1-18, 1992;
[22] Batt, G., and Braun, J., Geophys. J. Int., 136, 403-420, 1999;
[23] Willett, S.D., J. Geophys. Res., 28957-29981, 1999;
[24] Mugnier, J.L., Baby, P., Colletta, B., Vinour, P., Bale, P., and Leturmy, P. Geology, v. 25, 427-430, 1997;
[25] Persson, K.S., and Sokoutis, D. Tectonophysics, v. 19, 323-336, 2002;
[26] Norris, R., abstract, 2nd Intl Symposium on slip and flow processes in and below the seismogenic region, Tokyo, Mar 10-14, 2004;
[27] Savage, J., JGR 88, B6, 4984-4996, 1983;
[28] King, G., Stein, R., and Rundle, J., JGR, 93, B11, 13307-13318, 1988;
[29] Cohen, S., Advances in Geophysics, 41, 133-231, 1999;
[30] Cattin, R., and Avouac, J.P, J. geophys. Res., 105, 13 389-13 407, 2000;
[31] Chéry, J., Zoback, M.D., and Hassani, R., JGR, 106, B10, 22051-22066, 2001;
[32] Iio, Y., Sagiya, T., and Kobayashi, Y., abstract, Tokyo, Mar 10-14, 2004;
[33] Petrini, K, and Podladchikov, Yu., J. met. Geol., 18, 67-77, 2000;
[34] Upton, P., Am. J. Sci., 298, 296-323, 1998;
[35] Hobbs, B., Ord, A., and Regenauer-Lieb, K., abstract, 2nd Intl Symposium on slip and flow processes in and below the seismogenic region, Tokyo, Mar 10-14, 2004.

NUMERICAL MODELING OF EXHUMATION FLOWS AND P-T PATHS IN SUBDUCTION ZONES

2-09

Taras V. Gerya

Ruhr-University of Bochum, (Sonderforschungsbereich 526), Germany,
Geologisches Institut - ETH - Zürich, CH-8092 Zurich, Switzerland
Institute of Experimental Mineralogy, Russian Academy of Sciences, 142432 Chernogolovka, Moscow, Russia

High-pressure (HP) and ultrahigh-pressure (UHP) metamorphic rocks are evidence that in subduction - collision zones rocks can return from depths of more than 100 km to the surface. The pressure-temperature paths calculated from these rocks are variable while the time constraints are narrow and indicate that exhumation rates can be as fast (e.g., Rubatto and Hermann, 2001) and even faster than plate velocities (several tens of cm/yr). As such, subduction cannot be considered as a single burial process; instead, return flow of a considerable portion of crustal and upper mantle material must be accounted for. In recent years, several tectonic models relevant to exhumation of HP and UHP rocks were discussed. These studies identified at least five types of exhumation flows:

1) Forced return flow in a subduction/tectonic channel (e.g., Hsu, 1971; Cloos, 1982; Mancktelow, 1995; Roselle and Engi, 2002; Gerya and Stoeckhert, 2002) extending to asthenospheric depths thanks to rheological softening of the overriding plate by water-bearing fluids releasing from the slab (Gerya et al., 2002, 2004;).
2) Compressional squeezing of weak ductile rocks composing the subduction/tectonic channel during incipient collision (e.g., Burov et al., 2001).
3) Syn-collisional exhumation of coherent and buoyant crustal units (Chemenda et al., 1995).
4) Hydrated partially molten diapiric structures ("cold plumes") propagating from slabs into the asthenospheric portion of the mantle wedge (Tamura, 1994; Hall and Kincaid, 2001; Gerya and Yuen, 2003; Gerya et al., 2004).
5) Hydrated partially molten wave-like structures ("cold waves") propagating upward along descending slabs (Gerya et al., 2004).

However, the following key problems remain unresolved:

- Which physical parameters control the development of these different exhumation flows in subduction zones?
- What are in details the lithological contents, structures, evolutions and relationships of these flows?
- Which P-T-deformation-time paths of high and ultrahigh-pressure rocks are characteristic for the different exhumation mechanisms?
- How these different exhumation mechanisms may fit geological data on (U)HP metamorphic rocks of both crustal and mantle origin, which are found in modern and older orogens (e.g., Rosen et al., 1972; Chopin, 1984; Sobolev and Shatsky, 1990; Schertl et al., 1991; Dobrzhinetskaya et al., 1996; Wain, 1997; Perchuk et al., 1999; Willner et al., 2000; O'Brien et al., 2001; Stöckhert et al., 2001).

The pressure (P)-temperature (T)-time (t) path of a rock represents a long-term record of its movement within the Earth's interior. Therefore, P-T-t paths are powerful tools for understanding geodynamic processes, and in the last 25 years many P-T-t paths have been worked out for (U)HP metamorphic rocks. However, with only few exceptions (Allemand and Lardeaux, 1997; Guinchi and Ricard, 1999; Roselle and Engi, 2002; Gerya et al., 2002) most of numerical studies of subduction related processes do not address P-T paths of (U)HP complexes. The huge amount of empirical data available on the P-T-deformation-time evolution of crustal and mantle rocks is at present not adequately used to check and interactively optimize numerical models of subduction/collision processes. Therefore, more precise modeling is needed to compare numerical results with geological information.

We performed 2D numerical experiments (including the simulation of metamorphic P-T-time paths) for the following three tectonic settings: (i) oceanic subduction (Fig. 1), (ii) subduction under a continental margin (Fig. 2) and (iii) transition from subduction to continental collision. Our results suggest that in all these settings the formation and exhumation (U)HP metamorphic rocks often involves forced flow in a self-organising subduction/tectonic channel reaching down to depths of >100

km, with a geometry controlled by subduction of crustal rocks and progressive hydration of the overriding mantle lithosphere (Gerya et al., 2002, 2004; Stöckhert and Gerya, in preparation). We propose that the internal structures of orogenic belts, with nappes of HP and UHP metamorphic units showing variable P-T-t histories, may have partially formed by extrusion from a subduction channel during the active continental margin stage, hence prior to collision. On the other hand, our experiments suggest that the formation of large coherent UHP complexes in continental collision zones can result from the temporary expansion of the subduction/tectonic channel during incipient continental collision, when it can form a wider and deep-reaching (>150 km) wedge of subducted crustal material. In our simulations, this crustal wedge is often characterized by temperatures in excess of 800°C, shows internal circulation flow pattern and decays within a few million years by upward

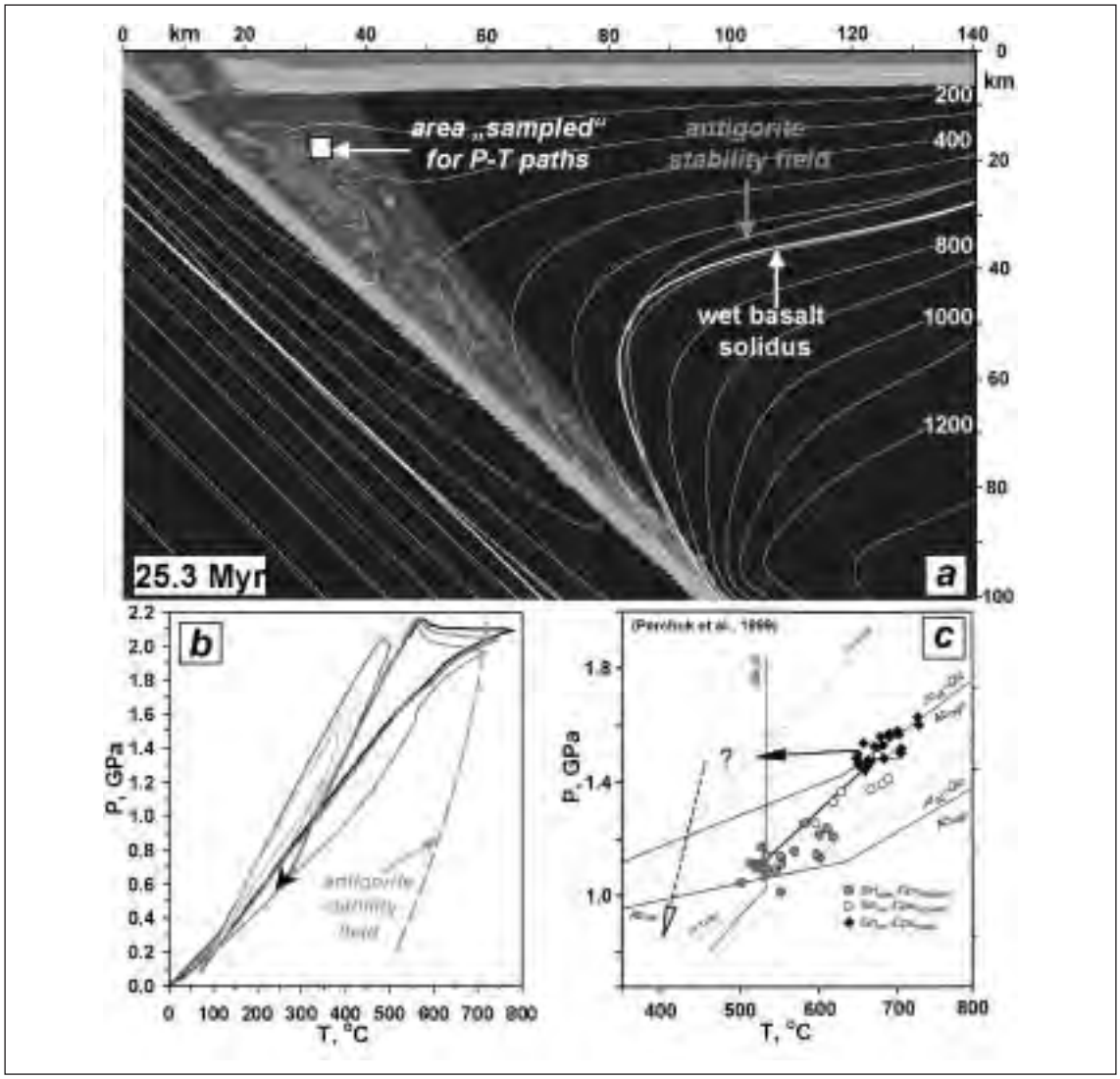

Figure 1. Development of simplified oceanic subduction model (a) and selected P-T paths (b) of high-pressure rock units (Gerya et al., 2002) compared with the counterclockwise P-T path (c) of high-pressure rocks of Yukon-Tanana terrane, Canada (Perchuk et al., 1999). Rock types in (a) are as follows (color code): red—sedimentary rocks; dark green and light green—basaltic and gabbroic oceanic crust, respectively; dark blue—unhydrated mantle; light blue—serpentinized mantle. White square in (a) show the area of numerical model where the P-T paths shown in (b) are sampled. Both clockwise and P-T paths are possible for slices of oceanic crust that became involved in the circulation. Counterclockwise P-T paths are found for slices that are accreted to the hangingwall at an early stage of subduction, and set free by the progress of hydration and softening in a more evolved stage, returning towards the surface in a cooler environment. This is consistent with tectonic interpretation for eclogites of Yukon-Tanana terrane (c) suggested by Perchuk et al. (1999).

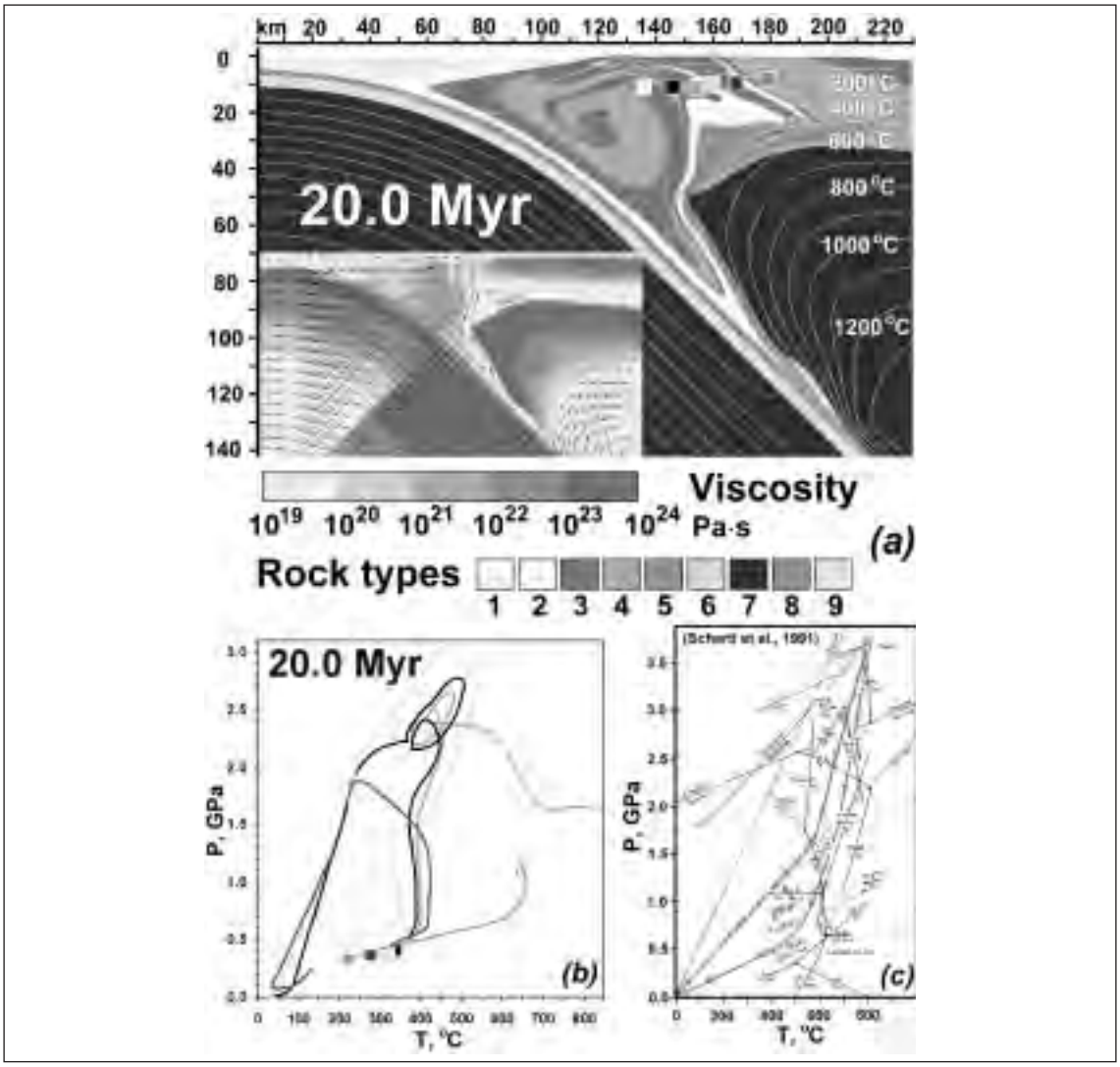

Figure 2. Development of continental margin subduction model (a) and selected P-T paths (b) of high-pressure rock units (Stöckhert and Gerya, in preparation) compared with the P-T path (c) of ultrahigh-pressure rocks of Dora-Maira massif, Western Alps (Schertl et al., 1991). Colored squares in (a) denote locations of modeled units. 1.5 million markers are used in this model to represent lithological field (a) with resolution about 300300 m. Staggered non-deforming grid resolution 1x1 km (~50 thousand nodes). See Fig. 2b for the model set-up. Rock types in (a) are as follows (color code): 1—weak layer on top of model (air, seawater), 2—sedimentary rocks; 3 and 4—upper and lower continental crust, respectively, 5 and 6—basaltic and gabbroic oceanic crust, respectively, 7—unhydrated mantle, 8—serpentinized mantle, 9—hydrated unserpentinized (i.e., beyond stability field of serpentine) mantle. Inset area in (a) shows viscosity (color code) and velocity (arrows) fields. Narrowed clockwise P-T paths are characteristic for ultrahigh-pressure rocks of crustal origin passed through the subduction channel. The shape of these paths is comparable with the P-T trajectory of ultrahigh-pressure rocks of Dora-Maira Massif, Western Alps (c) as constrained by Schertl et al. (1991).

extrusion. This buoyant escape of UHP crustal rocks may also be associated with necking and subsequent separation ("slab breakoff") of the subducted lithosphere, and related creation of an asthenospheric window. As the shape of the P-T path of an individual HP/UHP metamorphic unit depends on its specific trajectory in the subduction/tectonic channel or crustal wedge, an array of diverse, though interrelated, P-T paths rather then a single characteristic trajectory can be expected for (U)HP metamorphic complexes. The results of our siulations seem to reconcile with the metamorphic and structural record in several metamorphic belts: Franciscan Complex, Yukon-Tanana Terrain, Western Alps, Bohemian Massif, Hymalaya.

REFERENCES

• Allemand, P., Lardeaux, J.-M. (1997) Tectonophys., 280, 157-69.
• Burov, E., Jolivet, L., Le Pourhiet, L., Poliakov, A. (2001) Tectonophys., 342, 113-136.
• Chemenda, A.I., Mattauer, M., Malavieille, J., Bokun, A.N. (1995), EPSL, 132, 225-232.
• Chopin, C. (1984) Contrib. Mineral. Petrol., 86, 107–118.
• Cloos, M. (1982) Geol. Soc. Am. Bull., 93, 330-345.
• Dobrzhinetskaya, L.F., Green, H.W., II, Wang, S. (1996) Science, v. 271, p. 1841–1845.
• Gerya, T.V., Stoeckhert, B. (2002) Geophys. Res. Lett., 29(8), art. no. 1261, 102-1 – 102-4.
• Gerya, T.V., Yuen, D.A. (2003) EPSL, 212, 47-62.
• Gerya, T.V., Stoeckhert, B., Perchuk, A.L. (2002) Tectonics, 21, 6-1 – 6-19.
• Gerya, T.V., Yuen, D.A., Sevre, E.O.D. (2004) Geology, 32, 89–92.
• Guinchi, C., Ricard, Y. (1999) Geophys. J. Int., 136, 620-628.
• Hall P.S. and Kincaid C. (2001) Science, 292, 2472–2475.
• Hsu K.J., (1971) J. Geophys. Res., 76, 1162-1170.
• Mancktelow, N.S., (1995) J. Geophys. Res., 100, 571-583.
• O'Brien, P.J., Zotov, N., Law, R., Khan, M.A., Jan, M.Q. (2001) Geology, 29, 435-438.
• Perchuk, A.L, Philippot, P., Erdmer, P. Fialin, M. (1999) Geology, 27, 531-534.
• Roselle G.T., Engi, M. (2002) Am. J. Sci., 302, 410-441.
• Rosen, O.M., Zorin, Y.M., Zayachkovsky, A.A. (1972) Dokladi Akademii Nauk SSSR, 203, 674–676.
• Rubatto, D., Hermann, J. (2001) Geology, 29, 3-6.
• Schertl, H.-P., Schreyer, W., Chopin, C. (1991) Contrib. Mineral. Petrol., 108, 1-21.
• Sobolev, N.V., and Shatsky, V.S. (1990) Nature, 343, 742–746.
• Stöckhert, B., Gerya, T.V. Terra Nova, (in preparation).
• Stöckhert, B., Duyster, J., Trepmann, C., Massonne, H.-J. (2001) Geology, 29, 391–394.
• Tamura, Y. (1994) J. Petrol., 35, 619–645.
• Wain, A. (1997) Geology, 25, 927-930.
• Willner, A.P., Krohe, A., Maresch, W.V. (2000) Intern. Geol. Rev., 42, 64–85.

THE SEISMIC POTENTIAL OF THE INSUBRIA REGION (SOUTHERN ALPS): INSIGHTS FROM TOPOGRAPHIC AND RHEOLOGICAL MODELING 2-10

F. Giardina(*), A.M. Michetti(*), L. Serva(**), C. Doglioni(***)

(*) Dipartimento di Scienze Chimiche e Ambientali, Università dell'Insubria, Via Valleggio 11, 22100, Como, Italia
(**) APAT, Via Brancati, 48, 00144 Roma, Italia
(***) Dipartimento di Scienze della Terra, Università "La Sapienza", Piazzale A. Moro 5, Box 11, 00185 Roma, Italia

Introduction

The active tectonics of Northern Italy is characterized by the growth of the two thrust belts surrounding the Po Plain, the Southern Alps and the Apennines (Figure 1). As widely documented by regional geological data (e.g., Bigi et al., 1990; Doglioni, 1993), along the Apennines foredeep Quaternary deformation rates decrease westward from the Ferrara, to the Emilia and Monferrato Arcs; also, ongoing regional crustal movements as described by geodetic measurements seems to indicate a similar pattern. Most important for our study, this trend is in good agreement with the westward-decreasing level of seismicity shown by the historical catalog (e.g., Boschi et al., 2000; Camassi and Stucchi, 1997; Figure 1); moderate earthquakes (M 5 to 5.5) are more frequent in the east (Ferrara) than in the west (Monferrato). This is also true for the southern margin of the Southern Alps between Friuli and western Lombardia, notwithstanding the obvious difference in the structural evolution of the two thrust belts, which implies also a different seismic style in terms of maximum earthquake magnitude and recurrence behaviour, (e.g., Serva, 1990; Doglioni, 1993; Castellarin and Cantelli, 2000). In particular, based on the available observations during the historical time window, earthquakes in the Southern Alps show higher maximum magnitudes (in the order of M 6.5) then in the Northern Apenninic Arcs, as clearly illustrated by the Friuli (e.g., Slejko et al., 1987; Barbano,

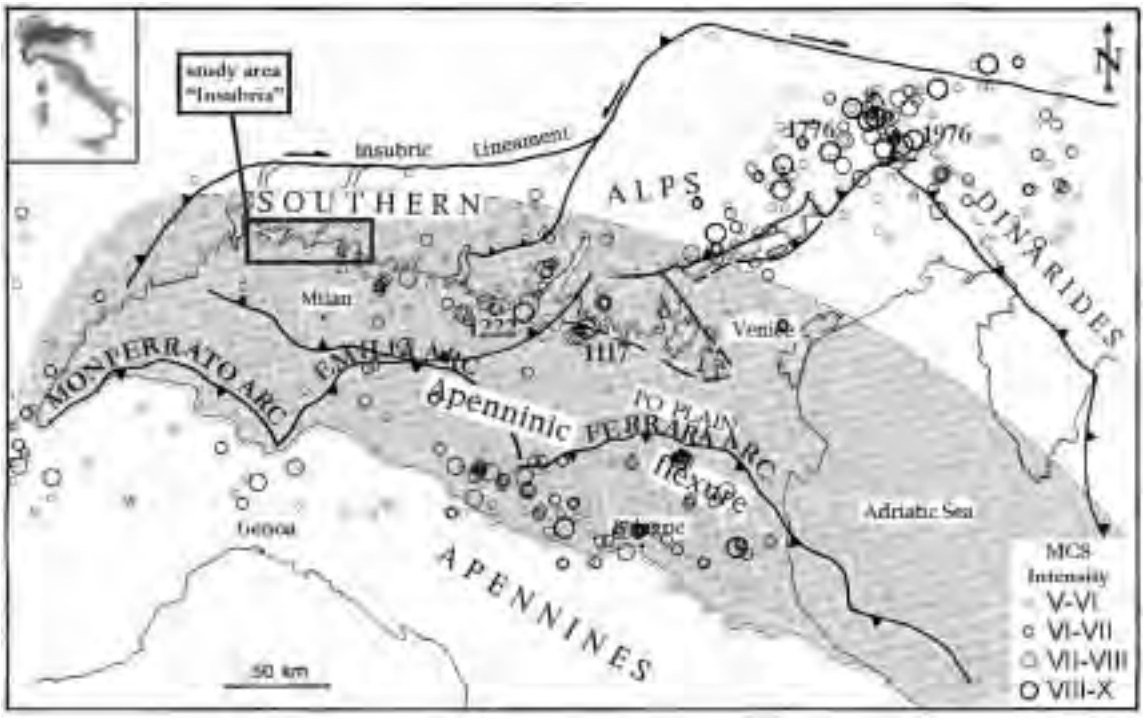

Figure 1: Epicentre distribution of the historical earthquakes (from Camassi and Stucchi, 1997) generated along the frontal sector of the Southern Alps and Northern Apennines (modified after Doglioni, 1993); 1117, 1222, 1776 and 1996 locate some of the strongest seismic events reported in the catalogues. The inset shows the area imaged in Figure 2, where several thrust along the piedmont belt show evidence for out-of-sequence Quaternary tectonic displacement.

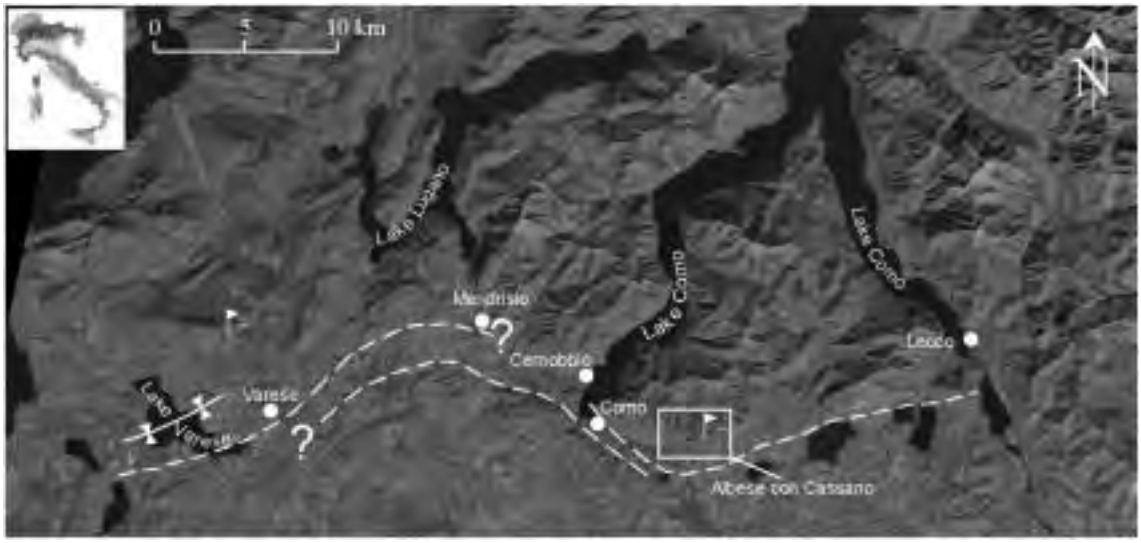

Figure 2: Landsat 5 TM image of the Southern Alps - Po Plain border in the Insubria region. Capable faults and fault propagation folds are locally influencing the topography of the piedmont belt more then the impressive Pleistocene glacial shaping. Dashed lines are thrust faults; the solid line indicates the Lake Varese synclinal; this is a preliminary interpretation from literature data (Biggioggero et al., 1981; Bernoulli et al., 1989; Gianotti and Perotti, 1986). The flags locate evidence of paleoseismicity described by Bini et al. (1992) near Varese, and by Zanchi et al. (1997) and our new field work along the Albese con Cassano Ridge. Inset shows the Albese con Cassano growing tectonic structure, first mapped by Orombelli (1976), and topographically modeled in Figure 3.

1993) and Garda areas (e.g., Magri and Molin, 1986; Serva, 1990; Curzi et al., 1992; Sauro and Zampieri, 2001; Galadini et al., 2001; Valensise et al., 2003); these strong historical seismic events have longer return periods in the west (Garda) then in east (Friuli). We argue, therefore, that the understanding of Quaternary tectonics and accompanying seismic potential around the Po Plain must be framed in a common regional geodynamic setting.
If this approach is correct, then a problem arises in the assessment of the seismic hazards in the region between western Lombardia and Ticino, at the Italy - Switzerland border, in the following referred to as the Insubria region (Figures 1 and 2). Indeed, in the Monferrato Arc (NW Apennines) significant recent tectonics deformation is associated to a seismicity level which, even if lower than in the Ferrara Arc, is far from being negligible in terms of seismic hazards. While in the Southern Alps, despite the clear evidence of Quaternary tectonics (e.g., Orombelli, 1976; Bini et al., 1992; Zanchi et al., 1997) that is described in some detail in the following, the Insubria region (W Southern Alps) shows no record of local earthquakes with epicentral Intensity greater than VI (MCS scale). Based on this lack of available historical data, the seismic hazard of the Insubria region is commonly regarded as insignificant (e.g., Stucchi, 2004). We argue that the geological evidence should be taken much more carefully into account before making suitable conclusions on the seismic potential of Insubria, an area that is one of the most economically developed and industrialized, and therefore exposed to seismic risks, of the whole Europe. In this paper we address this topic using the review of available literature, and new preliminary investigations by 1) airphoto interpretation and field mapping, 2) modeling of digital elevation data, and 3) modeling of rheological data.

Evidence of recent tectonics and paleoseismicity

Evidence of Quaternary tectonic deformation in the Insubria region has been described very clearly in the literature and since long time ago (e.g. Orombelli, 1976; Biggioggero et al., 1981; Gianotti and Perotti, 1986; Bernoulli et al., 1989; Curzi et al., 1992; Bini et al., 1992; Zanchi et al., 1997). We revised the available data and made reconnaissance field mapping and airphoto interpretation along selected structures in the area between Lecco and Varese. We focused firstly on the Albese con Cassano Ridge (Figures 2 and 3), where Orombelli (1976) described a tectonic structure which 1) uplifted a sequence of glacial to fluvio-glacial Middle Pleistocene deposits, 2) produced secondary faults within this sequence, 3) tilted more recent pro-glacial lake deposits, and 4) diverted the local drainage network. Our investigations allowed to confirm these data, and to propose that the Albese con Cassano Ridge is the morphological evidence of a growing anticline which accumulated ca. 200 m of vertical displacement during the Mid-Pleistocene to Present (?). Moreover, along this structure we identified liquefaction features within the pro-glacial lake deposits, whose sedimentological and stratigraphic characters seems to suggest the occurrence of strong local paleoearthquakes. Based on a) preliminary structural interpretation, b) geomorphic considerations, and c) the presence of uplifted Middle Pleistocene gravels at several others sites along the piedmont belt, the growth of the Albese con Cassano Ridge seems possibly to be controlled by a ca. 20 km long segment of the out-of-sequence, north-dipping thrust which bounds the mountain front between Lecco and Como (Figure 2). Literature data show that this is not a local style of deformation, but one that is common to at least the whole sector between Lecco and Varese. West of Como, a back-thrust (south-dipping) segment of similar (in the order of 20 km) length generates a mountain ridge that clearly controls the geomorphology of the valley between Cernobbio and Mendrisio. At the western margin of this structure, near Varese, a fault-bounded fold (Lake Varese syncline in Figure 2) is affected by an extensive karst system, which includes spectacular evidence for paleoseismic deformation in the caves of Monte Campo dei Fiori (broken speleothems and displaced phreatic conduits). These features were described by Bini et al. (1992) and Zanchi et al. (1997), who 1) estimated the age of deformation as younger than 350.000 years based on U/Th dating, and 2) interpreted this evidence of recent tectonic as due to the late Quaternary growth of the fault-bounded fold during repeated strong earthquakes.
These preliminary results indicate that the late Quaternary tectonics should be carefully taken into account in order to make a reasonable evaluation of seismic hazards in the Insubria region. However, interpreting these data in terms of earthquakes magnitude and rates of occurrence is presently unrealistic, since the following questions have not yet received a comprehensive answer:

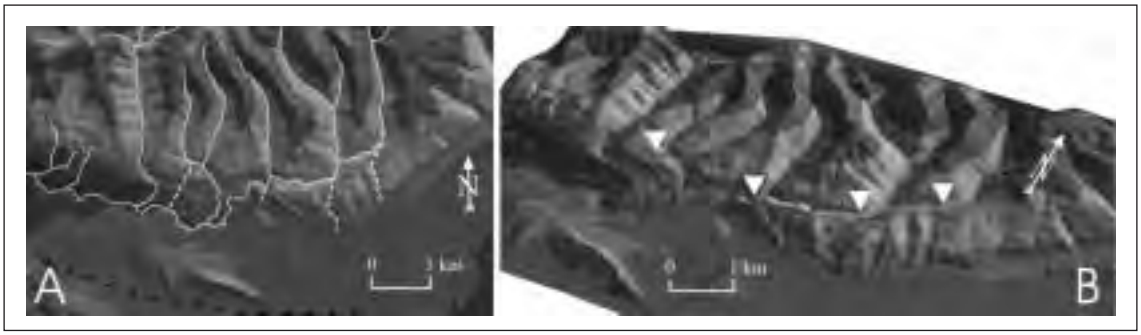

Figure 3: DTM of the Albese con Cassano Ridge; in A) the dashed lines represent the beheaded valleys; in B) the triangles indicate the wind gaps. These landforms are caused by the growth of the Albese con Cassano anticline, which dammed and diverted the local N-S trending drainages.

1) is there evidence of Holocene surface faulting or folding?
2) is tectonic creep a common feature in the area?
3) in the foothills area, what is the reasonable earthquake surface rupture length, if any?
4) what is the credible slip per event, if any?

In the next sections we begin to deal with some of these issues through 1) topographic modeling at Albese con Cassano Ridge site described above, and 2) rheological modeling of the lithosphere beneath the Insubria region.

Topographic modeling

In order to better define the morphological characters of the Albese con Cassano Ridge, we constructed a detailed digital terrain model (DTM) of the foothills belt at the base of the mountain front as shown in Figure 3. Our DTM clearly shows that the main features of the Albese con Cassano growing anticline are quite comparable with other active folds described in the world. The most similar example we found in the literature is Wheeler Ridge in California (e.g. Mueller and Suppe, 1997), which is generated by a ca. 20 km long thrust fault; capable structures of similar dimensions in California are typically associated with earthquake magnitudes in the order of 6.5 to 7, as illustrated by the 1994 Northridge earthquake (M6.8; e.g., Carena and Suppe, 2002). Due to the differences in strain rates, rheology and tectonic style between California and the Southern Alps of Italy, we believe that these data should be used with caution for estimating the size of the earthquakes possibly associated with the Albese con Cassano Ridge. For instance, it should be noted that Benedetti et al. (2000) based on the interpretation of growth folding models in the Veneto sector of the Southern Alps interpreted the Montello anticline as the cumulative result of repeated earthquakes with magnitude in the order of 6.

Rheological modeling

In order to compare the different parts of the Southern Alps and to estimate the possible presence of tectonic fault creep in the study area, we calculated a rheological model which provides some constrain about a) the crustal elastic thickness and b) the maximum supported differential stress of the Insubria lithosphere compared to the Friuli lithosphere.

The rheological model has been calculated using literature data about mineralogical composition and geothermal gradient of the lithosphere beneath the study area. We use the Sibson's law for the brittle behaviour at depths shallower than 10 km. The β parameter is assumed as 3 (as for regions characterized by thrust tectonics), the density ρ=2700 kg/m^3 , and an hydrostatic fluid pressure (λ=0.4). At depths higher than 10 km the brittle resistance to failure is likely not to follow Sibson's law, the brittle differential stress ($\sigma 1 - \sigma 3$) is kept constant and equal to that calculated with the Sibson's law at 10 km depth (Ord and Hobbs, 1989). For the ductile behavior we adopt the power law creep relation (Carter and Tsenn, 1987), which is mostly governed by temperature, strain rate and rheological parameters depending from the rock type. Since the strain rate (ε) largely affects the results we vary this parameter between 10^{-13} and 10^{-15} s^{-1} which are the most credible rates for this area

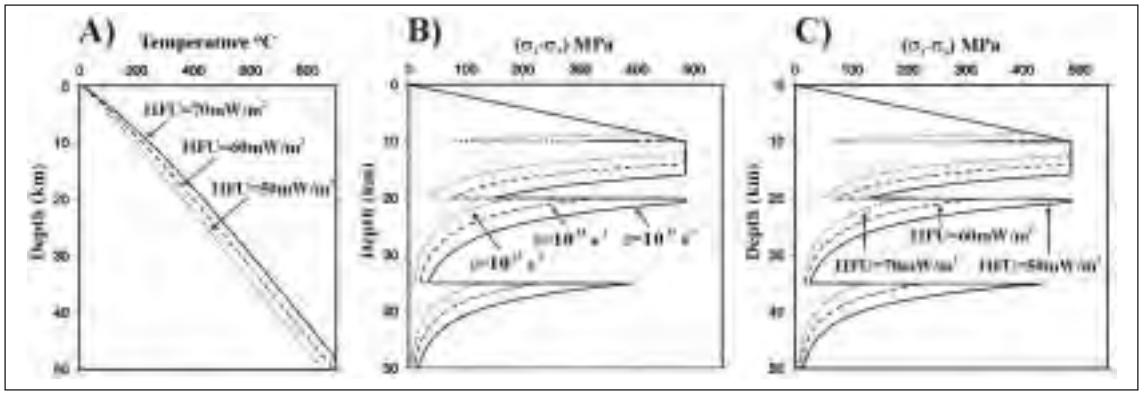

Figure 4: A) Geothermal gradients for different superficial heat flow, B) strength envelopes for different strain rates (from 10^{-15} to 10^{-13} s^{-1}) and a HFU of 60 mW/m^2 and C) strength envelopes for different HFU (between 50 and 70 mW/m^2) and a strain rate of 10^{-14} s^{-1}.

(Carminati and Siletto, 1997). The temperature distribution is modelled using superficial measured heat flow (HFU) which ranges in the studied area between 50 and 70 mW/m^2 (e.g. Della Vedova et al., 1995; Rybach et al., 1977), neglecting transient effects, assuming temperature to be a function of depth only, and thermal conductivity to be constant, we calculated the temperature distribution for HFU of 50, 60 and 70 mW/m^2. In figure 4 we give an example of our rheological model in strength envelopes which are calculated for different strain rates and for the different obtained geothermal gradients.

The used lithosphere composition and thickness is from the Schönborn (1992) section. The crustal parameters used for plastic flow are after Carter and Tsenn (1987). We used for the first 10 km of carbonatic cover the Solenhofen Limestone rheological parameters, for the upper crust (10-20 km) the Westerly Granite Dry parameters, for the lower crust (20-35 km) the Hale Albite Rock Dry parameters and for mantle (after Ranalli, 1997) the Peridotite Wet parameters. The depth of the first brittle-ductile transition in the upper crust is approximately from 8 to 15 km. Even if the structural setting of the eastern Southern Alps is quite different from the one of the western Southern Alps (e.g., Doglioni, 1993), it is important to note that the rheological parameters used in our model for the Insubria area are quite similar to those reported for the Friuli area, which is characterized by comparable HFU (e.g. Pasquale and Verdoya, 1990), lithospheric thickness and mineralogical composition (e.g. Bressan et al., 1992; Carulli and Ponton, 1992). The presence beneath the Insubria area of an elastic thickness of 8-15 km, a value that characterizes also the elastic thickness in the eastern Southern Alps, seems to rule out the possibility that creeping deformation can play an important role in the active tectonics of the study area. However, more work is needed in order to definitely assess the coseismic vs. aseismic nature of the recent tectonic deformation in the study area.

Discussion

The piedmont belt connecting the Prealps and the Po Plain in the Insubria region is bounded by several out-of-sequence thrusts which were certainly active during the Middle Pleistocene. Literature data, also supported by our new preliminary investigations, seems to indicate that these thrust faults can be also active today, and might be capable of producing significant surface deformation and faulting during future strong earthquakes. In order to verify this hypothesis, we are planning detailed field mapping and structural/geomorphic modeling of all the recent tectonic structures, also for identifying potential trench sites, and recognizing paleoseismic evidence that can allow to estimate for each structure 1) nature and age of the youngest fault displacement, 2) latest Pleistocene to Holocene slip rates, and 3) displacement per event and surface (or near surface) rupture length.

If this research will confirm our preliminary findings, and assuming that the historical seismic catalogue is really complete, the absence of significant historical earthquakes would imply that the Insubria region of the Southern Alps should be regarded as an important seismic gap. This might have significant societal impact in such a densely industrialized area, which is basically considered earthquake-safe in the Italian Seismic Code.

REFERENCES

• Barbano (1993) - Terra Nova, 5, 467-474.
• Benedetti et al. (2000) – Journal of Geophysical Research, 105, 739-766.
• Bernoulli et al. (1989) - Eclogae Geologicae Helvetiae, 82, 841-856.
• Bigi et al. (1990) - Prog. Fin. Geod., Quad. Ric. Scient., 114 (3).
• Bigioggero et al. (1981) - In: "Carta tettonica delle Alpi meridionali", di Castellarin A., Publ. n°441, Progetto Finalizzato Geodinamica (S.P.5) CNR, 185-189.
• Bini et al. (1992) - Karstologia 19, 23-30.
• Boschi et al. (2000) - Annali di Geofisica 43, 609-868.
• Bressan et al. (1992) - Studi Geologici Camerti, 1992/2, 89-98.
• Camassi and Stucchi (1997) - http://emidius.mi.ingv.it/NT/CONSNT.html
• Carena and Suppe (2002) - Journal of Structural Geology, 24, 887-904.
• Carminati and Siletto (1997) - Tectonophysics, 280, 107-123.
• Carter and Tsenn (1987) - Tectonophysics, 136, 27-63.
• Carulli and Ponton (1992) - Studi Geologici Camerti, 1992/2, 275-284.
• Castellarin and Cantelli (2000) - Journal of Geodynamics, 30, 251-274.
• Curzi et al. (1992) - Boll. Soc. Torricelliana di Scienze e Lettere, Faenza, 43, 3-111.
• Della Vedova et al. (1995) - Tectonophysics, 244, 57-74.
• Doglioni C. (1993) - Tectonophysics, 228, 1-20.
• Galadini et al. (2001) - T. Glade et al. (eds.), The use of historical data in natural hazard assessments, Kluwer Academic Publisher, 3-27.
• Gianotti and Perotti (1986) - Memorie della Società Geologica Italiana, 32, 67-99.
• Magri and Molin (1986) - ENEA-RTI PAS-IPS-GEOL-LO, (86) 2 (inedito).
• Mueller and Suppe (1997) - Journal of Structural Geology, 19, 383-396.
• Ord and Hobbs (1989) - Tectonophysics, 158, 269-289.
• Orombelli (1976) - Quaderno Gruppo di studio del Quaternario padano, 3, 25-37.
• Pasquale and Verdoya (1990) - Memoires de la Societe Geologique de France, Nouvelle Serie, 156, 135-143.
• Ranalli (1997) - Annali di Geofisica, 40, 671-680.
• Rybach et al. (1977) - Tectonophysics, 41, 113-126.
• Sauro and Zampieri (2001) - Geomorphology, 40, 169–184.
• Schönborn (1992) - Memorie di Scienze Geologiche, 44, 229-393.
• Serva (1990) - Boll. Soc. Geol. Ital., 109, 375-411.
• Slejko et al. (1987) - CNR, G.N.D.T, Rendiconti 1, 82 pp., Trieste.
• Stucchi (ed.) (2004) - http://zonesismiche.mi.ingv.it/documenti/rapporto_conclusivo.pdf
• Valensise et al. (2003) - Annali di Geofisica 46(5), 865-882.
• Wells and Coppersmith (1994) - Bull. Seismol. Soc. Am., 84, 974-1002.
• Zanchi et al. (1997) - Geologia Insubrica, 2, 137-142.

FINITE-ELEMENT MODELS OF SUBDUCTION AND MOUNTAIN BUILDING PROCESSES: CONCEPTS AND PRELIMINARY RESULTS

2-11

A. Hampel, A. Pfiffner

Institute of Geological Sciences, University of Berne, Baltzerstr. 1, 3012 Berne, Switzerland

Abstract

We present preliminary results from numerical simulations of processes contributing to mountain building in a subduction-zone setting. The Finite-Element models, performed with the software ABAQUS, are designed to decipher deformation patterns and particle paths in an orogenic wedge and to extract modes of material transfer.

All models include elasto-plastic oceanic and continental lithospheres, which rest on spring and dashpot elements to simulate isostatic effects. Two different types of model set-ups are realized: In a first 1500-km-long model set, an Arbitrary-Lagrangian-Eulerian formulation offered by ABAQUS (Hibbitt et al., 2002) is applied to the oceanic lithosphere (Figure 1), which allows to represent the subducting plate by a material flow through a deformable mesh. This approach has already been successfully applied to geodynamic problems with a rigid-plastic rheology to model large displacements (Fullsack, 1995; Ellis et al., 1999). In our ABAQUS models, the material enters the left Eulerian boundary (see Figure 1) with a velocity of 10 mm/a and leaves the subducting plate through the right Eulerian boundary. The continental plate has a Lagrangian mesh bounded to the material and is fixed in horizontal direction on its far right side, but free to move in vertical and horizontal direction

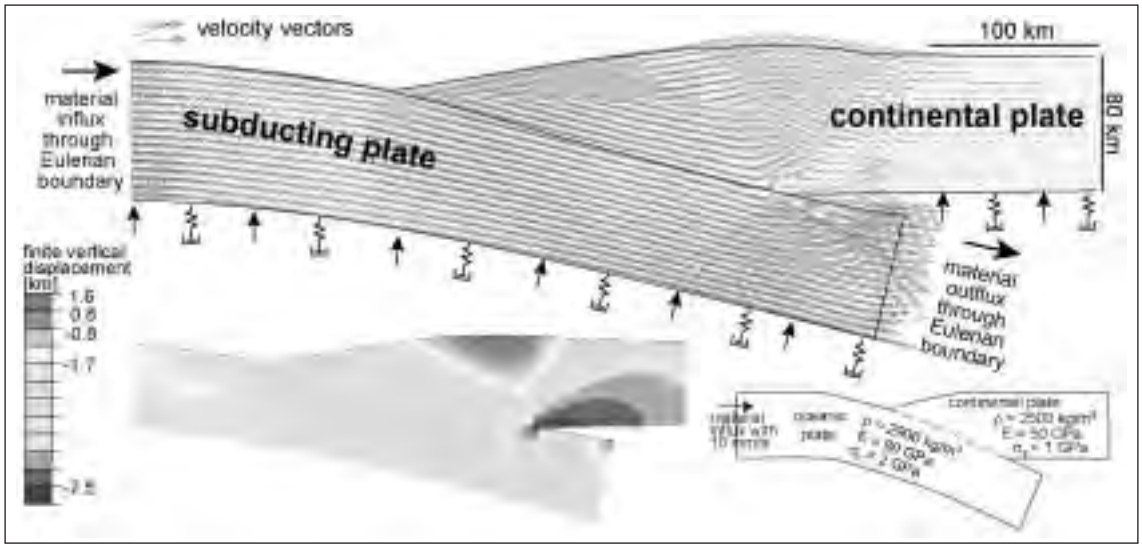

Fig. 1 – Subduction zone model with elasto-plastic oceanic and continental lithospheres, on which Arbitrary-Lagrangian-Eulerian and Lagrangian formulations are applied, respectively. Top: velocity vectors attached to the material. Bottom (left): vertical displacement of the mesh. Bottom (right): material properties for the oceanic and continental lithospheres with ρ density, E elastic modulus, σ_y plastic yield stress.

elsewhere. Material exchange between lower and upper plate is allowed across the plate interface in both directions. Therefore, this set-up enables to model subduction zones with considerable sediment cover on the oceanic plate, where accretion of material is expected, or collision settings where offscraped continental lithosphere leads to the formation of an orogenic wedge. The model presented in Figure 1 involves subduction of an oceanic plate. After ~30 km of convergence a particle displacement field as depicted in Figure 1 has developed. Major upward vertical displacement and associated development of topography in the upper plate is asymmetrically distributed above the lower end of the plate interface between the two plates.

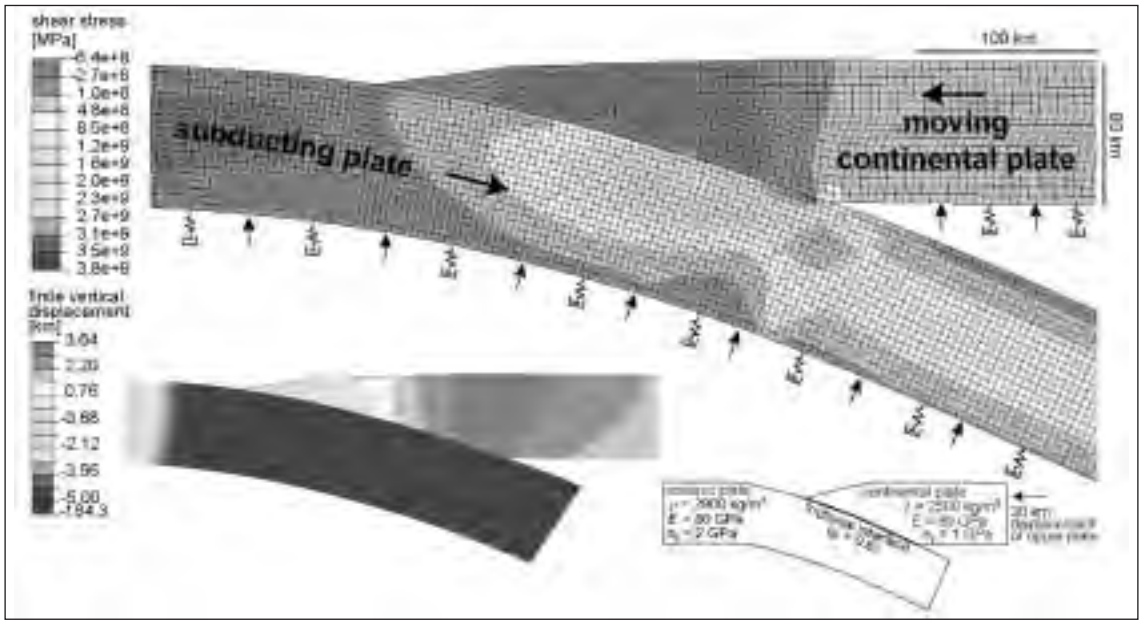

Fig. 2 – Model of a subduction zone with separate oceanic and continental lithospheres and frictional plate interface (μ=0.6). Top: Shear stresses (σ_{xy}). Bottom (left): vertical displacement. Bottom (right): material properties for the oceanic and continental lithospheres with ρ density, E elastic modulus, σ_y plastic yield stress.

In the second model set-up, a 1500-km-long oceanic and a 750-km-long continental plate are represented by two separate bodies, which are in contact along a frictional interface (Figure 2). Friction along the plate interface can be varied and thus allows to study the influence of this parameter on deformation patterns and the evolution of topography. In an initial phase, the model calculates the bending stresses in the down-flexed subducting plate. Afterwards, the upper plate is added and the model is allowed to react and to reach isostatic equilibrium again. In the main phase of the model, the continental plate moves toward the subducting plate. This set-up, which does not include material exchange between the two plates, is designed for application to natural settings like the Andean subduction zone where the sediment cover of the oceanic plate is negligible and friction along the plate interface is high. For such orogens, a close correlation between topography and variations of friction and shear stresses along the plate interface has been inferred (Lamb and Davis, 2003). Figure 2 shows the model with a friction coefficient of μ=0.6 after ~30 km of convergence. As in the first experiment, the largest upward vertical displacement is found above the lower end of the plate interface. Topography in the second model, however, is higher and distributed over a wider area than in the first model.
Future work will involve a detailed comparison between the two different types of models using similar rheologies as well as investigations on the influence of heterogeneities in the lithosphere and the implementation of surface processes.

REFERENCES

- Hibbitt, Karlson, and Sorenson (2002) ABAQUS/Explicit User's Manual, Hibbitt, Karlson and Sorenson, Inc. Pawtucket, RI, USA, version 6.3.
- Ellis, S., C. Beaumont, A. Pfiffner (1999) Geodynamic models of crustal-scale episodic tectonic accretion and underplating in subduction zones. J. Geophys. Res., 104, B7, 15169-15190.
- Fullsack, P. (1995) An arbitrary Lagrangian-Eulerian formulation for creeping flows and its application in tectonic models. Geophys. J. Int., 120, 1-23.
- Lamb, S., and P. Davis (2003) Cenozoic climate change as a possible cause for the rise of the Andes. Nature, 425, 792-797.

PHASE DEPENDENT STRAIN PARTITIONING IN OBLIQUELY CONVERGENT SETTINGS 2-12

A. Hoffmann-Rothe, N. Kukowski, O. Oncken

GeoForschungsZentrum Potsdam, Department of Geodynamics, Telegrafenberg, 14473 Potsdam, Germany, ahoro@gfz-potsdam.de

Summary

Physical (sandbox) simulations of obliquely convergent accretionary subduction margins show that the cyclicity of accretionary processes imposes a strong control on forearc deformation. Strain partitioning, i.e. the spatial separation of margin-normal and margin-parallel strain, is most dominant while new thrusts are forming at the deformation front. Shortening remains focused at the toe of the wedge, but the margin-parallel component reaches far into the forearc. Faults trending parallel to the trench are dominated by strike-slip motion. The results suggest that the forearc deformation pattern alternates with the characteristic time scale on which new thrust-slices are generated in the accretionary wedge (several 100.000 years).

Introduction

Forearcs of obliquely convergent subduction margins commonly exhibit spatial separation of deformation structures dominated by margin-normal (shortening) and margin-parallel (strike-slip) strain, respectively. The degree of deformation in the forearc is largely controlled by the efficiency of force transmission across the interface of the subducting and overriding plates (the area of force transmission defines the mechanic coupling zone). Forearc deformation patterns will further be controlled by kinematic boundary conditions which influence the material flow in the forearc. This

comprises any kind of structural heterogeneity within the continental wedge. Of particular importance is to differentiate between open subduction margins where resistance against margin parallel material transport is low (e.g. Sunda margin in front of Sumatra, trenchward convex shaped subduction margin, cf. Figure 1) and confined margins with high resistance against margin parallel material transport (e.g. Peru/Chile margin, trenchward concave shape).
In this study we focus on physical (sandbox) simulations of open subduction systems with accretionary margins. Our aim is to monitor the evolving forearc fault and sliver plate system and to derive the corresponding strain partitioning pattern. We emphasize the question of which spatio-temporal conditions in the accretive system favour the initiation or (re-) activation of margin-parallel faults. Do such faults exhibit phases of predominant accommodation of strike-slip motion, as it is inferred for many margin-parallel fault systems in oblique subduction settings (or oblique collision settings)?

Experimental setup

The experimental setup is shown on the left hand side in Figure 1: A conveyor belt (basal friction μ_b ~ 0.5) transports a sedimentary load (sieved sand, grainsize 0.02-0.63 mm, internal friction μ_i ~ 0.56; Lohrmann et al., 2003) toward the continental margin (deformable backstop). Shear force transmission at the base of the backstop ceases at the S-point (along the S-line in top view), which simulates the downdip limit of seismicity along the plate interface at an average depth of about 45 km (Tichelaar and Ruff, 1993). The obliquity of the system is set to 30°, an angle for which the occurrence of margin-parallel fault systems in physical simulations with sand was shown by Martinez et al. (2002). While one side of the experiment is closed with a glass panel in order to observe the internal deformation, the other side of the margin is open and allows for translational movement of the material. This simulates a trenchward convex shaped (open) subduction margin that evolves along its trenchline from transpressional to translational convergence (cf. bottom right hand side of Figure 1).
Surface deformation of the ongoing experiment is monitored with the help of two digital cameras in a stereo-setup. A set of pictures, used to calculate a digital elevation model of the surface, is taken every second. An image correlation system derives the incremental vector displacement field on the surface images of two successive time-steps (= convergence-steps). The area covered by the digital cameras reaches from the deformation front to the rigid backwall.

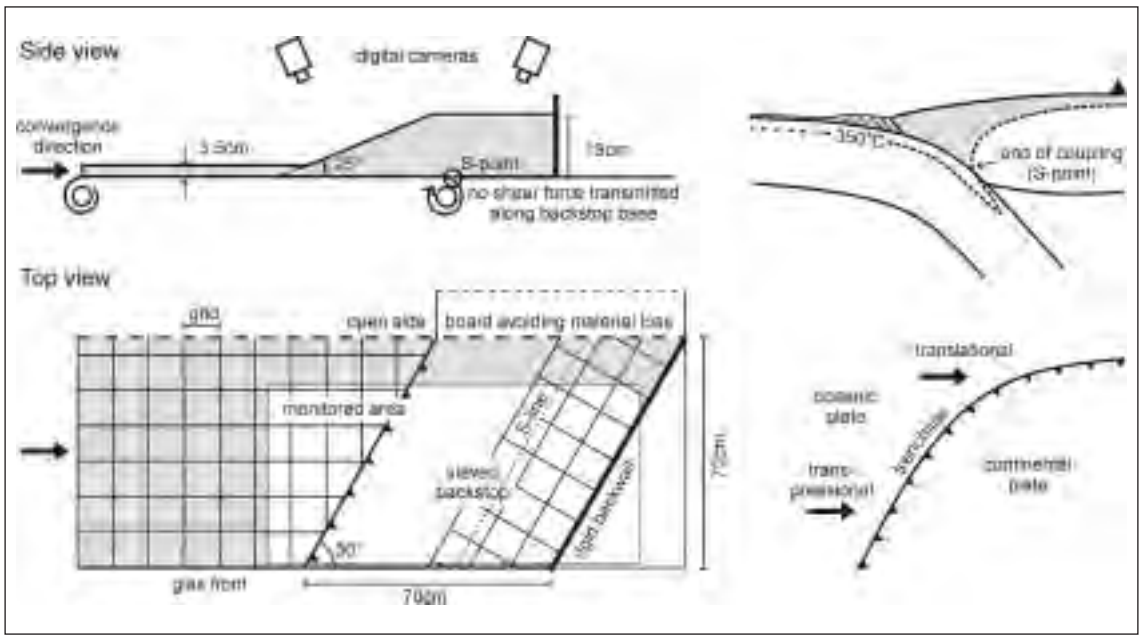

Fig.1 - Sketches of a trenchward convex accretionary subduction margin (right) and experimental abstraction (left).

What part of the subduction system is represented by this simulation? Strain localisation behaviour of quartz sand is similar to that of crustal rocks in the brittle field, exhibiting strain-hardening and -softening effects, and frictional ranges of sand and natural rocks are alike (Lohrmann, 2003). Owing to the effect that isotherms are downward deflected by the cold subducting plate, the continental wedge under brittle rheology (represented by the 350°C isotherm in the upper right part of Figure 1) may reach as deep as 50 km and up to 150 km into the forearc. The cold wedge therefore represents the volume for which conclusions can be drawn from the experimental studies. Note that its extent in nature is a function of the convergence rate, the age of subducted oceanic crust and the dip angle of the slab (Stern, 2002). Although proper geometrically scaled forearc dimensions would require a much greater sandbox, our setup allows a qualitative study of the conditions under which deformation reaches beyond the S-line and 'far' into the forearc.

First results and discussion

The analyses of the experiments show that strain distribution in the forearc varies in accordance with episodic thrust formation at the deformation front. This episodic behaviour of accretionary thrust cycles is well known from nature and physical experiments (Gutscher et al., 1998 and references therein). Two principle phases have been identified (Figure 2): (i) The relatively short thrust-initiation phase is marked by the formation of a new fore-thrust and pop-up structure at the deformation front. (ii) This is followed by the underthrusting phase in which the material transported into the trench is underthrusted beneath the continental wedge. The former fore-thrust evolves into a detachment zone. The accumulated displacement along this detachment zone (and its time of activity) is a function of the material thickness transported into the trench and the ratio between internal friction of this material and basal friction.

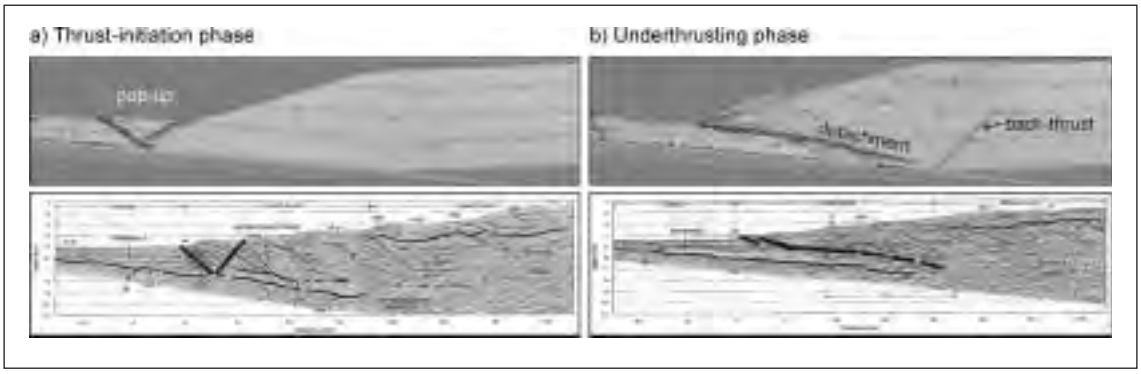

Fig.2 - Thrust-initiation (a) and underthrusting (b) phases of the accretionary thrust-cycle. The lower panels give two respective examples for these phases for the southern Chile margin (left: ENAP line 728, 36°S, right: ENAP line 732, 39°S, taken from Díaz-Naveas, 1999).

In the first thrust-initiation phase at the start of the experiment (cf. Figure 2a, top), a pop-up structure forms along the whole margin. The faults bounding the pop-up structure accommodate oblique slip, with the margin-normal shortening component being twice as high as the margin-parallel strike-slip component (this ratio will vary with obliquity). The striking observation is that all of the shortening is accommodated along the faults bounding the pop-up structure, while a translational component reaches beyond the pop-up into the rearward forearc. This form of spatial separation is common to all thrust-initiation phases, even in advanced stages of the experiment, when the deformation front becomes segmented into zones being in different phases of the accretion cycle. The surface image in the top panel of Figure 3a shows the formation of a new thrust-slice in the upper half of the image after 53 cm of convergence. The segment in the lower part is in an underthrusting phase. The analysis of how the displacement vectors split into the trench-normal (Vx) and trench-parallel (Vy) component along a profile that trends perpendicular to the margin, reveals the same strain partitioning pattern as described above (bottom diagram of Figure 3a): shortening is accommodated at the deformation front between points A and B; beyond B the remaining displacement field is almost entirely composed of

margin-parallel motion. The gradient of the Vy-curve at point C indicates the position of a strike-slip fault.

Spatial strain partitioning is less pronounced in the subsequent underthrusting phases. A profile view of the first underthrusting phase at the start of the experiment is shown in Figure 2b (top). Both, margin-normal and margin-parallel components, are transmitted from the underthrusting sheet across the detachment into the overlying wedge and backstop. Still, a large portion of strain is accommodated at the toe of the wedge, but the forearc sliver bounded by the deformation front and the back-thrust exhibits block-like oblique motion toward the open margin. Again, the incremental displacement field is generally the same for an advanced stage of the experiment, shown in Figure 3b: Along the toe of the wedge, between positions A and B, we observe accommodation of most of the strain. Margin-normal and -parallel motion of almost the same magnitude govern the rearward part of the forearc, which results in block-like motion obliquely to the trench, as indicated by the arrow. Pre-existing faults, however, such as in position C, may be active with a predominant strike-slip sense.

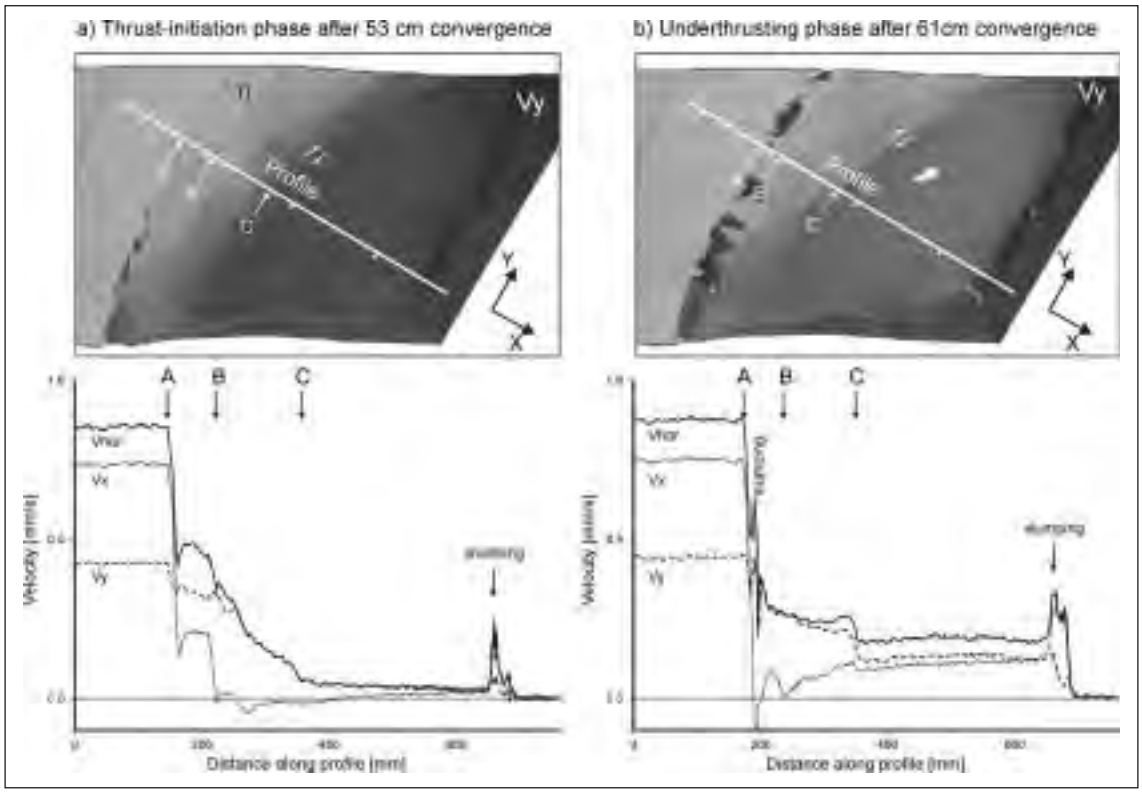

Fig.3 - Top: Surface images of thrust-initiation (a) and underthrusting phases (b) in an advanced stage of the experiment. TI marks the segment of the margin, where a new pop-up is just generated. Grey shades visualize the magnitude of lateral translation (the lighter the higher). Bottom: Diagrams showing the separation of incremental rates of horizontal motion Vhor into its trench-normal (Vx, shortening) and trench-parallel component (Vy, lateral translation) along the profiles shown on the surface images. Steep slopes cause noise in the curve due to slumping effects. Letters A, B and C are referred to in the text.

Obviously, the displacement field sampled along the shown profiles crossing the forearc is non-plane-strain. Particularly, in the rearward parts of the profile, material flow from neighbouring segments will contribute to the displacement signal. However, whereas individual underthrusting phases may exhibit different patterns of fault activation, the thrust-initiation phases are very systematically characterised by a lack of shortening in the rearward part of the forearc.

Will the observation of phase dependent partitioning of strain also be valid with modified boundary conditions, in particular for (i) lower basal friction or (ii) concave shaped margins? (i) Martinez et al. (2002) have shown that strain partitioning in sandbox models also develops if basal friction is low.

Additionally, 2D sandbox studies of frontally accreting systems also reveal that the margin-normal strain component (shortening) remains focussed to the deformation front while new thrust-slices are initiated. We therefore assume that a modification of the basal friction will not change the general partitioning pattern and phase dependency, however the magnitudes of displacement will vary. (ii) Results from Pinet and Cobbold (1992), who used an experimental setup that prohibits margin-parallel material flow beyond the edges of the obliquely convergent system (concave shaped margin), show the emergence of strain partitioning if a critical angle of obliquity is reached. This suggests that strain partitioning is not primarily controlled by kinematic boundary conditions facilitating margin parallel material flow. However, we expect the fault pattern, i.e. the position of faults relative to each other and the trench, to be different if resistance against margin-parallel material transport is high.

Conclusions

The experiments reveal phases of strong spatial separation of margin-normal and margin-parallel displacement. When compared to nature, our simple experimental setup produces fault patterns closely resembling those described for trenchward convex (open) subduction margins. In particular, comparison with the Sunda margin off Sumatra suggests similar processes of sliver plate formation (Molnar et al., 1996) as well as the formation of a prominent fault (system) at the rear of the accretionary wedge. In our models, these faults show episodic increase of strike-slip motion. This leads to the most notable result: forearc deformation (i.e. the degree of strain partitioning, initiation and reactivation of faults or the formation of basins) is subject to the cyclicity of the accretionary processes. Field studies of forearc deformation concentrate either on recent deformation (GPS surveys) or on the neo-tectonic record of deformation covering several millions of years. However, a thrust-cycle of the accretionary wedge lasts some 100.000 years, which may define the recurrence time for pronounced strain partitioning in the forearc. Moreover, recent deformation may vary significantly for segments along the trench, depending on the present phase of accretion. It is therefore necessary to identify the phase of accretion for a studied segment, e.g. by using offshore seismic lines, forearc bathymetry, the coastline uplift record or the sedimentation record of onshore and offshore basins.

Acknowledgements

We thank Silvan Hoth and Jo Lohrmann for valuable discussions and their help with the experiments. Günter Tauscher is thanked for his technical advice and for building the experimental setup.

REFERENCES

- Díaz-Naveas, J. L., Sediment subduction and accretion at the Chilean Convergent Margin between 35°S and 40°S, Dissertation, 129pp, University of Kiel, 1999.
- Gutscher, M.-A., N. Kukowski, J. Malavielle and S. Lallemand, Episodic imbricate thrusting and underthrusting: Analog experiments and mechanical analysis applied to the Alaskan Accretionary Wedge, J. Geophys. Res., 103: 10161-10176, 2000.
- Lohrmann, J., N. Kukowski, J. Adam and O. Oncken, The impact of analogue material properties on the geometry, kinematics, and dynamics of convergent sand wedges, J. Struc. Geol., 25: 1691-1711, 2003.
- Martinez, A., J. Malavielle, S. Lallemand, and J.-Y. Collot, Strain partitioning in an accretionary wedge in oblique convergence: analogue modelling, Bull. Soc. géol. France., 173/1: 17-24, 2002.
- Molnar, J. A. and B. M. Kemal, The Sumatra margin: oblique subduction and lateral displacement of the accretionary prism, in Hall, R. and D. Blundell (eds), Tectonic Evolution of Southeast Asia, Geol. Soc. Spec. Publ., 106: 19-28, 1996.
- Pinet, N. and P. R. Cobbold, Experimental insights into the partitioning of motion within zones of oblique subduction, Tectonophysics, 206: 371-388, 1992.
- Stern, R. J., Subduction Zones, Rev. Geophys, 40(4), 1012, doi:10.1029/2001RG000108, 2002.
- Tichelaar, B. W. and L. J. Ruff, Depth of seismic coupling along subduction zones, J. Geophys. Res., 98: 2017-2037, 1993.

LITHOSPHERIC INSTABILITIES AND THE CENTRAL ANDEAN OROGENESIS 2-13

L. Husson(*), Y. Ricard(**)

(*) Collège de France – Chaire de Géodynamique, Europôle de l'Arbois – Bat Laennec BP80, 13545 Aix-en-Provence, France.

(**) Université Lyon-1, Laboratoire de Géologie, UMR CNRS 5570, Lyon, France.

Summary

The disequilibrium between tectonic stresses and buoyancy stresses drives the orogenesis. The latter stresses includes the positive buoyancy of the light crust and the negative buoyancy of the cool and dense lithospheric mantle. Beneath the Eastern Cordillera of the Central Andes, the fast shear wave velocities outline a cool lithospheric keel. Converting the velocity anomalies into thermal anomalies and density anomalies for a peridotitic composition, we estimate the magnitude of the thermal moment of these thermal heterogeneities. In the Central Andes, its magnitude is comparable to that of the crustal moment, and its lateral variations are strong enough to significantly foster deformation in the Eastern Cordillera. All the components of the stress balance can then be restored and introduced in a mechanical model which in turns highlights the major role of the cool lithospheric keel in the Andean orogenesis.

Abstract text

The dynamics of an orogenesis is often regarded as the result of the disequilibrium between the tectonic stresses arising from global plate tectonics and the buoyancy stresses induced by the lateral density variations. The first term acts as boundary conditions either resulting from the far field tectonic regime or from the local coupling between the deforming lithosphere and the adjacent plate or even its friction with the asthenosphere.

Since Argand (1924), this disequilibrium have been mostly modelled considering the buoyancy stresses of the sole crust (e.g. England and McKenzie, 1982), although a significant contribution may arise from the lithospheric mantle (Houseman et al., 1981, Conrad, 2000). For a cooling Earth, the lithosphere is then a thermal boundary layer which is cooler and denser than the underlying asthenosphere. On average, the difference is lower than the difference between the crust and mantle densities, i.e. about 50 kg m^{-3}, but as the lithospheric mantle is thick with respect to the crust, its incidence can be large in some cases (Fig.1).

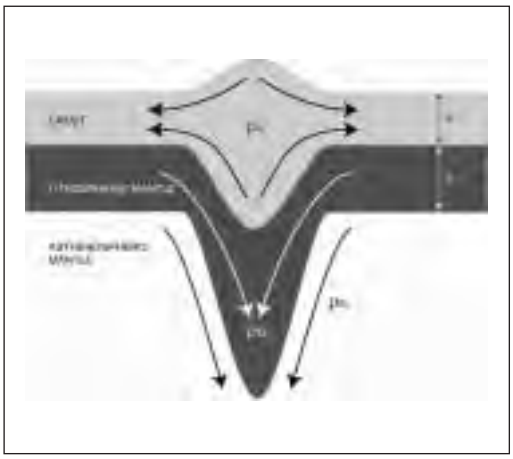

Fig.1: Incidence of a dense lithospheric mantle. Divergent arrows represent the positive buoyancy of the crust which tends to induce extension in thickened areas while convergent arrows show the negative buoyancy of the dense lithospheric mantle, which tends to induce compression. ρc is the density of the crust, ρm the density of the asthenosphere, and ρQ the density of the lithospheric mantle.

While the low density crust tends to restore a homogeneous thickness for the crust, the lithospheric mantle, on the contrary, enters a destabilisation mode: as it is dense with respect to its underlying media, any thickness variation is a density variation which tends to sink (e.g. Bercovici et al., 1998). The density of a particle at a given depth times this particular depth defines its potential incidence and is often called the stress moment law (Fleitout and Froidevaux, 1982). The lateral variations of this moment within the surrounding media gives the actual incidence of the particle on the dynamics. This quantity defines the buoyancy stresses.

The moments can write respectively for the crust (M_c) and the lithospheric mantle (M_Q)

$$M_c = \rho_c g \frac{1-\rho_c}{\rho_0} S^2$$

$$M_Q = \int_0^{L+h} z \rho_0 g \gamma \left(T - T0\right) dz$$

where ρ_c and ρ_0 are the densities of the crust and mantle (reference density), S the crustal thickness, g the gravitational acceleration, L the thickness of the lithosphere, z the depth, γ the thermal expansion coefficient, T the temperature and T0 the reference temperature. The total buoyancy stresses are given by the lateral variations of the sum of the moments.

In the Central Andes, the formation of the Altiplano is partly elucidated since Isacks (1988) which emphasized that a weakened lithosphere explains the width of the belt. In a previous paper (Husson and Ricard, 2004), we showed that introducing a slight viscosity decrease in our models corroborate this hypothesis. But this large-scale model does not explain the very little shortening of the Altiplano. In fact, shortening was actually concentrated in the Cordilleras and a lower-crustal flow towards the Altiplano acted as a piston for the last 10 to 20 Myrs, thickening its crust without shortening (Husson and Sempere, 2003). The weakness of the pre-Andean Eastern Cordillera triggered deformation in this area (Sempere et al., 2002), but as the moment increased whilst the crust thickened, deformation should at least have slow down and eventually migrated backward, in the Altiplano area. This suggests that another mechanism fostered deformation in this Eastern Cordillera after its onset.

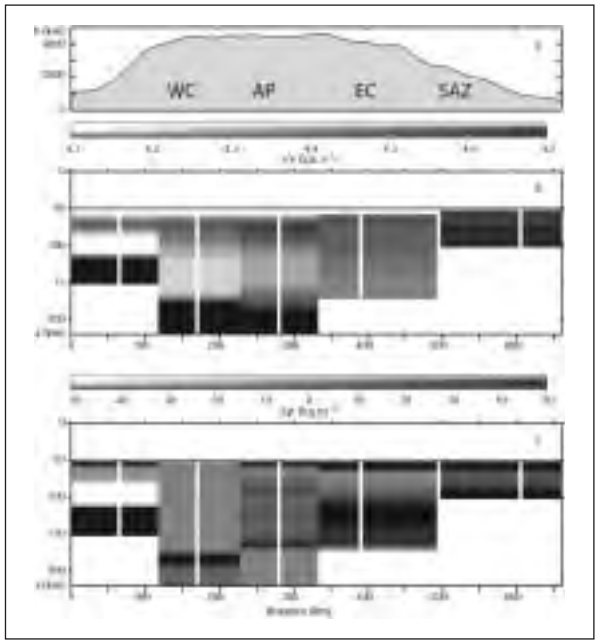

Fig.2: a) Topography and morphotectonic units in the Central Andes (20°S); b) Shear wave velocity in the Central Andes (after Baumont et al., 2002); c) Density variations in the Andean lithosphere deduced from the lateral shear wave velocity variations. WC: Western Cordillera, AP: Altiplano, EC: Eastern Cordillera, SAZ: Sub Andean Zone.

Local tomography in the Andes outlines a fast velocity unit below the Eastern Cordillera (e.g. Baumont et al., 2002). As shear waves velocities are very sensitive to temperature, this is interpreted as a cool lithospheric keel resulting from the subduction of the Brazilian shield beneath the Central Andes (Fig.2b). Assuming a homogeneous peridotitic composition for the mantle, we convert the lateral variations of densities into temperature variations using the results from Lee (2003). We take the minimum velocities at each depth as reference values for the asthenosphere, avoiding the Nazca cool slab. Note that the reference values do not have any incidence on the stress estimates which depends on the derivatives of the moment rather than its absolute value. We then convert the temperature variations into density variations (Fig. 2c, using a coefficient of thermal expansion of $2.4\ 10^{-5}$ K^{-1}). We neglect the velocity variations in the crust as they may as well reflect compositional heterogeneities, and also because the crust is in a regional isostatic

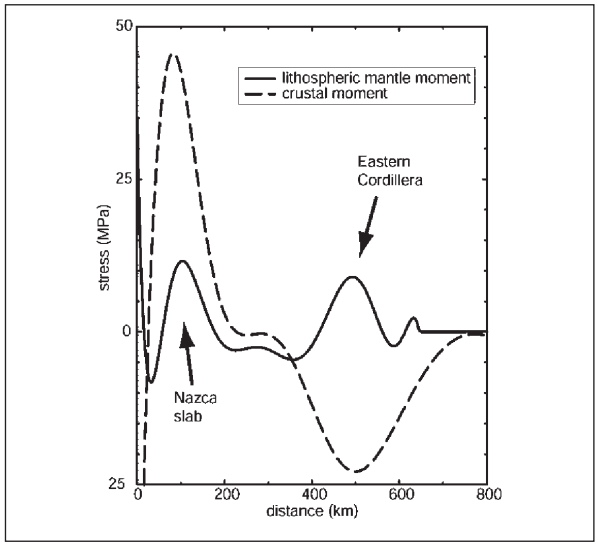

Fig.3: Buoyancy stresses arising from the crust (dashed curve) and lithospheric mantle (solid curve) in the Central Andes. At the longitude of the Eastern Cordillera, the lithospheric negative buoyancy almost balances the crustal positive buoyancy and annihilates their effects on the dynamics.

equilibrium which do not suggest that any significant density heterogeneity within the crust affects the crustal moment.
The integration of the density heterogeneities over the lithosphere thickness give the moment of the lithosphere. In the Central Andes, the magnitude of the variation in the moment reaches 10^{12} N m^{-1}, which is comparable to the ridge push. We fit the moment by a 10^{th} order polynomial curve previously to the calculation of the derivative, which then gives the lithospheric buoyancy stresses (Fig.3).
Next to the trench, the positive peak of the lithospheric buoyancy is due to the cool, sinking Nazca slab. It tends to induce compression in the westernmost 200 km. The second peak, of similar magnitude is located below the Eastern Cordillera. It almost annihilates the extensional stresses induced by the positive buoyancy of the crust. In our previous paper (Husson and Ricard, 2004), in order to fit the velocity field and to transmit deformation away from the trench, we were forced to assume that interplate friction could act over 300 km below the South American plate. In fact, it now comes out that the shear stresses that we called "interplate friction" somehow included the thermal moment. Establishing a new stress balance for the Central Andes including the effect of the thermal moment, a more realistic interplate friction profile is inferred, which is then also very similar to the formerly inferred interplate friction profiles of the "regular" segments of the Andes like Peru or Chile.
The occurrence of this dense lithospheric keel beneath the Eastern Cordillera highlights the fact the lithospheric moment in some cases might have to be accounted for. As shown in the Central Andean example, the present-day stress balance can then be better described adding the horizontal derivative of the lithospheric moment. Expanding our former thin viscous sheet approach, we need to add the transport equation for the lithospheric moment. Defining the lithosphere as a thermal boundary layer, the transport of the lithospheric moment can be described as the transport of the first temperature moment (Lemery et al., 2000) and writes, assuming the conservation of energy

$$\frac{\partial M_Q}{\partial t} + 2M_L \frac{\partial u}{\partial x} + u\frac{\partial M_L}{\partial x} = \kappa\left(\frac{\partial^2 M_L}{\partial x^2} - \rho_0 g\gamma T_s\right),$$

where u denotes the horizontal velocity, $\frac{\partial}{\partial t}$ the time derivative, $\frac{\partial}{\partial x}$ the horizontal derivative, κ the thermal diffusivity and T_s the temperature increase through the lithosphere. The transport of the thermal moment (=lithospheric moment) differs from the transport of the crustal moment because a diffusivity term is added. The transport of the crustal moment simply writes, assuming incompressibility,

$$\frac{\partial M_c}{\partial t} + 2M_c \frac{\partial u}{\partial x} + u\frac{\partial M_c}{\partial x} = 0$$

Running this model backwards in time allows estimating the evolution of the thermal moment and, in the case of the Central Andes, shows the drastic role of the lithospheric keel through time.

REFERENCES

- Argand, E. (1924), Comptes-rendus du 13eme congrès géologique international, Brussels.
- Baumont, D., et al. (2002), Lithospheric structure of the Central Andes based on surface wave dispersion, J. Geophys. Res., 107, doi.10.1029/2001JB000345.
- Bercovici, D., et al. (2000), The relation between mantle dynamics and plate tectonics: A primer, In: The History and Dynamics of Global Plate Motions, Richards, Gordon and Van der Hilst (eds), AGU Monograph 21, pp 5-46.
- Conrad, C. (2000), Convective instability of thickening mantle lithosphere, Geophs J. Int., 143, 52-70.
- England, P. and D. McKenzie (1982), A thin viscous sheet model for continental deformation. Geophys. J. R. Astr. Soc., 70, 295-321.
- Fleitout, L. & Froidevaux, C. (1982). Tectonics and topography for a lithosphere containing density heterogeneities, Tectonics, 143, 21-56.
- Houseman et al. (1981), Convective instability of a thickened boundary layer and its relevance for the thermal evolution of continental convergent belts, J. Geophys. Res, 143, 6115-6132.
- Husson, L., and Sempere, T. (2003), Thickening the Altiplano crust by gravity-driven crustal channel-flow; Geoph. Res. Lett., doi:10.1029/2002GL016877,

- Husson, L., and Ricard, Y., (2004), Stress balance above subduction zones - application to the Andes; in review, EPSL.
- Isacks, B.L. (1988), Uplift of the Central Andean Plateau and bending of the Bolivian Orocline, J. Geophys. Res., 93, 3211-3231.
- Lee, C.-T. A. (2003), Compositional variation of density and seismic velocities in natural peridotites at STP conditions: Implications for seismic imaging of compositional heterogeneities in the upper mantle, J. Geophys. Res., 108, doi:10.1029/2003JB002413.
- Lemery C., et al. (2000), A model for the emergence of thermal plumes in Rayleigh-Bénard convection at infinite Prandtl number. J. Fluid Mech. 414, 225-250.
- Sempere, T., et al. (2002), Late Permian – Middle Jurassic lithospheric thinning in Peru and Bolivia and its bearing on Andean age tectonics, Tectonophysics, 345, 153-181.

MODELLING THE DEFORMATION FRONT OF FOLD-THRUST BELTS CONTAINING MULTIPLE WEAK HORIZONS 2-14

H.A. Koyi(*), M. Sans(**), A. Bahroudi(***)

(*) Hans Ramberg Tectonic Laboratory, Department of Earth Sciences, Uppsala, Sweden Hemin.Koyi@geo.uu.se.

(**) Univeristat de Barcelona. Barcelona, Spain

(***) Geological Survey of Iran, P.O. Box 131851, Tehran, Iran

Summary

Fold-thrust belts (FTB) shortened above a weak horizon (e.g salt) possess a low taper, a wide deformation zone and contain structures with no preferred vergence. The sedimentary units of some fold-thrust belts contain more than one weak layer of salt (e.g. Zagros fold-thrust belt and Ebro Basin). Such multiple weak layers govern the style of deformation in a FTB and cause a complicated deformation history. In this study, we use results of sand-box models where a pack of layers of loose sand containing ductile layers simulating detachment horizons (salt or shale) at higher stratigraphic horizons, was shortened above a ductile layer simulating a basal detachment. Model results show that the ductile layers embedded within the sand layers (intermediate detachment horizons) govern the propagation style of the deformation front entirely. Upon reaching these detachment horizons, the deformation fronpropagates to upper stratigraphic horizons ahead of deformation in the deeper parts of the model. Applied to nature, this suggests that the surface expression of a deformation front in a FTB containing weak layers may not represent the active deformation zone in the deeper levels, which is decoupled from the shallower layers by weaker horizons at shallow stratigraphic levels (Fig. 1).

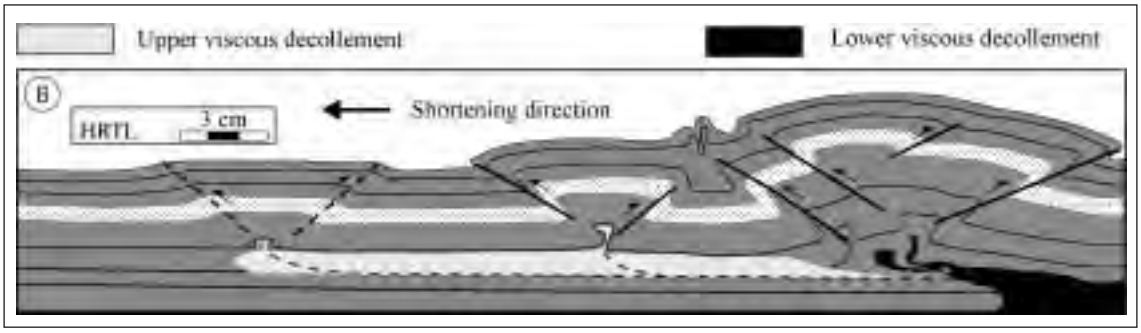

Figure 1. Line drawing of a model profile showing decoupling of deforamtion in the upper units from the lower units (undeformed) above an intermediate detachment horizon.

Models

Two models were designed to study the transference of deformation between detachments at different stratigraphic levels. Here, the results of one model is reported. The model consisted of three viscous layers interbedded with layers of loose sand (Figs. 1). The materials used were viscous SGM 36 simulating weak horizons and quartz sand simulating overburden units. SGM36 has an effective viscosity of 5x104 Pa s (density 987 kg m-3). The models with the above set-up was shortened to 22%

and photographed from the top at different time intervals. After completion, model was saturated with water and sections were cut for photographing (Fig. 1). The results of the model are applicable to fold-thrust belts where a sedimentary sequence containing different detachment horizons are subjected to shortening. Below, we give two examples of such areas.

Zagros fold-thrust belt

The Zagros fold-thrust belt is formed due to the subduction of Neo-Tethys beneath Iran and later suturing between Iran and Arabia along the main Zagros thrust (Fig. 2). More than 150 diapirs of Hormuz salt are known in southwest Iran and eastern part of Arabia (O'Brien 1957). The stratigraphy of southwest Iran and northeast Arabia are similar (Stocklin 1968, Kent 1970). The 1.3-km thick Hormuz salt is overlain by 6-7 km of lower Palaeozoic to upper Mesozoic sandy shale, carbonate and sandstone (O'Brien 1957). Rocks older than Jurassic are rarely exposed in the Zagros fold-thrust belt and are deeply buried beneath the foreland deposits. However, in addition to the basal detachment of Hormuz salt, the sedimentary sequence of the Zagros fold-thrust belt contains several "weak" horizons at intermediate and higher stratigraphic levels (e.g. evaporites; Miocene (Gachsaran Fm.) and Triassic salt (Dashtak Fm.) and shale; Kazhdumi and Gurpi Fms.). During the convergence between Arbia and Central Iran, these sedimentary units are shortened above the weak Hormuz salt (where present).

Since, intermediate weak horizons do exist in the Zagros stratigraphy, based on model results, we suggest that the deformation front in the sedimentary sequence of the Zagros fold-thrust belt, may only represent the extent of deformation in the shallow units. In the Zagros fold-thrust belt, the deformation front at deeper levels, which is detached above a layer of Hormuz salt, may be located towards northeast relative to the surface expression of the deformation front. Model results also show that strain distribution is heterogeneous in fold thrust belts with multiple weak zones.

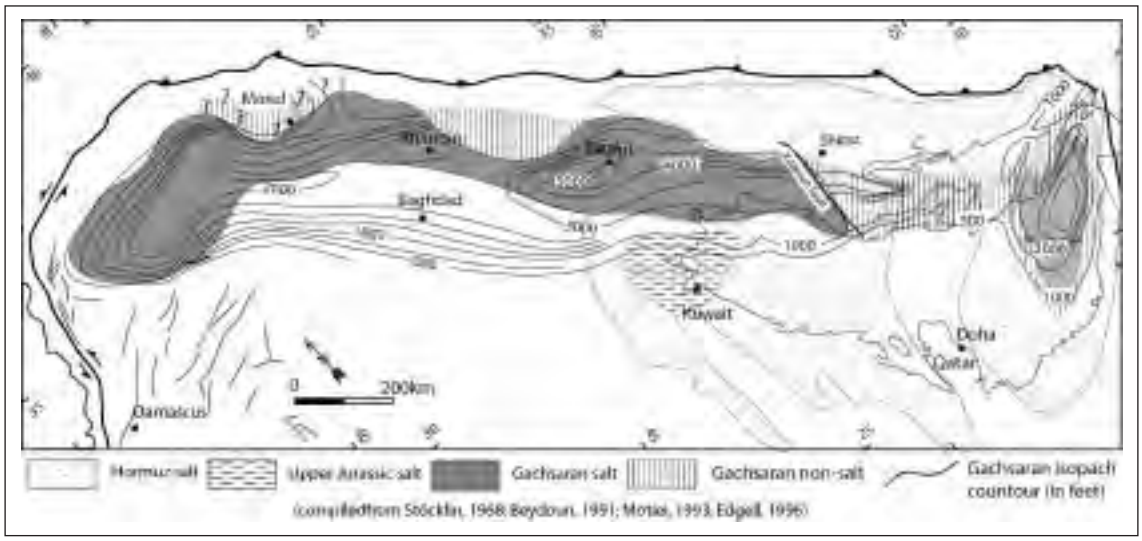

Figure 2. Distribution map of different evaporitic units in the Zagros basin.

The south Pyrenean Triangle zone

This zone is located in the southeastern Pyrenees where the basal thrust encounters detachment horizons at shallower levels to transmit deformation towards the foreland (Fig. 3; Sans et al., 1996). The south Pyrenean Triangle front is characterized at the surface by antiforms separating the undeformed subhorizontal beds of the Ebro basin from the deformed hinterland. The basal detachment of the triangle zone which is located in three different evaporitic levels, has a staircase geometry, stepping from the lower and northernmost Beuda formation to the higher and southwesternmost Barbastro formation. Wide flats are located in the evaporitic formations whereas ramps coincide with their southwestern edges and southeastern buried tip lines. This difference between the southwestern

and southeastern margins is related to the oblique thrust transport direction with respect to arrangement of the evaporitic basins (Vergés et al., 1992; Sans et al., 1996).
Three main thrust wedges developed along the southern margins of each of the evaporitic basins. The northern thrust wedge is located at the southern pinchout of the Beuda Formation where the basal thrust climbs up into the Cardona salt. The intermediate wedge coincides at the surface with the Santa Maria d´Oló, Súria and Sanaüja anticlines and it is related to the southern pinch-out of the Cardona salt. The southernmost wedge lies on top of a buried tip line located at the edge of the Barbastro Formation, and is represented at the surface by the Barbastro-Balaguer anticline.

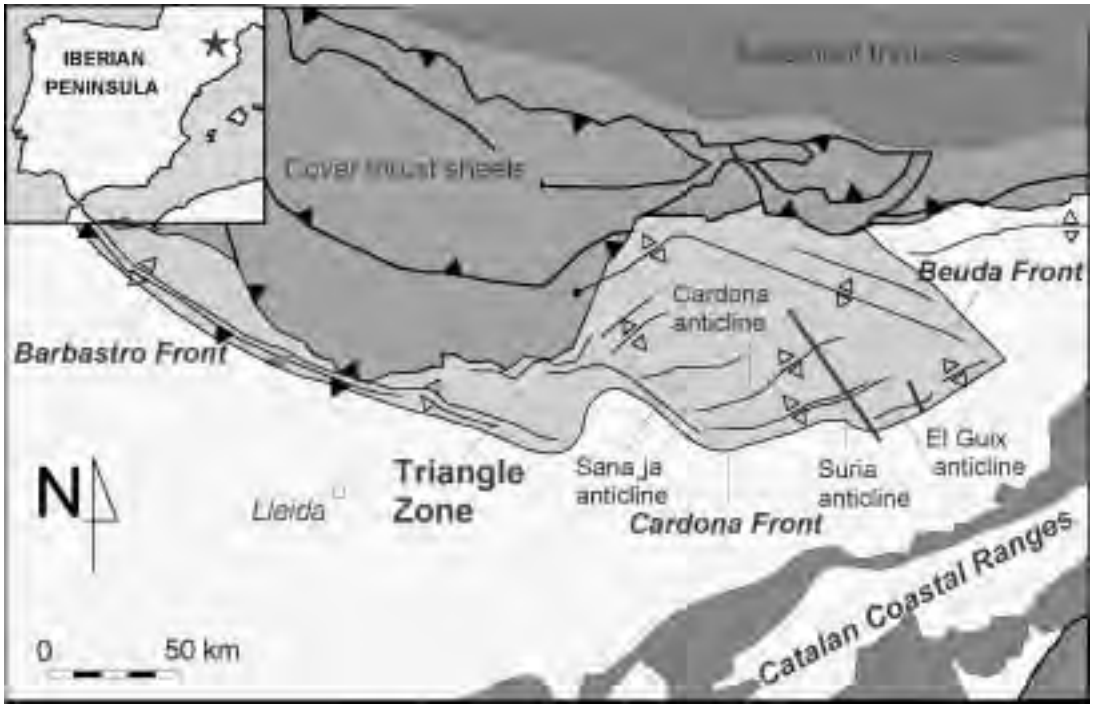

Figure 3. Map of the Southern Pyrenean Traingle zone showing three deformation fronts; Bueda, Cardona and barbastro, from bottom to top, respectively. These deforamtion fronts are associated with the pinch-out of three evaporitic units located at different stratigraphic horizons.

REFERENCES

- Beydoun, Z.R., 1991. Arabian plate hydrocarbon geology and potential- a plate tectonic approach. American Association of Petroleum Geologists Bulletin studies in Geology 33, 77p.
- Edgell, H. S. (1996), Salt tectonics in the Persian Gulf basin. In: Alsop, G. L, Blundell, D. L., Davison, I. (Eds.), Salt tectonics. Geological Society of London Special Publication 100, 129-151.
- Kent, P.E., 1970. The salt Plugs of the Persian Gulf Region.Leicester Literary and Philosophical Society Transactions 64, 55-58.
- Motiei, H. (1993), Stratigraphy of Zagros. Geological Survey of Iran (in Farsi), 536p.Stöcklin, J., 1968. Salt Deposits of the Middle East. Geological Society of America Special Paper 88, 158-181.
- O'Brien, C. A. E., 1957. Salt diapirism in South Persia. Geologie en Mijnbouw, v. 19, p. 337-376.
- Sans, M., Muñoz, J.A., and Vergés, J. (1996), Triangle zone and thrust wedge geometries related to evaportic horizons (southern Pyrenees). Bulletin of Canadian petroleum Geology, 44(2), 375-384.
- Stöcklin, J. (1974), Possible ancient continental margin in Iran. In: Burk, C.A., Drake, C. L. (Eds.), Geology of the continental margin. Springer, New York, 873-887.
- Vergés, J., Muñoz, J.A., and Martínez, A., (1992), South Pyrenean fold-and-thrust belt: role of foreland evaporitic levels in thrust geometry. In: Thrust tectonics, McClay, K.R. (ed.). Chapman & Hall, London, 255-264.

MATERIAL AND FLUID FLUX AT CONVERGENT MARGINS: WHAT ENDS UP IN THE FOREARC? 2-15

N. Kukowski

GeoForschungsZentrum Potsdam, Telegrafenberg, D-14473 Potsdam, Germany, e-mail: nina@gfz-potsdam.de

Introduction

During subduction of an oceanic plate beneath a continent material may be exchanged between the downgoing plate and the overriding plate. The amount and nature of material potentially being transferred to the forearc mainly depends on the composition and fluid content of the sediment cover entering a convergent margin at the deep sea trench. A wealth of geophysical data acquired during the past few decades clearly images different styles of sediment accretion at convergent margins. Accretionary wedges comprising an onshore portion, e.g. the rear 200 km of the Makran accretionary prism or paleo-accreted material now found onshore (e.g. Hirono and Ogawa, 1998) demonstrate that sediment accretion contributes to continent growth. However, about half of the entire world's margin length is non-accretive (von Huene and Scholl, 1991, Scholl and von Huene, 2001). At these margins, the forearc may lose considerable material through subduction erosion.

During accretion, sediment porosity loss not only results from vertical compaction but additionally from lateral tectonically driven porosity loss. Fluids being released by this process or chemical reactions, e.g. the smectite-illite transition, may considerably contribute to overpressuring (Bekins et al., 1995, Saffer and Bekins, 1998) and also significantly affect the wedge's thermal state (Kukowski and Pecher, 1999*).* Porosity distribution and released fluids also control the amount of solid and fluid fraction of material coming to the forearc - only the solid fraction of the incoming material may contribute to continent growth.

The structure, lithology, and tectonic history of forearcs as identified from geophysical and geology field observations hint to parameters possibly controlling material transfer at convergent margins. Among them, sediment supply, width of the subduction channel, and interplate frictional properties, which also exhibit control on plate coupling and therefore the seismic potential of a forearc, are suggested to be of major importance. To quantitatively understand the complex and coupled processes underlying material and fluid flux as well as related deformation, the combined employment of numerical and analogue simulation is the first choice strategy. Mirroring this concept, this contribution evaluates parameters controlling material transfer at convergent margins and the influence of fluid release and transport on forearc mechanics by reviewing recent analogue and numerical simulation studies. Similarities and differences between erosive and accretive margins will be discussed by addressing the central Andean margin as a long-term tectonically erosive forearc and the Makran (Figure 1) margin, which exhibit the largest amount of sediment supply among the Earth's margins, respectively.

Results of analogue and numerical simulations

There is a long tradition to simulate mass transfer and deformation in convergent systems employing scaled sandbox experiments. This approach is physically based on the self-similar elasto-plastic Mohr-Coulomb rheology. Very recently, a granular numerical approach, the distinct element method, also has been successfully applied to convergent systems (Burbridge and Brown, 2002, Huhn, 2002). According to its continuum based strategy, the finite element approach is the only method providing estimates of the stress tensor. It also is the first choice method to incorporate complex rheological behaviour and to simulate coupled processes.

Systematic series of accretive sandbox experiment revealed the dominant role of basal frictional properties in controlling global mass transfer modes in convergent systems. Basal accretion (underplating) only can occur above a considerably strong base, whereas above a weak base, frontal accretion will always take place (Gutscher et al., 1998). Weak layers within the incoming section will form a detachment and lead to simultaneous basal and frontal accretion (e.g. Kukowski et al., 2002, Huhn, 2002, Fig.1 F, G, H). Locally, activity of a wedge's thrust faults and therefore kinematic

segmentation is controlled by the frictional properties of the wedge material (Lohrmann et al., 2003). The position of the "global control point" (Lohrmann, 2002), which controls the width of the subduction channel (cf Lohrmann et al., this volume), together with the relative position of the décollement lastly determines the amount of material being added to the upper plate and potentially being transferred back to the mantle, respectively. These results from scaled sandbox experiments reveal the greater importance of basal frictional properties in controlling material transfer compared to the wedge's internal frictional properties.

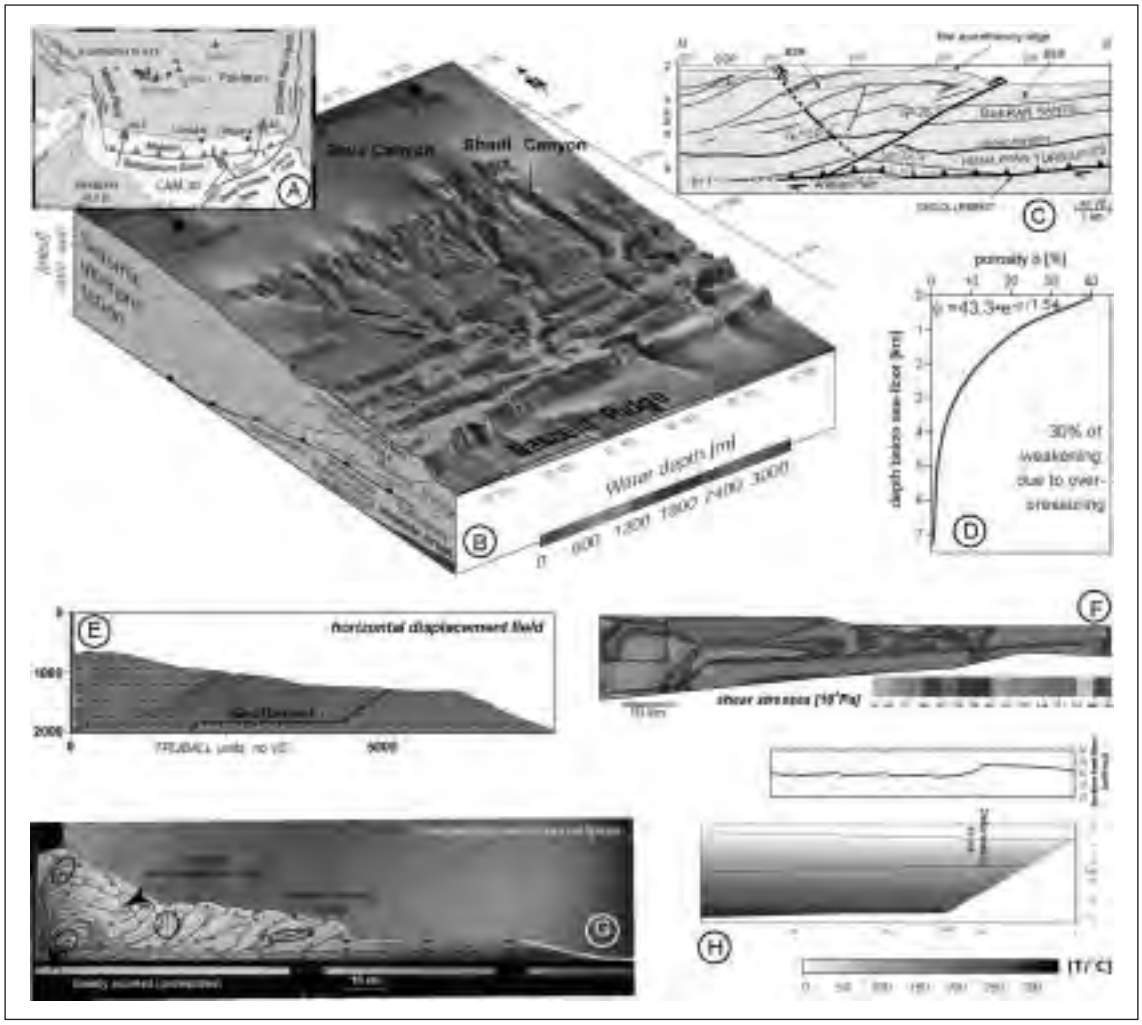

Fig.1 – Mechanics and thermo-hydraulics of the Makran accretionary wedge as deduced from geophysical data, finite element and distinct element simulation, and sandbox experiments. A) Location map, B) Swath bathymetry and interpretation of combined wide-angle and MC seismic data (after Kopp et al., 2000, Kukowski et al., 2001), C) Geometry of the frontal non-rotated conjugate thrusts (after Kukowski et al., 2001), D) Porosity-depth-distribution and overpressuring (after Fruehn et al., 1997), E) Result of distinct element simulation (after Huhn, 2002), Shear stress distribution as a results of finite element simulation (after Huhn, 2002), G) Final stage of a sandbox experiment with a weak layer in the incoming section, H) Temperature distribution and surface heatflow showing local anomalies in the neighbourhood of the thrust faults as obtained from coupled thermo-hydraulic simulation.

Sandbox experiments with no incoming sand layer show, that subduction erosion will only take place in the absence of sediment input. Additionally, basal tectonic erosion is a further mass transfer requiring high friction along the plate interface (Jarrard, 1986) and is furthermore facilitated by high roughness of the lower plate surface (Adam et al., 2002). Accordingly, erosive margins will build up a large taper. Basal tectonic erosion is restricted to the region close to the tip of the continent wedge where the interplate and wedge frictional properties are the same or only differ by less than a few

percent. As soon as the material in the subduction channel is weakened e.g. through dilatation, the strength contrast increases which inhibits further material removal. If the thickness of the basally transported layer exceeds the width of the subduction channel in term of the position of the global control point, basal accretion of subduction channel material may take place. Therefore, as material earlier eroded from the tip of a margin may be basally accreted in a more arcward position, the identification of underplated material beneath a continental slope does not allow draw conclusions about the accretive/erosive nature of a convergent margin, but only about the governing plate interface properties.

Following the results of analogue and numerical simulation, extension as often observed at the surface of a forearc may result from frontal mass wasting in the case of erosive margins as well as from sediment underplating in the case of erosive or complexly accretive forearcs. To decipher the cause of extension in a convergent setting in nature therefore requires independent analysis of related vertical tectonism.

Finite element simulation reveals that mass transfer scenarios (high basal friction/low basal friction, broad/narrow subduction channel) are mirrored in characteristic shear stress distributions. The more easily material may be basally dragged further arcward the smaller is the magnitude of shear stresses and therefore the potential of faulting.

Fluids released through tectonic dewatering or mineral reactions may lead in the case of sufficiently low permeability to enhanced pore pressures (Bekins et al., 1995), having considerable effects on the mechanical properties and therefore the strength of the overpressured regions. The amount of released fluids is mainly controlled by porosity distribution. If overall porosity is relatively small, the lower the permeability needs to be to cause overpressuring. Therefore, low porosity wedges are not favourable to strong overpressuring. Coupled simulations show that advection locally leads to strongly increased temperatures around active thrust faults. However, advection also contributes to the thermal field in the entire wedge, but mostly not more than about 10% (Kukowski and Pecher, 1999).

Application to natural systems

The central part of the Andean margin (5°S to 33°S) is a first priority location to study the modes of long-term tectonic erosion. Seismic and swath bathymetry data acquired off Peru at different latitudes reveal a nearly sediment-free oceanic crust of ultra-high roughness approaching the trench and the presence of only a small margin wedge. In northern Peru, the lowermost part of the slope slips trenchparallel as a whole along an at least 100 km long segment of the margin (Kukowski et al., 2004), whereas further to the south, subduction erosion seems to be strongest beneath Lima basin at some 80 km of the trench. Applying the results of erosive sandbox experiments to this margin suggests that in northern Peru the rough and high-friction plate interface causes basal erosion at the margin tip. Rates of erosion are enhanced if pre-weakened zones exist in the upper plate (Ranero and von Huene, 2002). Therefore, the presence of such zones may also shift the location of maximum erosion and may lead to the removal of large portions of the crust as suggested by the results of sandbox experiments with weak zones incorporated in the sand-wedge. As long-term erosion rates are higher than magmatic addition rates (Clift et al., 2003), the Peruvian margin seems to be a true sink for continental crust. Fluid pressure is unlikely to be significantly enhanced (Kukowski and Pecher, 1999) in the sub-marine part of the forearc which is in accordance with the probable strong base and large taper.

The Makran accretionary wedge off Pakistan results from the thickest sediment pile entering a subduction zone world wide (Fig.1). Only the upper part of this sediment is frontally accreted. The lower portion of the sediment is subducted and partly underplated beneath the mid-slope. Depth migrated MCS data reveal a pair of non-rotated conjugate thrust faults close to the deformation front (Fig.1). With the assumption of the toe of the wedge in a critical state this allows to determine frictional properties with a geometric approach following from critical taper theory (Davis and von Huene, 1087) and with pore pressure parameter was determined independently from seismic analysis (Fruehn et al., 1997). These results are shown in comparison with other margins in Table 1. A ratio of about 2.5 between internal and basal friction seems to be quite usual among margins. The values obtained from geometric analysis very well match frictional properties as obtained from laboratory measurements (Kopf and Brown, 2003). An exception is the Alaska wedge, however. There, long

undeformed units are underthrust, which argues for a relatively strong base (Gutscher et al., 1998). The material transfer mode proposed for the Makran also has explained deformation observed at the Mediterranean Ridge (Kukowski et al., 2002) and South Chile (Lohrmann, 2002) margins. Coupled thermo-hydraulic analysis shows a slight landward decrease of surface heat flow and local anomalies in the neighbourhood of the permeable, active thrust faults (Fig.1), which is in good agreement with heatflow obtained from needle probe measurements (Kaul et al., 2000). Overall porosity of the Makran wedge is relatively small and necessarily still decreases significantly arcward, indicating that most fluids originally contained in the sediment will be transferred back to the ocean and do not reach the mantle.

The influence of subducting asperities

Subducting asperities like seamounts or basement ridges may for a few millions of years very considerably enhance rates of tectonic erosion (Clift et al., 2003), however, they do not alter the original character of a margin. Whereas ridges do not cause major re-entrances (Hampel et al., 2004), seamounts generate a distinct scar in the wedge behind them (Ranero and von Huene, 2000). The evolution of faulting around a subducting asperity and related stress evolution has been successfully simulated with 3D analogue and numerical approaches (Dominguez et al., 1998, Hampel et al., subm., Mohr and Kukowski, 2001). Incorporating a rigid ridge or a seamount in sandbox experiments leads to characteristic patterns of local oversteepening and asymmetric uplift above the subducting ridge, compressional and extensional fault occurrence, and the formation of a gully-like track in the wake of a seamount. The observations made in the sandbox agree very well with the geological record in coastal Peru and off Costa-Rica, respectively.

	Internal friction	Basal friction	Ratio	Reference
Alaska	0.45 (24.2°)	0.28 (15.6°)	1.55	Davis & von Huene, 1987
Oregon	0.62 (31.8°)	0.23 (12.9°)	2.47	Lallemand et al., 1994
Nankai	0.50 (26.6°)	0.20 (11.3°)	2.35	Lallemand et al., 1994
Makran	0.42 (23.0°)	0.15 (8.5°)	2.80	Kukowski et al., 2001
Sunda	0.31 (17.2°)	0.13 (7.4°)	2.32	Kopp & Kukowski, 2003

Table 1: Internal and basal frictional properties of natural wedges determined with the method of Davis and von Huene (1987) which is based on the critical taper approach.

Concluding summary

Basal subduction erosion at the tip of a wedge and underplating beneath the rear of a wedge both are processes which require a strong basal interface. However, scaled sandbox experiments show that basal subduction erosion only occurs if no input is entering a convergent system. Underplating takes place in accretive as well as in erosive systems. As the release of fluids does not cause overpressuring in many wedges, geometric estimation of frictional properties will provide intrinsic values. Shear stress accumulation mainly is a function of i) the strength of the base and ii) the ability of subduction channel material to be further subducted. Therefore, the relative ease of basal material flux may be more important to build up high shear stress along the plate interface zone than fluid overpressuring. Basement ridges and seamounts have the potential to increase process rates, e.g. for tectonic erosion, however, will not change the overall mode of material transfer.

Acknowledgements

Many of the questions and conclusions addressed in this contribution result from intensive and stimulating discussions with S. Ellis, A. Hampel, A. Hoffmann-Rothe, K. Huhn, S. Hoth, J. Lohrmann, and O. Oncken.

REFERENCES

• Adam et al. (2002) EGS Meeting, Nice
• Bekins et al. (1995) Water Resources Research 31, 3205 - 3215

• Burbridge and Brown (2002), Geophys. J. Int. 148, 542 - 561
• Clift et al. (2003), Tectonics 22/3, doi:10.1029/2002TC001386
• Cloos and Shreve (1988), Pageoph 128, 455 – 500 and 501 - 545
• Davis and von Huene (1987), Geology 15, 517 - 522
• Dominguez et al. (1998), Tectonophysics 293, 207 - 224
• Fruehn et al. (1997), Terra Nova 9, 101 - 107
• Gutscher et al. (1998) J. Geophys. Res.
• Hampel et al. (2004), J. Geophys. Res. 109 B2101, doi:10.1029/2003JB002593
• Hampel et al. (subm.)
• Horono and Ogawa (1998) , Geology 26, 779 - 782
• Huhn (2002), PhD Thesis, GFZ STR02/02
• Jarrard (1986), Rev. Geophys. 24, 217 - 284
• Kaul et al. (2002), Marine Geology 164, 37 - 51
• Kopf and Brown (2003), Marine Geology 202, 193 - 210
• Kopp and Kukowski (2003), Tectonics 22/6, doi:10.1029/2002TC001420
• Kukowski and Pecher (1999), J. Geodynamics 27, 373 - 402
• Kukowski et al. (1994) Geol. Rundschau 83, 822 - 831
• Kukowski et al. (2001), Marine Geology 173, 1 – 19
• Kukowski et al. (2002) Marine Geology 186, 29 - 42
• Kukowski et al. (2004), EGU Meeting, Nice
• Lallemand et al. (1994), J. Geophys. Res. 99, 12033 - 12055
• Lohrmann (2002), PhD Thesis, GFZ STR02/10
• Lohrmann et al. (2003), J. Struct. Geol. 25, 1691 - 1711
• Lohrmann et al., this volume
• Mohr and Kukowski (2001), GV Meeting, Kiel
• Ranero and von Huene (2000), Nature 404, 748 - 752
• Saffer and Bekins (1998) J. Geophys. Res. 103, B12, 30351 - 30370
• Scholl and von Huene (2001), GV Meeting, Kiel
• von Huene and Scholl (1991), Rev. Geophys. 29, 279 – 316

COMPLICATED FOLDING AND 3D-MODELING OF PRECAMBRIAN FORMATIONS

2-16

Laine Eevaliisa

Helsinki University of Technology, P.O. Box 6200, 02015 HUT, eevaliisa.laine@hut.fi

The geometry of Precambrian formations is complex (Fig. 1). Several consequent tectonic events have folded and faulted the rocks. In addition, partial melting and intense metamorphism have changed the original textures and structures of rocks. Estimation of rock properties between known values may be done

- manually, which is perhaps the best alternative in interpretation of rock contacts,
- using mathematical interpolation, or
- by using interpolation or sequential simulation based on statistical modeling of spatial continuity using a semivariogram calculation and modeling.

The objectives of the present study were the estimation of properties associated with folded rock layers, resolving complex tectonic events by spatial statistics, modeling complex anisotropies and creating an algorithm for using this model in estimation. The case studies included virtual geological formations that were created to resemble epithermal gold deposits in Finland using geological 3D-models and sequential indicator simulation (Journel and Alabert, 1989). One of the realizations was chosen as a virtual deposit.

Estimations were done using geostatistical interpolation - kriging. The ordinary kriging assumes that the used variables have symmetric distribution. However, the Earth science data sets have mostly skewed distributions, thus, a non parametric indicator kriging (Journel, 1983), was applied. In addition to estimation of local probability distributions, the binary coding was used to detect tectonic orientations (Fig. 2).

The following approaches were tested:

1. variogram modeling of indicator transforms in detecting and analyzing tectonic orientations,
2. ordinary and indicator kriging using global coordinates in estimations,
3. unfolding techniques and kriging in estimations and
4. variogram modeling and kriging at local coordinates in estimation of rock properties at deformed rock formations.

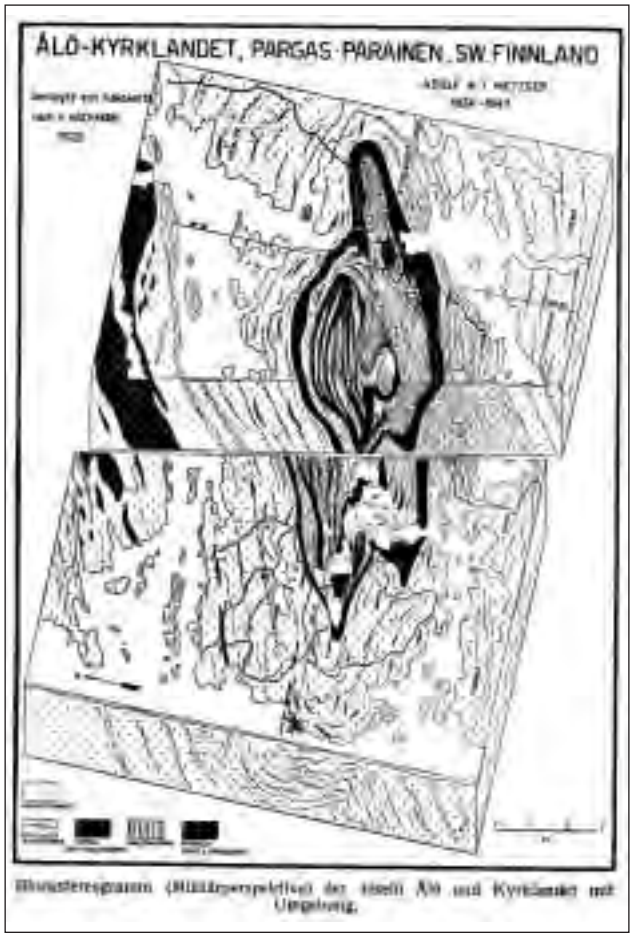

Figure 1. A 3D model of Parainen limestone deposit made by Adolf Metzger 1924-44.

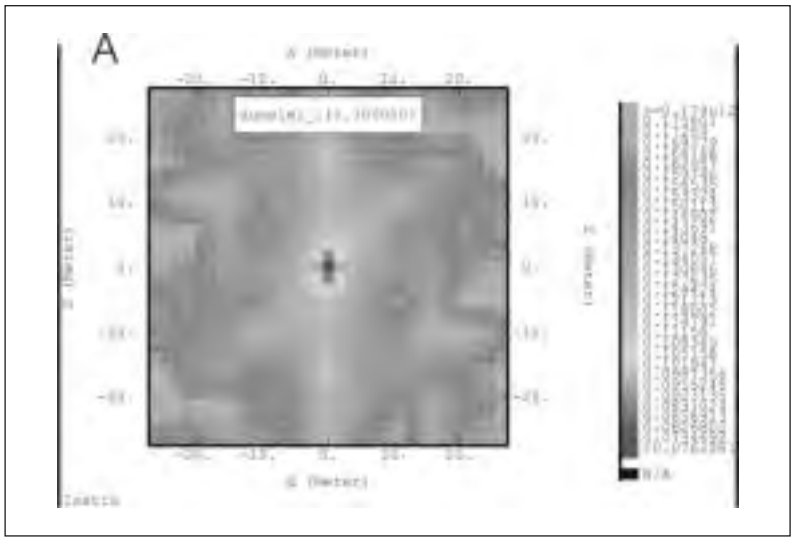

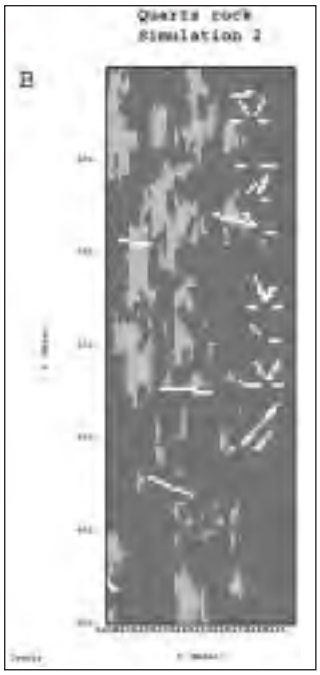

Figure 2. A) A variogram map of a indicator transform for a threshold of gold content of 5.3 g/t shows a vertical continuity at Kutemajärvi gold deposit. B) A simulated realization of the distribution of quartz rich rocks at the Kutemajärvi gold deposit.

As a result:
- The indicator kriging is better than ordinary kriging in resolving anisotropies in complex geological formations
- The use local coordinates is needed in estimation of rock properties along folded formations because all the properties are not following the layring, and the unfolding may destroy these orientations.
- Finally, there exist often more than one direction of maximum continuity, for example, in the case of rock properties associated with fracturing.

REFERENCES

- Journel, A. G. 1983. Non-parametric estimation of spatial distributions. Math. Geol., 15, pp. 445-468.
- Journel, A. and Alabert, F., 1989. Non-Gaussian data expansion in the earth sciences. Terra Nova, 1, pp. 123-134.

WHICH PARAMETERS CONTROL KINEMATICS AND MASS TRANSFER WITHIN SUBDUCTION CHANNELS? 2-17

J. Lohrmann, N. Kukowski, C.M. Krawczyk, O. Oncken

GeoForschungsZentrum Potsdam,Telegrafenberg D-14473 Potsdam, jo@gfz-potsdam.de

Abstract

Two series of scaled sandbox experiments were carried out to simulate accretive forearcs with different modes of mass transfer. By analysing the incremental displacement-gradient field, we define criteria to determine subduction channel geometries. The results show that each accretion mode exhibits an unique pattern of material flow-rate within the subduction channel.
Among the controlling parameters, the gradient of mechanical material properties at the top of the subduction channel and the amount of rearward material loss are of predominant importance. The vertical load and the activity of faults in the overlying wedge exert only minor control on the mass-transfer mode. However, it is very difficult to unequivocally identify the set of parameters that controls the mass budget of a specific forearc in nature, as demonstrated by the South-Chilean Forearc.

1. Introduction

Subduction channels are thin zones at the interface between the subducting and overriding plates, where highly diverse material (a melange of oceanic crust, pelagic and continentally derived sediments, and continental basement) is transported landward (e.g. Fig. 1). They are one of the most important geodynamic elements of subduction scenarios, as they control the whole mass budget of forearcs (Cloos and Shreve, 1988a/b): If the material flow-rate through the subduction channel is higher than the supply rate of new sediment from the trench, the forearc has a net-negative mass balance, i.e. tectonic erosion occurs. In contrast, a flow rate of the channel material that is lower than the supply rate of new sediments, forces growth of the forearc by frontal or basal accretion. These growth modes are responsible for the internal architecture of forearc wedges and vertical surface movements.

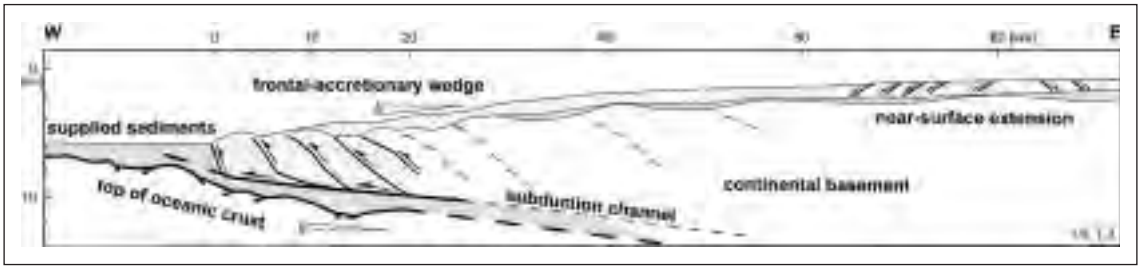

Figure 1: Cross-sectional sketch of the South-Chilean Forearc based on interpreted reflection seismic sections of RC 2901/730,732, modified after Díaz-Naveas (1999).

Theory argues that the channel geometry predominantly governs the material velocities and, thus the mass-transfer mode (Cloos and Shreve, 1988b). In nature, the geometry of fossil subduction channels, which are exposed at the surface, can be determined by mapping the highest displacement gradient between the constant velocity field of the upper and lower plate, respectively. This method provides a geometry that integrates all material that was transported through the channel and may have left it also by basal accretion. The question remains open, whether this finite displacement gradient is appropriate to understand the dynamics of mass-transfer modes. Moreover, the influence of various parameters (e.g. vertical load, mechanical material properties and rearward material loss, see section 2) possibly controlling the material flow-rates in the subduction channel is unknown.
Our study attempts to address this issue with focus on processes in the brittle field of accretive subduction channels. Subduction zones in nature are unsuitable for this investigation, as the controlling parameters are not accessible by geophysical or geological techniques. The observable features (e.g. vertical surface movements, tectonic structures) are caused by a combination of several parameters. Thus, field investigations cannot separate the effect of a single parameter. Therefore, we simulated subduction scenarios in series of scaled sandbox experiments, in which only one parameter per experiment was changed. We compared the experiments to identify the specific influence of each parameter. The experimental results were tested against data obtained from a 'real-world' subduction scenario to demonstrate the reliability and applicability of the simulations. We chose the South-Chilean Forearc (37-38°S), since the onshore-offshore reflection seismic profiles of the survey SPOC at 38°S (Subduction Processes Off Chile; Krawczyk et al., 2003) show that this forearc has established a subduction channel. In the study area, frontal accretion of the upper part of the incoming sediments and basal accretion of the lower sediments occur coevally (as seen for example in a marine reflection seismic line RC-2901/730 at 37.55°S, Fig. 1). Along-strike variations of the surface kinematics suggest a lateral change in the recent, deep-seated mass-transfer mode. In this study, we also attempt to identify the parameter causing this change.

2. Experimental Setup

The analogue experiments were performed in a glass-sided box (320–380 cm length and 20 cm width; for details see Tab. 1 and Fig. 2a) at a scale factor of 105. We chose granular analogue materials, which deform similarly to brittle crustal rocks with a strain-hardening and strain-softening phase prior to stable sliding (Lohrmann et al., 2003). In the device, a conveyor belt was drawn toward the rigid backwall along a 5° inclined base. The conveyor belt was covered with sandpaper and simulated the rough top of the oceanic crust. In front of the backwall, a wedge-shaped body (i.e. deformable backstop; 115–135 cm initial length, 2–6° initial surface slope) acted as a continental forearc wedge in a subduction scenario. A sand layer (2–3.5 cm thickness) that was sifted on top of the conveyor belt simulated the sediments that are supplied to the forearc by convergence of the subducting plate. We varied the following parameters in two series of experiments to investigate their specific influence (Tab. 1, Fig. 2b):

- **Rearward material loss** through the subduction channel is experimentally shown as a parameter strongly influencing the mass-transfer mode of forearc settings (e.g. Kukowski et al., 1994; Lohrmann, 2002). Also in nature, parts of the sediments, which are transported from the trench into the forearc, can be moved to greater depths (e.g. Morris et al., 1990). In our experiments, this was simulated by lifting the rigid backwall (i. e. open setup) and allowing material loss of 50% of the underthrust sediments.
- **Vertical load** was varied by changing the initial thickness of the backstop without changing its surface slope. This parameter was chosen because Cloos and Shreve (1988b) showed that the vertical load resulting from forearc geometry and rock density can significantly influence the amount and position of rearward material loss.
- **Friction contrast** along the transition of subduction-channel material and primary wedge material was varied by choosing different material combinations. The use of the same kind of sand in an experiment produces only a very minor friction contrast. Incorporation of a thin layer of glass-beads, which is significantly weaker than sand, in the incoming sand-layer increases the friction contrast along the entire length of the subduction channel. Adding the glass-beads only in the rear

of the deformable backstop simulates depth-dependent softening along the top of the subduction channel. The justification for this comes from rheological studies indicating depth- and material-dependent friction contrasts in nature (e.g. Hacker et al., 2003).

The first series of experiments focused only on the fundamental processes of subduction channels. A strongly-idealised open setup was chosen with a homogenous incoming layer and deformable backstop, both consisting of sifted sand (sifting height ca. 20 cm, rate 130 cm^3 min^{-1}). In this series, we tested the influence of depth-dependent softening of top of the channel and vertical load (Tab. 1, Fig. 2a).

The second experiment series aimed at an application to the South-Chilean Forearc. In this case, we used a mechanically-stratified incoming sand/glass-bead layer and a deformable backstop consisting of mortar. The former allows to simulate the decoupling between the upper and lower part of the incoming sediments and the latter represents the continental basement wedge. The initial geometry of these experiments was adopted from seismic lines across the South-Chilean Forearc (Tab. 1, Fig. 1, F We monitored the experiments with a PIV System (Particle Imaging Velocimetry; Adam et al., 2002). This image-correlation technique provides a precise measure of the incremental displacement field every 4 seconds (equivalent to 3.8 mm of convergence) with a spatial resolution of 1.4 mm. From the displacement field all components of the displacement gradient tensor were calculated. These components allow to study the influence of the aforementioned parameters on kinematics, growth mechanisms, and internal deformation patterns of the convergent sand wedges.

experiment		varied parameters			stable-dynamic friction and cohesion [Pa]				thickness of sand layer	surface slope	convergence
		backstop	material loss (setup)	friction contrast	sand paper/sand	sand	glass beads	mortar			
1st series	KOL	thicK	10 mm (Open)	Low	0.55±0.002; 44±10	0.57±0.002; 67±5	...	...	20 mm	2°	330 cm
	NOL	thiN	10 mm (Open)	Low	0.55±0.002; 44±10	0.57±0.002; 67±5	...	...	20 mm	2°	390 cm
	KOI	thicK	10 mm (Open)	Increase	0.55±0.002; 44±10	0.57±0.002; 67±5	0.43±0.014; 34±2	...	20 mm	2°	300 cm
2nd series	KOH	thicK	7 mm (Open)	High	0.55±0.002; 44±10	0.57±0.002; 67±5	0.43±0.014; 34±2	0.66±0.004; 24±13	14+20 mm	6°	180 cm
	NOH	thiN	7 mm (Open)	High	0.55±0.002; 44±10	0.57±0.002; 67±5	0.43±0.014; 34±2	0.66±0.004; 24±13	14+20 mm	6°	200 cm
	NCH	thiN	0 mm (Closed)	High	0.55±0.002; 44±10	0.57±0.002; 67±5	0.43±0.014; 34±2	0.66±0.004; 24±13	14+20 mm	6°	240 cm

Table 1: Setup and nomenclature of the experiments.

3. Experimental Results

In every experiment a subduction channel developed, i.e. material was transported from the wedge tip along a thin zone (< 3 cm) at the wedge base, even though each sand wedge underwent rather different modes of accretion (pure frontal or basal accretion in the 1st series, coeval frontal and basal accretion in the 2nd series; Fig. 2c).

The displacement-gradient fields show that the geometry of the subduction channel was distinctly variable within each thrust cycle in all experiments. For example, a cycle of a purely basally-accretive wedge started as soon as a new ramp was initiated at the tip of the wedge. In this stage, only the basal detachment on top of the sand paper was active and no material was transported at the base of the wedge. However, basal transport was subsequently initiated by reactivation of a roof thrust (Fig. 2d). During a later stage of the thrust cycle, geometry and position of the slip planes at the top and bottom of the channel underwent fast fluctuations and their shear-strain magnitudes strongly changed. Further convergence forced the initiation and reactivation of branch thrusts and duplexes left the channel by accretion into the overlying wedge. This basal accretion caused uplift and bending of the overlying material (i.e. previously-accreted material and primary wedge material) and was confined to the rear by discontinuously-active backthrusts. Beneath active backthrusts, higher material flow-rates occurred. Their activity encouraged accretion of material further to the rear, compared to situations with inactive backthrusts.

We used the highest displacement gradient in the time increment representing one thrust cycle to determine the channel boundaries. This provided channel geometries, in which the whole range of geometric fluctuations are considered without the displacement signal of material that has left the subduction channel by accretion. These channel geometries and related material flow-rates show distinct patterns indicative for each of the accretion modes.

Comparison of the experiments shows that an initially lower vertical load on the subduction channel maintains a higher flow rate than an initially higher vertical load. This effect occurs in both series (Fig. 2c). Thus, the influence of vertical load is independent of the friction contrast at the top of the channel (if the friction contrast is constant). The material loss of an open setup also results in a more rearward position of basal accretion. This parameter is more dominant than vertical load, as material beneath an initially thinner wedge in a closed setup is accreted in a more frontal position. In the range of parameters tested in this study, the most dominant parameter was the friction-contrast gradient at the top of the channel. Its variation forced a complete change in the mass-transfer mode: glass beads at the rear of an initially thick wedge caused basal accretion, whereas the sand wedge of the same thickness without the friction-contrast gradient was purely frontally-accretive.

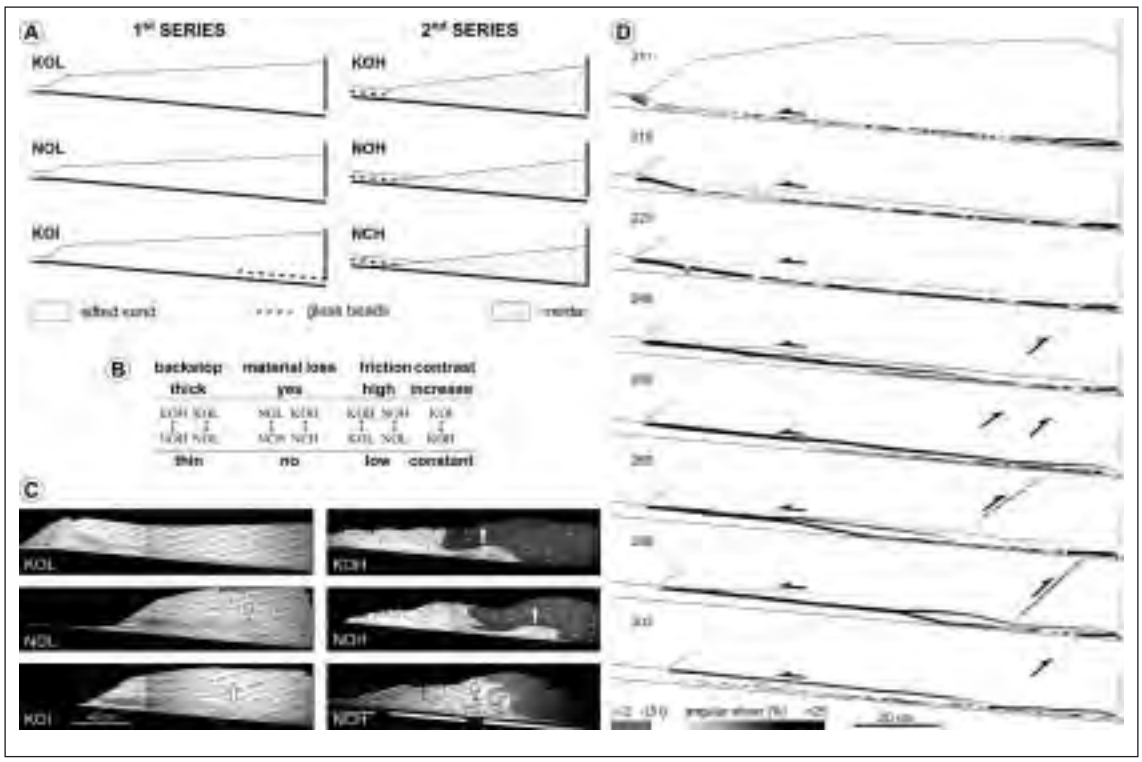

Figure 2: a) Setup of the experiments. b) Overview of the pairs of experiments compared to identify the influence of the parameters. c) Final stages of the experiments. Arrows indicate the position of the centre of uplift after 150 cm of convergence. d) Evolution of one thrust cycle in the NOL experiment. The incremental angular shear accumulated during 3.8 mm of convergence image the magnitude and shear sense of instantaneously-active faults. Numbers denote centimetres of total convergence.

4. Application to Nature

All sandbox experiments of the 2nd series formed a detachment along the glass-bead horizon. This enabled frontal accretion of the upper part of the incoming sand-layer. The lower part of the incoming sand-layer was underthrust within the subduction channel and basally accreted (Fig. 2c). Basal accretion produced convex-upward thrust units and bending of the overlying wedge, which showed near-surface extension above the centre of basal accretion. To accommodate the uplift, several steep backthrusts were subsequently initiated. These young toward the rear and early-formed backthrusts were reactivated due to underthrusting of thickened duplexes.

The structural features of this mode of basal accretion are comparable to structures observed at the South Chilean Forearc: In the SPOC on-shore reflection seismic profile at 38°S, strong reflective elements are observed above the top of the oceanic crust. These structures are interpreted as the top of the subduction channel, which is at least 3 km thick. In this cross-section, steeply W-dipping fault traces dissect the whole imaged forearc down to the top of the channel. Slightly to the north of the

SPOC profile, a cluster of earthquakes was recorded during the ISSA 2000 campaign (Integrated Seismological experiment in the Southern Andes). This cluster define an aligned, W-dipping zone of compressive activity from the plate interface up to depth of 3 km (Melnick et al., 2003). The geometrical similarity of this zone of seismicity to the fault traces in the SPOC profile suggests that these faults might represent backthrusts. Trenchward of these inferred backthrusts, a domain of syn-uplift extension was interpreted in a marine reflection seismic section (RC-2901/730; Fig. 1; Díaz-Naveas, 1999). This kinematic domain is comparable to the area of uplift due to basal accretion in the sandbox simulation. In addition, the relative position of the backthrusts at the South-Chilean Forearc are in accordance with that of the reactivated backthrusts of the basally-accretive experiments.
However, further to the north (37°S) a domain of syn-uplift extension is in more landward position as defined by geological mapping. Therefore, we suggest a shift in the position of basal accretion along strike. The off-shore SPOC-data show that the slab is shallower inclined (13°) in the northern uplift area than in the south (15°) and indicate an along-strike increase of thickness of the wedge. This might imply that the shift of basal accretion results from a related increase in vertical load. However, the experiments reveal that the change of each investigated parameter would be able to cause such a shift. Thus, a distinct parameter combination that controls the mass-transfer mode of the South-Chilean Forearc, cannot yet be identified.

5. Conclusions

Our results confirm that subduction-channel geometry and material flow-rate mainly govern the accretion mode. However, the time increment, in which the channel geometry is determined from the displacement-gradient field, has to be carefully chosen. The finite displacement-gradient field (integrating over the whole time span of channel activity) is unsuitable: It includes the signal of material that has left the subduction channel by accretion. To avoid this ambiguity and to consider the whole range of channel-geometry fluctuations, only the record over one thrust cycle should be used as a valuable time increment.
This parameter-sensitivity study shows that friction-contrast gradients at the top of the subduction channel and rearward material loss dominate over the influence of the vertical load. Reactivated inherited structures in the overlying wedge, such as backthrusts, minorly influence the mode of accretion, but they are crucial for local transport rates. All investigated parameters show the same kind of bulk effect on the mass-transfer mode: The variation of parameters results in a shift of the position of basal accretion. Hence, lateral changes of forearc architecture in nature, which indicate a shift of basal accretion, cannot be unequivocally ascribed to one specific parameter or parameter combination.

Acknowledgements

This study was financially supported by the DFG (SFB 267). Technical support in the lab came from Günter Tauscher, Alex Kurta, Kerstin Mittelhaus, Anja Pigowske and Ulrike Schönrock. Special thanks to Dave Tanner for correcting the English.

REFERENCES

- Adam, J., Lohrmann, J., Hoth, S., Kukowski, N., Oncken, O. (2002): Strain variation and partitioning in thrust wedges: High-resolution data from scaled sandbox experiments by 2D-3D PIV analysis. Bol. Geofisica 42, 123-125.
- Cloos, M. and Shreve, R.L. (1988a): Subduction-channel model of prism accretion, melange formation, sediment subduction, and subduction erosion at convergent plate margins; Part I, Background and description. Pure Appl. Geoph. 128(3-4), 455-500.
- Cloos, M. and Shreve, R.L. (1988b): Subduction-channel model of prism accretion, melange formation, sediment subduction, and subduction erosion at convergent plate margins; Part II, Implications and discussion. Pure App. Geoph. 128(3-4), 501-545.
- Díaz-Naveas, J.L. (1999): Sediment subduction and accretion at the Chilean convergent margin. PhD-Thesis, Ch. Albrechts Universität Kiel. pp. 130.
- Hacker, B. R., G. A. Abers, et al. (2003): Subduction factory 1. Theoretical mineralogy, densities, seismic wave speeds, and H2O contents, Journal of Geophysical Research, 108(B1): 10-1 - 10-26.
- Krawczyk, C.M. and the SPOC Team (2003): Amphibious seismic survey images plate interface at 1960 Chile earthquake. EOS, 84 (32), 301, 304-305.
- Kukowski, N., von Huene, R., Malavieile, J., Lallemand, S.E. (1994): Sediment accretion against a buttress beneath the Peruvian continental margin at 12°S as simulated with sandbox modeling. Geol. Rundsch., 83, 822-831.
- Lohrmann, J., Kukowski, N., Adam, J., Oncken, O. (2003): The impact of analogue material properties on the geometry, kinematics,

and dynamics of convergent sand wedges. J. Struc. Geol., 25, 10, 1691-1711.
• Lohrmann, J. (2002): Identification of Parameters Controlling the Accretive and tectonically Erosive Mass-Transfer Mode at the South-Central and North Chilean Forearc using Scaled 2D Sandbox Experiments. STR02/10, pp. 233.
• Melnick, D., Echtler, H., Pineda, V., Bohm, M., Manzanares, A., Asch, G. (2003): Active growing of the Arauco Peninsula, Southern Chile (37°30'S). 10th Congresso Geológico Chileno, Conception.
• Morris, J.D., Leeman, W.P. and Tera, F. (1990): The subducted component in island arc lavas; constraints from B-Be isotopes and Be systematics. Nature 344(6261), 31-36.

TESTING THE MINIMUM DISSIPATION THEORY IN SAND-BOX EXPERIMENTS 2-18

B. Maillot(*), H.A. Koyi(**)

(*) Département des Sciences de la Terre, UMR7072, Université de Cergy-Pontoise, France. Bertrand.Maillot@geol.u-cergy.fr
(**) Hans Ramberg Tectonic Laboratory, Dept. of Earth Sciences, Villav. 16, 752 36 Uppsala, Sweden. Hemin.Koyi@geo.uu.se

Summary

The results of a series of sand-box models consisting of layers of different mechanical properties (Nemours sand and glass beads) are presented here. The aim of this study is to check the principle of minimum dissipation applied to the passage through a lower flat-ramp transition of a frictional multi-layered material. The theory predicts the dips of back-thrusts developing in the hanging wall by minimising the overall dissipation occurring along the ramp and the back-thrusts. Previous experiments on a single homogeneous layer, made at the Institut Francais du Pétrole (IFP, Reuil-Malmaison, France), are satisfactorily described by the theory (Luu et al., 2003) However, in this work, we introduce mechanical anisotropy in the deformed granular layers and compare the results to the theoretical predictions. The results of the current models are in agreement with the theoretical predictions; 1, the dip of back-thrusts change across a mechanical discontinuity that provides a lower friction than the basal friction. In such a scenario, the back-thrusts become steeper upwards. And 2, a granular package with layered anisotropy do not develop any "visible" back-thrusts when shortened and transported above a ramp with zero friction.

The theory

The theory for a single frictional layer, and for the micro-laminate ductile materials is presented in Maillot and Leroy (2003). The theory for a frictional multi-layer is developed in Luu's Master Thesis (2003) in the framework of the theory of limit analysis, with examples with a three-layer sample. Here, we present the theory for a two-layer sample as illustrated in Figure 1.

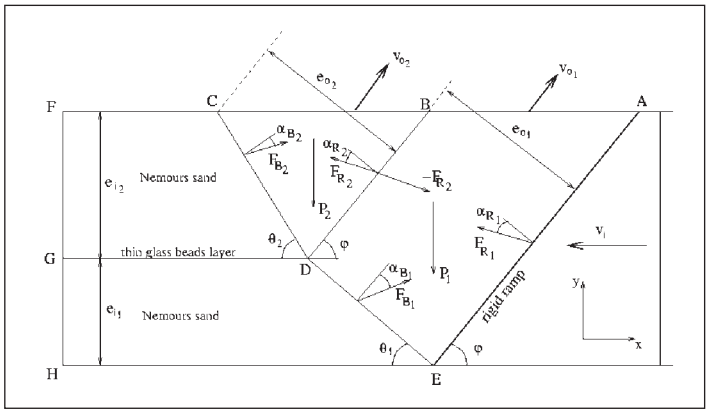

Figure 1. Illustration of the kinematics and definition of the parameters and of the forces.

A rigid ramp (AE) dipping with an angle φ is moving horizontally at a velocity υ_i towards a granular material sample (AFHE) made of two layers of Nemours sand separated by a thin layer (GDB) of glass beads. This shortening results in the upward movement of the two layers (ABDE) and (BCD), at respective velocities υ_{o1} and υ_{o2}, which are fully eroded along the line (AF). We assume that there is no internal deformation and that the movements therefore occur only along the thrust planes (EA) and (DB), which we will call "ramps" 1 and 2, and along (ED) and (DC), which we will call "back thrusts" 1 and 2, respectively. We further assume that the deformation is isochoric and stationary. The goal is to find the back thrust dips θ_1 and θ_2 which minimise the overall dissipation of energy. With the assumptions mentioned above, the dissipation of energy occurs solely along the two ramps and the two back thrusts. It is defined as the product of the shear force along the plane with the jump in tangential velocity across the plane:

$D_{R1} = F_{R1} \sin \alpha_{R1} \upsilon_{o1}$ jump (1)
$D_{R2} = F_{R2} \sin \alpha_{R2} (\upsilon_{o2}-\upsilon_{o1})$ (2)
$D_{B1} = F_{B1} \sin \alpha_{B1} (\upsilon_{o1} \cos (\theta_1 + \varphi) - \upsilon_i \cos \theta_1)$ (3)
$D_{B2} = F_{B2} \sin \alpha_{B2} (\upsilon_{o2} \cos (\theta_2 + \varphi) - \upsilon_i \cos \theta_2)$ (4)

where D_{R1}, D_{R2}, D_{B1}, D_{B2}, are respectively the dissipations along the thrust planes (EA), (DB), (ED), (DC). α_{R1}, α_{R2}, α_{B1}, α_{B2}, are the friction angles along these planes (cohesion is neglected). The four unknown forces F_{R1}, F_{R2}, F_{B1}, F_{B2} are determined by writing the global equilibrium of the two parts of the hanging wall (BDC), and (AEDB), while the weights P_1 and P_2 are directly calculated from figure 1. The total dissipation may be written

$D = D_{R1} + D_{R2} + D_{B1} + D_{B2} = F \upsilon_i$,

where

$$F = \tfrac{1}{2}\rho g e_{i1} e_{i2} . k(\varphi, \theta_1, \theta_2, \alpha_{R1}, \alpha_{R2}, \alpha_{B1}, \alpha_{B2}, e_{i1}/e_{i2}) \quad (5)$$

is the force conjugate to υ_i in the sense of dissipation. Finally, the optimal back thrust dips θ_1 and θ_2 are determined by solving

$$\frac{\partial k}{\partial \theta_1} = 0, \text{ and } \frac{\partial k}{\partial \theta_2} = 0 \quad (6)$$

Two solutions are analysed for ramp dips $\varphi = 30°$ and 45°. Other parameters were set as follows: α_{R1} varying from 0.5° to 40°, $17° \leq \alpha_{R2} = 24.5° \leq 24° \leq \alpha_{B1} = \alpha_{B2} \leq 32°$, and $e_{i1} = 11.5$ mm, $e_{i2} = 10.5$ mm.

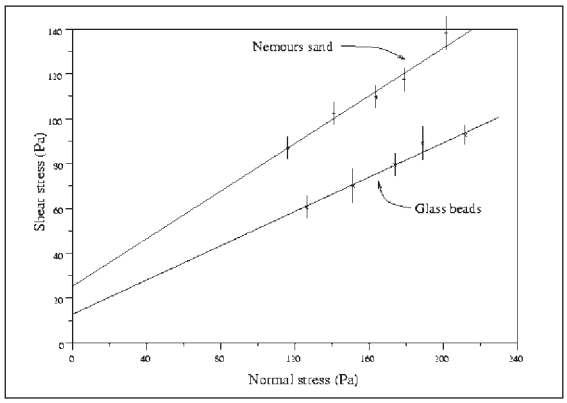

Figure 2. Failure envelopes for the Nemours sand and the glass beads. A linear regression with error bars gives a friction coefficient of 0.531 ± 0.087 and a cohesion of 25.1 ± 13.7 Pa for the Nemours sand, and a friction coefficient of 0.382 ± 0.072 and a cohesion of 12.7.1± 12.9 Pa for the Glass beads.

Model materials, preparation and kinematics

Two different granular materials (Nemours sand and micro glass beads) were used in the models described here. The mechanical properties of these two materials were measured with a newly designed apparatus that possess a minimum apparatus friction. The grain size of the sand range between 80 and 120 μm, with a sharp peak at 100 μm. Figure 2 shows he internal friction angle of the Nemours sand and glass beads. In all experiments, we have tried to be consistent during the preparation of the layers; pouring sand in small amounts on the surface of the model and scraping the sand pile to a horizontal layer. Coloured marker horizons (each less than one mm thick) were sprinkled on the surface of the models to act as strain markers.

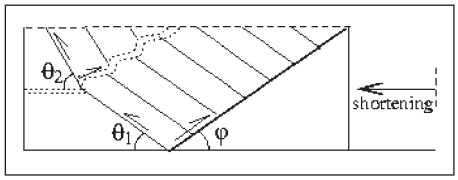

Figure 3. A theoretical sketch of a model with a discontinuity that provides a lower friction than that of the basal friction. Note that the back-thrusts are steeper (θ_2) above the discontinuity (dashed) layer.

The current experiments aimed at testing the theory of limit analysis in the case of a sample material made of two frictional layers separated by a thin layer with a different internal friction (Figure 3). The models with the above setting (25 mm thick, 200 mm wide and 200 mm long) were shortened by a backstop ramp with various dips. The box used for these experiments had the dimensions 200 x 200 x 100 mm. Friction along the ramp was varied in the models; zero friction in some models (the ramp was driven under a fiberglass sheet above which the granular layers were placed), low friction in some models (a fiberglass sheet was glued on the surface of the ramp) and high friction in some other models (a sand paper was glued on the ramp surface). During shortening, the ramp (with different friction) was pushed towards the layers which were transported above the ramp. Any topography that formed during the shortening were eroded by removing all sand accumulating above the ramp (i.e., conditions of full erosion). The sample is expected to slide upward along the ramp where a series of back-thrusts, with possibly different dips in each layer, were formed in the displaced layers. Once the maximum shortening was reached, allowed by the geometry of the box , the experiment was stopped, and the sample was cut to measure the dips of the back-thrusts to be compared with the theoretical predictions.

Results and discussion

During shortening of the models, the granular package was transported above the ramp which was moved in the model. In the models with low and high friction, a series of back-thrusts formed when the granular layers were transported above the ramp. In the models with no zero ramp friction, no back-thrusts were visible. Models results are in good agreement with the theoretical predictions (Figure 4).

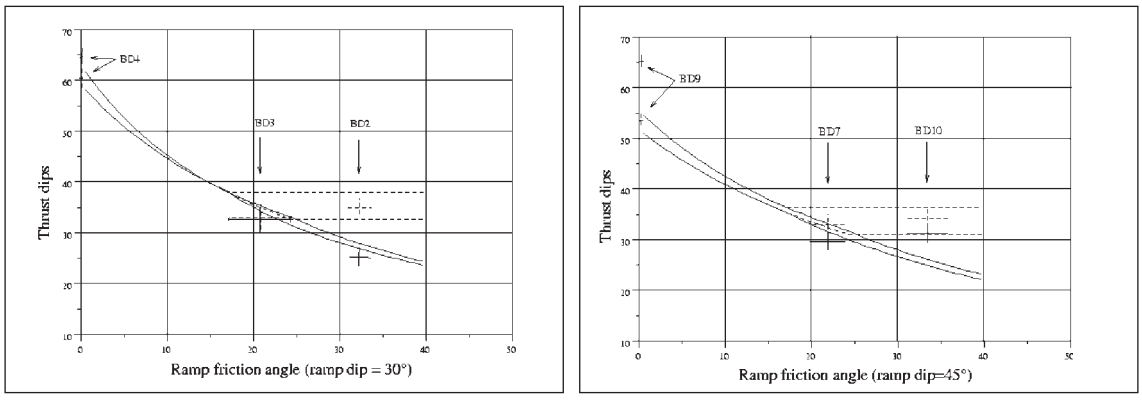

Figure 4. Comparison between theoretical and observed thrust dips for a variable friction on the ramp, dipping at a, 30° and b, 40°. Solid and dashed lines: range of theoretical thrust dips for the upper and lower units. Ranges are due to uncertainties on the determination of friction angles. Solid and dashed crosses: experimental data for upper and lower units, with error bars on both axes.

In general, two main features can be summarised from these experiments: First, the back thrust dips depend mainly on the friction along the rigid ramp (ramp 1). If this friction is lower than the interlayer friction (ramp 2), then the back thrusts exhibit no refraction, i.e., they exhibit similar dips, and there is no, or little, slip along the interlayer bed. If on the contrary, the interlayer friction is lower than that of the rigid ramp, then slip will occur between the top and bottom layers which will exhibit different back thrust dips. Moreover, the top layer will have steeper back thrusts than the bottom layer, as predicted by our theory. Second, the experiments BD4 and BD9, with zero friction along the ramp, do not show any staircase shape of the passive markers in the hanging wall: the back thrusts thus form continuously, or, equivalently, the distance between them tends to zero. Friction on the ramp thus appears to play a key role in the development of thrusts in the hanging wall.

REFERENCES

- Bonini, M., D. Sokoutis, G. Mulugeta, and E. Katrivanos (2000), Modelling hanging wall accommodation above rigid thrust ramps, J. Struct. Geol., 22, 1165-1179.
- Cobbold, P.R., and L. Castro (1999), Fluid pressure and effective stress in sandbox models, Tectonophysics, 301,1-19,
- Erickson, J.P., and W.R. Jamison (1995), Viscous-plastic finite element models of fault-bend folds, J. Struct. Geol., 17 (4), 561-573.
- Krantz, R.W. (1991), Measurements of friction coefficients and cohesion for faulting and fault reactivation in laboratory models using sand and sand mixtures, Tectonophysics, 1888, 203-207.
- Luu, T. T. (2003), ``Application du calcul a la rupture a un pli de rampe", Master's Thesis (Directors: B. Maillot and Y. Leroy), École Nationale des Ponts et Chaussées.
- Maillot, B., and Y. M. Leroy (2003), Optimal dip based on dissipation of backthrusts and hinges in fold-and-thrust belts, Jour. Geophys. Res., 108(B6), 2320-2339.
- Luu, T.T., Maillot, B., and Y. M. Leroy (2004), A mechanical analysis of the lower flat-ramp transition in a multi-layer hanging wall, Poster presentation, XVIth Geol. Winter Meeting, Uppsala, Sweden.
- Merchant, E. (1945), Mechanics of the Metal Cutting process. II. Plasticity conditions in orthogonal Cutting, J. Appl. Phys., 16, 318-324.
- Merchant, E. (1944), Basic mechanics of the metal-cutting process. J. Appl. Mech., 168-175.
- Merle, O., and N. Abidi (1995), Approche expérimentale du fonctionnement des rampes émergentes, Bul. Soc. géol. Fr., 166, 5, 439-450.
- Persson, K.S. (2001), Effective indenters and the development of double-vergent orogens: Insights from analogue sand models, In Koyi H.A., and Mancktelow, N.S., eds., Tectonic modelling: a volume in honor of Hans Ramberg: Boulder, Colorado, Geol. Soc. Am. Memoir 193, 191-206.
- Schellart, W.P. (2000), Shear test results for cohesion and friction coefficients for different granular materials: scaling implications for their usage in analogue modelling, Tectonophysics, 324, 1-16.

NUMERICAL MODELLING OF ASYMMETRIC SINGLE- AND MULTI-LAYER FOLDS

2-19

Neil Mancktelow

Geologisches Institut, ETH-Zentrum, CH-8092 Zürich, Switzerland

Asymmetric folds are common in nature and indeed the change in vergence of mesoscopic parasitic folds is an accepted criterion for mapping regional-scale fold structures. The asymmetry of intrafolial folds in shear zones is also often used to imply the sense-of-shear. However, most theoretical and modelling studies of fold development have concentrated on symmetric folding developed by shortening parallel to layering. The development of asymmetric folding is analysed here using finite-element numerical models of layers in oblique orientations or deformed under simple and general shear. Both viscous and viscoelastic rheologies are considered. In general, the effects of rotational deformation or oblique shortening are similar. For single layers, the shape of the folded layer remains symmetric up to quite high amplitude, but the strain distribution in the matrix is clearly asymmetric from the outset. Strongly asymmetric forms are difficult to generate in isolated single layers. As the layer rotates during ongoing deformation, it eventually enters the field of incremental extension and tends to unfold again. Boudins are not readily developed in viscoelastic materials, and may require pressure-sensitive rheology (e.g. Mohr-Coulomb plasticity). Differing boundary conditions produce

an increase in the asymmetry of single-layer folds in the order: (1) simple shear of an oblique layer, (2) pure shear of an oblique layer, and (3) transtension (combined pure and simple shear with shortening parallel to shear direction) of a shear-zone parallel layer. Infinite multi-layers readily develop strong asymmetric folds, in which the axial plane tracks a material plane. As established by Ramberg (see summary in Ramberg, 1981), below a critical spacing in an infinite multi-layer there is no dominant wavelength and the growth rate increases monotonically with increasing wavelength. As a result, polyharmonic folds do not develop in a multi-layer of alternating strong layers and weak matrix. Even in a three-material layered system, true polyharmonic folds with clearly asymmetric parasitic folds are difficult to develop in models made up of homogeneous, isotropic, viscoelastic materials.

REFERENCES

• Ramberg, H. 1981. Gravity, Deformation and the Earth's Crust. Academic Press, London.

STRUCTURAL EVOLUTION OF FOLD-THRUST STRUCTURES DEVELOPED IN ANALOG (CENTRIFUGE) MODELS 2-20

Todd E. Noble, John M. Dixon

Department of Geological Sciences and Geological Engineering –Queen's University,Kingston, ON, Canada, K7L 3N6

Summary

We investigate the structural evolution of fold-thrust systems by analog scale modelling by the centrifuge technique, using a large geotechnical centrifuge. Multilayer models are constructed of plasticine and silicone putty to simulate foreland stratigraphic sequences and are shortened horizontally to simulate the nucleation and progressive growth of fold-thrust structures and fold-thrust systems as a whole. The models accurately reconstruct the structural evolution and geometrical development of duplex structures and provide insight into the temporal development of fold-thrust phenomena. An evolutionary relationship between folding and faulting exists; the low-amplitude buckling instability of the competent unit localizes and controls the spacing of thrust ramps in duplex structures. Internal laminations in the competent units reveal the spatial and temporal interplay of faulting, folding and layer-parallel shortening during the development of the individual overthrust structures. The deformation mechanisms active in the development of model overthrust structures are similar to those documented from natural prototype structures.

Abstract text

Modelling of fold and thrust structures is carried out in the C-CORE centrifuge facility that houses an Accutronic 680-2 centrifuge with a radius of 5.5m, capable of a maximum rotational speed of 189 rpm or exerting 200 times the force of gravity at the platform. The payload platform measures 1.4 m long by 1.1 m wide with a capacity of 130 g-tonnes at 200 g. The capacity of the centrifuge is large enough to accommodate a servo-controlled mechanical drive system and load-monitoring devices to measure stress/strain/strain-rate relationships during shortening of a model.

Models representing a stratified foreland sedimentary succession are typically 950 mm long, 100 mm wide and 60-80 mm thick. The linear scale ratio is ~$2x10^{-5}$ (20 mm = 1 km). The models are constructed of the materials plasticine modelling clay (Harbutts Gold Medal Brand) and silicone putty (Dow Corning Dilatant Compound 3179). Competent stratigraphic units are composed of laminated plasticine, and are mechanical analogs for limestones or coarse clastics. Incompetent units are composed of alternating silicone putty and plasticine layers that represent shale interbedded with sandstone, limestone or siltstone. The thin internal laminations in both the competent and incompetent units act as strain markers that reveal the spatial and temporal interplay of faulting, folding and layer-parallel shortening (LPS) during the development of the fold-thrust structures.

The models deformed at C-CORE replicate dynamically scaled models previously deformed in the smaller but higher-**g** centrifuge at Queen's University (Dixon & Liu, 1992; Liu & Dixon, 1995). Physical scale modelling at both Queen's University and C-CORE follows scale-model theory to ensure that the selected set of length, density and acceleration ratios lead to the development of realistic representations of geologic structures. According to scale theory, by maintaining a similar stress ratio between the models deformed at C-CORE and Queen's as well as the natural prototype system, the analog structures in both types of models should evolve in a kinematically and geometrically similar fashion to natural prototype structures (Table 1).
Model TN16, one of a series of models deformed at C-CORE, is composed of five internally layered stratigraphic units of alternating bulk competency, with an incompetent unit at the base. It was deformed at a constant shortening rate of 0.05 mm/s from an initial length of 904 mm to a total of 35% shortening in two stages of deformation (Fig. 1). During the first stage of deformation, a buckle-fold train propagates serially from hinterland to foreland in the competent units with diminishing fold amplitude toward the foreland. During continued deformation to 35% bulk shortening, the buckle-fold train propagated further towards the foreland in both competent units. In addition, the hinterland region of the lowermost competent unit that was previously pervaded by buckle folds had developed into a series of thrust horses bounded by thrust ramps with regular spacing and consistent structural style. An evolutionary relationship between folding and thrusting can be observed; the low-amplitude buckling instability of the lowermost competent unit localizes and controls the thrust ramps in duplex structures. The regular spacing of the thrust horses in model TN16 is inherited from the buckling wavelength of the competent unit, with an average thrust spacing of 87mm; scaled at 20mm = 1km, the 1 km thick competent unit has an average thrust spacing of 4.35 km.

	Queen's Model Ratio	C-CORE Model Ratio	Equivalence for C-CORE Models and Prototype
Length	$l_r=1.0x10^{-6}$	$l_r=2.0x10^{-5}$	20mm=1km
Specific Gravity	$\rho_r=0.6$	$\rho_r=0.6$	1.60=2.67 (bulk value for the whole stratigraphic column)
Time (strain rate)	$t_r=1.0x10^{-11}$	$t_r=1.0x10^{-11}$	e.g. 10^{-4} s^{-1} = 10^{-15} s^{-1}
Viscosity	$\mu_r=2.4x10^{-14}$	$\mu_r=2.4x10^{-14}$	$2.4x10^{2}$ Pa s =10^{16} Pa s
Acceleration	$a_r=3.2x10^{3}$	$a_r=1.6x10^{2}$	160g = 1g
Stress	$\sigma_r=\rho_r\ l_r\ a_r=1.9x10^{-3}$	$\sigma_r=\rho_r\ l_r\ a_r=1.9x10^{-3}$	(calculated from other ratios)

Table 1- Scale ratios of models deformed at Queen's University and C-CORE and equivalence to the natural prototype.

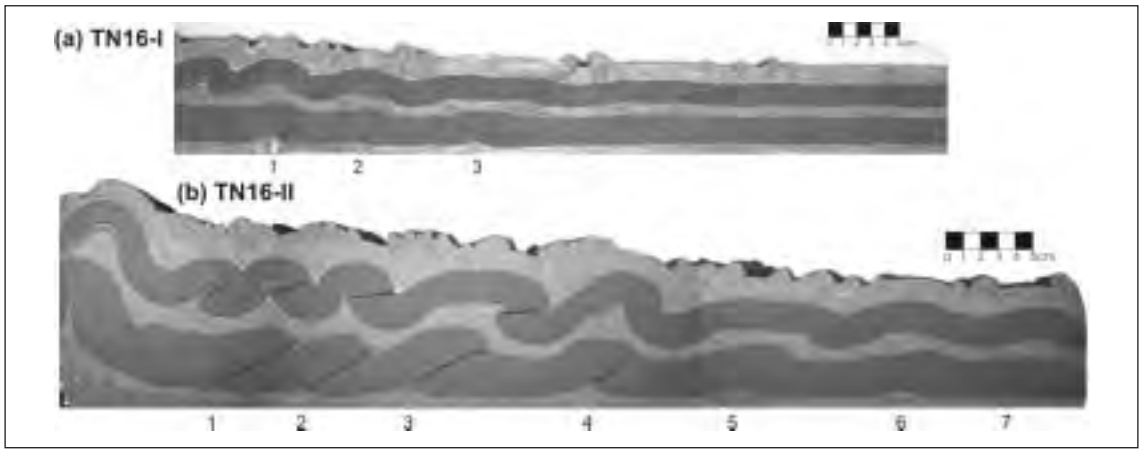

Figure 1 - Transverse profiles of model TN16 taken after two stages of deformation. The model was horizontally shortened at a constant shortening rate by 15% during stage I, (a), then to a total of 35% shortening during stage II, (b). The buckle folds and associated thrust structures in the lower competent unit are numbered (1-7) in order of their sequential development on both the stage I and stage II photographs.

The temporal development of fold-thrust structures revealed by observing progressively younger structures towards the foreland end of the models provides insight into the timing of different deformation mechanisms that contribute to the development of an individual overthrust. Individual fold-thrust structures develop in the following progression: a buckle-fold train propagates serially from hinterland to foreland through a competent unit; each buckle fold develops foreland vergence and small reverse faults localize in the steeply dipping forelimb (Fig. 2, structure 5); a thrust ramp then cuts through the forelimb generating a fault-propagation fold (Fig.2, structure 4) where displacement on the thrust diminishes to zero at the fault tip and internal strain is taken up by folding at the tip of the propagating thrust; the thrust ramp cuts through the entire competent unit and the hanging-wall panel is further displaced over the footwall ramp (Fig. 2, structure 3). We interpret that during the structural evolution of the overthrust structures the fault tip cuts both up-section towards the foreland through the forelimb of the fold in the competent unit, and down-section on a listric trajectory towards the hinterland into the underlying incompetent unit.

As observed in natural prototype structures, overthrust structures in model TN16 have hanging-wall panels that do not match footwall ramps because of differences in the internal strain above and below the thrust. The relative stretch values, ε_r, between the hanging wall and footwall panels along the major thrust faults for structures 2, 3 and 4 range from 0.75-0.8. Natural fold-thrust structures described by Williams and Chapman (1984) with a relative stretch of ~0.75 share a similar evolutionary history and geometry to those in model TN16. The asymmetrical fold grows well in advance of the propagating thrust, creating steeply dipping beds in the forelimb and a footwall syncline; a thrust then cuts up-section through the forelimb of the fold at a fast rate relative to fault slip, further modifying the fold profile by steepening the beds in the hanging wall immediately in front of the thrust (Chapman and Williams, 1984).

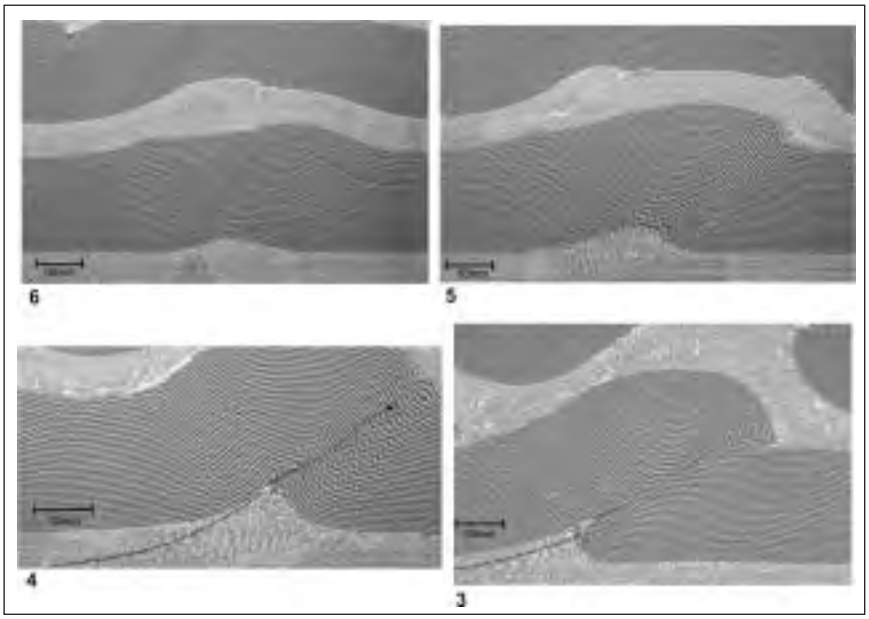

Figure 2 - Enlarged images of the sequential development of thrust structures in the lowermost competent unit of model TN16. The structures are numbered as in Figure 1(b).

Thrust sheets in the lowermost competent unit of model TN16 accommodate internal strain during overthrust development by generating arrays of planar, low-angle, minor contraction faults that accommodate horizontal shortening and vertical thickening of the units. Two fault arrays are present across each of the overthrust structures; an array of foreland-verging reverse faults initiating from the lower boundary of the competent unit, and a conjugate array of hinterland-verging reverse faults that develop at the upper boundary as a response to slip on their counterparts at the base of the unit (Fig. 3). The displacement on the contraction faults is greatest at the boundaries of the competent units, diminishing to zero at various distances inwards from the boundaries. Contraction faults that develop at the base of the unit are initially planar and form consistently at 30-35º to the structural dip

of the bedding laminations. In the case of tectonically mature structures near the hinterland end of the model, contraction faults form at 30-35º relative to the underlying thrust fault.

During the initial stages of overthrust development (Fig. 3, structures 5 & 6), regularly spaced contraction faults develop on the back-limb of the fold, initiating at the lower boundary of the competent unit as the sheet accommodates internal strain during development of the asymmetrical fold. In addition, foreland-verging contraction faults concentrate in the forelimb of the asymmetric fold. Internal strain is accommodated by contraction faults at the base of the forelimb, whereas folding accommodates internal strain at the upper boundary of the forelimb. Planar contraction faults that are partially incorporated into hanging-wall syncline develop a sigmoidal shape as the back limb is back-rotated during fold development (Fig. 3, structure 4). When the fold shape has reached maturity and the main thrust begins to cut through the forelimb, internal strain is concentrated in the hanging-wall panel during emplacement of the thrust sheet. Further internal strain in the hanging wall is accommodated at the base of the thrust sheet by an increase in the density of foreland-verging contraction faults (Fig. 3, structure 3). Thrust sheets in the Appalachians exhibit a similar deformation style where families of consistently oriented minor fault populations shorten and vertically thicken rocks nearest to the thrust (Wojtal, 1986). At the leading edge of the hanging-wall panel, continued folding and thinning of the forelimb is facilitated by relative displacement and rotation of fault-bounded blocks as the sheet undergoes internal strain during emplacement (Fig. 3, structure 3).

Thrust sheets undergo additional horizontal shortening and vertical thickening after the generation of contraction faults by homogeneous LPS and by displacement and rotation of blocks that are bounded by contraction faults. These internal deformation mechanisms can be distinguished by variations in the intersection angles between the bedding laminations and the planar contraction faults (B-F intersections). Internal strain that is accommodated by homogeneous LPS increases the B-F intersection angles, whereas additional strain that is accommodated by fore- or back-rotation of fault-bounded blocks decreases the B-F intersection angles. In the lowermost competent unit of model TN16, B-F intersection angles typically increase inwards toward the center of the unit to ~45º as additional internal strain is accommodated by homogenous LPS in the center of the unit. A decrease in B-F intersection angles by back-rotation of fault-bounded blocks occurs in the core of folds at the base of the thrust sheet, and in the hanging-wall syncline (areas indicated by grey fill in Fig. 3). In addition, a decrease in B-F angles by forward rotation of fault-bounded blocks occurs near the leading edge of the hanging-wall panel during folding and continued overthrust development. Wojtal (1986) likened the ductile deformation accrued by displacement and rotation of blocks bounded by contraction faults that occurs during emplacement of a thrust sheet to mesoscopic grain boundary sliding. Variations in B-F angles caused by internal strain indicate regions within the overthrust structure where, and the timing when, different deformation mechanisms are active: the development of contraction-fault arrays is dominant near the boundaries of the unit and particularly near underlying thrust faults; LPS is dominant in the center of the competent unit; and ductile strain achieved by relative displacement, rotation and internal strain of the fault-bounded blocks is dominant in the cores of buckle folds and on the fore- and back- limbs of overthrusts.

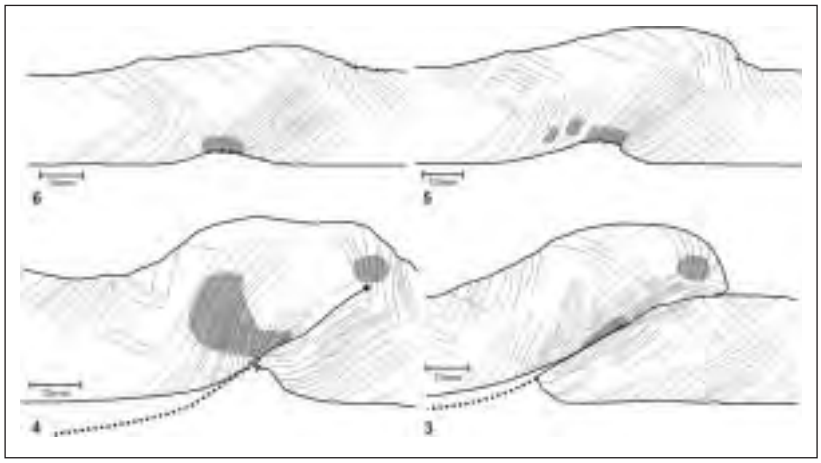

Fig. 3 – Structural outlines showing the orientation and distribution of contraction fault arrays for the development of overthrust structures in the lowermost competent unit of model TN16. Grey fill represents the regions where B-F angles are reduced by distributed strain within fault-bounded blocks.

Although the modelling materials do not generate the same suite of mesoscopic sub-fabrics as rocks systems during overthrust development (brittle faults, fractures, stylolites, *etc*.), the deformation mechanisms active in model TN16 are similar to those documented from natural overthrust structures. Further work will examine the timing, distribution and types of deformation mechanisms active throughout the development of the model overthrust structures in order to gain insight into understanding the kinematic implications of sub-fabrics observed in natural overthrust structures.

REFERENCES

- Chapman, T.J. & Williams, G.D. 1984. Displacement-distance methods in the analysis of fold-thrust structures and linked fault systems. J. Geol. Soc. London, Vol. 141, pp. 121-128.
- Dixon, J.M. & Liu, S. 1992. Centrifuge modelling of the propagation of thrust faults. In: McClay, K.R. (Ed.), Thrust Tectonics. London: Chapman & Hall, pp. 53-70.
- Liu, S. & Dixon, J.M. 1995. Localization of duplex thrust-ramps by buckling: analog and numerical modelling. Journal of Structural Geology, Vol. 17, pp. 875-886.
- Wojtal, S. 1986. Deformation within foreland thrust sheets by populations of minor faults. Journal of Structural Geology, Vol. 8, pp. 341-360.

CRUSTAL SCALE BUCKLING IN THE PRESENCE OF THERMAL ANOMALIES WITH SPECIAL REFERENCE TO THE ARCHEAN 2-21

A.P. Peschler [(1)], K. Benn [(1)], W.R. Roest [(2)]

(1) Ottawa-Carleton Geoscience Centre and Department of Earth Sciences, University of Ottawa, Ottawa, ON K1N6N5, Canada,

(2) IFREMER centre de Brest, B.P. 70, 29280 Plouzane, France, peschler@apeschler.net

Summary

Analog experiments of crustal scale folding, including the presence of younger and more mature thermal anomalies, were carried out primarily to investigate tectonic deformation of Archean crust. Our results suggest that the scales and styles of crustal scale folding are strongly affected by the location and maturity of the thermal anomaly. A comparison is made between the experimental results and one well studied Late Archean greenstone belt, the Abitibi belt, Canada.

Abstract

We use analog experiments to investigate folding of continental crust subjected to different geothermal gradients and displacement rates. The experiments are designed with an eye to deformation of Archean greenstone belts, however, the results may also be pertinent for younger terranes. Different thermal gradients are used to investigate the effects of major additions of heat to the crust, such as might occur above a plume or in response to magmatic underplating.

In the particular case of the Archean, the natural prototype corresponds to a portion of an evolved Archean lithosphere (400X400 km) where a linear thermal perturbation occurred (150 km wide), adding heat to the base of the crust and creating both vertical and lateral thermal gradients. The analog model is made of 5 layers (Fig.1); the upper crust composed of greenstones is modeled by silica sand and silicone gum to represent the brittle and ductile parts of the upper crust. The middle crust is mainly composed of granitoids with a TTG composition and is modeled by a paraffin wax layer with a melting temperature of 55°C. The lower crust composed of gneiss is modeled by another paraffin wax layer with a melting temperature of 52°C. The viscosities of paraffin waxes are modified by addition of heat from a source below the models, which leads to lower viscosities and eventually to melting. Finally, the upper mantle is modeled by a 3 cm-thick layer of the same silicone gum used in the lower part of the upper crust. The analog model is scaled to the natural prototype with down scaled factors of 10^{-6}, for linear dimensions; around 1 for the density ratios of the layers, and 15 for the temperatures (Fig.1).

The experimental apparatus (Fig.2) corresponds to a squeeze box. Its internal dimensions are 42X40 cm. The basal heating surface is 15 cm wide. Bakelite plates have been added to allow a minimal

lateral heat propagation (Fig. 2). A stepper-motor is used to shorten the models at two different displacement rates, 1cm/hr and 4 cm/hr. The experimental apparatus did not allow free lateral surfaces and no material was added or lost during the experiment. Erosion rates were not taken into account, though mass wasting occurred on steep surface slopes during some experiments.
A series of 10 experiments was completed, with variation of the displacement rates and of the thermal gradients. Each experiment was heated between 10 and 20 hours prior the start of deformation. The experiments were run until a maximum of 20% shortening, then cooled down before they were sliced. For each experiment, a dome was formed above the thermal anomaly prior to deformation. The dome is higher and more localized for cooler geothermal gradients. The warm geothermal gradients required longer heating times; therefore lateral thermal relaxation occured which caused the height of the dome to diminish. The domes correspond to what is expected to form in a crust as a response to the arrival of a plume at the base of the lithosphere.

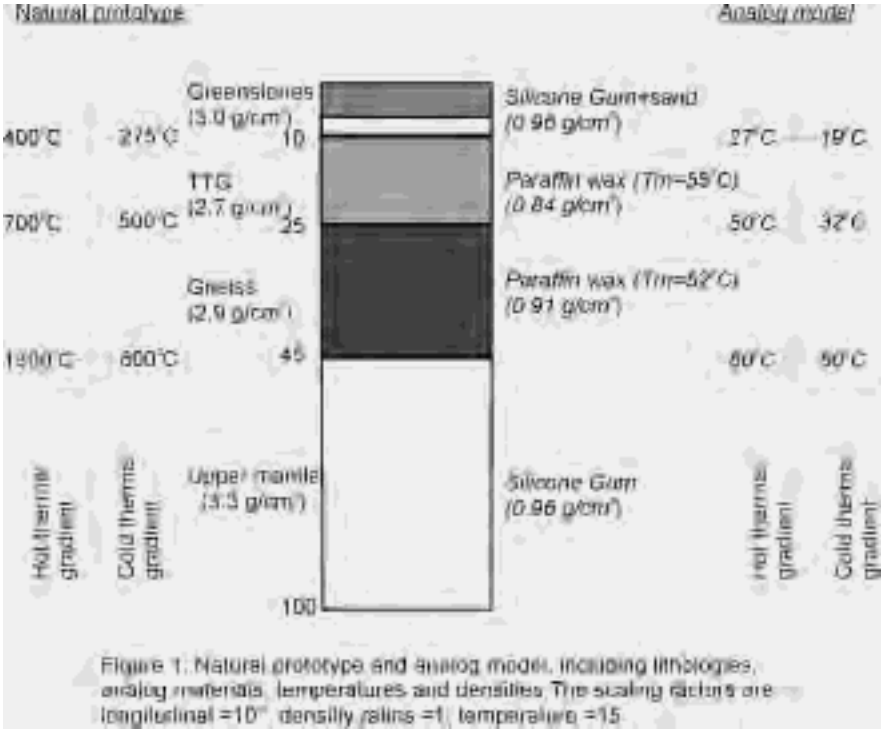

Figure 1. Natural prototype and analog model, including lithologies, analog materials, temperatures and densities. The scaling factors are longitudinal =10⁻⁵, density ratios =1, temperature =15

Fig. 3 displays two examples of the experimental results, using a 1 cm/hr displacement rate, and two different thermal gradients. We imposed a cold thermal gradient in experiment 3 and a hot one in experiment 8. Both thermal gradients are within the range of geothermal gradients for the Archean, proposed by Richter (1985) or established by numerical simulations for this study.
In our experiments, folding is the main response to shortening of the analog crust. The middle and lower crust analogs behave essentially as one ductile layer and respond to the shortening by buckling. Folding is accompanied by thickening of the paraffin wax layers in the intrados of folds and thinning in the extrados. In the upper crust analog, the first-order folding imposed by the middle and lower crustal layers is accompanied, in some experiments, by higher-order folding, by the formation of grabens above anticlines, and by reverse shear zones located near inflection lines on limbs of synclines (Fig. 3, experiment 3). The synclines form basins that receive material by mass wasting. For the coolest thermal gradients, one anticline-syncline pair is formed. For warmer gradients, multiple folds develop that have shorter wavelengths and smaller amplitudes. The modeled crustal folds may also be asymmetical, and the thermal regime causes the sense of asymmetry to change (compare experiments 3 and 8 in Fig. 3).
Changing the displacement rates used in the experiments influences the style of deformation only in

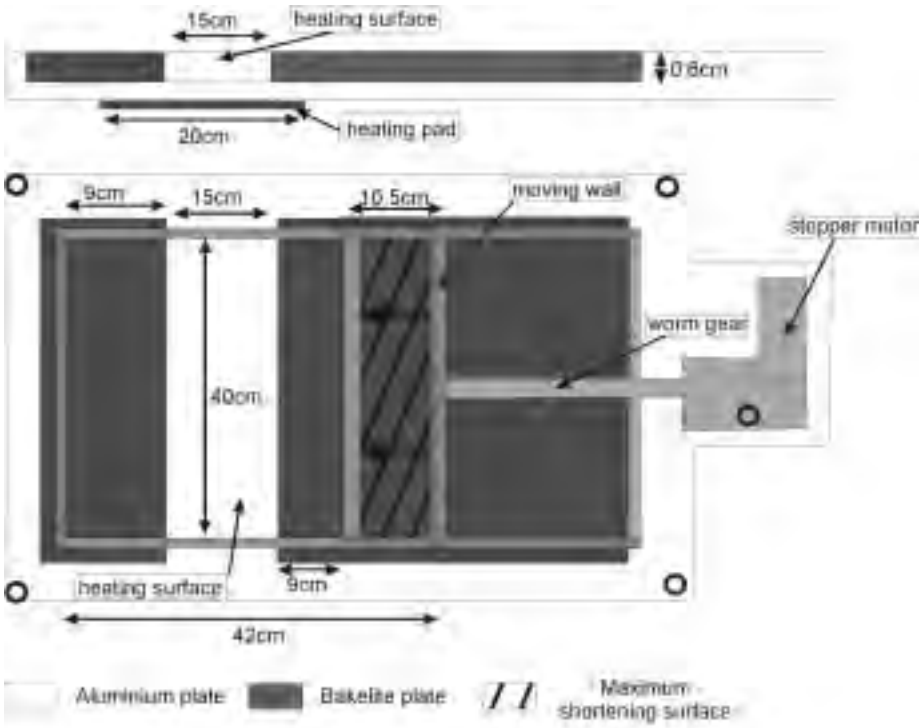

Figure 2: Design of the apparatus used for the analogue experiments

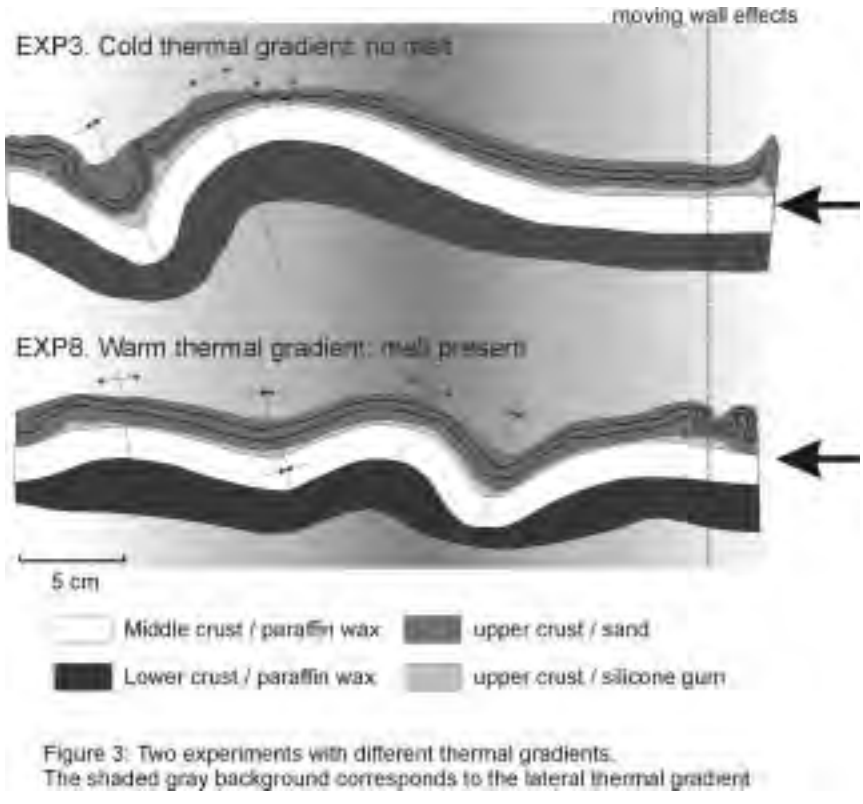

Figure 3: Two experiments with different thermal gradients.
The shaded gray background corresponds to the lateral thermal gradient

that a slower displacement rate allows for thermal relaxation of a larger volume of the wax layers, which affects fold amplitudes.
Our results suggest that the deformation style preserved within folded Archean greenstone belts is strongly influenced by the syndeformational thermal regime. The scales and styles of folding, the development of sedimentary basins and the formation of shear zones in the upper crust should depend critically on the time lag between plume activity and the onset of folding. If the time lag is shorter, the thermal anomaly is more localized. If the time lag is longer (e.g. ca. 5 Ma) then shorter wavelength, and smaller amplitude folds would be formed. Reverse shear zones show a larger development for cooler thermal gradients. The vergence of the folds, as well as the location of the sedimentary basin vary with the thermal gradient: from a foreland fold vergence and basin location for the coolest gradients, to an hinterland fold vergence with a central basin location for the warmest gradients.
A comparison is made between the experimental results and the Late Archean Abitibi Subprovince, Canada, which has implications for the crustal structure and the tectonic history of that greenstone terrane.

REFERENCE

• Richter J.M. 1985. Earth Planet. Sci. Lett. 73, 350-360.

INTERPRETING STAGE WARPING EVENTS USING 3D SIMULATION: AN EXAMPLE FROM THE PLATTENGNEIS SHEAR ZONE, EASTERN ALPS 2-22

Martin Putz*, Kurt Stüwe*, Mark Jessell**, Philippe Calcagno***

* *Institut für Geologie und Paläontologie, Universität Graz, Heinrichstr. 26; A-8010 Graz, Austria*
** *Laboratoire des Mécanismes et Transferts en Géologie, Université Paul-Sabatier, 38 rue des Trente-six Ponts, 31400 Toulouse cedex, France*
*** *BRGM - 3, avenue Claude-Guillemin - BP 6009 - 45060 Orléans Cedex 2 - France*

Summary

The Plattengneis is a flat lying shear zone (600 km^2 outcrop area) within the Koralpe Complex in the Eastern Alps. The shear zone formed during the eclogite facies Eo-Alpine metamorphic event in the Cretaceous. During its subsequent exhumation, it was warped into open folds with a 10 km wavelength. Because of the long wavelength, the patchy outcrop conditions and the ill-constrained nature of shearing process, the overall geometry of the shear zone has not been understood and the late folding event has so far escaped interpretation. Here we use field and literature date to generate a 3D-model of the shear zone which allows us to interpret the geometry of the shear zone and the fold pattern. The fold pattern is then interpreted in terms of the stress regime during the late Cretaceous exhumation of the region using a finite element simulation. A kinematic model for the exhumation is suggested.

Abstract Text

The mylonitic Plattengneis (Koralpe Complex, Austria) forms one of the major transport horizons during the Eo-Alpine orogenesis in the Eastern Alps. The Koralpe is a high-grade metamorphic complex, also known for the eclogite type locality (e.g. Hauy, 1821; Stüwe & Powell, 1995; Tenczer & Stüwe, 2003). The structural evolution of the Plattengneiss shear zone during the Eo-Alpine high grade metamorphism has been studied in some detail (e.g. Krohe, 1981; Kurz et al., 2002). However, the post Eo-Alpine deformation of the region is less well understood and is the subject of this contribution. Here, we describe a 3D model that was designed to explain a late stage warping event that folded the shear zone on a 10 km wavelength into open folds (Fig. 1).

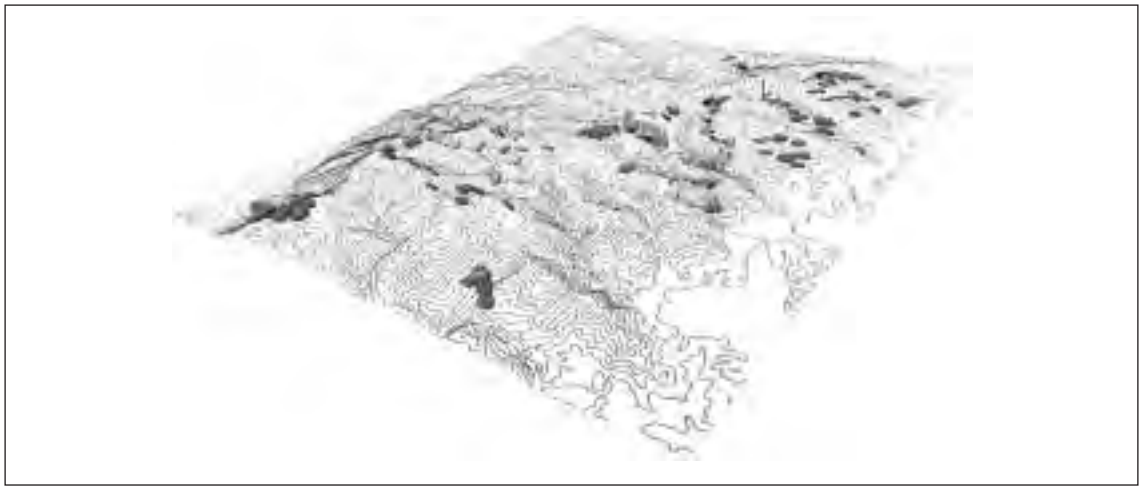

Fig. 1: Orientation of foliations within and around the Plattengneis. Circular disks show the orientation and position of foliation measurements, colour coded according to steepness of dip (red=shallow, green=steep). Contours are displayed at 50m intervals. Model viewed from South-East.

The geometry of the late stage warping event described here is difficult to understand because outcrop conditions are patchy and the shear zone contacts intersect with the surface topography at very shallow angles. Moreover, the open folds are highly non-cylindrical and outcrops are distributed over more than 600 km^2 of area. For these reasons it is not trivial to understand the three dimensional geometry of the shear zone. Nevertheless, it is important to interpret this warping event because it occurred simultaneously with the subsidence of the adjacent Gosau Basin in the upper Cretaceous, which is an important part of the evolution of the Alpine orogen. In order to understand this warping event and the overall geometry of the shear zone (for example whether it forms one single sheet or several sub parallel splays), a three dimensional model has been developed. The idea was to generate a 3D-Model with the point data that we gain from geological mapping with no contribution by geophysics. We used a number of about 350 outcrops. The only depth information was given due the topography with a relative difference in elevation of about 2000 meters. Most commercial 3D visualisation packages cannot handle this sort of input data or would require a great amount of interpretation in advance of the modelling process. For these reasons we used the non-commercial software package “the Geological Editor”, developed by the French Geological Survey (BRGM). The main advantage of this package for our purpose was that “point information” (as single outcrops) could be directly used as input data (Courrioux et al., 2001, Calcagno et al., 2004).
The model shows that the shear zone is made up of a single 250 m to 600 m thick layer that is folded into 4 open synforms and 5 antiforms with a mean distance of about 5 km. In the south of the working area these folds strike WNW-ESE and turn towards a N-S orientation to the north (Fig. 2).

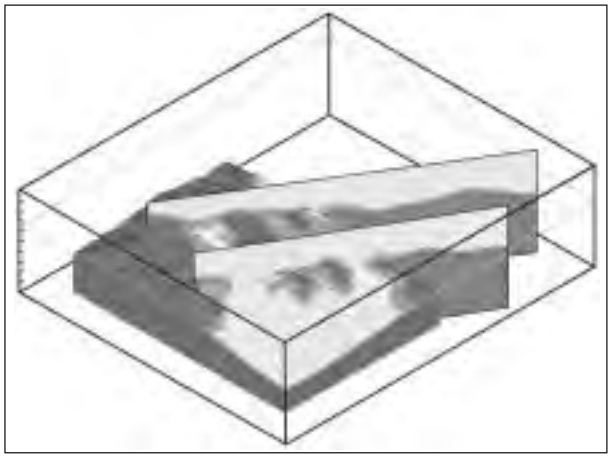

Fig 2: 3D model of the Plattengneis cut off by the topography (DTM), combined with two NW-SE cross-sections. Blue: units below Plattengneis, Orange: Plattengneis, Yellow: Units above Plattengneis. Model viewed from South-West.

This geometry indicates that the folding event has been highly non-coaxial. Even though the overall longitudinal shortening was less than 5%, the fold pattern can be used to interpret the stress regime during late Cretaceous exhumation of the region. The fold pattern in the Koralpe region suggests a dominance of N-S directed shortening in the south but a rather E-W orientated stress field in the north.

According to Neubauer et al. (1995) doming and exhumation of the Gleinalpe, to the north of the investigated area, is related to shortening in the lower crust and a series of major vertical, sinistral NE-SW striking shear zones that separate the Koralpe from the Gleinalpe Complex (Fig. 2). Following this model we suggest that folding of the Plattengneis must have occurred while these shear zones were still active, but when the Gleinalpe dome already provided a rigid backstop. Thus we propose a southward propagation of folding and exhumation of the region during the late Cretaceous. Within this model, the formation of the Gosau basin is intimately related to the folding event in the Koralpe but postdates the formation of the Gleinalpe dome.

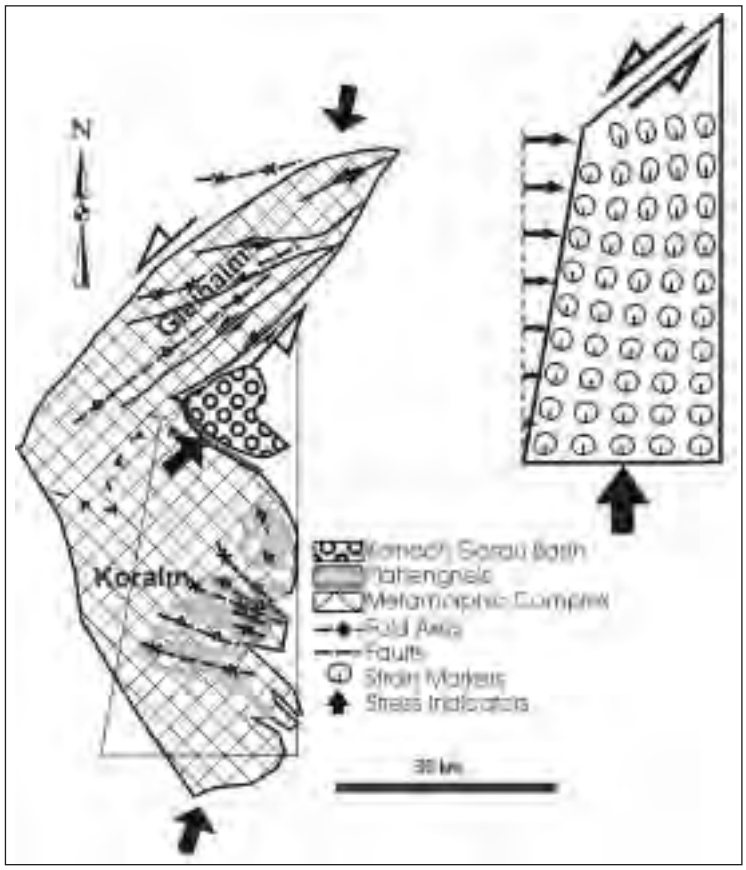

Fig. 3: Tectonic sketch of the proposed model. The left hand figure shows a simplified geological map of the Koralpe and its relationship to the Gleinalpe complex to the north. The right hand figure shows a simple finite element mechanical model calculation which produces strain ellipses with east-west orientation in the south and strain ellipses with a north south orientation in the north.

With this contribution we want to show that three dimensional modelling based on pure geological field data can enhance the understanding of complex structures and thus can be seen as a practical tool for mapping geologists to save time and improve the output of their work.

REFERENCES

- Tenczer, V., Stüwe, K., 2003; The metamorphic field gradient in the eclogite type locality, Jouranl of Metamorphic Geology, V. 21, Nr. 4, S. 377-393
- Hauy, R. J., 1822. Traité de mineralogie. 2nd ed., 2. 594 pp., Paris (Bachelier).
- Krohe, A., 1987. Kinematics of Creatceaous nappe tectonics in the Austroalpine basement of the Koralpe region (eastern Austria). Tectonophysics, 136, 171-196.
- Neubauer, F., Dallmeyer, R.D., Dunkl, I. & Schirnik, D., 1995. Late Cretaceous exhumation of the metamorphic Gleinalm dome, Eastern Alps: kinematics, cooling history and sedimentary response in a sinistral wrench corridor. Teconophysics, 242, 79-98.
- Stüwe, K. & Powell, R., 1995. PT paths from modal proportions: application to the Koralm Complex, Eastern Alps. Contributions to Mineralogy and Petrology, 119, 83-93.
- Kurz, W., Fritz, H., Tenczer, V. & Unzog, W., 2002. Tectonometamorphic evolution of the Koralm Complex (Eastern Alps): Constraints from microstructures and textures of the „Plattengneis“ – shear zone. Journal of Structural Geology, 24, 1957-1970.
- Courrioux, G., Nullans, S., Guillen, A., Boissonnat, J., Repusseau, P., Renaud, X. & Thibaut, M., 2001; 3D volumetric modelling of Cadomian terranes (Northern Brittany, France): an automatic method using Voronoi diagrams. Tectonophysics, V. 331, S. 181-196
- Calcagno et al. (2004), GeoMod2004, this volume

ANALOGUE EXPERIMENTS OF INDENTATION TECTONICS AND BREAK-OFF: INSIGHT TO ARABIA INDENTATION

2-23

V. Regard(*), C. Faccenna(**), J. Martinod(***), O. Bellier(*)

(*) *Centre Européen de Recherche et d'Enseignement en Géosciences de l'Environnement – CEREGE, UMR CNRS 6635, Université Aix-Marseille III, Europôle de l'Arbois BP80, 13545 Aix-en-Provence cedex 4, France*

(**) *Dipartimento di Scienze Geologiche, Università Roma tre, Largo S. L. Murialdo 1, 00146, Roma, Italy*

(***) *Laboratoire des Mécanismes et Transferts en Géologie – LMTG, 38 rue des 36 ponts, 31400 Toulouse, France*

Summary

We investigate, using 3D laboratory experiments, how the dynamics of indentation process are affected by the evolution at depth of the oceanic and continental subductions. Lithospheric plates are modelled by sand-silicone plates floating on glucose syrup, and the density contrast between oceanic and continental lithospheric plates and asthenosphere is reproduced. Analogue experiments model the convergence between two lithospheric plates, a small continent indenting a large continental plate. We show that the surface deformation in front of the indenter and above the oceanic subduction zone depends on the behaviour of the slab below the collision zone. Slab break-off following the subduction of the small continent favours the indentation process, because it results in an increasing compression in front of the indenter, and extension above the neighbouring oceanic subduction, both of them being responsible for the appearance of the indenter-like geometry of the plate boundary. When the slab does not deform significantly at depth, in contrast, the closure of the oceanic domain in front of the indenter is followed by a longer period of continental subduction, during which the tectonic regime within the large continent remains quite homogeneous. Comparing the presented analogue experiments with the subductions both part of the Arabian indenter within Eurasia, our results suggest that the different tectonic regime on both sides of the Arabia indenter may partly result from the probable occurrence of a detachment at depth under Eastern Anatolia.

Introduction

Indentation is defined as the collision of a relatively small "indenter" with a large continental domain, generally flanked on its sides by subduction zones. The "indenter" is globally buoyant and has been drifted towards the indented continent by subduction of the oceanic domain that initially separated them. Presently, many studies argue in favour of combined or successive vertical/horizontal extrusion to explain deformation related to collision (Johnson, 2002). Consequently, to understand collision processes, it appears necessary to look at the indentation mechanisms in the 3 dimensions. An interesting example of indenter is Arabia, since the indentation of Arabian within Eurasia is differently expressed to the East (Iran) than to the West (Aegean-Anatolian domain).

The tectonic process driving and accompanying indentation has been investigated especially for those aspects concerning the way the upper plate deforms. In particular, it has been pointed out that a major role is played by the strength of the upper plate, providing the possibilities to squeeze and thicken the crust or producing the lateral escape of crustal block along strike-slip faults (e.g., Molnar and Tapponnier, 1975; Shen et al., 2001). In particular, it seems that a tectonic escape must be allowed by the presence, at the sides of the indented continent of free boundaries, i.e., not exerting any confining force. Whether western pacific subduction zones are free boundaries is currently a subject of debate. Indeed, if one compare upper plate deformation over subduction zones, it is evident that the effects of the subduction dynamics vary, for upper plate, from compressional to extensional de formation (for example, respectively, rocky mountains and Aegean domain). Thus the role played by subduction zones laterally bounding the "indenter" must be of high importance, but has not received the interest it deserves.

We present 3D-laboratory experiments performed to define the role of subduction in the tectonics of indentation. These experiments are part of an experimental program devoted to the investigation of the physical parameters that drive collision processes. In a previous paper (Regard et al., 2003), we have

described 2D experiments to illustrate the way continental lithosphere subducts prior to collision, and following oceanic subduction. The results of this set of experiments show that the possibility for the continent to subduct is related to the pull exerted by the previously subducted oceanic lithosphere, and, therefore to the way the slab deforms at depth. We express our results by means of two dimensionless numbers (F) where the slab pull force is normalised to the strength of the slab: favourable conditions for continental subduction require low values of F, or, in other words, the oceanic slab is more prone to maintain its integrity and to exert an higher pull on the subducting continent. Here, we extend this analysis to a more complex 3D configuration with a lateral transition from oceanic to continental subduction.

Experimental setup

We simulate the stratified lithospheric rheological profile (e.g., Ranalli and Murphy, 1987), by constructing a brittle-ductile layered model, with sand mixture to model the brittle behavior of the upper crust and silicone putty to model the ductile behavior of the lower crust and mantle lithosphere. The sand-silicone layering rests on honey, which simulates the upper mantle (Fig. 1). We use two different kinds of sand-silicone layers, either lighter or denser than the glucose syrup, to represent continental or oceanic lithospheres, respectively. Continental and oceanic plates differ in thickness, density and viscosity of the upper silicone layer, and in thickness and density of the sand layer. The lower boundary of the box approximates a high gradient viscosity transition. Models are constructed inside a rectangular plexiglas tank (50 cm long, 30 cm wide and 11 to 19 cm deep; Fig. 1). Horizontal shortening is achieved displacing a rigid piston at constant velocity perpendicular to the plate margins. A squared grid of passive sand markers enables visualization of the surface deformation.

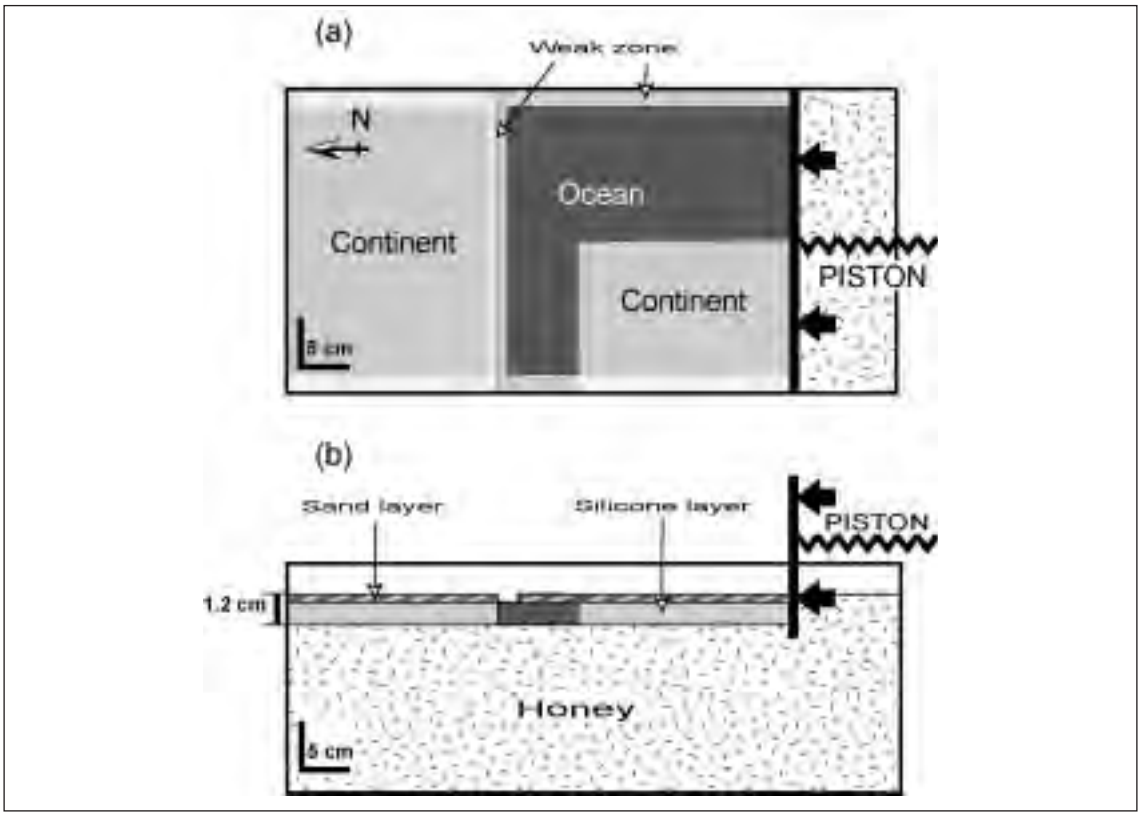

Fig. 1. Experimental set up: (a) upper view and (b) cross-section of the western part of the model. Sand/silicone plates modelling the lithosphere are lying above honey that represents the asthenosphere. These plates are lighter or denser than honey, to represent continental or oceanic lithospheres, respectively. The piston is pushing northward at a constant velocity of 4.4 mm/h scaled to represent 2.3 cm/y in nature. The oceanic plate will subduct below the northern continent, the subduction place being controlled by the removal of a 1 cm-wide band of sand that weakens the northern margin of the oceanic plate.

Results

Our experiments show that the way the upper plate deforms during indentation depends much on the characteristics of the subduction system and on the history of subduction. Comparison between experiments highlights the dependence of the pattern of collision and deformation in 3D on the way the subduction process develops. We check that the behaviour of the slab in 3D experiments fits predictions based on the F_1-F_2 diagram constructed using the 2D experiments described in Regard et al. (2003): viscous blubs only appear when F_2 is larger than about 3, and break-off occurs when F_1 also is large (larger than 1.2).

Exp. 1 demonstrates that the plate boundary is likely to absorb several hundreds of kilometres of continent-continent convergence before an indenter-like geometry appears, particularly when the slab does not break or stretch at depth, as already evidenced by published 2D experiments (Chemenda et al., 1996; Regard et al., 2003). In 3D configuration, subduction of indenting continent is favoured both by the pull of the previously subducted oceanic plate, and by the pull resulting from the lateral active oceanic subduction. In exp. 2, the ocean initial width, and consequently the slab pull, are larger, and the slab breaks (cf. Regard et al., 2003). This break-off process laterally propagates (several cm/yr), and slab pull concentrates at the tip of the propagating tear (Yoshioka and Wortel, 1995). This, in turn, induces large-scale back-arc extension within the upper plate above the oceanic subducting plate (Wortel and Spakman, 1992; Buiter et al., 2002), favouring the appearance of an indentation-like geometry between the two lithospheric plates (Fig 2.).

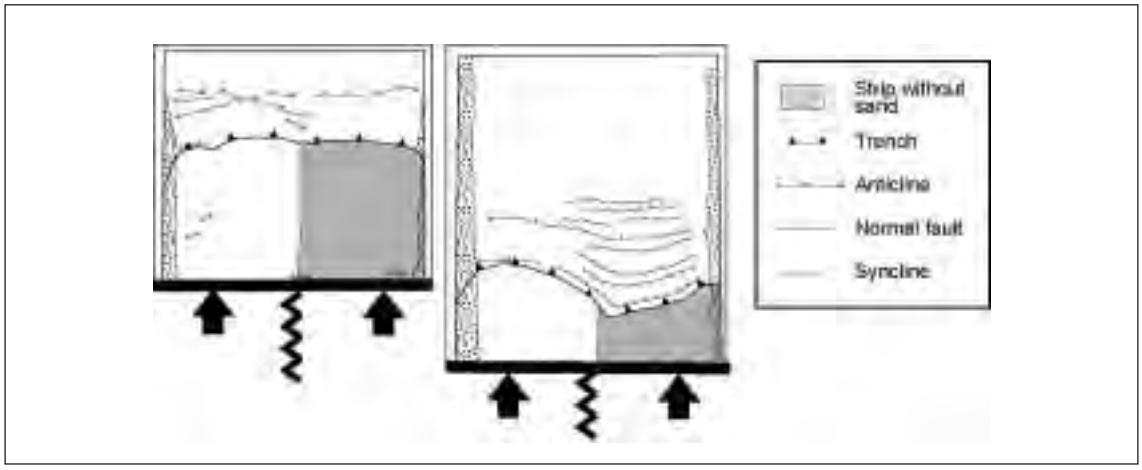

Fig. 2. Experiments 1 and 2 described here, in a mature stage. Continental are white, oceanic ones are grey.

On the contrary to most of the experimental sets previously built, our experimental set-up takes into account the rheology of the colliding/subducting plate. The indenter and the oceanic plate, however, generally correspond to the same drifting plate, and their motion is not independent. We observe that break-off permits to diminish the linkage between the indenter and the oceanic plate. In turn, the tectonic regime within the large continent passes from shortening in front of the indenter, to back-arc extension above the oceanic subduction. Moreover, back-arc extension above the oceanic subduction sharply accelerates as soon as the slab below the collision zone breaks, partly decoupling the motion of the indenter from that of the ocean. Before the onset of break-off, in contrast, the tectonic regime in the large continent remains rather homogeneous. In the first experiment, the slab below the collision zone and below the oceanic subduction preserves its integrity, smoothing the tectonic regime within the large continental plate, and only small amounts of back-arc extension are observed above the subduction zone. This extension is smaller and appears later than in the second experiment, because the deformation of the entire upper plate above the subduction zone is largely influenced by the shortening that is developing in front of the indenter.

Our results first underline that the way continental lithosphere deforms during indentation depends not only on the upper plate strength or the lateral boundary conditions. A strong and rigid cratonic area should be more prone to escape in rigid block than a softer, post-collisional lithosphere. This mechanism can be very pronounced if a pre-existing weakness zone exists. However, the rheology of the indenter-bearing plate must also be considered. In this sense our experiments can provide insights into natural situations where the indenting plate shows a transition from ocean to continent, as for the case of the Arabia-Eurasia convergence (Fig. 3, cf. Regard, 2003).

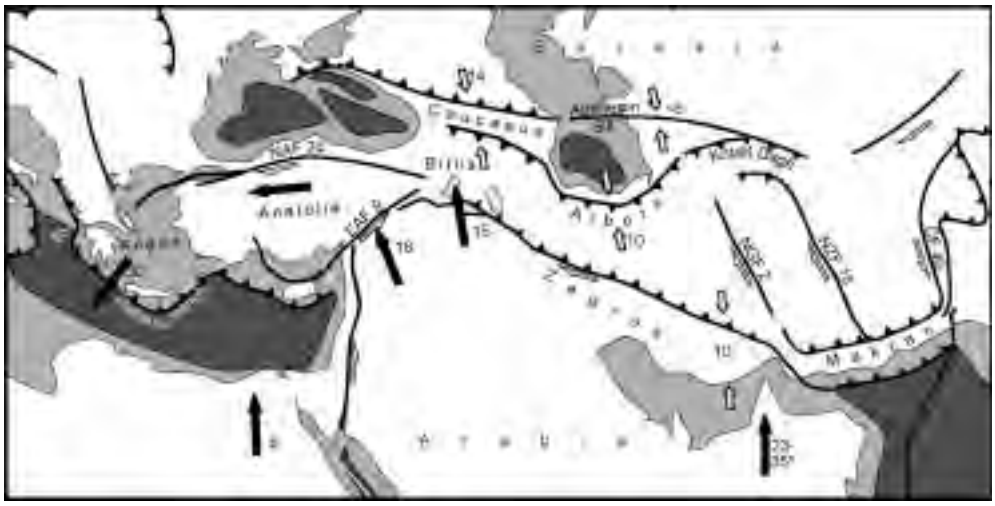

Fig. 3. Present-day tectonics of the Middle East, modified after Dercourt et al. (1986). White arrows indicate local deformation and solid arrows indicate velocities with respect to stable Eurasia (DeMets et al., 1990; McClusky et al., 2000; Vernant et al., in press). KF: Kephalonia fault; NAF: North-Anatolian fault; EAF: East-Anatolian fault (McClusky et al., 2000); NGF: Nayband and Gowk faults (Walker and Jackson, 2002); NZF: Neh and Zahedan faults (Freund, 1970; Tirrul et al., 1983; Walker and Jackson, 2002); CF: Chaman fault (Lawrence et al., 1992).

Conclusion

We explore, using laboratory experiments, how the deep behaviour of the subducting plates affect the style and occurence of indentation. These simple experiments highlight that the tectonics within the large continent does not only depend on the rheology of this continental plate, as often assumed in analogue or numerical models, but is also strongly dependant on the behaviour of the small indenting continent and of the neighbouring oceanic plate. As a matter of fact, it is necessary to deform both the upper plate, and the subducting/colliding oceanic/continental plate, to obtain the formation of an indenter-like geometry of the plate boundary.

In particular, we observe that slab break-off following the continental subduction of the small continent favours the indentation process, because it increases compression in front of the indenter, and extension above the neighbouring oceanic subduction. Our observations could give a new sight on the evolution of the entire Arabia-Eurasia indentation related processes, from Aegean extension to Zagros collision within Iran.

REFERENCES

- Buiter, S.H.J., Govers, R. and Wortel, M.J.R. (2002), Tectonophysics, 354, 195-210.
- Chemenda, A.I., Mattauer, M. and Bokun, A.N. (1996), Earth Planet. Sci. Lett., 143, 173-182.
- DeMets, C. et al. (1990), Geoph. J. Int., 101, 425-478.
- Dercourt, J. et al. (1986), in J. Aubouin, X. Le Pichon and A.S. Monin (Eds), Tectonophysics, 123, 241-315.
- Freund, R. (1970), J. Geol., 78, 188-200.
- Johnson, M.R.W. (2002), Earth Sci. Rev., 59, 101-123.
- Lawrence, R.D., Khan, S.H. and Nakata, T. (1992), Ann. Tectonicae, Spec. Issue. - Suppl. to vol. VI, 196-223.
- McClusky, S. et al. (2000), J. Geophys. Res., 105, 5695-5719.

- Molnar, P. and Tapponnier, P. (1975), Science, 189, 419-426.
- Ranalli, G. and Murphy, D.C. (1987), Tectonophysics, 132, 281-296.
- Regard, V. et al. (2003), J. Geophys. Res., 108, 2208, doi:10.1029/2002JB001943.
- Regard, V. (2003), PhD thesis, University of Aix-Marseille III, available on-line at http://tel.ccsd.cnrs.fr/documents/archives0/00/00/37/77/index_fr.html.
- Shen, F., Royden, L.H. and Burchfiel, B.C. (2001), J. Geophys. Res., 106, 6793-6816.
- Tirrul, R., et al. (1983), Geol. Soc. Am. Bull., 94, 134-150.
- Vernant, P. et al. (in press), Geophys. J. Int.
- Walker, R. and Jackson, J. (2002), J. Struct. Geol., 24, 1677-1698.
- Wortel, M.J.R. and Spakman, W. (1992), Proc. Kon. Ned. Akad. v. Wetensch., 95, 325-347.
- Yoshioka, S. and Wortel, M.J.R. (1995), J. Geophys. Res., 100, 20223-20244.

THE ROLE OF INDENTER RHEOLOGY DURING CONTINENTAL COLLISION: CONCEPTS AND APPLICATION TO THE EASTERN ALPS 2-24

J.C. Robl, K. Stüwe

Institut für Geologie & Paläontologie, Universität Graz, Austria

Summary

Numerical models describing continental collision processes on the orogenic scale in plan-view, generally assume an infinitely rigid indenter that drives deformation. This is in contrast with many orogens where substantial deformation occurs in both plates involved in the collision process. Here we present a plan-view model for continental collision with a finite indenter rheology. It is shown that both the size of the indenter and its rheology contrast with the foreland play a critical role in the partitioning of deformation between the two involved plates. Parameter space is explored with a simple numerical model. Application to the European Alps shows that the rheology contrast between Adriatic plate and Alpine orogen is currently no more than 3.

Abstract text

The process of a continent-continent collision is generally described with an indentation geometry: A rigid indenter is assumed to deform a significantly weaker plate. The crust in front of the indenter is thickened and forms an orogen while the indenter itself remains unaffected by the large scale deformation. This scenario is well explored by analogue- (e.g. Tapponier et al., 1982) and numerical models (e.g. England and Houseman, 1986) and has been successful in describing the India-Asia collision zone where most of the deformation is indeed partitioned into the Asian plate.

In contrast, many orogens show that substantial deformation occurs in both plates involved with the collision process. For example, in the European Alps, the Adriatic micro-plate indents the European foreland, but both plates are highly deformed. In fact, most of the seismicity in the Alpine orogen currently occurs within the Adriatic micro-plate. In two dimensions, this deformation partitioning between plates can be well-described on cross sections by employing asymmetric boundary conditions at the base (e.g. Beaumont et al., 1996). However, in plan-view, partitioning of deformation between two colliding plates can only be described by assuming a finite rheology contrast between the two plates involved. Here we present an extension of the classic thin viscous sheet model for continental collision (England and McKenzie, 1982; England and Houseman, 1986) in which we explore the influence of finite rheology contrast between indenter and foreland on the deformation partitioning. A somewhat more refined model is then applied to explore the rheology of the Adriatic micro-plate in the European Alps.

Model setup

The simple numerical model expands on the “elongate model geometry” of Houseman and England (1986). We use the finite element model of Barr and Houseman (1996) to describe thin viscous sheet deformation. A quadratic region with a dimensionless side length 1 is considered (Figure 1a). The

indenter is a block of length 0.25 and variable width w, initially located in the center of the southern boundary of the model region. The southern boundary is moving north with the velocity U_0 over the width of the indenting block and tapers to zero outside the indenter.
In order to apply this model to the Alps we have refrained from finite strain calculations and focused on describing the present day deformation regime with incremental calculations. For this we have made the following changes to the model: (1) Potential energy was interpolated onto the finite element mesh using a filtered digital elevation model for the Alps and assuming that potential energy is directly related to topography. (2) Thin viscous sheet calculations were performed in spherical coordinates. (3) A number of regions of finite viscosity contrasts were implemented to describe realistic geological units (Figure 2b). For this a general triangulation routine was used.

Numerical model results

Within our simple model, four parameters play an important role in the deformation partitioning between the two plates. The width of the indenter w, the viscosity contrast between indenter and foreland η, the Argand number Ar, and the non-linearity of viscous deformation as described by the power law exponent n. Figure 1b explores this parameter space for three pairs of Ar and n suggested to cover a characteristic range of geological settings by Houseman and England (1986). The curves shown in Figure 1b show the lines where the maximum thickening in the indenter is equal to that of the foreland. In general, crustal thickening dominates in the indenter for large w and small η, while crustal thickening dominates in the foreland if the indenter is small and strong. For $w = 0$ the model is equivalent to that of Houseman and England (1986) and can be compared directly with their results. For a viscosity contrast of $\eta = 3$ and an indenter width of 0.15, thickening in the indenter is the same as that in the foreland and is robust towards power law exponent and Argand number.

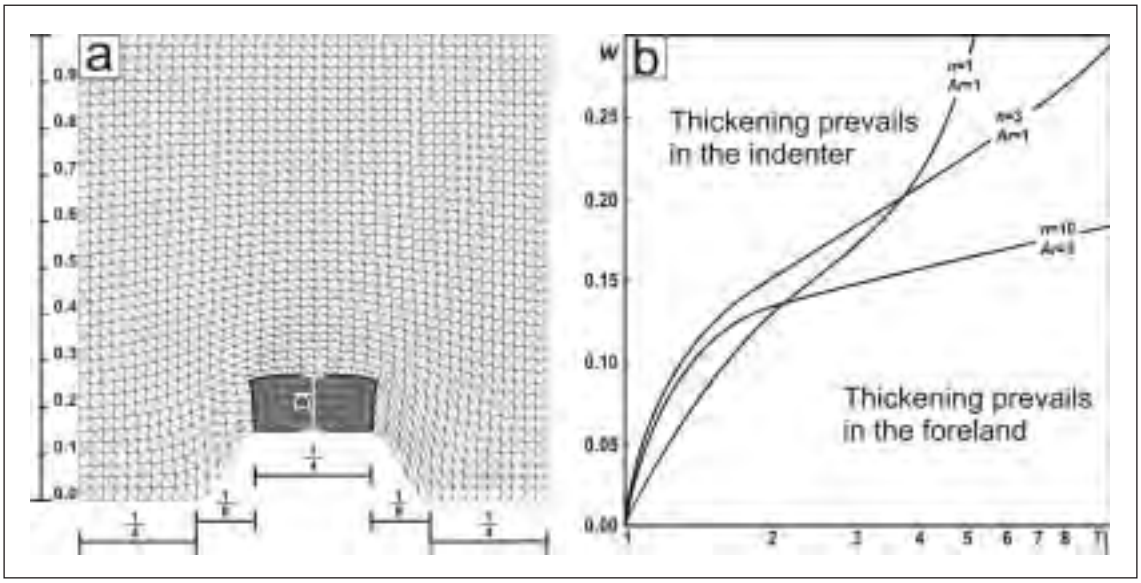

Fig. 1 Simple numerical model for the exploration of the role of indenter rheology in deformation partitioning between two plates. (a) Model set up. The dark shaded region is referred to as the "indenter", the light triangulated region as the "foreland". (b) The contours delineate the parameter space where the maximum thickening in both the indenter and the foreland are equal. η is the viscosity contrast between indenter and foreland. w is the width of the indenter. Note the logarithmic scale of the viscosity contrast.

Application to the Alps

A refined model was used to explore the indenter rheology in the Alpine orogen. For this, the region limits in the north and east were set in the aseismic European foreland and were ascribed zero velocity boundary conditions. The western boundary was placed in the central Alps where we assume symmetry of deformation across the boundary. The southern boundary is defined by zero stress and zero velocity except the boundary segment where the Adriatic plate indents into the orogenic wedge.

This segment is described by an increasing north directed velocity from west to east, according to the Euler pole of the Adriatic plate at 45.36°N 9.10°E and a counter-clockwise angular velocity at 0.52°/my (Nocquet and Calais, 2003). Over a width of 2° a $\cos^2$ function tapers the velocity smoothly down to zero at the eastern edge of the indenter (Fig. 2a).

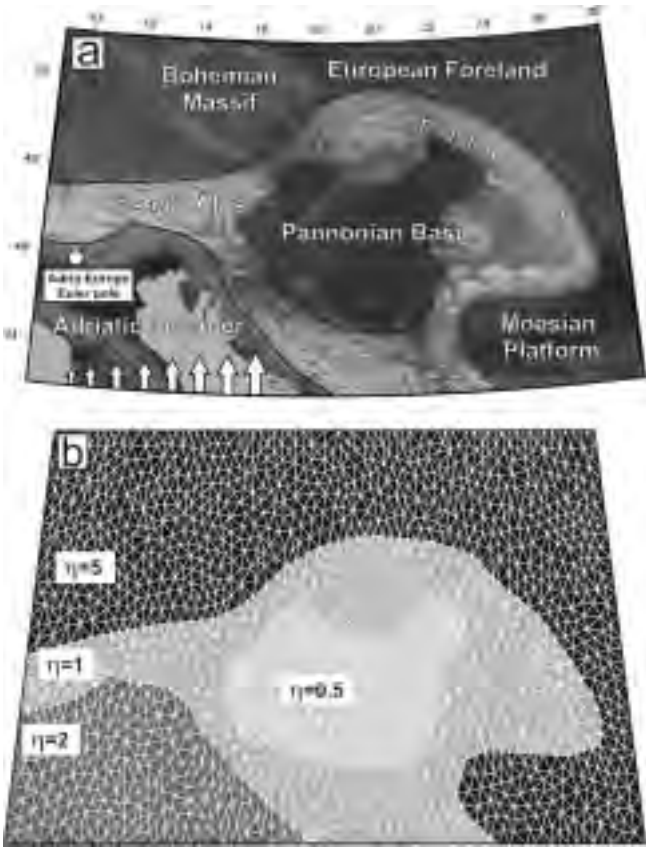

Fig. 2 Numerical model used to explore the rheology contrast between Adriatic plate and Alpine orogen. (a) Model region and boundary conditions. The arrows along the southern margin indicate the eastwards increase in north velocity. (b) Finite element grid used for the model calculations. Viscosity contrasts are labelled.

Within the modeled region we assumed 4 regions of different viscous rheology (Figure 2a). The European foreland including the Bohemian massif shows only minor internal deformation and is therefore defined arbitrarily to be 5 times more viscous than the Eastern Alps. Similarly, we assume that the lithosphere in the Pannonian basin is thin and warm and ascribe it a viscosity contrast of 0.5. The rheology of the Adriatic indenter plays a crucial role for the collision process and we explore this parameter in some detail.

Model results that match the intraplate stress field, the seismicity distribution and the GPS-determined velocity field suggest that the Adriatic indenter is 1.5 to 3 times as viscous as the Eastern Alps. While this estimate is very preliminary in our work, it is consistent with cross sectional models along the TRANSALPS profile by Willingshofer and Cloetingh (2003).

REFERENCES

- Beaumont, C., Ellis, S., Hamilton, J. and Fullsack, P., 1996. Mechanical model for subduction-collision tectonics of Alpine-type compressional orogens. Geology, 24: 675-678.
- Barr, T.D. and Houseman, G.A., 1996. Deformation fields around a fault embedded in a non-linear ductile medium. Geophysical Journal International, 125: 473-490.
- England, P.C. and Houseman, G.A., 1986. Finite strain calculations of continental deformation; 1, Method and general results for convergent zones. Journal of Geophysical Research, 91(3): 3664-3676.
- England, P.C. and McKenzie, D., 1982. A thin viscous sheet model for continental deformation. Geophys J Roy Astron Soc, 70: 295-321.
- Houseman, G.A. and England, P.C., 1986. Finite strain calculations of continental deformation; 1, Method and general results for convergent zones. Journal of Geophysical Research, 91(3): 3651-3663.
- Nocquet, J.-M. and Calais, E., 2003. Crustal velocity field of western Europe from permanent GPS array solutions, 1996-2001. Geophysical Journal International, 154: 72-88.
- Tapponier, P., Peltzer, G., Le Dain, A.Y., Armijo, R. and P., C., 1982. Propagating extrusion tectonics in Asia: new insights from simple experiments with plasticine. Geology, 10: 611-616.
- Willingshofer, E. and Cloetingh, S., 2003. Present-day lithospheric strength of the Eastern Alps ant its relationship to neotectonics. Tectonics, 22(6): 1-15.

COEVAL SHORTENING, THICKENING AND OROGEN-PARALLEL EXTENSION: LABORATORY MODELS APPLIED TO THE EASTERN ALPS 2-25

Rosenberg C.L.(*), Brun J.P.(**), Cagnard F.(**), Gapais D.(**)

(*) Institut für Geologie, Freie Universität Berlin, Germany
(**) Géosciences Rennes, UMR 6118 CNRS, Université de Rennes 1, Rennes, France

Introduction and Geological setting

Miocene tectonics of the Eastern Alps were characterized by contemporaneous shortening and extension perpendicular and parallel to the orogen, respectively (Ratschbacher et al., 1989). Extension was accommodated in front of the Southalpine indenter, along eastward diverging sets of strike-slip faults (Fig. 1; Ratschbacher et al., 1991a), whose conjugate activity resulted in eastward-directed extrusion. Major vertical displacements, leading to exhumation of middle/lower ductile crust in the Tertiary were confined to a sharply bounded area, known as the Tauern Window (TW). This 160 km long, E-W striking metamorphic dome (Fig. 1), exposes amphibolite facies rocks with Miocene cooling age within the brittle Austroalpine "lid". The Tauern dome is bounded by low-angle extensional faults both on its western (Brenner Line) and its eastern (Katschberg Line) sides (Fig. 1), whereas its northern margin is defined by a sinistral strike-slip fault (SEMP Line; Fig. 1). The present-day surface of the Brenner Line is folded with E-W-striking and steeply-dipping axial planes. Mutual overprinting between folding and normal faulting suggest that E-W extension occurred contemporaneously with N-S shortening (Behrmann, 1988; Selverstone, 1988).

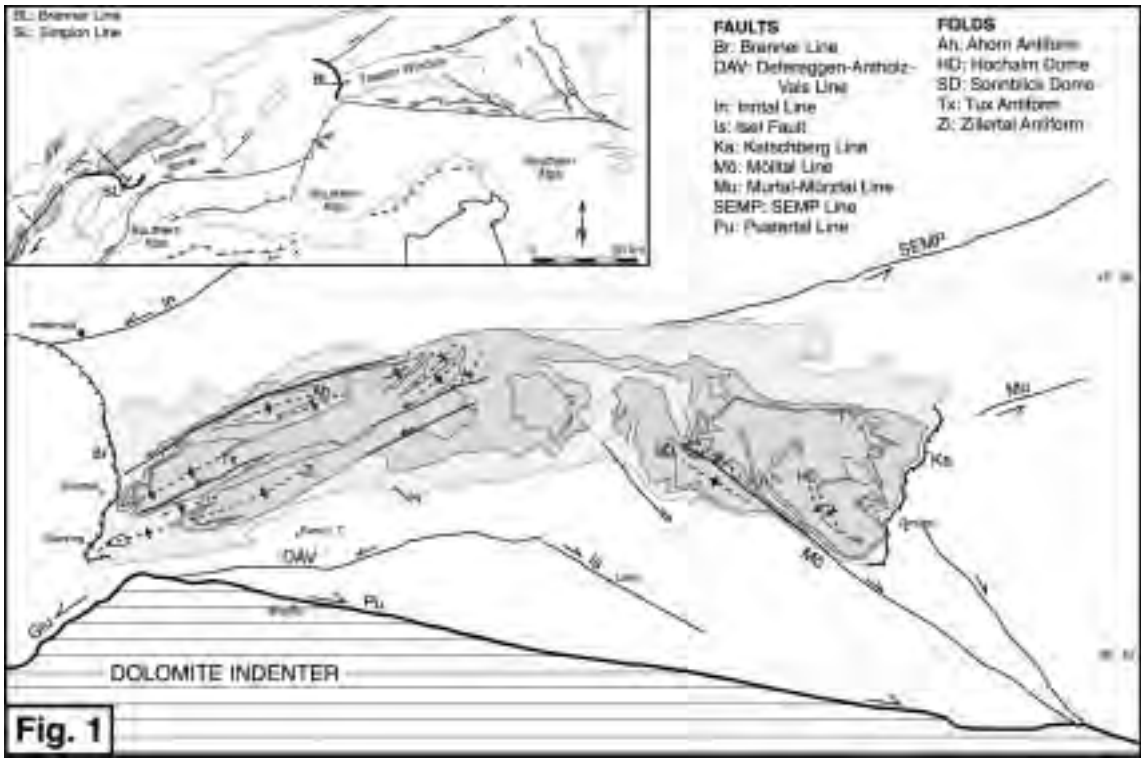

Fig. 1: Tectonic map of the Tauern Window. Inset modified after Mancktelow and Pavlis, 1994

In the present paper we investigate experimentally the effect of indentation geometry, indentation direction, and lithosphere rheology on the formation of domal structures and orogen-parallel extension. The experimental models are compared with the Eastern Alps, with special emphasis on the TW.

Experimental materials and boundary conditions

Laboratory experiments scaled for density and viscosity were carried out in a plexiglass box of 80 cm x 50 cm x 12 cm. The model lthosphere consisted of a ductile mantle layer of silicone, with density 1.45 g/cm^3 and viscosity 10^5 Pa s, a ductile lower crust with density 1.30 g/cm^3 and viscosity 10^4 Pa s and an upper brittle crustal layer of sand mixed with ~10% of ethyl-cellulose with density 1.3 g/cm^3. This stratified lithosphere lied above the model asthenosphere, represented by honey, with density 1.5 g/cm^3 and viscosity 10^1 Pa s. The models were confined along three sides by plexiglass and only the fourth margin was deformable, consisting of silicone. In the following we will refer to this margin as the eastern one.

Experimental results

A first set of experiments was carried out by shortening the model lithosphere up to 50% between two parallel plexiglass plates in a direction perpendicular to these plates (Fig. 2). These conditions have been tested both on 4-layer models, including a brittle upper mantle layer, and on 3-layer models without brittle mantle. Irrespective of the rheological layering, the amount of shortening, and the convergence velocity, these models shortened mainly by thickening along conjugate sets of thrusts, striking at high angles to the convergence direction (Fig. 2). Lateral extrusion never exceeded a few percent.

Fig. 2: Surface of 3-layer model (ductile upper mantle, ductile lower crust, brittle upper crust) after 50% shortening between parallel boundaries. Convergence direction was at 90° to the long side of the picture.

In a second set of experiments the mobile plexiglass plate was replaced by a rigid indenter (Fig. 3), whose shape reflects the South-alpine Dolomite indenter. The western margin of the indenter represented the sinistral, transpressive Giudicarie Line (Fig. 1) and the northern margin, represented the dextral Pustertal Line (Fig. 1). In order to investigate the effect of the convergence angle, the piston direction was changed from perpendicular (90° to the northern plate) to oblique (70° and 60° to the northern margin).

Perpendicular convergence of the indenter resulted in fold and thrust belts flanking the western end and the northern edge of the indenter (Fig. 3a), before passing to the northern border of the model, whilst the southern margin of the model remained relatively undeformed. No lateral extrusion occurred, in spite of the divergent geometry of the plates (Fig. 3a).

Oblique convergence of the indenter with an angle of 20° towards the NNE, localized shortening and thickening adjacent to the northern border of the indenter (Fig. 3b), especially, along its western part. This area, which was marked by tight folds of large amplitude, also accommodated significant E-W extension, locally attaining 50% in front of the leading edge of the indenter (Fig. 3b). To the East, these folds pass into a zone of conjugate transpressive thrust belts. The combined activity of these conjugate systems resulted in limited lateral extrusion (≤ 15%).

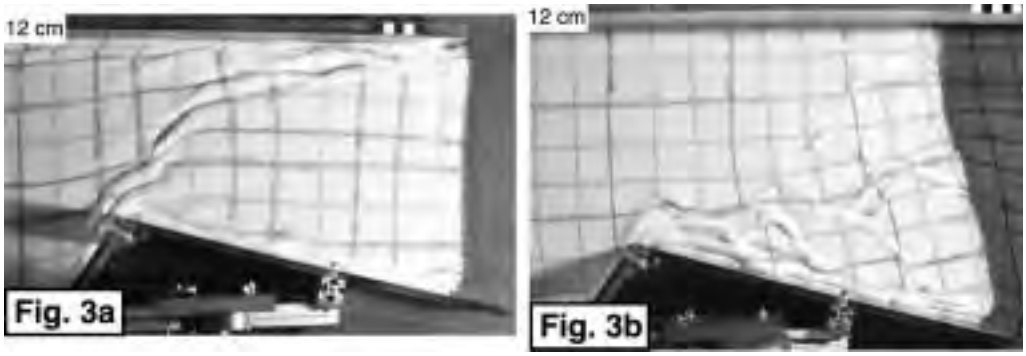

Fig. 3: Surface of 3-layer models shortened to 40% by a rigid block whose shape reflects the Dolomite indenter. a) Convergence direction perpendicular to N-margin. b) Oblique convergence direction (20° to the NNE).

Oblique convergence with an angle of 30° towards the NNE, also showed a zone of localized shortening adjacent to the northern border of the indenter, but also a significant amount of shortening at the north-eastern margin of the model. In addition, a series of N-S striking normal faults formed in front of the western margin of the indenter, separating the part of the model that did not suffer any deformation, from that which was shortened.
In a last series of experiments, the thickness of the ductile crust was doubled in the central part of the model. Deformation rapidly propagated from the indenter into the orogen (Fig. 4), localizing first along sets of conjugate, transpressive thrust belts (Fig. 4), which nucleated at the tip of the indenter (Fig. 4a). These conjugate pairs of thrusts evolved into tight folds with increasing shortening, forming an arcuate fold belt (Figs. 4b and c). This folded structure accommodated most of the bulk shortening by folding and thickening, but also by significant E-W extension, reaching up to 100% in the western part and 50% in the eastern part (Fig. 5). East of the folded structure, extension is transferred into eastward diverging transpressive strike-slips, as observed in the 20° oblique convergence with no initial thickening of the ductile crust (Figs. 4 and 5).

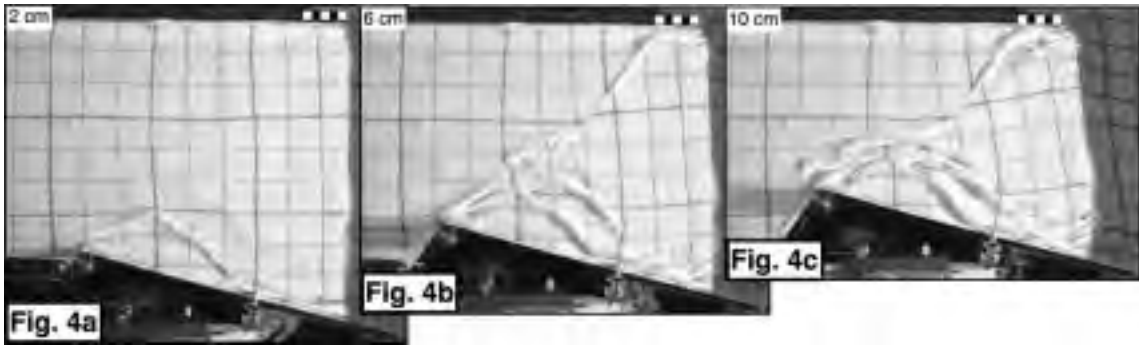

Fig. 4: Surface of 3-layer model with thickened ductile crust. Oblique convergence (20° to the NNE).
a) 7% shortening, b) 20% shortening, c) 30% shortening

Fig. 5: Same model as Fig. 4 at 40% of shortening.

Discussion and Conclusion

The latter model (Figs. 4 and 5) shows the greatest similarities with the Tertiary deformation pattern observed in the Eastern Alps: 1) A zone of tight folds accommodating most of the shortening, thickening, and E-W extension formed in front of the leading edge of the indenter. These folds correspond to the Ahorn, Tuxer and Zillertal antiforms of the western TW (Fig. 1) and to the Sonnblick and Hochalm domes of the eastern TW (Fig. 1). It is interesting to note that shortening in the model induces the formation of three major antiforms in the West, just like in the TW (Fig. 1). 2) The folds of the model are associated with sinistral displacements in the West and dextral ones in the East (Fig. 5). The same is true in the TW, where the antiforms of its western part are separated by sinistral strike-slip faults, striking subparallel to the folds (Fig. 1). Similarly, the antiforms of the eastern TW are separated by dextral strike-slip faults, subparallel to the antiforms (Fig. 1). 3) The axial planes of the folds in the western and eastern parts of the dome make an angle of 120° to each other, both in the model and in the TW (Figs. 1 and 5). 4) A triangular, nearly undeformed region occurs between the northern margin of the indenter and the folded region, as also observed between the Periadriatic Fault and the DAV Line (Fig. 1), which is inferred to represent the southern border of the Tauern Window (Frisch et al., 2000). 5) The aspect ratio of the folded region in the model is ~5:1, and the ratio of the indenter- vs dome length is ~2:1. These ratios are close to those measured in map view for the TW and the Dolomite indenter (Fig. 1). 6) An area of significant E-W extension coinciding with the western part of the folded region characterizes both the model (Fig. 5) and the western margin of the TW (Brenner Line). 7) A series of NE- and SE- striking transpressive sinistral and dextral faults respectively, transferred E-W extension from the arcuate fold zone to the eastern boundary of the model, inducing a modest amount of lateral extrusion. These structures correspond to the sinistral SEMP and Murtal faults, and to the dextral Mölltal Line (Fig. 1)

The convergence direction of the Southalpine indenter with respect to the European foreland is contradictory discussed in the literature. The inferred direction varies from SE-NW (Lammerer, 1988; Ratschbacher et al., 1989), to SSE-NNW (Mancktelow and Pavlis, 1992; Frisch et al., 2000), to S-N (Ratschbacher et al., 1991b), to SW-NE (for the Oligocene to early Miocene; Neubauer et al., 1999). The present models suggest that the formation of the Tauern domes and the entire deformation pattern of the eastern Alps were strongly influenced by small changes in the convergence direction of the indenter. Based on the analogy between structures in the model and map view, it is suggested that E-W extension and the formation of the Tauern domes were triggered by an indenter motion from SSW to NNE. Our confined models show that bulk lateral extrusion never exceeds 15-20%. Unconfined models (e.g., Ratschbacher et al., 1991b) do show larger (>50 %) extrusion, reproducing a fault pattern similar to that observed in the E-Alps, but the spatial distribution of finite strain in such models is very different from that inferred from structural investigations of the eastern Alps. In the latter models strain increases along the extrusion direction. This trend is opposite to the one inferred for the Eastern Alps, where E-W extension is maximum in the western TW and minimum East of the TW (e.g. Frisch et al., 1998, Fig. 2). This westward increase of orogen-parallel extension occurs in our model (Figs. 4 and 5), which is laterally confined.

One effect of doubling the thickness of the ductile crust is to reduce the strength of the lithospheric column at depth. As a consequence, thickening of the lithosphere during indentation cannot be supported to the same extent as in experiments with a lower thickness of ductile crust. Hence, lateral flow in the form of orogen-parallel extension takes place in the area that suffers the greatest amount of thickening, in front of the leading edge of the indenter.

Acknowledgements

The Deutsche Forschungsgemeinschaft is greatly acknowledged for financial support (Project RO 2177/2-1). J.-P. Caudale and J.-J. Kermarrec, helped resolving all technical aspects of the models. J. Smit helped to construct many experiments.

REFERENCES

- Behrmann, J. H., 1988, Geodyn. Acta, 2, 63-73.
- Frisch, W., Kuhlemann, A., and Dunkl, I., and Brügel, A., 1998, Tectonophysics, 297, 1-15.
- Frisch, W., Dunkl, I., and Kuhlemann, J., 2000, Tectonophysics, 327, 239-265.
- Lammerer, B., 1988, Geologische Rundschau, 77/1, 143-156.

• Mancktelow, N. S. and Pavlis, T.L., 1994, Tectonics, 13, 668-685.
• Neubauer, F., Genser, J., Kurz, W., and Wang, X., 1999, Phys. Chem. Earth (A), 24, 675-680.
• Ratschbacher, L., Frisch, W., Neubauer, F., Schmid, S. M., and Neugebauer, J., 1989, Geology, 17, 404-407.
• Ratschbacher, L., Frisch, W., and Linzer, H.-G., 1991a, 10, 257-271.
• Ratschbacher, L., Merle, O., Davy, P., and Cobbold, P., 1991b, Tectonics, 10, 245-256.
• Selversone, J., 1988, Tectonics, 7, 87-105.

DEFORMATION OF UNCONFORMABLE SEQUENCES: A FIELD CASE STUDY AND PRELIMINARY ANALOGUE MODELLING

2-26

E. Saura(*), H.A. Koyi(**), A. Teixell(*)

(*) Departament de Geologia (Geotectònica), Universitat Autònoma de Barcelona – 08193 Bellaterra, Spain

(**) Hans Ramberg Tectonic Laboratory–Department of Earth Sciences, Uppsala University, Villavägen 16, S-753 26 Uppsala, Sweden

Summary

The thrust deformation of angular unconformable sequences in the upper crust is investigated by sandbox modelling and structural analysis of a field example from the Spanish Pyrenees. The models used in this study are made of loose sand and glass microbeads and consist of a lower part with inclined layers truncated by an upper part with horizontal layers. Differences in dip and composition of the sub-unconformity layers have been introduced in the models to evaluate the influence of the unconformity angle and, preliminary, the effect of the mechanical stratigraphy. The natural example is from inverted extensional basins located at the leading edge of the Axial Zone antiformal stack of the Pyrenees. Extensional basins, of Stephano-Permian age, were originally unconformably overlapped by Triassic series. In thrust sheets involving a Stephano-Permian antithetically-inclined sequence, backthrusting parallel to the syn-rift sequence is a common feature, resulting from the incompatibilities derived from divergent slip directions associated to each sequence, above and below the Triassic unconformity. Analogue models also show backthrusting parallel to inclined markers with suitable orientations, indicating that there is a range of orientations for which slip along bedding will take place, in preference to the formation of new faults. Once nucleated, backthrusts usually do not refract when crossing the unconformity. Mechanical contrasts introduced in the lower sequence control nucleation of structures but do not act as gliding surfaces if their orientation is outside the favourable range for slippage.

Abstract text

We investigate the structural geometry and kinematics of deformed unconformable sequences based on a field example of positively inverted basins from the leading edge of the Pyrenean Axial Zone antiformal stack (AZAS), and on analogue modelling using frictional granular materials. The deformational geometry of unconformable sequences has been discussed by some authors (Ramsay, 1967; Suppe, 1983; Alonso, 1989; etc.) but an analogue modelling approach has never been reported. Alonso (1989) analytically studied the deformation of unconformable sequences, based on a natural example of reactivated folds in a basement overlain by a horizontal cover. This author described features as change of the unconformity angle, reactivation of basement faults, formation of faults parallel to basement bedding, and gliding along the unconformity.

The AZAS is formed by a stack of three highly far-travelled thrust sheets (Fig. 1), which are downward facing and unrooted in the frontal part (Nogueres Zone; Séguret, 1972). The thrust sheets at the Nogueres Zone are made up of a Hercynian basement, discontinuous Stephano-Permian red beds and volcanics deposited in small extensional basins, and a Triassic Buntsandstein unconformable cover. The occurrence of the extensional basins in the basement-involved thrust sheets strongly influences the deformation style, where the unconformity between Paleozoic and Triassic appears as a major issue.

A structural section of the field case study is shown in figure 2, where the names of the major thrust faults and overlying sheets are indicated. The Erta thrust sheet contains an inverted Stephano-Permian

basin that is overthrust beyond the initial null point. Layer-parallel backthrusting is conspicuous in the sub-unconformity sequence in this inverted basin, and the overlying Triassic unconformity appears sheared (Saura, 2000), The Nogueres thrust sheet is composed by several minor thrust slices, occasionally showing the Triassic directly overlying the Hercynian basement. When an extensional basin occurs in one of these slices, the extensional feature has also controlled its thrust sheet attitude and dimensions (fig 2), and short-cut features are common. As a general rule thrust sheets only involving Hercynian basement and Triassic cover are bigger, and their displacement is larger.

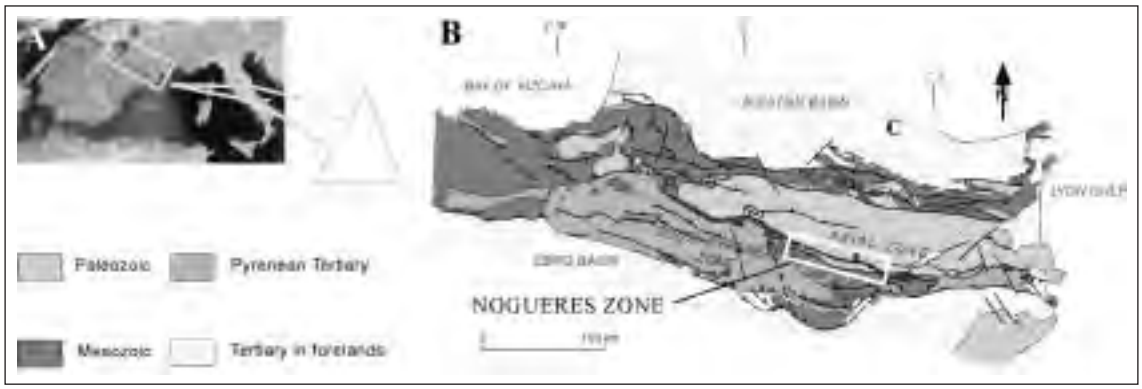

Fig. 1 - Situation of the study area. A) Satellite view of the Western Mediterranean region. B) Geological sketch of the Pyrenees, with the field case study area marked in white.

To validate the present-day cross-section and to obtain a restored version previous to the Pyrenean convergence, we have attempted a kinematic modelling approach with the software 2DMove (Midland Valley Exploration Ltd.). Kinematic modelling was performed using the Fault Parallel Flow algorithm (Egan et al., 1997), following a workflow designed specially for this field area. This method involves the kinematic restoration of available data (surface data), the completion of the restored cross-section, and subsequent forward modelling of the new restored section. The algorithm used simulates flexural slip emplacement by using an adequate angular shear value (ϕ, user's input). To avoid unrealistic deformation patterns resulting from repeated thrust sheet superposition, some assumptions and slight simplifications were needed. The obtained computer balanced section (fig. 3) slightly modifies the original section (always within the admissible range).The most important differences are: a thickness increase of Erta thrust sheet and localised thickness variations of the Triassic Buntsandstein. These divergences are mainly a consequence of the algorithm limitations (e.g., Savage & Cook, 2003), but the results validate the original field section.

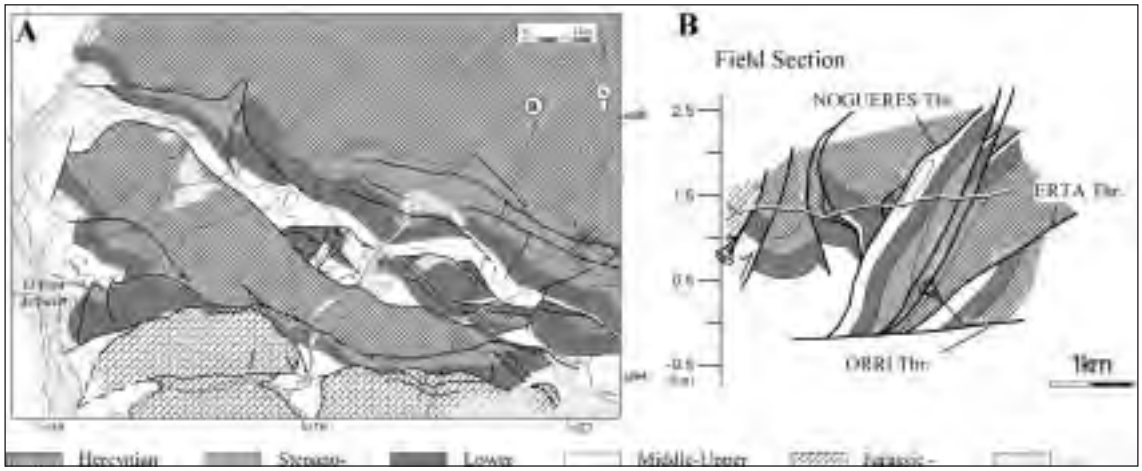

Fig. 2 - A) Geological map B- Balanced field section through the eastern edge of Gotarta thrust sheet (Nogueres Zone), showing the Orri, Erta and Nogueres units. In B, indicate the topographic line (the white and black line).

The restored section shows the original geometric characteristics of the Stephano-Permian basins. The syn-extensional volcano-sedimentary sequence was tilted 5º to 30º antithetically (fig.3). The bedding nature of both sequences, above and below the Triassic unconformity, enhances layer-parallel slip, and the mechanism of thrust emplacement was flexural shear. Consequently, this implies the existence of two slip directions during the emplacement, one for each sequence, and hence, problems of accommodation of the deformation arise at the unconformity surface. The sheared aspect of the unconformity in the field suggests that it may have acted as a decoupling surface, separating the two domains with different slip direction. As the preserved basin has been rotated but not much internally folded (fig. 2), the main effect of the divergent slip directions is the development of backthrusts, to accommodate deformation mainly in the sub-unconformity sequence.

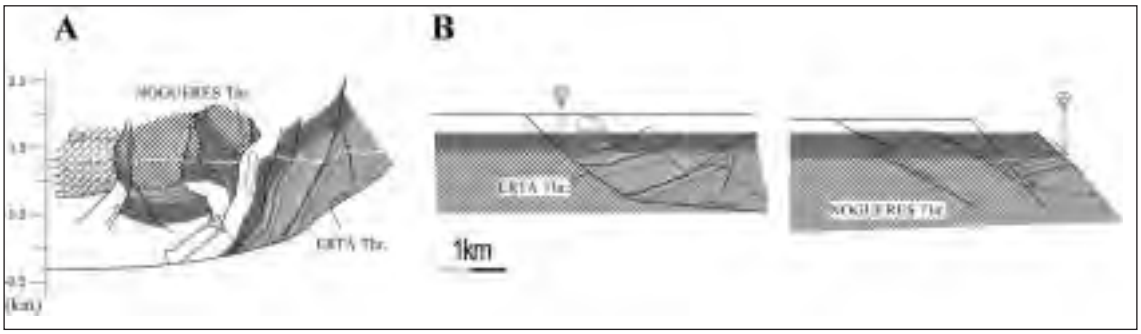

Fig. 3 - Kinematic modelling of Section B with 2DMove. A) Present-day cross-section showing the Erta and Nogueres thrust sheets. The Orri unit has not been modelled. B) Kinematic restoration. Dashed lines correspond to present-day topography. Same legend as fig. 3.

To investigate the effect of the orientation of the inclined sub-unconformity sequence and the influence of mechanical contrasts, three sandbox models have been designed at the Hans Ramberg Tectonic Laboratory. The models are divided in two parts, a lower sequence with foreland-dipping markers, and an upper sequence with horizontal markers, separated by an angular unconformity. Models 1 and 2 consist of loose sand, and display different dip (15º and 5º, respectively). The lower sand units in model 3 have the same dip as in Model 2, but a glass microbeads layer is introduced in the lower sequence (table 1). In some of the models, the backthrusts are parallel to the layering, which may have acted as a detachment. However, we have not been able to quantify this in detail. No ductile decollement was introduced in the models; hence, the contact between the sand pack and the basal plate acts as a frictional decollement, although of relatively low friction.

	Model dimensions		Lower Sequence			Upper Sequence	Shortening
	Thickness	Length	Thickness	Dip angle	MA	Thickness	
Model 1	2.5 cm	40 cm	1.5 cm	15º	No	1 cm	35 %
Model 2	2.5 cm	40 cm	1.5 cm	5º	No	1 cm	35 %
Model 3	2.5 cm	40 cm	1.5 cm	5º	Yes	1 cm	35 %

Table - Analogue model specifications. M.A.- mechanical contrast (glass microbeads layer).

Model results obtained after 35% shortening (fig. 4**A**) show some structural variations, although the general evolution of the models follows a similar pattern. Major forethrust sheets formed in a piggy-back sequence. At initial stages, a box fold (with both a forethrust and a backthrust) forms in front of the backstop. This structure is associated with the development of a sand wedge acting as an indenter stuck to the backstop at the base of the models (fig. 4.**A**), With further shortening, new forethrusts form as new material is incorporated in front of the wedge. These forethrusts develop from rotated forekinks along which deformation is localised. Although backthrusts are common in all models, because of the dominance of forethrusts, the result is a reduction of the wedge taper angle from around 20º at first stages of shortening, decreasing rapidly below 10º (fig. 4**B**).

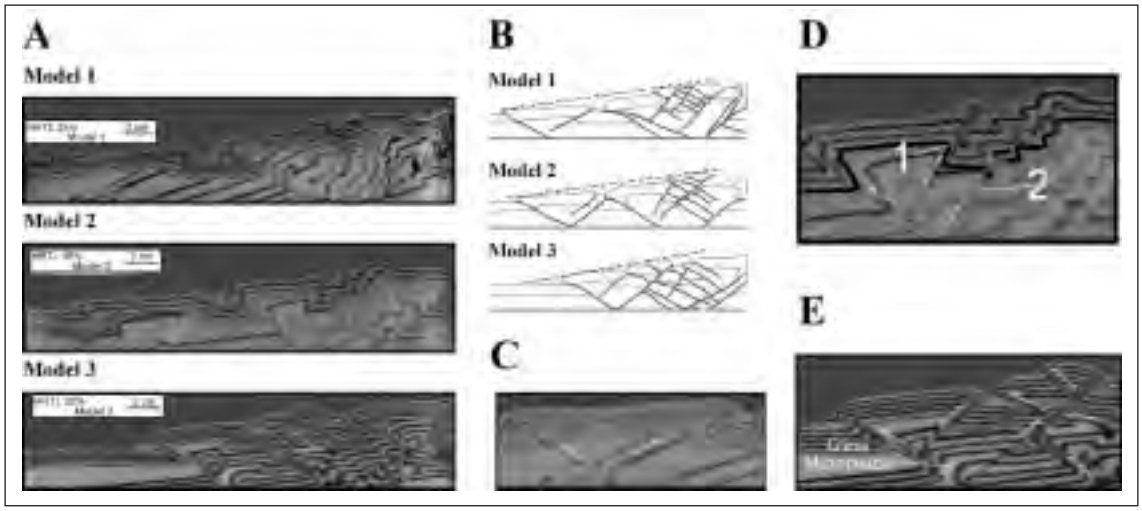

Fig. 4 - A) Profiles of models 1, 2 and 3. For identical shortening the deformation front is more advanced in models 1 and 2 than in model 3. B) Sketches of the model profiles shown in A. Bold lines: faults. Thin lines: Upper and lower boundary of the horizontal sequence. Dashed lines: wedge taper. C) Detail of profile of model 1 showing a low angle layer-parallel backthrust. D) Detail of Model 2 showing two high angle backthrusts. Backthrust 2 changes its orientation at the uncomformity, which is indicated by a Bold line. E) Detail of Model 3 showing the basal step-up of its frontal thrust at the pinch out of the glass microbeads layer.

Models 1 and 2 are similar, but they show differences in backthrust dip related to the original dip of the inclined sequence (fig. 4**B**). This is illustrated in figure 4**C**, from model 1, where a backthrust following a marker of the inclined sequence can be seen, indicating that the markers configure an effective gliding anisotropy. This feature has not been observed in model 2, where all backthrusts form with an initial steeper dip (40º-50º) that cross-cuts bedding. On the other hand, in all models, several backthrusts may use previously rotated marker beds as gliding surfaces, or even change their orientation to become subparallel to bedding (fig. 4**D**), when the marker presents a suitable orientation. Sandbox modelling shows that although the orientation of the sub-unconformity sequence controls backthrust dip, the orientation of the forethrusts appears independent, i.e., there is a range of orientations whose potential activation as gliding planes requires a shear stress lower than the one required to generate new thrusts.

The glass microbeads layer in model 3 exerts a control on the nucleation of foreland-verging thrusts. While in models 1 and 2 the fault cutoff of the unconformity of the frontal forethrust is close to the frontal static wall (only 3 to 5 cm apart), in model 3 it is farther (10 cm). The basal step-up of the frontal thrust of model 3 is located at the basal pinch-out of the glass microbeads layer (fig. 4**E**). On the other hand, forethrust dips are continuous from base to top in all models (being around 30º), and do not experience any refraction when passing from the sub-unconformity sequence to the unconformable one. Neither do the backthrusts. The only exception to this rule is the forethrust that just passes through the unconformity truncation of the glass microbeads layer. This thrust has an initial dip of 27º, then becomes parallel to the unconformity when encountering the microbeads layer, to ramp up again to cut the unconformable sequence at 34º. Model 3 suggests that the mechanical contrast between loose sand and glass microbeads is only effective at the tips of the microbeads layer, but the rheological step at this layer is not enough to overcome the effect of its very gentle dip (5º) and to induce gliding along it.

Conclusions

Preliminary analogue models and a field example from the Pyrenees show how thrust deformation of unconformable sequences may be influenced by the dip of the sub-unconformity sequence. If bedding orientation is favourable, gliding along bedding surfaces will occur, expressed by conspicuous backthrusting in foreland dipping sub-unconformity successions. However, in both field example and

analogue models, backthrust do not experience refraction when passing through the unconformity. In addition, at any stage of the progressive deformation, a planar anisotropy that acquires a suitable orientation by rotation may become a gliding surface, and accommodate slip as seen both in the sandbox models and in nature. Single mechanical steps as a glass microbeads layer do not control backthrusts orientation if its orientation is not suitable for gliding, but can induce the nucleation of major structures. New modelling is in progress to evaluate the effects of enhanced anisotropy at the lower sequence and stronger contrast of material properties at the unconformity.

Aknowledgements

This work benefitted from a travel grant BE 2002BEAI200200 of the Generalitat de Catalunya and from MCYT project BTE2003-00499 (Spain). We thank Midland Valley Exploration Ltd. for license to use 2Dmove.

REFERENCES

- Alonso, J.L. (1989), Fold reactivation involving angular unconformable sequences: theoretical analysis and natural examples from the Cantabrian Zone (Northwest Spain), Tectonophysics, 170, 57-77
- Egan, S.S., Buddin, T.S., Kane, S.J. & Williams, G.D. (1997), Three-dimensional modelling and visualisation in structural geology: New techniques for the restoration and balancing of volumes, In: Proceedins of the 1996 Geoscience Information Group Conference on Geological Visualisation, Electronic Geology, 1, Paper 7, 67-82
- Ramsay, J.G. (1967), Folding and fracturing of rocks. McGrau-Hill, New York, 568 pp
- Saura, E. (2000), Les unitats de les Nogueres i la seva relació amb els conglomerats oligocens entre les valls del Flamissell i el Manyanet (Pirineus Centrals), Treball de Recerca, Univ. Autònoma de Barcelona. 118pp
- Savage, H.M. & Cook, M.L. (2003), Can flat-ramp-flat geometry be inferred from fold shape? A comparison of kinematic and mechanical folds, Journal of Structural Geology, 25, 2023-2034
- Séguret, M. (1972), Etude tectonique des nappes et séries décollées de la partie centrale du versant sud des Pyrénées. Thèse Doct., Publ. USTELA. Série Géol. struct. 2, Montpellier, 210 pp
- Suppe, J. (1983), Geometry and kinematics of fault-bend folding. American Journal of Science, 283, 684-721

GROWTH OF AN OROGENIC WEDGE BY FRONTAL ACCRETION: FIRST RESULTS OF A NUMERICAL MODEL STUDY 2-27

C. Selzer(*), S. Buiter(**), A. Hampel(*), A. Pfiffner(*)

(*) Institute of Geological Sciences, University of Bern, Baltzerstrasse 1, CH-3012 Bern, Switzerland
(**) Geodynamics Group, Department of Oceanography, Dalhousie University, Halifax, Nova Scotia, Canada

Abstract

Our numerical model study presents preliminary results from investigations of the dynamics of orogenic wedges We particularly focus on the process of frontal accretion. The models computed by the finite element code Microfem, show that mechanically weak inclusions and weak “model basins” affect the progression of shear zones, and that erosion slows down the growth of an orogenic wedge.

Introduction

Orogenic wedges form in the foreland of orogens at convergent margins. With progressing convergence, crustal material is added by frontal accretion near the toe and/or by underplating at the base of the wedge (Dahlen et al. 1984; Davis et al., 1983). Orogenic wedges raised above or formed above sea level may undergo subaerial erosion.

In this study we concentrate on the process of frontal accretion, i.e. the incorporation of material at the toe of the wedge, above an inclined basal detachement and in front of a buttress. We are particularly interested in the wedge attaining a critical taper by internal deformation, as well as the nature of this internal deformation such as the stacking of thrust sheets. The dynamics and thus the shape of an orogenic wedge is influenced by frontal accretion, underplating, erosion, sedimentation, and changes in the basal shear stress. In order to achieve high resolution we limit the model to crustal deformation.

Modelling methods

For the numerical investigation we apply the finite element code Microfem, specifically developed for geodynamic applications by the Geodynamics Group of Dalhousie University (Fullsack, 1995). Microfem enables to calculate two-dimensional, plane-strain models applying the arbitrary Eulerian-Lagrangian formulation. This allows to study large deformation processes, through which large strains are achieved and shear zones develop. Material behaviour can be defined as rigid-plastic or viscous-plastic. So far, our models only apply rigid-plastic rheology.

First modelling results

We have performed calculations for three different models: (1) a basic model with a homogenous crust, (2) a model containing weak inclusions 2 km beneath the surface of the incoming crust, and (3) a model with weak "model basins" at the top of the incoming crust. The basal detachment represents the situation where the lower lithospere (mantle and lower crust) is subducted, whereas the upper lithosphere (sediments in case of oceanic lithosphere, upper crust in case of continental lithosphere) is offscraped to form an accretionary or orogenic wedge. The theoretical critical taper angle in these models equals approximately 7°. Model set-up and material properties are given in Fig. 1.

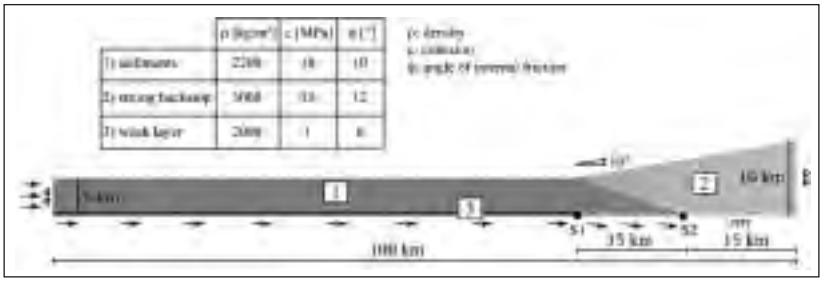

Fig. 1 - Sketch of model set-up for frontal accretion experiments. Material behaviour is rigid-plastic, the Coulomb internal angle of friction is an effective angle which takes into account the effect of pore fluid pressure. Material is fed into the grid from the left side at a velocity of 1 cm/yr. Up to point S1 the base moves horizontally at a velocity of 1 cm/yr, between S1 and S2 material exits downward at an angle of 5° and the velocity remains constant. The strong material to the right of S2 acts as backstop. The weak layer at the base of the model is intended to act as basal detachment.

Model 1

Results of the basic model are given in Fig. 2. As a result of convergence, shear zones develop. The first starts at point S2 and spreads to the toe of the newly built orogenic wedge. With ongoing convergence a basal shear zone develops. Further shear zones always extend from the end of the basal shear zone to the toe of the orogenic wedge. They are about equally spaced and have a dip of approximately 45° at formation. Continued convergence decreases this dip and results in self-similar growth of the orogenic wedge. Its top surface consists of several bulges that form due to intersection with shear zones. The overall dip in front of the first shear zone decreases from 7 to 5°. The taper angle is 7°, i.e. close to critical. Accumulation of sediment underneath the strong backstop has caused its uplift and a clock-counterwise rotation.

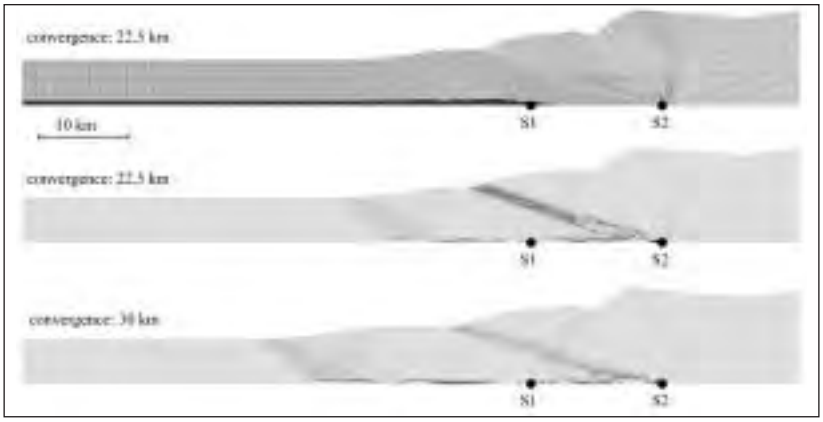

Fig. 2 - Accumulated deformation (shown by Lagrangian grid) and instantaneous strain rates of basic model.

Model 2

Weak inclusions of the second model are located 2 km underneath the surface of sediments. They have a width of 10 km, a height of 1 km and an equal spacing from each other of 15 km. They have identical material properties as the weak layer (see Fig. 1). These inclusions are intended to represent mechanical heterogeneities in the incoming crust in a simple generic way. Calculations have been performed without and with erosion. A slope-dependent erosion model has been applied with an erosion rate corresponding to a denudation of 1 mm/yr for a slope of 45°.

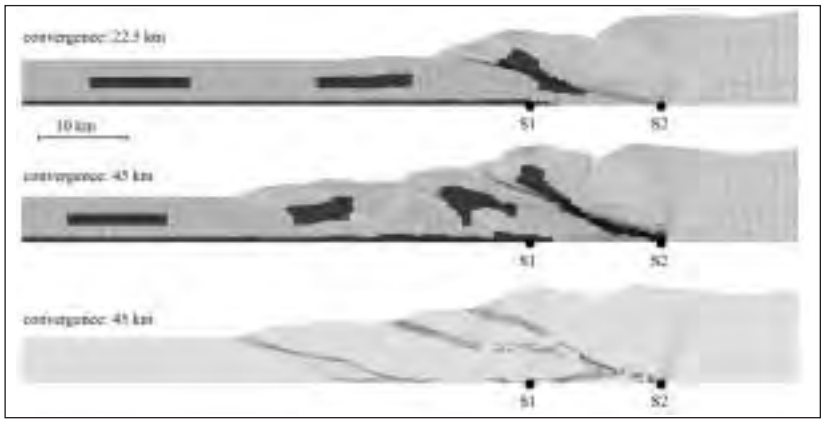

Fig. 3 - Accumulated deformation (shown by Lagrangian grid) and instantaneous strain rates of model containing weak inclusions - without erosion.

Similar to the homogeneous basic model the first shear zone spreads from S2 to the toe of the newly built orogenic wedge. Its progression, however, is influenced by the arrival of the first weak inclusion. Subsequently, shear zones emerge from the end of the basal shear zone to the toe of the orogenic wedge. Their progression is also influenced by the weak inclusions. With further convergence, later-built shear zones connect to the first one, in a way that an upper detachment level is developed. The weak inclusions interact with the shear zones: initially inclusions are flexed and form weak cores of broad antiforms building-up the orogenic wedge. Subsequently they are dissected by the shear zones, markedly stretched and pulled downwards. Finally, they stack underneath formerly accreted weak inclusions. In comparison with the basic model, the orogenic wedge has a topography containing more pronounced bulges. The overall surface slope decreases from 12 to 8° in the course of the experiment, but is always shallower towards the toe. The reduction of the surface slope is slower in the model with erosion. Because of accumulation of sediments, the strong backstop is uplifted and rotated. This uplift is more marked if modelling considers the effect of erosion. Another consequence of erosion is that formation of new shear zones, as well as their connection to the upper detachment level is delayed. Thus, growth of the wedge is slower if erosion is included.

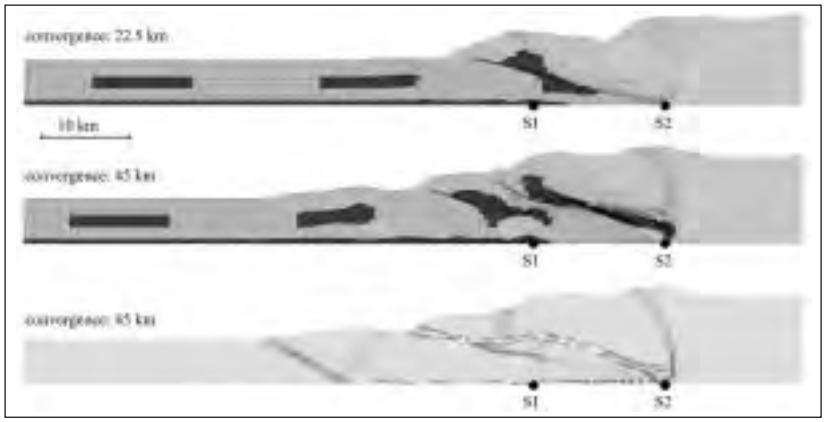

Fig. 4 - Accumulated deformation (shown by Lagrangian grid) and instantaneous strain rates of model containing weak inclusions - with erosion.

Model 3

The top of the sediment layer of the third model contains trapezoidal shaped "model basins". These are 25 km (top)/15 km (base) wide, 1 km deep, and arranged at an equal spacing of 25 km. Except for the cohesion, for which a value of 10 MPa has been assumed, they have identical mechanical properties as the weak basal layer (see Fig. 1). Calculations have again been performed without and with erosion, applying the same slope-dependent model as for Model 2.

Similar to the models discussed before, the first shear zone develops from S2 to the toe of the orogenic wedge. It is influenced by the weak layer on top of the sediment layer, however, it does not cut across this weak layer but follows its base. As a consequence of this, material transport into the orogenic wedge occurs along this shear zone, thus the "basement high" between basin 1 and 2 is subducted along this detachment. In later stages (97.5 km of convergence) a shear zone develops at the base of model basin 2 during its incorporation into the orogenic wedge. Simultaneously, a further shear zone develops at the base of the model. The basal shear zone gradually propagates outward connecting to the surface by step-up shear zones. The latter develop preferentially at the leading and trailing edges of the model basins. Like in the basic and the second model, the strong backstop material is uplifted and rotated. Erosion delays the formation of the frontal shear zone and the growth of the orogenic wedge, and induces a more pronounced uplift of the strong backstop.

Concluding remarks and outlook

Our preliminary results indicate that growth and internal deformation of an orogenic wedge is influenced by the presence of weak inclusions, or weak basins, and by erosion. Weak inclusions and weak basins control the progression of shear zones, and thus the internal deformation. Erosion slows down the growth of the orogenic wedge. Similarly, the critical taper angle is achieved in a later stage. This can be explained by enhanced internal deformation (as shown by the total accumulated strain), which tends to raise and thus maintain the surface slope. In further investigations with Microfem we aim to analyse the sensitivity of our model orogens to material properties, to different types of erosion (diffusive versus slope or height dependent) and to flexural bending.

We also plan to study the growth of orogenic wedges using the commercial code ABAQUS (Hibbitt et al., 2002). ABAQUS-models will be computed using comparable set-up and material properties. In particular, elastic-plastic material behaviour will be studied.

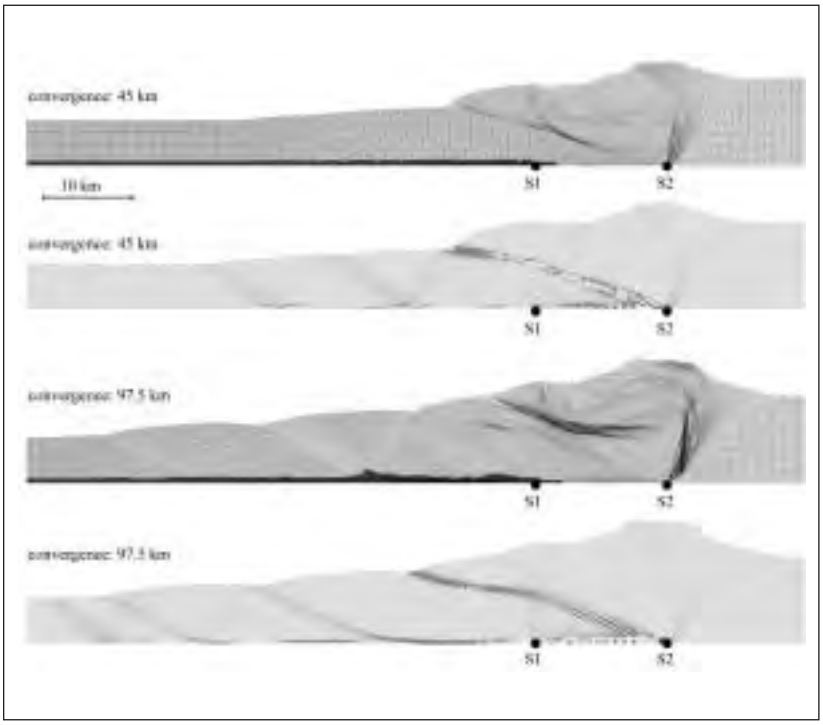

Fig. 5 - Accumulated deformation (shown by Lagrangian grid) and instantaneous strain rates of model with weak model basins in top of the sediment layer - with erosion.

REFERENCES

- Dahlen, F. A., J. Suppe, and D. Davis (1984), Mechanics of fold-and-thrust belts and accretionary wedges: Cohesive Coulomb theory, J. Geophys. Res. , 89 , 10087-10101.
- Davis, D., J. Suppe, and F. A. Dahlen (1983), Mechanics of fold-and-thrust belts and accretionary wedges, J. Geophys. Res., 88, 1153-1172.
- Fullsack P. (1995), An arbitrary Lagrangian-Eulerian formulation for creeping flows and its application in tectonic models, Geophys. J. Int., 120, 1-23.
- Hibbitt, H. D., Karlson, B. I. and Sorenson, E. P. (2002), Theory Manual, Hibbitt, Karlson and Sorenson, Inc. Pawtucket, RI, USA, version 6.3.

MODELING SUBDUCTION OROGENY IN THE CENTRAL ANDES 2-28

S. Sobolev, A. Babeyko

GeoForschungsZentrum-Potsdam – 14473 POTSDAM Germany

Summary

A number of hypotheses have been invoked to explain extreme subduction orogeny in the Central Andes in Cenozoic time. However, none of them has been tested so far by fully coupled and internally consistent thermomechanical modeling involving both subducting slab and overriding continental plate. Filling this gap we show that intensive tectonic shortening in the Central Andes might have been driven by fast (2-3 cm/yr) westward motion of the South America plate combined with the regionally high resistance of the subducting Nazca plate due to the relatively high friction coefficient in the subduction channel. The modeling also demonstrates an important role of the mechanical weakening processes at the South America plate margin before and during tectonic shortening, including mantle lithosphere delamination.

Introduction

Thermo-mechanical interaction of the subducting oceanic plates with the overriding continental plates may result in various deformation scenarios ranging from the strong extension (backarc spreading) to the strong compression (subduction orogeny). Factors controlling such behavior remain poorly understood. Here we present a fully coupled thermo-mechanical model of the extreme case of the subduction orogeny, a development of the Altiplano-Puna plateau in the Central Andes in Cenozoic time. The Altiplano-Puna plateau of the Central Andes is the second greatest plateau in the world after Tibet with average elevation of about 4 km and area of more than 500,000 km^2. The plateau resulted from the crustal shortening of the western edge of South America plate overriding subducting Nasca plate, which generated unusually thick, hot and felsic continental crust (Isacks, 1988; Allmendinger et al., 1997; Lamb et al., 1997; Kley and Monaldi, 1998; Yuan et al, 2000, Yuan et al., 2002, Beck and Zandt, 2002, Lamb and Davis, 2003).

The Cenozoic orogeny in the Central Andes was attributed to the weakening of the South American plate margin (Isacks, 1988), or to the increase of the Nazca-South America convergence rate (Pardo-Casas and Molnar, 1987; Somoza , 1998), or to the increase of the overriding rate of the South America plate (Silver et al., 1998) as well as to the anomalously high shear stress (friction) at the interface between Nazca and South America plate (Lamb and Davis, 2003). However, none of these hypotheses has been tested so far using fully coupled and internally consistent thermo-mechanical modeling. The reason for that is that treatment of the delicate force balance between subducting and overriding plates requires to include into analyses also the elastic and friction forces, which is very difficult to do in the spatial (1000 km) and temporal (30 Myr) scales of interest. We attempt to fill this gap here. In our modeling we address the following intriguing features of the Andean orogeny:

(1) The high mountain belt has been developed only in the Central Andes and only during the last 30-40 Myr although the Nazca plate has been subducted along the entire western margin of the South America during ca. 200 Myr;

(2) The large-scale tectonic shortening in the Central Andes and uplift of the plateau are accelerating during the last 10-15 Myr although the Nazca- South America convergence rate is markedly decreasing;
(3) Deformation was concentrated first in the western and central parts of the plateau and it was shifted to the east in the last 10 Myr;
(4) There is no evidence for strongly increased thickness of the mantle lithosphere below the plateau although crust there is doubled;
(5) The major part of the thick crust beneath the plateau is felsic and very hot, even partially molten in places.

Model

We use a 2D parallel thermo-mechanical finite element code, which combines the explicit lagrangian FLAC algorithm (Polyakov et al., 1993; Cundall and Board, 1988) with the marker technique similar to the particle-in-cell method (Sulsky et al., 1995; Moresi et al., 2001). Markers track material properties and full strain and stress tensors minimizing numerical diffusion related to remeshing. The explicit lagrangian time-marching algorithm allows for strongly non-linear rheologies. We employ realistic temperature- and stress-dependent visco-elastic rheology, as well as Mohr-Coulomb elasto-plasticity for oceanic crust and mantle and for two layer continental crust, mantle lithosphere and asthenosphere (Fig. 1), with the parameters taken from published experimental studies (e.g. Gleason and Tullis, 1995; Hirth and Kohlstedt, 1996; Rybacki and Dresen, 2000). We also include friction- and viscosity- strain softening, which allows for spontaneous strain localization and self-generation of faults. The initial friction angle of 30 ° and cohesion of 20 MPa as well as viscosity in all materials decrease by factor of 10 at finite strain of 1 with exception for Pz sediments in Subandean Zone (Fig. 1), which are assumed to soften quicker (by factor of 10 at finite strain of 0.25-0.5).
Our model explores the interaction of the subducting Nazca plate with the overriding South America plate during the last 35 Myr in the 1200 km long and 400 km high model box (Fig.1). The model includes shear heating and gabbro-eclogite phase transformation. The velocities at which overriding plate enters the model box (overriding rate) and the subducting plate leaves the box (subduction rate) are prescribed by boundary conditions (Fig.1) and are taken from plate tectonics reconstructions (Samosa, 1998, Silver et al. 1998). All other parts of the model box boundary (Fig.1) are open for free motion of the material. The interface between the slab and the upper plate is modeled as a few km thick subduction channel with particularly low-friction Mohr-Coulomb rheology. The friction coefficient in the subduction channel is major model parameter and it was varied from 0 to 0.06.

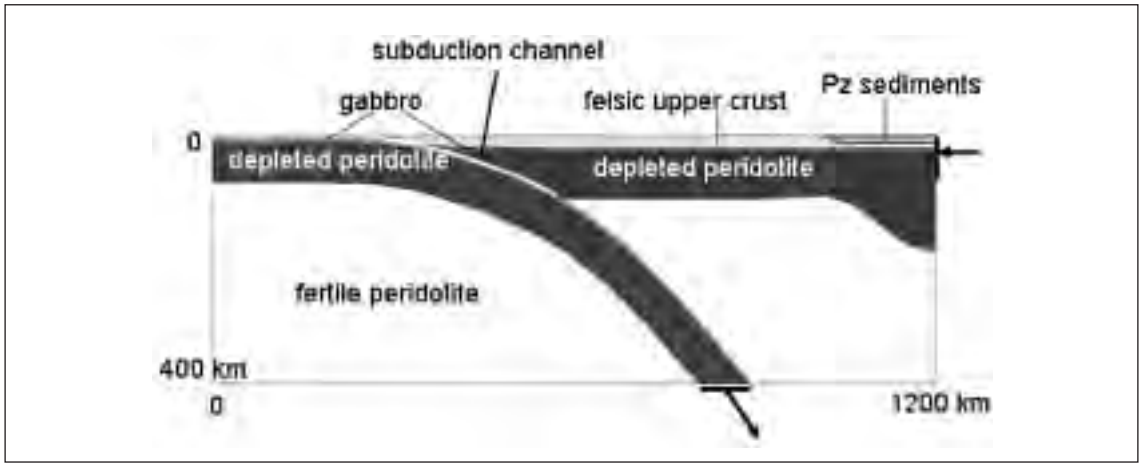

Figure 1. Model setup. Modeling starts at 35 Ma and finishes at present time. The Nazca plate is subducting with variable velocity, increasing up to 12 cm/yr at model time 10 Myr and slowing down to 5 cm/yr at present time in accord with plate motion reconstruction (Samosa, 1998). The South American Plate is moving west (to the left) with velocity increasing from 1,5 to 3 cm/yr during 35 Myr (Silver et al. 1998). Finite element size is 4 X 4 km. In the "best fit" model the starting crustal thickness is 40-50 km.

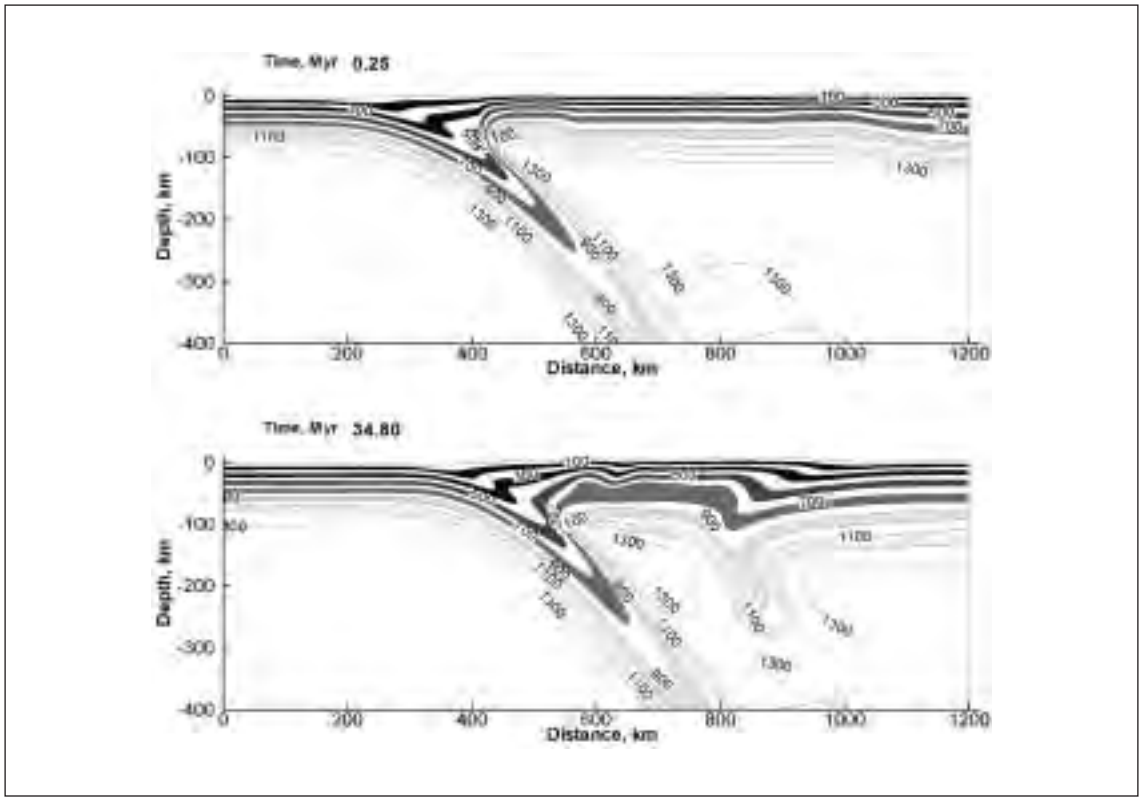

Figure 2. Initial temperature (upper section) and final temperature (lower section) distributions in the best-fit model for the Central Andes. The subducting plate is 50 Myr old. Initial thickness of the continental lithosphere is 80-120 km, with the thickest lithosphere in the eastern (right) part of the model corresponding to the Brazilian Shield margin. Note the field corresponding to the temperature range of 700-800°C when partial melting of the water containing felsic rocks occurs. In the starting model, these temperatures are achieved only in the lower mafic crust without partial melting. In the final model they are achieved within thickened felsic crust (see also Fig. 3) where partial melting and convection may be expected (Babeyko et al., 2002).

Results

Systematic exploration of the model parameter space shows that variations of the overriding plate velocity from 1 to 3 cm/yr and friction coefficient in subduction channel from 0 to 0.05 (parameters ranges expected for the Andes) may strongly change deformation regime in the upper plate. Variations of the subduction velocity by 7 cm/yr, reported for the Andes in Cenozoic time, appear to have less important impact.

The modeling suggests that the tectonic shortening in the Central Andes may have been driven by the Mid Atlantic Ridge push (possibly powered by the East-West sub-lithospheric mantle flow, Silver et al., 1998) which forced the South America plate to override the Nazca plate with increasing velocity, and by the resistance of the Nazca plate controlled by the friction coefficient in the subduction channel. The model replicates very well the Cenozoic evolution of the Central Andean lithospheric structure (Fig. 3a), surface topography (Fig. 3b) and distribution of the strain in the crust (Fig. 3c), if the time-averaged friction coefficient in the subduction channel is set to 0.03-0.05. These relatively high, for the subduction zones values (Peacock, 1996), are likely due to the lack of sediments in the trench in the arid Central Andes (Lamb and Davis, 2003). Note, however that our estimates of the friction coefficients are about 1.5-2 times lower than friction coefficients required to achieve excessively high shear stresses at the slab interface suggested by Lamb and Davis (2003).

Our modeling suggests that Andean subduction orogeny took place at the time and in the place when and where at least two major conditions met: (i) high overriding rate of the South America plate (likely achieved during the last 30 Myr and particularly during the last 10 Myr) and (ii) friction coefficient

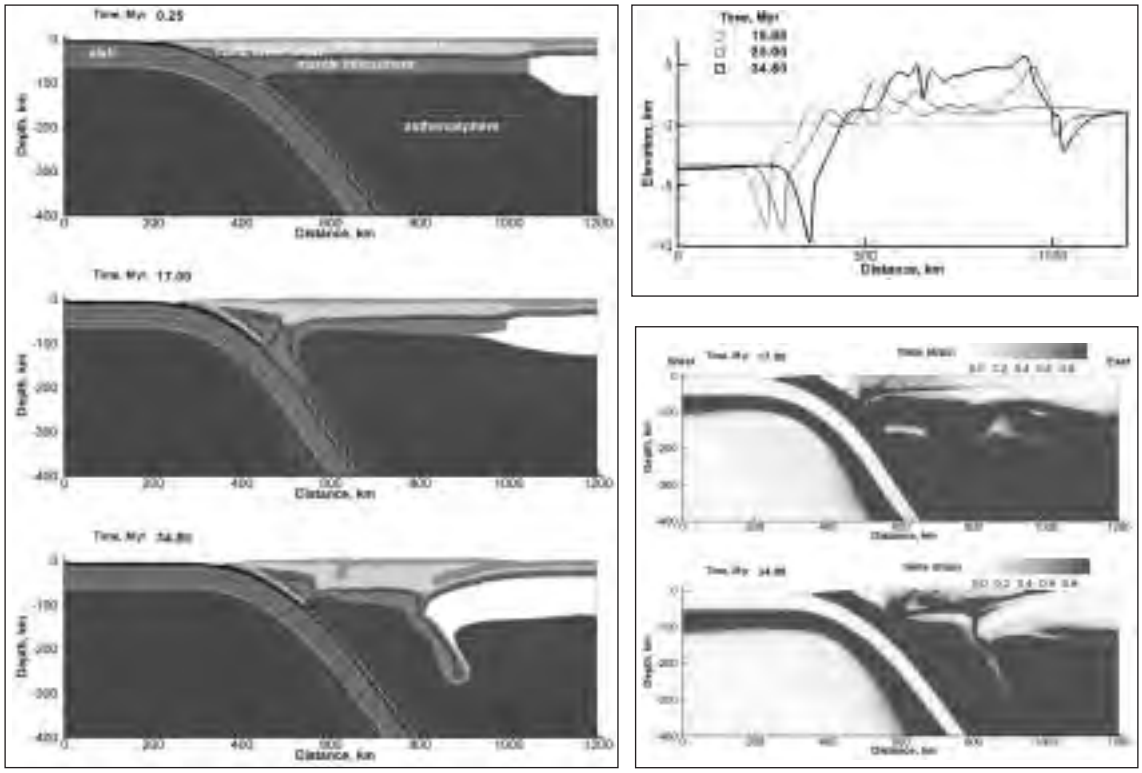

Figure 3. Modeling results for the best-fit model for the Central Andes. (a) Time snapshots of the evolution of tectonic shortening. Color codes correspond to the rock types. Note intensive thickening of the felsic upper crust (light and intermediate gray in the upper part of the continental crust) and loss of the mafic lower crust (intermediate gray color in the lower part of the continental crust) during the last 18 Myr. Note also that mantle lithosphere is becoming thinner during tectonic shortening. (b) Evolution of surface topography. Note formation of high plateau during the last 10 Myr (model times 25-35 Myr). (c) Distribution of finite strain at two model times. Note that tectonic deformation in the upper plate crust first concentrates in the western (left) part of the plate and then moves to the eastern (right) part. This motion is accompanied by generation of low-angle mega-thrust fault and lower crustal flow.

of 0.03-0.05 in the subduction channel (achieved only in the most arid central Section of Andes).
The above-mentioned conditions were likely necessary but not sufficient to create the Andean high plateau. Our models also demonstrate an important role of several processes of the internal mechanical weakening (softening) of the South America plate during the tectonic shortening. The major of these processes is mantle lithosphere delamination (Fig. 3a), which is triggered by the gabbro-eclogite transformation in the thickened continental lower crust (Kay and Kay, 1993). As it is seen from Fig 3a, due to the delamination, mantle lithosphere significantly thins during tectonic shortening. The delamination also leads to the loss of mafic lower crust and strong heat input into the crust from the asthenosphere both resulting in mechanical weakening of the lithosphere. The direct consequence of this weakening is acceleration of shortening, which we observe in all our models. Another consequence is heating and partial melting of the felsic continental crust (Fig. 2) (Babeyko et al., 2002).
Our models also suggest that it would be much easier to form the Andean high plateau during some 30 Myr if before the beginning of the deformation, the lithosphere of the upper plate was rather thin and weak (in accord with Isacks, 1988). For instance, our best-fit model has rather high initial temperatures (Fig. 2) and relatively week “wet” rheological laws for upper crust (wet quartzite by Gleason and Tullis, 1995), lower continental crust (wet feldspar by Rybacki and Dresen, 2000) and continental mantle lithosphere (wet olivine by Hirth and Kohlstedt, 1996). In addition the best-fit model has thick (up to 45-50 km in places) initial crust, which favors early gabbro-eclogite transformation in the lower crust.

REFERENCES

- Allmendinger et al. (1997), Annu. Rev. Earth Planet. Sci., 25, 139-174
- Babeyko et al. (2002), Earth. Planet. Sci. Lett., 199, 373-388.
- Beck and Zandt (2002), J. Geoph. Res., 107, 2230, doi:10.1029/2000JB000124
- Cundall and Board (1988), In: 6th Interna-tional Conference in Numerical Methods in Geomechanics (ed. Swoboda, G.), A. A. Balkema, Brookfield, Vt., 2101-2108.
- Gleason and Tullis (1995), Tectonophysics, 247, 1-23.
- Hirth and Kohlstedt (1996), Earth Planet. Sci. Lett., 144, 93-108.
- Isacks (1988), J. Geophys. Res., 93, 3211-3231.
- Kay and Kay (1993), Tectonophysics, 219, 177– 189.
- Kley and Monaldi (1998), Geology, 26, 723–726.
- Lamb et al. (1997), In: Orogeny Through Time (eds. Burg J.-P. and Ford M.), Geol. Soc. Spec. Publ., 121, 237–264.
- Lamb and Davis (2003), Nature, 425, 792-797
- Moresi et al. (2001), In: Proceedings of the Fifth International Workshop on Bifurcation and Localization in Geomechanics (ed. Mühlhaus et al.), Balkema, Rotterdam, ISBN 90265 18234, 345–355.
- Pardo-Casas and Molnar (1987), Tectonics, 6, 233–248.
- Poliakov et al. (1993), in: Flow and Creep in the Solar System: Observations, Modelling and Theory, eds. Stone, D.B. and Runcorn, S.K., Kluwer Academic Publishers, p. 175-195.
- Peacock (1996) in Subduction, Top to Bottom (eds Bebout, G. E. et al.), Geophys. Monogr. 96, American Geophysical Union, Washington, p. 119–133.
- Rybacki and Dresen (2000), J. Geoph. Res., 105, 26017-26036.
- Silver et al. (1998), Science, 279, 60-63.
- Somoza (1998), J. S. Am. Earth Sci., 11, 211– 215.
- Sulsky et al. (1995), Comput. Phys. Commun., 87, 236–252.
- Yuan et al. (2000), Nature, 408, 958-961.
- Yuan et al. (2002), Earth Planet. Sci. Lett., 199, 389-402.

GEOMETRICAL MODELLING OF COMPRESSIONAL ANALOGUE SANDBOX EXPERIMENTS: WHAT THE DIFFERENCES MEAN 2-29

D.C. Tanner(*), J. Adam(**)

(*) Geological Institute, RWTH-Aachen, Wüllnerstr. 2, 52056 Aachen, Germany, tanner@geol.rwth-aachen.de

(**) Department of Earth Sciences, Dalhousie University, Halifax, Nova Scotia B3J 3J5, Canada, j.adam@dal.ca

Summary

We present geometrical models, based on compressional analogue sandbox experiments, to show the differences between observed and modelled geometries obtained from the two methods, and use these to decipher the role of geological deformation mechanisms in the sandbox. In addition, we demonstrate displacement field results from particle-imaging velocimetry of the analogue models and geometrical models, and discuss the implications of both.

Introduction

Analogue sandbox modelling is increasingly used to decipher the parameters controlling the development of tectonics in compressional and extensional settings. Techniques such as Particle Imaging Velocimetry (PIV) have pushed back the boundaries of the analysis of such models, as they allow detailed, three-dimensional imaging of the displacement field over time (White, 2001: Adam et al., 2002: Adam et al, in review). Nevertheless, it is still difficult to interpret the resulting velocity, strain, and area fields over time in terms of the (bulk) deformation processes which occur during the experiment.

Geometrical kinematic modelling, based on either finite elements or geometrical three-dimensional surfaces, is able to back- or forwards (retro)-deform natural and artificial models to obtain geological data and verify the geometry of a model. The techniques available, especially in three dimensions, are based on geometrical/structural modelling concepts as well as bulk mathematical approximations of rock deformation, such as flexural slip or inclined shear. They suffer from the fact that they are unable

to combine rock deformation mechanisms, and need to approximate deformation. All models, whether analogue or geometrical are susceptible to scaling problems.
We present a series of geometrical kinematic models, of which the starting geometries were derived from images of two-dimensional compressional scaled sandbox models. The geometrical models were then forward-deformed using two algorithms (fault-parallel flow, flexural slip), which are widely used for thrust fault analysis and restoration. The differences between the geometrical and analogue deformation are then discussed in detail, as are strain results from both methods. In the discussion, reasons for both the deformation mechanisms in the compressional sandbox experiments and natural thrust faulting and the shortcomings of the geometrical analysis are shown, as well as the implications of the study on geometrical/kinematical modelling of natural thrust faults.

The sandbox experiments

2D contractional sand-wedge experiments, with different friction contrast between the basal detachment and the deforming sand (low friction contrast - LF; high friction contrast - HF) were carried out at the analogue laboratory at the GeoForschungsZentrum in Potsdam, Germany. The experimental device consists of a glass-sided 2D shear box of 200 cm length and 20 cm width. Convergence was simulated by a conveyor belt that was pulled towards the rigid rear wall at ca. 10 cm/min. The input layer, with a thickness of about 3.5 cm (scales to 3.5 km in nature), was made of mechanically-homogeneous sifted sand, which deforms similarly to brittle crustal rocks, with a strain-hardening and softening phase prior to stable sliding. The density and cohesion scales with a factor of 10^5 to natural systems.

Figure 1: Incremental shear strain indicating active deformation, obtained by PIV image analysis of the two sandbox models (left – LF, right – HF), at the point just before the new imbricate block is initiated by shear localisation. White areas indicate areas of particles undergoing shear (between arrows) and thus the new imbricate block.

During the experimental run, the sand layer was transported on top of the conveyor belt and was deformed in front of the rear wall. The incoming sand layer was successively detached from the basal interface and formed an imbricate thrust wedge (cf. Fig. 1).
The HF sand wedge was transported on a smooth foil with a basal friction coefficient significantly lower than the sand itself (friction contrast (fc) = 1.89, basal: 0.352; intern: 0.536). This corresponds to a situation in nature where pore fluid pressure has reduced the effective friction. In this experiment, the basal detachment developed as a shear plane directly on top of the basal foil. The HF wedge grew dominantly by frontal accretion with characteristic short thrust displacements. This lead to pronounced lateral growth with a small wedge taper.
The LF sand wedge rested on sandpaper. This interface was characterized by significant roughness and strong mechanical coupling to the sand layer (fc = 1.03, basal: 0.55; intern: 0.536). A natural analogue would be, for instance, when rough oceanic crust topography is subducted. In this experiment, the basal detachment was formed as a broad shear zone from the top of the interface up to 6 mm within the overlying sand layer. In contrast to the HF sand wedge, the LF wedge grew mainly by frontal underplating. Individual thrust faults were characterized by large thrust displacements. The entire thrust wedge showed a large taper and dominant vertical growth (e.g. Huiqi et al. 1992).

Methods of geometrical kinematic modelling

The starting geometries for the models were taken from digital images of the sandbox models in a similar stage of thrust wedge development. From each of the HF and LF models we took the image

of an active imbricate block, at the point were it was clear from particle displacements that a new fault was developing at its leading edge (Fig. 1). The modelling was carried using the 2/3DMove software package from Midland Valley Exploration Ltd. Two algorithms were used to forward deform the geometry models: fault-parallel flow and flexural slip.

Fault-Parallel Flow: This new algorithm was designed by a consortium from Midland Valley Exploration Ltd and Keele University, UK. (Egan et al. 1999). It envisages that all node points in the hanging wall of a fault are displaced parallel to the fault. This simple philosophy means it can cope with complex convoluted faults and hanging wall geometries. In addition to displacement, nodes need to undergo simple shear, parallel to the fault surface, if they pass through a net number of convex or concave fault-dip domains (Tanner et al. 2003). A consequence of this method is that bed length is conserved parallel to the fault.

Flexural Slip: This algorithm is based on the classic work of Suppe (1983). In his method, Suppe suggested only beds moving over ramps are deformed (by simple shear), and that when a node passed through the bisectors of two ramp/flat angles, it is effectively sheared and then unsheared, i.e., the equal, but opposite amount of shear is applied. Bed length is maintained in the transport direction, excess bed length being either placed on the trailing edge or at the leading edge as a steep overturned fold.

Geometrical models were forward deformed until the leading edge of the imbricate block was in the same position as the imbricate block reached in the sandbox experiment, before a new imbricate block developed at its leading edge. In an attempt to compare strain results, images of the final sandbox models were used to build grids representing the whole fault imbricate in its deformed position. These were then retro-deformed using fault-parallel flow. Strain results were recorded from the grid displacement field.

Results

Figure 2 shows the results of the geometrical forward modelling compared to the analogue experiment.

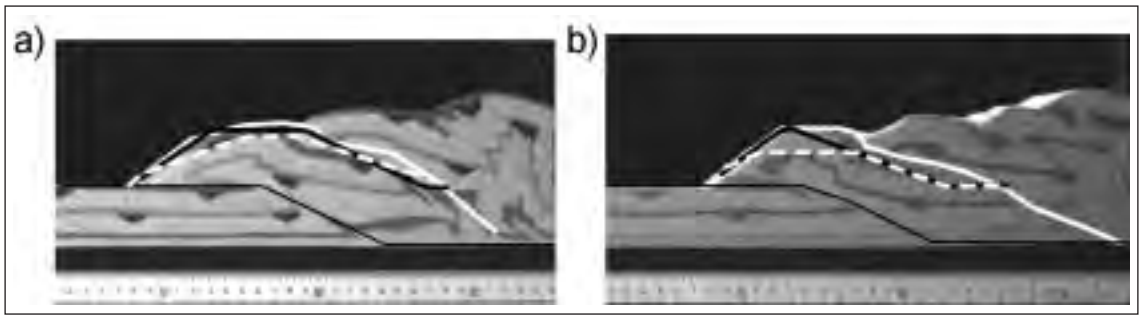

Figure 2: Results of the forward geometrical modelling, compared to the actual final sandbox model (background). a) LF and b) HF. Line coding; white – outline of sandbox imbricate block, black – geometrical modelling using fault-parallel flow, dashed white – geometrical modelling using flexural slip.

Clearly, geometrical modelling was not able to raise the imbricate block up as far as the analogue experiments. The closest fit was achieved by fault-parallel flow, in both HF and LF models. Fault-parallel flow was able to most closely fit the leading edge angle in both cases. The areal difference between the results is given in Table 1.

Experiment	Fault-parallel flow (%)	Flexural slip (%)
LF	94	78
HF	83	78

Table 1: Apparent percent area of geometrical forward models with respect to the appropiate analogue model.

Since the leading edge of the analogue model imbricate block is an erosional surface, which during and after deformation corresponds to the angle of repose for the sand, the amount of fault

displacement was underestimated in the geometrical model by ca. 5 mm (slightly higher for the HF experiment). This would increase the results of Table 1 by ca. 2-3%.
Strain in the analogue modelling was imaged using PIV to calculate the amount of shear strain. Note strain is accumulated only at the base of the imbricate block and in the footwall. (Fig. 3).

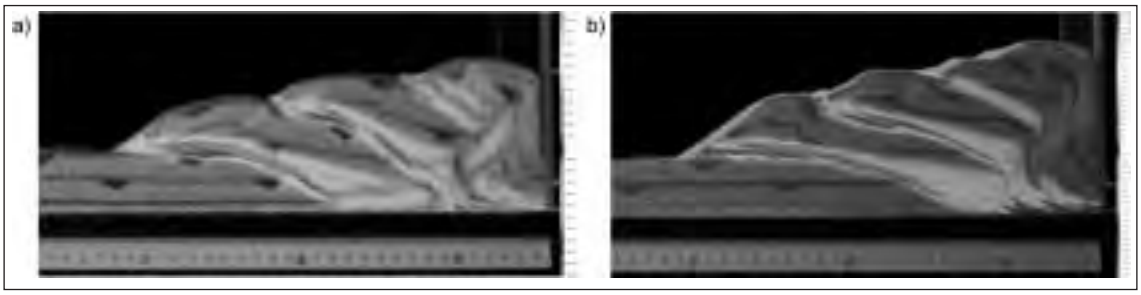

Figure 3: Total shear strain obtained by PIV image analysis of sandbox models, a) LF and b) HF, showing the amount of shear strain accumulated by the modelled imbricate block (furthest left). Lowest strain is transparent, white highest.

In contrast, geometrical algorithms such as fault-parallel flow assume strain is distributed throughout the imbricate block (Fig. 4). The amount of strain depends on the number of flat/ramp angles a node point has crossed.

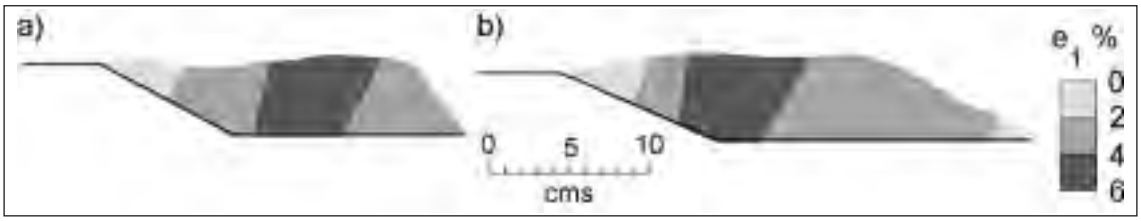

Figure 4: Results of retrodeforming (i.e. removing deformation in reverse) the final analogue sandbox model geometries with a) LF and b) HF, using fault-parallel flow. Note the inability of the geometrical modelling to return the final model to the starting geometry (cf. Fig. 2). Colours represent amount of strain (in percent maximum strain), which was accumulated within the imbricate block during geometrical modelling.

Discussion

In all cases, geometrical modelling was not able to lift the imbricate block as high as the sandbox model, and apparent thickening of the imbricate block is thus recognisable in the analogue experiment. As pointed out previously, the amount of displacement necessary is an underestimate due to the erosional nature of the leading edge in the sandbox experiment. However, this does not account for the largest part of the discrepancy. We propose that the following processes were active:

1. layer-parallel shortening before and during the bounding fault formed, by diffuse deformation,
2. material decompaction during shear localisation, and
3. simultaneously-active conjugate forethrust and backthrust in the initial phase of thrust formation.

Although there is some evidence of 3. in Fig. 1 (esp. the HF experiment), backthrusting was inactive after slip on the forethrust. Lohrmann et al. (2003) have shown that under shear sand increases in volume due to 2. by up to 5%. Therefore we suggest the former two hypotheses are jointly responsible for the area discrepancy.
Fault-parallel flow is better at following the analogue model because it does not require “bedding” slip to maintain area. However shear is required in fault-parallel flow to counteract the net concave fault bend, i.e. the majority of the imbricate block nodes cross only one ramp/flat bisector. However, since this cannot be varied in the transport direction, the leading edge of the geometrical model is always over-sheared. As such, it is partly responsible for the over-steepening of the leading-edge angle.
Geometrical algorithms distribute the changes in node position, which causes strain, throughout the modelled unit. The amount of strain is directly proportional to number of ramp/flat fault bends a node has passed over, and not the distance from the fault.

In contrast, analogue modelling shows that strain is not only accumulated passively in the hanging wall of the thrust fault and the fault imbricate as governed by transport along the fault geometry. In addition, as a consequence of the complex brittle strain-dependent deformation behaviour of sand that is similar to nature, more strain is accumulated by pre-failure diffuse deformation and progressive shear localisation in the hangingwall and footwall host material of active shear zones. PIV analysis shows that the shear strain is concentrated within the basal third of the imbricate block. However, similar to geometrical modelling predictions, strain is higher in the frontal part of the imbricate block, which passed over more fault bends.

An important implication of this comparison for geometrical/kinematic modelling of natural thrust faults is the consequent under-estimation of strain in the faulted rock volume, or often the complete neglection of pre-failure strain and progressive shear strain accumulation, as frequently observed in natural fault rocks. Whereas this processes result only in a minor modification of modelling results for regional-scaled strain analysis and restoration of thrust system, they are of major importance for strain accumulation on the scale of individual faults and their associated secondary structures. Here, geometrical strain modelling without the incorporation of the proper physical rock deformation mechanism results in the underestimation of strain in the faulted rock volume.

To model the strain history and the total strain of individual faults at outcrop scale, e.g. the "subseismic" strain of subsurface fault structures in 2D/3D seismic studies, and to use this strain data as proxy for the fracture modes, pattern and densities on structural and regional scale, appropriate physical fault simulations with realistic mechanical boundary conditions must be applied. This type of more detailed strain data are of crucial importance for applied environmental problems, hydrogeology and hydrocarbon exploration/production (characterisation of fractured reservoirs).

Acknowledgements

Jo Lohrmann is thanked for her critical review of the manuscript. Technical support in the GFZ lab came from Günter Tauscher.

REFERENCES

- Adam, J., Hoth, S., Kukowski, N. & Oncken, O., 2002. Bollettino di Geofisica teorica ed applicata, 42, 1/2, p. 123-126.
- Adam, J., Urai, J., Wienecke, B., Oncken, O., Pfeiffer, K. , Kukowski, N., Lohrmann, J., Hoth, S., v.d. Zee, W. & Schmatz, J., in review, J. Struc. Geol.
- Egan, S.S., Kane, S., Buddin, T.S., Williams, G.D., Hodgetts, D., 1999. Computers and Geosciences 25, 283–297.
- Huiqi, L., McClay, K. R., Powell, D., 1992. In: Thrust tectonics. Chapman & Hall, London, 71-81.
- Lohrmann, J., Kukowski, N., Adam, J., Oncken, O. 2003. J. Struc. Geol., 25, 10, 1691-1711.
- Suppe, 1983. American Journal of Science 283, 684-721.
- Tanner, D. C., Behrmann, J.H. & Dresmann, H. 2003. Journal of Structural Geology 25, 737-748.
- White, D. J., Take, W. A. & Bolton, M. D., 2001. 10th International Conference on Computer Methods and Advances in Geomechanics, Tucson, Arizona, 2001.

NUMERICAL AND ANALOGUE MODELLING OF METAMORPHIC CORE COMPLEX DEVELOPMENT 2-30

C. Tirel(*), J-P. Brun(*), E. Burov(**), D. Sokoutis(***)

(*) Géosciences Rennes, Université de Rennes 1, UMR CNRS 6148, Rennes, France
(**) Laboratoire de Tectonique, Université de Paris 6, UMR CNRS 7276, Paris, France
(***) Vrije Universiteit Amsterdam, De Boelelaan 1085, 1081 HV Amsterdam, The Netherlands

Introduction

Metamorphic core complex appeared to be symptomatic features of lithosphere-scale extension following crustal thickening. A number of famous examples has been described in the Basin and Range (Western US) and Aegean. A considerable debate, still continuing, concerns in particular the origin and significance of the so-called "detachment faults" associated in core complexes to the exhumation of metamorphic rocks from the middle to lower crust. On the other hand, the dynamics of

core complexes at crust and lithosphere scales also remain poorly understood. We here attempt, using numerical and analogue models to discuss the structure and development of core complexes within a thick and hot continental crust. Models simulate the asymmetric extension of a hot lithosphere with a 60 km thick crust. A heterogeneity mimicking a granitic intrusion in the ductile crust is used to initiate deformation. Results illustrate graben formation, dome shape evolution, channel flow in ductile crust and patterns of shear zones at the crustal scale.

Modelling

Numerical models

The large-strain thermo-mechanical code PAROVOZ (Poliakov et al., 1993) used for our model is a hybrid finite element/finite differences, fully explicit, time-marching Lagrangian algorithm, derived from FLAC® (Cundall, 1989). This widely used algorithm was described in details in several previous studies (Cundall, 1989; Poliakov et al., 1993). The code solves equilibrium problems for brittle-elasto-ductile media using general Newton law equations of motion in the continuum mechanics formulation coupled with the heat transport equation. The model setup is shown in Fig. 1. Lithosphere models have spatial dimension of 400 km x 100 km and numerical grid dimension of 200 x50 quadrilateral bilinear elements. The thickened crust has a pre-collapse thickness of 60 km which corresponds to a typical Alpine orogenic belt. The structure of the model is constituted of a continental crust and a lithospheric mantle which have an average quartz-diorite and olivine composition respectively. For a better visual tracing of the developing structures, the crust is divided into four marker layers (see Figure 1). A low density heterogeneity, mimicking an intrusion which has granite composition, is located at the center of the model. The rheology of the materials in the model is non-linear, brittle-elasto-ductile (see legend of Fig. 1). Ductile creep is described by a power law relationship between strain rate and stress (Kirby and Kronenberg, 1987). The brittle rheological term is approximated by Mohr-Coulomb plasticity with a friction angle of 30° and a cohesion of 20 MPa (Gerbault et al., 1999).

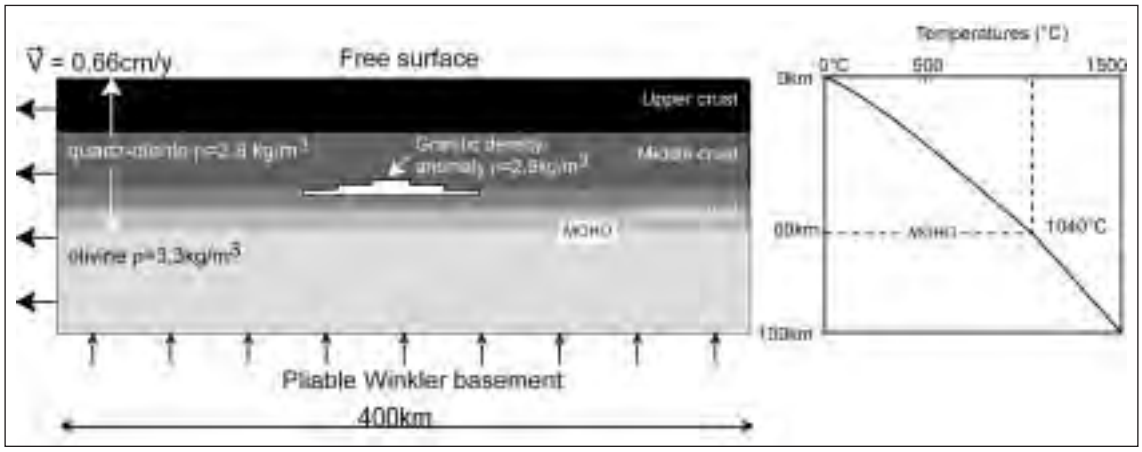

Fig. 1 - Model geometry, velocity boundary condition (0.66cm/y), and initial geotherm with Moho temperature T_M = 1040°C at 60km depth. Material constants used in model are the power law constant A, the power law constant n, the creep activation enthalpy H: Quartz-diorite $A_1 = 1.26 \times 10^{-3}$ MPa^{-n}.s^{-1}, $n_1 = 2.4$, $H_1 = 219$ kJ.mol^{-1} (Ranalli and Murphy, 1997); Granite $A_2 = 1.25 \times 10^{-9}$ MPa^{-n}.s^{-1}, $n_2 = 3.2$, $H_2 = 123$ kJ.mol^{-1} (Kirby and Kronenberg, 1987); Olivine $A_3 = 7 \times 10^4$ MPa^{-n}.s^{-1}, $n_3 = 3$, $H_3 = 520$ kJ.mol^{-1} (Brace and Kohlstedt, 1980). The thermal conductivities are $k_1 = 2.5$ W.m^{-1}.K^{-1} and $k_2 = 3.3$ W.m^{-1}.K^{-1} for the crust and mantle respectively.

Analogue models

Following Brun et al. (1994), the experimental apparatus used to model metamorphic core complex consists of a rectangular box with a movable wall (Fig. 2). The two-layer system simulates of a 20 km thick brittle upper crust lying above a 40 km thick ductile lower crust, composed of sand and silicone putty, respectively. Sand is a Mohr-Coulomb material with a 30° friction angle. Silicone putty is a Newtonian fluid of 1.4g.cm^{-3} density and 10^4 Pa.s viscosity at room temperature. A local zone of

weakness, represented by a silicone putty with 1 g.cm^{-3} density and 0.6x10^{3} Pa.s viscosity, is located just beneath sand-silicone contact. It may correspond in nature to a partially molten zone, like a granitic intrusion at the brittle-ductile transition. The basal boundary and the walls in contact with the silicone putty are lubricated to avoid perturbations due to boundary shear. At variance with the previous experiments of Brun et al. (1994), the movable wall velocity is here constant (30 cm/h), controlled by a stepping motor. The velocity is chosen significantly lower than the natural spreading rate of the model.

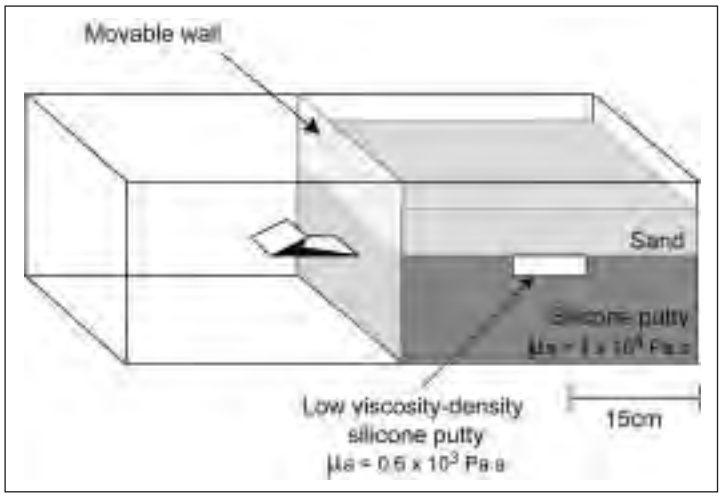

Fig. 2 - Apparatus and initial geometry of analogue models

Results

The deformation history of both numerical and analogue models can be divided into two successive stages, called here "upper crust necking" and "dome amplification". The upper crust necking stage is produced for each case beneath the weak zone in the ductile layer (Fig. 3a, 3c and 4a). The necking is accommodated by conjugate normal fault (Fig. 4a) and an upper central zone of deformation in numerical model (Fig 3c), that correspond to a graben in the brittle crust. On both graben sides, the upper crust remains mostly undeformed. In Fig 3c, contours of bulk shear strain intensities reveal a pattern of flat lying shear zones with conjugate senses of shear that results from channel flow in the lower crust. During dome amplification stage, the upper crust undergoes extreme thinning and rupture (Fig 3b and 4c). In numerical model, the dome shape becomes progressively asymmetrical whereas the velocity field remains almost the same since the first steps of extension. The middle crust shear zone, forming the right dome limb is the major zone of localized displacement that represents an

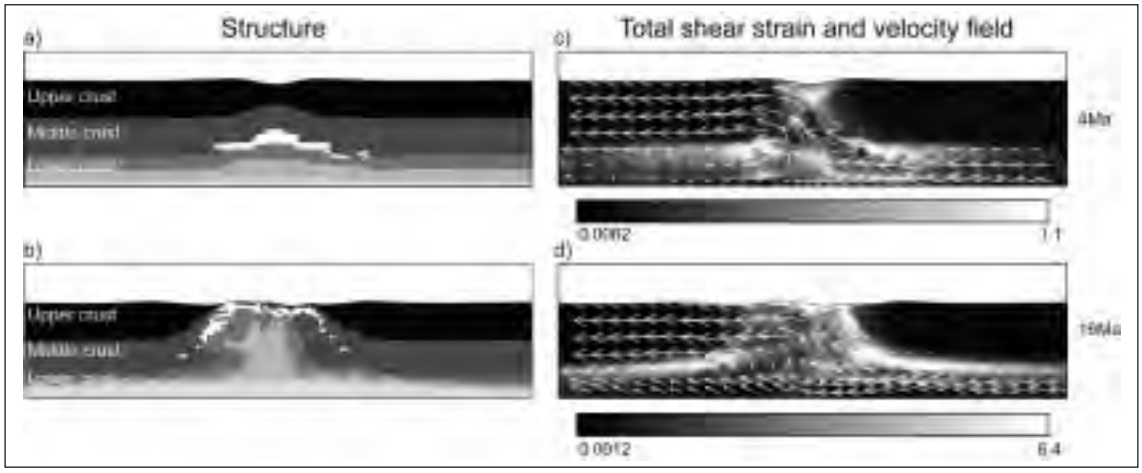

Fig. 3 - Structure and bulk shear strain with superposed instantaneous velocity fields of model. Stages of evolution, given in Ma, illustrate the stages of "upper crust necking" (4 Ma) and "mature dome" (16 Ma).

extensional detachment. This detachment zone displays a sigmoid shape made of three main parts: flat at the dome top, steeply dipping along the dome limb and flat again in the middle of the crust (Fig. 3d). The evolution during experiment shows the progressive connection between a zone of high strain intensity located at graben base and a basal middle crust shear zone that accommodates channel flow (Fig. 3c). In analogue model, the left border faults of graben rotate to a lower dip, becoming progressively a detachment fault, allowing dome rising (Fig. 4b and 4c). Here the detachment becomes flat on dome top and more steeply dipping along the right dome side, like in numerical experiments. However, the analogue experiments do not bring detailed information on the flow pattern within the ductile layer.

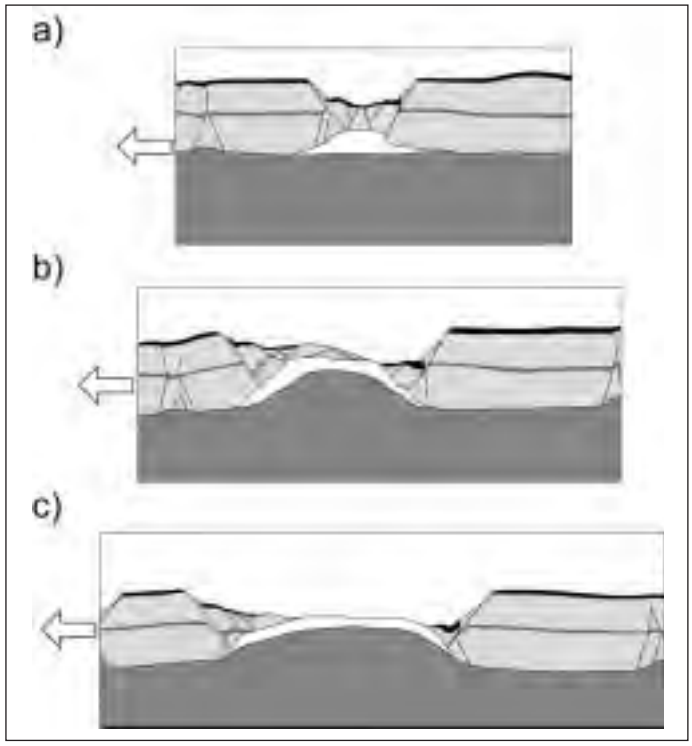

Fig. 4- Evolution of pattern deformation in model containing low-viscosity-density heterogeneity. a) 33% of extension. b) 66% of extension. c) 100% of extension. Images are focalized just on the middle of the total structure.

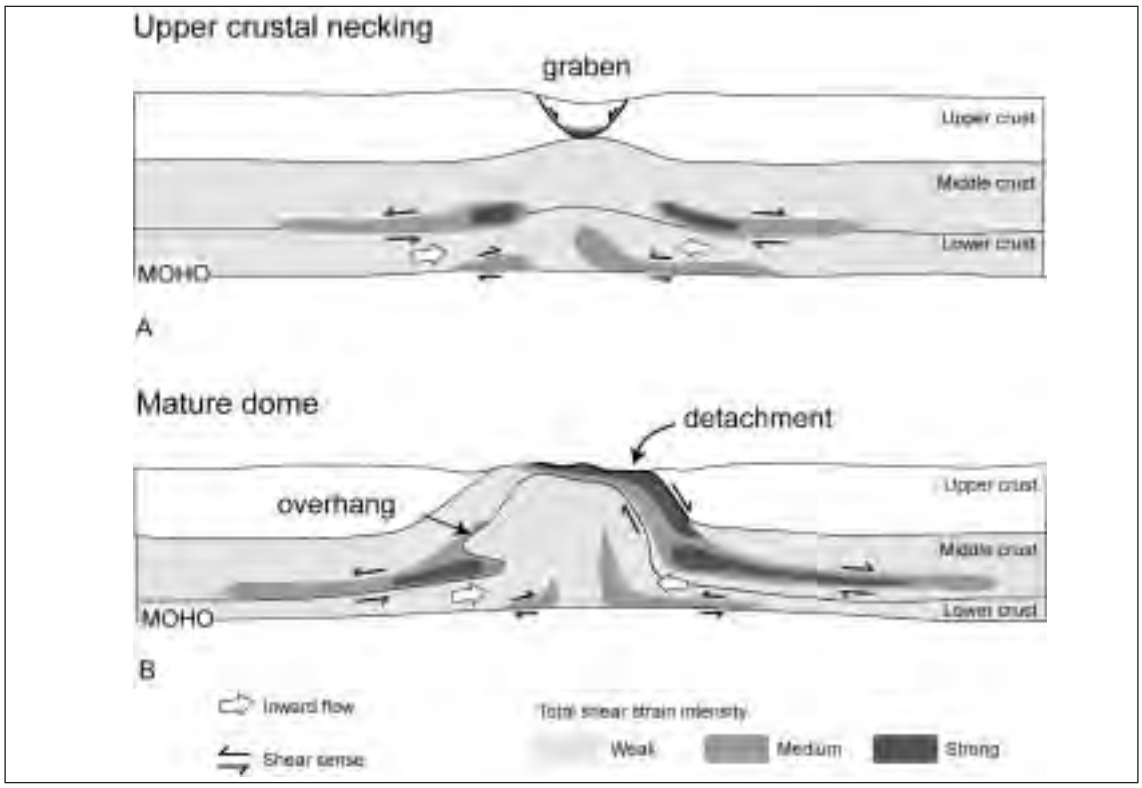

Fig. 5- Shear zone patterns associated with extensional gneiss dome evolution at the crustal scale.

Discussion

These results provide new insights on the development and structure of metamorphic core complex at crustal scale. In the two types of models, deformation is characterized by two successive stages. At upper crust necking stage (Fig. 5A), crustal scale deformation is close to pure shear with a symmetrical graben in the upper crust and a symmetrical pattern of shear zones, associated with lower crustal flow, with opposite senses of shear. At the mature dome stage (Fig. 5B), deformation is strongly asymmetrical with a detachment shear zone, on one dome limb, and an overhang at the dome base, on the opposite limb (see corresponding bulk shear strain distribution in the two stages respectively in Fig. 3). The sigmoid shape of the detachment results from the connection, during dome amplification, of the shear zone that accommodates graben opening, at the brittle-ductile interface, with the base middle crust shear zone. Our models show that extensional detachment zones at crustal scale result from an interaction between faulting, extreme thinning and rupture of the upper brittle crust, and lower crustal flow. Note that the detachment results form progressive deformation and, therefore, is not present at the onset of extension.
In the numerical models, the Moho remains rather flat even below the dome as a result of very efficient lower crustal flow. This is in agreement with the flat basal boundary condition imposed in the analogue experiments.

It is finally noteworthy to point out the complementarity of numerical and analogue modelling methods. Numerical experiments provide a full description of the dynamic evolution and step by step images of strain pattern evolution within the ductile crust. Conversely, the analogue experiments give far more realistic simulations of faulting within the upper brittle crust.

REFERENCES

- Brace W.F. and Kohlstedt D.L. (1980), Journal of Geophysical Research, 85, B11, 6248-5252
- Brun, J-P. et al. (1994), Geology, 22, n°4, 319-322
- Cundall, P.A. (1989), Ing. Arch., 59, 148-159
- Gerbault M. et al. (1999), Geophysical Research Letters, 26, 2, 271-274
- Kirby S.H. and Kronenberg A.K. (1987), Reviews of Geophysics, 25, n°6, 1219-1244
- Poliakov A.et al. (1993), in Flow and creep in the solar system: observations, modelling and theory, dynamic modelling and flow in the Earth and planets, 175-195
- Ranalli, G. and Murphy D.C. (1987), Tectonophysics, 132, n°4, 281-295

OBLIQUE RAMPS AFFECTING THE NORTHERN APENNINE FRONT: INSIGHTS FROM SEISMIC DATA AND ANALOGUE MODELS 2-31

G. Toscani, A. Ravaglia, S. Seno

Dipartimento di Scienze della Terra - Università di Pavia – via Ferrata, 1 – 27100 PAVIA Italy

Summary

The aim of this work is to reconstruct and elucidate the latest tectonic deformations of the Northern Apennine looking at the boundary of the chain with its foreland, the Po Plain. The study area is located inside the Emilian arc of folds, a group of thrust sheets with a strong salient geometry forming the buried outer fronts of the Northern Apennine. More than 400 km of seismic data (courtesy of ENI-AGIP) located across the foothill and the Po Plain were interpreted and depth-converted. This job allowed us to study in detail the geometry of the basal thrust fault that carried the External Ligurid tectonic units on the Late Miocene stratigraphic horizons belonging to the foreland. In some places, transverse lineaments interrupt the continuity of the structural arc; lack of seismic data in correspondence of one of these lineaments (in the Tidone valley) led us to model this tectonic setting in order to better understand arrangements and kinematics of this part of the chain.

Geological setting

The study area is located in the Northern part of the Apennines, close to the Po Plain. Northern Apennine is a continuous thrust-fold belt ranging from Tuscany to the Po Plain,its present foreland (Kligfield, 1979). The belt is formed by a stack of tectonic units belonging to different palaeogeographic domains. The buried front of the chain can be divided into three different salients: arc of the Monferrato folds (in the western part of the Po Plain, mostly deformed from Messinian to Pleistocene time), arc of the Emilian folds (in the central part of the Po Plain, mainly active from Messinian to Late Pleistocene time) and arc of the Ferrara folds (in the eastern part of the Po Plain, active from Late Pliocene to Pleistocene time) (Perotti, 1991). Inside these salients, most of the thrusts show an Apennine vergency (NE-ward) but there are sectors where different structural directions are present; all the salients are strongly asymmetric having southeastern parts more developed than the northwestern ones. Going from west to east (i.e. from the arc of the Monferrato folds toward the Ferrara one) a progressive raise of shortening happens: this is consistent with the hypothesis of a counter clockwise rotation of the entire orogen during its emplacement (Castellarin, 1985). The most external outcropping tectonic units are the "External Ligurids" and their basal thrust sheet is the object of this paper. Their footwall is the Po Plain foredeep sediments; the youngest tectonic event that involved the Apennines happened mainly on the basal thrust of these units and on these sediments.

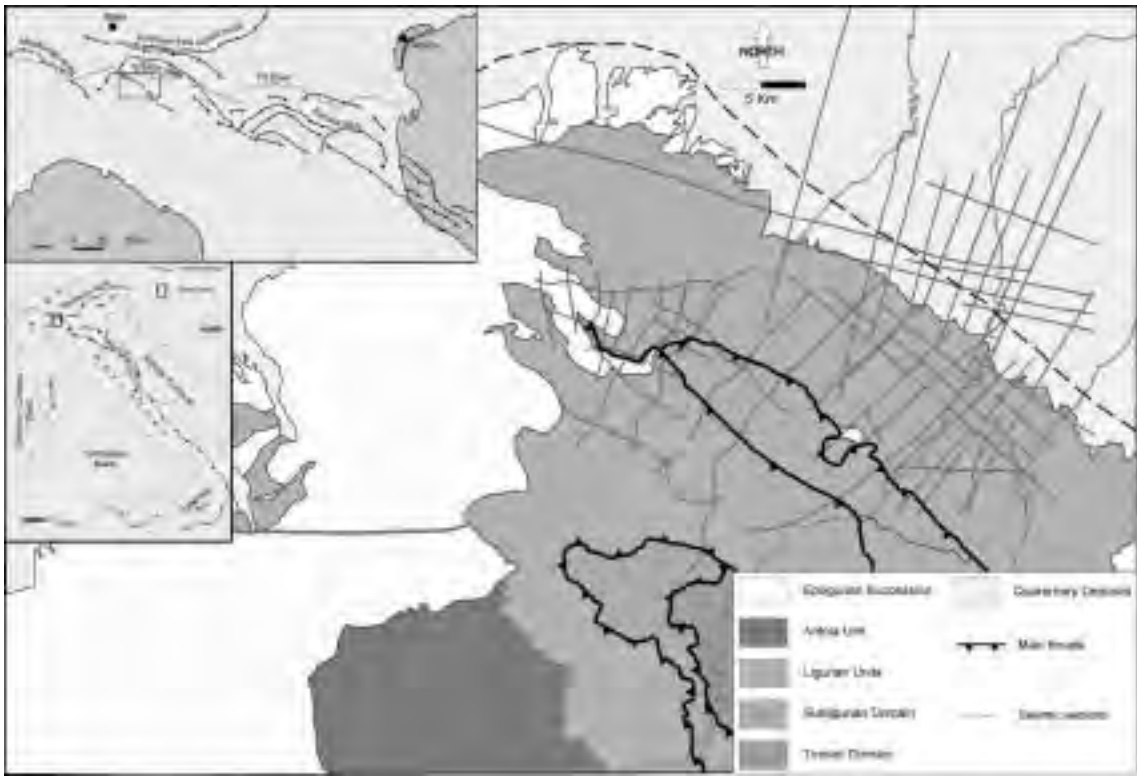

Fig.1 - Geological setting of the study area. In the picture seismic data considered are plotted.

Data

We analyzed 400 km of seismic data and four oil well stratigraphies. Seismic lines cross the outermost Apennine tectonic unit and the Po Plain sediments; Ligurids basal thrust and foreland stratigraphic horizons are clearly detectable on the external lines and also on the most internal ones. Strike seismic lines (fig.1) were used used to reconstruct the three dimensional model, whereas dip seismic lines were only considered to constrain data. A limited number of the lines have not been considered in the model in order to check if the reconstruction was consistent with these data. Thanks to the good

quality of the lines and to their short spacing it have been possible to analyze in detail the relationships between the chain and its foreland.

Digital model

We automatically traced contour lines of the External Ligurids basal thrust and footwall cut-off lines of the foredeep sediments treating all the previous data with a structural analysis software (3DMove) (fig.2). The External Ligurids basal thrust fault shows an increasing elevation going from the outermost outcropping thrust in the Ligurian complex toward the Po Plain boundary where it reaches altitudes close to the sea level. The thrust front is buried under Pliocene to Quaternary sediments in the foothill zone. In a very general way, the fault shows the typical low angle geometry with an increment in elevation going toward the foreland. The structure contour map highlights an important difference in elevation within different sectors of the External Ligurids basal thrust. In particular, in the inner part of the map this difference is evidenced by the strip of land where contour lines are not correlated. Lack of seismic data in this area did not enable us to detect why the opposite sectors are differently elevated. The presence of a transfer fault or a oblique/lateral ramp must be hypothesized to justify these differences. A sand-box model where we reconstructed fault geometry provided some insights for a plausible explanation.

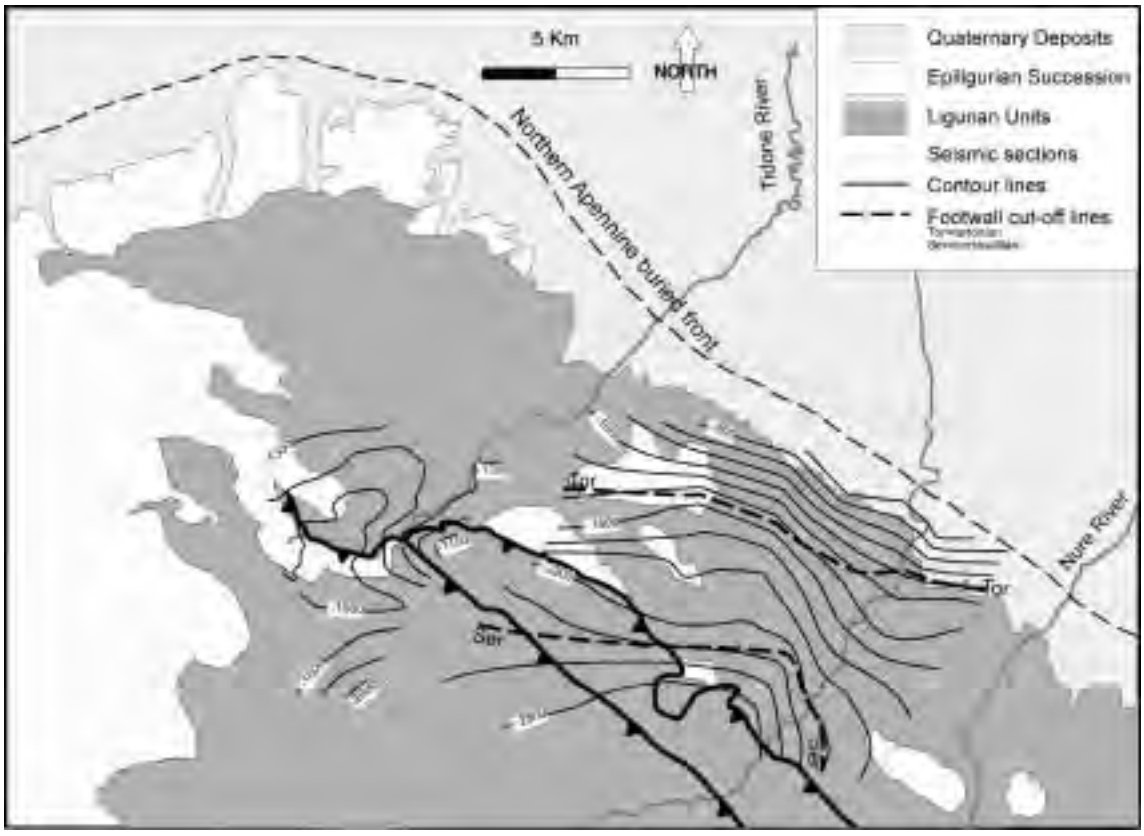

Fig.2 - Contour and footwall cut-off lines of the Ligurids basal thrust.

Analogue model

The modelling initial constraints were built to simulate non-cylindrical deformation (Fig. 3a). The final map view reveals a complex braided architecture of faults that characterized the portion of the model within the two rigid ramps (Fig. 3b). There, lateral terminations and anastomoses of faults occur. As an example, two frontal segments connected by an oblique sector form thrust front A. Such

surface geometry reflects fault surface at depth. The reconstruction of the surface from several cross sections displays an oblique ramp connecting two frontal ramps. The comparison of the modelled geometry with the hardly interpretable natural example gives some hints for a plausible completion of the Ligurids basal thrust fault.

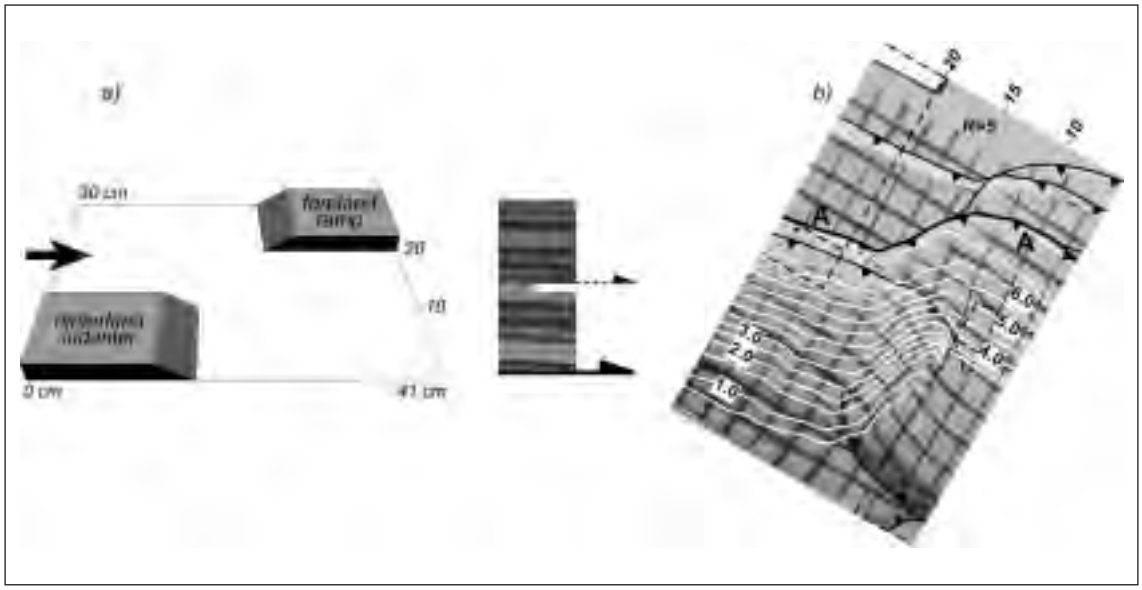

Fig. 3 – (a) Initial set up of the experiment and the sand/microbeads stratigraphy used in the modelling. Initial thickness is 5 cm. Sand has an angle of internal friction ϕ_i= 33°; glass microbeads ϕ_m= 24°; the friction at the base of the model is ϕ_b= 30°. The hinterland indenter and the rigid ramp are 2.5 cm high and 10 cm wide. Backstop moves from the left to the right. (b) Contouring of fault A on the final map view of the model; labels are in cm from the base of the model. Final shortening, Sh = 12 cm (28 %). Foreland regional elevation, R = 5 cm. The black squared grid on the surface of the models was 2 cm. The black dashed lines are the outlines of the rigid ramps.

Conclusions

Combining observation from the reconstruction of the natural case and from the sand-box experiment, it's possible to observe how differences in altitude between different sectors of the same thrust sheet have been recreated. Data available from the model are continuous and directly observable from "real" sections and this allowed us to reconstruct in three dimensions a primary lateral ramp whose geometry and setting is consistent with the data set coming from the basal thrust of the Northern Apennine.

REFERENCES

- Castellarin et al., 1985. Giornale di Geologia, 47/1, 47-75.
- Kligfield R., 1979. American Journal of Science, 279, 676-691.
- Perotti C.R and Vercesi P.L., 1989. Memorie Descrittive carta Geologica D'Italia, XLVI, 313-326.

INFLUENCE OF THE INITIAL GEOMETRY OF LATERAL STRENGTH VARIATIONS DURING CONTINENTAL CONVERGENCE: AN ANALOGUE MODELLING STUDY

2-32

E. Willingshofer(*), D. Sokoutis(*), J-P. Burg(**)

(*) Faculty of Earth and Life Sciences, Vrije Universiteit Amsterdam, De Boelelaan 1085, 1081 HV Amsterdam,The Netherlands

(**) Geologisches Institut, ETH-Zürich, Sonneggstrasse 5, 8092 Zürich, Switzerland

Summary

The influence of a pre-existing weak zone and its initial geometry on the structural/tectonic evolution of a continental collision zone is investigated through lithospheric-scale analogue modelling. Strength heterogeneities were incorporated by varying the strength of the layers analogue to the crust and the upper mantle and by implementing a weak plate or part-of-a-plate between two strong lithospheres. Plate boundaries are orthogonal to the convergence direction. Three (brittle crust/viscous crust/strong viscous upper mantle) layer models were bordered by a weak silicone layer on one convergence-parallel side in order to contain but not oppose to lateral extrusion. Three cases are discussed where the weak zone is separated from the strong plates by 1) vertical boundaries 2) one and 3) both boundaries dipping towards the weak zone. Experimental results show that thrust fault propagation away from the weak zone only occurred in the case of initially vertical boundaries. In the experiments with inclined boundaries thrusting remained localisedlocalized along the boundaries and resulted in underthrusting of the strong plates beneath the weak one. Uni-polar underthrusting was obtained for initially asymmetric geometries of the weak zone (one side inclined). In this case the strong platestrong withplate with inclined boundary underthrusted the weak zone and the strong plate with vertical boundary remained nearly undeformed. In contrast, a symmetric initial setup (both sides inclined) resulted in a bi-vergent thrsusting system involving both strong plates that also experienced lithospheric-scale buckling.

The modelling results have implications for interpretation of deep seismic and tomographic data, which in the case of the European Alps suggest lateral changes in polarity.

Introduction

The mechanical properties of the continental lithosphere are subject to variations in space and time, primarily due to changes in composition and thermal conditions. The most important compositional change within the continental lithosphere occurs at the crust-mantle boundary.,boundary. The rheology of the continental lithosphere may change laterally because of tectonics; for example, the separation or collision of continents are associated with fault activity and are connected with pronounced thermal perturbations that result in changes of composition and lithospheric thickness. As a consequence the continental lithosphere exhibits lateral strength variations, which control the localization of shear and the structural, geometrical, and topographic evolution upon subsequent deformation of the lithosphere.

In this study we use physical modelling to address the fundamental question of: “How strongly the initial geometry of a pre-existing weak zone influences the structural evolution of a compressed continental lithosphere?” Emphasis is put on the upper-mantle-lower-crust structures and their relationship to higher-level deformations.

Modelling Setup

The experimental continental lithosphere consisted of three layers representing the brittle crust, ductile crust, and ductile mantle in nature (Fig. 1). Lateral changes of lithospheric strength were incorporated by laterally varying the thickness of the brittle and ductile crustal layers and the rheology of the brittle or ductile upper mantle. In this study we discuss cases having a weak zone separated from stronger zones by 1) vertical, 2) one side inclined, and 3) both sides inclined boundaries (Fig. 1). Dry quartz sand, a Mohr-Colomb-type material, and mixtures of Rhodorsile Gomme-type (silicone mix I) or PDMS-type silicone (silicone mix II) with barite powder, exhibiting slightly non-Newtonian properties, were used as rock analogues for the brittle crust, the viscous crust and the viscous upper

mantle, respectively. The experiments have been conducted within a 50 x 40 x 15 cm plexiglass tank. Glass walls attached to the long sides of the box reduced friction. Solid walls confined three sides of the model while the 4th, a layer of silicone putty labelled "Lateral Confinement" (Fig. 1), allowed limited amounts of lateral escape. During modelling, the surfaces of all experiments have been scanned with a 3-D video-laser every 30mn. The data have been converted to digital elevation models (DEM), which are crucial for the understanding of the relationships between evolving structures and topography.

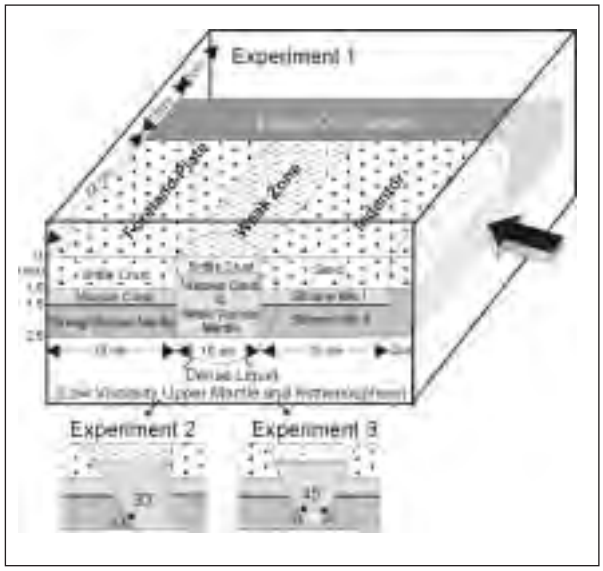

Fig. 1 - Initial setup for lithospheric-scale analogue experiments.

All experiments have been performed under normal gravity conditions. Geometrically the experiments were scaled by applying a length ratio of 5 x 10^{-7}, equating 1 cm in the models to 20 km in nature. The Ramberg number (Weijermars & Schmeling, 1986; Sokoutis et al., 2000) has been adopted as a measure for dynamic similarity between model and natural examples. Shortening, imposed by the advancing wall, was at a constant rate of 0.7 cm/h.

Modelling Results

For descriptive convenience, we call the strong plate at the side of the moving wall "indentor" and refer to the strong part of the lithosphere on the opposite side of the weak zone as "foreland plate".

Experiment 1

Deformation commenced at the boundaries between the strong and weak plates by thrusting after 1.5% bulk shortening. As convergence continued thrusting propagated outwards with respect to the central weak plate (Fig. 2a). A sequence of backthrusts developed within the brittle crust of the indentor. After 10% bulk-shortening thrusting flipped to the foreland side of the weak plate. The weak plate folded while thrusting propagated away into the indentor and foreland plates. Consequently, the uplifted weak plate had an antiformal surface flanked on both sides by depressions. After 20% bulk shortening outward thrust propagation stopped and convergence was taken up by out of sequence thrusting reactivating earlier thrusts. Coeval folding continued and led to surface uplift on the weak plate and subsidence in the backthrust region. Until the end of the experiment shortening was mainly taken up by out-of-sequence thrusting (Fig. 2a). Dextral strike slip faulting on the lateral confinement side was related to the low resistant lateral material.

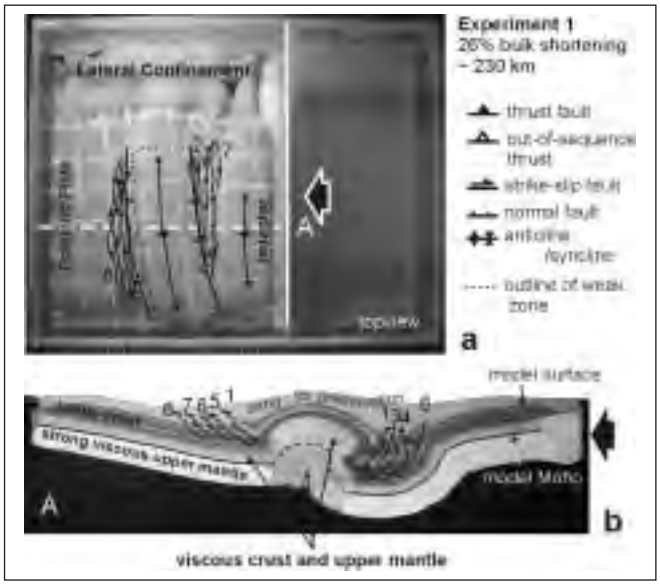

Fig. 2 - Experiment 1 after 26% bulk shortening. (a) Photograph of model surface, (b) cross-section. Numbers indicate the sequence of deformation.

Sections of experiment 1 document the complex interplay of thrusting and folding (e.g. Fig. 2b). The implemented weak zone turned into an anticline with a thick core of ductile crust and upper mantle. The anticline is asymmetric, exhibiting an overturned limb facing the indentor. Thrusting led to considerable thickening of the brittle crust, especially in the backthrust area where initial thickness has doubled (Fig. 2b). These backthrusts rotated towards steeper dips to accommodate folding of the indentor. In contrast, the brittle layer of the weak plate was not faulted. Shortening was taken up within the lower crusts of the foreland and indentor plates by homogeneous thickening, which is largest (~25%) close to the back wall and the moving wall and least (~13%) at the boundary with the weak plate.

Experiment 2

In experiment 2, deformation started at the boundary between the weak zone and the foreland plate, which was progressively tilted towards the weak zone (Fig. 1) before underthrusting beneath it. Within the weak zone shortening was accommodated by folding in the hangingwall of the main thrust fault (thrust No. 1 in Fig. 3) and by foreland-directed thrusting (No. 2). After 10% bulk shortening back-thrusting (No. 6) commenced at the weak zone-indentor interface and a major dextral strike-slip fault (No. 7) developed close to the weak lateral confinement in response to continued motion on the main thrust. At 20% bulk shortening the model orogen already advanced 4 cm over the foreland plate and the weak zone was shortened by ca. 30%. Contraction within the weak zone caused overturning of the fold in the hangingwall of the main thrust and further movement along thrust No 2. At the end of the experiment (24% bulk shortening) a mature foreland-type basin had developed on the underthrusting plate (Figs. 3a & b). The topography of the weak zone was mainly controlled by thrusting along thrust plane number 2. Additional to underthrusting of the foreland plate and folding and thrusting within the weak zone, part of the shortening was accommodated by heterogeneous lateral material transfer, which increases towards the lateral confinement.

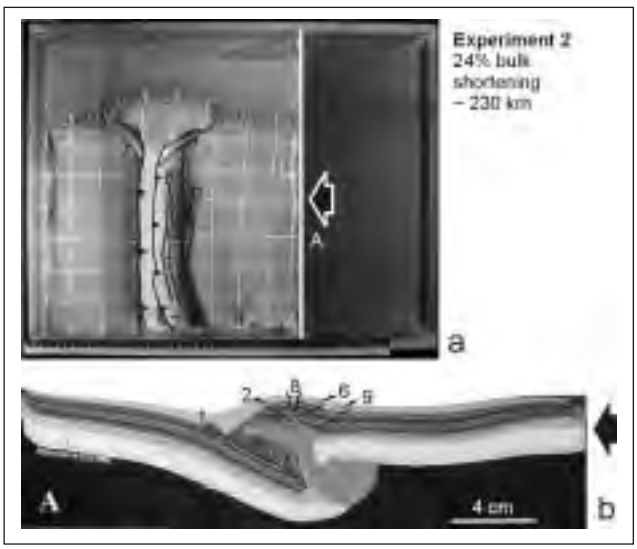

Fig. 3 - Experiment 2 after 24% bulk shortening. (a) Photograph of model surface, (b) cross-section. Legend as Fig. 2.

Sections reveal the asymmetric lithospheric structure, which is dominated by underthrusting of the foreland plate (Fig. 3b). As shortening is mainly taken up by motion along thrust N1 and to a lesser extent within the brittle layer of the weak zone, the indentor plate remained nearly unfaulted. The foreland-facing side of the weak zone forms a recumbent fold cored by the ductile crust. The foreland and indentor plates are separated by a broad ductile shear zone of ductile crust and upper mantle material. The Moho topography of the foreland plate documents bending whereas that of the indentor plate remained flat.

Experiment 3

In experiment 3 both boundaries of the weak zone were initially inclined inward (Fig. 1). Deformation started within the weak zone close to the indentor by fore- and back-thrusting (No. 1 in Fig. 4). The area between these faults definearea between these faults defines a pop-up structure and was subsequently uplifted. Simultaneously, thrusting at the foreland plate-weak zone boundary (No. 3) initiated together with backthrust No. 4 within the weak zone, defining another pop-up structure. Thereafter, shortening was mainly taken up by motion along the main thrusts (No 1 & 3) bordering the weak zone. The weak zone itself was squeezed between the strong plates and, therefore,

experienced surface uplift. From 15 % bulk shortening onward, contraction also resulted in large-scale folding of the indentor and foreland plates. Until the end of the experiment (26 % bulk shortening) further shortening did not change the overall geometry of the model but mainly affected the fold amplitudes, which distinctly increased.
Cross-sections (e.g. Fig. 4b) impressively document the dominance of lithospheric-scale folding of the foreland and indentor plates. The weak zone turned into a vertically barrel-shaped structure bordered on both sides of the upper brittle layer by thrust faults defining a large-scale pop-up. In contrast, no faulting affected the brittle crusts of both strong plates. Instead deformation remained localized on the early-formed thrust planes for a long period of time. Furthermore, both, the foreland and the indentor plates exhibit a similar lithospheric-scale structure describing a steeply dipping, bi-polar system.

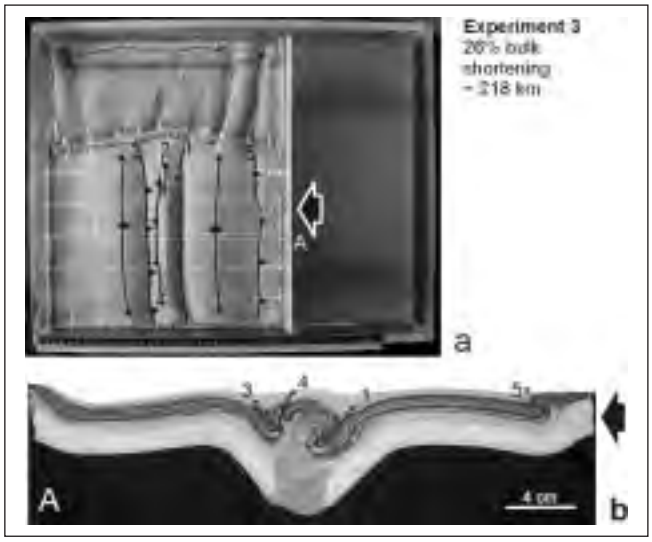

Fig. 4 - Experiment 3 after 26% bulk shortening. (a) Photograph of model surface, (b) cross-section. Legend as Fig. 2.

Discussion of modelling Results

Experimental results show that the initial orientation of the boundaries between weak and strong lithospheres exerts a strong control on the structural evolution of continental collision zones. In particular, initially symmetric boundariessymmetric boundaries, either vertical (experiment 1) or inclined (experiment 3), yield close to symmetric modelling results, whereas asymmetric setups result in a strongly asymmetric structure. Slight asymmetry from symmetric setup appears to be mainly controlled by the direction of push (proximity to moving wall). In both, symmetric and asymmetric systems, inclined, inclined boundaries produced underthrusting of the strong plates beneath the weak one (Fig. 3b and 4b). This large-scale geometry has implications for natural systems, as they would be imaged through deep reflection seismic profiling or P-wave tomography. Experiment 2 with a down-flexed foreland plate underthrusting the deformationthe deformation (orogen) zone andzone and the indentor is in its basic lines comparable to the deep structure of the Alps along the EGT traverse (e.g. Schmid et al., 1996). In experiment 3 however, no clear hangingwall-footwall relations can be established between the foreland and the indentor plates. Folding is a dominant deformation mechanism, which determines the finite structure of the lithosphere. Conversely, such a scenario would be imaged as doubly vergent orogen with a steep mantle root. A comparable situation is depicted for the upper mantle structure across the eastern Alps close to the western margin of the Tauern Window, where the upper mantle resembles a vertical slab geometry (Lippitsch, 2002).
The initial orientationinitial orientation of boundaries controls both the experimental lithospheric-scale geometry andgeometry and strain localisation. Experiments with inclined boundaries document deformation histories where the main movements takemovements take place on the thrust planes initiated at the inclined boundaries. As a consequence, the strong plates show little evidence of deformation (Fig. 3b). The opposite holds for the experiment with the initially vertical boundaries (experiment 1, Fig. 2). In this case deformation through thrusting involved large parts of the foreland and indentor plates. We conclude that the initial orientation geometry of weakness boundaries zones within continental lithosphere is an important factor controllingfactor controlling the deformation history and the large-scale structure of collisional orogoens.

Acknowledgements

E. Willingshofer is grateful to Ffunding of this work by NWO-ALW, the Dutch Organisation for Scientific Research, grant 810.31.003 (E. Willingshofer) and ISES (D. Sokoutis) is gratefully acknowledged.

REFERENCES

- Lippitsch, R., Lithosphere and upper mantle P-wave velocity structure beneath the alps by high-resolution teleseismic tomography, PhD-thessis, 155 pp., ETH-Zürich, Zürich, 2002.
- Schmid, S.M., O.A. Pfiffner, N. Froitzheim, G. Schönborn, and E. Kissling, Geophysical-geological transect and tectonic evolution of the Swiss-Italian Alps, Tectonics, 15, 1036-1064, 1996.
- Sokoutis, D., M. Bonini, S. Medvedev, M. Boccaletti, C.J. Talbot, and H. Koyi, Indentation of a continent with a built-in thickness change: experiment and nature, Tectonophysics, 320, 243-270, 2000.
- Weijermars, R., and H. Schmeling, Scaling of Newtonian and non-Newtonian fluid dynamics without inertia for quantitative modelling of rock flow due to gravity (including the concept of rheological similarity), Phys. Earth.Planet. Inter., 43, 316-330, 1986.

ANALOGUE AND DIGITAL MODELLING OF ACCRETIONARY PRISMS WITH GRANULAR MATERIALS 3-33

Yasuhiro Yamada[1], Satoshi Ueda[1], Kokoro Kaneda[1], Kei Baba[2], Toshi Matsuoka[1]

1) Department of Civil and Earth Resources Engineering, Kyoto University, Kyoto 606-8501 Japan
2) JAPEX Research Center, Chiba 261-0025 Japan

Summary

The accretion process of sediments at subducting margins can be modelled and examined by using analogue experiments and numerical simulations. Previous research suggests that granular materials can appropriately model the upper crustal deformation, which characterized by brittle (frictional) behaviour. This presentation includes some of our results of physical experiments employed dry sand and micro glass beads and numerical simulations based on the discrete element method (DEM). Using micro glass beads to act as a decollement in a pile of dry sand in the experiments, we succeeded accurately to reproduce the structure observed at the toe of the accretionary wedge off Muroto. The simulation results showed a drastic change in the strain and stress field within the particle assembly as the deformation propagates. This is strongly related to the stick-slip motion of the fault surfaces, which might be a common feature of the brittle deformation.

Introduction

The Nankai Trough is one of the most typical accretionary wedges in the world and a number of geoscientists have been working for earthquake mechanism, deformation-fluid flow interactions and methane hydrate exploration. The trough lies off the Southwest Japan, where the Philippine Sea Plate is subducting underneath the Eurasian Plate (Seno *et al.*, 1984) (Fig. 1). The sediments accreting to the prism are mostly supplied from the island arc, and this is why a large quantity of methane hydrates is expected at the wedge. In order to examine how, where and how much methane hydrates accumulate, it is essential to evaluate the distribution and development of inter-granular porosity as migration pathways of formation fluids including methane. The accretionary prism is known for its highly deformed geometry and this should affect the

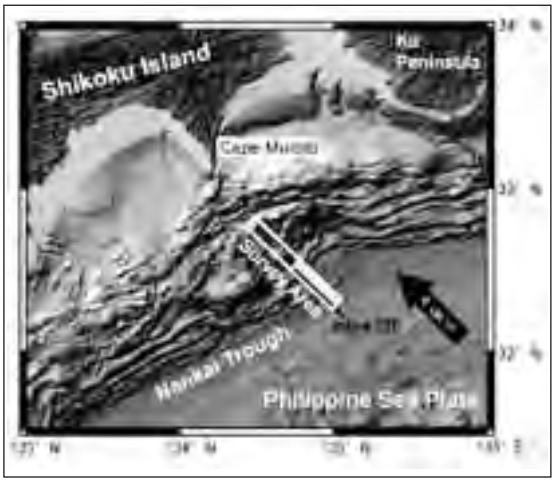

Fig 1. Bathymetric map of the Nankai Trough area including the Shikoku Island and Southwest Japan (Tsuji et al., 2004). The box is the area of a 3D

fluid migration. Thus we focused to model the faults during the acrretionary process. The purpose of this study is to reproduce the fault growth accurately with analogue experiments and numerical simulations, and apply the results to construct a fluid flow model in the accretioanry prism for methane hydrate exploration.

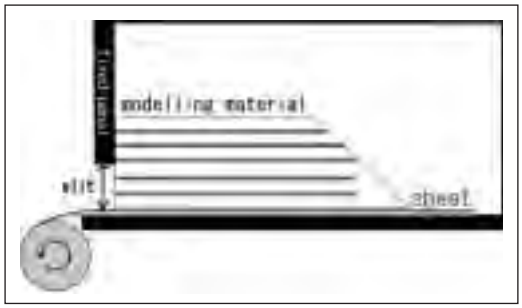

Fig 2. Schematic side-view of the physical modelling sand box.

Analogue Experiments

The experimental rig in this study is an acrylic box (25 cm x 150 cm x 50 cm) with a flat sheet (Fig.2). Layers of modeling material are piled on the sheet,which is pulled by a motor at a constant speed of 1 cm / minute through a slit under the fixed end wall. This slit is to produce the detachment horizon within the modelling material, similar to a characteristic of the Nankai prism, where the decollement is seen at the middle of a thick mudstone. The modeling materials are dry sand and micro glass beads, which are suitable to simulate the brittle deformation of the upper crust (Yamada *et al.*, 2002, Lohrmann *et al*., 2003). Our shearing tests showed that the cohesion and the angle of internal friction of the glass beads are much smaller than those of the dry sand. This suggests that the micro beads may be a better material for a detachment layer within sediments (e.g. Massoli *et al.*, 2002). In reality, the decollement is a layer of high pore pressure which significantly reduces the friction along the detachment. In the model, micro beads reduces the friction due to the lower friction coefficient.
A series of experiment were performed to examine possible combinations of the modelling materials to reproduce a better geometry of the Nankai wedge.

Results of Experiments

The experiments are aimed at reproducing the geometry of the accretionary wedge. Fig.2a is a seismic profile illustrating the characteristic structural style at the toe of the Nankai accretionary prism off Muroto. The profile has no vertical exaggeration (i.e. the vertical scale equals to the horizontal scale), thus can be directly compared with experimental results.
In Experiment-I, a homogeneous dry sand model, reproduced structures similar to the real wedge; such as the piggyback sequence of thrusting, the landward tilting thrust geometry and formation of the wedge geometry (Fig. 2b). We also succeeded to make the horizontal detachment within the sand pack. The angle of the prism surface (line linking the tips of the thrusts) is, however, much steeper than that of the real. In addition, the distance between the thrusts is significantly closer than that seen offshore Muroto.

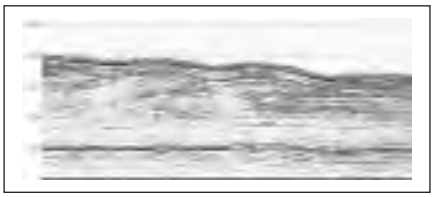

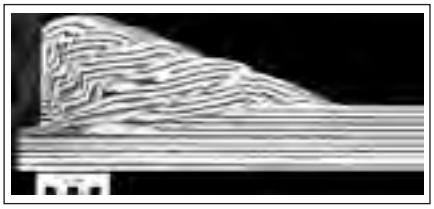

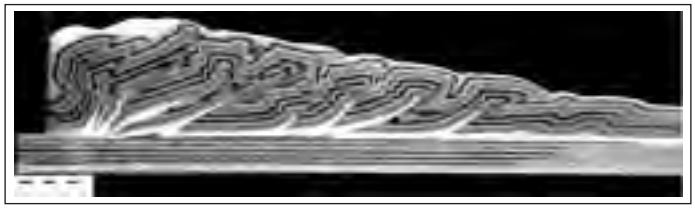

Fig. 2 - A seismic profile and experimental results.
a) A part of a seismic profile at the toe of the Nankai accretionary wedge off-shore Muroto (Bangs et al. 2004). Note that the detachment horizon is at the middle of the mud stone (low reflective sediments) and not at the upper-most horizon of the basaltic basement (the strong reflector).
b) Experiment-I with pure dry sand (from Yamada et al., 2004a). A typical sand-wedge experiment with a piggy-back sequence of thrusts.
c) Experiment-II with dry sand and a layer of micro glass beads. The beads layer behaved as the detachment horizon, from which the thrust sequence developed. Note that the geometry of the wedge is strongly controlled by the physical property of the detachment.

Then we put a micro beads layer within the sand to change the physical property of the detachment. The results (Experiment-II) showed that the micro beads layer perfectly formed the horizontal detachment. The sand layers below the detachment did not deform but those above the beads layer did as expected (Fig. 2c). In the sand layers above the detachment, a series of thrusts were formed and converged on the beads layer. The characteristics of the structures formed in the Experiment-II coincided with that of a real prism toe. In addition, the angle of the prism surface (line linking the tips of the thrusts) was gentler and the distances between the fault planes were larger than that in the Experiment-I. These suggest that the Experiment-II reproduced a geometry closely similar to that observed at the toe of the Nankai accretionary wedge.

Numerical Simulations

We employed the discrete element method (DEM) as the simulation technique (also see Yamada *et al.*, 2004b). The DEM assumes that the subjects of investigation consist of particles. There are two steps in each calculation cycle: the first step is to evaluate interaction forces for every particle, and the second step is to move these particles according to numerical integration following to the Newton's equation of motion for the given external forces. The interaction forces can be evaluated from the force-displacement law (Cundall and Strack, 1979). The software employed in this paper is based on that by Matsuoka *et al*. (2001), which includes a brief description of the algorithm, and further developed since then.

In order to make the initial conditions of the simulations similar to those of the experiments, we determined the input parameters equivalent to the experimental set-ups. For instance, randomised grain size distribution, quasi-static deformation, no initial cohesion between the particles, and low friction coefficient and shear stiffness at the detachment.

The simulation results showed the quite unstable nature with frequent changes in the strain and stress field within the particle assembly as the deformation propagates from the moving end-wall. Such a feature can also be found in other simulations for a brittle deformation (i.e. Yamada *et al,* 2004b). This might be, therefore, strongly related to the stick-slip motion of the fault surfaces, which will be a common feature of the brittle deformation.

Conclusions

We succeeded to reproduce a better geometry of the structure observed at the toe of the accretionary wedge offshore Muroto, by using glass beads to act as the decollement in the sandbox experiments. The simulation results also provide internal information of the particle assembly, which is extremely difficult from analogue expereiments. The information obtained by these experiments constrain where, how and how much methane hydrates migrate and accumulate during the deformation process of accretionary prisms. Further research is aimed at analyzing the results quantitatively and constructing a model for fluid flow along thrusts.

REFERENCES

- Bangs, N. L. et al. (2004): Evolution of the Decollement from the Trench into the Seismogenic Zone Inferred from Mapping Nankai Trough Decollement Seismic Reflections in 3-D, Muroto Transect. Geology, in press.
- Cundall, P.A. and Strack, O.D.L. (1979): A discrete numerical model for granular assemblies. Geotechnique, 29, 47-65.
- Lohrmann, J., Kukowski, N., Adam, J., Oncken, O., 2003. The impact of analogue material properties on the geometry, kinematics, and dynamics of convergent sand wedges. Journal of Structural Geology 25 , pp. 1691-1711.
- Matsuoka, T., Yamada, Y., Tamagawa, T. and Ashida, Y. (2001): Computer simulation for sandbox experiments. Extended abstract of the Annual meeting, the Society of Exploration Geophysicists. San Antonio, TX, USA.
- Massoli, D., Koyi, H.A., Barchi, M.R., Rogledi, S. (2002): Analogue modelling of the Po Plain: structural evolution of a fold & thrust belt generated by multiple decollement. Bollettino di Geofisica teorica ed applicata, 42, 1/2 supplement, 200-202.
- Seno, T., Maruyama, S., 1984. Paleogeographic reconstruction and origin of the Philippine Sea. Tectonophysics, 102, pp. 53-84.
- Tsuji, T., Yamada, Y., Matsuoka, T., Nakamura, Y., Tokuyama, H., Kuramoto, S.(2004): Evolution of the Décollement in Nankai Trough off Muroto: Insights from Seismic Reflection data and ODP data. Proceedings of the International Symposium on Methane Hydrates and Fluid Flow in Upper Accretionary Prisms (PrismFluid2004). Kyoto, Japan, 26-30.
- Yamada, Y. Tanaka, A., Matsuoka, T. (2002): Analogue experiments of domal upwelling under tectonic stresses. Bollettino di Geofisica Teorica ed Applicata, 42, 1/2 supplement, 326-329.
- Yamada, Y., Kaneda, K., Baba, K., Matsuoka, T. (2004a): Analogue Modeling of Accretionary Prisms With Granular Materials. Proceedings of the International Symposium on Methane Hydrates and Fluid Flow in Upper Accretionary Prisms (PrismFluid2004). Kyoto, Japan, 14-17.
- Yamada, Y., Tanaka, A., Matsuoka, T. (2004b): Velocity and Stress Distributions during Continental Collision; Insights from Discrete Element Simulations. Bollettino di Geofisica Teorica ed Applicata, (this volume).

VELOCITY AND STRESS DISTRIBUTIONS DURING CONTINENTAL COLLISION; INSIGHTS FROM DISCRETE ELEMENT SIMULATIONS 3-34

Yasuhiro Yamada, Atsushi Tanaka, Toshifumi Matsuoka

Department of Civil and Earth Resources Engineering, Kyoto University, Kyoto 606-8501 Japan

Summary

The Discrete Element Method (DEM) as a digital sandbox simulator can be a powerful tool, in particular, to simulate fault related structures and also to analyse the deformation quantitatively. The DEM approximates the geologic body as an assembly of particles, similar to the sandbox experiments, which can properly simulate the brittle behaviour of the upper crust. As an example of DEM simulation of large-scale tectonic deformation, we examined the collision process of the Indian sub-continent to the Eurasian Plate by using the Tapponnier's geologic model. The simulations reproduced the deformation geometry similar to their analogue models. Velocity and stresses of each particle extracted during the deformation were quite unstable showing a characteristic feature of the brittle behaviour of the upper crust. A comparison of these results with GPS and in-situ stress data of the eastern Asia suggests that the Tapponnier's tectonic model may have a strong boundary effect, particularly to the stress field within the model.

Introduction

Deformation processes of geologic structures have been modelled by analogue physical experiments for a century. In particular, such experiments using granular materials, i.e. dry quartz sand, can properly scale the brittle behaviour of the upper crust, thus successfully applied to various sedimentary basins by the petroleum exploration industry. The knowledge obtained by the 'sandbox' experiments forms the core of modern structural geology and has been employed to interpret geophysical data, to understand structural development processes and also to predict sub-seismic fracture systems.

Since the experimental material is an assembly of grains, the deformation of such particles can also be examined with a numerical technique, the Discrete Element Method (DEM). We believe that the DEM can replace at least partly the role of the sandbox experiments and be applied to various scales of tectonic deformations. This paper presents some results of the DEM simulation applied to the Indian collision to the Eurasia.

DEM simulation

The DEM assumes the geologic body to be consisted of particles (Fig. 1). There are two steps in each calculation cycle: the first step is to evaluate interaction forces for every particle, and the second step is to move these particles according to numerical integration following to the Newton's equation of motion for the given external forces (Matsuoka et al., 2001b). The interaction forces can be evaluated from the force-displacement law (Cundall and Strack, 1979). The software employed in this paper is based on that by Matsuoka et al. (2001a), which includes a brief description of the algorithm, and further developed since then.

One of the significant advantages of the DEM is that some data can be extracted from each particle during deformation, such as displacement path (velocity) and stress fields. When applied to real geology, these can be compared with GPS and in-situ stress/seismicity data, which represent the current deformation of the region.

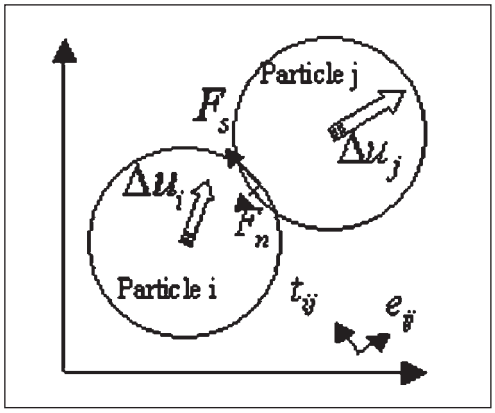

Fig. 1 - Basic idea of the DEM. The motion of each particle is defined by the given external forces.

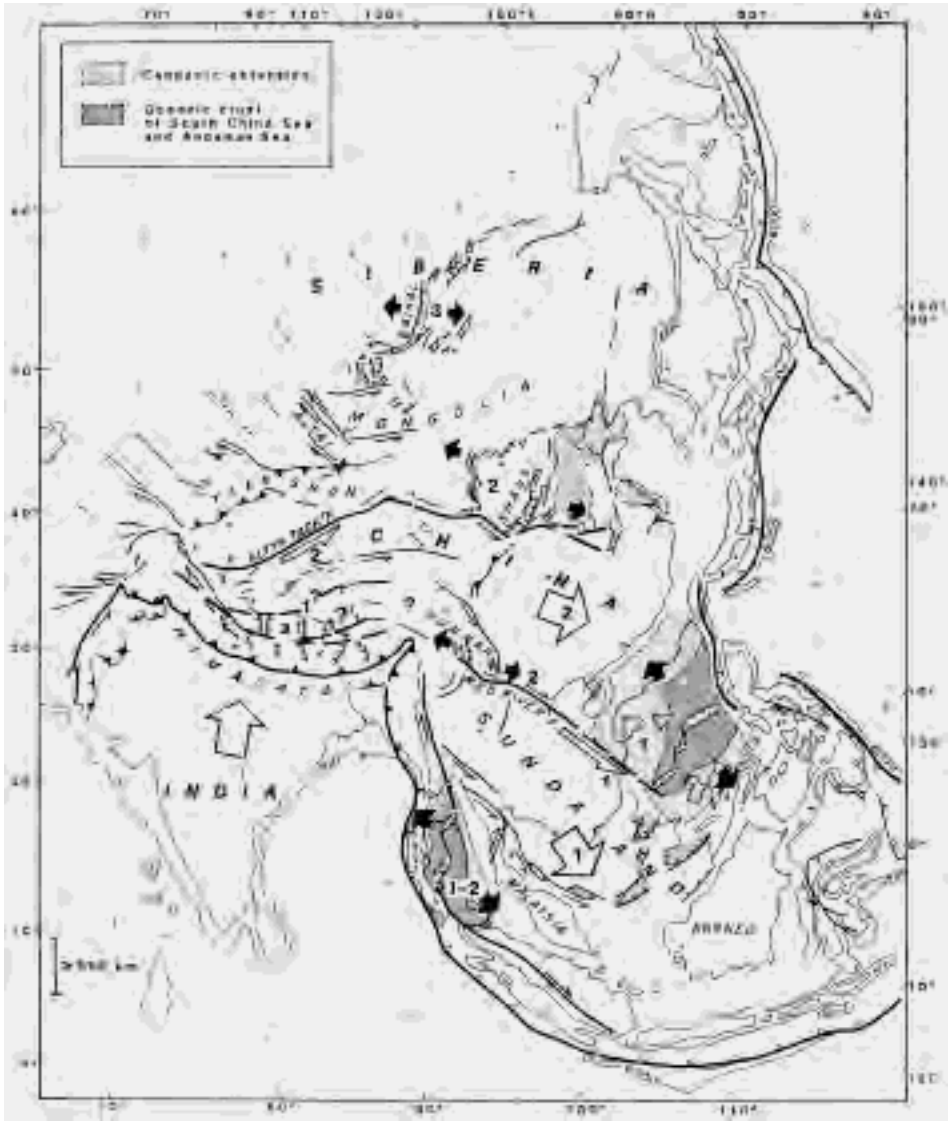

Fig. 2 - Deformation of eastern Asia due to the Indian collision (Tapponnier et al., 1986).

Indian Collision to Eurasia

The collision tectonics of the Indian sub-continent to the Eurasian Plate is one of the most spectacular current tectonic events of the Earth (Fig. 2). In order to investigate its lithospheric deformation processes, a series of physical experiments have been conducted using analogue materials, such as combinations of dry quartz sand and silicone polymer (Davy and Cobbold, 1988) and layered plasticine (Tapponnier et al., 1982, 1986, Peltzer and Tapponnier, 1988). Basic assumptions of these experiments included 1) rigid Indian continent, 2) deformable Eurasian Plate, 3) constrained northern and western margins of the experiments, and 4) unconstrained southern and eastern margins. The experimental results suggested that their simple tectonic models could explain the major tectonic features in the Eastern Asia.

Simulation Results

A series of DEM simulations following the same assumptions as those of the analogue experiments above were conducted to examine the input parameters including the relative position of the indenter (corresponding to India) and the bonding condition between the particles (Yamada et al, 2002a, 2002b, 2004). In all simulations, the particle size was randomized in a range between 0.06 and 0.14 to avoid potential weak planes due to the 'perfect' initial packing arrangement by a homogeneous size of the particle.

Fig. 3a shows a simulation result with a condition of homogeneous bonding and the indenter position at the centre of the particle assembly. The collision produced progressive development of fault systems, the lines of gap between the particles, which were propagated from the left corner of the indenter to the unconstrained right margin. The outline of the right- hand-side of the particle assembly is broadened to overcome the space problem due to the collision.

During the deformation, the velocity and stresses of each particle were also extracted and their time-laps variations were examined. Fig. 3b is the velocity vector diagram of each particle at the same time step as Fig. 3a. The figure shows the segmented blocks are moving to the east, as assumed by the deformation geometry of Fig. 3a. However, the region in front of the indenter has no systematic direction, suggesting that the region is highly fragmented. This velocity distribution is quite unstable and easily changed the direction and magnitude during the deformation.

From the resultant force on each particle, the normal (Fig. 3c) and tangential (Fig. 3d) components of stresses were calculated for the same time step of Fig. 3a and 3b. The normal stress distribution suggests that the fragmented blocks in east of the indenter are not highly compressed at this stage (Fig. 3c). This may correspond to the boundary condition of the unconstrained right margin. Fig. 3c also shows that the normal stress in the particles is not homogeneous and some chain-like structures of high stresses are formed from the indenter to the constrained walls. The tangential stress diagram shows that the collision produced a broad shear band in the particles (Fig. 3d). The black particles correspond to a strong shear in the anti-clockwise direction, whereas the white ones represent clockwise shear. Thus the major black shear band corresponds well with the sinistral shear seen in Fig. 3a.

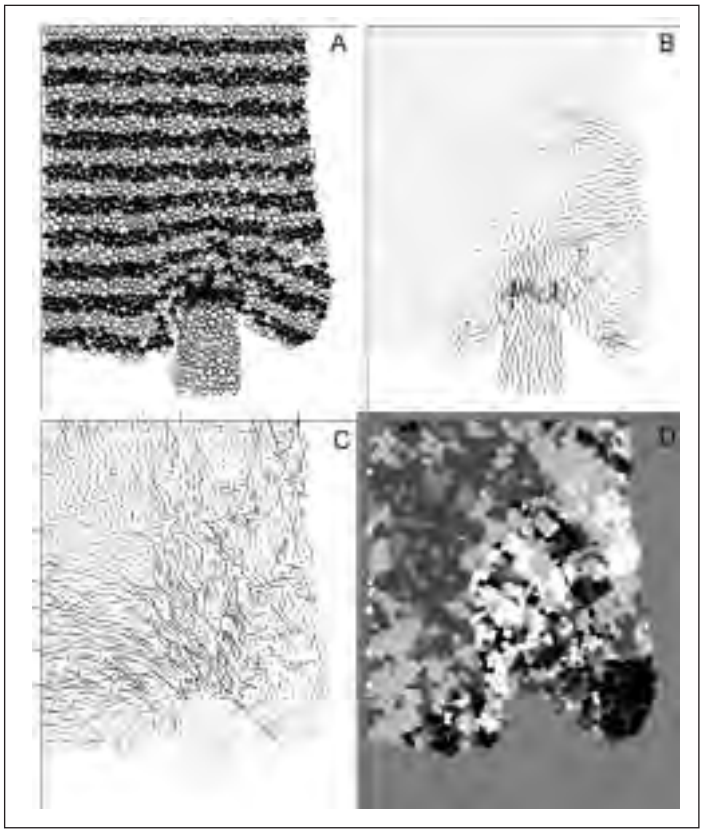

Fig. 3 - DEM results. a) A deformation geometry of the particle assembly. b) The velocity distributions at the same time step. c) Stresses in the normal (inter-particle compression) direction of each particle at the same time step. The fragmented blocks in east of the indenter are not highly compressed at this stage. Note some chain-like structures of high stresses are formed from the indenter to the constrained walls. d) Stresses in the shear (inter-particle shear) direction of each particle at the same time step. Particles in dark colors are rotating in a clock-wise direction, whereas those in light colors acquiring shear forces in anti-clock wise rotation. The collision produced a broad shear band corresponds with the sinistral shear seen in Fig. 3a

Comparison with Experiments/GPS/In-situ Stress Field

The plasticine models by Tapponnier et al. (1982, 1986) are characterized by sequential development of major fault systems and rotation of fragmented continental blocks. Davy and Cobbold (1988) conducted analogue models, which were properly scaled to the lithospheric deformation, and founded that formation of major single shear zone is the common feature of this tectonic setting. Our DEM simulation produced both types of faulting with similar geometry; initiation at the left corner of the indenter and propagation to the right margin of the particle assembly. This suggests that the parameters we examined can be major factors to control the deformation style. In the frontal region of the indenter, thrust faults are produced perpendicular to the indentation in the experiment and the layers were thinned at the corresponding position in the DEM (Fig. 3a).

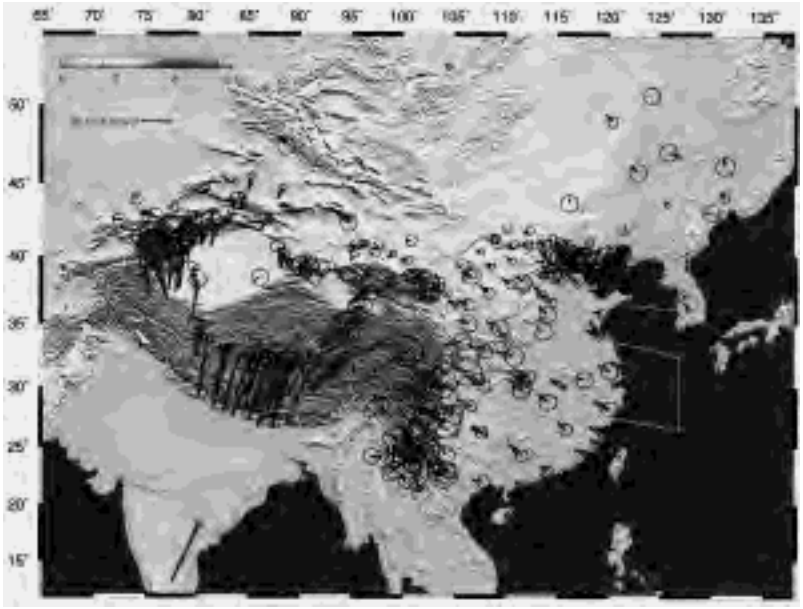

Fig. 4 - Current velocity field in the eastern Asia obtained by GPS data (Wang et al., 2001), shows the vectors run along smooth lines, suggesting that the deformation may be strongly controlled by the ductile deformation of the lower crust.

Major features of the DEM results different from the analogue experiments are related with the larger size of the particles in the simulation, which significantly affects the resolution of deformation structures.

The velocity distributions of the particles in the DEM are equivalent to GPS when applied to the real deformation in the eastern Asia. As described earlier, the velocity distributions are quite unstable during the deformation and commonly showed unsystematic variations in front of the indenter (Fig. 3b), whereas GPS vectors are generally continuous from the colliding Indian continent (Fig. 4). This could also be explained by the particle size problem, but may suggest that the DEM parameters need to be altered to incorporate the effect of ductile deformation of the lower crust more.

It is generally difficult to obtain precise vectors of the current stress fields, and only the directions of the maximum horizontal compressional stresses can be available (Fig. 5). This data can be compared with the directions in the normal stress diagram of the DEM particles (Figs. 3c). The directions of the stresses in both Figs. 3c and 5 can be approximated to a radial pattern from the northern boundary of the Indian Plate. The characteristic clockwise rotation of the stress direction at the east of the Himalaya is not significant in the DEM, but a group of particles nearby to the right-front corner of

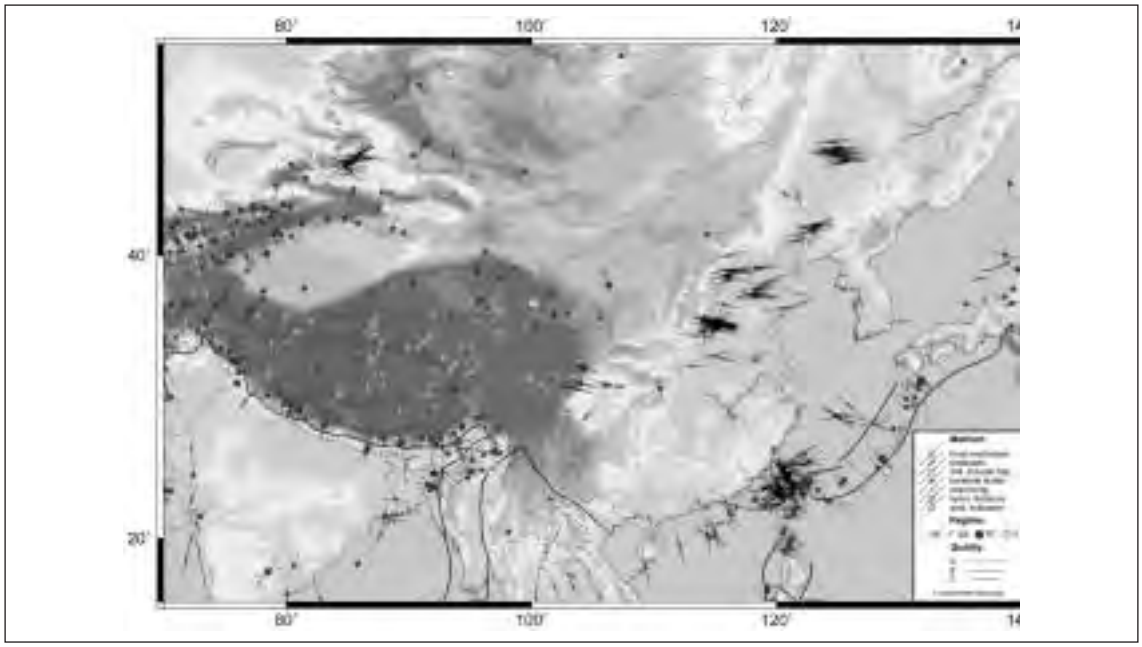

Fig. 5 - The directions of maximum horizontal compressional stress axis, compiled by the WSM project (Reinecker et al., 2003), show that the directions are roughly parallel to the GPS vectors.

the indenter show such rotation in a minor degree (Fig. 3c). These particles have tangential stresses in the clock-wise rotation (Fig. 3d), which also agree with the stress rotation.

Conclusions

The DEM simulation results can be correlated with the scaled physical experiments done under similar boundary conditions, and also with natural deformations including GPS and in-situ stress data. Therefore the method can be a powerful tool to analyse natural geologic deformations, to validate quantitatively the parameters that control the deformation, and also to construct dynamic models of structural deformation with a variation in time and space.

REFERENCES

- Cundall, P.A. and Strack, O.D.L. (1979): A discrete numerical model for granular assemblies. Geotechnique, 29, 47-65.
- Davy, P. and Cobbold, P. R. (1988): Indentation tectonics in nature and experiment. 1. Experiments scaled for gravity. Bulletin of the Geological Institutions of Uppsala, N. S., 14, 129-141.
- Matsuoka, T., Hasegawa, T., Yamada Y. and Ashida, Y. (2001a): Analogue and digital modelling in structural geology. Proceedings of the Recent Advances in Exploration Geophysics. Kyoto, Japan.
- Matsuoka, T., Yamada, Y., Tamagawa, T. and Ashida, Y. (2001b): Computer simulation for sandbox experiments. Extended abstract of the Annual meeting, the Society of Exploration Geophysicists. San Antonio, TX, USA.
- Peltzer, G. and Tapponnier, P. (1988): Formation and evolution of strike-slip faults, rifts, and basins during the India-Asia collision: an experimental approach. J. Geophys. Res., 93, B12, 15085-15117.
- Reinecker, J., Heidbach, O. and Mueller, B. (2003): The 2003 release of the World Stress Map (available online at www.world-stress-map.org).
- Tapponnier, P., Peltzer, G. Armijo, R. Le Dain, A.-Y. and Cobbold, P. (1982): Propagating extrusion tectonics in Asia: new insights from simple experiments with plasticine. Geology, 10, 611-616.
- Tapponnier, P., Peltzer, G., and Armijo, R. (1986): On the mechanics of the collision between India and Asia. In Collision Tectonics, (ed.) Coward, M. P., and A. C. Ries, Geological Society Special Publication, 19, 115-157.
- Wang, Q., Zhang, P.Z., Freymueller, J.T., Bilham, R., Larson, K.M., Lai, X., You, X., Niu, Z., Wu, J., Li, Y., Liu, J., Yang, Z., Chen, Q. (2001): Present Day Crustal Deformation in China constrained by Global Positioning Measurements, Science, 294, 574-577.
- Yamada, Y., Tanaka, A. and Matsuoka, T. (2002a): DEM Simulation of Indentation Tectonics: Continental Collision of Indo-Eurasia. Proceedings of the 6th International Symposium on Recent Advances in Exploration Geophysics in Kyoto (RAEG2002), 28-32.
- Yamada, Y. Tanaka, A., Matsuoka, T. (2002b): DEM simulation of continental collision; Insights for indentation tectonics in Asia. Bollettino di Geofisica teorica ed applicata, 42, 1/2 supplement, 245-249.
- Yamada, Y., Matsuoka, T. (2004): Digital Sandbox Modelling using Discrete Element Method (DEM): Applications to Fault Tectonics. In: Sorkhabi, R. and Tsuji, Y. (Eds.), Faults and Petroleum Traps, AAPG Memoir, in press.

Session 3

SEDIMENTARY BASINS

A 3D IMAGE OF THE VENETIAN FORELAND BASIN (NE ITALY) THROUGH A 2D (PLANFORM) ANALYSIS

3-01

C. Barbieri(*), D. Garcia-Castellanos(**)

(*) Department of Earth Sciences, University of Pavia, via Ferrata 1, 27100 Pavia, Italy

(**) Department of Earth Sciences, Vrije University of Amsterdam, De Boelelaan 1085, 1081HV Amsterdam, The Netherlands

Summary

The Venetian Basin (NE Italy) evolved as the foreland of the Dinarides, Eastern Southern Alps and Northern Apennines which underwent their main orogenic phases during Paleocene-early Eocene, late Miocene-early Pliocene and Pliocene-early Pleistocene, respectively. A 2D (planform) analysis is here proposed to reconstruct a flexural model of this sector of the Adria plate and identify the contribution of each belt to the total deflection observed at present. In particular, results show that the Northern Apennines only influenced the southernmost part of the Venetian Basin, as the deflection occurred in its northern sector was mainly affected by the Eastern Southern Alps related flexure.

Introduction and aim of the present work

The Venetian Basin (NE Italy; Fig.1) is characterised by a complex geometry due to the partial superposition of three partly overlapping foredeeps (Fantoni et al., 2002 and references therein), different in both age and polarity, associated to the development of the surrounding belts, namely Dinarides, Eastern Southern Alps and Northern Apennines, which underwent their main orogenic phases through Tertiary time. Therefore, the Venetian Basin represents an interesting area to observe and better understand the interplay between the evolution of several mountain belts and the response of the adjacent foreland. However, in spite of its interesting position, this basin has received little attention in modelling studies, mainly because of the lack of well constrained data.

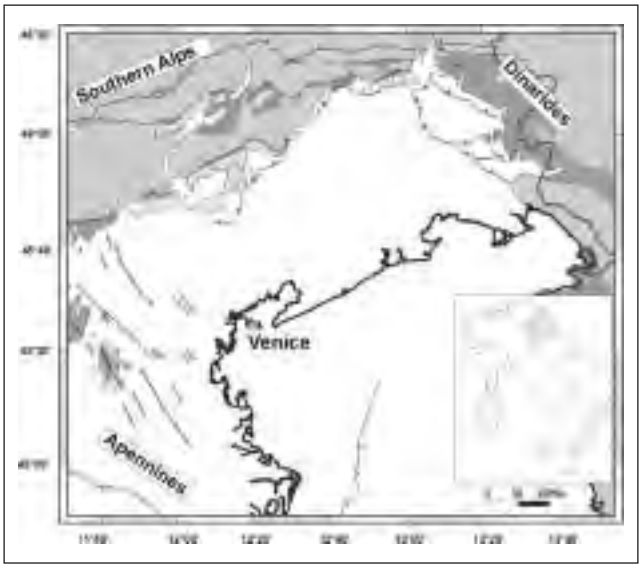

Fig. 1 - Map showing the studied area. Dinarides are characterised by Paleocene-early Eocene SW verging structures which developed in front of a N-NE dipping foredeep. The following Southalpine main orogenic phases (late Miocene, early Pliocene) occurred contemporaneously with a second N-NW dipping foredeep developed N of Venice. The latest Apenninic phases (Pliocene-early Pleistocene) were finally responsible for the south-westward flexure of the Adria plate.

During the last decade, many geophysical and geological works, for the most part related to the TRANSALP project (i.e. TRANSALP working group, 2002), were carried out in this zone giving new insights in crustal geometries and on the timing of orogenic growth. On the basis of this new interest for the Venetian Basin, geohistory curves were calculated along the strike direction of the Eastern Southern Alps (Mellere et al., 2000) to reconstruct the Oligocene-Miocene subsidence on the area and recognise the effects of the Dinaric and Southalpine thrusting.

Moreover, the deflection associated to the Northern Apennines has been recently tested as a possible controlling factor for the Pliocene – early Pleistocene subsidence occurred in the south-westernmost

part of the Venetian Basin, on the basis of the subsurface geometries of the sedimentary infill (Carminati et al., 2003).
The existing models give only a partial image of the complex subsidence history occurred in the Venetian Basin and the mutual effect of the three orogeneses in this sector is still debated. Planform flexural studies have shown their ability to constrain the spatial distribution of lithospheric rigidity and the relative importance of each tectonic unit involved in similar multi-vergent orogenic settings such as the Ebro Basin (Gaspar-Escribano et al., 2001; Garcia-Castellanos et al., 2003). Here we propose to apply similar 2D (planform) techniques to analyse the main processes controlling the subsidence of the Venetian Basin and to constrain their area of influence.

Data and method

In this work, the flexural response of the Venetian Basin to the present loads has been studied using the code tao3D (Garcia-Castellanos et al., 1997; Garcia-Castellanos, 2002). The calculated model is mainly focused on the analysis of the deflection produced by the eastern Southern Alps and the Northern Apennines, as the older Dinaric flexural effect is hard to constrain being largely obliterated by the following tectonic events.
Therefore, the reference surface for the calculated deflection is represented by the isobaths of the bottom of the Upper Miocene succession (Fig.2) which has been reconstructed through wells and seismic data (courtesy of ENI).

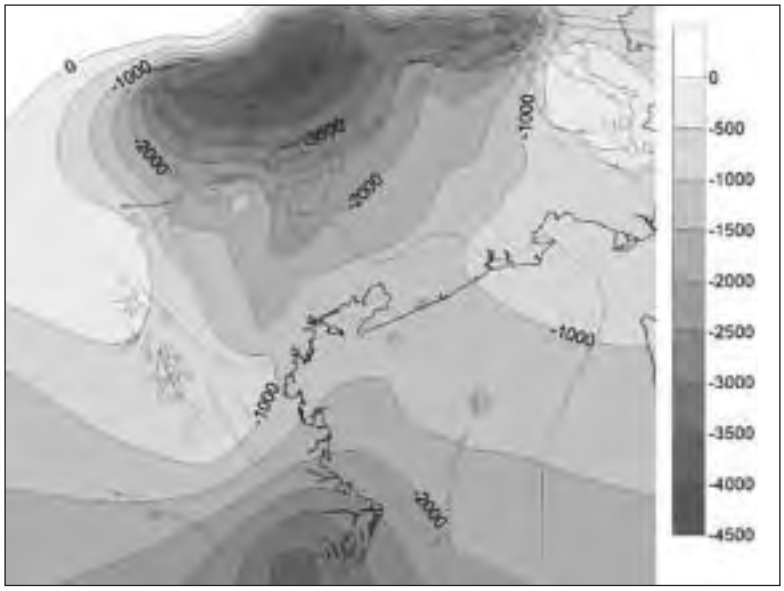

Fig. 2 - Isobaths map of the bottom of the Upper Miocene succession.

Due to the dramatic erosion event occurred during Messinian, the base of the upper Miocene succession could not be accurately constrained South of the present coast line, however, the depths measured in a few wells suggest that only a few tens metres deposited during late Miocene in both the Apenninic sector and the northern Adriatic region. Therefore, it is reasonable to assume that the sedimentary thickness separating the base of the Upper Miocene from the lower Pliocene is negligible if compared to the overlying Plio-Quaternary succession. For this reason, the calculated deflection in front of the Apennines is compared to the isobaths map representing the base of the Plio-Quaternary succession proposed by Bigi et al., (1990).
Calculations have been carried out over an area of about 276.000 Km^2 wide, centred on the analysed basin, in order to avoid errors related to the boundary effects in the study area. The mountain load is represented by the present topography of the surrounding belts. On the contrary, the initial water depth has not been taken into account due to the scarce constraints existing on the initial water depth all over the study area. Hidden loads can be added to solve the difference between calculated and observed flexure. Effective elastic thickness (Te) values represent a further input used in tao3D. In this work (Fig.3a), a Te value of 20 Km has been applied to the northern area of the Venetian Basin. and Te

values ranging between 15-25 Km have been used to the South according to values inferred from flexural modelling of the Adria plate by several authors (i.e. Kruse & Royden, 1994; Buiter et al., 1998; Kroon, 2002).

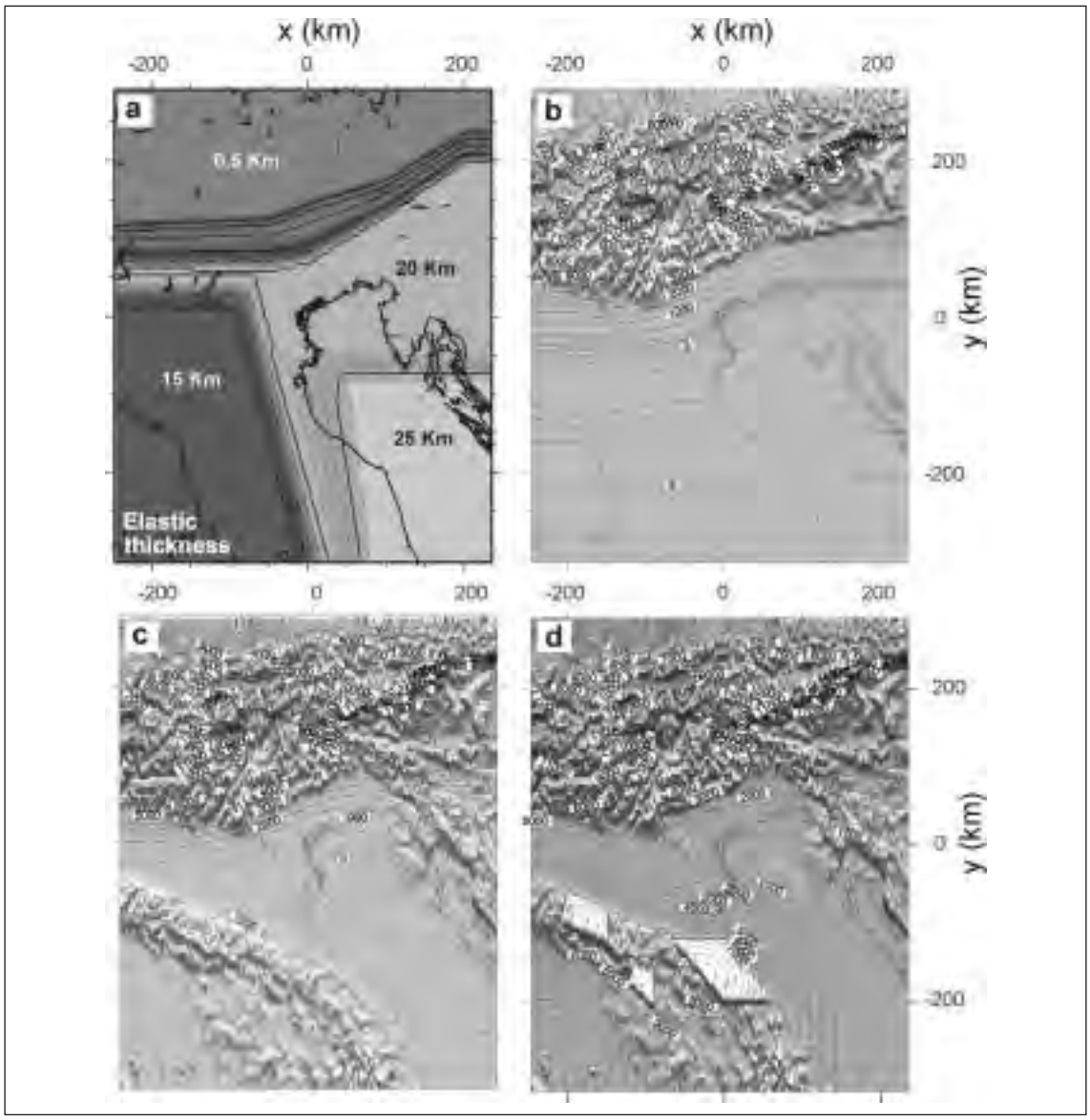

Fig. 3 - a) Te distribution on the modelled area. b) deflection calculated taking into account only the Eastern Southern Alps load. In the Venetian Basin, a NW dipping foredeep forms which is bounded, just South of the present coast line, by a few metres high zone. c) Deflection calculated for the total present relief. A forebulge forms in the present Northern Adriatic Sea. d) Best fit with the observed deflection obtained by adding hidden loads beneath the Apennines.

The implemented algorithm do not allow sharp changes in Te values to be accounted for and this limitation may represent a problem while simulating a broken plate condition. However, it is possible to approximate an abrupt change in this parameter by calculating a gradient within a narrow band, consistently with the numerical stability of the algorithm. Finally, all calculations have been performed assuming the Adria plate to behave as a thin elastic plate.
In order to separate the contribution to flexure of the surrounding belts, mountain load is considered in two steps which investigate the flexural effect related to the mountain load produced by the Eastern Southern Alps only and by the whole present relief, respectively (Fig. 3b-c).

Results

The best fit in the area which corresponds with the Venetian Basin (Fig. 3b-d) has been obtained assuming a broken plate condition to occur beneath the Eastern Southern Alps, close to the Valsugana Thrust System. In particular, the broken plate condition has been simulated through a transition from 0.5 Km to 20 Km along a narrow band centred on the fore mentioned tectonic lineament. The very low Te value applied to the northern block allows the mountain load located North of the Valsugana Thrust System to be locally compensated rather than distributed over the modelled plate. By applying the Southalpine belt load only (Fig. 3b), a N-NW dipping foreland system forms which is bounded by a few metres high located just South of the present coast line. In further step (Fig. 3c), calculated taking into account all the presently existing mountain loads, a forebulge forms in the central part of the Northern Adriatic Sea, between the Istrian peninsula and the present Po delta. At this point, as the Apenninic load is not sufficient, in itself, to reproduce the present deflection in the Northern Adriatic Sea area, hidden loads have been applied beneath this belt to fit the deflection highlighted by the Plio-Quaternary isobaths reported in the Structural Model of Italy (Bigi et al., 1990). The increased deflection (Fig. 3d) allows the model to fit the Apenninic foredeep and the forebulge to be shifted toward the Dalmatian region, to the East, consistently with the present-day topography of the Adriatic region. It is important to highlight that the applied hidden loads could be partly due to the lack of information on the initial bathymetry.

Conclusions

As a whole, the 2D (planform) models shed light on the effects of both Southalpine and Northern Apennines loads on the western part of the Venetian Basin. In particular, the calculated models have demonstrated that the Southalpine load is responsible for the formation of a NE-SW trending foredeep around 100 Km wide bounded, to the South, by a few metres high forebulge in the area corresponding to the present northernmost sector of the Adriatic Sea. At present, this latter feature cannot be observed, whereas the adjacent foredeep has been preserved Barbieri et al., (2002). It has been demonstrated that the addition of the present topography of the Northern Apennines as a further load allows this bulge to be shifted southward, towards the centre of the Northern Adriatic sea. This feature is eventually shifted toward the Dalmatian region by adding hidden loads beneath the Apennines.
The second point to be stressed concerns the extension of the area affected by the Apenninic deflection. Results show that the southern sector of the Venetian Basin, corresponding, at present, to the Lagoon of Venice, was significantly affected by the Northern Apennines load which could contribute for up to 500 m to the total occurred subsidence. In contrast, the Apennines did not affect the northernmost sector of the studied basin, whose deflections seems to be only related to the growth of the Eastern Southern Alps, in contrast with the interpretation given by Doglioni & Carminati (2002) who hypothesised the Apennines related deflection to influence the Southern Alps.

REFERENCES

- Barbieri et al. (2002), Memorie di Scienze Geologiche, 45 (Spec. Vol.), 135-138
- Bigi et al. (1990), Structural model of Italy, scale 1:500000, CNR, progetto finalizzato Geodinamica, printed by SELCA, Florence.
- Buiter et al. (1998), Tectoniphysics, 296, 249-268
- Carminati et al. (2003), Geophysical Research Letters, 30, 13, 50-1 50-4
- Doglioni and Carminati (2002), Memorie di Scienze Geologiche, 45 (Spec. Vol.), 1-4
- Fantoni et al. (2002), Memorie della Società Geologica Italiana, 57, 301-313
- Garcia-Castellanos et al. (1997), Computers and Geosciences, 23, 9, 993-1003
- Garcia-Castellanos (2002), Basin Research, 14, 89-104
- Garcia-Castellanos et al. (2003), Journal of Geophysical Research, 108 (B7), 2347, 10.1029/2002JB002073
- Gaspar-Escribano et al. (2001), International Geophysical Journal, 145, 2, 349-368
- Kroon (2002), PhD Thesis, Vrije University of Amsterdam, NSG publication nr. 20020803, pp.112
- Kruse and Royden (1994), Tectonics, 13, 2, 278-302
- Mellere et al. (2000), Basin Research, 12, 159-182
- TRANSALP working group (2002), Geophysical Research Letters, 29, 10, 92-1 92-4.

RELATING VERTICAL MOVEMENTS AND STRESS/STRAIN FIELDS IN SEDIMENTARY BASINS AND ADJACENT OROGENS FOLLOWING THE MAIN STAGES OF CONTRACTION: MODELLING AND REALITY OF LITHOSPHERIC/CRUSTAL BUCKLING

3-02

G. Bertotti

Department of Tectonics/Structural Geology, Vrije Universiteit, De Boelelaan 1085, 1081HV, Amsterdam (NL) – Giovanni.Bertotti@falw.vu.nl

Introduction

Vertical movements, both uplift/exhumation in orogens and subsidence in the adjacent sedimentary basins are traditionally related to horizontal deformations. Shortening, for instance, causes thickening of the crust and of the lithosphere, consequent modifications of the weight of the lithospheric column and eventually vertical movements. These are exhumation/uplift in the orogen and subsidence in the adjacent foredeep basin. One can describe these movements as associated with vertical loads. One of the implicit consequence of the causal relation between horizontal shortening and vertical movements is that these are supposed to cease once convergence ends. It is now increasingly well-known that this is often not the case and that vertical movements continue after the end of shortening. In this contribution I will constrain the post-orogenic vertical movements observed in mountain belts and in the adjacent sedimentary basins. I will then present main results from modeling studies and explicitly discuss the contribution they provide for the understanding of vertical movements.

Post-orogenic vertical movements

Subsidence

A large body of data is now available demonstrating that subsidence persists also following the main stages of contraction. In several cases one documents even an increase in subsidence rate and a widening of the area affected by subsidence. Well-documented cases are the Focsani Depression, a segment of the Carpathian foredeep (Tarapoanca et al. 2004), the western Po Plain, the South Adriatic basin (Bertotti et al., 2001) and the Oman Interior Basins (Bertotti and Immenhauser, submitted). It is striking that this "abnormal" subsidence has received little attention. Very few, data-constrained quantitative models have been developed to understand these first order patterns (see Tarapoanca et al., in press for an exception).

Exhumation/uplift

In the last years, the accuracy of low temperature geochronometers such as apatite fission track and, more importantly, (U-Th)/He on apatites has allowed the detailed reconstruction of vertical movements in the orogens within the uppermost few kilometers of the Earth's crust. Similarly to what observed in the sedimentary basins, such methods have demonstrated that vertical movements in the orogens continue or even intensify after the cessation of shortening. This is observed, for instance, in the Ligurian Alps (Foeken et al. 2003) and in the segment of the Carpathians adjacent to the Focsani Depression (Sanders et al., 1999).

Regional patterns

Studies on vertical movements rarely consider both the orogen and the adjacent basin. Indeed the two regions are studied by different geological communities working often with quite different tools. The integrated analysis of the entire system, however, is interesting in that it shows that, following orogeny:

a) vertical movements of **different sign** take place **at the same time**. This is to say that, for instance, exhumation/uplift in the mountains is contemporaneous with subsidence in the adjacent basin. This is the case for the Plio-Quaternary of the Ligurian Sea – Western Po Plain system, for the Miocene to Quaternary Adriatic-Albanide and for the Quaternary of the Carpathian – Focsani Depression region (Fig. 1a).

b) Some specific regions, change the sign of their vertical movements during time and shift, for

instance, from subsidence to exhumation/uplift. This is a typical pattern of the transition zones connecting the orogen to the sedimentary basin.

Tectonic models for post-orogenic vertical movements

A few models have been proposed in the past to explain post-contractional vertical movements. Most of them are associated with vertical loads. The presently most popular is that of slab detachment and of its lateral migration (Wortel and Spakmann 2000 and references). In brief, the model predicts that
a) Strong subsidence should take place in the regions prior to the detachment of the hanging slab. Once the tear has reached a specific region, this should experience rapid uplift
b) The two types of movements should occur over the entire system, namely the orogen and the adjacent sedimentary basin (Fig. 1b).

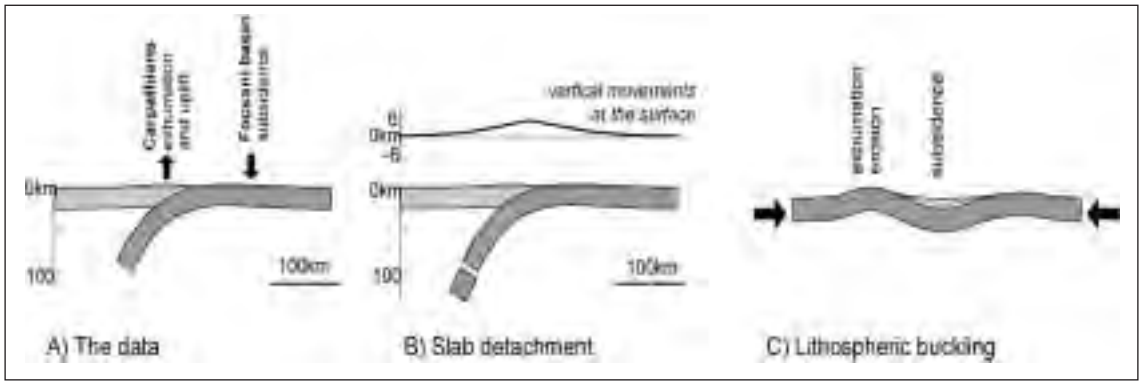

Fig. 1 - Cartoon of vertical movements observed in the Carpathian domain and predicted by the slab detachment and by the buckling model

Lithospheric buckling: inferences from numerical models

It is now generally accepted that buckling is a "normal" way for the lithosphere to accommodate shortening (Cloetingh et al. 1999). This major advancement was made possible by increased computing power and by the improvement of existing codes. Indeed, crustal/lithospheric buckling can only be modeled by taking into account the full dynamic behavior of a mechanically complex object such as the lithosphere.
Once subjected to compression, the lithosphere develops synclines and anticlines the wave lengths of which depend on the its mechanical state. A typical continental lithosphere in an orogenic domain, for instance, is expected to develop folds with two wavelengths, a large one associated with mantle folding and a shorter one related to crustal folding (Fig. 2)

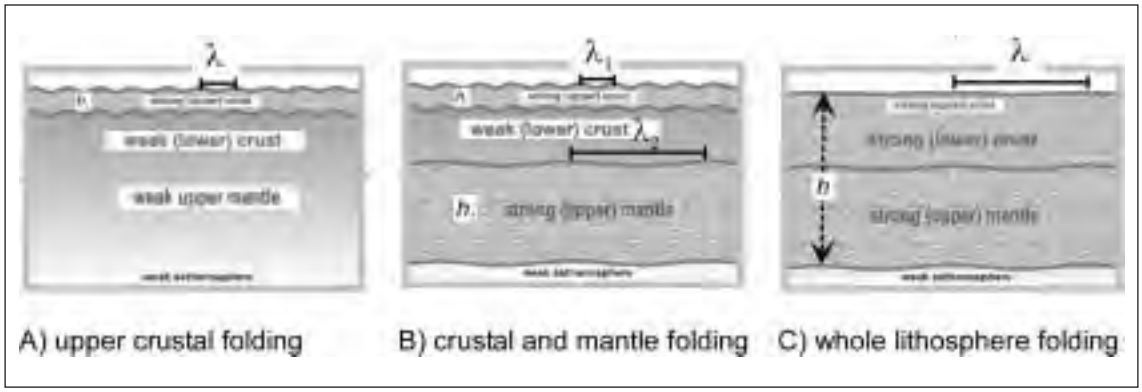

Fig. 2. - Cartoon showing relations between lithosphere mechanics and folding patterns (from Cloetingh et al., 1999).

The buckling model is a convincing model to explain post-orogenic movements such as those described above:
a) It is compatible with the observations that uplift/exhumation and subsidence can take place during the same time (Fig. 1c).
b) Produces wave lengths compatible with those observed in nature
c) Produces substantial vertical movements in the absence of strong localized deformations

State of the art of numerical models

Numerical models of crustal/lithospheric buckling are, however, still in their infancy and there are still unable to provide detailed predictions which can be tested in the field. Movements in the uplifting domains are extremely sensitive to erosion patterns and these are described in a fairly qualitative manner so that more and more understanding is gained (see however Avouac and Burov, 1996; Burov and Cloetingh, 1997; Cloetingh et al., 2003) but detailed tests are still to become possible. Subsidence in the basins cannot be compared with real world because of insufficient sedimentological realism.
Although not at a detailed enough level, numerical models of buckling do provide further information on on poorly understood phenomena which are a valuable source of inspiration. I will discuss two of such features in the following.

Implications and conclusions

Changing vertical movements

One of the most interesting conclusions obtained from numerical modeling is that different domains can experience at the same time quite different patterns of vertical movements and that these can change through time. This is exemplified in Fig. 1c. A more detailed prediction on vertical movements during buckling is given in Fig. 3. Three "localities" are marked in this figure. Points A and B have a simply history of vertical movements in that they experience constant upward or downward movement respectively. In geological terms, these domains will correspond to mountains and sedimentary basins respectively.

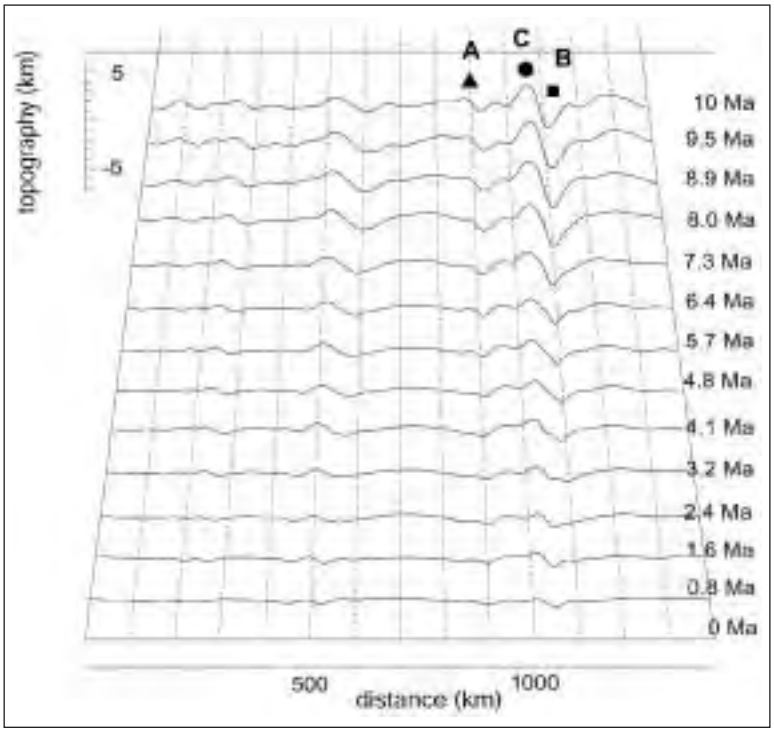

Fig. 3 - Evolution of the topography of a lithospheric system undergoing buckling. Note how certain localities (A and B) do not change the sign of their vertical movements during shortening. This is the case of point C. Numerical experiment by Ingrid Kroon.

More interesting is point C which initially moves downward and then changes to an upward displacement. It is important to note that this shift occurs within a frame where boundary conditions such as shortening rate etc remain perfectly constant. In other words, the transition from one

movement to the other does not result from any noticeable tectonic change (tectonic phases) and is merely the result of the complex interactions between the growth potential of different folds.
There are numerous examples testifying these changes. In the Central Adriatic, the Pelagruza high experienced Miocene to Pliocene uplift and erosion and began, in the Pleistocene to subside (Bertotti et al., 2001). In the same area, the orogenic wedge of the Albanides underwent post-orogenic subsidence during Serravallian to Pliocene times and was subsequently uplifted to its present day position (Bertotti et al., 2001). The external zones of the Carpathians, at the transition with the Focsani Depression subsided by few kilometers and was then tilted and uplifted forming high Quaternary high relief (Tarapoanca et al., 2004).

Stress and strain fields

Buckling systems are characterized by compression the boundaries of the system. The associated shortening is not accommodated by localized deformation, that is, major faulting, but rather by large wave length folding. Consequently compressional stresses are predicted to be present over the entire width of the model with limited amounts of deformation affecting large domains of the model mainly concentrated in the areas of folding.
In the field, such low-strain deformations are joints, veins and or small-scale faults. Each of these features will accommodated small deformations (tens to tens of meters) but will be spatially very widespread thereby provoking major changes in physical properties of rocks and, for instance, patterns of basin-scale fluid flow. A beautiful example of such behaviors has been recently documented in the Oman Interior where joints parallel to the direction of s1 affect areas of several hundreds of square kilometers (Bertotti and Immenhauser, submitted).
In theory, the regional compression could be compensated and even overruled by local stress fields associated with folding. Anticlinal folding, for instance, could become so accentuated that the stress axis perpendicular to the fold could become tensional (local field dominating on the regional). Numerical models show that the curvatures needed for such a shift are generally not realized. However, some specific areas display tensional axes perpendicular to the folds. These are indeed areas where the curvature is extremely high.
The knowledge that stress and strain in a given system are controlled by lithospheric/crustal buckling is of major importance because it allows a meaningful extrapolation of outcrop data to non-exposed target areas such as hydrocarbon reservoirs.

REFERENCES

- Avouac, J.-P. and Burov, E.B. 1996. Erosion as a driving mechanism of intracontinental mountain growth. J. Geophys. Res., 110, 17747-17769.
- Bertotti, G., Picotti, V., Chilovi, C., Fantoni, R., Merlini, S. And Mosconi A. 2001. Neogene to Quaternary sedimentary basins in the South Adriatic (central Mediterranean); foredeeps and lithospheric buckling. Tectonics, 20, 771-787.
- Bertotti, G., Matenco, L., Cloetingh, S. 2003. Vertical movements in and around the SE Carpathians: Lithospheric memory and stress field control. Terra Nova. 15, 299-305.
- Bertotti , G. and Immenhauser, A. submitted. Stratigraphic and regional distribution of fractures in Barremian-Aptian carbonate rocks in Eastern Oman: Outcrop data and extrapolation to Interior Oman hydrocarbon reservoirs. Int. J. Earth Sciences.
- Buiter, S., Wortel, M. and Govers, R. 1998. The role of subduction in the evolution of the Apennine foreland basin. Tectonophysics, 296, 249-268.
- Burov, E.B. and Cloetingh, S. 1997. Erosion and rift dynamics: New thermomechanical aspects of post-rift evolution of extensional basins. Earth Planet Sc. Lett., 150, 7-26.
- Cloetingh, S., Burov, E. and Poliakov, A. 1999. Lithospheric folding: Primary response to compression? (from central Asia to Paris basin). Tectonics, 18, 1064-1083.
- Cloetingh, S., Burov, E., Maßenco, L., Toussaint, G., Bertotti, G., Andriessen, P., Wortel, M. and Spakman, W. 2003. Thermo-mechanical controls on the mode of continental collision in the SE Carpathians (Romania). Earth Planet. Sc. Lett., 6931, 1-20.
- Foeken, J., Dunai, T., Bertotti, G. And Andriessen, P. 2003. Late Miocene to Present exhumation in the Ligurian Alps (SW Alps) with evidence for accelerated denudatio during the Messinian Salinity Crisis. Geology, 31, 797-800.
- Kroon, I. 2002. Strength of the Adriatic lithosphere: Inferences from tectonic modeling. PhD Thesis Vrije Universiteit Amsterdam,11 pp.
- Sanders, C., Andriessen, P. and Cloetingh, S. 1999.
- Tarapoanca, M., Bertotti, G., Matenco, L., Cloetingh, S. and Dinu, C. 2004. Architecture of the Focsani Depression: A 13 km deep basin in the Carpathian Bend Zone (Romania). Tectonics. 22/6, 13-1 to 13-18.
- Tarapoanca, M., Garcia-Castellanos, D., Bertotti, G., Matenco, L., Cloetingh, S.A.P.L. And Dinu, C. In Press. Role of 3D distribution of load and lithospheric strength in arcuate orogens: poly-stage subsidence in the Carpathian foredeep. Earth and Planet. Sc. Lett.
- Wortel, M.J.R and Spakman, W. 2000. Subduction and slab detachment in the Mediterranean-Carpathian rgeion. Science, 290, 1910-1917.

FORMATION OF EXTENSIONAL SEDIMENTARY BASINS: THE ROLE OF SURFACE PROCESSES IN MODE SELECTION

3-03

Susanne J.H. Buiter, Ritske S. Huismans, Christopher Beaumont

Geodynamics Group, Department of Oceanography, Dalhousie University, Halifax (NS), Canada, susanne.buiter@dal.ca

Summary

We analyse the formation of extensional basins and the influence of surface processes on the dynamic evolution of the extensional system. We present: a) An analysis of the rate of energy dissipation for simple models with a frictional-plastic upper crust welded to a linear viscous lower crust and a prediction of extensional modes; b) Equivalent numerical models to test our analytical predictions; c) An analysis of the role of surface processes in these simple two-layer models; and d) An evaluation of the effect of surface processes on thermo-mechanical crustal-scale models of extension.

Introduction

Observations show that extension of the Earth's lithosphere typically leads to localisation of deformation in the crust in the form of extensional sedimentary basins. These basins have geometries varying from symmetric, with displacements on the normal faults bounding the basin being of equal magnitude, to asymmetric, with displacement focussed on one planar or listric basin-bounding fault (e.g., *Cheadle et al*, 1987; *Marsden et al*., 1990). Our goal is to determine factors which control whether a sedimentary basin will evolve in a mainly symmetric or asymmetric manner. In an accompanying paper (*Huismans et al*, this volume) we show that on a lithospheric scale, extension may be accommodated in an asymmetric manner, in a symmetric manner, or by pure shear. The main control determining this behaviour is the competition between the viscosity of the lower lithospheric layer and strain-softening of the frictional-plastic upper layer.

Here we focus on the crustal scale. We first examine whether the controls that we found for the lithospheric scale operate in a similar manner for the crustal scale. Our next aim is to evaluate the role of sedimentation and erosion. We show how sedimentation promotes the formation of symmetric sedimentary basins.

We first consider simple two-layer models of the crust, with an upper frictional-plastic layer welded to a lower linear-viscous layer. We calculate analytically the internal rate of dissipation of energy and the gravitational rate of work. By assuming that this simple model will deform in a manner which minimises the sum of both rates of energy dissipation, we predict the modes of deformation in the order of decreasing viscosity of the lower crust: 1) pure shear, 2) multiple plugs, 3) single symmetric plug, and 4) single asymmetric plug. We then perform numerical experiments of equivalent two-layer models to examine whether these agree with the analytic prediction. We examine how these modes are modified by sedimentation and erosion.

Our interest in an analysis of the rate of energy dissipation is motivated by our aim to try to understand the behaviour of more complex thermo-mechanical extension models. How are extensional sedimentary basins which form in a crust with a viscous-plastic rheology influenced by surface processes?

Analytical estimates of the dissipation of energy

We analytically calculate the rate of energy dissipation for simple two-layer models assuming that they will deform in one of the four deformation modes shown in Figure 1. The internal rate of dissipation of energy is given by

$$\frac{1}{2}\int_A \sigma \cdot \dot{\varepsilon} dA$$

where σ is the stress tensor, $\dot{\varepsilon}$ the strain-rate tensor, and the integration is over model area A and per unit length for 2D models. For pure shear extension this integral is easily calculated following pure shear extension fields for the plastic and the viscous layer. For the three plug modes, contributions to

this rate come from (Fig. 1): a) shear zone(s) in the plastic layer, b) bending of footwall block(s), c) a Couette-type flow in a boundary layer which accommodates the velocity difference between the plastic upper layer and the viscous lower layer, and d) a pure shear flow in the lowermost part of the viscous layer. The rate of gravitational work is given by:

$$\int_A \rho g V_z dA$$

for density ρ, gravitational acceleration g and vertical component of velocity V_z. We have build on our previous analytical analysis by adding a prediction of the multiple plug mode, footwall bending terms, an evaluation of the effect of Airy isostasy, and an evaluation of the role of surface processes.
We calculate the total dissipation for each of the four modes shown in Figure 1 and assume that the deformation mode which has the least dissipation of energy will be the one selected by the system. A main control is the viscosity of the lower layer. We predict the following deformation modes (using the values given in Table 1): asymmetric plug for viscosities below approximately $4x10^{19}$ Pa s, symmetric plug for approximately the interval $4x10^{19}$-$2x10^{21}$ Pa s, and pure shear for higher viscosities. A marginal preference for a multiple symmetric plug mode is predicted around 1-$2x10^{21}$ Pa s.

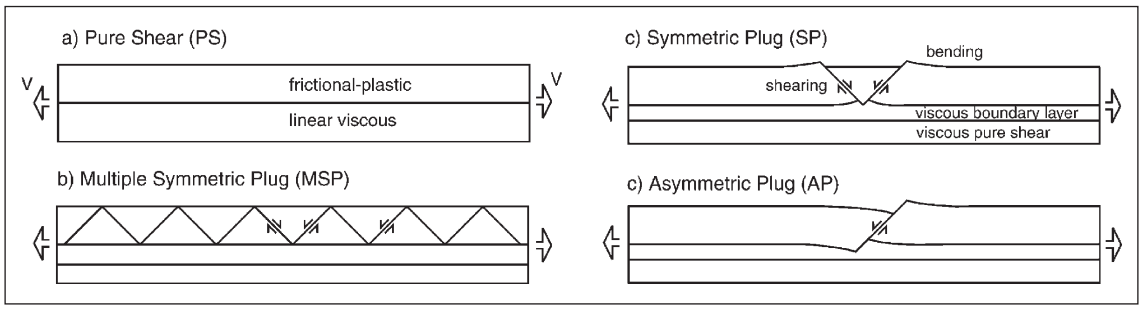

Fig. 1 - Schematic representation of deformation modes expected in crustal-scale simple two-layer extension models.

Simple crustal-scale two-layer models

Next, we perform numerical experiments of the extension of simple crustal-scale models consisting of a frictional-plastic upper crust welded to a linear viscous lower crust. We use a two-dimensional plane-strain mechanical model (*Fullsack*, 1995). The mechanical equilibrium equations are solved on an Eulerian grid to which material properties are assigned using Lagrangian tracking points. We use a Coulomb failure criterion for the upper crust and strain softening occurs through a reduction of the angle of internal friction with increasing strain. A small volume of weak material (considered to have completely strain-softened) acts as a seed to initially localise deformation.
For a low-viscosity (10^{19} Pa s) lower crust extension in the brittle crust is mainly focussed on one shear and the surface depression is asymmetric (Fig. 2). If we do not allow for strain-softening of the frictional-plastic upper crust, the equivalent model is symmetric. With a slightly higher viscosity (10^{20} Pa s) for the lower crust, the surface depression becomes symmetric and increasing the viscosity further (to 10^{22} Pa s) forces the upper crust to follow pure shear behaviour (Fig. 2). Interesting to note is that the model with a lower crust viscosity of 10^{21} Pa s continues to deform in a multiple plug mode with increasing extension (not shown here). These modes of extension agree with the analytical predictions.

The sequence of asymmetric, through symmetric to pure shear deformation with increasing viscosity for the lower layer is the same as that seen for lithospheric-scale models (*Huismans et al*, this volume). The difference is that the transition from asymmetric to symmetric deformation, and the transition from symmetric to pure shear extension, occurs at much lower values for the viscosity of the lower layer. This difference is explained by the scale difference in the models. In particular, a thinner brittle layer lowers both transition viscosities.

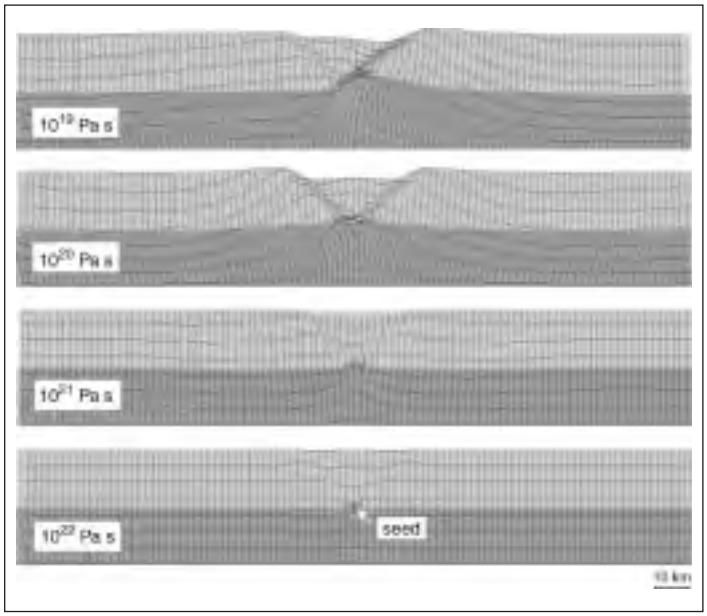

Fig. 2 - Four models with different values for the uniform viscosity of the lower crust. The value for viscosity is shown in each panel. The upper crust is frictional-plastic and follows a Coulomb failure criterion. The models are 400 km wide and 35 km high and the figure shows the centre 200 km. The basal boundary condition is a roller. These models have no sedimentation or erosion. All models are after 10 km of extension.

Table 1: model parameter values

Cohesion	20 MPa
Angle of int. friction	30° • 4°
Softening interval (strain)	0.5-1.5
Pore-fluid factor	0.357
Density	2800 kg/m^3
Extension V (per side)	0.5 cm/yr

We evaluate the effect of sedimentation and erosion by examining different surface processes models. As an example, Figure 3 shows the results of one end-member model. Any depression that forms is filled with sediments with the same properties, and therefore also the same density, as the crust. Sedimentation clearly enforces the formation of a symmetric basin. The models that already developed a symmetric depression in the absence of sedimentation (Fig. 2) have now become deeper under the weight of the sediments filling the basin. More gravitational energy is released owing to the subsiding basin and its fill, and no work is now done against gravity to uplift footwall blocks.

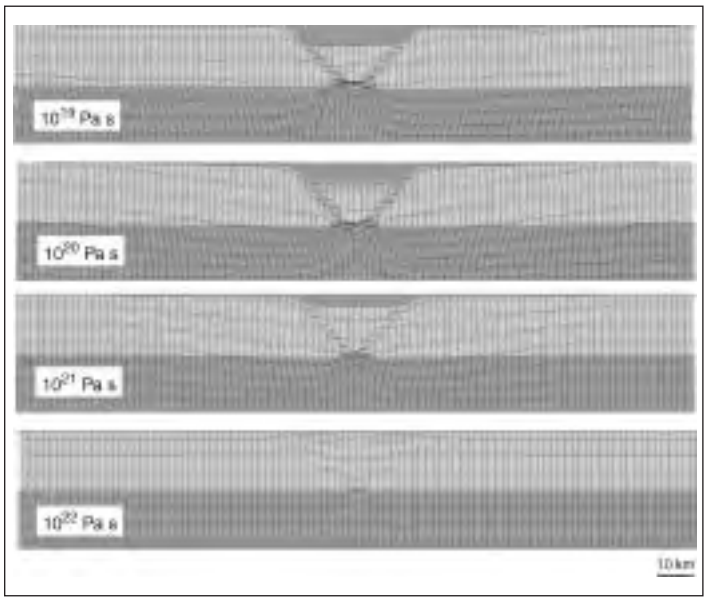

Fig 3 - Four models with different values for the uniform viscosity of the lower crust. The value for viscosity is shown in each panel. This series shows the effect of sedimentation. Any depression that forms is immediately filled with sediments which have the same properties as the crust. All material properties as in Table 1. All panels are after 10 km of extension.

The model that was asymmetric for the case of no sedimentation (lower crust viscosity 10^{19} Pa s in Fig. 2) develops in a symmetric manner when sedimentation is included. This is examined further in Figure 4. The model initially starts extending in a symmetric mode with two unsoftened shears. When no sedimentation is included, one of the shears preferentially softens and the strain-softening feedback

effect allows shear to localise on one side, leading to the formation of an asymmetric depression (Fig. 4a,b). However, in case the depression is immediately filled with sediments, this tendency is suppressed (Fig. 4c,d). We interpret the role of surface processes in terms of differences in the rate of work against gravity.

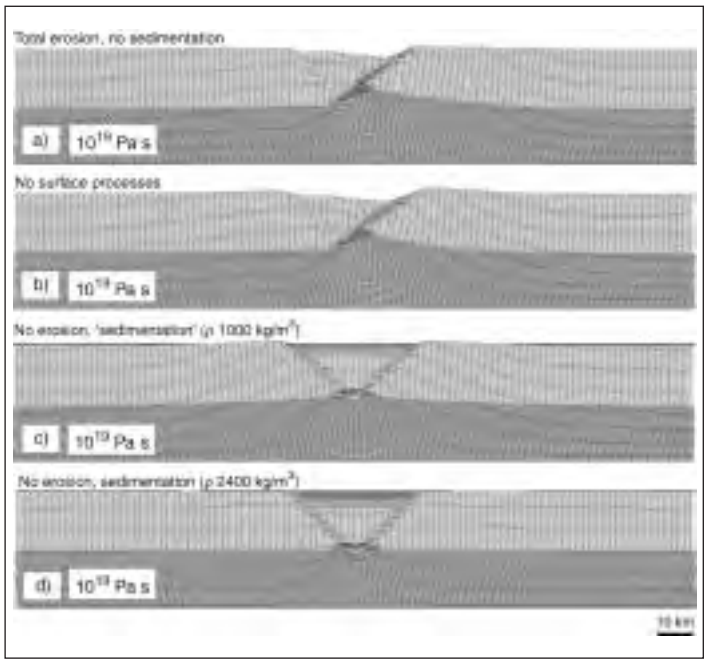

Fig 4 - The effects of erosion and sedimentation for a model with a lower crust viscosity of 10^{19} Pa s. All panels are after 10 km of extension. a) Total erosion and no sedimentation, b) No erosion and no sedimentation, c) Intermediate model with no erosion and sedimentation with material with a density of 1000 kg/m^3, d) No erosion and sedimentation with a sediment density of 2400 kg/m^3. All other material properties as in Table 1.

Temperature-dependent viscous-plastic model

A primary aim of the consideration of the dissipation of energy in extension, both analytically and in the simple numeric models, is to help us understand the behaviour of models with more complex pressure- and temperature-dependent rheologies. Figure 5 shows an example of the results of a thermo-mechanical model. The material of the upper crust deforms in a frictional-plastic manner while the lower crust follows the power-law flow-law for wet quartz of *Gleason and Tullis* (1995). The transition between frictional-plastic and power-law behaviour is determined by the model itself and not specified to be at a certain depth. Flexural isostatic compensation is included through an elastic beam which underlies the model and which is loaded by the weight of the evolving model.

Extension is first accommodated by pure shear until approximately 20 km of extension (Fig. 5a). Subsequently, a symmetric basin is formed in the case of full sedimentation (Fig. 5 b,c) and also in the case of no surface processes (Fig. 5e). This can be explained by the strength distribution, which has a high viscosity in the boundary layer just below the frictional-plastic upper crust (Fig. 5d). It is this relatively high viscosity in the boundary layer which promotes symmetric extension (see also Fig. 2). Sedimentation again promotes the formation of a deep basin.

We use this model to examine the effects of variations in crustal strength. This is done in a simple manner by scaling the flow-law for power-law creep. A weak flow-law leads to a thin brittle upper crust and a thick weak lower crust. In this case small half-graben basins form in the upper crust and they propagate outward along with the lower crustal viscous flow. A strong flow-law leads to a thick brittle upper crust. In this case a deep sedimentary basin forms and new shear zones form internally. We analyse and interpret these results using an analysis of the rate of energy dissipation and our findings for the simple two-layer models.

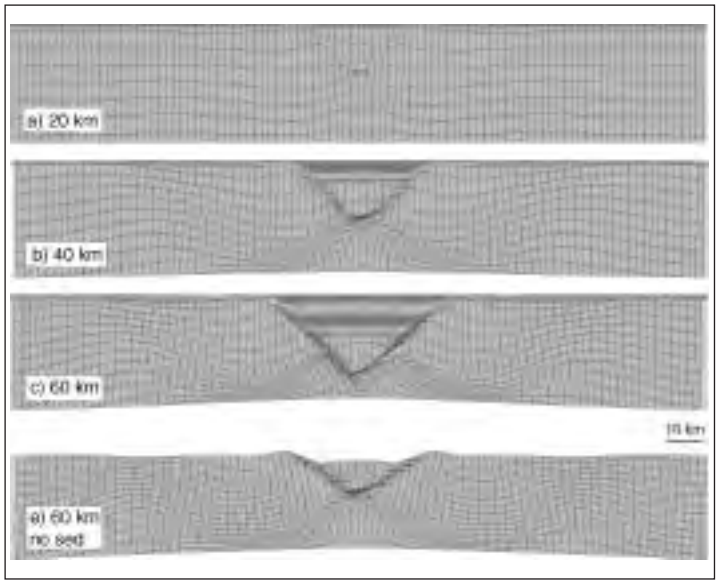

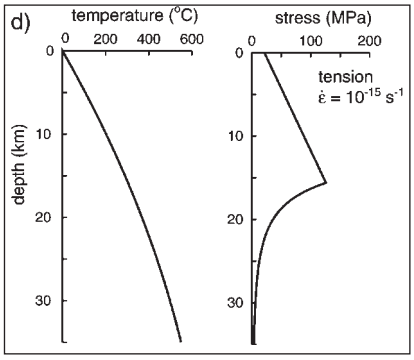

Coulumb failure criterion:
$\sigma_y = P_e(1-\lambda)\sin\phi + C\cos\phi$
C 20 MPa
λ 0.357
ϕ 30° softening to 4° over a finite strain interval of 0.5-1.5
P_e dynamic pressure

Power-law flow-law for wet quartz of *Gleason and Tullis* (1995)

Fig 5 - a-c) Evolution of a thermo-mechanical model of crustal-scale extension. The initial temperature and strength distribution are shown in d). The models have full sedimentation. The sediments have the same properties as the crust, only the density is lower (2400 kg/m^3 for the sediments and 2800 kg/m^3 for the crust). The shade of gray of the sediments changes with every 10 km of extension. The elastic beam used for flexural isostatic compensation of the model has a flexural rigidity of $5x10^{21}$ Nm. A roller basal boundary condition is applied. e) Same model, only now without surface processes.

REFERENCES

- Cheadle, M.J., S. McGeary, M.R. Warner and D.H. Matthews (1987) Geol. Soc. Spec. Publ. 28, 445-465.
- Fullsack, Ph. (1995) Geophys. J. Int., 120, 1-23.
- Gleason, G.C. and Tullis, J. (1995) Tectonophysics, 247, 1-23.
- Huismans, R.S., S.J.H. Buiter, C. Beaumont (2004) this volume.
- Marsden, G., G. Yielding, A.M. Roberts and N.J. Kusznir (1990) Tectonic Evolution of the North Sea Rifts, Oxford Science Publications, 240-261.

PASSIVE EXTENSION IN SALT-BEARING PASSIVE MARGINS: NEW INSIGHTS BY ANALOGUE MODELING 3-04

Costa Elisabetta[1], Cavozzi Cristian[1], Doglioni Nicolò[1]

1 Dipartimento di Scienze della Terra, Parco Area delle Scienze 157/A, 43100 Parma (Italy)

Introduction

This study analyzes the kinematics of thin-skinned, gravitational extension, due to salt spreading and/or sliding, by means of analogue modeling. Our models do not reproduce any particular natural settings. They have been designed to reproduce the phenomenon of passive extension of a cover resting on a low viscosity horizon: for this aim we eliminated the buttressing effect due to any kind of obstacle to the forward propagation of the models' front. The first part of our study, presented here, was aimed in particular at balancing the influence of 1) the thickness of rock salt, 2) the thickness of the cover and 3) the angle of slope on : a) geometry of deformation, b) localization and width of the deformed areas and c) sequence of nucleation and growth of normal faulting.

Model set up and deformation

The data presented in this study show the geometrical and kinematic differences obtained by eighth models deforming by passive extension. The models, built with dry sand and silicone (Table I), had the same size (200 x 200 mm) and one side unconfined, where the viscous silicone was free to spread and/or slide under its own weight and that of the overlying brittle overburden (see Table II for details on model features). Every model was run both horizzontally and on a 6° slope.

Table I - Physical parameters of the materials used in the models

Materials	Density [g/cm^3]	Grain size [μm]	Angle of internal friction φ	Dynamic shear viscosity η[Pa s]
Sand	1,75	300	30°	- - - - -
Silicone SGM36	0,976	- - - - -	- - - - -	2 x 10^4

All the models were free to deform until their forward extension stopped (movement rate < 1 mm/day): in practice every model was allowed to deform as much as possible. The total deformation time is then very different in the various models (Table II), depending on their total thichness.

Table II – Models' features

Model	Thickness of sand (mm)	Thickness of silicone (mm)	Slope (°)	Total time (h, m)	Final length of model (mm)	Bulk stretching (%)
STA3	18	10	6°	04, 30	284	42
STA5	10	5	6°	07, 35	252	26
STA7	10	10	6°	05, 00	280	40
STA9	5	5	6°	13, 45	255	27,5
STA2	18	10	0°	05, 00	260	30
STA4	10	5	0°	08, 00	226	13
STA8	10	10	0°	06, 40	250	25
STA10	5	5	0°	22, 15	230	15

The movies of the models' top surface during deformation allowed to completely reconstruct the timing and sequence of structure nucleation and growth. After deformation, models were wet and cut along various cross sections and line drawings obtained from their pictures.

Model results

The line drawings obtained from the cross sections cut at the centre of each model show a series of extensional structures represented by normal faults generating either simmetrycal or asimmetrical grabens (Figs. 1and 2), which delimit tilded blocks (Fig. 1 model STA 4, Fig. 2 model STA 3). In all the models most of the faults form during the first 2,5 cm of extension; these structures then evolve to grabens and tilted blocks

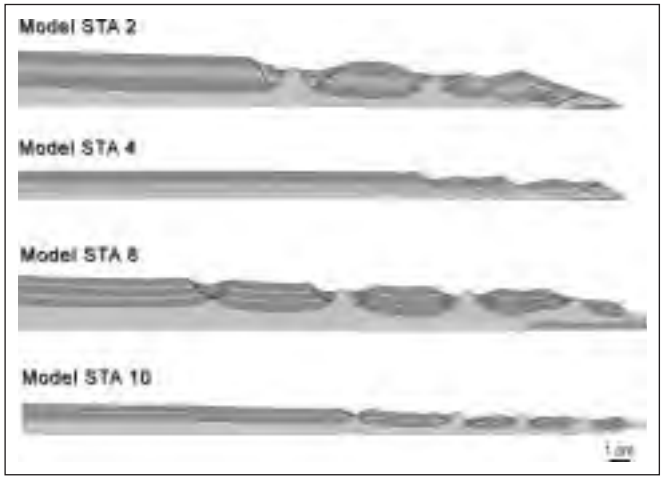

Fig. 1 - Line drawing of orizzontal models (grey: silicone; green and blue: sand)

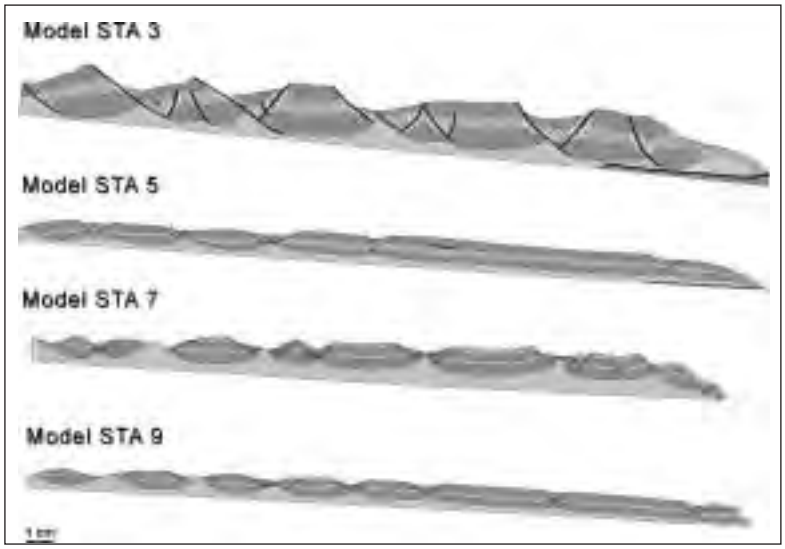

Fig. 2 – Line drawing of tilted models (grey: silicone; green and blue: sand)

The horizontal models never deformed at their rear and the deformed frontal areas are whider when the silicone is thicker but, the thickness of the silicone being equal, they are whider when the cover is thinner. The tilted models deformed at both their front and rear at the same time (Mauduit et al., 1997). It is noteworthy that deformation structures form following a back and forth sequence of propagation. Deformation moving toward the center of the system occurs by faults dipping foreward while deformation moving away from the center occurs by faults dipping backward. Our models show two different deformation bands having amplitudes proportional to the angle of slope and to the thickness of the viscous layer, but inversely proportional to the thickness of the brittle cover.
Only in the thicker models the two deformed parts merge toward tthe models' centre (STA3 and STA7) whereas the models STA 5 and STA 9 have undeformed, or less deformed zones in their central part.
In all the models the viscous layer pierces where the cover is weakened and thinned by normal faulting (Vendeville and Jackson, 1992), and in some models diapirs extrude. All the gravitational models after a phase of instantaneous acceleration (that brings them to the maximum speed), progressively decelerate until the speed settles down to limit values that precede thier complete stop. The maximum and minimal values of velocity are more influenced by the increased thickness of both viscous and brittle layers, rather than by the slope increase. The tilted models, show a more regular deceleration curve than the horizontal models.

Discussion

Our models were designed by varying simple parameters and relationships; they represent only a first step of our study. Further models scaled down to real geodynamic systems, will reproduce variations of the cover thickness through time (progradation, sin-tectonic sedimentation) and variations of the angles of slope as well. This first part of our study is thus aimed at partitioning the effect of the different variables acting on a geodynamic system and reproduced by more realistic and thus inherently more complicated models.

REFERENCES

• Mauduit, T., Guerin, G., Brun, J.P., Lecanu, H., 1997. Raft tectonics: the effects of basal slope angle and sedimentation rate on progressive extension. J. Struct. Geol. 19, 1219-1230.
• Vendeville, B. C., Jackson, M. P. A., 1992. The rise of diapirs during thin-skinned extension. Marine & Petroleum Geology 9, 331-353.

FOUR-DIMENSIONAL MODELLING OF SEDIMENTARY BASIN ARCHITECTURE AND HYDROCARBON MIGRATION 3-05

S.M. Clarke*, S.D. Burley*&**, G.D. Williams*, A.J. Richards*, D.J. Merredith*

(*) Basin Dynamics Research Group, School of Earth Sciences & Geography, Keele University, Staffordshire, ST55BG, England

(**) BG Exploration and Production India Ltd, Midas Building, Sahar Plaza, M.V. Road, East Andheri, Mumbai, 400 049, India

Summary

Structural restoration, fault-seal analysis and hydrocarbon migration are largely treated as separate, predictive approaches to investigating basin geohistory and petroleum systems. Basin and fault-seal modelling techniques use geometrical and geo-mechanical solutions to static problems of basin architecture, structural restoration modelling uses geometrical models of basin geohistory, whilst hydrocarbon migration modelling approaches employ fluid dynamic solutions to flow through geometrically static basins. Each of these separate modelling approaches in their own fields are advanced and sophisticated but not integrated with each other. Lack of integration results in a static solution to migration modelling and renders a risk-driven, multiple realisation approach to petroleum systems analysis impractical. In this paper, we describe an integrated, 4D basin modelling workflow in which structural restoration and fault-seal analysis, together with their evolving geohistories and geometries, can be incorporated into an invasion percolation (IP) hydrocarbon migration modelling technique.

Four-Dimensional Basin Analysis

Basin modelling, or 'petroleum systems analysis', is a powerful approach for predicting the timing of petroleum generation and the distribution of hydrocarbon phase in the sub-surface to reduce exploration risk (Burley et al., 2000). Basin architecture and its evolution are two of the essential inputs to building a basin model. Basin geohistory influences the sediment infill, whilst evolving fluid conduit geometries define potential hydrocarbon migration pathways and thus hydrocarbon accumulations.

Commercial and research basin modelling tools already enable many petroleum system processes to be predicted with considerable usefulness, including subsidence, compaction, pressure, maturation, secondary migration and trapped hydrocarbon phase and volumes (Mann et al., 1997; Wendebourg, 2000). These processes are dynamic, evolving through time and may occur in different areas of a basin at the same time. Fluid flow conduits, and potential migration along them, are also 3D networks throughout the basin. Accurate prediction of hydrocarbon accumulations therefore requires modelling in four dimensions: 3D space and time. Without the time component, basin models are essentially static, retaining Present Day geometries. However, incorporation of basin architecture and its evolution into 4D basin models is still simplistic in its approach. Commercial, 3D, secondary migration simulators do not directly incorporate structural restoration beyond vertical decompaction and backstripping, whilst commercial structural restoration tools do not simulate hydrocarbon generation and migration processes.

The importance of structural restoration in determining basin geohistory, for incorporation into predictive petroleum system simulators, is considered in this paper. Initial results of a new, integrated, modelling methodology linking 4D fault restoration software with a hydrocarbon migration simulator based on *Invasion Percolation* (IP) techniques are presented. Accurate restoration of a basin geohistory is demonstrated to be critical to the modelling of hydrocarbon migration, and thus for petroleum system analysis.

Sequential Restoration and Basin Modelling in Four Dimensions

Accurate estimation of the evolution of subsurface geometry through time requires reconstruction of the regional to local scale tectonics and the simulation of porosity reduction through compactional processes. The key to incorporating structural restoration in basin simulators is to represent basin geometry and fault restoration as a geometrical modelling environment. Until now, two different

techniques have been used to tackle the problem of subsurface geometry, porosity and pressure prediction. Traditionally, the gross geometry has been estimated using inverse models that range from large-scale tectonics to structural reconstruction with mechanical decompaction, and the generated time steps used as input into hydrocarbon migration modelling (e.g. Huggins et al., 2004). However a more detailed estimate of porosity and pressure can be obtained through forward simulation integrated with a coupled pressure-temperature model, resulting in a further reduction of porosity through diagenesis.

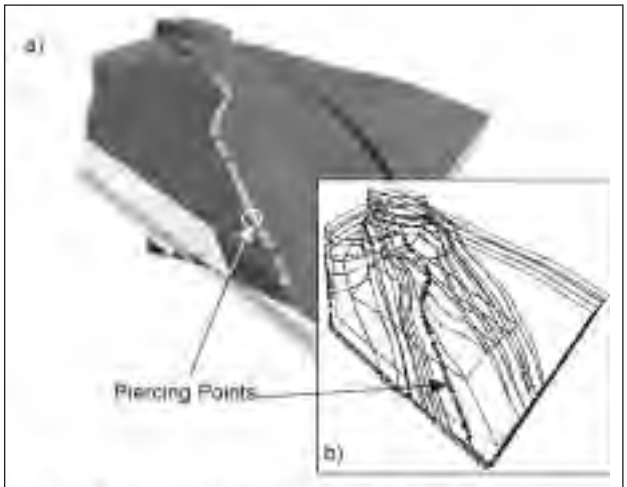

Figure (1) - A 3D model containing multiple faults. (a) shows the location of calculated piercing points used to determine the restoration azimuth and heave values. (b) shows the same model in outline and the location of the piercing points in relation to the footwall and hanging-wall cut-offs on the fault surfaces.

Structural restoration through time involves a retro-deformational process in which sequential 'snapshots' of the basin evolution are portrayed. Automated retro-deformation can be achieved using a 'piercing point' technique (fig. 1), which analyses and automatically computes the required displacement vector field needed to restore the displaced geometry. This modelling approach uniquely defines matching points on the fault hanging-wall and footwall cut-offs and computes the required heave vectors for each restoration step. Restoration is performed using a well-known geometrical technique – the vertical/inclined shear algorithm – which results in a volume balanced solution, key to the successful geometrical modelling of basin stratigraphy (Williams et al., 1997). Geometrically perfect restorations are achieved without stratigraphical surface gaps or overlaps in the restored model.

Four-Dimensional Fault Seal Analysis

Faults, their geometries, and their movement histories through time are important controlling elements of hydrocarbon migration and entrapment within sedimentary basins. When faults undergo displacement, their fluid transmissibility properties change as a result of juxtaposed strata and the development of a fault zone of material between faulted blocks. These effects have to be combined with structural restoration and basin modelling and incorporated into models of hydrocarbon migration for accurate migration pathways to be predicted through time. By adopting a 4D modelling approach to the prediction of fault transmissibilities resulting from the processes of *cross-fault juxtaposition* (Allan, 1989) and *argillaceous fault rock* development (Fristad et al., 1997) these processes can be incorporated into basin modelling and hydrocarbon migration simulation.

Cross-fault juxtaposition can be modelled by constructing a *fault-surface section* (Allan, 1989) to investigate seal and leak points resulting from juxtaposed combinations of reservoir and non-reservoir lithologies. This technique produces a static, 2D model that demonstrates juxtaposition relationships for a given temporal stage (usually Present Day) in the deformational history of the fault. Accurate modelling relies on the correct interpretation of faulted structural geometry and stratigraphy. The geometry of a fault that is curved along strike will not be represented correctly in the fault-surface section and, if a curved fault is resolved onto a flat plane, stratigraphical cut-off areas will not necessarily be preserved. Furthermore, the representation of a fault as a fault-surface section does not allow the interaction of multiple faults on sealing capacity to be investigated, or the juxtapositions of lithologies at other temporal stages in the structural evolution of the fault to be analysed. Using a 4D solution these problems can be addressed. By mapping properties of the faulted blocks to the footwall and hanging-wall of the fault surface directly in 3D, inaccuracies inherent in the 2D solution are reduced (fig. 2). Furthermore, the interaction of juxtaposition seal between multiple faults can be

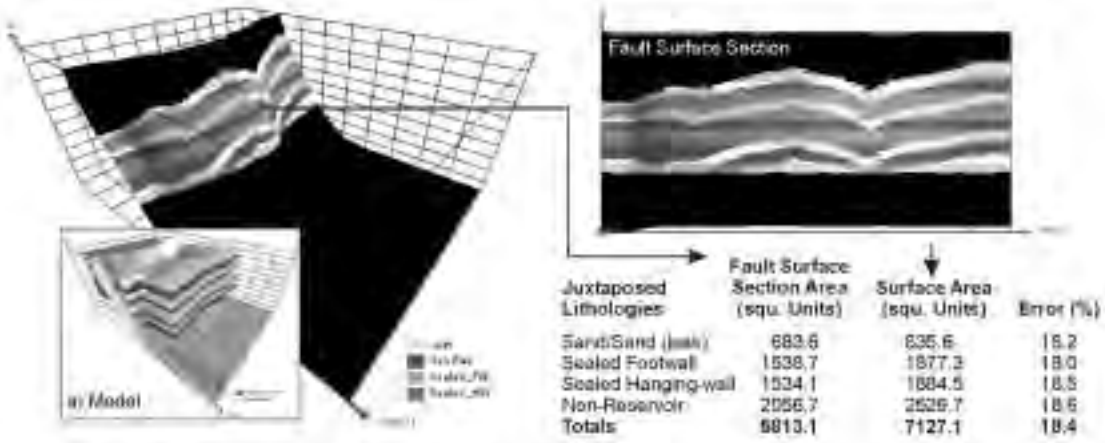

Juxtaposed Lithologies	Fault Surface Section Area (squ. Units)	Surface Area (squ. Units)	Error (%)
Sand/Sand (juxt.)	683.6	835.6	18.2
Sealed Footwall	1538.7	1877.3	18.0
Sealed Hanging-wall	1534.1	1884.5	18.5
Non-Reservoir	2056.7	2529.7	18.6
Totals	6813.1	7127.1	18.4

Figure (2) - The lithological juxtaposition relationships for a simple, synthetic, 3D model with one fault cutting an interbedded arenaceous and argillaceous sequence. The same relationships are shown projected to a fault surface section. Note the large differences in juxtaposed areas between the true 3D analysis and the fault surface section. For faults with tight surface curvature, these errors will increase.

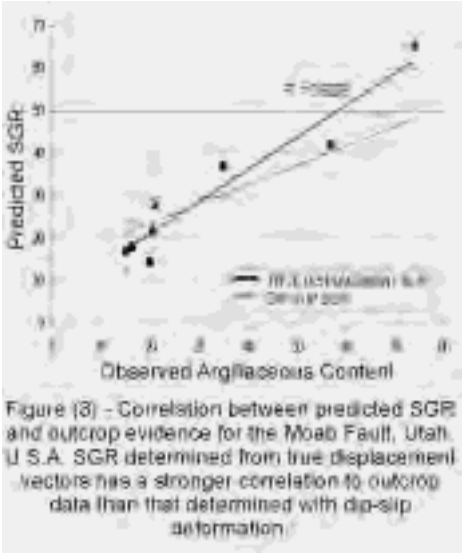

Figure (3) - Correlation between predicted SGR and outcrop evidence for the Moab Fault, Utah, U.S.A. SGR determined from true displacement vectors has a stronger correlation to outcrop data than that determined with dip-slip deformation.

explored and, by working in 4D, the juxtaposition relationships at other temporal stages in the evolution of the fault(s) can be determined.

There are many examples of faulted, hydrocarbon-bearing, sedimentary basins in which faults can seal hydrocarbons even in the presence of juxtaposed reservoir units (e.g. Fristad et al. 1997). In these cases, fault transmissibility is dependent on the properties of the fault zone. Argillaceous smearing is an example of a fault-zone process that can affect transmissibility. This process has attracted much attention due to its particular relevance to mixed arenaceous and argillaceous sequences and calibration with field examples (Foxford et al., 1996). Many workers have produced 1D and 2D models to quantify argillaceous smearing and, of these models, the *Shale Gouge Ratio* or SGR (Fristad et al., 1997) is commonly employed for the analysis of fault transmissibility.

By developing a 4D solution to the SGR it is possible to incorporate the true 3D variations in fault surface and block geometry through time into the prediction. Using this approach (fig. 3) an increased correlation between predicted gouge and outcrop examples can be demonstrated (Clarke et al., 2004). Moreover, by integrating argillaceous gouge modelling into the basin workflow it is possible to explore the effects of gouge from multiple linked faults on the sealing capacity of a reservoir, determine gouge at other temporal stages in the evolution of the fault (fig. 4) and incorporate these effects into models of hydrocarbon flow**.**

Hydrocarbon Migration

Hydrocarbon migration simulators rarely consider the effects of structure on migration and entrapment (see Huggins et al., 2004). Previous attempts at integrating the effects of faults into migration simulators have employed the results of fault analysis methods to provide a *transmissibility multiplier* applied to the cellular grid of a finite element (FE) migration model (e.g. Manzocchi et al., 1999), but these tools are designed for static reservoir models. They go some way to introducing the effects of faults into migration simulators but the geometry and evolution of the fault is not carried forward and the migration model becomes structurally static. Furthermore, the lengthy process times

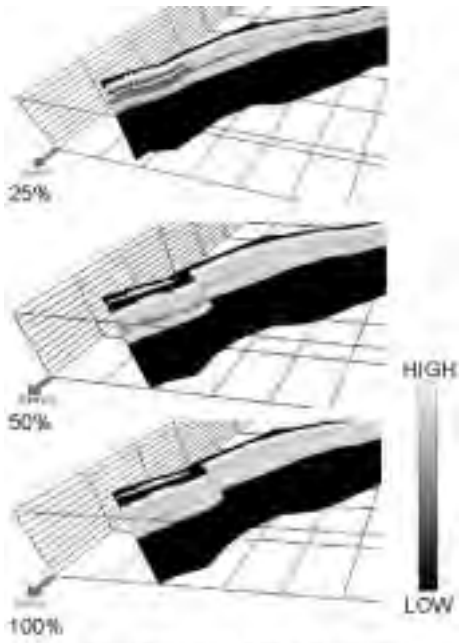

Figure (4) - Variation in SGR with percentage deformation on part of the Moab Fault (Utah U.S.A.)

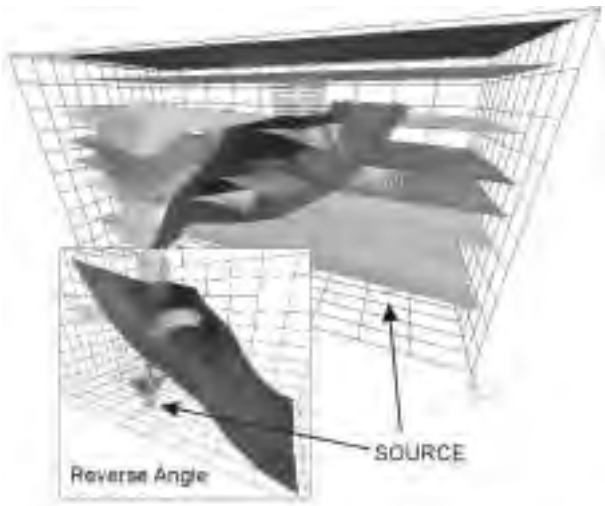

Figure (5) - IP-driven migration pathway simulations through a synthetic basin model. The effects of cross-fault juxtaposition have been included and control migration from source to various traps in fault blocks

of FE-driven migration simulation renders a risk-driven approach to basin analysis and migration impractical. The effects of poorly constrained input parameters on potential outcomes cannot be adequately assessed.

By adopting a 4D approach to migration modelling based on *Invasion Percolation* (IP) techniques (Meakin et al., 2000; Cathuruthers, 2003) it is possible to integrate the 4D effects of basin architecture and geohistory with hydrocarbon migration simulation. The technique models flow pathways (not properties) based on the statistical determination of the easiest path through the basin model. The effects of 3D fault-block geometry, transmissibility, and their temporal variation, can be incorporated (fig. 5). Using this technique, migration pathways can be simulated in minutes (rather than days or weeks) allowing multiple realisations of the same model to analyse risk associated with possible trap fill. This approach does not replace full FE-driven simulation since these techniques determine properties of the flow (such as quantities and phases) essential to the evaluation of the economic viability of the modelled accumulations. However, IP-driven flow modelling provides multiple realisations that enable the sensitivity of models to input geological parameters to be investigated and high-risk prospects to be eliminated.

Conclusions

The integrated modelling of basin architecture, geohistory, fault-seal analysis and hydrocarbon migration produces a valuable tool for a risk-driven, basin analysis workflow. Using this workflow, it is possible to explore the structural evolution of hydrocarbon-bearing basins in 4D and integrate this with fault-seal analysis and migration pathway modelling to produce a model in which the effects of structure, rock properties and basin geohistory on hydrocarbon migration can be explored. Using IP-driven hydrocarbon migration results in model process times of the order of minutes (rather than days) and the effects of poorly constrained input parameters, varying structural geometries, deformation stages, approximated rock properties and changes in fault seal capacity on trap fill can be determined to minimise risk in hydrocarbon exploration.

REFERENCES

• Allan, U.S. 1989 Model for hydrocarbon migration and entrapment within faulted structures. AAPG Bul..,73 803-81
• Burley, S.D., Clarke, S., Dodds, A., Frielingsdorf, J. Huggins, P., Richards, A., Warburton, I.C. and Williams, G.D. 2000 New

insights on petroleum migration from the application of 4D basin modeling in oil and gas exploration. Jl Geochem. Exploration, 70, 465-470.
- Carruthers, D.J. 2003 Modelling of secondary petroleum systems migration using invasion percolation techniques. Ch 3 in: Duppenbecker, S and Marzi, R. (eds) Multi-dimensional Basin Modelling. AAPG Discovery Series, No. 7.
- Clarke, S.M., Burley, S.D. & Williams, G.D. 2004 (In Press) Dynamic fault seal analysis and flow pathway modelling in three-dimensional basin models. Proceedings of the 6th Petroleum Geology Conference. London
- Foxford, K.A., Garden, I.R., Guscott, S.C., Burley, S.D., Lewis, J.J.M., Walsh, J.J. & Watterson, J. 1996 The field geology of the Moab Fault. In Huffman, A.C., Lund, W.R. & Godwin, L.H. (eds.) Geology & Resources of the Paradox Basin Special Symposium. Utah Geological Association & Four Corners Geological Society Guidebook 25
- Fristad, T., Goth, A., Yeilding, G. & Freeman, B. 1997 Quantitative fault seal prediction: a case study from Oseberg Sud. In Moller, P. & Koestler, A.G. (eds.) Hydrocarbon Seals: Importance for Exploration & Production. NPF Special Pub. 7 107-124
- Huggins, P., Burley, S.D., Sylta, O., Tommeras, A., Bland.,S, Kape, S., and Kusznir, N. 2004 (In press) Structural Restoration Techniques in 3D Basin Modelling: Implications for hydrocarbon migration and accumulation. Mar Pet.Geol.
- Mann, U., Hantschel, T. Schaefer, R.G., Kroos, B., Leythaeuser, D., Littke, R. and Sachsenhofer, R.F. 1997. Petroleum migration: mechanisms, pathways, efficiencies and numerical simulations., p403-509. In: Welte, D.H., Horsfield, B. and Baker, D.R. (eds) Petroleum and Basin Evolution. Springer. 535pp.
- Manzocchi, T., Walsh, J.J., Nell, P. & Yeilding, G. 1999 Fault transmissibility multipliers for flow simulation models. Petroleum Geoscience 5 53-63
- Meakin, P., Wagner, G., Vedvik, A., Amundsen, H., Feder, J. & Jossang, T. 2000 Invasion percolation and secondary migration: experiments and simulations. Marine & Pet. Geol. 17 777-795
- Wendebourg. J. 2000 Modelling multicomponent petroleum migration in sedimentary basins. Jl Geochem. Exploration, 70, 651-656.
- Williams, G., S. Kane, Buddin, T.S. and Richards, A. 1997, Restoration and balance of complex folded and faulted rock volumes: flexural flattening, jigsaw fitting and decompaction in three dimensions. Tectonophysics, 273, 203-218

LITHOSPHERIC MEMORY, STATE OF STRESS AND RHEOLOGY: NEO-TECTONIC CONTROLS ON EUROPE'S CONTINENTAL TOPOGRAPHY AND SEDIMENTARY BASINS

3-06

S. Cloetingh(*), F. Beekman(*), P. Andriessen(*), G. Bada(*), L. Matenco(*), P. Ziegler(**), D. Garcia-Castellanos(*), D. Sokoutis(*), N. Hardebol(*), P. Dezes(**)

(*) Faculty of Earth and Life Sciences, Vrije Universiteit, De Boelelaan 1085, 1081 HV Amsterdam, the Netherlands

(**) University of Basel, Bernouillistrasse 32, 4056, Basel, Switzerland

Summary

To date, research on neotectonics and related continental topography development has mostly focused on active plate boundaries characterised by generally high rates of deformation. The intraplate sedimentary basins and rifts of the northern Alpine foreland are associated with a much higher level of neotectonic activity than hitherto assumed. Seismicity and stress indicator data, combined with geodetic and geomorphologic observations, demonstrates that Europe's intraplate lithosphere is being actively deformed. This has major implications for the assessment of its natural hazards and environmental degradation. The lithosphere has undergone a polyphase evolution with an intense interplay between upper mantle thermal perturbations and stress-induced intraplate deformation that points to the importance of lithospheric folding of the thermally weakened lithosphere. Below we will address relationships between deeper lithospheric processes, neotectonics and surface processes with special emphasis on tectonically induced topography. The objectives are to quantify the effects of ongoing Alpine collision and Atlantic ridge push on the intraplate deformation in Europe and its impact on topography evolution and related natural hazards.

This presentation reviews the 4-D topographic evolution of the European lithosphere through a multidisciplinary approach linking geology, geophysics and geotechnology. Until now, research on neotectonics and related topography development of intra-plate regions has received little attention. Our study examines a number of selected natural laboratories in continental Europe. From orogen through platform to continental margin, these natural laboratories include the Alps/Carpathians-Pannonian basin, the NW European platform, Iberia and the Atlantic continental margin. We focus on lithosphere memory and neotectonics with special attention to thermo-mechanical structure of the lithosphere, mechanisms of large-scale intraplate deformation, Late Neogene anomalies in subsidence and uplift, and links with surface processes and topography evolution.

The northwestern European platform

The lithosphere of the Alpine foreland system has undergone repeated tectonic reactivation (Ziegler et al., 1995; 2004), expressed by significant differential vertical motions and the development of dynamic topography at large distances from plate boundaries. The nature of intraplate stress fields in continental lithosphere and its relationship to plate-tectonic driving forces has been subject to a large number of observational and modelling studies (e.g. Bada et al., 2001). These studies have revealed the existence of consistently oriented first order patterns of intraplate stress. The effect of these stresses on vertical motions in the lithosphere expressed in terms of, for example, apparent sea level fluctuations (Cloetingh et al., 1985), foreland bulges (Ziegler et al., 2002), basin inversion (Ziegler et al., 1995; 1998) and lithosphere folding (Cloetingh et al., 1999) has been demonstrated to be an important element in the dynamics of intraplate continental interiors (Bertotti et al., 2002).

Stress propagation occurs in lithosphere, which is significantly weakened by inherited structural discontinuities as well as by thermal perturbations in the upper mantle (e.g. Goes et al., 2000). Below we present thermo-mechanical models for large-scale intraplate deformation, and we discuss constraints on these models inferred from different studies carried out in the last few years on the rheology of the European lithosphere.

The Carpathians – Pannonian basin natural laboratory: Neotectonic control on continental topography

In the Carpathians – Pannonian basin natural laboratory the lithospheric to surface controls on tectonic topography have been investigated. Between processes taking place at depth and at the surface, the focus was put on the interplay between basin evolution, active tectonics, topography evolution and drainage pattern development. The principal aim has been to understand and quantify neotectonic processes controlling landscape formation and natural hazards in the light of the late-stage (late Neogene - Quaternary, 0-10 Ma) evolution of the Pannonian basin - Carpathian system. Activities aim at the understanding of topography-building processes in the aftermath of the continental collision (Cloetingh and TECTOP team, 2003). This is being achieved by acquisition of new data, interpretation of existing and novel data, and process oriented modelling studies (see Cloetingh et al., 2004,; Cloetingh and TECTOP team, 2003 and references therein).

The Carpathians – Pannonian basin system is a key locality to pursue research in the quantification of 4D topography evolution. Of particular importance is the reconstruction and modelling of neotectonic and landscape forming processes, the development and validation of a new generation of models for ongoing orogeny and its effect on the evolution of continental topography. The results obtained so far have demonstrated the importance of recent crustal deformation, particularly the substantial differential vertical movements taking place during the last several million years up to present times (Horváth and Cloetingh, 1996; Cloetingh et al., 2003, 2004). A crucial element is the investigation of the mechanics of coupling between back-arc deformation in the Pannonian basin and continental collision and foreland basin evolution along the Carpathian arc.

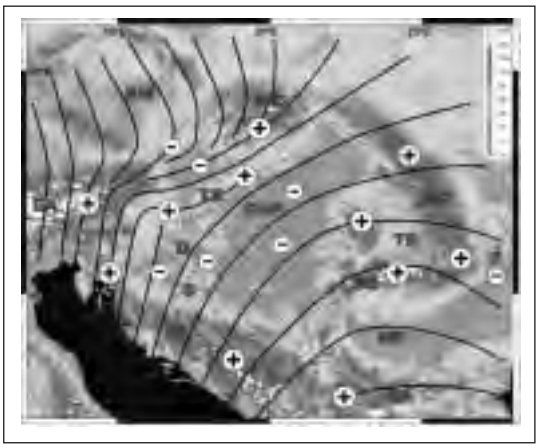

Figure 1 - Topography of the Pannonian-Carpathian system and present-day maximum horizontal stress (SHmax) trajectories (after Bada et al. 2001). + and – signs mark areas of Quaternary uplift and subsidence, respectively. L: high-resolution seismic profile in Figure 3.3. BA: Balkanides; BM: Bohemian Massif; D: Drava trough; DI: Dinarides; EA: Eastern Alps; EC: Eastern Carpathians; F: Focsani depression; MP: Moesian Platform; PB: Pannonian Basin; S: Sava trough; SC: Southern Carpathians; TB: Transylvanian basin; TR: Transdanubian Range; WC: Western Carpathians.

The back-arc domain: inversion of the Pannonian Basin

Research in the Pannonian basin has established, through a combination of dynamic and kinematic modelling, the fine structure of the mechanics of back-arc extension coupled with continental subduction dynamics in an orogenic arc system. The Pannonian basin evolved from its syn-rift to post-rift phase during Early to Late Miocene times (cc. 20-5 Ma), when back-arc extension was coupled with subduction dynamics in the Carpathian orogenic arc system (Wortel and Spakman, 2000). A close relationship has been demonstrated between the timing and nature of stress changes in the extensional basin and structural episodes in the surrounding thrust belts, pointing to an intrinsic mechanical coupling between the basin, the orogen and its foredeep (Huismans et al., 2001). In Quaternary times the basin system reached an advanced stage of evolution with respect to other Mediterranean back-arc basins with positive structural inversion taking place for the last few million of years. Basin inversion is related to changes in the regional stress field, from one of tension that controlled basin formation and subsidence, to one of compression resulting in active faulting, increased level of seismicity, and contraction and flexure of the lithosphere associated with differential vertical movements.

Modelling tectonic topography

Analysis of the geometry and kinematic evolution of the Carpathian foreland has been combined with process-oriented modelling (e.g. Cloetingh et al., 2004), both towards the reconstruction of its Tertiary evolution and the quantification of continental topography evolution and drainage pattern development in recent times (Matenco et al., 2004). Subsidence in the Focsani basin was initiated by Badenian extension, and by subsequent Late Miocene to Quaternary flexural response to the SE-ward movement of the orogenic wedge. Modelling demonstrates (Tarapoanca et al., 2004) that the extension modified the rheology of the Moesian lower plate and induced significant changes of the typical orogenic loading flexural models during subsequent Late Miocene collisional stages. Using only the present topography as a load, the 3D flexural modelling predicts the development of Focsani basin as a result of a mechanically weak Moesian platform. Differences between the thrust loading/collision mechanisms in the northern part and the bend zone of the East Carpathians rely on the much younger mechanical thermal age of the Moesian platform. The latter is affected by Early to Middle Miocene extension and post-rift thermal subsidence, equilibrating the shortening and subsequent deformations in the Carpathians bend region. As a direct result, for around 6 Ma (between Middle and Late Miocene) shortening and subsequent deformations in the Bend region proceeded without creating relief, paleobathymetry being always close to sea level. Thus, the extensional subsidence effect had to be taken into account together with the effect of N-S compressive intraplate stresses, inducing an 9 km-deep syn and post-collisional basin in the Focsani Depression (Tarapoanca et al., 2004). In order to link multi-scale observations

Intraplate deformation of Iberia

Integration of stress indicator data, gravity data, crustal kinematics data and analysis of topography and recent vertical motions demonstrates the occurrence of consistently oriented spatial patterns of large scale Alpine to recent intraplate deformation in Iberia (Cloetingh et al., 2002). The inferred upper crustal and lithospheric deformation patterns and the timing of the associated expressions at or near the surface support the existence of a close coupling with plate boundary processes operating at the margins of Iberia. Patterns of lithosphere and upper crustal folds are oriented perpendicular to the main axis of present-day intraplate compression in Iberia inferred from structural analysis of stress indicator data and focal mechanism solutions. These findings suggest the presence of lithospheric folds, with wavelengths compatible with theoretical predictions of folding wavelengths of Variscan lithosphere. Stress-induced intraplate deformation set up by plate interactions is compatible with indications for the absence of present-day deep mantle -lithosphere interactions inferred from seismic tomography.

The Norwegian rifted continental margin

The pre-rift lithosphere configuration has an important control on the rifting process (Ziegler and Cloetingh, 2004). Because of the presence of the Vøring Basin close to the final rift location, crustal

temperatures are expected to be lower on the Norwegian side than on the Greenland side. Modelling studies (Van Wijk and Cloetingh, 2002) indicate that this could result in an increased movement of material towards the Norwegian side of the break-up axis. As a consequence, according to this model, the crust is expected to be locally thickened during the final rift phase while the surface is uplifted. Both predictions will be rigorously tested, but no clear answer has been obtained. A pre-rift Moho configuration can be reconstructed from seismic data by backstripping and isostatic compensation. The newly collected and available fission track data will allow us to test the predictions on uplift (Hendriks et al., 2004).

Modelling studies have shown that the dynamics of continental rifting and break-up, and of associated basin evolution, are strongly influenced by the rheological behaviour of the crust and upper mantle (Burov and Cloetingh, 1997; Van Wijk and Cloetingh, 2002). Of particular importance is the rheological, localisation and re-activation behaviour of large scale fault and shear zones that transect the crust and possibly the upper mantle. Dynamic models have been developed for the quantification of melting processes in volcanic rifted margins (Van Wijk et al., 2001) in order to address the lateral migration of rifting and associated vertical motions established by kinematic modelling studies (Reemst and Cloetingh, 2000). It appears that break-up processes set the stage for subsequent tectonic reactivation in a compressional stress regime overprinted by upper-mantle thermal anomalies. The systematic quantification of surface uplift and erosion by thermo-chronology has revealed pronounced lateral variation of late-stage uplift along strike of the northern Atlantic.

Quantification of erosion and sedimentation through integrated analogue and numerical experiments

Laboratory experiments are very well suited to study tectonic processes in space and time, including techniques to simulate erosion and sedimentation. The quantification of the amounts and rates of erosion and sedimentation currently poses serious problems in analogue modelling. In contrast, numerical modelling (e.g. Garcia-Castellanos et al., 2003) enables us to successfully model the link between erosion/sedimentation and tectonic processes. These models, however, are less detailed in representing structural complexities and fault control. A full feedback between the two methods will make both stronger (Persson et al., 2004). Ideally, in such a setup the numerical model would indicate where and how much to erode/sediment in the analogue model for a given time step using a surface scan of the analogue model as input parameter.

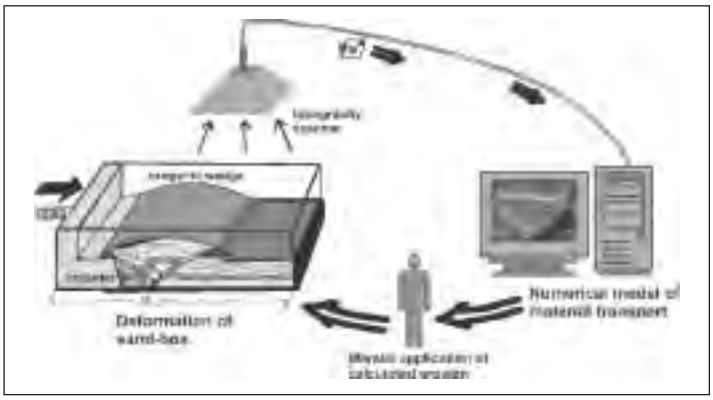

Figure 2: Added value of a coupled analogue-numerical modelling system. The analogue modeling facilities of the ISES TecLab are used to simulate the upper crustal deformation and its dynamic response to the surface erosion and sedimentation predicted by the numerical models developed in the ISES Numerical Lab. The scanner is used to transmit the surface topography of the analogue model to the numerical model. Later the calculated erosion / deposition is manually applied to the analogue model (e.g. Persson et al., 2004)

Since laboratory models are strain-rate dependant and therefore can not be stopped, it is essential to reduce the time from acquisition of the models surface scan via the numerical calculation to the actual erosion-sedimentation in the laboratory experiment as short as possible. Advanced scanning devices generate data files of 4D displacement fields, allowing close tracking and detailed interpretation of ongoing structural deformation in the simulated systems.

SELECTED REFERENCES

- Bada, G., Horvath, F., Cloetingh, S., Coblentz, D.D., Toth, T., 2001. Role of topography-induced gravitational stresses in basin inversion: The case study of the Pannonian Basin. Tectonics 20, 343-363.
- Bertotti, G., Schulmann, K., and Cloetingh, S.A.P.L. (Eds.), 2002. Continental collision and the tectono-sedimentary evolution of forelands. European Geosciences Union Stephan Mueller Special Publication Series 1, 236pp.

- Burov, E., Cloetingh, S.A.P.L., 1997. Erosion and rift dynamics: new thermo-mechanical aspects of post-rift evolution of extensional basins. Earth Planet. Sci. Letts 150, 7-26.
- Cloetingh, S.A.P.L., Burov, E., and Poliakov, A., 1999. Lithosphere folding: primary response to compression ? (from central Asia to Paris Basin). Tectonics 18, 1064-1083.
- Cloetingh, S.A.P.L., Burov, E., Beekman, F., Andeweg, B., Andriessen, P.A.M., Garcia Castellanos, D., de Vicente, G. and Vegas, R., 2002. Lithospheric folding in Iberia. Tectonics 21, 10.1029/2001TC901031.
- Cloetingh, S., Ziegler, P., Cornu, T., ENTEC Working Group, 2003a. Investigating environmental tectonics in northern Alpine foreland of Europe. EOS, Transactions, American Geophysical Union 84 (36), 349+356-357.
- Cloetingh, S., Horváth, F., Dinu, C., Stephenson, R.A., Bertotti, G., Bada, G., Matenco, L., Garcia-Castellanos, D. and the TECTOP Working Group, 2003b. Probing tectonic topography in the aftermath of continental convergence in Central Europe. EOS, Transactions, Am. Geophys. Un. 84, 89-93.
- Cloetingh, S., Burov E., Matenco, L., Toussaint G., Bertotti G., Andriessen P.A.M., Wortel M.J.R., Spakman W., 2004. Thermo-mechanical controls on the mode of continental collision in the SE Carpathians (Romania), Earth Planet. Sci. Letts. 218, 57-76.
- Garcia-Castellanos, D., J. Verges, J.M. Gaspar-Escribano & S. Cloetingh, 2003. Interplay between tectonics, climate and fluvial transport during the Cenozoic evolution of the Ebro Basin (NE Iberia). Journal of Geophysical Research 108, doi:10.1029/2002JB002073.
- Goes, S., Govers, R., Vacher, P., 2000a. Shallow upper mantle temperatures under Europe from P and S wave tomography. Journal of Geophysical Research 105, 11153-11169.
- Hendriks, B.W.H., Andriessen, P.A.M., Dunai, T.J., Cloetingh, S.A.P.L., 2004 (submitted). Denudation history of the Northern Scandes range; Comparison with the record from southern Norway. Tectonophysics.
- Horváth, F. and Cloetingh, S., 1996. Stress-induced late stage subsidence anomalies in the Pannonian Basin. Tectonophysics 266, 287-300.
- Huismans, R.S., Podlachikov, Y.Y., & Cloetingh, S.A.P.L., 2001. Transition from passive to active rifting: Relative importance of asthenospheric doming and passive extension of the lithosphere. Journal of Geophysical Research 106, 11271-11291.
- Maßenco, L., Bertotti, G., Marin, M., Cloetingh, S. and Schmid, S., 2004 (submitted). Pliocene to Quaternary tectonics of the SE Carpathians foreland (Romania), Tectonophysics.
- Persson, K.S., Garcia-Castellanos, D., Sokoutis, D., 2004. River transport effects on compressional belts: First results from an integrated analogue-numerical model. Journal of Geophysical Research 109, 10.1029/2002JB002274.
- Reemst, P.A., and Cloetingh, S., 2000. Polyphase rift evolution of the Voring margin (Mid Norway): constraints from forward tectono-stratigraphic modelling. Tectonics 19, 225-240.
- Tarapoanca, M., Garcia-Castellanos, D., Bertotti, G., Matenco, L. and Cloetingh, S., 2004. Role of the 3D distributions of load and lithospheric strength in arcuate orogenic arcs: poly-stage subsidence in the Carpathians foredeep. Earth Planet. Sci. Letts., in press.
- Van Wijk, J.W., Cloetingh, S., 2002. Basin migration caused by slow lithospheric extension. Earth Planet. Sci. Letts. 198, 275-288.
- Van Wijk, J.W., Huismans, R.S., ter Voorde, M., and Cloetingh, S., 2001. Melt generation at volcanic continental margins: no need for a mantle plume? Geophys. Res. Letts. 28, 3995-3998.
- Wortel, R., Spakman, W., 2000. Subduction and Slab Detachment in the Mediterranean-Carpathian Region. Science 290, 1910-1917.
- Ziegler, P.A., Cloetingh, S., 2004. Dynamic processes controlling evolution of rifted basins. Earth Science Reviews 64, 1-50.
- Ziegler, P.A., Cloetingh, S., van Wees, J.D., 1995. Geodynamics of intraplate compressional deformation; the Alpine foreland and other examples. Tectonophysics 252, 7-61.
- Ziegler, P.A., Schumacher, M.E., Dezes, P., van Wees, J.D., Cloetingh, S., 2004. Post-Variscan evolution of the lithoshere in the Rhine Graben area: constraints from subsidence modeling. Geol. Soc. Lond. Spec. Publ., in press.

CENTRIFUGE MODELLING OF PERIODIC INSTABILITIES DURING CONTINENTAL EXTENSION 3-07

G. Corti

Dipartimento di Scienze della Terra, Università degli Studi di Firenze, via G. La Pira, 4, 50121 Firenze, Italy

Summary

In this work I present centrifuge models investigating the development of periodic instabilities during continental extension. The results of modelling suggest that unstable lithospheric extension is accompanied by development of regularly-spaced structures at two characteristics wavelength: a crustal (shorter) wavelength and mantle (longer) wavelength. The thickness of the brittle upper crust and the strain rate have a major influence on the spacing of instabilities: an increase in the brittle layer thickness and a decrease in the strain rate lead to an increase in both crustal and mantle wavelengths. Wavelengths for crustal deformation varies from ~10 km to ~45 km for typical crustal thicknesses and strain rates of ~10 mm yr^{-1}; for lower strain rates (4 mm yr^{-1}) these values varies from ~20 km to ~55 km. Mantle wavelengths are typically in the range of ~60-140 km for high strain rate and ~75-100 km for high strain rate. The characteristics wavelengths also increase increasing the amount of total extension, whereas variations in the thickness of the ductile lower crust have little effects on the

spacing of structures. These results are similar to previous numerical and analytical models and match the patterns of periodic basins and ranges in regions undergoing wide rifting.

Abstract text

Wide rifts, characterised by deformation distributed over areas as wide as 1000 km, are documented in many regions undergoing active extension such as the Basin and Range of Western United States, the Aegean, the West Antarctic Rift System. Both numerical and analogue models of continental extension agree in that wide extensional regions develop in regions of relatively low bulk strength of the continental lithosphere resulting from high geothermal gradients (Buck, 1991; Brun, 1999; Corti et al., 2003). This high gradients are normally related to thermal relaxation during post-orogenic collapse (e.g., Brun, 1999). In case of such distributed deformation, many studies have shown that normal faults and sedimentary basins develop at a regular spacing giving rise to lithospheric-scale periodic instabilities. Particularly, numerical and analytical models of whole-lithospheric extensional flow have shown the development of periodic instabilities during extension at two different scales. Short-wavelength instabilities develop in association with necking of the brittle upper crust, whereas long-wavelength instabilities are associated with an upward deflection of the Moho and a regional thinning of the lithospheric mantle. These dominant wavelengths are primarily controlled by the thickness of the strong layers, with the upper crust thickness having the major influence on the spacing of structures (e.g., Zuber et al., 1986; Martinod and Davy, 1992). Many quantitative relations between the upper crust thickness and the dominant wavelengths of perturbations have been developed in previous numerical models commonly showing that ratio between the spacing of structures and the thickness of the upper brittle crust (normalized wavelength) is approximately 3-4 for short-wavelength instabilities (e.g., Fletcher and Hallet, 1983; Ricard and Froidevaux, 1986; Zuber and Parmintier, 1986; Zuber et al., 1986; Martinod and Davy, 1992). For long-wavelength instabilities the normalized value increases to about 11-15 (e.g., Zuber et al., 1986). However, these values depend on the assumed rheological stratification of the lithosphere and the number of plastic and viscous layers using during the modelling.

Analogue models are less prone to develop stretching instabilities, as in many case the extensional deformation is obtained by applying a velocity discontinuity that localises deformation and focus extension on a narrow zone. However, 3-layer analogue models by Benes and Davy (1996) showed the development of periodic instabilities at two dominant wavelengths controlled by the thickness of the upper brittle layer. Normalized wavelengths in these experiments are 2-3.5 and ~8 for short- and long-wavelength instabilities, respectively.

In this modelling work, centrifuge models are used to investigate the mechanics of wide continental extension and to model the control of rheological stratification and the strain rate in the development of periodic instabilities. Particularly, the centrifuge forces imposed a uniform stress field on the models and the different distribution of deformation was only imposed by the different rheological stratification of the models, representing a good approximation of the natural case. The model rheology approximates a 3-layer continental lithosphere with a strong brittle upper crust and strong ductile mantle separated by a weak lower crust (e.g., Zuber et al., 1986). This rheology well applies to regions undergoing wide rifting as the Basin and Range of western US or the Aegean, where the geothermal gradient is high and the occurrence of a brittle mantle is prevented, as indicated by seismic activity which is restricted to the upper brittle crust (e.g., Parsons, 1995; Gautier et al., 1999). Strength profiles for thickened lithospheres undergoing extension and characterised by high heat flows shows that the contribution of the strength of the mantle is normally subordinated to that of the upper brittle crust. In the modelling, the scaled thickness of the brittle upper crust was varied in the range of 5-30 km; two different series were performed at strain rates of 4 and 10 mm yr^{-1}. All the models were stretched up to 40% bulk extension.

Results of the experiments show that continental extension is accommodated by regular boudinage of the brittle upper crust, accommodated by passive flow of the lower crust and folding of the lower-upper crust boundary. Results support that the crustal wavelength is primarily controlled by the thickness of the brittle upper layer and the strain rate (Figures 1, 2). In particular, the crustal wavelength increases increasing the upper crust thickness and decreasing the strain rate (Figure 1).

For high scaled strain rates (10 mm yr^{-1}), the scaled wavelength varies from ~10 km (for scaled upper crust thickness of 5 km) to ~45 km (for scaled upper crust thickness of 30 km; Figure 2). For low strain rates (4 mm yr^{-1}) these values varies from ~20 km (for scaled upper crust thickness of 10 km) to ~55 km (for scaled upper crust thickness of 20 km; Figure 2). Normalized wavelength are of 1.5-2.5 and 2-3 for high and low strain rates, respectively (Figure 1). Similarly, the amplitude of lower crustal upraising increases increasing the upper crust thickness and decreasing the strain rate (Figure 1). A similar trend is displayed by the mantle wavelength: its scaled values are in the range of ~60-140 km for high strain rate and ~75-100 km for high strain rate; the normalised values are in the range of 5-12 (Figure 1). Notably, increasing the upper crust thickness and decreasing the strain rate the number of sedimentary basins decreases whereas their length increases.

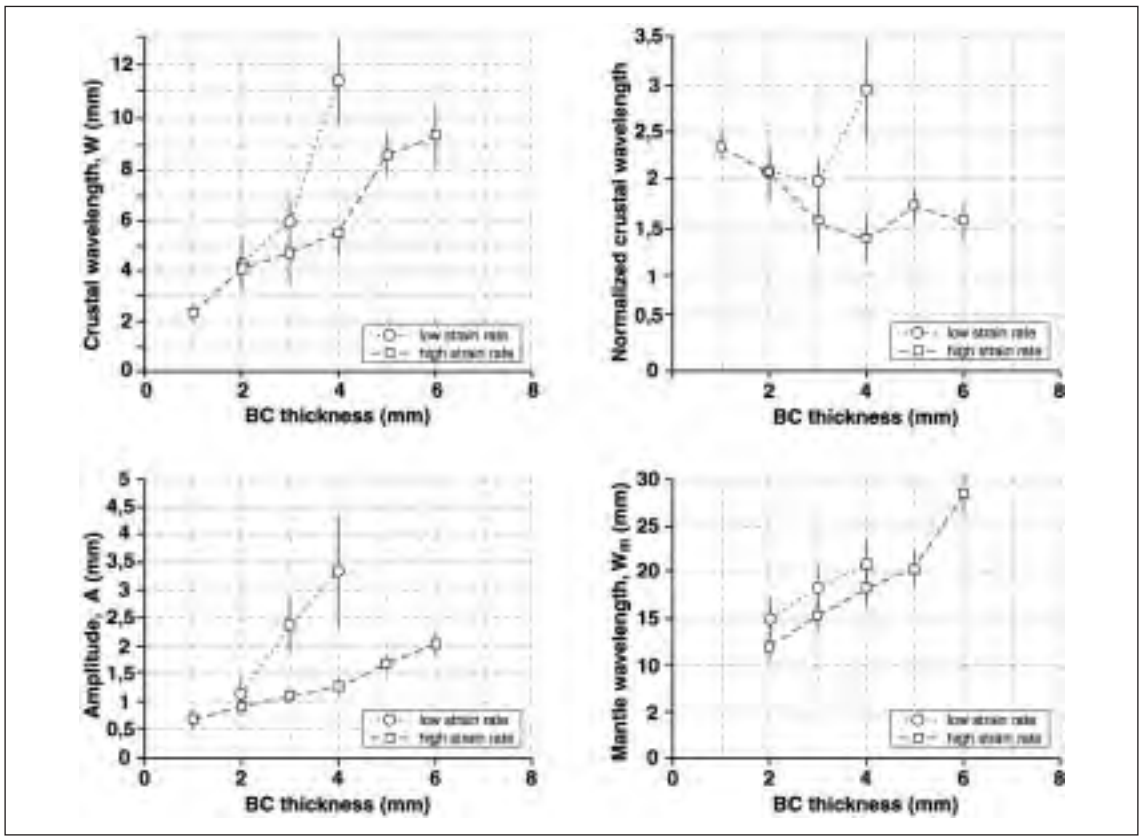

Fig.1 - Experimental results.

The characteristic mantle and crustal wavelength are also dependent on the amount of total extension, an increase of which shift the scaled spacing of instabilities to higher values (Figure 2). Conversely, variations in the thickness of the ductile lower crust have minor effect on the characteristic wavelengths. In particular, a decrease in the thickness of the ductile crust decreases the long wavelengths, but has no effect on the shorter ones.

These results are in agreement with previous analogue modelling results of Benes and Davy (1996) as well as previous numerical modeling works. In particular, current results well accord with previous models (e.g., Zuber et al., 1986) in that (1) increasing the thickness of the upper crustal layer (keeping the thickness of both lower crust and mantle constant) increases both short and long dominant wavelengths and (2) a decrease in the thickness of the ductile crust decreases the long wavelengths, but has no effect on the shorter ones. In addition, similarly to previous models the current experiments suggest the short-wavelength deformation nearly vanishes at the crust-mantle boundary, predicting a nearly flat Moho despite strong folding of the upper-lower crust boundary. A flat Moho is a characteristic of Basin and Range-like deformation.

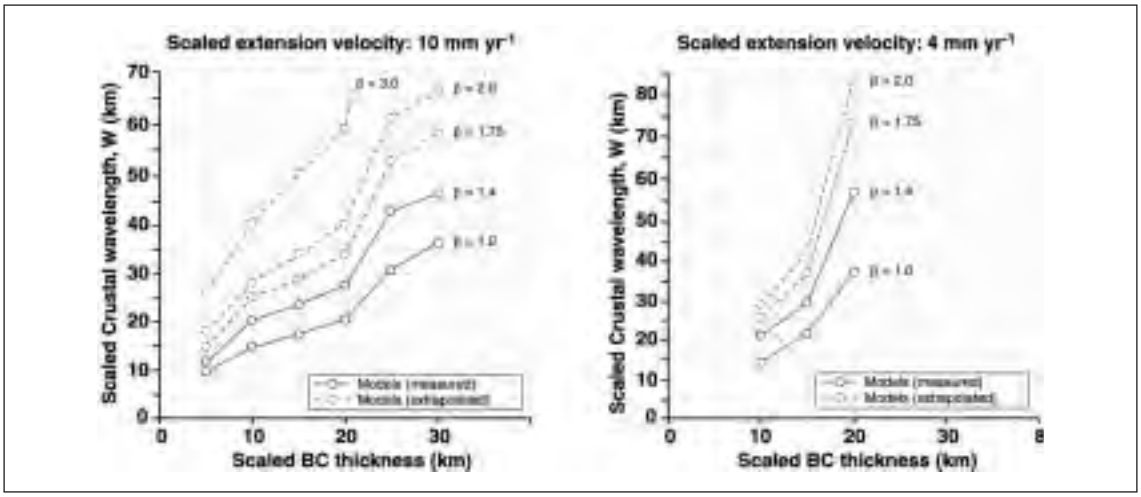

Fig. 2 - Scaled spacing of instabilities results as a function of the beta factor (final/initial width of models).

Comparison of the current model results with natural examples show a very close similarity in terms of geometry and wavelengths of deformation. In particular, characteristic wavelengths fit well the reported spacing of structures in the Basin and Range, the Aegean (Cyclades, Rhodopes, Menderes Massif) and the West Antarctic Rift System.

REFERENCES

- Buck, W.R. (1991). Journal of Geophysical Research, 96, 20161-20178.
- Brun, J.-P. (1999). Philosophical Transactions of the Royal Society of London, A, 357, 695-712.
- Corti G., et al. (2003) Earth-Science Reviews, 63, 169-247.
- Fletcher, R.C., and Hallet, B. (1983). Journal of Geophysical Research, 88, 7457-7466.
- Ricard Y., and Froidevaux C. (1986). Journal of Geophysical Research, 91, 8314-8324.
- Zuber, M.T., and Parmentier E.M. (1986). Earth and Planetary Science Letters, 77, 373-383.
- Zuber M.T., Parmentier E.M., and Fletcher R.C. (1986). Journal of Geophysical Research, 91, 4826-4838.
- Martinod, J., and Davy, P. (1992). Journal of Geophysical Research, 97, 1999-2014.
- Parsons, T. (1995). In: Olsen. K.H. (ed.), Continental Rifts: Evolution, Structure, Tectonics, Developments in Geotectonics, 25, 277-324.
- Gautier, P. et al. (1999). Tectonophysics, 315, 31-72.

INTERACTION BETWEEN NORMAL FAULTS AND PRE-EXISTING THRUST SYSTEMS IN LABORATORY PHISICAL MODELS 3-08

S. Lucia(*), G. Corti(*), M. Bonini(**),F. Sani(*), F. Mazzarini(***)

(*) Dipartimento di Scienze della Terra, Università degli Studi di Firenze, Via La Pira, 4 – 50121 Firenze (Italy)

(**) CNR-IGG, Sezione di Firenze, La Pira, 4 – 50121 Firenze (Italy)

(***) CNR-IGG, Via G. Moruzzi, 1 – 56124 Pisa (Italy)

Summary

We present the results of analogue models designed to investigate the interactions between normal faults and pre-existing thrusts. Experiments considered a first compressive phase followed by extension at variable obliquity angles (α). Results of experiments allow to identify three different main modes of interactions between pre-existing compressive structures and later extensional ones, depending on the kinematics of extension. (1) For orthogonal extension (α=0°) compressive structures strongly influence the development of normal faults: graben structures nucleate within previous thrust anticlines and the normal faults reactivate thrust faults at depth (*branching at depth mode of*

interaction); (2) For highly oblique extension ($\alpha \geq 45°$), no influence on later extension-related faults in exerted by compressive structures and extension-related steeply-dipping faults (characterised by oblique component of movement) displace thrust faults (*no interaction mode*); (3) For intermediate obliquity angles (α=15°, 30°), an *intermediate mode of interaction* characterise the experiments, as the two above-described behaviours (*no interaction + branching at depth*) coexists in different regions of the models.

Abstract text

It has been shown that in many cases pre-existing thrust systems play an important role in controlling the architecture of superimposed normal faults. Mechanical theory suggests that the probability of reactivation of pre-existing thrust faults depends on their orientation respect to the superimposed extensional stress field (e.g., Sibson, 1985). The process was investigated in previous analogue models (Krantz, 1991; Faccenna et al., 1995) suggesting that the initial dip of thrust faults has a major control on the development of successive normal faults. Both works considered a first phase of compressional deformation designed in order to obtain progressively steeper thrust faults prior to extension. In models by Krantz (1991) extensional reactivation of reverse faults was restricted to structures initially dipping at angles >40°, in accord with prediction based on the Mohr envelope for reactivation of faulting in sand. In these models two different categories of normal faults formed: linked faults were influenced by the presence of pre-existing thrust faults, determining atypical fault geometry especially in terms of anomalously low dip; unliked faults displayed evolution and geometrical features that did not link to pre-existing structures. Results of models by Faccenna et al. (1995), suggested that three different types of interactions between pre-existing thrusts and successive normal faults may arise: (1) *No interaction* occurs in case of low-dip thrusts (<32°±1°) and normal faults form independently displacing pre-existing thrusts; (2) *branching at depth* of normal faults onto thrust planes is observed for intermediate dip angles (32°±1°-41°±1°); (3) total reactivation occurs on thrust planes dipping at angles higher than 41°±1°. These three basic models of interactions between normal faults and thrust systems have been recognised and described in natural systems (e.g., Williams et al., 1989; Faccenna et al., 1995).

In this study, we present a series of analogue models investigating the interactions between pre-existing thrusts and successive normal faults when a first orthogonal compressive phase is followed by extension occurring at variable obliquity angles (α) to the main compressive structures, with angles α of 0°, 15°, 30°, 45° and 60°. The experiments have been performed at the Tectonic Modelling Laboratory of the CNR-IGG settled at the Earth Science Department of Florence University (Italy) and deformed through the use of a pure and simple shear deformation apparatus. A 5-cm thick sand pack represented a sedimentary cover in nature, overlying a décollement layer modelled by silicone (Mastic Rebodissant 29, produced by CRC France). Compression and extension at different angles have been obtained by movement of two orthogonal motors controlled by a central unit. Deformation during the extensional phase was localised by a thin acetate sheet at the base of the model creating a velocity discontinuity (VD). Compression has been driven at the constant velocity of 40 mm/h (corresponding to a scaled value of ~10 mm/yr) up to 25% bulk shortening. Extension has been applied at 6 mm/h (corresponding to a natural rate of ~1,5 mm/yr) up to 10% local extension in the central part of the model.

Orthogonal compression during the first deformative phase resulted in regularly-spaced fore- and back-thrusts defining anticline structures distributed over the whole model surface. Dip of thrusts was typically in the range of 32°-35°. During the second phase, the structural pattern was highly dependent on the obliquity angles a. For low angles (α=0°), normal faults sub-parallel to the main thrusts were distributed over a wide area in the central part of the model, in correspondence of the VD. These faults mainly localised in correspondence of the anticlines defined by fore- and back-thrusts. A narrower deformed zone centred above the VD characterised higher obliquity angle ($\alpha \geq 30°$) models, with faults were exhibiting an important transcurrent component of movement. Overall, comparison of the different models suggests that increasing the obliquity angle, the models showed a decrease in both the width of the deformed zone and fault density, whereas the dip of main faults increased as expected by the higher transcurrent character of the fault for high obliquity angles (α=45°, 60°).

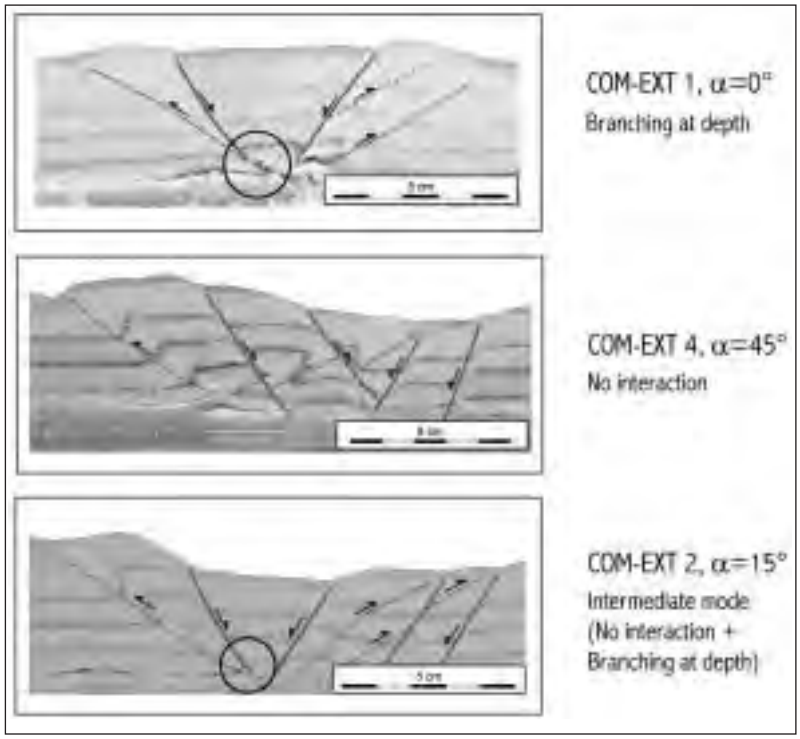

Fig. 1 - Modes of interaction between pre-existing thrusts and normal faults.

Interpretation of model results allows to highlight three different main modes of interactions between pre-existing compressive structures and later extensional ones (Figure 1). The difference is mainly a function of the obliquity angle (α).

(1) For α=0° early compressive structures strongly influence the development of successive normal faults that give rise to graben structures nucleating within and dismembering previous thrust anticlines. In this case, the master fault of the grabens join at depth with the thrust planes, inverting the movement on these faults and thus reactivating their deepest portions. The geometry of this fault is similar to the linked faults of Krantz (1991) and the mode of interaction between thrusts and later faults is analogous to the *branching at depth mode* obtained by Faccenna et al. (1995) for similar thrust initial dips (32°-35°). The antithetic fault cuts through the whole sand pack not interacting with thrust faults (unlinked faults of Krantz, 1991).

(2) For high obliquity angles ($\alpha \geq 45°$), no influence on later extension-related faults in exerted by compressive structures, in a similar fashion to the *no interaction mode* of Faccenna et al. (1995). Steeply-dipping faults characterised by important transcurrent motion displace thrust faults and nucleate above the VD, showing no relations with previous anticline structures (unliked faults of Krantz, 1991). Notably, although the *no interaction mode* was suggested by Faccenna et al. (1995) to characterise dip of thrusts <32°±1°, in the current models this behaviour is also obtained for initial thrust dips in the range of 32°-35°.

(3) For intermediate obliquity angles (α=15°, 30°), an *intermediate mode of interaction* characterises the experiments, as the two above-described behaviours (*no interaction + branching at depth*) coexists in different regions of models.

The above results suggest that the mode of interaction between pre-existing thrusts and newly-formed normal faults is not only influenced by the dip of thrusts but also by the kinematics of the extensional phase. However, total reactivation was never observed in the models, supporting theoretical predictions from Mohr envelopes for reactivation of pre-existing faults in sand as well as observations by Krantz (1991) and Faccenna et al. (1995) in that initial thrust dip higher than ~40° is needed for this mode of interaction.

REFERENCES

- Faccenna, C. et al. (1995). Journal of Structural Geology, 17, 1139-1149.
- Krantz, R.W. (1991). In: The Geometry of Normal Faults (edited by Yielding A.M. and Freeman, B.), Spec.Publ. Geol. Soc., 56, 219-229.
- Sibson, R.H. (1985). Journal of Structural Geology, 7, 751-754.
- Williams, G.D. et al. (1989). In: Inversion Tectonics (edited by Cooper M.A. and Williams, G.D.), Spec.Publ. Geol. Soc., 44, 3-15.

USE OF STRATIGRAPHIC MODELLING IN SEDIMENTARY BASINS 3-09

D. Granjeon, J.-M. Daniel
Institut Français du Pétrole - 1 et 4 avenue de Bois Préau - 92500 Rueil Malmaison - France

Summary

Thanks to the recent developments in numerical modelling, study of the relationship between tectonics and sedimentation can now be investigated using coupled stratigraphic and structural numerical models. This paper is focused on this new technology, and in particular on the stratigraphic modelling : its principles and some applications.
A forward stratigraphic simulation is based on the modelling of three main geological "processes" through time : creation of accommodation space, supply and transport of sediment. An application on the Colorado Basin, Argentina, is presented to illustrate these principles. Stratigraphic forward model was used in this frontier area to optimise and validate the geological model, to simulate in 3D the stratigraphic architecture, and finally to asses location of generative source-rocks and review the basin hydrocarbon potential.
This stratigraphic model was then coupled to a structural model, and tested on the Central Apennines, Italy. The studied area is situated in the East of the Umbria-Marche Apennines, where Messinian to Pliocene synflexural and synkinematic series crop out. Given the eastward migration of the foredeep depocentres with time, the series deposited in a flexural foreland setting were progressively involved in thrusting, uplifted and eroded. The main results of the coupled modelling allowed us to iteratively correct and refine the structural interpretation of the seismic data, define the sedimentary mass balance of the studied region and establish the chronology of the major faults by fitting the simulated facies, thickness and lithology of the synkinematic sediments to our observations in the field and on seismic.
Stratigraphic models, and moreover coupled stratigraphic and structural numerical models, are a dreamed key to decipher the stratigraphic records in synkinematic series, but great scientific effort still have to be put on their developments to close the process-deposit loop in complex tectonic settings.

Abstract text

The study of the relationship between tectonics and sedimentation can be a key to decipher stratigraphic records in synkinematic series, such as in foreland basins (e.g. Canadian Foothills), or in deltaic series affected by growth faulting (e.g. offshore West Africa) or salt tectonics (e.g. Gulf of Mexico, Brazilian margin). Thanks to recent developments in numerical modelling, this relationship can now be simulated and quantified using coupled stratigraphic and structural modelling. This paper is focused on this new technology, and in particular on the stratigraphic modelling : its principles and some applications in a relatively quiet sedimentary basin (Colorado Basin, Argentina), and a more tectonically active foreland basin (Central Apennines, Italy).

Principles of stratigraphic modelling

Stratigraphic forward models have been developed since the 1970s (Harbaugh and Bonham-Carter, 1970), and are more and more used in universities to teach sequence stratigraphy and sedimentology, and in petroleum industries to help explorers and reservoir engineers to define a play concept, characterise field architectures and petrophysical properties.
A forward stratigraphic simulation is based on the modelling of geological processes through time in a sequence of time step, from the past up to the present, using deterministic rules. At each time step, three main "processes" are taken into account : creation of accommodation space, supply of sediment, and transport of sediment. Stratigraphic forward models can be roughly divided into three main classes, depending on the way they simulates the transport of sediment : geometrical, fluid-flow and process-base models.
The geometrical models (e.g. Jervey, 1988, Cross and Lessenger, 1999), are mainly based on an 2D equilibrium profile defined by some empirical rules ; dynamics of sediment transport is not

considered. Due to the increasing power of computers, they are progressively neglected and replaced by fluid-flow and/or dynamic-slope models. The fluid-flow models (e.g. Tetzlaff and Harbaugh, 1989, Syvitski and Bahr, 2001), use very detailed equations to simulate the movement in three dimensions of each grain of sediment; they are commonly used in fluvial and coastal engineering but, as they require very detailed and complex parameters, and are still highly computer time consuming, they are still difficult to condition on real outcrop, well or seismic data. The dynamic-slope models (e.g. Paola *et al*, 1992, Granjeon and Joseph, 1999, Warrlich *et al,* 2002, Clevis *et al*, 2003), are an intermediary between these two previous model families : they use deterministic empirical laws to simulate the transport of sediment. Their pragmatic philosophy allows to (1) simulate large-scale physical behavior of sedimentary systems, and (2) fit model outputs on real data and rapidly test geological scenarii (one simulation can be performed in a few minutes on PC or Unix workstations).
Stratigraphic forward models can also divided into sub-classes depending on their ability to simulate clastic, and/or carbonate, and/or mixed sedimentary systems, but it's beyond the scope of this paper to present a full review of all of them. The key point is that they quantify interactions between the three main "processes" that control sedimentation : accommodation, sediment supply and sediment transport.
To illustrate the potential gains provided by such a stratigraphic model, let us focus on one of them, named Dionisos, and have a look on some of its recent applications. Dionisos (Granjeon and Joseph, 1999) has been built to study the evolution of sedimentary basin stratigraphy at a large scale (tens to hundreds of kilometers, hundreds of thousands to hundreds of millions of years). The three main "processes" (accommodation space, supply and transport) are simulated using the following assumptions or empirical laws :
(1) Accommodation space is defined as the sum of a vertical subsidence (defined by users and/or computed using a 3D elastic flexural model), and an eustatic curve (also defined by users and/or predefined using the Haq's curve). Compaction may be simulated using simple burial-depth laws to take into account additionnal accommodation space created by synsedimentary differential compaction.
(2) The supply of sediment may be an inflow (volume of water and sediment coming into the basin from the erosion of adjacent source areas), or an *in situ* production (volume of carbonated sediment produced in marine environments, or dissolved in continental areas, ...), controlled by physical parameters (bathymetry and wave energy) and/or ecological rules (competition between species, requirements of a hard-ground, ...).
(3) The transport of sediment is finally simulated using three empirical laws, which described (1) the low-energy long-term fluvial and gravity-driven transport (using a water-driven diffusion equation controlled by long-term climatic parameters), (2) the high-energy short-term transport induced by catastrophic floods and hyperpycnal flows (using a simplified Saint-Venant equation controlled by short-term climatic parameters), and (3) the catastrophic slope failure (using a Coulomb criteria) and debris flows associated to (using a Newton equation). To be transported by one of these three processes, sediment must first be produced by weathering processes, depending on the shear stress induced by the local water discharge.
The behavior of Dionisos may be either thus of a detachment limited erosion model (when wheathering is low or localised, such as in mountainous areas, or in submarine canyons) or transport capacity limited model (when weathering is high, such as in deltaic plain).

Applications of stratigraphic modelling in sedimentary basins

The Colorado Basin, Argentina (Mancilla *et al*, 2002), is located along the Atlantic margin of Argentina, and records 12000 meters of continental and marine sediments mainly explored by seismic since the ´60. Eighteen exploration wells located on the basin borders investigated only the upper-third of the sedimentary column, from the Upper Cretaceous to Quaternary. Existence of an active petroleum system is proven by several oil shows.
Stratigraphic forward model was used in this frontier area, where relatively few data are available, to optimize and validate the geological model, to simulate in 3D the stratigraphic architecture, and finally to asses location of generative source-rocks and review the basin hydrocarbon potential. The

Colorado basin was initiated during an early Mesozoic rifting period, followed by a Cretaceous to Miocene sag period, to ultimately reach the present day passive margin configuration.
A stratigraphic simulation was constraint by excellent seismic data and these few wells, to quantify the geological parameters (accommodation, supply and transport) and evaluate the facies distribution in the non-drilled areas (Jurassic and Lower Cretaceous, in the eastern part of the basin). It indicates a drastic change from (1) alluvial fans, lacustrine and restricted marine environments, to (2) fluvial plaines and open marine environments, around the Atlantic spreading period corresponding to the beginning of the sag phase.
The 4D stratigraphic gridded model was integrated in a basin software which provides the kitchen evolution for the different potential source-rocks, to evaluate the exploration potential of this basin.

Principles of coupled stratigraphic and structural modelling

Classical stratigraphic models work on a cartesian numerical grid, and take into account only vertical basin deformation. Their use is thus restricted to relatively quiet basin, and in particular they cannot be applied on complex tectonic settings, with thrusts, growth faults, or shale/salt diapirsms. On the contrary, forward and backward structural models are able to deal with such complex systems, but they usually represent only large-scale basin deformation, without any detailed description of the stratigraphy of the sedimentary layers. They usually deforme, break and move homogeneous sedimentary layers.
A coupled stratigraphic and structural model has been the dream of sedimentary and structural geology expected since a long time, and thanks to the recent developments in computers and numerical modelling, its birth is approaching at a fast rate now. To illustrate the gains of such a dream, the link between Dionisos and Thrustpack, the structural model developed at IFP, is presented here.
The Thrustpack model allows to model 2D geological cross sections of foreland and fold-and-thrust belt areas. It comprises a forward structural module used to reproduce the evolution of the geometry of the different structural units through time, allowing thrusting and backthrusting using a flexural-slip deformational mode, syn-orogenic sedimentation and erosion, and basement subsidence. This 2D structural model was linked to Dionisos using the following methodology. Each sedimentary layer is described as a set of cells, each of them having a more or less square shape before thrusting. At each stratigraphic time step, (1) Thrustpack provides a first estimation of the deformation of the basin, using a very simple erosion / sedimentation law (assuming a geometrical equilibrium profile). (2) This estimated deformation allows to define displacement vectors of each sedimentary layer, and in particular of each cell of these layers. These displacements are then split in two parts : a vertical and horizontal components. (3) A classical stratigraphic simulation is then used, taking into account only the vertical component. (4) The new depositional profile, and the lithology content of each cell of each sedimentary layer, which have been created (sedimentation of a new layer) or updated (erosion of an ancient layer) by the stratigraphic model, are then sent to the structural model to update the cross section, the geometry of each layer, and the sedimentary characteristics of each cell of each layer.
Also this methodology is quite heavy, it allows to test rapidly the link between stratigraphic and structural model. To really model the structural and stratigraphic evolution of sedimentary systems in three dimensions, it is clear that we need to develop a fully integrated model, but this simple link already provides interesting outputs.

Applications of coupled stratigraphic and structural modelling in foreland basins

The Central Apennines, Italy (Albouy *et al*, 2003), is a dreamed area where the link between stratigraphic and structural numerical models is enhanced. The studied area is situated in the East of the Umbria-Marche Apennines, where Messinian to Pliocene synflexural and synkinematic series crop out. Given the eastward migration of the foredeep depocentres with time, the series deposited in a flexural foreland setting were progressively involved in thrusting, uplifted and eroded. Four regional seismic sections were interpreted, unfolded and balanced.
To build a fully 2D gridded model of this area, where foreland basin turbidites are an exploration target, stratigraphic (Dionisos) and structural (Thrustpack) numerical models were linked. During each time step of the forward simulation, Thrustpack defined the basin deformation ; this

deformation, with thrusts involving the basement, induced a total shortening of around 20%, which represent a relative horizontal movement of sedimentary units up to several tens of kilometers. Then Dionisos simulated the evolution of the stratigraphy, controlled by the three main stratigraphic parameters (accommodation defined by Thrustpack, supply and transport).
The results of the coupled modelling allowed us to iteratively correct and refine the structural interpretation of the seismic data, define the sedimentary mass balance of the studied region and establish the chronology of the major faults by fitting the simulated facies, thickness and lithology of the synkinematic sediments to observations in the field and on seismic. For example, the modelling shows that sediment deposited during the Messinian in this flexural foreland basin context is mainly derived from a source lying to the North of the study area. After deposition, they were progressively reworked and involved in the thrusting since the Lower Pliocene.

Conclusion

In fine, the coupled stratigraphic and structural numerical models allow us to better quantify in 3D the stratigraphy of sedimentary basins, and constrain the chronology of major faults and structural events. This new approach has great potential both (1) for teaching and academic studies to quantify the relative influence of accommodation, supply and transport on sediments and stratigraphy, and (2) for petroleum exploration in peri-orogenic basins.

Stratigraphic models, and moreover coupled stratigraphic and structural numerical models, are a dreamed key to decipher the stratigraphic records in synkinematic series, but great scientific effort still have to be put on their developments to close the process-deposit loop in complex tectonic settings.

Acknowledgments

Dionisos is a 3D stratigraphic forward model, developed by IFP and a consortium of petroleum companies including Shell, Total, Repsol-YPF, Chevron-Texaco, Petrobras, ENI and PRC, while the Thrustpack consortium is sponsored by Chevron-Texaco, IMP, Enterprise-Shell and Conoco-Philips.

REFERENCES

- Albouy E., Casero P., Eschard R., Barrier L., Rudkiewicz J.L., and Sassi W. (2003) Coupled structural / stratigraphic forward modelling in the Central Apennines. AAPG Annual Meeting 2003
- Clevis Q., de Boer P. and Wachter M., 2003, Numerical modelling of drainage basin evolution and 3D alluvial fan stratigraphy. Sedimentary Geology 163, pp. 85-110.
- Cross, T.A., and Lessenger, M. A., 1999, Construction and application of a stratigraphic inverse model. In Harbaugh, J.W., et al (eds), Numerical Experiments in Stratigraphy., SEPM Sp. Pub. 62, p. 69-83.
- Granjeon, D. and Joseph, Ph., 1999, Concepts and applications of a 3D multiple lithology, diffusive model in stratigraphic modeling. In Harbaugh, J.W., et al (eds), Numerical Experiments in Stratigraphy., SEPM Sp. Pub. 62
- Harbaugh, J.W., and Bonham-Carter, G., 1970, Computer Simulation in Geology. Wiley-Interscience, New York, 575 p.
- Jervey, M.T., 1988, Quantitative geological modeling of siliciclastic rock sequences and their seismic expression. In Sea Level changes - an integrated approach. SEPM Sp. Pub. 42, p. 47-69.
- Mancilla, O.H., Salinas, A., Soubies, E.D., Debarre, R., and Granjeon, D., 2002, Exploration of a frontier area using numerical stratigraphical modeling - Application to the offshore Colorado basin of Argentina. AAPG Annual Meeting 2002, March 10-13, Houston.
- Paola, C., Heller, P.L., and Angevine, C.L., 1992, The large scale dynamics of grain size variation in alluvail basins, 1 : Theory. Basin research, 4, p. 73-90.
- Syvitski, J.P.M., and Bahr, D.B., 2001. Numerical Models of Marine Sediment Transport and Deposition. Computers and Geosciences, 27(6), p. 617-753.
- Tetzlaff, D., and Harbaugh, J.W., 1989, Simulating Clastic Sedimentation. Computers Methods in the Geosciences, Van Nostrand Reinhold, New York, 202 p.
- Warrlich, G., Waltham, D. and Bosence, D., 2002, Controls on atoll stratigraphies; insights from 3D forward computer modelling. Basin Research, 14, 416- 430.

THE ROLE OF STRESS ORIENTATION ON FAULT REACTIVATION: AN ANALOGUE MODELLING APPROACH 3-10

C. Del Ventisette(*),(**), D. Montanari(**), F. Sani(*),(**), M. Bonini(*)

(*) Istituto di Geoscienze e Georisorse – IGG, Via la Pira 4 – 50127 FIRENZE - Italy

(**) Università degli Studi di Firenze – Dipartimento di Scienze della Terra, Via la Pira 4 – 50127 FIRENZE - Italy

Abstract

A series of analogue models have been performed to get insights into the relationships between reactivation of pre-existing extensional structures and the orientation of a successive compressive stress field. Influence of rheological behaviour of syntectonic sedimentation (pure brittle or brittle-ductile) during the extensional phase has been also taken into account. The models consisted of two deformational phases: 1) a first extensional phase ($\sigma_h=\sigma_3$) during which a graben delimited by major faults developed, and 2) a successive compressive phase with the orientation of maximum stress axis σ_1 ($\sigma_h=\sigma_1$) variable between 0° and 90° (obliquity angle α to the trend of faults bounding the first-phase graben. The experimental results suggest that the development of compressive structures is strongly controlled by the pre-existing extensional structures and by the obliquity angle α. All the experiments have shown that the extensional structures were invariably reactivated during shortening. Notably, the shortening was firstly accommodated by the reactivation of the pre-existing structures and localized preferentially in correspondence of lateral rheological discontinuity, whereas new faults developed only successively. In all models, the dip rotation of major fault planes took place and increased with angle α. Mean horizontal displacement vectors illustrate the role of basin fill ductile layers and obliquity angle (α) on strain partitioning and brittle-ductile decoupling.

Introduction

The final deformational pattern of extensional rift basins reactivated in compression is strongly influenced by the geometry of early normal faults. In this geodynamic context the compressive deformation shows geometries and time-space evolution strongly different with respect to those simply due to shortening. The early normal faults are generally zone of weakness with different mechanical properties (cohesion and internal friction) in comparison with the un-deformed rocks. This variation of mechanical properties along the fault plane favours its reactivation, since it necessitates minor stress then that necessary for the development of new structures.

The dynamics of fault reactivation is influenced by many factors. In this work we examine, through an analogue modelling study, the role of 1) a basal ductile layer within the graben and 2) the direction of shortening with respect to the main fault trend on the deformation pattern resulting from basin inversion.

Experimental procedure

Scaling of analogue models to the natural prototype requires the geometrical, rheological, kinematical and dynamical similarities to be satisfied (e.g., Hubbert, 1937, Ramberg, 1981; Weijermars and Schmeling, 1986; Weijermars et al., 1993; Brun, 1999).

The model had initial dimensions of 45.5cm x 42cm x 7cm and consisted of a pure brittle system representing the crystalline basement of a natural prototype (e.g. Nalpas and Brun, 1993). 3.5 cm-wide bands with different colours were introduced in the model parallel to the extension direction (CML layer). In this way we could appreciate the strike-slip reactivation of the earlier extensional normal faults in the basement during the successive compressive phase cutting model cross-section.

The models were extended at a constant velocity of 10 mm/h for seven hours up to the bulk extension (BE) of about 16.5%. After 1 hour of deformation (approximately 2.3% BE), when the graben was 1 cm deep, a mixture of silicone and oleic acid (Newtonian behaviour, $\rho=1060$ kg m^{-3}, $\eta=10^3$ Pa s) was placed into the graben to simulate the ductile behaviour of salt layers that are generally associated whit this geodynamic contest. The successive syn-tectonic sedimentation consisted of dry quartz sand layers (Fontainbleau sand with grain dimension lower than 250 μm) with different colours sieved at regular time intervals (1 mm every 30 minutes).

The following deformational phase simulating a compressive stress field ($\sigma_1 \cong \sigma_h$) was applied at the constant velocity of 10 mm/h for seven hours.
To investigate the role of ductile layers on fault reactivation and final deformational patterns a parallel-model without the silicone layer at the base of the graben fill, deformed with α=50°, was performed.

Summary of experimental results

1. The deformation during the shortening is strongly influenced by previous extensional structures and by the associated rheological discontinuities.
2. In all models, the major extensional faults are invariably reactivated during the compressive phase. For low obliquity angles (α<40°), pre-existing structures acted prevalently as dislocation zones and tear-faults for newly formed thrust, while for high obliquity angles (α>40°) the deformation is mostly accommodated by pre-existing structures with strike-slip component decreasing with a (Figure 1).

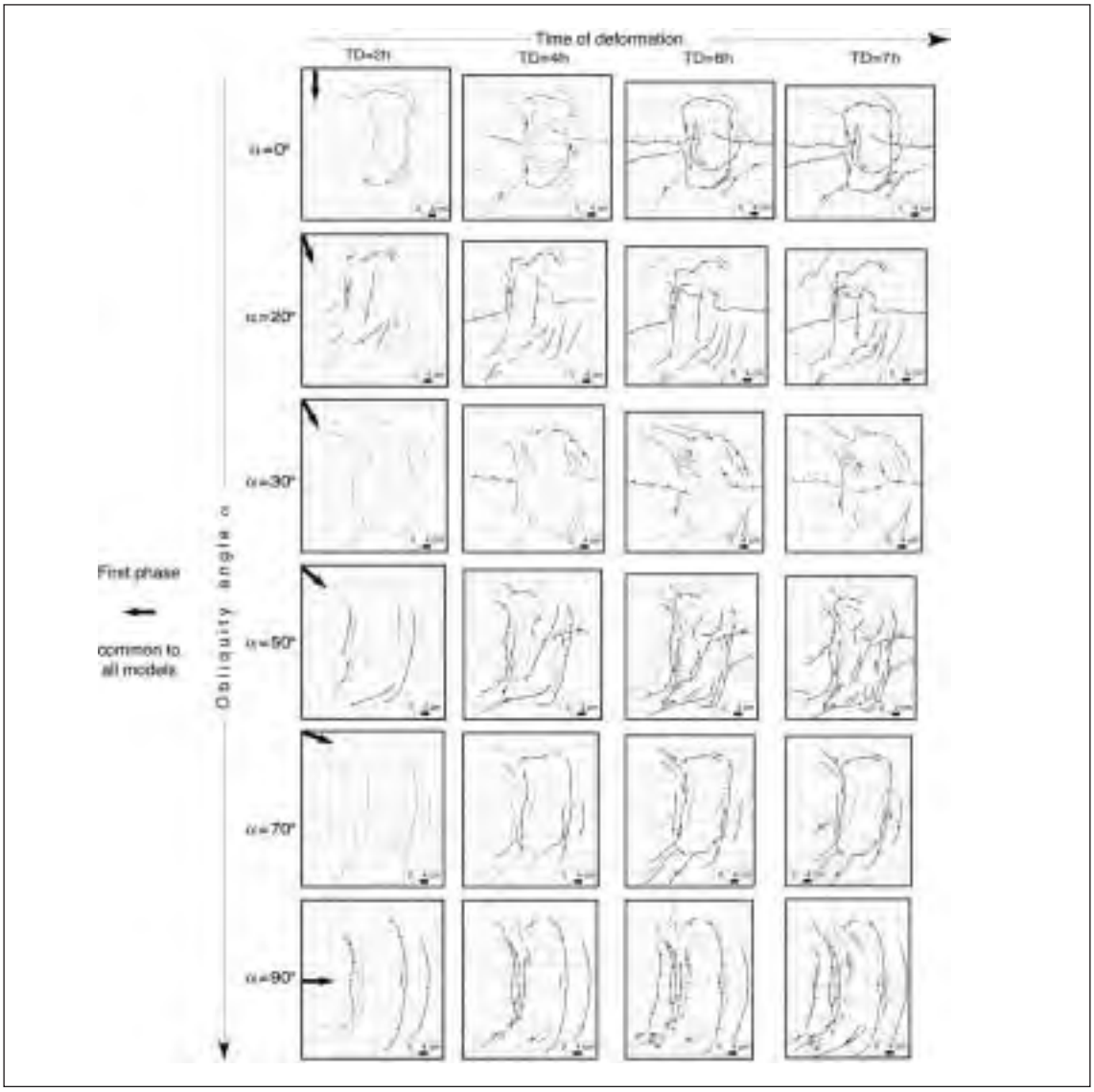

Figure 1 - Line drawing of top view for all models at different times of deformation. Along the axes Y increases the obliquity angles α (0°, 20°, 30°, 50°, 70°, and 90°) while along axes X increases the time of deformation after 2, 4, 6 and 7 hours.

3. For high obliquity angles (α=70° and 90°), a salt wall-like structure formed above an early major normal fault within the graben. This structure was initially triggered by high dip-slip component of reactivation of the same fault. This favoured a rising of the silicone putty that successively evolved in a diapiric fashion (Figure 2).

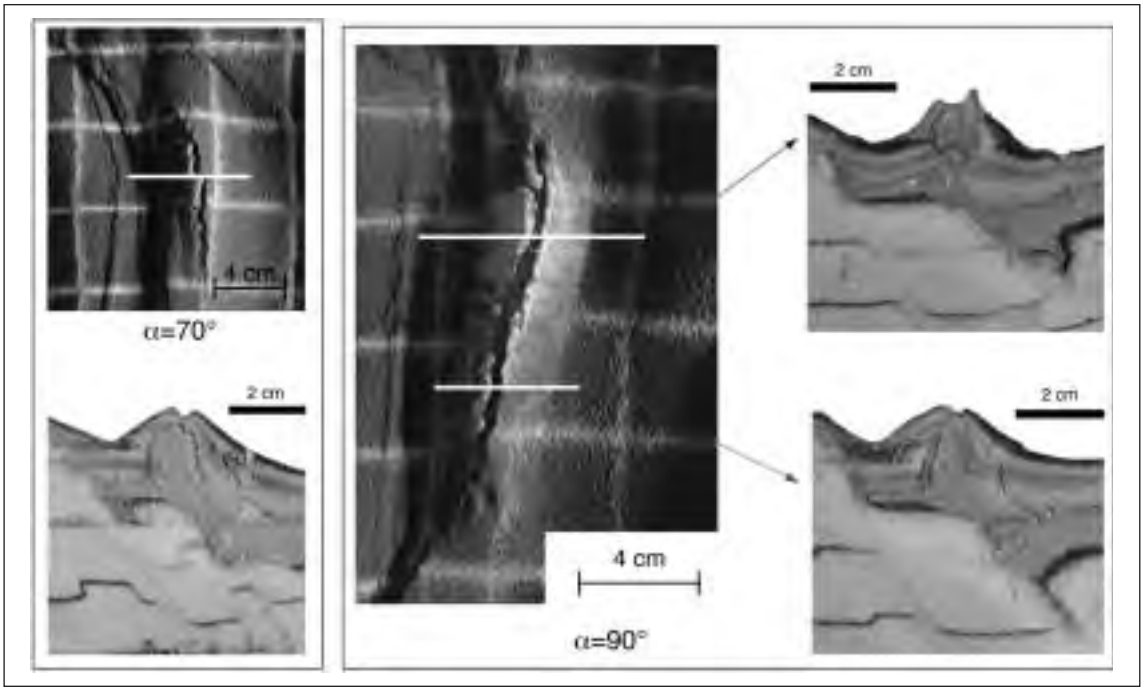

Figure 2 - Well-developed diapiric structures (salt-wall) triggered by strong dip-slip positive inversion of pre-existing normal fault developed for high obliquity angle α.

4. Dip rotation of major faults and the variations in graben width have been considered from a quantitative point of view:
   - The dip rotation of fault plane is invariably present (except for α=0°) showing linear relation to the obliquity angle (α) of shortening. This can indicate a reorientation of the pre-existing structures before their reactivation.
   - The graben width exhibits two different behaviour for high and low obliquity angles respectively, with the boundary around α=40°.
5. The horizontal displacement vectors give quantitative indications on the influence of pre-existing structures and rheological discontinuities on different strain partitioning and final deformational patterns.
6. The presence of a shallow décollement strongly modifies the deformational pattern in the sedimentary cover. The lateral rheological discontinuities between the ductile base of the graben fill and the brittle basement are able to create relevant local stress field reorientation.

REFERENCES

- Brun, J.P., (1999), Philosophical Trasnactions of the Royal Society of London, A, 357, 695-712.
- Hubbert M.K (1937), Geol. Soc. Am. Bull., 48, 1459-1520.
- Nalpas T., Brun J.P. (1993). Tectonophysics 228, 349-362.
- Ramberg H. (1981). Gravity, deformation and the Earth's crust (2nd edition). Academic Press, London.
- Weijermars, R., and Schmeling, H. (1986), Physics of the Earth and Planetaty Interiors, 43, 316-330.
- Weijermars et al. (1993), Tectonophysics, 217, 143-174.

GEOLOGICAL CONSTRAINTS ON POROSITY EVOLUTION, PERMEABILITY, AND FLUID MIGRATION IN CARBONATE-RESERVOIRED PETROLEUM SYSTEMS: A GLOBAL VIEW

3-11

G. Darke, P. Nadeau, J. Garland
STATOIL, N-4035, Stavanger, NORWAY

Summary

Geological processes for the evolution of porosity and permeability in carbonate rocks, as a function of burial and thermal history, are under evaluation. The primary objective of this work is to provide observational constraints for quantitative predictions and risk reduction in the hydrocarbon exploration setting.

Abstract text

Traditional carbonate petrology studies have not provided readily applicable models for the quantitative prediction of porosity and permeability as a function of burial history. Whilst petrophysical models used for the classification of reservoir heterogeneity (eg. Lucia 1999) are useful for a specific reservoir at the hydrocarbon field scale, they do not provide predictive models at basin scale. Recent advancements in siliciclastic diagenesis have resulted in predictive models as a function of burial and thermal history (Bjørkum et al., 1998). This paper establishes an observational framework for the establishment of similar models in carbonates. Global data of carbonate reservoirs and their top seals are examined here for their use in predicting the distribution of porosity, permeability and hydrocarbon migration at the basin scale.

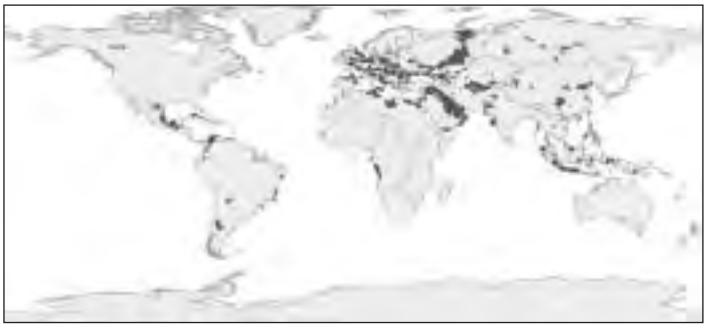

Figure 1 - Global distribution of oil and gas reservoirs/pools data for carbonate reservoirs. The data set includes subsurface information 9,128 resource accumulations from a variety of industrial, government and academic sources.

Compilation of a database representing 9,128 carbonate reservoirs (Figure 1) provides the basic input for this analysis. The parameters under examination include rock and fluid properties, subsurface temperature and pressure, as well as geological setting. The data allow reservoir quality and heterogeneity quantification which can provide valuable constraints, particularly during the early stages of exploration when detailed information is typically unavailable.

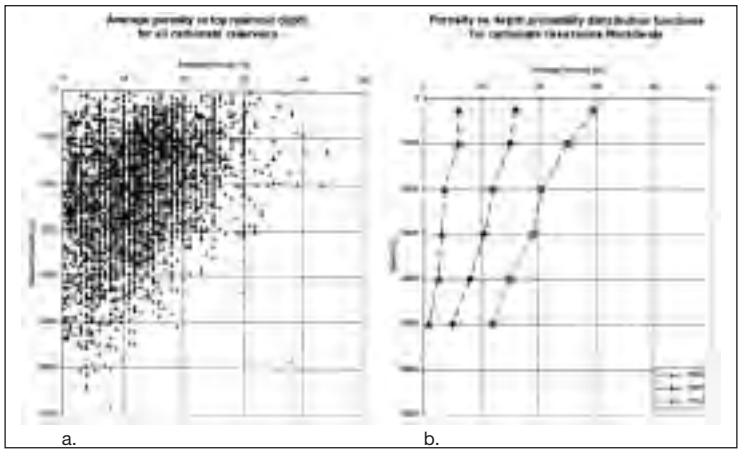

Figure 2 - a) Cross-plot of porosity versus reservoir depth for carbonate reservoirs, showing a well-defined porosity maximum b) Probability distribution functions (P90, P50, P10) for the same data

The data for mean reservoir porosity versus burial depth (Figure 2), as well as porosity versus mean permeability, demonstrate a wide but systematic variation. The data provide useful information on the relative heterogeneity of carbonate reservoirs, which often exists at the reservoir as well as the basin scale. More importantly for our purposes, they define quantitative constraints on porosity distribution as a function of burial depth. This is particularly important in carbonate rock sequences, where diagenetic processes of porosity enhancement as a function of burial history complicate modelling of basin scale geologic processes, most notably for fluid migration.

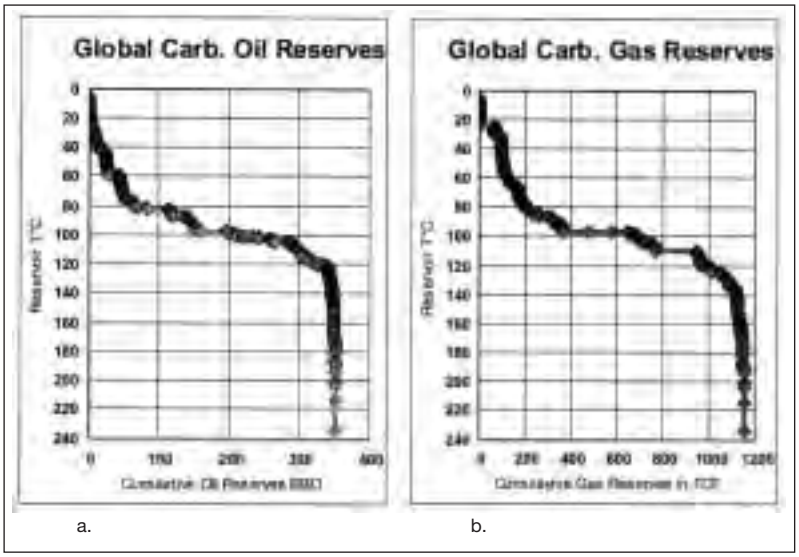

Figure 3 - Cummulative distribution of a) oil and b) gas reserves in carbonate reservoir pools. More than 75% of total reserves occurs between 80° and 120°C

The data base also provides information on the distribution of oil and gas reserves as a function of reservoir temperature. Globally, 75% of total reserves (86% of oil) in carbonate reservoirs occur within the range of c. 80° and 120°C (Figure 3). This result differs somewhat from hydrocarbon accumulations in general, where the temperature range is typically 60° to 120° C (Bjørkum & Nadeau, 1998). The strong thermal controls on petroleum distributions within sedimentary basins are focus areas of our research, as well as the candidate geological processes responsible for them.

There is evidence that this phenomenon can be linked to top-seal diagenesis. Here we observe that top seal lithology, notably shale/mudstone, is more often associated with enhanced reservoir properties, when compared to carbonate reservoirs with evaporite top seals. This could possibly result from a greater probability for enhanced vertical fluid flow in the former, particularly during the early stages of diagenesis. Nadeau et al. (2002, 2003) have presented data demonstrating an exponential relationship to exploration risks as a function of reservoir temperature, relating them to thermal controls on porosity loss rates, as well as permeability reduction in shales/mudstones. The industry, however, often drills beyond the optimal entrapment zone, with corresponding reductions in exploration efficiency. This is particularly relevant for carbonate-reservoired petroleum systems, where occurrence rates for economic reserves can be c. 2%/°C. Assuming a typical geothermal gradient of 30°/km, this can constrain the majority of the economic resources to a zone less than c. 1.5 km in thickness. Further research is required, however, to better incorporate thermal controls on geological processes into basin scale models of rock properties and fluid migration within carbonate sequences.

REFERENCES

- Bjørkum, P.A. & Nadeau, P.H. 1998. Temperature controlled porosity/permeability reduction, fluid migration, and petroleum exploration in sedimentary basins. Australian Pet. Prod. & Expl. Assoc. Journal, 38, p. 453-464.
- Lucia, F.J,. 1999, Carbonate reservoir characterisation: New York, Springer-Verlag, 226p.
- Nadeau, P.H., Walderhaug, O., Bjørkum, P.A. & Hay, S. 2002. Clay Diagenesis, shale permeability, and implications for petroleum systems analysis. EAGE Florence 2002: Proceedings Abstract G003.
- Nadeau, P.H., Bjørkum, P.A. & Walderhaug, O., 2004. Petroleum system analysis: Impact of shale diagenesis on reservoir fluid pressure, hydrocarbon migration and biodegradation risks. In: Doré, A. G. & Vining, B. (eds) Petroleum Geology: North-West Europe and Global Perspectives – Proceedings of the 6th Petroleum Geology Conference. Geological Society, London, (in press).

THE DEVELOPMENT OF INVERTED FAULTS: RESULTS FROM ANALOGUE PLASTER MODELS

3-12

I. Grunnaleite

RF-Rogaland Research, Thormøhlensgt. 55, N5008 Bergen, Norway

Summary

The background for this study was a seismic interpretation of fault complexes in the Barents Sea, revealing structures indicative of positive structural inversion. (Gabrielsen et al, 1992, 1997, Grunnaleite, 2002) The scope of this work is to study structural evolution and deformation during positive structural inversion in analogue models in order to enhance the understanding of how these structures are initiated and how they develop, and thus to aid interpretation of inverted structures in field and in seismic data.

The geometry of four plaster cast experiments of inversion were carefully analysed during intermediate stages of deformation. The chosen experiments show variation in fault geometry, from simple planar faults to arrays of synthetic, listric- and planar-, faults and complex deformation zones consisting of interconnected blind faults and extensive- and compressional duplexes. The analyses comprised structural evolution, variations of area and length, displacement, dip of horizons and faults, block deformation and shear angles during deformation. The analysis is summarized in a general five-stage evolution of inversion structures: 1) Early extension stage, 2) Extensional faulting stage, 3) Early inversion stage, 4) Reverse faulting stage and 5) Thrusting stage. Such detailed analyses of inverted faults have not previous been presented and it is believed that it may increase the understanding of inversion and help identify such structures in field and on seismic data and understand their evolution history.

Introduction

Plaster cast analogue models

Using plaster as modelling medium has many advantages compared to sand, clay and other materials. Plaster is inelastic and preserves structures in great detail, and as the experiments are self-hardening it's easy preserved for later display. Structures derived in plaster cast experiments display great similarity to real brittle structures observed in seismic data or in field, and different kinds of observed structures can easily be modelled using this technique

In the present study, the method described by Fossen & Gabrielsen (1996) and Gabrielsen & Clausen (2001) has been utilised. The experiments are mechanically homogeneous and the strain markers are painted on the inside of the glass box. The black markers contrast excellently to the white plaster. This allows even very small and subtle faults to be identified giving the plaster model an appearance of a very well defined seismic section. The plaster is self-hardening and no glue- or epoxy injection is needed to conserve the models. Good control with the strength of the plaster is performed by using miniature slump test to determine the time for deformation. The results of the slump test can be cross-referenced against the profile of repose of the overall finished model, since both are conserved in the model (Sales 1989a).

Inversion

Inversion is related to reactivation of old structures with an inverted (reversed) stress regime relative to the stress situation at the initiation of the structure. It is usually applied to extensional structures that have been reactivated and deformed by compression, but should also imply extensional reactivation of compressional structures. These two cases are defined as positive inversion and negative inversion respectively (Williams et al., 1989, Hayward & Graham, 1989). The identification of inversion structures on seismic data can be difficult, for instance, a weakly inverted normal fault may show small drag phenomena and signs of contraction (positive inversion) but may still have a large normal fault throw. These experiments were made and analysed to increase the general understanding of how (positive) inversion structures develop and how they would appear after varying amounts of compression.

Description of experiments

Four out of totally 15 inversion experiments done, were chosen for analysis of fault initiation and geometrical development, fault and horizon rotation and internal block deformation. They represent a range of complexity from one single planar fault (Experiment A), to a complex deformation zone with extensional- and compress ional- duplexes (Experiment D), see Fig 1. All experiments are drawn at initial position (e0), maximum extension, end of contraction (final stage of model) and at various intermediate stages. The number of deformation stages used for each model depends on the complexity of the structures.

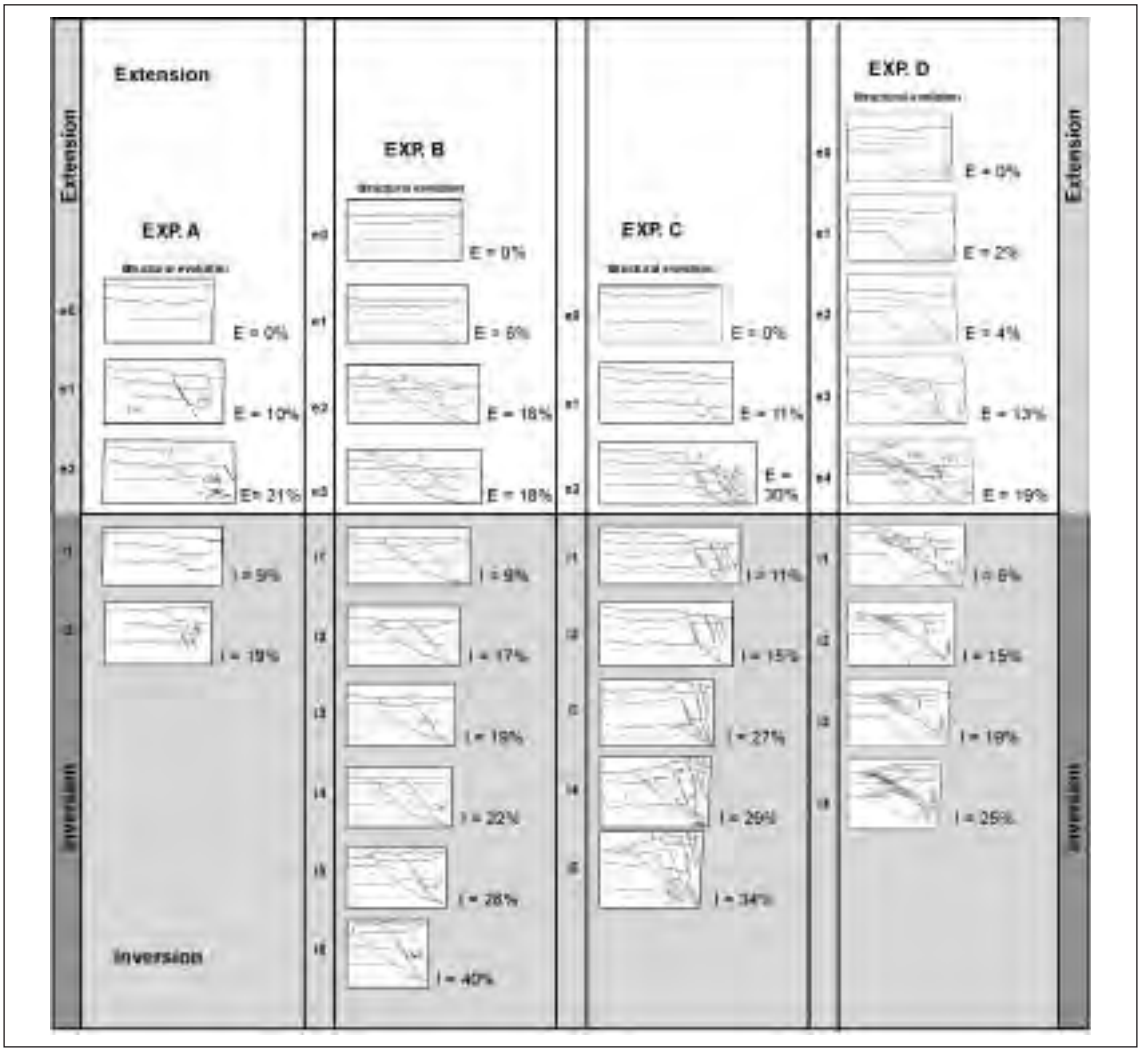

Fig 1 -Experiments used for fault analysis. E% refers to amount of extension, I% refers to amount of inversion (i.e. compression after max. extension) Upper part, (white box): extensional stages-, and lower part, (grey box) compressional stages of deformation.
Experiment A: One single planar fault
Experiment B: Two simple planar and listric faults.
Experiment C: A series of parallel extensional fault blocks and new thrust faults developed into the footwall.
Experiment D: Extensional faults linking into a complex deformation zone with duplexes.

Analysis of experiments

Analyses are based on observations from one side of the experiments, which were traced from still photos and video at certain time steps. The drawings were analysed and measured using technical drawing software. Table 1 lists the analyses that were performed on all experiments. The analyses are

based on observations from certain time steps in the evolution of the experiments. The measured data are thus point observations in time, and a linear evolution between observation time steps cannot always be assumed. Time evolution charts for the different effects of deformation during extension and subsequent inversion will be presented and analysed

Analysis	Description
Structural evolution:	General observations of faulting process, timing of deformation, comparison between experiments etc.
Extension/inversion:	Amount of extension and compression (relative to length at stage of maximum extension)
Length and area:	Variations of length and area for the whole model and for individual fault blocks during deformation.
Fault displacement:	Fault throw measured at each horizon during deformation. Heave measured on surface.
Fault rotation:	Change in fault dip angle during deformation.
Horizon rotation	Rotation of fault blocks
Horizon drag against faults:	Change in horizon dip during deformation on hanging wall- and footwall- side against faults.

Table 1 - Parameters analysed at given time steps in the evolution of the experiments A-D.

Summary and conclusions

The main conclusions of the experiment analyses indicate that complete inversion of extensional faults can be divided into 5 stages (Figure 2). More detailed results and observed differences related to initial fault geometry will be presented. The typical deformation seen at these stages are:

1. Early Extensional stage

- Flexuring and dipping of the shallower horizons down in the direction of extension prior to first extensional faulting.

2. Extensional faulting stage

- Faulting and rotation of faults to a shallower dip angle.
- Development of extensional duplexes and splay faults
- Increasing normal throw usually developed first and largest on deepest horizons.
- Larger stretching and rotation at base leads to development of listric faults.
- Development of normal drag against both side s of fault planes.
- Horizons in the hanging wall side of fault blocks rotate down against the fault plane.
- Horizons in the footwall side of fault blocks rotate in the fault dip direction.
- Horizon dip against the fault varies typically between +10° to –30° to 50° both in footwall and hanging wall blocks.
- Typical shear angles observed range from –45-50° to -90°.

3. Early inversion stage

- Normal throw decreases on upper surfaces.
- Normal throw may still increase on deeper horizons.
- Steepening of faults
- Inversion of throw starts along the faults with the largest normal throw, if the main parts of these faults get steeper than 60-65º it will not be inversed into reverse throw.
- Generally horizon rotation in the direction of fault dip, some exceptions occur.
- A wide range of shear vectors, increasingly wider spread backward in hanging wall.

4. Reverse faulting stage

- Continued steepening of faults and rotational shearing of fault blocks.

- Sequential development of inversion in the direction of compression.
- Linking of splay faults into reverse duplexes.
- Diverse horizon rotation and drag evolution as faults enter from inversed normal state into reverse state.
- Faults are steeper when throw are nulled out at surface than they were when extension started.
- Increasing range of horizon dip against faults, largest dip range in hanging wall block.
- Narrower range of shear vectors in hanging wall, steeper upward direction during inversion

5. Thrusting stage

- Thrusting on the foremost inverted fault.
- New shallower dipping reverse faults develop in the footwall block.
- Reverse faults flatten towards the surface giving faults and hanging wall blocks a sigmoid shape.
- Internal shearing in fault blocks as they are pushed up, stretched in upper frontal part and thinned in lower parts.
- Horizons in outer hanging wall areas and footwall horizons beneath the thrust front rotate against the position of compression.
- Horizons on upper hanging wall side of thrusts steepen towards the thrust fault.
- Positive relief created by the uplifted hanging wall section.
- Reverse throw increases, but may actually decrease at surface as more of the displacement is taken up as horizontal heave over the footwall crest.
- Gravitational collapse of hanging wall as compression stops may reduce reverse throw or increase normal throw on incompletely inversed hanging wall faults.
- The range of horizon dip against fault planes narrows in both footwall and hanging wall block. Generally negative dip angles caused by extensive reverse drag.
- Increasing horizontal shear vectors within footwall blocks. Separation of shear vectors in hanging wall into two groups; Upward thrusting in deeper and central parts and horizontal to downward directed in upper thrust front.

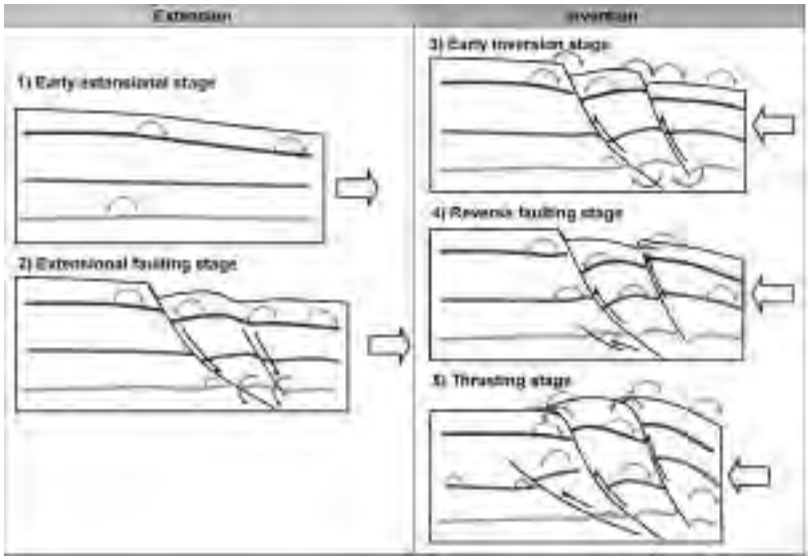

Fig. 2 - Main deformational stages and direction of internal rotation during positive structural inversion.

Acknowledgement

The experiments were made at the Structural Laboratory of Geological Institute, University of Bergen. Thanks to Professor Roy H. Gabrielsen and his students for help with making the experiments. The video- and graphical analyses were made at RF-Rogaland Research, Bergen. This work was done as a part of my PhD degree at University of Bergen, Oct. 2002.

REFERENCES

- Fossen, H. & Gabrielsen, R.H., 1996: Experimental modelling of extensional fault systems by use of plaster. Journal of Structural Geology, 18, 673-687.
- Gabrielsen, R.H., Grunnaleite, I. & Ottesen, S., 1992: Reactivation of faults complexes in the Loppa High area, southwestern Barents Sea., in: T.O.Vorren, E.Bergsager, Ø.A.Dahl-Stamnes, E.Holter, B.Johansen, E.Lie & T.B.Lund: Arctic Geology and Petroleum Potential., Norwegian Petroleum Society Special Publication, 2, 631-641.
- Gabrielsen, R.H., Grunnaleite, I. & Rasmussen, E., 1997: Cretaceous and Tertiary inversion in the Bjørnøyrenna Fault Complex, south-western Barents Sea., Marine and Petroleum Geology, 14, 2, 165-178.
- Grunnaleite,I., 2002: Late Cretaceous to Tertiary inversion in the southwestern Barents Sea, In: Inversion in the Norwegian continental shelf with particular emphasis on the areas N of 62oN., unpublished PhD thesis, ISBN 82-497-0115-1, UiB, 2002.
- Gabrielsen, R.H. & Clausen, J.A., 2001: Horses and duplexes in extensional regimes: A scale modelling contribution. In: H.A.Koyi & N.S.Mancktelow (eds.): Tectonic Modeling: A Volume in Honor of Hans Ramberg. Geological Society of America Memoir, 193, 219-233.
- Hayward, A.B. & Graham, R.H., 1989: Some geometrical characteristics of inversion. In: Cooper, M.A. & Williams, G.D. (eds.): Inversion tectonics, Geological Society London, Special Publication, 44, 17-39.
- Sales, J., 19989: Plaster structure modelling (PSM) A versatile tool for structure analysis (Procedures). In Abstract volume: Structural and tectonic modelling and its Application to Petroleum Geology, NPF Conference, Stavanger, Norway, Oct. 1989.
- Williams G.D., Powell, C.M. & Cooper, M.A., 1989: Geometry and kinematics of inversion tectonics. In: Cooper, M.A. & Williams, G.D. (eds.): Inversion tectonics, Geological Society London, Special Publication, 44, 3-15.

CAN CENOZOIC UPLIFT AND FLEXURING EXPLAIN OCCURRENCE AND DISTRIBUTION OF STRUCTURAL INVERSION IN THE SW BARENTS SEA? RESULTS FROM NUMERICAL MODELLING

3-13

I. Grunnaleite*, Z. Huang**

* *RF-Rogaland Research, Thormøhlensgt. 55, N5008 Bergen, Norway*
** *RF-Rogaland Research, Ullandhaug, N4068 Stavanger, Norway*

Summary

Compressive structures and signs of structural inversion are widespread in the southwestern Barents Sea. A series of processes have been suggested as the mechanisms responsible for these structures, including thermal heating and volcanic processes associated with opening of the North Atlantic and transform spreading along the Barents margin. Cenozoic uplift, ridge push, shearing, compression and orogenesis on Spitsbergen and east Greenland, shift in plate motion during rifting, intra-plate stress, loading effects associated with uplift, erosion and glaciations are also considered to have had important effects on regional or more local scale. Most of the observed inversional structures are found along the main NNE-SSW striking main fault complexes and adjacent basins along the SW margin of the Barents Sea. Theses structures generally display strike compatible with ESE directed compression. On the other hand a few of the observed inversional structures are found on the flank of uplifted structural highs, and their position indicate compression directed towards NW, directly opposite to the generally assumed ESE-directed compression direction from the oceanic crust towards the continental crust. Another problem in relating the observed inversion to processes associated only with the opening of the North Atlantic and sea-floor spreading in the Norwegian-Greenland basin is the timing. Detailed seismic interpretations indicate that large scale folding and inversion occurred from Cretaceous time, well before the Cenozoic sea-floor spreading started and associated ridge-push and thermal effects could be expected.

Regardless of what is taken as the cause it is inevitably shown that the structural highs in the southwestern Barents Sea have been uplifted and eroded by as much as 1000-3000m from latest Cretaceous and through Cenozoic time. The areas of maximum uplift coincide with the areas where inversional structures are observed. To examine this we did numerical modelling of the stress-effect of uplift and flexuring of the structural highs. The results indicate that compressive stress directed against the expected ridge-push can occur in the eastern flanks of the uplifted highs. Reverse faults with up to NW-directed compressive motion are described from seismic data and are difficult to explain by other mechanisms, generally creating SE-directed compression. The main conclusion is that the mechanical effect locally of uplift must be taken into consideration and may explain the

observed distribution of compressional structures no matter what regional mechanism caused the observed uplift or contemporaneous compression. Regional uplift and associated bending of the structural highs and their border faults were found to directly affect deformation in the adjacent basins and in the uplifted highs themselves.

Introduction

The large uplift, rotation and erosion of the structural highs in the western Barents Sea had a quite dramatic effect for the evolution of the area. Uplift and erosion in the order of thousands of meters totally changed the subsidence pattern and probably had a dramatic effect for the hydrocarbon potential, Kjemperud & Fjeldskaar (1992), Nyland et al., (1992). It is obvious that large-scale uplift and rotation of the high areas must affect the fault complexes defining these uplifted highs. Tilting of a stiff basement block must also rotate the bounding faults, and uplift will cause a vertical upward push above these faults. The adjacent basin with soft sediment fill is much more prone to take up this deformation and its associated spatial problems than the older, compacted and lithified footwall-blocks.

In the SW Barents Sea, the eastern deep part of the Bjørnøya Basin, consisting of thick Cretaceous and Tertiary units is confined between two uplifted and rotated platform areas, the Stappen High and the Loppa High. Both extensional and compressional structures of approximately same age are seen in the seismic data. Our theory is that the rotation and uplift deformed the existing fault zones and the adjacent basin sediments were affected by both extensional and compressional stress. (Figure 1a-c). To quantify the effect of uplift and flexuring and to test how the modelled stress distribution would compare to the observed structures, we did some simple numerical modelling using the 2-D distinct element UDEC code.

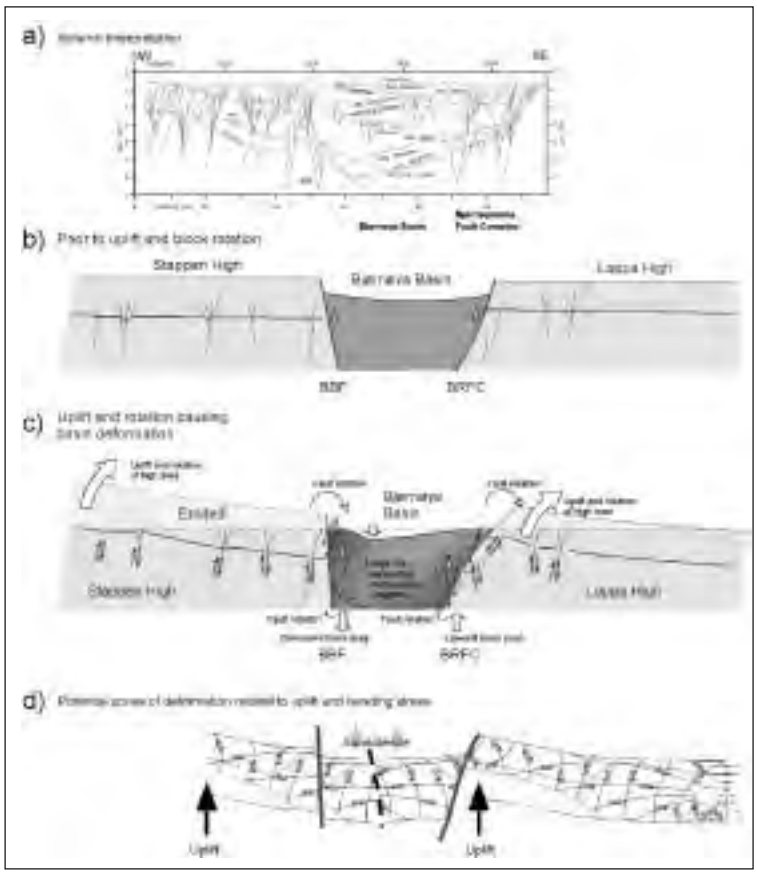

Fig. 1 - Uplift and block rotation of the Stappen and Loppa Highs and associated basin deformation in the Bjørnøya Basin.
a) Interpretation of regional NW-SE seismic profile. b) Situation prior to the major uplift and rotation. c) Rotational effects of rotation and uplift.
The basin-bounding main faults (BBF and BRFC) rotate, bend and deform differently according to downward directed drag or upward directed push from the footwall block respectively. Likewise the Bjørnøya Basin experience different deformation on the opposing flanks. Deep-seated upward compression and shallow extension dominated on the south-eastern side whereas shallow compression and deep subsidence and extension occurred on the north-western side. A hinge-line defined by sharp change of dip direction of reflectors defines the two opposed deformation regimes. Internally the rotated highs deform by shearing along rotated flower structures and faults creating distinct dip differences between adjacent blocks. d) Expected pattern of deformation due to flexuring of a rigid body. Figure d) based on figure from Sandford (1959) doing sand-box experiments on uplift and bending.
BBF = Bjørnøya Basin Fault, (informal name used in Grunnaleite, 2002), BRFC=Bjørnøyrenna Fault Complex.

Numerical modelling

To check this hypothesis and further investigate the mechanism of inversion and compression in the southwestern Barents Sea, numerical modelling was carried out using the 2-D distinct element UDEC code, to simulate the uplift of the basement/sediment under vertical basement movement and horizontal ridge-push force. Both elastic and plastic properties were included.
The model has a dimension of 100 km (length) X 30 km (height), with a sedimentary layer of 10 km thickness. A sinusoidal vertical displacement along the basement is applied. Due to symmetry in the vertical dimension, all grid points at the side boundaries were fixed in the horizontal direction. Vertical stress was assumed equal to the gravitational stress.

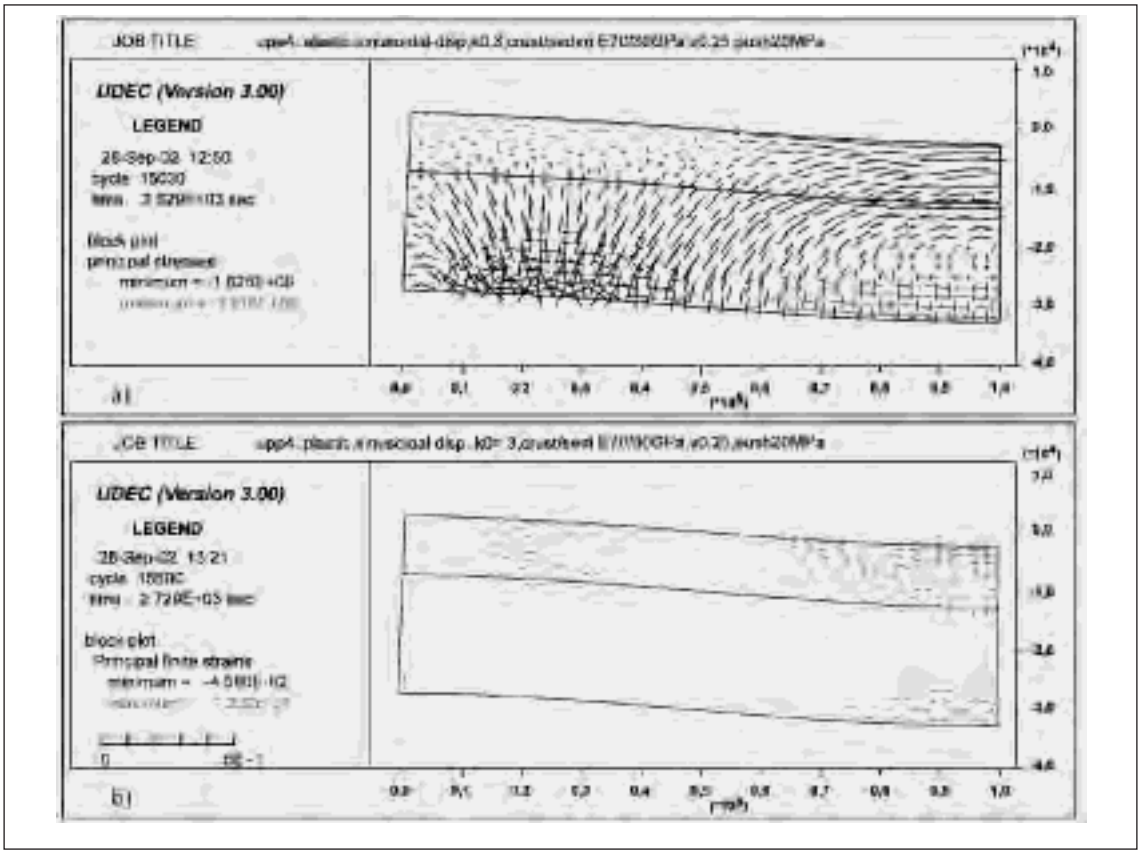

Fig. 2 - Results of numerical modelling of stress caused by a 3000m uplift of a structural high with dimensions 100x30 km under a ridge-push stress of 20MPa. A 10km sedimentary sequence is assumed on top of a 20km thick basement.
a): Using elastic properties: Stress state under sinusoidal displacement in the basement of crust/sediment and ridge-push force at the left boundary. Positive stress values = tensile stress, negative values= compressive stress.
b): Using plastic properties: Principal strains. Horizontal tensile strain in upper left part supporting vertical fracturing, vertical tensile strain, i.e. horizontal compressive strain in upper right part.

Elastic modelling results

The model shows theoretically that in response to the loading and displacement boundary conditions given above large horizontal tensile stress/strain developed at the left upper and right lower parts. These tensile stresses are entirely theoretical, that is potential stresses and would not be reached in the rocks themselves as failure of the rock would occur long before theses stresses could be reached. At the right upper part of the model compressive horizontal stresses and tensile vertical stresses indicate that inversion faults have the great potential to occur here (Figure 2a).
There are potential large tensile zones at the left upper and right lower parts of the model due to uplift along the basement, which means failure of the rock occurs long before these stresses could be reached. With ridge-push force applied, the horizontal tensile stresses at the left (uplifted) upper part

are reduced, and the potential for tensile fracturing is reduced accordingly. This ridge-push force does not have much effect on the right upper part due to uplift that is mainly caused by the sinusoidal vertical displacement applied along the basement.

Plasticity modelling

In the plasticity analysis, the Coulomb failure criteria were used with non-associated flow rule, in coupling with tension cut-off with associated flow rule (Huang, 2001):
The displacement field of the plastic model has the same pattern as for the elastic modelling. The principal strain shown in Figure 2b) indicates horizontal tensile strain at the left upper part, which may cause vertical tensile fractures. The horizontal ridge-push at the left side boundary tends to cause the vertical fractures to become inclined slightly. Hence normal faults with steep dip angle probably will develop at the left upper part.
The vertical tensile strain at the right upper part in Figure 2b), shows horizontal cracks may be expected in that area. In combining with the horizontal compression strain, the plastic zones at the right upper part may form low angle planes of potential shear, and thus reverse faults may dominate in this area.

	Young's modulus (GPa)	Poisson ratio	Density (kg/m^3)	Cohesion (MPa)	Friction angle (°)	Tensile strength (MPa)
Basement	70	0.25	2100	30	40	10
Sediment	30	0.25	3000	25	35	5

Table 1 - Parameters used in the modelling.

Summary and conclusions

The main conclusion is that the mechanical effect locally of regional uplift must be taken into consideration and may explain the observed distribution of compressional structures no matter what regional mechanism caused the observed uplift or contemporaneous compression. Numerical modelling results have supported our theory that the stress applied locally as an effect of uplift and bending and flexuring of structural highs may explain the distributions of faults and compressive structures and especially it may explain occurrence of local anomalies in the general regional scale stress pattern. Stress distribution in the numerical models may be used to directly explain structures in seismic sections and thus it may contribute to a better understanding of the structural evolution of the Barents Sea. Such modelling may prove extremely important in petroleum exploration as it may be used to focus on areas of potential seal-breakage, hydrocarbon migration pathways and possible leakage. The method may indicate where fractures and faults on a sub-seismic scale may be expected. This modelling could prove specially important along the North-Atlantic passive margins which were subject to rapid vertical motions by glaciations and differential loading during Cenozoic time.

ACKNOWLEDGEMENT

The regional seismic data set used in this study was provided by NPD, the Norwegian Petroleum Directorate, and Harstad. The interpretation was done at Geological Institute, University of Bergen as part of a PhD project. (Grunnaleite, 2002). Numerical modelling was done at RF-Rogaland Research, Stavanger.

REFERENCES

- Grunnaleite,I, 2002: Late Cretaceous to Tertiary inversion in the southwestern Barents Sea, In: Inversion in the Norwegian continental shelf with particular emphasis on the areas N of 62oN., unpublished PhD thesis, ISBN 82-497-0115-1, UiB, 2002.
- Huang, Z. P. 2001. Stabilizing of rock cavern roofs by rock bolting. Ph.D thesis. Norwegian University of Science and Technology
- Kjemperud, A. & Fjeldskaar, W, 1992: Pleistocene glacial isostacy – implications for petroleum geology. In: Larsen, R. M., Brekke, H., Larsen B.T. and Talleraas, E. (editors): Structural and Tectonic Modelling and its Application in Petroleum Geology. Norwegian Petroleum Society, Special Publication No. 1.pp. 187-195. Elsevier, Amsterdam,.
- Nyland, B., Jensen, L.N., Skagen, J., Skarpnes, O. & Vorren, T., 1992: Tertiary Uplift and Erosion in the Barents Sea: Magnitude, Timing and Consequences., in: R.M.Larsen, H.Brekke, B.T.Larsen, & E.Talleraas (eds): Structural and Tectonic Modelling and its Application to Petroleum Geology., Norwegian Petroleum Society Special Publication (Elsevier), No. 1,pp.153-162.
- Sandford, A.R., 1959: Analytical and experimental study of simple geological structures. Geol.Soc. Am. Bull., 76, pp.19-52.

THE FLYSCH TO MOLASSE TRANSITION – INSIGHT FROM SCALED SANDBOX SIMULATIONS

3-14

S. Hoth(*), N. Kukowski(*), O. Oncken(*), J. Pfeifer(**)

(*) GeoForschungsZentrum Potsdam, Telegrafenberg, 14473 Potsdam, Germany; shoth@gfz-potsdam.de

(**) Colorado School of Mines, 1500 Illinois Street, Golden, CO, 80401 USA

Summary

Based on scaled sandbox experiments we investigate the influence of the lateral and vertical growth of bivergent sand–wedges subject to denudation on the geometric evolution of a hypothetic foreland basin system and its sediment infill. Our results suggest that the imposed kinematic boundary condition, i.e. asymmetry of convergence and the associated singularity, favour a wedge growth which can be best described by a power law. Based on these observations we propose a simplified kinematic model for the flysch to molasse transition. A power law of the wedge growth implies that the incremental lateral and vertical growth decreases over time and so does the respective load of the wedge. Accordingly, the addition of flexural induced subsidence of a hypothetical foreland at a given position decreases over time as well. If one further assumes a constant hypothetic sedimentation rate in this foreland basin system, a change from underfilled (fast addition of new accommodation), to overfilled (slow addition of new accommodation) would result. This transition would be thus an emergent consequence of the imposed kinematic boundary conditions. A further implication is that there is no need to necessarily invoke a halt of convergence or a slab breakoff as a cause for the flysch to molasse transition.

Introduction

Peripheral foreland basin systems (DeCelles & Giles 1996) result from the flexural down–bending of continental lithosphere in response to tectonic and topographic loading during continent–continent collision (Price 1973). The spatial evolution of the associated depozones (wedge–top, foredeep, forebulge, backbulge) and their respective sedimentary infill, is strongly dependent on (i) the effective elastic thickness (T_e) of the involved lithospheres, (ii) the level of horizontal stresses, (iii) the magnitude of the loads imposed on the foreland by the orogenic wedge and the subducted lithospheric slab, (iv) the dip–angle of the latter, (v) the rate and direction of convergence, (vi) the amount of erosion of the orogenic wedge and the dispersal system within the foreland and (vii) eustasy (Allen et al. 1991; Sinclair 1997; Ziegler et al. 2002).

Numerous field studies have demonstrated that almost all foredeeps evolve from an underfilled to a filled or overfilled depositional state (Covey 1986; Sinclair 1997). The underfilled state is characterised by deep–marine (flysch type) sediments, high thrust advance rates and low exhumation rates. In contrast, the overfilled state shows shallow marine to continental (molasse type) deposits and a dominance of exhumation versus frontal advance of the orogen (Sinclair and Allen 1991). Classically, the flysch to molasse transition is interpreted as recording the migration of the thrust wedge and the associated foredeep over the hinge line of the inherited passive margin of the underthrusted plate (Dewey 1982). Numerical simulations however, suggest that the rate of frontal advance of the orogenic wedge and the sediment transport coefficient (K) are the main control on the state of the foredeep infill, whereas an increase in flexural rigidity or the surface slope of the orogenic wedge are only of minor importance (Sinclair et al. 1991). This is supported by field observations from the Swiss Alps (Sinclair 1997).

The objective of this study, which is based on scaled–sandbox simulations, is to investigate the link between the geometric evolution of foreland basin systems and their respective sedimentary infill and the growth of the associated bivergent orogen subject to different denudation modes. Finally, we propose a simplified kinematic model for the flysch to molasse transition.

Experimental set up

Granular flow of sieved, dry quartz sand (0.02–0.63 mm) which is characterised by a strain dependent deformation behaviour with pre–failure strain hardening and post–failure strain softening is similar to

the non–linear deformation behaviour of crustal rocks in the brittle field (Lohrmann et al. 2003). Based on the mechanical properties of the used sand, a geometric scaling factor (ca. 10^5) was derived (Hubbert 1937). The kinematic boundary conditions inferred for natural bivergent orogens are simplified and integrated in a 2D sandbox approach which shows the following characteristics: Elastic upper and lower plates, which overlap in the centre and are only fixed at their respective outward sides to allow for load driven flexure. The lower plate is supported by a spring to adjust its stiffness. As a first order approximation, a plate–spring combination was chosen to ensure a linear increase of the flexural rigidity as a function of added load. The corresponding dip angle β changes from about 5° to about 6° during experimental runs. Lower plate subduction and basal shear is simulated by a conveyor belt, made of sandpaper, which covers only the lower plate. The sandpaper is drawn by a motor (9 cm/min) beneath the tip of the upper plate. Convergence is in the order of 150 cm (~150 km in nature) and is thus similar to medium sized orogens like the European Alps or the Pyrenees. To promote frontal accretion in the developing retro-wedge, a thin glass–bead layer was introduced as a potential detachment horizon between the sand and the upper plate. An additional glass–bead layer was incorporated in the lower third of the 6 cm thick sand–layer, which covers the upper and lower plate equally, to allow for coeval frontal and basal accretion. During the experiments, the two sand layers converged, which resulted in the development of an asymmetric bivergent sand–wedge (Fig. 1a).

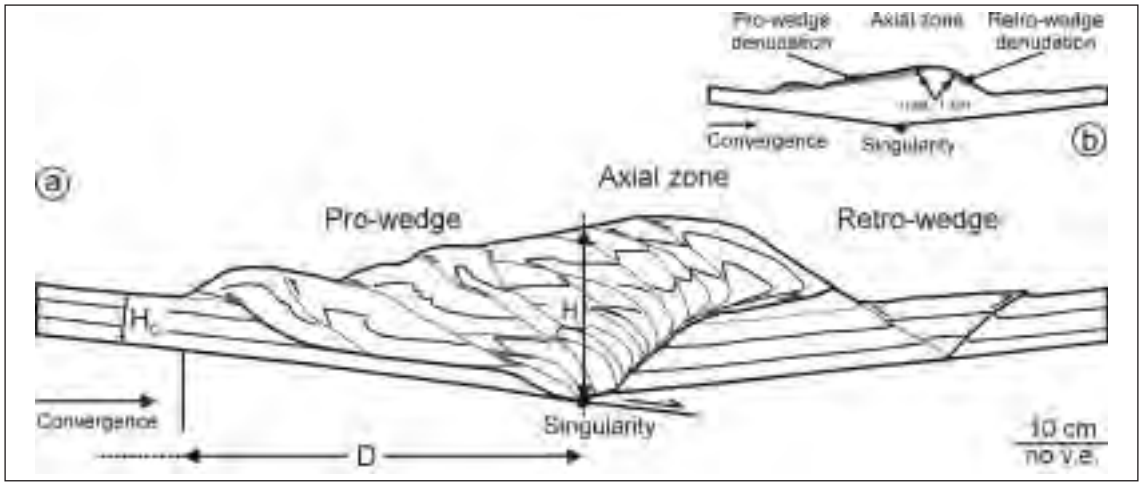

Fig. 1 – a) Outline and structural inventory of a bivergent sand–wedge after 100 cm of convergence. Measured parameters i.e. propagation of the deformation front of the pro–wedge [D] and height above the Singularity [H] are indicated. b) Schematic bivergent sand–wedge and geometry of simulated denudation.

In order to determine the influence of the location of denudation with respect to the convergence geometry on the lateral and vertical growth of bivergent sand–wedges, a reference experiment without denudation was carried out. In the two denudation experiments, the sand wedge was allowed to produce an initial topography during the first 40 cm of convergence. Incremental denudation at every ten centimetres of convergence was simulated with a vacuum cleaner. Denudation was decreased linearly from the top of the sand wedge to the toe of either the pro– or the retro–wedge (Fig. 1b). All experiments were monitored in 2D (profile–view) with two high speed, high resolution, digital cameras. Images were taken at every two seconds.

From these images two time series of (i) the distance between the deformation front of the pro–wedge and the singularity [D] and (ii) the height of the wedge above the singularity [H] are derived. Both geometric parameters are measured at every fifth image which equals 1.5 cm of convergence and are normalised with respect to the thickness of the incoming layer [H_0]. These time series in turn are used for the calculation of the flexure of a hypothetic foreland lithosphere in response to orogenic loading for each time (convergence) step according to the formulae provided by Allen and Allen (1990). Thereby we assume an elastic and broken plate and a complete fill of the foredeep with sediments. Thus, for each time (convergence) step we derived a flexure profile. All individual flexural profiles were finally combined and displayed as a flexure map.

Results and discussion

The imposed kinematic boundary conditions exert a strong control on the growth of the bivergent sand–wedge. Key kinematic characteristics of the latter are: (i) a polarity associated with the horizontal tectonic mass–transfer, (ii) the formation of a pro–wedge with a gentle topographic slope, an axial zone and a retro–wedge with a significantly steeper topographic slope, (iii) coeval frontal and basal accretion in the pro–wedge, (iv) a predominance of the accumulation of deformation in the pro–wedge during early to more advanced stages of convergence (v) late stage frontal accretion in the upper plate, (vi) upward motion of material due to thickening and (vii) flexural bending of the converging plates associated with the formation of foreland basins. Thus, the simulated bivergent wedge resembles the first order features of natural bivergent orogens such as the European Alps or the Pyrenees. Changes of either the flexural rigidity or the mechanic stratigraphy or the simulation of denudation evoke only minor modifications in the kinematic evolution of the bivergent sand–wedges. Results from physical simulations (Storti et al. 2000; Rossetti et al. 2002) do suggest that this is also the case for sedimentation or even for a different rheology. Thus, given these kinematic boundary conditions, the kinematics of such a bivergent wedge are considered to be very robust.
Time series data of the propagation of the deformation front of the pro–wedge (Fig. 2a) derived from the reference experiment show footwall shortcuts and the initiation of individual thrust imbricates. Whether the former or the latter occurs depends on the work necessary to either initiate a new thrust in the foreland, a shortcut or to reactivate an already existing thrust. The resulting overall trend of the propagation of the deformation front of the pro–wedge thus reflects the adjustment of the wedge to the incoming layer and the imposed boundary conditions. This trend is best described by a power law. In the reference experiment the width of the pro–wedge grows proportional to the convergence (x) by $x^{0.44}$, which is close to the theoretically predicted value of $x^{0.5}$ (Dahlen 1990). Time series data for the height above the Singularity (Fig. 2a) suggest a power law as well (Table1).

	Best fit curve (D)	Best fit curve (H)
No denudation	$y=1.0299x^{0.44}$	$y=1.0104x^{0.26}$
Retro–wedge denudation	$y=1.0328x^{0.43}$	$y=1.0692x^{0.25}$
Pro–wedge denudation	$y=0.97049x^{0.39}$	$y=1.0410x^{0.20}$

Table 1 – Power laws of best fit curves for the propagation of the deformation front of the pro–wedge (D) and for the height above the Singularity (H) for three experiments [x equals convergence, y is either D or H].

The observed power laws for both parameters imply that the incremental lateral and vertical growth of the pro–wedge decreases over time and so does the respective incremental addition of load. Accordingly, the addition of flexural induced subsidence of a hypothetical foreland at a given position decreases over time as well. If one further assumes a constant hypothetic sedimentation rate in this foreland basin system, a change from underfilled (fast addition of new accommodation), to overfilled (slow addition of new accommodation) would result. This transition would be thus an emergent consequence of the imposed kinematic boundary conditions.
Experiments with either pro– or retro–wedge denudation, however, reveal different power laws for the measured geometric parameters (Table1 and Fig. 2b). This results from the adjustment of the wedge by out–of–sequence thrusting or prolonged displacement along the deformation front to changes of the load distribution caused by denudation. Based on the same assumptions made above, our results suggest that the transition from an underfilled to an overfilled state is highly (minor) promoted for the pro–wedge (retro–wedge) denudation scenario.

Altogether, these results and the assumption that the kinematic boundary conditions are not subject to change as well as a constant sediment accumulation rate within the foreland basin system lead us to propose a two–staged evolutionary model: During the early stages of convergence the rate of orogenic growth/advance is high and so is the rate of flexure induced subsidence within the foredeep. Debris derived from the orogen is deposited in a deep and probably underfilled foredeep (flysch–type). At a later stage of convergence the rate of flexure induced subsidence within the foredeep decreases. The

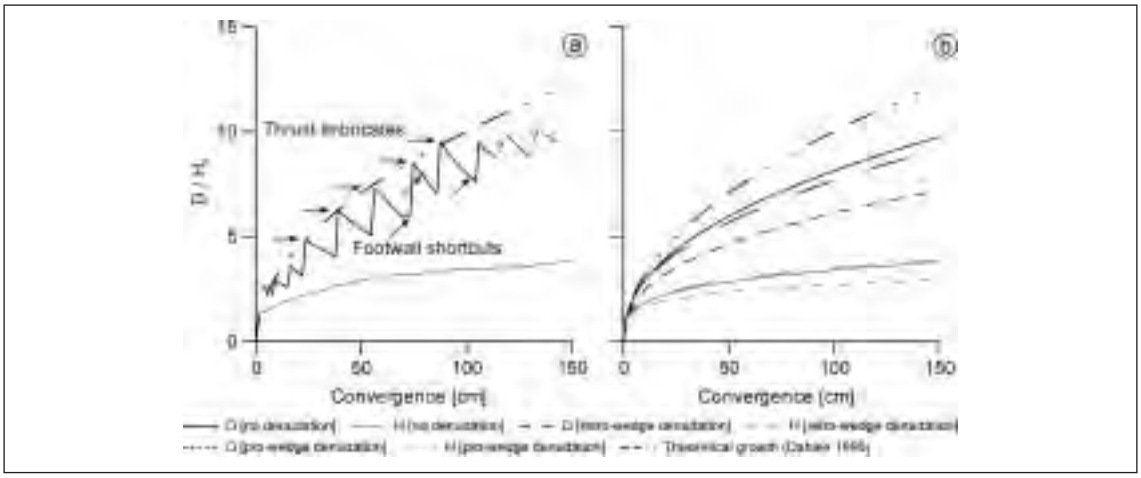

Fig. 2 – a) Time series data derived from the reference experiment; D is propagation of the deformation front of the pro–wedge; H is the height above the Singularity. b) Best fit curves for D and H for the reference and the experiments with either retro- or pro-wedge denudation.

latter is successively filled and may reach a point in its evolution where all sediments are bypassed (overfilled or molasse–type). Thus, we do suggest that the flysch to molasse transition is an emergent phenomenon solely arising from the imposed boundary conditions. Changes of the latter such as the flexural rigidity, the thickness and mechanic stratigraphy of the incoming plate or denudation/sedimentation would only retard or promote the flysch to molasse transition. The influence of denudation would be twofold: First, denudation controls the geometry and the propagation of an orogenic wedge and thus determines the incremental addition of load responsible for the flexure. Second, denudation provides the debris with which the foreland basin system is filled. A further implication is that there is no need to necessarily invoke a halt of convergence or a slab breakoff as a cause for the flysch to molasse transition.

Outlook

One of the main observations made in this study is, that the imposed kinematic boundary conditions result in a decay of the lateral and vertical growth of bivergent sand–wedges while convergence at constant rates continues. A similar slowdown has been observed for the Swiss Alps (Sinclair 1997) and for the Pyrenees (Labaume et al. 1985). In the case of the Swiss Alps and probably also for the Pyrenees, this slowdown is associated with the underfilled to overfilled transition and would thus support our model (Labaume et al. 1985; Sinclair 1997).

We further speculate upon the following: The geometric evolution of ancient foreland basins and their infill might once be used to decipher the position and magnitude of denudation with respect to the convergence geometry of bivergent orogens, now levelled down to their roots. Pro–wedge denudation significantly promotes the transition from an underfilled to an overfilled state and would thus lead to a short–lived underfilled foreland basin system. This might explain the scarcity of early flysch deposits in the foredeep of the Himalayas, Taiwan and the Pyrenees, which were subject to intense denudation on their respective pro–wedges (Covey 1986; Fitzgerald et al. 1999). A further implication of the results is that the magnitude and the location of denudation (pro– or retro–wedge) controls the height and the migration of the forebulge. Forebulge unconformities are preferred sites of Mississippi Valley Type deposits (Bradley and Leach 2003). Their formation might be induced by a denuding orogen, hundreds of kilometres away.

Acknowledgements

T. Vietor helped to clarify some aspects of this study. T. Lohr and R. Bachmann are thanked for their help while compiling the database necessary for the calculations. G. Tauscher build the experimental set up.

REFERENCES

• Allen P. & Allen J. (1990), Blackwell Science.
• Allen et al. (1991), Basin Research, 3, 143-163.
• Bradley D, & Leach D, (2003), Mineralium Deposita, 38, 652-667.
• Covey M. (1986), Spec. Publs. int. Ass. Sediment., 8, 77-90.
• Dahlen F. (1990), Annual Review of Earth and Planetary Sciences.
• DeCelles P. & Giles K. (1996), Basin Research, 8, 105-123.
• Dewey J. (1982), Geological Society of London, Journal, 139, 371-414.
• Fitzgerald P. et al. (1999), EPSL, 173, 157-170.
• Hubbert M. (1937), Geol. Soc. Am. Bull., 48, 1459-1520.
• Labaume et al. (1985), Tectonics, 4, 661-685.
• Lohrmann J. et al. (2003), Journal of Structural Geology, 25, 10, 1691-1711.
• Price R. (1973), Gravity and Tectonics, Wiley.
• Rossetti F. et al. (2002), Journal of Structural Geology, 24, 5, 953-962.
• Sinclair H. (1997), Geology, 25, no. 12, 1123-1126.
• Sinclair H. & Allen P. (1992), Basin Research, 4, 215-232.
• Sinclair H. et al. (1991), Tectonics, 10, 599-620.
• Storti F. et al. (2000), Tectonics, 19, 378-396.
• Ziegler P. et al. (2002), EGU Stephan Muller Special Publication Series 1, 17-56.

THE EFFECT OF PLASTIC-VISCOUS LAYERING AND STRAIN SOFTENING ON MODE SELECTION DURING LITHOSPHERE EXTENSION 3-15

Ritske S. Huismans, Susanne J.H. Buiter, Christopher Beaumont

Geodynamics Group, Department of Oceanography, Dalhousie University, Halifax (NS), Canada.
Ritske.Huismans@dal.ca

Summary

We investigate factors controlling the mode of extension in simple two layer systems. We present: 1) analytical estimates of the rate of energy dissipation for three modes, pure shear (PS), symmetric plug (SP) and asymmetric plug (AP); 2) criteria that control which of these modes is selected based on minimisation of the rate of energy dissipation; 3) numerical models of extension of the same simple two layer system, that confirm the analytic mode transition criteria. The main factor controlling the mode of deformation is the relative trade-off between two differential forces, the differential 'viscous penalty force' incurred by deforming of a viscous boundary layer in the symmetric and asymmetric plug modes versus the differential 'plastic gain force' owing to strain weakening that may occur in the plastic layer upon localised deformation.

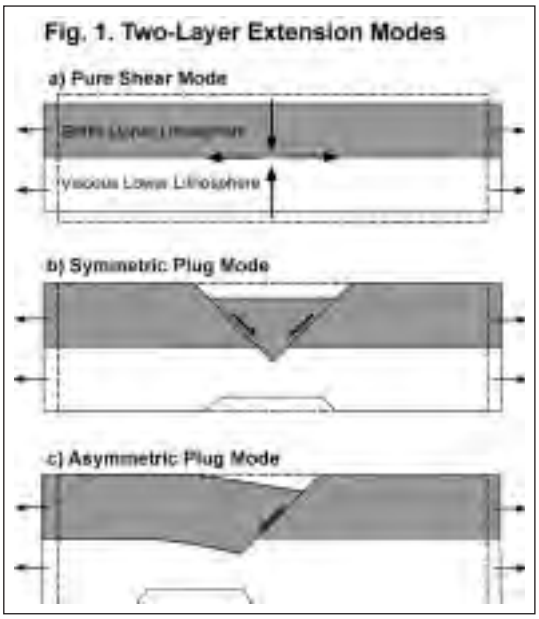

Introduction

Whether extension at the crustal or lithosphere scale may be symmetric or asymmetric is part of the larger question concerning the factors that control the styles or modes of continental extension (*McKenzie*, 1978; *Wernicke*, 1982). Observations of major detachments along passive margins, as well as asymmetric half grabens and asymmetric exhumation of high grade core complexes along single detachments indicate that extension may be asymmetric (Fig. 1). On the other hand a range of rift basins and core complexes with multiple opposite verging detachments indicate that extension may also be symmetric at different scales (Fig. 1). Although these observations

demonstrate the importance of symmetry and asymmetry and the role of faults and ductile detachments, other modes including lithospheric scale uniform pure shear without focused deformation are also theoretically possible.
Some insight exists concerning: 1) the factors that control asymmetry and symmetry during the early stages of extension, and; 2) the factors that cause a given mode to be abandoned during extension. Previous work (e.g. *Lavier et al.*, 1999; *Lavier and Buck*, 2002; *Huismans and Beaumont*, 2002, 2003) indicates that strain softening (or strain rate softening, *Behn et al.*, 2002) may be requirements for the initiation of asymmetric extension. Geometric hardening has been suggested (*Buck*, 1988; *Buck*, 1993; *Lavier et al.*, 1999; *Lavier and Buck*, 2002) as a main control that terminates asymmetric extension. However, strain softening and geometrical hardening, are probably universal lithospheric properties and, therefore, extensional zones would have similar geometries if these were the only important controls.
We propose at least a partial answer to the questions of the factors that control the modes of lithospheric extension, and which mode is selected in a particular circumstance. We base our approach on the view that the lithosphere is a composite laminated system, with viscous and plastic layers, in which the plastic layers weaken by focused deformation on faults and shear zones. We then use the principle of minimum rate of energy dissipation to predict the extensional mode that will be selected. The predictions of mode selection from the approximate rate of dissipation analysis is confirmed by a series of finite element model experiments. These experiments range from the model used for the approximate analysis through models with more realistic rheological layering. The overall results demonstrate that the mode preference in decreasing order is AP, SP and PS, and the modes will be selected in this order depending on the relative penalty of the viscous boundary layer rate of internal energy dissipation incurred by each mode.
We present: 1) the results of the dissipation analysis for the simple system, 2) the results of the numerical experiments; 3) the comparison of the numerical model results with the predictions of the dissipation analysis.

Analytical estimates of the rate of energy dissipation

The dissipation in a simple two-dimensional, plane-strain system (Fig. 2) comprising a uniform brittle-plastic layer overlying and bonded to a uniform linear viscous layer is analyzed approximately to estimate the rate of internal energy dissipation during the early stages of extension for three possible modes: 1) the PS Mode, distributed uniform (pure shear) extension; 2) the SP Mode, the symmetric single `plug' mode, and; 3) the AP Mode, the asymmetric single 'plug' mode. The plastic layer may either be a von Mises or a frictional-plastic material, respectively characterized by the cohesion or internal angle of friction. Strain softening results in a decrease in the value of these parameters with increasing strain, thereby weakening the plastic layer when deformation is focused on shear zones.

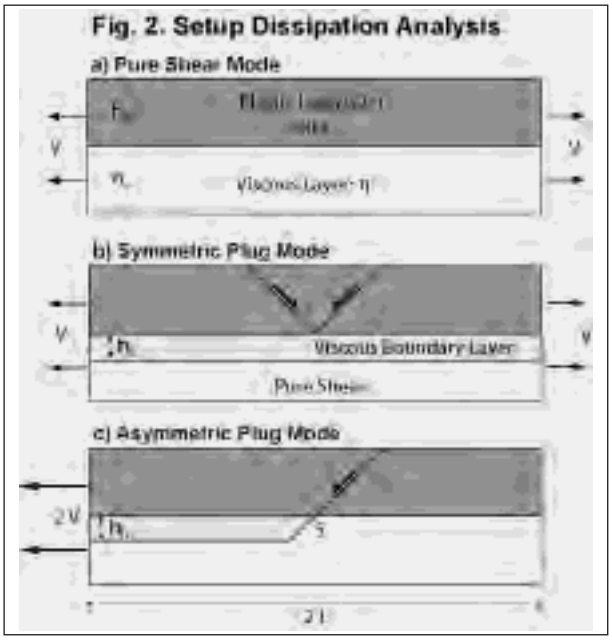

There are two main contributions to the rate of internal energy dissipation. 1) Plastic layer: this rate of dissipation is the same for each of the modes except when it is reduced by strain softening of the localized shears. 2) Viscous layer: this rate of dissipation ranges from that owing to pure shear in PS to a combination of pure shear and shear of the boundary layer at the top of the viscous layer when there is differential extension between the two-layers in SP and AP. Which mode is selected depends on the trade-off between the reduction of the plastic dissipation owing

to strain softening in SP and AP, versus the penalty of the increased rate of dissipation owing to the viscous boundary layer in SP and AP. By considering these trade-offs the mode selection can be predicted as a function of the layer properties and the rate of extension. The latter is important because the rate of dissipation depends on the strain rate.

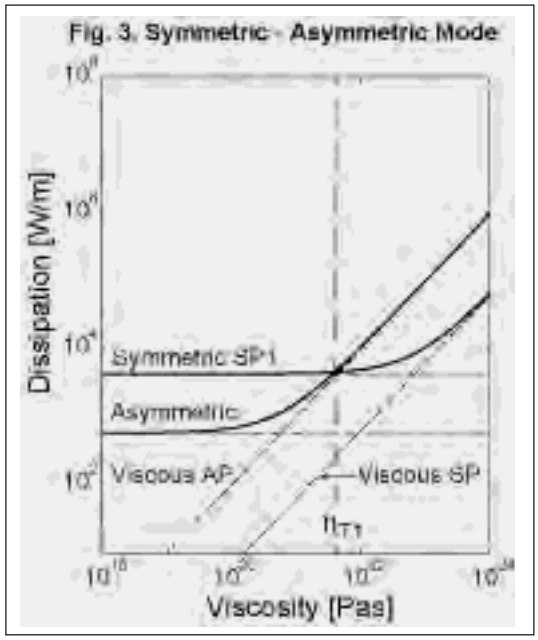

We derive approximate velocity fields and corresponding rates of energy dissipation for each of the three modes (Fig. 2). The criteria for mode selection are based on the minimization of dissipation. In the two-layer system the upper uniform cohesive or frictional-plastic layer is bonded to the underlying uniform linear viscous layer. The system extends under velocity, V, applied uniformly with depth and equally and oppositely to both ends. The base is free to slip horizontally but does not move vertically and there is a stress free upper surface. The results from the dissipation analysis show that the pure shear PS, symmetric plug SP1 and SP2 (where the latter includes the effect of strain softening on the bounding shears) and asymmetric plug AP modes may be selected.

We derive the transition viscosities that demark the viscosity dependence of the minimum dissipation modes. Here we discuss, as an example, the transition between the SP1 and AP Modes (Fig. 3). Equating the total dissipations found for the SP and AP modes and solving for the transition viscosity has the following result:

$$\eta_{T1} = \frac{1}{VL^*} h_p \, (C^{pss}(\varepsilon) - C^{ss}(\varepsilon))$$

Where V is the extension velocity, L^* is a characteristic dimensionless length scale that depends on the style of deformation in the boundary layer, h_p is the thickness of the brittle layer, and C^{pss} and C^{ss} are the partially and fully strain softened plastic cohesion values that depend on strain, ε. An equivalent transition viscosity, η_{T2}, is derived for the transition between SP2 and PS modes. The frictional plastic case will also be presented.

Numerical Models of Extension

We present finite element model experiments designed to test the approximate analytical theory. An Arbitrary Lagrangian-Eulerian (ALE) finite element method for the solution of mechanical plane-strain, incompressible, viscous-plastic creeping flows (*Fullsack*, 1995) is used to investigate extension of models with simple geometry and rheological structure. Plastic deformation has a pressure-dependent Drucker-Prager yield. Strain softening is introduced by linear decreases of respectively cohesion and friction angle over a range of strain.

Here we show one model series as an example (Fig. 4). A strain-softening frictional-plastic layer overlies a uniform constant linear viscous layer, and the viscosity ranges 10^{21} to 10^{23} Pas. The results are shown after 40 km total extension at 1 cm/yr. At low viscosity the AP Mode is selected. Strain softening has focused the plastic deformation onto one shear and the extension is highly asymmetric. When $\eta = 10^{22}$ Pas asymmetry is suppressed and extension in the plastic layer occurs along two symmetric shears in the SP Mode. At high viscosity ($\eta = 10^{22}$ Pas) local deformation in the plastic layer is completely suppressed and extension of both layers occurs by pure shear, the PS Mode.

The results of the numerical models are in qualitative agreement with the predictions of the dissipation analysis in that the modes selected for the strain-softened, SS, state change from AP to SP to PS as

the viscosity of the lower lithosphere increases. The results also indicate that the transition viscosities η_{T1}, and η_{T2} fall between 10^{21} and 10^{22} Pas, and 10^{22} and 10^{23} Pas, respectively, for the parameter values used in the numerical models. Numerical model experiments with depth dependend rheology and with more realistic basal boundary conditions confirm the mode predictions shown here. In an accompanying paper (*Buiter et al.*, this volume), which focusses on the role of surface processes during crustal scale extension, we confirm the main controls found here.

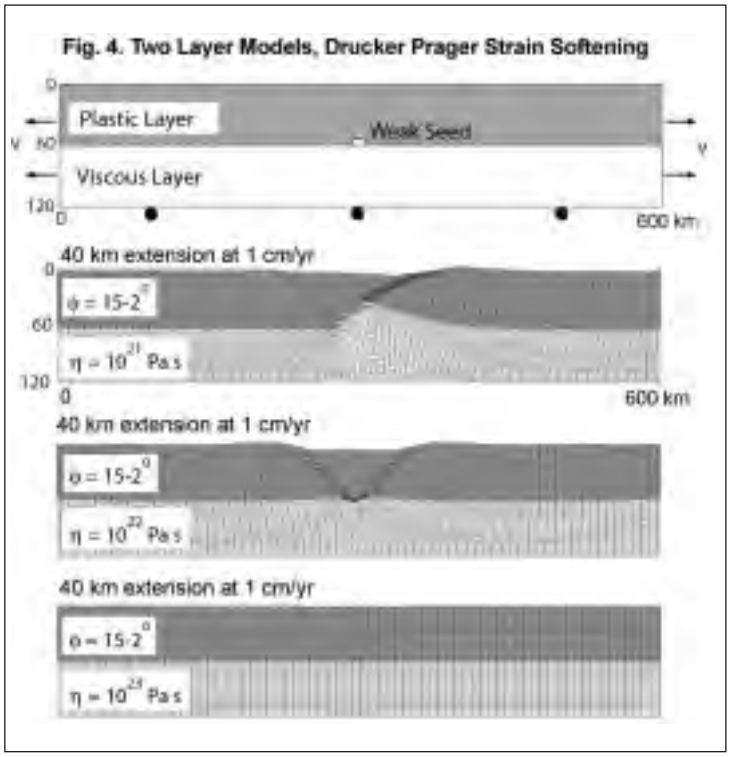

Conclusions

We demonstrate that mode selection in models of lithospheric extension can be predicted based on the minimization of rate of energy dissipation. The basic analytical mode predictions are confirmed by the numerical models. The predictions apply equally to the numerical models with the more advanced rheologies and more realistic basal boundary conditions.

The results presented illustrate the application of the principle of minimum rate of dissipation to a simplified model of the lithosphere comprising a cohesive, or frictional-plastic upper layer bonded to an underlying linear viscous lower lithosphere. Figure 5 illustrates the predicted mode selection pathways during strain softening of the plastic upper lithosphere (NSS → PSS → SS) and the control of the mode selection by the viscosity of the underlying viscous layer. These conclusions are derived from an approximate analysis and are supported by the finite element experiments.

Depending on the viscous dissipation the mode that is chosen during the early phase of extension, before the onset of strain softening (i.e. the NSS regime), will be the symmetric plug, SP1, or pure shear, PS, if the viscosity of the lower layer is greater than the critical value, η_{T2}. Later, during partial strain-softening, PSS, systems with viscosities greater than η_{T2} will ignore the possibility of strain softening on the shears bounding the plug and remain PS as they evolve. Systems with viscosity lower than η_{T2} will adopt either the asymmetric plug, AP Mode, or the strain-softened symmetric plug, SP2 Mode, if the viscosity is greater than the critical value, η_{T1}.

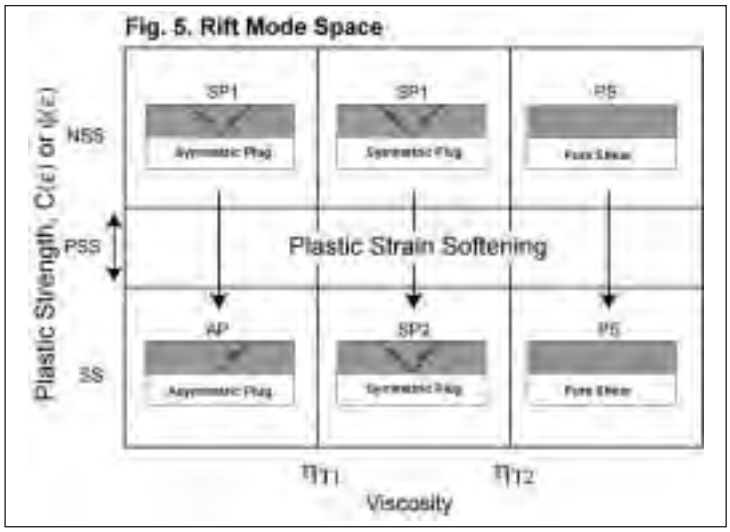

The potential application to crust and lithospheric extension is that the AP Mode is preferred when the dissipation in the viscous crust or lower lithosphere is

small, for any of the reasons that make η sub-critical with respect to η_{T1}, for example, extension is slow and the strain rates are low, or the effective viscosity is intrinsically low because the lithosphere is hot and weak. The AP Mode is therefore likely to be preferred for slow extension and/or hot lithosphere, but there are other possibilities that make η_{T1} greater than η, for example, factors that make η_{T1} large; so the selection is always a relative one. Equivalently, the SP2 Mode is predicted for faster extension of colder, higher effective viscosity lithosphere but this is not unique, any factor that makes η_{T1} less than η and η_{T2} greater than η will select this mode.

REFERENCES

- Behn, M.D., Lin, J., and Zuber, M.T., (2002), Earth Planet. Sci. Lett., 202, 725-740.
- Buck, W.R., (1988), 7, 959-973.
- Buck, W.R., (1993), Geology, 21, 933-936.
- Buiter, S.J.H., Huismans, R.S., and C. Beaumont, (2004), this volume, xxxx, this volume.
- Fullsack, P., (1995), Geophys. J. Int., 120, 1-23.
- Huismans, R.S., and Beaumont, C., (2002), Geology, 30, 211-214.
- Huismans, R.S., and Beaumont, C., (2003), J. Geophys. Res., 108, doi:10.1029/2002JB002026.
- Lavier, L.L., Buck, W.R., and Poliakov, A.N.B., (1999), Geology, 27, 1127-1130.
- Lavier, L.L., and Buck, W.R., (2002), J. Geophys. Res., 107, doi:10.1029/2001JB000513.
- McKenzie, D., (1978), Earth Planet. Sci. Lett., 40, 25-32.
- Wernicke, B., (1985), Can. J. Earth Sci., 22, 108-125.

INFLUENCE OF PORE PRESSURE ON SECONDARY HYDROCARBON MIGRATION, TUNE AREA, VIKING GRABEN 3-16

A.E. Lothe(*), Ø. Sylta(*), O. Lauvrak(**), S. Sperrevik(**)

(*) SINTEF Petroleum Research, N-7465 Trondheim, Norway

(**) Norsk Hydro ASA, P.O. Box 7190, N-5020 Bergen, Norway

Summary

Pressure and hydrocarbon migration modelling has been carried out in the Tune Field area, Viking Graben, offshore Norway. The pressures are considered to be controlled by compartments bounded by mapped faults. Two different interpreted fault maps at the top reservoir level (Brent Group) are used as input to the modelling. First, a low-resolution fault map is used, with only the large faults interpreted, and next, both large and small faults are included.

The simulations show high overpressures generated in the deeper parts of the Viking Graben, and hydrostatic in the eastern areas. A sharp pressure transition zone results from using the low-resolution fault map in the simulations. The secondary oil migration models show that overpressures have major effect on the hydrocarbon migration pathways. The level of detail in the fault interpretation is important for the simulation results, both for pressure distribution and for hydrocarbon migration.

Introduction

Faults may control lateral water flow and hydrocarbon migration in sedimentary basins. They can act as barriers to flow, but also as conduits or partial-conduits, depending on the involved lithologies and the geohistory. The flow transmissibility of faults is an important parameter when the pressure distribution and compartmentalization is modelled in a basin (Borge & Sylta 1998, Borge 2000).

The fluid flow properties of each fault is of importance when calculating lateral fluid flow in sedimentary basins. The fault interpretations from reflection seismic data of the dip-slip displacement and fault pattern are crucial for the pressure simulations. This implies that the level of details that the fault interpretations are carried out affect the pressure simulation results strongly. Understanding which fault map resolution is needed to obtain a good match to the observed pressure distribution will help in designing interpretation strategies. Probably, hydrocarbon migration modelling needs a higher resolution in the input data than simulations of the pressure distribution. The level of detail needed in

the input fault pattern, both to do pressure simulations and hydrocarbon migration, is one of the questions this work aim to answer.

The present study was carried out using a dataset from the Viking Graben in the northern North Sea. The data set covers both Oseberg South and the Tune Field, but the analysis was focused on the overpressured Tune Field (Figure 1). It is obvious in highly overpressured areas like the Halten Terrace area, Gulf of Mexico and the Northern Viking Graben, that the overpressure has a large impact on hydrocarbon migration. However, will the pressures also influence migration, when the pressure is low to moderate as is the case in the Tune area?

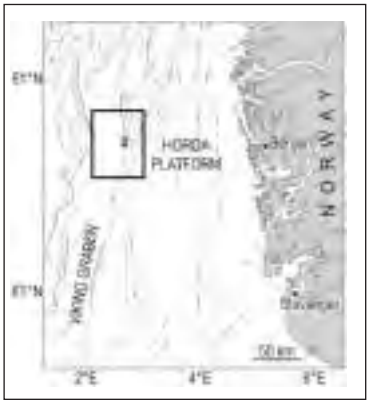

Fig.1 - Overview map from the northern North Sea. Main faults are shown. Large frame marks the study area.

Methods

The pressure simulator used ("Pressim"; Borge 2000, Lothe et al. in press), was developed to simulate pressure dissipation and migration at basin scales. The pressure compartments are defined by fault patterns interpreted at top reservoir level. The flux between the compartments is modelled. The shales above and below the reservoir form seals to the compartments. Fault transmissibility properties depends on the burial depth, the length, width and dip-slip displacements of the faults, thickness of the reservoir layers and the permeability inside the fault block (Borge & Sylta 1998). The most controlling factor for the transmissibility is the dip-slip displacement. The permeability versus depth is defined for all faults in the basin. However, the transmissibility across individual faults can be varied if local effects in the basin should be tested. In this work, the word "corrected" is used, if the transmissibility across individual faults has been changed to match measured pressures in particular wells. Hydraulic fracturing and leakage from the reservoir unit is estimated using the Griffith-Coulomb failure criterion for the first failure, and a frictional sliding criterion for reactivation of faults (Lothe et al., in press). The minimum horizontal stress is formulated as an empirical relationship versus depth. The vertical stress was varied as a function of time, depending on sedimentary loading. In the secondary hydrocarbon migration modelling the "Semi" modelling software was used (Sylta 1993). Semi employs a ray tracing modelling approach, assuming that hydrocarbons migrate along the top of a permeable carrier bed and upwards along the most steeply dipping rock horizon, governed by buoyancy. Hydrocarbon charge from a source layer within the model area or from injection points at the edges of the model at locations defined from regional migration studies is assumed. Burial histories, hydrocarbon maturation, expulsion and secondary migration are calculated at discrete time-steps. The fault sealing potential is related to the percentage shale within the part of the sequence that has moved past a point on the fault surface; termed the Shale Gouge Ratio (Yielding 1997). The SGR values on the fault surfaces are calculated from the dip-slip displacement to the faults and Vclay logs at the fault interpolated from Vclay-logs from nearby wells (Childs et al. 2002b, Sylta et al. 2003). The empirical estimations of fault rock properties presented by Sperrevik et al. (2002) are incorporated in the Semi modelling software (Sylta et al. 2003). Fault rock entry pressures are estimated from the clay content, maximum burial depth and depth at time of deformation. These properties are simulated to affect hydrocarbon migration, but not the water fluid flow modelled in the presented simulator. Sylta et al. (2003) used a multi-carrier model, while the present study is less complex, with only one carrier modelled.

Input data

To build the pressure simulator model, different input parameters are needed: a fault trace map at top reservoir level, depth-converted horizons for different time steps, paleo-water depths to the corresponding time steps, isopach map of the reservoir unit and measured pressure data from wells. In accordance, oil and gas expulsion maps and Vclay-logs from wells are needed to do the

a) b)

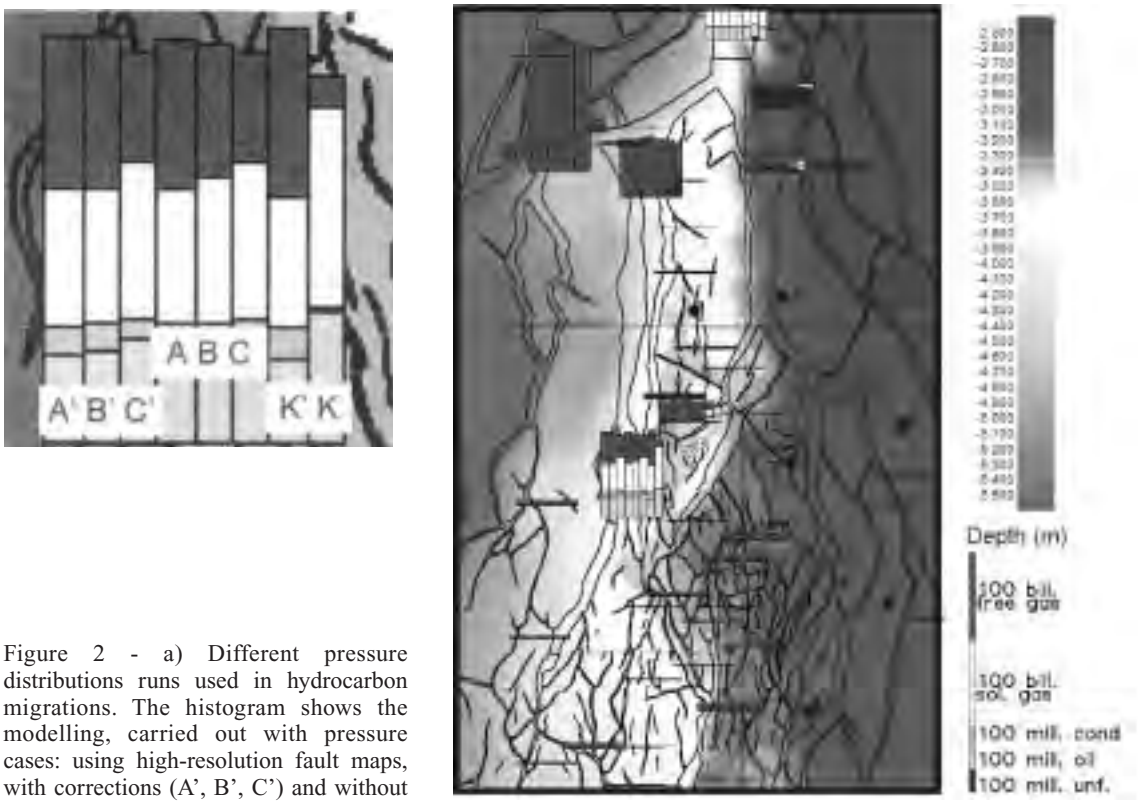

Figure 2 - a) Different pressure distributions runs used in hydrocarbon migrations. The histogram shows the modelling, carried out with pressure cases: using high-resolution fault maps, with corrections (A', B', C') and without corrections (A, B, C). The two last histograms show expected hydrocarbon columns using the low-resolution fault maps, with and without corrections (K' and K).b) Histograms shows expected hydrocarbon-columns using the different fault maps. White frame mark maps shown in Figures 3 and 4.

hydrocarbon migration modelling. The different paleo-pressure maps are used as input in the hydrocarbon migration modelled.

The fault trace maps are interpreted from seismic at the top Brent Group horizon in this study (Figure 4). Data from different seismic surveys are combined in the two fault map versions: Low-resolution fault map: Interpretation carried out on 2D lines, 125 m grids. High-resolution fault map: Combined grids with low resolution in some areas, and high resolution in central areas (16 m grids), partly interpreted from 2D lines and partly from 3D lines.

Results

In order to test how different pressure histories will influence the simulated migration, the different pressure maps were used as input for the secondary oil migration modelling. The high-resolution fault map was used in six cases. Simulations were carried out with pressure cases A', B' and C' with corrections first, and cases A, B and C were simulated without corrections. Finally, two simulations have been carried out using the low-resolution fault maps; with and without corrections (Figure 2a).

The results of all the different cases are presented in map view in Figure 2b. The figure contains histograms of the hydrocarbons trapped through time. The histograms show the amounts of oil, condensate, solution gas and free gas. A major gas trap is simulated to occur west of Tune, and also some smaller amounts in the Tune Field area.

Different models have been carried out using the different pressure cases as input. The first three histograms from the left in Figure 2a show the resulting hydrocarbon columns in case A, B and C. The three next show the results from A', B' and C'. The two last histograms to the right show the results using the low-resolution fault map to model the pressure distribution. The cases using the high-

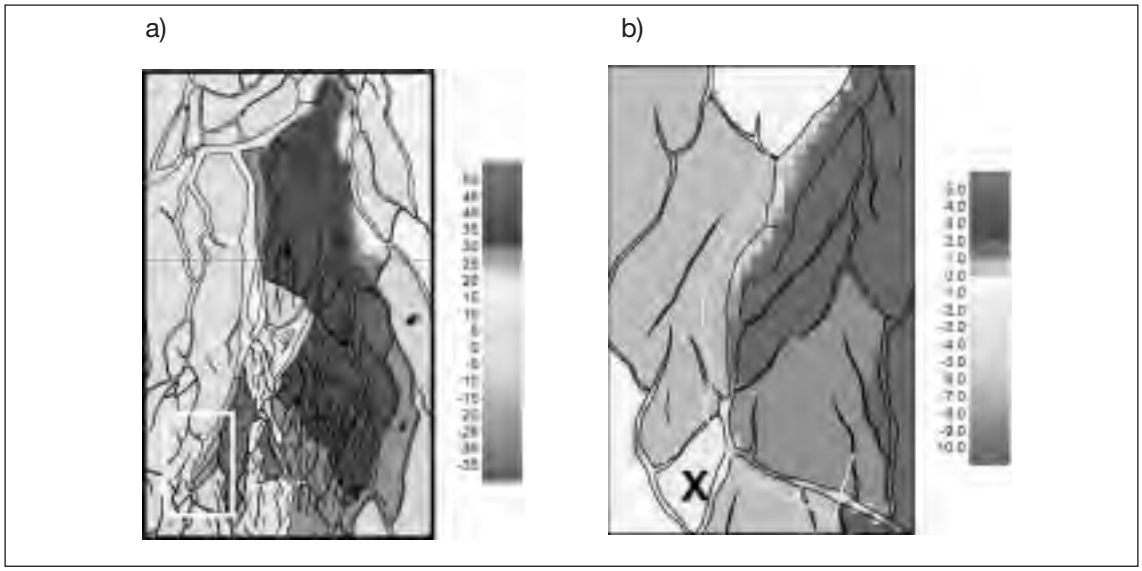

Figure 3 - a) Difference in the simulated pressure between case A' and C' (colour scale in bar). b) The changes in one pressure compartment marked X, seems to have a major influence on the hydrocarbon column in the nearby traps.

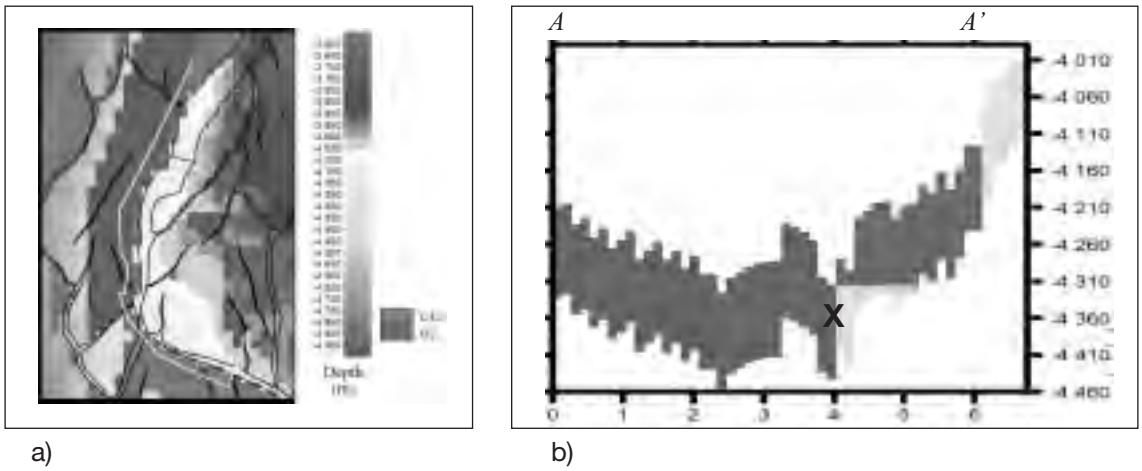

Figure 4 - a) Map showing the gas-flow rate in area marked on Figure 2. b) Profile A-A' shows that the oil-gas contact is situated on the fault in this area. Then, changes in pressure in compartment X changes the migration path in to the prospect west of Tune.

resolution fault map show small variations in simulated hydrocarbon columns. Starting out with the high-resolution fault map with corrections, there are some variations in the resulting gas columns depending on the depth where the cap rock starts to seal. Case A' has a thicker gas column developed (Figure 2b) and lower pressure build up than case B' and C'. If one compares case A' and case C', the difference in simulated pressure is mainly seen in the eastern part of the area (Figure 3a). In the southwestern part, however, there is a small compartment, which experiences a small pressure change between the two runs (A' & C'; Figure 3b). This small pressure change (3 bar) also changes the oil migration in the area (Figure 4a). A profile is shown across the structure to illustrate the oil-and gas distribution in the area (Figure 4b). The gas-water contact is situated directly on the fault, with oil on the other side. A small increase in the simulated fluid pressure in this compartment (marked X; Figure 4), will influence the simulated gas column in the prospect.

Case A, B and C (without corrections) show the same trend in oil and gas accumulations as described for case A', B' and C'. The reason is probably that the overpressure changes between, for example case

A and A', is in the eastern part of the area with generally lower pressure. Also, the hydrocarbon modeling shows that the oil migrates from west towards east. The pressure changes in west become the most critical factor for the hydrocarbon migration.
Secondary oil migration modelling has also been carried out, keeping the high-resolution fault map for the hydrocarbon migration simulations, but using the pressure distribution history simulated using the low-resolution fault map runs presented. Figure 2 shows the filling history, using the low-resolution fault map, with and without corrections. Run K (without correction) gives the lowest pressure in the western area, including Tune, and therefore more gas is dissolved in the oil in this case. The free gas cap therefore fills less of the pore space and more oil can be trapped before spill starts.

Conclusions

Simulations using a low-resolution fault map give a large-scale understanding of the major trends in the pressure distribution throughout the sedimentary basin. In the Viking Graben study area large overpressures are simulated in the deepest western part of the basin, and close to hydrostatic pressures in the eastern area. A rather narrow indermediate zone with intermediate pressure is simulated. The modelled pressures have a controlling effect on the hydrocarbon migration even in intermediate pressured areas. Changes in the fault interpretation will modify the overpressure distribution and therby significantly modify the modelled trapped oil and gas accumulations.

REFERENCES

- Borge, H. 2000. Fault controlled pressure modelling in sedimentary basins. An thesis for the degree of Doktor Ingenør of the Norwegian University of Science and Technology, Trondheim, 148 pp.

Borge, H. & Sylta, Ø. 1998. 3D modelling of fault bounded pressure compartments in the North Viking Graben. Energy, Exploration and Exploitation, 16, 301-323.

- Childs, C., Sylta, Ø., Moriya, S., Walsh, J.J. & Manzocchi, T. 2002b. A method for including the capillary properties of faults in hydrocarbon migration models. In: Koestler, A.G. & Hunsdale, R. (eds), Hydrocarbon Seal Quantification. NPF Special Publication. Elsevier Science, Amsterdam, 127-139.
- Lothe, A.E., Borge, H. & Gabrielsen, R.H. in press. Modelling of hydraulic leakage by pressure and stress simulations: An example from the Halten Terrace area, offshore Mid-Norway. Submitted to Petroleum Geoscience.
- Sperrevik, S., Gillespie, P.A., Fisher, Q.J. & Knipe, R.J. 2002. Empirical estimation of fault rock properties. In: A.G. Koestler & R. Hunsdale (eds), Hydrocarbon Seal Quantification. NPF Special Publication. Elsevier Science B.V., Amsterdam, 109-125.
- Sylta, Ø. 1993. New techniques and their application in the analysis of secondary migration. In: Doré, A.G. (eds), Basin Modelling: Advances and Applications. NPF Special Publications, Amsterdam, 385-398.
- Sylta Ø., Childs C., Sperrevik S. & Tømmerås A. 2003. On the use of multi-carrier hydrocarbon migration modelling with clay-smearing in faults. EAGE Conference: Fault and Top Seals. What do we know and where do we go?, Montpellier, France. Abstract only.

EXTENSION THROUGH A HETEROGENEOUS CRUST. THE CASE OF GULF OF CORINTH (GREECE). PART I: ANALOGUE MODELLING 3-17

L. Mattioni, I. Moretti, L. Le Pourhiet

Institut Français du Pétrole, 4 Av de Bois Preau, 92852 Rueil Malmaison, France. (luca.mattioni@ifp.fr)

Summary

We used analogue models to study the normal fault patterns produced by extension through a heterogeneous crust. The boundary conditions have been designed to correspond to the western part of the Gulf of Corinth where old thrust sheets are likely to be reactivated as décollement levels during the Quaternary extension. Our preliminary results show that the occurrence of an inherited weak nappe can act as a localising factor of the deformation and thus can behave as detachment level.

Introduction

Orogenic phases result in a stack of nappes that may correspond to different lithologies and result in heterogeneous mechanical behaviour of the area during post-orogenic structuration. In the Mediterranean area, the best examples of orogens that are currently affected by extension are the

Italian Apennines (see, among others, Faccenna et al., 1995) and the Hellenides, in Greece (Jolivet, 2001). In this paper, we approach the problem of the influence of the inherited heterogeneities on normal fault genesis and evolution by means of small-scale model experiments (Exadaktylos et al., 2003). The results of our analogue models discussed here may be applied anywhere, however the boundary conditions have been chosen to provide insight on the fault pattern and evolution of the Gulf of Corinth (Greece) case-history.

The Gulf of Corinth (Greece) is a N100°E oriented elongate graben 105 km long, bounded by systems of very recent, roughly E-W normal faults (Fig. 1a), that are thought to be younger than 1.2 Myr (Moretti et al., 2003 and references therein). The extension affecting this area started in Miocene times, and is clearly superposed on an earlier compressive tectonic phase, responsible for the development of the Hellenides thrust belt (Jolivet, 2001). This compressive phase is characterised by structures striking roughly N150°, which are therefore oblique with respect to the direction of extension, which is N-S oriented. Interpretation of subsurface data (Moretti et al., 2003, and references therein) has shown that the Gulf of Corinth is not an asymmetric simple half graben as previously believed, rather, there are active normal faults on both sides of the Gulf. The more active faults that localize the current depocentre are located near the Southern shore and dip northward in the Eastern part of the Gulf, whereas in the Western part of the Gulf they are located near the Northern shore and dip southward. The seismogenic zone presents different characteristics from East to West: it is flat and rather deep (12 km) in the East, whereas it dips to the north and is rather shallow (up to 5 km under the North Peloponneous) in the West (Rigo et al., 1996). In outcrop, the faults have a high-angle dip and are planar structures; one may suggest that they root onto the gently dipping (roughly 20° to the north) plane defined by the cluster of microseismicity (Fig.1b) (Rigo et al., 1996). Further particular characteristics of the area have been well summarized by Moretti et al. (2003) and include (i) the occurrence of the Hellenic nappes westward, whereas the eastern part has been poorly affected by the compression, (*ii*) variation of the crustal thickness from west (about 40 km) to east (20 km), and (*iii*) variations, through time and space, of the location of the depocentre.

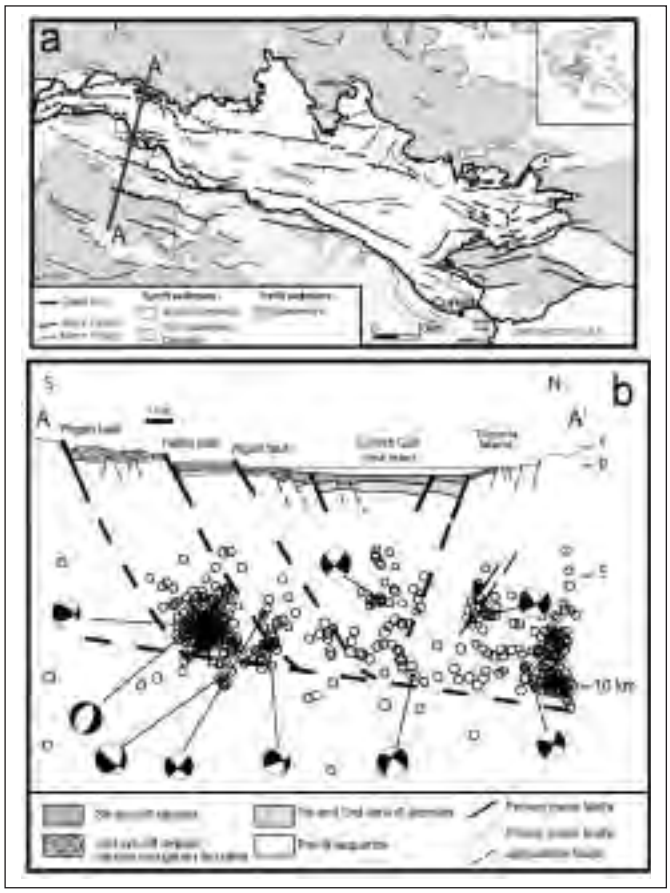

Fig. 1. (a) Geological sketch map of the Gulf of Corinth (modified from Moretti et al., 2003). A-A': trace of the cross section. (b) Schematic cross section through the Gulf of Corinth (modified from Moretti, 2003). Interpretative fault-plane solutions have been also projected (reproduced from Rigo et al., 1996)

Analogue modelling

In the experiments, upper-crustal brittle rocks are simulated with sand having a very low/negligible cohesion value, an angle of internal friction varying from 23° to 45° and a density ranging from 1500 and 1700 kg/m^3. The ductile behaviour of rocks in the lower crust, and/or of weak layers within the brittle upper crust is simulated by silicone putty (PDMS). This latter is a nearly Newtonian fluid, with a density of 0.965 g cm^{-3} and a viscosity of 5 x 10^4 Pa at room temperatures and at strain

rates below 3 x 10^{-3} s^{-1}. Our models were scaled for lengths, viscosities and time, following the basic principles discussed in detail by Hubbert (1937) and Ramberg (1981).
The experimental set-up consists of a wooden box (Fig. 2a), with two free sides. The other two sides of the box are represented by two sliding backstops attached to two base plates, and driven by a double conveyor belt system, that moves by means of computer-controlled stepper motor. The conveyor belt system allows the deformation to be localised at the base of the model near its central part (i.e. where the two base plates are in contact), where a velocity discontinuity occurs.
As can be seen in Fig. 2b, the models consisted of a 1-cm-thick silicone layer directly above the plates, overlain by a 4-cm-thick sand pack. During construction of this latter, we placed a gently dipping silicone layer 0.4-cm-thick, thus simulating a ductile level embedded within a more mechanically competent series. A set of experiments with a systematic variation of the strike direction of the gently dipping décollement level was carried out to test the influence of this parameter on normal fault patterns. The angle α of apparent dip of the silicone layer (e.g. the angle measured along a vertical section perpendicular to the velocity discontinuity) was maintained fixed at 20° (Fig. 2b). All the models were subjected to symmetric extensional deformation. The applied extension was characterised by a direction perpendicular to the velocity discontinuity and by a velocity fixed at 1 cm/h. A square grid of coloured sand markers was traced on the uppermost surface of the model.
As the deformation was applied, the central part of the sandbox was scanned by means of X-ray computerised tomography (CT), thus allowing a detailed analysis of their internal geometry and kinematic evolution (Colletta et al., 1991).

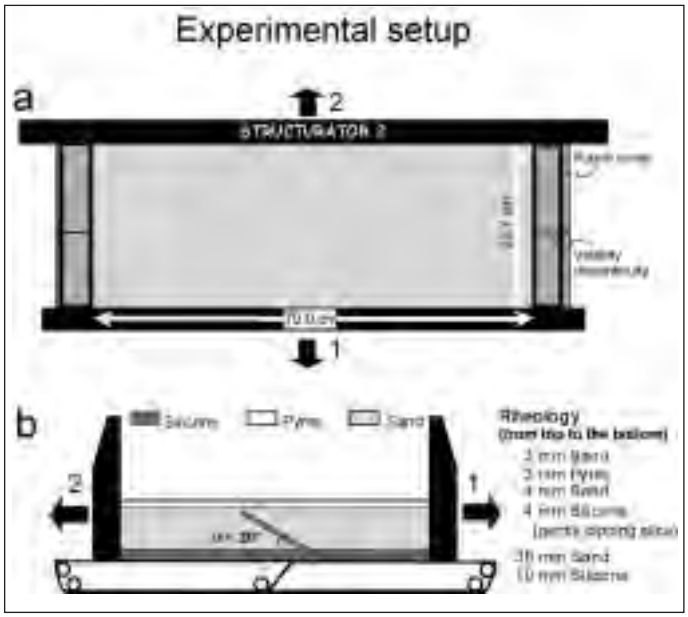

Fig. 2. Experimental set-up for analogue model experiments. (a) Plan view of the sandbox. Arrows indicate the direction of applied extension. (b) Section through the model.

Discussion and conclusions

The results of our small-scale experiments allowed us to draw some preliminary conclusions.
1. In all the models, the occurrence of a gently inclined ductile level interlayered within a more competent sand pack, produces a strong localisation of the extensional deformation within the part of the sand directly above the décollement level. In fact, in the early stages of deformation, a system of conjugate high-angle normal faults initiates at the tip of the gently dipping décollement level nearest the free surface. For practical reasons, we will call those faults dipping in the same dip direction as the décollement level "synthetic faults" and all the faults dipping in the opposite dip direction "antithetic faults". This language convention will be used throughout the paper. The set of conjugate normal faults propagates upwards with increasing displacement on the detachment level, thus resulting in a more or less symmetrical graben configuration. With increasing deformation, the main fault within the system becomes the one bordering the left side of the rifted zone, as it exhibits much higher and more localised displacement with respect to both minor synthetic and antithetic faults. This feature results in a progressive asymmetry of the graben. Further minor synthetic faults progressively develop in the hanging wall of the older ones; new antithetic faults form in the footwall of the older antithetic ones, thus producing a gradual migration downward the detachment level of the right side of the rifted zone. Associated with such asymmetric opening of the graben, a progressive shift to the right of the depocentre occurs (Fig. 3a).

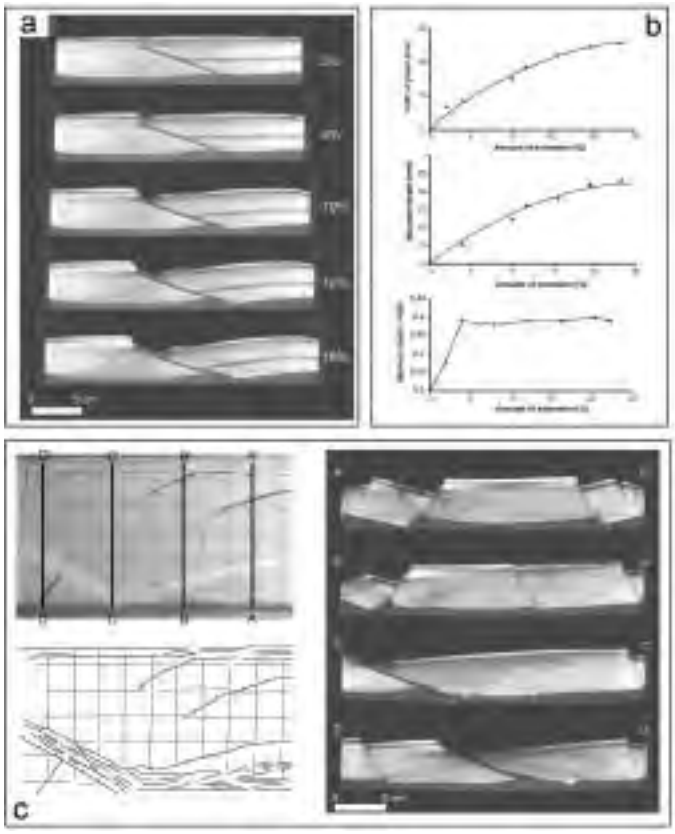

Fig. 3. Analogue model results. (a) Vertical sections showing fault evolution at four stages within the analogue model (the images refer to the experiment where the angle comprised between the direction of extension and the strike of the detachment was 90°). (b) Representation of relationships between the width of graben and the rate of extension (upper graph), the maximum depth of the graben at the free surface and the rate of extension (central graph). Evolution of the ratio between maximal depth/width of the graben vs. amount of extension is also shown in the lowermost graph. (c) Line drawing after photograph of surface and vertical sections through the model, describing the fault pattern at the end of experiments where the angle comprised between the direction of extension and the trend of the décollement level were less than 90° (in this case 60°). Position of vertical sections is indicated in accompanying photograph of surface.

2. Model results indicate that both the maximum depth and the width of the graben increase roughly proportionally with increasing shear displacement along the gently inclined detachment level (Fig. 3b) (Exadaktylos et al., 2003). Considering the ratio between the maximum depth and the width of the graben at different stages of the extension, we see that this value is roughly constant during the evolution of the deformation. However, this is not observed in the initial phases of deformation, when this ratio is at its minimum value. This suggests that in the early stages of extension the rifted zone grows mainly in width rather than in depth, whereas as deformation continues, the amount of offset increases and the trough quickly deepens.

3. In experiments where the angle between the direction of extension and the trend of the décollement level is less than 90°, all the new faults that root on the ductile silicone layer develop with a strike that is not necessarily orthogonal to the direction of extension. Rather, they run parallel to the trend of the ductile layer, and accommodate a transtensional displacement. However, the strong contrast of competency between the two experimental materials used, i.e. sand and silicone, could explain this control on normal fault orientation.

4. Rheological differences between areas where low-angle detachment layers occur and adjacent domains without a décollement level can lead to some differences in strain distribution, that result in different patterns of normal fault distribution and evolution. This is shown in Fig. 3c, where the detachment layer, striking with an angle of 60° with respect to the direction of extension, occurs only in the lower left corner of the sandbox, and is completely absent in the right-hand part of the model. Thus, in the presence of a gently dipping detachment, the resulting deformation is highly concentrated in a narrow area; within such a zone, apart the main synthetic fault displaying larger displacements, the extension is homogeneously accommodated by means of several minor faults oriented obliquely (i.e. parallel to the trend of the décollement level) with respect to the direction of extension. Where there is no décollement, the deformation affects a wider zone, however it is accommodated by few faults showing larger displacements. As a whole, such features seem to suggest an important control played by the presence of a décollement level on graben dimensions and on the distribution of

deformation. However, this part of the work is still in progress, as only few experiments have been carried out with this configuration.
Summarising, our results show that the occurrence of structural heterogeneities within the brittle crust can strongly influence the subsequent fault pattern and the distribution of the deformation during a rifting episode. In particular, our analogue results predict a fault pattern similar to that of the Gulf of Corinth, i. e. a system of synthetic and antithetic faults that root on the décollement level constituted by the thrust sheet (Fig. 1b). The graben gets wider as the extension increases and new faults appear towards the right of the model (the equivalent of northward in the Western Corinth case study). As a result, the external margin of the rift zone progressively migrates to the right (i.e. northward), together with the depocentre of the basin, that progressively migrates towards the dip direction of the detachment. The above results are rather similar to those obtained in the numerical models performed by Le Pourhiet et al. (2004).
Furthermore, the presence of a pre-existing discontinuity can lead to remarkable differences in strain distribution, as well as in the dimensions and orientation of the resulting rifted zone. This is shown in Fig.3c, where a low-angle detachment is present only in the left part of the model. Up to now only a few experiments have been performed with this configuration, so that the results shown are preliminary. Nevertheless, they seem to be very interesting and represent a good basis for future work aimed to elucidating the role of pre-existing discontinuities in extension tectonics.

REFERENCES

- Colletta B., Balé P., Ballard J. F., Letouzey J. and Pinedo R.; 1991: Computerized X-ray tomography analysis of sandbox models: examples of thin-skinned thrust systems. Geology, 19, 1063-1067.
- Exadaktylos G. E., Vardoulakis I., Stavropoulou M. C. and Tsombos P.; 2003: Analogue and numerical modeling of normal fault patterns produced due to slip along a detachment zone. Tectonphysics, 376, 117-134.
- Faccenna C., Nalpas T., Brun J. P., Davy P and Bosi V.; 1995: The influence of pre-existing thrust faults on normal fault geometry in nature and experiments. J. Struct. Geol., 17, 1139-1149.
- Hubbert M. K.; 1937: Theory of scale models as applied to the study of geologic structures. Geol. Soc. Am. Bull., 48, 1459-1520.
- Jolivet L.; 2001: A comparison of geodetic and finite strain pattern in the Aegean, geodynamic implications. Earth Plan. Sci. Lett., 187, 95-104.
- Le Pourhiet L., Moretti I. and Mattioni L.; 2004: Extension through a heterogeneous crust. The Gulf of Corinth (Greece) case-history. Part II: Numerical modelling. Boll. Geof. Teor. Appl., this issue.
- Moretti I., Sakellariou D., Lykousis V. and Micarelli L.; 2003: The Gulf of Corinth : a half graben? J. Geod. 36, 323-340.
- Ramberg H.; 1981: Gravity, Deformation and the Earth's Crust. Academic Press, New York.
- Rigo A, Lyon Caen H., Armijo R., Deschamps, A., Hatzfeld D. Makioupoulos K, Papadimitriou P. and Kassaras I.; 1996: A microseismic study of the western part of the Gulf of Corinth (Greece): implications for the large-scale normal faulting mechanisms, Geophys. J. Int., 126, 663-688.

EXTENSION THROUGH A HETEROGENEOUS CRUST. THE CASE OF THE GULF OF CORINTH (GREECE). PART II: NUMERICAL VERSUS ANALOGUE MODELING APPROACH

3-18

L. Le Pourhiet, I. Moretti, L. Mattioni

Institut Français du Pétrole, 4 Av de Bois Préau, 92852 Rueil Malmaison, France

Summary

We use numerical models to study the normal faults pattern produced by extension through a heterogeneous crust. Two set of runs will be discussed. Set 1: the boundary conditions have been designed to correspond to the western part of the Gulf of Corinth where old thrust sheets (the Phylliades Nappe) are likely to be reactivated as decollement levels during the Quaternary extension. Set 2: the runs have been designed to compare the numerical approach with the analogue one developed previously. Results show that the boundary conditions, especially the fixed bottom in regular sand box models preclude the quantification of realistic vertical movements.

Introduction

Orogenic building leaves a complex heritage consisting of a stack of nappes that may have contrasting lithologic structures resulting in heterogeneous mechanical behaviour of the system during the post-orogenic stages. While the thermal state of the region is re-equilibrating, strong lateral variations of the depth to the brittle-ductile transition develop as a consequence of these pre-existing heterogeneities. We use a thermo-mechanical model to quantify how an inherited weak nappe influences the development of fault patterns resulting from post-orogenic extension. The numerical code Para(o)voz (developed by Y.Y Podladchikov and A.N.B Poliakov) has been used for the experiments; the description and benchmarks of the algorithm can be found in the FLAC-related literature (e.g., Cundall, 1989; Poliakov et al., 1993).

A first series of experiments aimed to test the influence of a weak nappe with thermo-dependant non-Newtonian visco-elasto-plastic rheology and realistic boundary conditions.

The second aimed to benchmark the cylindrical analogue model (Mattioni et al., this issue) with a purely mechanical model and much simpler rheology.

Applicability of inherited weak nappe structure to the case of the Corinth Gulf

The Gulf of Corinth is an active rift zone associated with very high seismicity and strain rates. It is located between Peloponnesus and continental Greece. All recent studies confirm that the rifting was initiated 1My ±0.2 ago [Sorel, 2000; Westaway, 2002; Moretti et al., 2003]. The recent GPS data [Briole et al., 1999] infer an opening direction N00 with opening velocity decreasing eastward from 1.5cm/yr, at Rio, to 0.5cm/yr, at the level of the Isthmus of Corinth.

The main inherited features in the region of Corinth are pre-existing variations in crustal thickness (discussed in [Le Pourhiet et al., 2003]) and stack of thrust sheet, including the Phyllades nappe that outcrops south of the Gulf. Both are related to the orogenic building and to the Miocene times extension. The Phyllades nappe is mainly composed of weak phyllosicates [Ghorbal, 2002] (see map Fig.1) and shows lineation of extension N30 to N50. We proposed to apply our model to the Phyllades nappe which is the major lithological contrast in the area. Considering this, the initial conditions of the models correspond to a simplified cross-section of the Gulf of Corinth with a top-flattening part at the level of the tectonic window of Pheneos where the Phyllades nappe outcrops under the Tripolista nappe and the Pindos nappe (Fig 1).

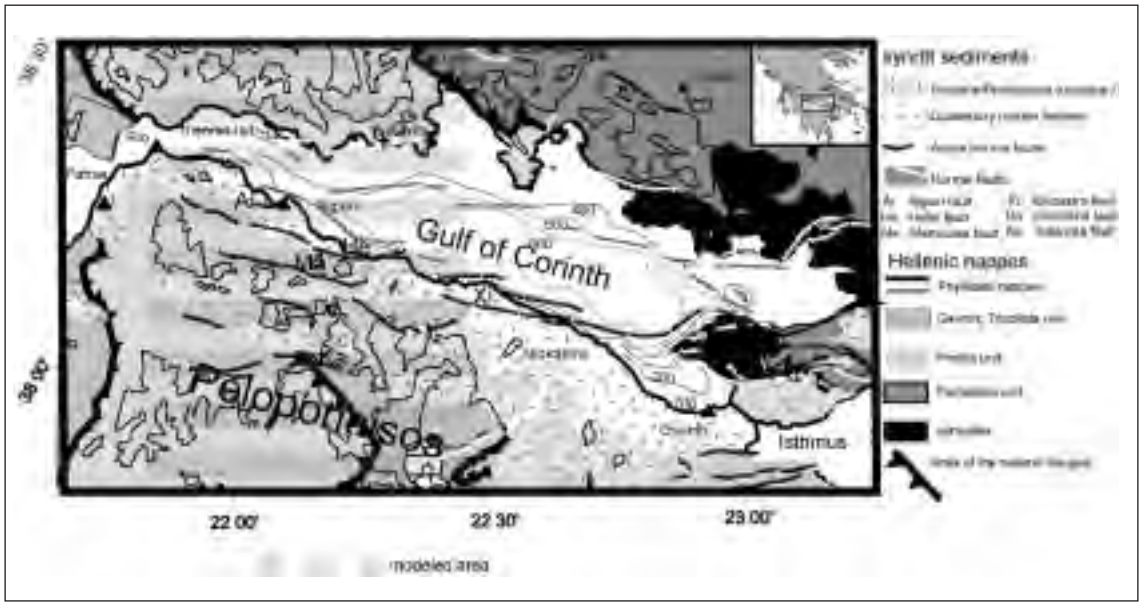

Fig. 1. Geological map of the Gulf of Corinth. The extensional lineations trend N30-50° in the metamorphic window of Pheneos [Ghorbal, 2002]. Hellenic nappes after [Jacobshagen et al., 1978], recent faults after [Rigo et al., 1996, Ghisetti et al., 2001; Moretti et al., 2003]

2D Thermo-mechanical experiments

In the first set of numerical experiments the influence of numerous parameters has been tested including the dip angle of the thrust sheet, the competence contrast between the weak nappe and the host rock as well as the competence of the host-rock itself. Fig 2a presents the boundary and initial condition used. The rheological parameters are summarised in table 1 and 2.

Table 1:

Phases	Density, ρ, (kg.m^{-3})	A (MPa^{-n})	n	E (J mol^{-1})	shear modulus, G (Pa) = bulk modulus K(Pa)	Cohesion (Pa), C_0	Friction angle ϕ, (°)	Dilata., angle,
Nappe	2600	$5x10^{3}$	3	$1.9x10^{5}$	10^{10}	$2x10^{7}$	30°	0°
Host-rock	2600	$5x10^{-6}$	3	$1.9x10^{5}$	10^{10}	$2x10^{7}$	30°	0°

Table 2:

Phases	Vis (Pa.s)	Lambda (Pa)	G = K (Pa)	Friction angle	Dilatation angle
Nappe	10^{19}	10^{10}	10^{10}		
Host-rock		10^{10}	10^{10}	42°	0°

The results are fully described in Le Pourhiet et al. [2004] and presented here on phase diagram on Figure 2b. To sum up those results:
1) A weak horizontal layer would result in decrease of the global effective elastic thickness of the upper crust and permit the formation of upper crustal scale faults with shorter spacing than what would be attended without the weak heterogeneity. The fact that this thick weak planar heterogeneity possesses a dip results in lateral variation of the effective elastic thickness of the upper crust and localization effect. A dipping weak nappe introduces thus a lateral velocity discontinuity and serves as a localization factor for deformation.
2) In the case of a low competence contrast between the weak nappe and the surrounding rocks, the presence of the nappe is sufficient to localize strain and to lead to the formation of a flexural rolling hinge but the contrast is not sufficient to decoupled elastically the stronger phases situated above and below. The migration of the basin depotcenter is slow, continuous and limited by gravity driven processes that lead to the rise of hot (weak) material under the subsiding basin.
3) In case of a high competence contrast, overall crustal strength is reduced by a 'dipping pie' effect. By 'pie', we mean a layered media. Assuming overall high crustal strength, the presence of a contrasting nappe leads to bimodal fault pattern governed by two types of faults: crustal scale planar faults rooting on the brittle ductile transition of the crust and thin-skinned listric faults rooting on the nappe itself. This bimodality results is a jump-like migration of the basin downward the dipping weak nappe.

What competence contrast to explain the kinematics of normal faults in Corinth Gulf?

Application of the numerical results to the case of Gulf of Corinth (Greece) allows us to explain, in case of assumed high competence contrast with a brittle ductile transition situated at 12 km, the observed micro-seismicity patterns, the asymmetry of the Gulf and the kinematics of fault migration within the basin (Fig 5).
Nethertheless**,** the 2D assumption can be discussed because the dipping direction of the Phyllades nappe in the Gulf of Corinth is 30°/50°N while the stretching is directed along 00°N. This difference can produce either 'en echelon' structures following the iso-depth of the nappe, or re-orient the fault in the dipping direction of the nappe. In fact, both of these structural patterns ('en echelon' faults and 30°N oriented faults) exist in the Gulf of Corinth.
To test these hypothesis, 3D analogue model have been run (Mattioni et al. 2004). The second part of this contribution aimed to test if comparison between analogue and numerical model is justified.

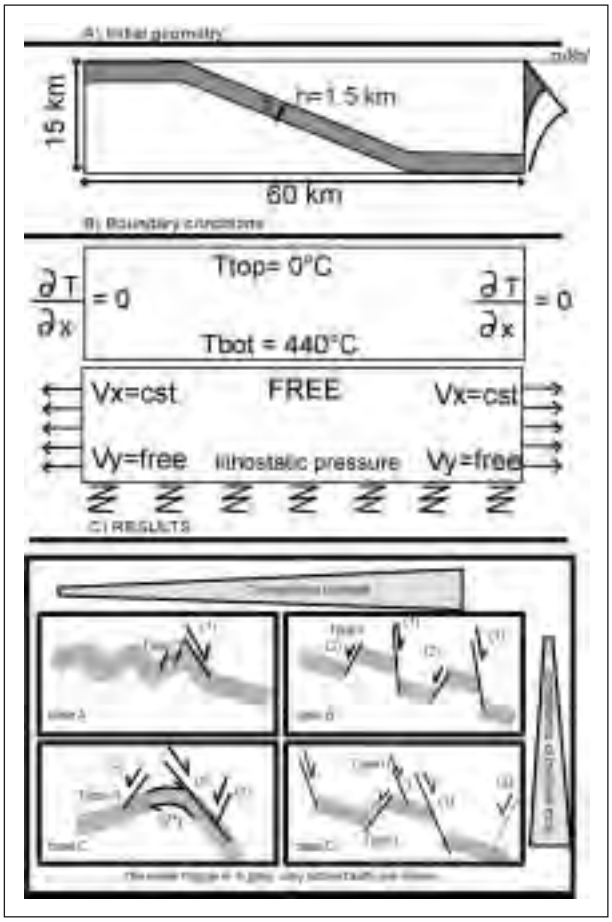

Fig 2a. boundary condition and initial setup for thermo-mechanical run.
The model box is 60 km long and 15 km deep. A non-planar heterogeneity corresponding to the nappe is introduced in the box. This heterogeneity presents a 1.5 km wide band characterized by a weak material phase. The introduced "nappe" flattens at the horizontal borders of the model to reproduce the usual flat and ramp geometry of real nappes. Mechanically speaking, the upper flat portion of the nappe does not affect the predicted deformation patterns because the near-surface deformation is dominated by elasto-plastic behavior, whereas the imposed elasto-plastic properties are the same both for the heterogeneity and for the host rock. The presence of a flat weak segment at the bottom of the model does not really reduce the integrated strength of the upper crust because the strength of the host rocks is already low at depth
Boundary conditions correspond to symmetric stretching with free vertical slip on the left and right borders, Winkler basement at depth and true free surface boundary condition is applied at the top. The temperatures are kept constant at the top and at the bottom (0°C and 440°C, respectively), while the lateral boundary conditions correspond to zero lateral outflows.

Fig 2b. Phase diagram for faulting pattern. The figure presents four cases of the computed fault patterns predicted as a function of the competence contrast ($A_{host\ rock}/A_{nappe}$) and of the competence of the host rock ($\alpha A_{host\ rock}$). For thin nappes, the competence of the host rock constrains the wavelength of the deformation while the competence contrast constrains the type of accommodation of flexure beyond the major normal fault (1). For low competence contrast, flexure is accommodated on the nappe by flexural slip (2*). For high competence contrast, flexure is accommodated on antithetic faults (2).
The three types of out-of-sequence faults are described. Type III corresponds to a very late stage of deformation and develops only when the down-dip direction of the nappe switches from north to south at the back of the major faults. Type I and II are characteristic of the high competence contrast mode. Type I corresponds to the antithetic faults described by Axen & Bartley [1997] for the Basins and Ranges; they help to accommodate flexure and uplift. The antithetic faults of type II are characteristic of the high competence contrast mode with high competence of the host rock, they develop to accommodate stretching in the upper block during its uplift.

To be able to compare sand box results to the 2D model proposed earlier for the Gulf of Corinth, the initial geometry of the sand box model has been chosen to simulate high competence contrast between the weak heterogeneity and its surroundings.

Benchmark of cylindrical sandbox experiments

A second set of experiments has been done to benchmark the numerical code with the sand box using simple mechanical model. The competent host rock was modelled with Morh-Coulomb elasto-plasticity and visco-elastic Maxwell rheology has been used for weak nappe to reproduce the same set up but, at scale, of the sand box cylindrical case (see Mattioni et al. 2004). The rheological parameters used in the computation can be found in table 1. Results plotted on figure 4 show the topography evolution through time, the second invariant of strain rate tensor and the cumulative plasticity. The same general evolution than the physical model is observed e.g. high degree of flexural deformation acquired in the hanging wall and a rather narrow graben localised above the décollement level. The external border of the graben migrates slightly through time in the direction of the thrust dip direction

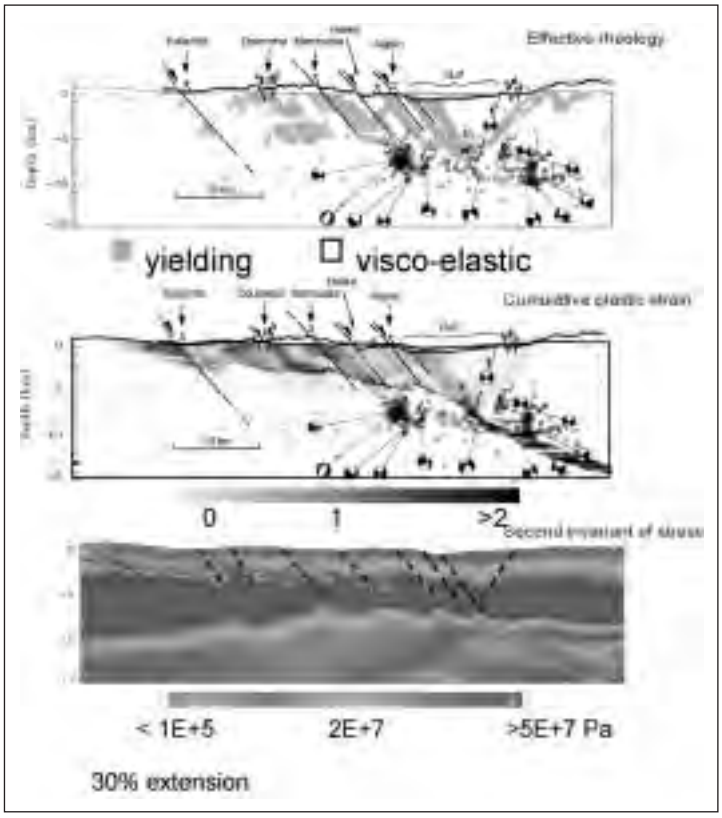

Fig. 3. Effective rheology as to be understanding as instantaneous brittle (yielding) elements in grey or instantaneous visco-elastic elements in white. This model fits well with the microseismicity observed by Rigo et al. [1996]. Cumulative plastic strain indicates a fault spacing rather similar to the one observed in the Gulf of Corinth and that some of the fault roots on the BDT of the crust while others, more listric, root on the nappe. The second invariant of stress show that deformation is not localised at the place of the nappe because short wavelength flexural deformation is observed and accommodated on active faults.

and the basin get wider. In the showed case, the graben is about 6 km wide after 2% of extension and reaches 12 km at 16% of extension. The topographic evolution Fig 4a shows a strong subsidence in the through from 400 to more than 2000 m when extension increase from 2 to 16%. Strain rates and cumulative plastic strain indicates clearly that both antithetic and synthetic faults are simultaneously active and that the "last" antithetic fault which borders the graben is migrating downward the thrust sheet. These results are rather similar to what was obtained in the physical model. Nevertheless, few differences can be observed in terms of width of the graben and topography. Those can be related to the extreme difficulties related to the choice of elastic parameters as they are not taking into account in the scaling of analogue experiments we had to set them to be realistic for rocks.

Comparison with Corinth Gulf thermo-mechanical model

Important discrepancies can be observed between thermo-mechanical and analogue modelling approaches. In the analogue model, as in its numerical benchmark, the competence contrast is very high but bimodality of faulting or 'dipping pie' effect, which fits the geological observations, does not occurs.

However, the only major important difference between both sets of experiments is the bottom boundary condition. The thermo-mechanical approach use Wrinkler basement (i.e. vertical viscous dash-pot mixed with horizontal free slip condition) while the analogue experiments, as well as their numerical benchmarks, have null vertical velocity as bottom boundary condition. The layer of weak silicon at the base of the model is to thin to permit any flexural bending of the lower elasto-plastic bloc. This annihilates the formation of upper crustal scale faults to develop. As a result, flexural bending of the upper strong bloc becomes the only way to accommodate strain.

Conclusion

2D thermo-mechanical models (first set of experiments) have shown that assuming weak and thick lower crust, the presence of a weaker dipping nappe in the upper crust results in particular fault patterns depending on the importance of the competence contrast between the weak nappe and its

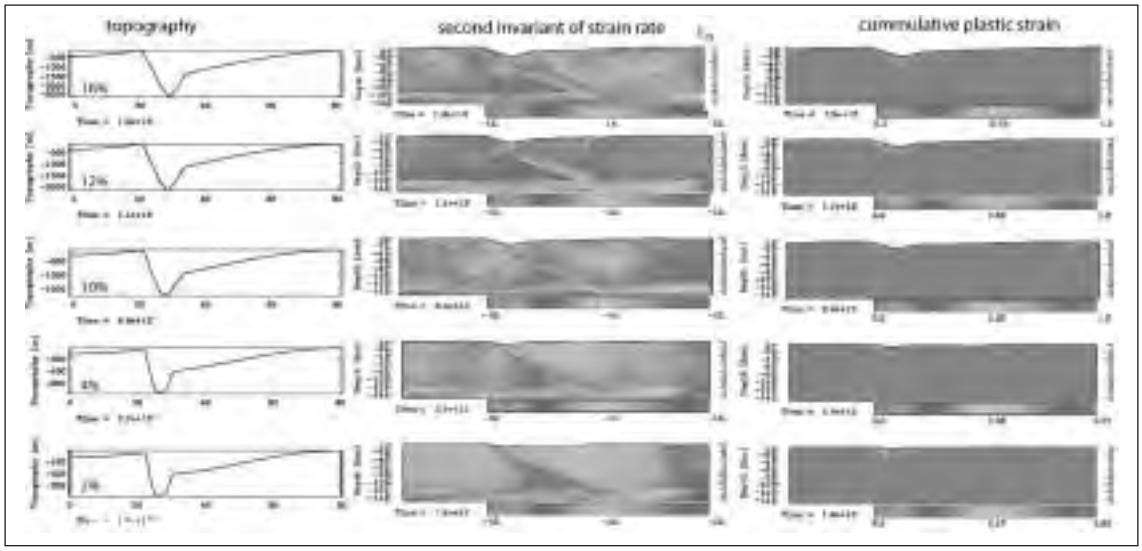

Fig. 4 – Topography, second invariant of stress and cumulative plastic strain for purely mechanical benchmark The dark grey (red on the numerical version) bands correspond to the places where the strain localises instantaneously. Similarly, the dark grey (red) part of cumulative plastic strain pictures could be interpreted as faults. The synthesis of both indicates clearly that in the numerical model, both antithetic and synthetic faults are simultaneously active and that the "last" antithetic fault which borders the graben is migrating downward the thrust sheet. Rounded aspect of the topography denotes important flexural bending.

surrounding. In the case of the Gulf of Corinth, the fault patterns and the kinematics of the faults can only be explained by a very high competence contrast. As the Corinth Gulf is a 3D feature rather than a 2D one, we have tried to extend the proposed model to 3D by using analogue modelling (Mattioni et al. 2004). After benchmarking our numerical code with cylindrical analogue experiment using the same boundary conditions and mechanical behaviour for the phase (second set of experiments), we found that the patterns obtained were very similar. Nevertheless, to run those analogue experiments and their numerical benchmark we had to change the boundary conditions at bottom from Wrinkler basement to fixed vertical velocity. This change has caused the annihilation of the development of upper crustal scale normal faults because the lower elasto-plastic bloc of the model was not able to bend flexuraly anymore. For this reason, it is not really possible to use the 3D analogue model to extend our thermo-mechanical study (first set of experiments) to 3D. We thus like to focus our conclusion on the fact that important care should be given to the boundary conditions of analogue model because fixed vertical velocity at the base of the model imposes very important change in the mechanical behaviour of the model compare to more geologically relevant boundary conditions. There is still a possibility to rule this problem by using a higher box which could allow us to add 5 more centimetres of silicone at the base of the analogue model.

REFERENCES

- Axen, G.J., and J.M. Bartley, 1997: Field tests of rolling hinges; existence, mechanical types, and implications for extensional tectonics, Jour. Geophy. Res., 109, 20515-20537.
- Briole, P., A. Rigo, H. Lyon Caen, J. Ruegg, K. Papazissi, C. Mistakaki, A. Balodimou, G. Veis, D. Hatzfeld, and A. Deschamps, 1999: Active deformation, of the gulf of Korinthos, Greece: results from repeated GPS surveys between 1990 and 1995, J.G.R., 105, 25605-25625.
- Cundall, P.A., 1989: Numerical experiments on localization in frictional materials, Ing.-Arch., 59, 148-159.
- Ghisetti, F.C., L. Vezzani, F. Agosta, R. Sibson, and I. Moretti, 2001: Tectonic setting and sedimentary evolution of the south-west margin of the Corinth rift (Aigion-Xylocastro area), Institut francais du pétrole, Rueil Malmaison, Report no 562 11, pp 22.
- Ghorbal, B., 2002: Quels arguments en faveur d'un détachement Plio-Quaternaire au sud du Golfe de Corinthe? : Etudes tectono-métamorphique des Phyllades du Péloponnèse septentrionnal., (master thesis, Paris VI).
- Jacobshagen, V., S. Duerr, F. Kockel, K. Kopp, and G. Kowalczyk, 1978: Structure and geodynamic Evolution of the Aegean Region, in Alps Apennines Hellenides: Geodynamic investiagtions along Geotraverses by an international group of geoscientists, vol. 38, Inter-Union Commission Geodynamics Scientific Report, E. Schweizerbart'che Verlagsbuchhandlung, Stuttgart, p. 537-620,

- Le Pourhiet, L., E. Burov, I. Moretti, 2004; Rifting through a stack of inhomogeneous nappe (the dipping pie concept), Submitted to Tectonics
- Le Pourhiet L., E Burov et I. Moretti; 2003; Initial crustal thickness geometry controls on the extension in a back arc domain: The case of the Gulf of Corinth, Tectonics, v 22, n 4, 1032-1041.
- Mattioni L., I. Moretti, L.Le Pourhiet; Extension through a heterogeneous crust. The Case of The Gulf of Corinth (Greece). Part I: Analogue Modelling, extended abstract for geomod 2004, this issue.
- Moretti, I., D. Sakellariou, V. Lykousis, and L. Micarelli, 2003: The Gulf of Corinth : a half graben ?, J. Geodynamics, 36, 323-340.
- Poliakov, A.N.B., Y.Y. Podladchikov, and C. Talbot, 1993: Initiation of salt diapirs with frictional overburden: Numerical experiments., Tectonophysics, 228, 199-210.
- Rigo, A., H. Lyon-Caen, R. Armijo , A. Deschamps, D. Hatzfeld, K. Makropoulos, P. Papadimitriou, and I. Kassaras, 1996: A microseismic study in the western part of the gulf of Corinth (Greece) implications for large-scale normal faulting mechanisms, Geophys J. Int., 126, 663-688.
- Sorel, D., 2000: A Pleistocene and still active detachment fault and the origin of Corinth Patras rift, Greece, Geology, 28, 83-86.
- Westaway, R., 2002: The Quaternary evolution of the Gulf of Corinth, central Greece: coupling between surface processes and flow in the lower crust, Tectonophysics, 348, 4, 207-246.

THE ZAGROS FOREDEEP EVOLUTION 3-19

G. Minelli [1], S. Scarselli [2], G. Simpson [2]

1 Dipartimento di Scienze della Terra, Università di Perugia,
2 Earth Science Department, ETH Zurich)
gminelli@unipg.it; sonia.scarselli@erdw.ethz.ch; guy.simpson@erdw.ethz.ch

Summary

In this project we have analysed several data regarding the mechanical characteristics (elastic thickness, Young modules, etc…) of the flexuring crust and geophysical features of the orogen in order to better confine the evolution of the Persian Gulf Foredeep and to better understand the origins of various anomalies present in this area

Abstract text

The Zagros Thrust and Fold Belt (ZFTB) (Fig.1) are part of the Alpine-Himalayan orogenic system; the inner portion of the orogen has been subject to intermittent deformation extending at least as far back as the late Palaeozoic (Berberian & King, 1981); by contrast, the modern fold and thrust belt was a relatively quiescent region of sediment accumulation until the latest episode of shortening and uplift began in the late Miocene or early Pliocene (James & Wynd, 1965; Falcon, 1974; Berberian & King, 1981).The exact timing for the onset of the most recent period of deformation, which apparently extends throughout much of Iran, is not well constrained. Berberian & King (1981) estimated that deformation began about 5 Ma, which coincides with the beginning of a second phase extension along the Red Sea and Gulf of Aden.

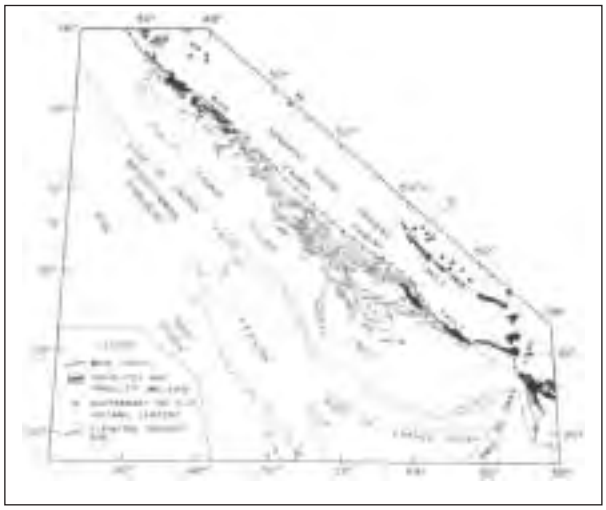

Fig 1: Schematic map of the ZFTB and Persian Gulf (Berberian,1981)

The ZFTB building is related to deformation which has propagated from northeast to southwest through time (Oberlander, 1965; Falcon, 1974; Berberian & King, 1981) and continues to the present day; ZFTB extends laterally for a distance of about 1500 Km along the SW part of Iran and NE of Iraq. Mirroring this evolution from NE to the SW, are observes a decrease in crustal thickness (Snyder

& Barazangi, 1986), topography, intensity of deformation (Falcon, 1961, 1969, 1974), fold amplitude, reverse fault displacement, relative shearing along the Hormuz decollment detachment and age of the folded and faulted sedimentary rocks decrease from the High Zagros and the Zagros suture in the N and NE toward the Zagros Foredeep in the S and SW. Compression within the fold belt is manifested by a series of large, doubly plunging folds that verge to the Southwest (Fars Zone) and imbricated thrusts in the West (Dezful and Lorestan).The ZFTB are subject to a wide spectrum of studies. The first interest of the area concerns its abundance in very rich hydrocarbon sources and the second one is related to its unexplained geophysical anomalies. We are engaging to link the main stratigraphic, structural and geophysical features in order to develop an evolution model of the orogen.

Geological setting

The ZFTB stratigraphic sequence is divided in 5 main groups (Colmann & Sadd, 1978; James & Wynd ,1965)

1) Basament Group (Precambrian): consisting of a Precambrian metamorphic basement (Falcon, 1967; Berberian & King, 1981);
2) Lower Mobile Group (Proterozoic): (1-2 km) Infra-Cambrian evaporite facies of the Hormuz Series (Ala, 1974);
3) Competent Group (Early Cambrian-Lowest Miocene): platform cover, deposited on the subsiding basement of the Arabian continental margin from (Stocklin 1978, Koop & Stoneley, 1982).

The sedimentary cover ranges from about 5 to 10 km in thickness (Morris 1977; James & Wynd, 1965; Afshar et alii, 1976) and contain numerous salt and anhydrite horizons interbedded with limestones (Berberian & King, 1981), the main are the Upper Mobil group (Low- Middle Miocene) and the Incompetent Group (Upper Miocene-Actual).

The thickness of the sedimentary cover and the crust in the ZFTB are suggested to change from 12-14 Km (Inose &Wynd, 1965, Huber, 1997; Mostafazadeh, 1994).

Decoupling of the Phanerozoic sedimentary cover from the Precambrian basement has occurred along the Lower-Cambrian Hormuz salt and above the Eocene-Oligocene Asmari Limestone along the Miocene Gachsaran Evaporites.

In the ZFTB can be distincted 3 geographycal and geological areas (Colman and Sadd , 1978):

1) “Simple folding belt” characterized by Precambrian/Pliocene shelf sediment, folded into a series of large anticlines and synclines and localized in the Fars Zone (SSW of Zagros Belt), this belt has a NW-SE trend that changes to EW in the SE region.
2) Imbricated belt characterized by the same sediments as the Fars Zone but more deformed with the development of a series of thrust faults, localized in the Dezful and Lorestan region;
3) Thrust belt characterized by a wide variety of lithologies including ultrabasic and metamorphic rocks intensely thrust faulted, localized in the NNE portion of the Zagros system.

The boundaries of these units are defined on the basis of: surface topography and morphotectonic features, style of deformation, subsurface geologic-tectonic data and regional seismicity. Berberian (1995) suggests these boundaries are marked by master “blind” thrust faults; similarly. Jackson et al (1981) considered the majority of these structures as high angle reverse faults (dipping 40°/50°) developed along pre-existing Permian normal faults.

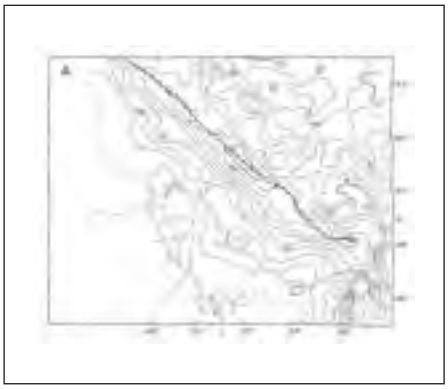

Fig.2: Gravimetric map, Deghani & Makris (1984)

The foredeep in the Zagros system is localized in the coastal Plain and Persian Gulf. The Coastal Plain is narrow feature that slopes gently to the S with an area of about 226.000 km^2, the Persian Gulf is a shallow epicontinental sea with a tectonic origin (foreland depression) which covers the Arabian shelf platform with water depths less than 100 m (average depth ≈35 m, maximum depth ≈110 m).The evolution of the area can be subdivided into 3 main steps (Koop & Stoneley, 1982) The first step is characterized by a rifted continental shelf phase (Permian

and Triassic) with thick marine deposition followed by thinning due to uplift and pre-Jurassic truncation associated to drift separation of the Arabian Plate. In the second step (Jurassic to Mid Cretaceous) thin sequences typical of arid climates were deposited. In the early Cretaceous uplift is regionally replaced by subsidence, except the Arabian plate which remained elevated. In the Mid Cretaceous the first pre-tectonic effects are found and the Neotethys began to close. The third step concerns the collision and Zagros orogeny; at first a regional uplift is recognized in the whole area while in the Palaeocene-Eocene the subsidence starts and the first flysch sediment are deposited in an elongate foredeep with NW/SE direction. In fig. 3 we report the Miocene Recent isopach and facies distribution map showing that the foredeep associated with Zagros belt presents, in front of the Dezful and eastward to the Fars, thicknesses ranging from 4.5 to 5.5 km. It is important to note that the thicknesses of sediment deposited are reflected in the present day stratigraphic distribution.

Main Anomalies

The first incongruence observing the ZFTB and its topography is that the Zagros higher elevations are not properly located to produce an effective load to elastically flex the Arabian plate, in other words the Zagros exhibits no direct evidence of topography or subsurface loads in order to explain the degree of flexure in the Persian foredeep (Snyder & Barazangi, 1986). Snyder & Barazangi (1986) hypothesized a combination of isostatic, elastic flexure and horizontal compression forces to best model the features observed in the Zagros region. For the same authors the Zagros Collision Zone incorporates a Lower crust that is deforming plastically between a brittle upper crust and a rigid uppermost mantle lid. In this hypothesis, isostatic forces dominate in the Arabian craton area and near the Main Zagros Thrust where the plastic lower crust hydraulically raises the surface and depresses the Moho in local isostatic balance; unfortunately this solution lacks any geophysical evidence.

Fig. 3: Miocene to Recent post Asmari isopach and facies distribution (Koop & Stoneley, 1982).

In the gravimetric anomaly map (Fig. 2, Deghani & Makris, 1984) we have a wide spectrum of the anomalies ranging between -20 mGal (in the Persian Gulf foredeep) and -225 mGal (in the Main Zagros Thrust). The most visible discrepancy is that the maximum negative of the anomaly is not exactly below the maximum topographic high but is displaced 50-150 Km towards the SW (Snyder & Barazangi, 1980). Deghani & Makris (1984) supposed that high negative values below the Main Zagros Thrust are produce by crustal thickening, while the small negative values in the Elbers Mountain are probably ascribed to crustal thinning and major isostatic disturbance. In Fig.2 the regional gravity map shows that above the Zagros an average negative value of -170mGal is registered while in the Centre of Iranian range the anomaly is very small, -50/-100mGal. To the NE and SW of the Zagros the gravimetry is characterized by a relative gravity high separated by a small area around Zabol. On the basis of the gravity anomaly distribution, Deghani & Makris measured the crustal thickness, obtained values ranging between 50-55km below the Zagros to 40-48 km in the East Iran region and 40km in the Lut depression. Finally they produce a map of the isostatic conditions indicating that the majority of the area is in isostatic equilibrium, with the exception of the Fars Zone and Main Zagros Thrust which is strength undercompensated. Another poorly understood feature of the ZTFB has been noted by Seber et al. (1997) who have reconstructed a compilation map for the Moho depth combining more than 50 crustal refraction profiles with gravity maps, surface-wave tomographic studies and Bouguer gravity data in Iran. The higher crustal thickness is located towards the southern limit of the Zagros System which is displaced S relative to the high topography.

Final considerations

The situation described above reveals incongruities between the models adopted to explain the Zagros and Persian Gulf evolution and the data. Essentially, the previous works point out the impossibility of explaining the evolution of the ZFTB as a simple collisional system with sufficient loads to elastically flex the Arabian plate to the degree observed. We suggest that the key to explaining this discrepancy lies in recognizing the implications of the Palaeozoic paleogeography and tectonics and resulting crustal thickness distribution, which are closely related to the style of deformation and subsidence and the mechanical properties of the lithosphere. On the basis of the geometries we recognize two different structural styles separated by the Kazerun tectonic lineament; the Fars Zone to the SSE is characterized by broad and regularly spaced anticlines whereas Dezful and Lorestan region is characterized by imbricated thrust faults. Interestingly the region characterized by simple folding corresponds spatially with the greatest thickness of Palaeozoic rift sediments, whereas in the region where salt was thin or absent, deformation is characterized by imbricated thrust faults. In addition, the Moho thickness underneath the Fars Zone varies between 30-40 km whereas in the Dezful and Lorestan Zones it varies between 60-80 km. We suggest that this difference in crustal thickness reflect the fact that Palaeozoic rifting significantly thinned the crust in the Fars Zone. These different tectonic domains behave very differently during the subsequent Tertiary collision. Evidence for this is represented by the depth and the geometry of the foredeep. It's seen that in front of the Dezful and Lorestan, the sequence has thickness ranges between 4.5/5.5 km (isopach maps,fig.3) while in front of the Fars Zone the thickness is reduced to 2/3 km. We have modellled this geometry with Flex by Hinojosa & Mickus (1993).

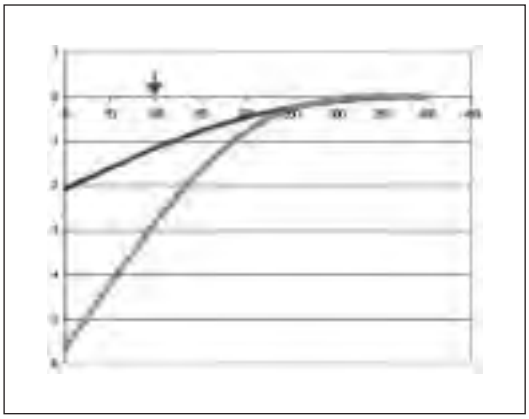

Fig.4: Modelling of the foredeep depth variation from the crustal thicknesses

In both the models the considered Mantel density is 3290 (kgm^{-3}), the Crustal density is 2800 (kgm^{-3}) and the Sediment density is 2650 (kgm^{-3}). For the thinner elastic litosphere (35 km) the Young's modul is 8.00E+11 (Pa) and for the thickest (70 km) is 8.70E+10 (Pa). Different values are also for the Poisson ratio that for the thinner elastic litosphere is 0.2 and for the thickest is 0.15. We have obtained values of foredeep depth closely similar of those observed on the Persian Gulf using crustal thicknesses (fig.4).

REFERENCES

- Berberian M., King G.C.P.(1981): Canadian J. Earth Science, 18(2), 210-285.
- ColmanS.P- Sadd , (1978) A.A.P.G., v.62, 6, 984-1003.
- Deghani G.A. & Makris J. (1984), J. Geol. Palaont. Abh., 168, 215-229.
- Falcon, N.L.(1969): Special Publisher Geol. Soc. of London 3, 9-22.
- Falcon, N.L.(1974): Special Publisher of Geol. Soc. of London, 4, 199-211.
- Hinojosa, J.H., Mickus,K.L.(1993):Computers and Geoscience,19(9),1321-1332.
- Jackson J.A., Fitch T.J. & McKenzie D.P., (1981).Thrust and Nappe tectonic, Geological Society of London
- James, G.A., Wynd, J.G.(1965): AAPG Bulletin, 49, (12), 2182-2245.
- Koop W.J. $ Stoneley R., Phil.Trans.R.Soc.Lond., 305, pp.149-168 (1982).
- Oberlander T.(1965): Syracuse geography, Serie 1.
- Snyder D.B. & Barazangi M., Tectonics(1986)., 361-373, 5,3

COMPARISON BETWEEN ANALOGUE AND NUMERICAL MODELS OF BASIN INVERSION PROCESSES. 3-20

Marion Panien(*), Susanne Buiter(**), Guido Schreurs(*), Adrian Pfiffner(*)

(*) Institute of Geological Sciences, University of Berne, Baltzertrasse 1, 3012 Bern - Switzerland. panien@geo.unibe.ch

(**) Geodynamics Group, Department of Oceanography, Dalhousie University, Halifax, B3H 4J1-Canada. susanne.buiter@dal.ca

Summary

We present results of analogue and numerical experiments of inversion of a symmetric basin. By combining the two techniques we hope to profit from the strengths of each method and obtain more insight in basin inversion processes. The results of both methods show that most of the shortening is accommodated by the graben fill. There is only limited reactivation of the pre-existing (but weakened) faults. In general, forward thrusts and backthrusts nucleate at the transition strong/weak and cut across the graben-bounding faults. The overall evolution of the analogue models is quite similar to that of the numerical models.

Introduction

Analogue and numerical modelling are two different methods which are used in geology to investigate natural geological structures in order to understand mechanisms controlling their geometry and dynamics. By combining these two techniques, it is possible to overcome the weaknesses inherent in each of the methods and to get more insight into natural processes (see, for example, Ellis et al, 2004). We present results of analogue and numerical models of basin inversion. By basin inversion we understand the process of shortening a sedimentary basin that was created in extension. During the shortening, the basin fill is typically uplifted and faults are reactivated (Cooper et al, 1989). Most previous analogue experiments on basin inversion have focussed on hanging wall deformation using rigid footwalls (e.g. Koopman et al., 1987; McClay, 1989; Buchanan & McClay, 1991;Yamada & McClay, 2003). These footwall blocks usually represented a structural basement with varied geometries, e.g., listric, planar or ramp/flat listric. In this type of experiment, inversion results in both the reactivation of the main detachment and the initiation of new thrust faults. A major disadvantage of these models is that the rigid footwall is unable to undergo deformation. Among the few previous numerical experiments of basin inversion is the work of Nielsen and Hansen (2000) who show the formation of flexural marginal troughs, Hansen and Nielsen (2003) who explain how rifting leads to sufficient weakening to allow inversion, and Buiter and Pfiffner (2003) who focussed on the inversion of half-graben basins.

Here, analogue experiments on basin inversion are described and compared with equivalent two-dimensional numerical models in which both footwall and hanging wall are free to deform. The experiments start with a pre-existing basin. The main motivation for this set-up is to have the same starting geometry for the analogue and the numerical experiments, which would be difficult to achieve if we would also model the basin formation phase. In our experiments only granular materials are used as analogues for upper crustal rocks. Based on the fact that sedimentary deposits in basins are generally less competent than adjacent basement rocks, part of the graben fill consists of granular materials that are weaker than the surrounding material.

The aim of our experiments is to determine factors affecting the style of deformation during inversion and the factors which could contribute to the reactivation of the graben-bounding normal faults during shortening. We focus here on the effects of variations in graben location and graben width.

Analogue model set-up

The models were built in a sandbox, 40 cm length, 15 cm width and 15 cm height, with glass side panels. Models consisted of alternating layers of quartz and corundum sands that were sieved in the sandbox to obtain 3 horizontal layers, each 1 cm thick. The graben was created by means of two tilted metallic plates that were driven at a dip angle of 60° into the multilayer model. The layers between the plates were then removed and replaced with alternating strength brittle layers. The graben fill consists

of weak microbeads overlain by strong corundum and quartz sands. The metallic plates were subsequently pulled out (Fig. 1). The normal arrangement of grains was disturbed along narrow areas, which act as potential weak zones. An additional 0.5 cm thick layer of corundum sand was sieved on top of the model to simulate a post-rift sequence. Marker particles consisting of coloured sand at layer interfaces were used to track the evolution of the structures.

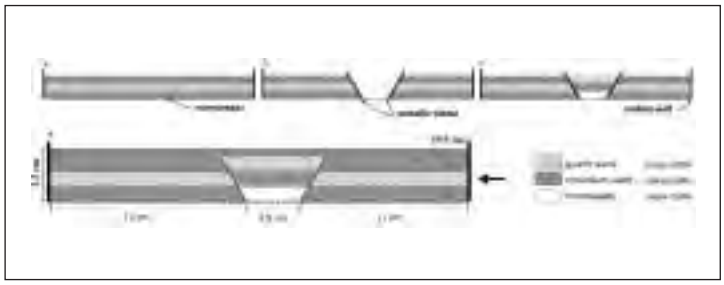

Fig. 1- Set-up of the analogue model. (a) Three layers are sieved in the sandbox. (b) Two tilted metallic plates are then driven at a dip angle of 60° into the model. The layers are removed and (c) replaced with alternating strength brittle layers. The metallic plates are subsequently pulled out and (d) an additional 0.5 cm thick layer of corundum was sieved on top of the model to simulate a post-rift sequence.

The grain size of corundum and microbeads is around 088-125 μm, and 125-175 μm for quartz sand. The internal friction of our analogue materials was measured using a ring-shear tester. The results show that granular materials are characterized by an elastic frictional-plastic material behavior with an initial strain-hardening phase preceding failure (peak strength) that is followed by a transitional phase of strain-softening until stable sliding (dynamic-stable strength) (Lohrmann et al., 2003; Ellis et al., 2004; Panien et al., in prep). Angles of internal peak friction and dynamic-stable friction are 36° and 31° for quartz sand, 37° and 32° for corundum sand, 22° and 20° for microbeads, respectively. All materials have a low cohesion, the value of which is poorly constrained at very low normal stresses. The angle of basal friction between corundum sand and the bottom of the sandbox was reduced to 14° by sieving a 0.5 mm thin layer of microbeads at the base of the model.

Numerical model set-up

A two-dimensional plane-strain mechanical model (Sopale, developed by Fullsack and Beaumont, Fullsack (1995)) was used for the numerical experiments. The model is Arbitrarian Lagrangian Eulerian-type (ALE-type): the equations are solved on an Eulerian grid to which material properties are assigned using Lagrangian tracking points. The numerical model uses a rigid-plastic rheology for brittle behaviour of ‘sand’, ‘corundum’ and ‘microbeads’, which are governed by the frictional-plastic Coulomb criterion. A small amount of strain-softening of the angle of internal friction is included to mimic the strain-softening which has been measured for the analogue materials. The softening occurs over a finite strain interval of 0.5 to 1.0. Cohesion is kept constant.

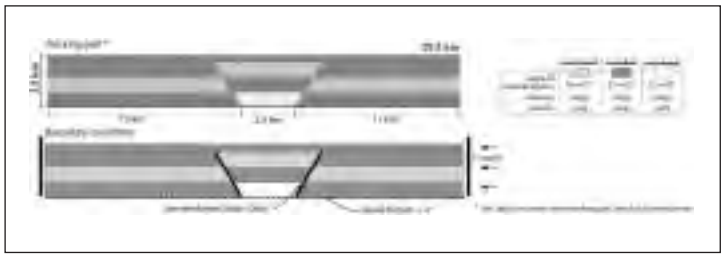

Fig. 2- Set-up of the numerical model and material properties.

The boundary conditions of the numerical model follow the analogue model as closely as possible. The left vertical side is held fixed, while the right vertical side is moving with a velocity of 1 cm/yr to the left. The base is kept fixed as well. The surface is a free surface to which a small amount of diffusive erosion is applied, with a diffusion coefficient of 5e-9 m^2/s. This simulates the small amount of sand redistribution along the surface that occurs in the analogue models. To take into account the disturbance of the graben sides when building the analogue models, the basin sides of the numerical models are pre-weakened by defining bands of quartz and corundum sands with a low value for the

angle of internal friction (31 and 32° respectively). The basin sides and their parallel zones of weakness dip at 60° and are not continuing into the post-rift layers (Fig. 2).
The numerical models are scaled such that similarity with the analogue models is as close as possible. The values of density and angle of internal friction are the same as those of the analogue materials. 1 km in the numerical models is chosen to correspond to 1 cm in the analogue model. According to the theory of mechanical scale models (Hubbert, 1937 and 1951; Ramberg, 1981), a cohesion of 0.1MPa in the numerical models is equivalent to 1 Pa in the analogue model. The main exception to the attempted similarity between the numerical and the analogue model is formed by the basal thin layer of microbeads. It is twice as thick in the numerical model (equivalent to 1 mm) to facilitate shearing in this layer. We also found that this layer needs to be much weaker. When we use the friction angle, which was measured in the ring-shear tester for the friction between microbeads and a basal sheet (14°), all thrusting localises at the moving wall. The models we present here have an angle of internal friction of 4° for the basal layer of microbeads. It is clear that more research is needed to understand the mismatch between the measured analogue basal friction and the behaviour of the numerical models using these measured friction values. However we note in support of the numerical models that with our choice of parameters the results do seem to be in good agreement with the analogue experiments.
Caution is required when comparing results of continuum type numerical experiments with those of sandbox experiments. Due to its manual set-up, an analogue model will intrinsically have more heterogeneities than a numerical model. Furthermore, our numerical models do not include elasticity and dilatancy, whereas the analogue model materials do have these properties. As a consequence, shear zones in the numerical model initially develop at angles of around 45°.

Results

Two series of experiments were performed: the first series tests the influence of the graben location in the model and the second series examines the effect of graben width on the resulting deformational structures. The evolution of the structures during shortening is quite similar for all models. Deformation is mostly accommodated by the graben fill.
In the analogue reference model (GL-11 in Fig. 3 or GW-3.5 in Fig. 4), the graben-bounding block closest to the mobile wall acts as a rigid block during the early stages of shortening. It transmits the horizontal displacement produced by the mobile wall to the graben. The width of the graben decreases, leading to the bulging of the layers between the two major graben-bounding weak zones (potential faults). Contractional faults nucleate at the basal transition from strong footwall to weak graben fill and behave a dip of ± 40°. There is no or little movement along the weak zone dipping at 60° closest to the mobile wall: only its deeper part is reactivated as a reverse fault. A new fault branches off this reactivated fault (short-cut fault) and propagates upward at a shallower dip into the footwall of the graben and the postrift sediments. At the same time a forward thrust initiated in the graben accommodates most of the bulk shortening. It propagates through the graben and across the post-rift sediments. It passively transports the reverse fault in its hanging-wall. With continued shortening, additional forward thrusts form in sequence and new backthrusts initiate in the footwall of the graben. The weak basin fill at the base of the graben localises the position of the forward thrusts, the partial reactivation of the graben-bounding fault and its upward propagation as short-cut fault in post-rift layers. The contractional faults nucleate at the basal transition from weak to strong brittle layers.
We see the same general features in the numerical model. With increasing shortening a second set of shear zones forms closer to the moving wall than in the analogue experiment. This may result from irregularities in the thicker basal microbeads layer caused by the movement of the overlying sand/corundum.

Graben location

In these experiments, the graben width is held constant, whereas the location of the graben with respect to the right mobile wall is changed (Fig. 3). We see that the length of the right graben-bounding block does have effects on the resulting structures. In a case of a short right-graben bounding block (GL-9), deformation is concentrated in the graben fill leading to an enhance bulging

and inversion of the graben fill. In contrast, when the right-graben bounding block is longer (GL-13), it indergoes internal deformation (backthrusts in the analogue set-up, shear zones in the numerical model). As a consequence, less graben fill is expulsed at identical stages of shortening.

Graben width

In the second series of experiments, the width of the graben is varied (Fig. 4). In model GW-3.5, the forward thrust connects with the top of the left graben-bounding fault. This may be because of the graben geometry (the fault dip connects the base of the graben on the right with the shoulder on the left). When the basin becomes wider (GW-8) the dip of the forward thrust diminishes to 30° in the analogue model (and 45° in the numerical model). A comparison between 3 experiments shows that the initiation of the forward thrust is independent of the graben width whereas its dip seems to be influenced by the top left graben-bounding fault (GW-3.5 and GW-5). For both analogue and numerical models, forward propagation of the thrusts is more clearly developed for the wider graben (GW-8), where initially these faults form entirely within the graben fill.

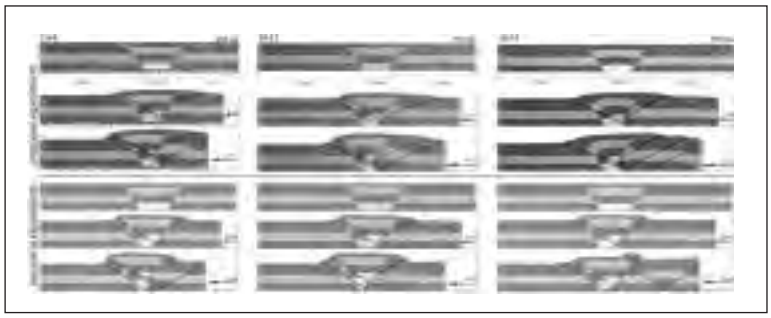

Fig. 3- Cross-sections of the analogue and numerical experiments GL-9, GL-11 and GL-13 before shortening, after 2 cm and 4 cm, 2 km and 4 km of shortening respectively. This series examines the effect of variations in the location of the graben with respect to the mobile wall.

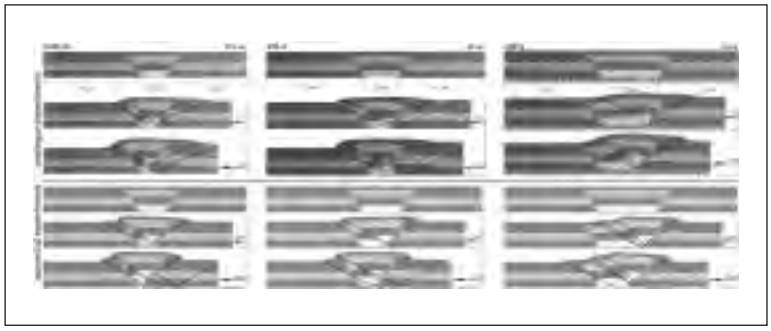

Fig. 4- Cross-sections of analogue and numerical experiments GWL-3.5, GW-5 and GW-8 before shortening, after 2 cm and 4 cm, 2 km and 4 km of shortening respectively. This series tests the effect of basin width.

REFERENCES

- Buchanan & McClay (1991), Sandbox experiments of inverted listric and planar fault systems, Tectonophysics, 188, 97-115.
- Buiter & Pfiffner (2003), Numerical models of the inversion of half-graben basins, Tectonics, 22, 11-1, 11-16.
- Cooper et al. (1989), Inversion tectonics – A discussion, Geol. Soc. Spec. Publ., 44, 335-347.
- Ellis, Schreurs and Panien (2004), Comparison between analogue and numerical models of thrust wedge development, Journal of Structural Geology, in press.
- Fullsack (1995), An arbitrary Lagrangian-Eulerian formulation for creeping flows and its application in tectonic models, Geophys. J. Int., 120, 1-23.
- Hansen & Nielsen (2003), Why rifts invert in compression, Tectonophysics, 373, 5-24.
- Hubbert (1937), Theory of scale models as applied to the study of geologic structures, Bull. Geol. Soc. America, 48, 1459-1520.
- Hubbert (1951), Mechanical basis for certain familiar geologic structures, Bull. Geol. Soc. America, 62, 355-372.
- Koopman et al. (1987), Sandbox model studies of inversion tectonics, Tectonophysics, 137, 379-388.
- Lohrmann et al. (2003), The impact of analogue material properties on the geometry, kinematics and dynamics of convergent sand wedges, Journal of Structural Geology, 25, 1691-1711.
- McClay (1989), Analogue models of inversion tectonics, Geol. Soc. Spec. Publ., 44, 41-59.
- Nielsen & Hansen (2000), Physical explanation of the formation and evolution of inversion zones and marginal troughs, Geology, 28, 875-878.
- Panien et al. (in prep), Mechanical properties of materials used in analogue modelling.
- Ramberg (1981), Academic Press, New York.
- Yamada & McClay (2003), Application of geometric models to inverted listric fault systems in sandbox experiments, Journal of Structural Geology, 25, 1551-1560.

IMPACT OF LITHOSPHERIC HETEROGENEITIES ON RIFTING; NUMERICAL MODELLING OF THE OSLO GRABEN, NORWAY

3-21

C. Pascal, S. Cloetingh, G.R. Davies

Faculty of Earth and Life Sciences, Vrije Universiteit, De Boelelaan 1085, 1081 HV Amsterdam

Summary

Compared to other Permo-Carboniferous rift basins of northwest Europe, the Oslo Graben has two distinct characteristics. First, it initiated inside cold and stable Precambrian lithosphere, whereas most Permo-Carboniferous basins developed in weaker Phanerozoic lithosphere, and second, it is characterised by large volumes of magmatic rocks despite relatively little extension. Seismic reflection surveys show that the crust thickens from southern Norway to southern Sweden, the most significant Moho deepening occurring from the Oslo Region eastwards. Deep seismic studies also suggest that the base of the lithosphere deepens markedly eastwards from the Oslo Region. Such a long-wavelength lithospheric geometry cannot be explained by the Permian or post-Permian evolution of the area, hence the Oslo Graben appears to have evolved at the transition between two lithospheric domains with contrasting thickness. Numerical thermo-mechanical modelling is applied to test if this transitional position can influence the dynamics of rifting. Different models with varying lithosphere thickness contrast are considered. Model results show that a crust and lithosphere thickness contrast comparable to the Oslo Region can explain rifting and focussing of magmatism in a narrow zone with minor thinning of the crust. Models also account for the major characteristics of the Oslo Graben in terms of location and strain distributions in the crust.

Abstract text

The Oslo Graben (Fig. 1) is part of the wide Permo-Carboniferous (hereafter P-C) rift and magmatic system that affected NW Europe from ~310 Ma to ~250 Ma. In contrast with most P-C basins of northwest Europe, the Oslo Graben formed inside Precambrian lithosphere. The presence of huge volumes of syn-rift magmatic rocks (>95000km^3, Neumann 1994) with little crustal extension (less than 16 km or $\beta < 1.3$, Pallesen 1993) remains enigmatic. To account for these observations it has been proposed that the lithosphere was stretched uniformly above an underlying mantle temperature anomaly. However, the involvement of a mantle thermal anomaly in the rift process (i.e. active rifting) is contradicted by the pre-rift stratigraphic record that points to pre-rift subsidence (Olaussen et al. 1994). In addition, estimation of extrusion temperatures of basaltic lavas from whole rock major element compositions points to "normal" mantle temperatures or a moderate thermal anomaly (Neumann 1994). An alternative model has been proposed by Pedersen and van der Beek (1994). This model, a derivative of the non-uniform stretching model, leads to the conclusion that the observed magmatic rocks can be produced at "normal" mantle temperatures if the mantle lithosphere is made of wet peridotite and stretched three times more than the overlying crust. Pedersen and van der Beek's model assumes differential stretching between crust and mantle lithosphere but does not explain its cause. All the models proposed for the Oslo Rift assume that rifting took place in a laterally uniform lithosphere (i.e. with homogeneous crust and mantle lithosphere thickness). An increasing number of geophysical studies have, however, established pronounced variations in Moho and base lithosphere topography in southern Scandinavia.

A compilation of deep seismic lines (Kinck et al. 1993) has revealed that the Moho deepens ~10 km from southern Norway to southern Sweden (Fig. 1a). Deepening occurs from the Oslo Graben eastwards. This Moho topography is also confirmed by recent seismic studies (Thybo 1997). Because the post-Permian evolution of southern Scandinavia is mainly characterised by a few km of uplift and denudation (Riis 1996), it is difficult to explain the pronounced contrast in crustal thickness by post-Permian tectonics. Such a long-wavelength crustal asymmetry cannot result from Permian rifting, which was restricted to relatively narrow zones in southern Scandinavia, and is likely to be inherited from Precambrian times. Also, teleseismic studies carried out along the 60th parallel suggest that deepening of the base lithosphere occurs abruptly from west to east across the Oslo Region (Fig. 1b). Hence there is compelling evidence of both crust and mantle lithosphere thickening when crossing the Oslo Region from southern Norway to southern Sweden.

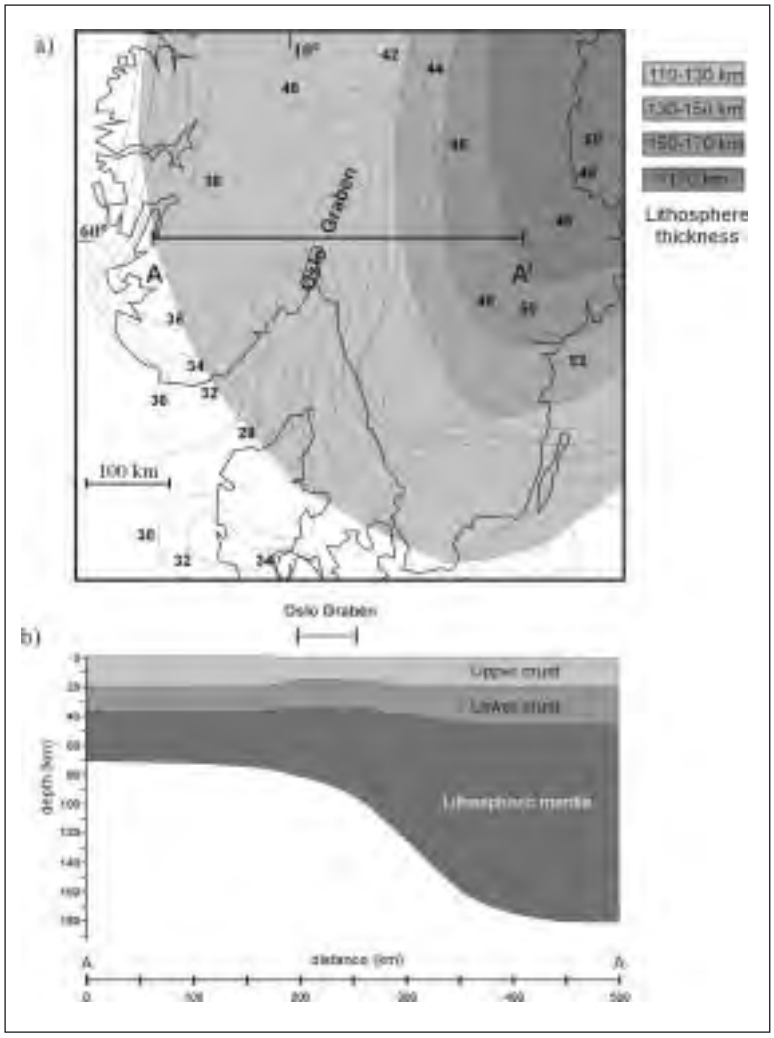

Figure 1. a) Moho depth in km in southern Scandinavia (Kinck et al. 1993) and lithosphere thickness in km as deduced from surface wave dispersion analysis (Calcagnile 1982). b) Present-day lithosphere structure along the modelled section A-A´ as deduced from deep seismic data and P-wave residual analysis (Plomerová et al. 2001). Note that both surface wave dispersion analysis and P-wave residuals analysis argue for base lithosphere deepening in the eastern part of section A-A´. Note also that results from both methods do not give exactly the same lithosphere configuration but that the study by Plomerová et al. (2001) uses a better constrained Moho topography.

2D numerical models were designed to explore the impact on rift dynamics of varying lithosphere thickness and particularly varying mantle lithosphere thickness below the eastern part of the models (Pascal et al. 2002, 2004). Lithosphere thickness was varied from 150 km to 200 km. These values imply lithosphere thickness contrasts, between the western and eastern parts of the models (hereafter referred to as Δthi), ranging from 25 to 75 km. The mantle lithosphere thickness in the western part of the model and the crust geometry were kept constant in the models. The commercial Finite Element Modelling package Ansys was used in the numerical study and a visco-elastic rheology, dependent on temperature, strain-rate and composition, was applied. In contrast with most academic FEM codes specifically developed to solve geodynamical problems, the engineering code Ansys has the advantage of remaining stable when the geometry of the studied system becomes complex. Computations were performed on two separate but interactive grids, a thermal one and a mechanical one.

The modelling results (Fig. 2), in agreement with a large range of different geological and geophysical observations, suggest that a pronounced lithosphere thickness contrast (i.e. > 55 km) pre-existed the Oslo Graben and had a strong control on its development, in particular in focussing deformation and causing decompression melting at the lithosphere-asthenosphere boundary. The models succeeded in accounting for localisation of rifting (e.g. Fig. 2d), horizontal offset of stretching between the crust and the lowermost lower crust-upper mantle and melt initiation in the first few million years of the rifting. It is suggested that relatively high stretching velocities (i.e. a few cm/y) prevailed during the early stages of development of the Oslo Graben. In addition, modelling shows that increasing the pre-

existing lithosphere thickness contrast does not automatically lead to more efficient strain concentration in the Oslo Graben, but can result in diffuse strain over the entire modelled section (e.g. compare Fig. 2b with Fig. 2c).

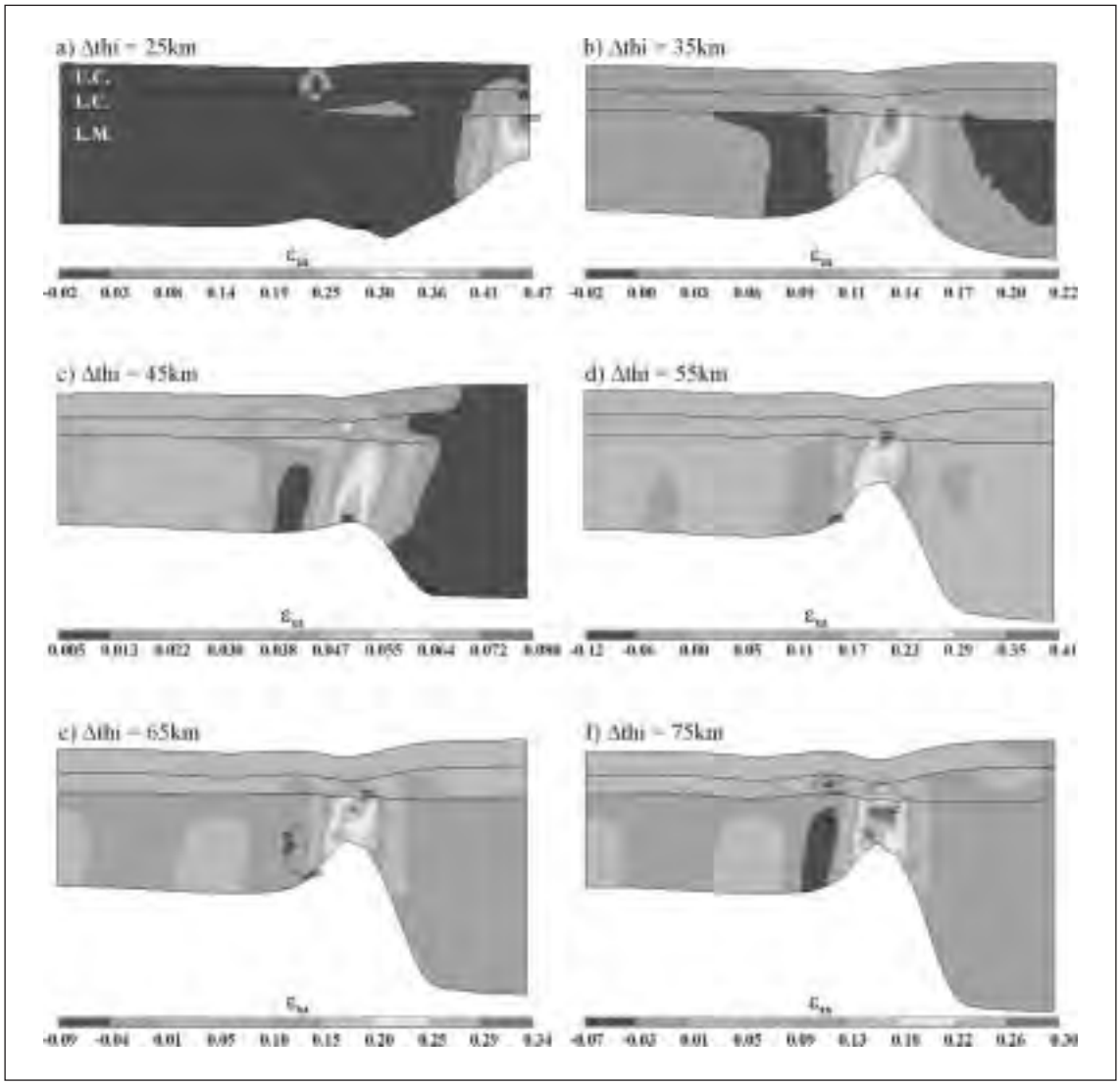

Figure 2. Horizontal strain (ε_{xx}) distributions computed for the last Myr of stretching. The key-parameter explored here is the lithosphere thickness contrast (Δthi) between eastern and western parts of the models. Positive strain values indicate stretching. Models are stretched for 10 Myr with a velocity of 1.6 cm/y. Note the different scales for strain in each figure. U.C. = upper crust, L.C. = lower crust, L.M. = lithospheric mantle.

REFERENCES

- Calcagnile G. (1982), Tectonophysics, 90, 19-35.
- Kinck et al. (1993), Precambrian Research, 64, 23-51.
- Neumann E.-R. (1994), Tectonophysics, 240, 159-172.
- Olaussen et al. (1994), Canadian Soc. Petrol. Geol. Memoir., 17, 175-197.
- Pallesen S. (1993), Tectonophysics, 221, 155-172.
- Pascal et al. (2002), Geophysical Research Letters, 29/9, 69/1-4.
- Pascal et al. (2004), Spec. Pub. Geol. Soc. of London, in press.
- Pedersen and van der Beek (1994), Earth and Planetary Science Letters, 123, 317-329.
- Plomerova et al. (2001), Tectonophysics, 332, 1-21.
- Riis F. (1996), Global and Planetary Change, 12, 331-357.
- Thybo, H. (1997), Geological Magazine, 134, 597-606.

THERMAL EVOLUTION OF THE PERMIAN-MESOZOIC POLISH BASIN – MODEL PREDICTIONS CONFRONTED WITH ANALYTICAL DATA 3-22

Pawel Poprawa, Izabela Grotek

Polish Geological Institute, Department of Regional and Petroleum Geology, ul. Rakowiecka 4, 00-975 Warszawa, Poland; ppop@pgi.waw.pl; igro@pgi.waw.pl

Summary

Debates regarding tectonic model of development of the Polish Basin (PB) concentrates recently on an alternative between simple-shear and pure-shear rifting models. Each model predicts an alternative patterns of heat flow changes in time and space. In location of each borehole with given vitrinite reflectance (VRo) profile a maturity predicted from the heat flow model could be confronted with analytical data. In general the measured VRo profiles are not qualitatively compatible with parameters of both simple-shear and pure-shear rift models, published for the PB. Instead other significant perturbations of the thermal regime were reconstructed, partly with clear convective mechanism of heat transport. The most important positive thermal anomalies are related to presumed hot fluid activity and phases of structural activity. These are the Early-Middle Jurassic one, reconstructed for the southern part of Kujawy segment of the Polish Trough (PT), and the Oxfordian one reconstructed for the southern-most part of the PB. Additionally along the most of the PT a significant regional cooling is observed for the Late Cretaceous, and to the systematically lesser degree for the Early Cretaceous and the (Middle?-) Late Jurassic.

Geological setting

Polish Basin (PB) is a part of the system of the Permian-Mesozoic sedimentary basins of the Central and Western Europe (fig. 1). The basin developed along the major crustal boundary of Europe, i.e. on the Trans-European Suture Zone. The PB accumulated a thick pile of shallow marine and continental sediments, reaching up to 10-11 thousand metres, with a vast volumetric contribution of the Upper Permian-Lower Triassic, Upper Jurassic and Upper Cretaceous deposits (e.g. Dadlez et al., 1995). Characteristic feature of the basins is a continuous sedimentation throughout the late Permian to late-most Cretaceous in its main depocentre, often referred to as the Polish Trough (PT).

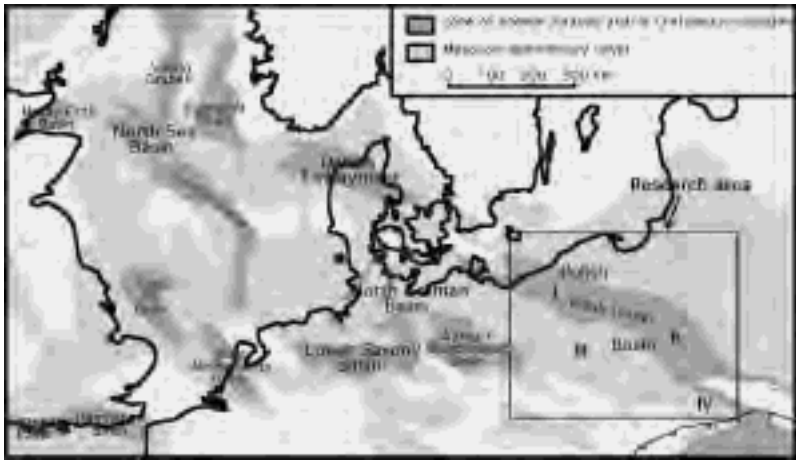

Fig. 1 - Permian-Mesozoic sedimentary basins of the Central and North-Western Europe (after: Ziegler, 1990, simplified) with location of studied area. Discussed zones of the PB: I – Pomerania; II – Kujawy; III – South-west (area of the Fore-Sudetic monocline); IV – South (area of the Miechow Trough).

Recent structure of the PB is significantly affected by two major phases of erosion. South-western part of the PB was uplifted and intensively eroded during the Early Cretaceous (before the Late Albian) and the late-most Cretaceous-Paleocene. During the second of the above mentioned phases also the PT was tectonically inverted, uplifted and intensively eroded. The PB is unconformably overlained by relatively uniformed, few hundred metres thick, cover of the Cenozoic (without the Lower Paleocene) continental to shallow marine sediments.

Previous tectonic and thermal models

The PB is commonly regarded as a rift basin, however there is much of debate regarding mode of rifting. Dadlez et al. (1995) advocated for pure-shear rifting, suggesting two main phases of extension: the late Permian-Early Triassic and Late Jurassic one. The Late Cretaceous subsidence event they explained by foreland reaction to transmition of compressional stress from the Carpathian collision zone. A consequence of pure-shear model are relatively high extension factors calculated for both phases of rifting, reaching up to ß=1.74 and ß=1.29 for the late Permian-Early Triassic and Late Jurassic respectively. Modification of the above model is given by Van Wees et al. (2000), who proposed that during the late Permian-Early Triassic sediments filled accommodation space created partly by rifting, partly by thermal subsidence following previous, i.e. early Permian magmatic activity. Such assumption allows to calculated lower extension factors for the first rifting phase. Pure-shear model for the PB generally predicts significant increase of heat flow during the late Permian-Early Triassic in the PT and its exponential decrease afterwards. For the southern part of the PB it should be repeated during the Late Jurassic. In this model the exact calculated value of palaeoheat flow anomaly related to each rifting event strictly depends on reconstructed extension ß factor (e.g. fig. 2).
To explain tectonic evolution of the PB Kutek (1997) and Karnkowski (1999) applied Wernicke's model of simple shear extension. In particular with this model they aimed to explain general geometric asymmetry of the PB and a Moho topography below the basin. A consequence of simple shear rifting model is a prediction of syn-rift thermal anomaly in the SW part of the basin (zone III on fig. 1) leading to relatively high maturity of basin's sedimentary fill in this zone (Karnkowski, 1999).
Relative role of strike-slip movements as a subsidence mechanism for the PB late Permian, was additionally discuss e.g. by Poprawa (1997) and Hakenberg & Świdrowska (1997). Transtensional regime was suggested for the late Permian-Early Triassic, Late Triassic, Early-Middle Jurassic and early-most Cretaceous tectonic subsidence events. Each of this events could theoretically create a shot time positive thermal anomaly.

Thermal history of the Polish Basin – constraints from maturity modelling

1-D maturity modelling was conducted for a dense grid of boreholes, covering all the PB. For each analysed well section maturity profile was determined by vitrinite reflectance (VRo) measurements. During the modelling alternative scenarios of heat flow history were tested; in each case maturity predicted by model was confronted with VRo measurements to discriminate between realistic and not relevant thermal history scenarios.
Modelling performed for the Kujawy segment of the PT (fig. 1) clearly shows that thermal history predicted by pure-shear model results with maturity by far to high with compare to VRo profile (fig. 2). This indicates, that syn-rift heat flow anomalies, as postulated by McKenzie model, did not dominate thermal history of the PT. Therefore pure-shear model, if applicable to the PB, would require in this case very limited extension ß factor. This is in agreement with very small ß factor for the PT calculated from extensional structures.

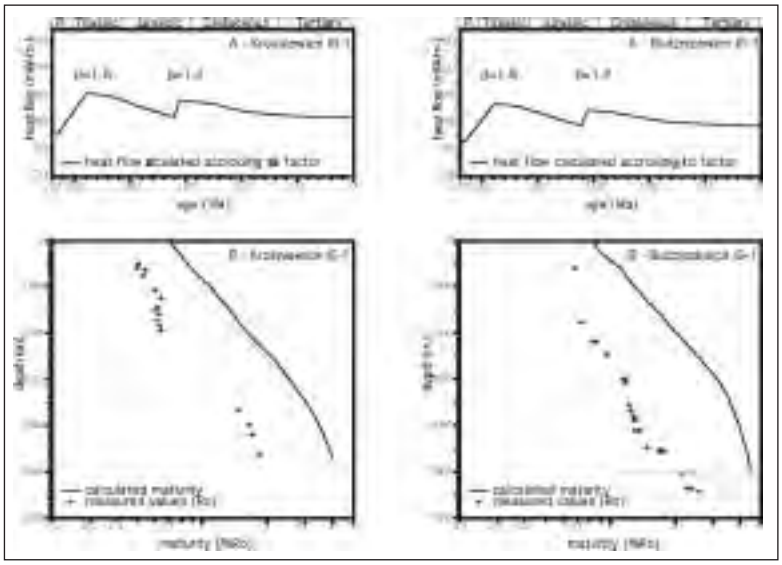

Fig. 2 - Consequences of pure-shear model for the PB, with ß factor after Dadlez et al. (1995), calculated for two borehole sections (Krosniewice IG-1 and Budziszewice IG-1; zone II on fig. 1): A – heat flow distribution in time calculated according to the ß factors; B – measured versus calculated thermal maturity profile. The figure illustrates misfit between predictions of McKenzie rift model for the PB and the analytical data (VRo).

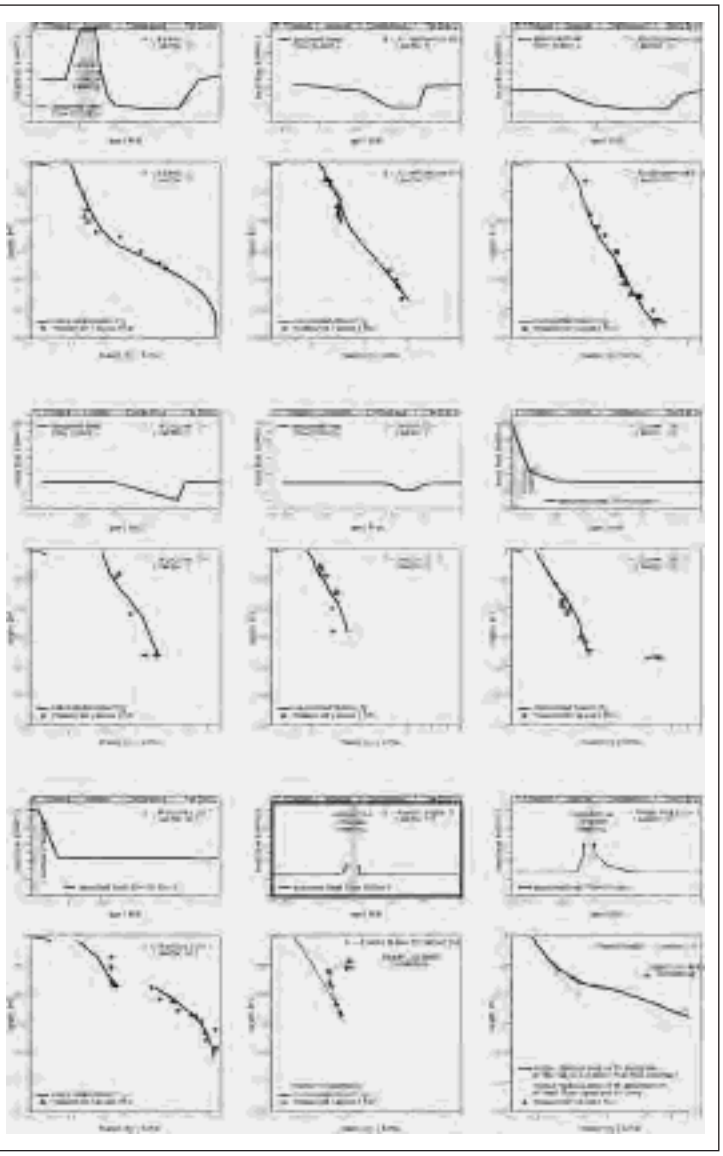

Fig. 3 - Models of thermal history (heat flow scenarios versus their calibration by VRo data) for the chosen well sections representative for the following zones of the PB: I – Pomerania; II – Kujawy; III – South-west (area of Fore-Sudetic monocline); IV – South (area of Miechow Trough).

Application of the alternative, simple-shear model for the PB was partly justified based on suggestion that zone of syn-rift high heat flow was shifted towards SW (zone III on fig. 1) with respect to the main depocentre (Karnkowski, 1999). However this model predicts to high thermal maturity in the the SW part of the PB. The misfit is clearly seen e.g. at the level of the Main Dolomite sediments (Zechstein), for which model predicts VRo higher than 2 % Ro in some locations (op. cit.), while measurement indicate maturity between 0.6-1.0 % Ro. High maturity of the underlying Carboniferous sediments also do not confirm the concept of high Mesozoic heat flow, because it is results of the late Carboniferous and/or early Permian heating (Poprawa et al., 2002). This is clearly illustrated by unconformity in thermal maturity profile between the Carboniferous and Upper Permian strata (fig. 3f-3g).

Except of quantitative limits on both of the above discussed models, there is generally little of constrains from the maturity modelling on the Permian-Triassic thermal history of the PB. On a contrary, measured VRo profiles allows for higher resolution of reconstruction of the PB thermal regime for the Jurassic and Cretaceous.

In the southern part of the Kujawy segment of the PB (fig. 1) the Early to Middle Jurassic thermal anomaly was revealed. This was based on maturity modelling (fig. 3a) (Poprawa et al., 2002), supplemented with thermochronological constrains obtained from K/Ar dating of diagenetic illite (Kozlowska & Poprawa, 2004). Values of paleoheat flow calculated for this relatively fast decaying thermal anomaly are extremely high (up to ~130 mW/m^2), indicating convective mechanism of heat transport. The anomaly is coeval in time with phase of tectonic reactivation of the PB and development extensional to transtensional faults in this part of the basin (Hakenberg & Swidrowska, 1997; Poprawa, 1997). This allows for interpretation, that the thermal anomaly was caused by migration of hot fluids from sedimentary basement of the PB though hydraulically opened structures.

Additional thermal perturbation took place during the late Jurassic further to the South, i.e. in the area of the Miechow Trough (zone IV on fig. 1). The modelling reveals increase of heat flow at that time in most of the analysed sections (Poprawa et al., 2002). In some cases inversion of thermal maturity profile is observed, with the highest values obtained in the Oxfordian sediments (fig. 3h, 3i), sugges-

tive that source of additional heat was related to this stratigraphic level. The Oxfordian thick brittle limestone formation is engaged by the late Jurassic extensional structures (Kutek, 1994), possibly related to rifting in the northern part of the Tethyan domain (Poprawa, 1997). Based on above we conclude that the late Jurassic thermal anomaly in the southern-most part of the PB could be related to both tectonically driven increase of conductive heat transport, as well as hot fluid migration though the hydraulically opened extensional structures, well developed in the Oxfordian limestone.
The Polish Trough, i.e. the main depocentre of the PB, during the late Cretaceous and/or Paleocene underwent inversion and significant erosion. As a result maturity of pre-Paleogene sediments in this zone are not influenced by recent burial and thermal regime, therefore it records paleothermal conditions. For most of the PT, and particularly for its Kujawy segment, this allows to reconstruct significant decrease of thermal gradient/heat flow, which took place in the Late Cretaceous, prior to inversion (Poprawa et al., 2002). Heat flow calculated for the late-most Cretaceous could be lower then recent one even by 30-40% (fig. 3a-3e). In most of the analysed sections in the PT a less pronounced decrease of heat flow is reconstructed also for the Early Cretaceous, and to even lesser degree for the (Middle-?) Late Jurassic. It is difficult to discriminate between conductive and convective mechanisms for this perturbation of thermal regime. A contribution to the observed phenomena could be paid by post-rift cooling, however this would require an additional Tertiary thermal event to explain recent thermal regime of the Polish Lowlands. The late-most Cretaceous stage of the low heat flow period could be genetically related tectonic inversion of the PT as well. Nonetheless, other convective mechanisms could be also regarded to explain the observed phenomena.
It could be summarised, that there is little of correlation between tectonic models for the PB development and relevant predictions of the thermal evolution with observed maturity profiles. Instead other significant changes in time, as well as lateral changes, of thermal regime are reconstructed, partly characterised by clear convective mechanism of heat transport and coeval in time with phases of structural activity.

REFERENCES

- Dadlez R., Narkiewicz M., Stephenson R.A., Visser M.T.M. & van Wess J-D. (1995), Tectonic evolution of the Mid-Polish Trough: modelling implications and significance for central European geology. Tectonophysics, 252: 179-195
- Hakenberg M. & Swidrowska J. (1997), Propagation of the south-eastern segment of the Polish Trough connected with bounding fault zones (from the Permian to Late Jurassic). Comptes Rendes de l'Academie Science, Paris, 324: 793-803
- Karnkowski P.H. (1999), Origin and evolution of the Polish Rotliegend basin. Polish Geological Institute Special Papers, 3: 1-93
- Koz≥owska A. & Poprawa P. (2004; in print), Diagenesis of the Carboniferous sediments of the Mazowsze region and the northern Lublin region related to their burial and thermal history. Przeglad Geologiczny (in Polish with English abstract)
- Kutek J. (1994), Jurassic tectonic events in the south-eastern cratonic Poland. Acta Geologica Polonica, 44(3-4): 167-221
- Kutek J. (1997), The Polish Permo-Mesozoic Rift Basin. IGCP 369 - Abstracts book of 4th Annual Meeting and Fieldtrip, Barcelona
- Poprawa P. (1997), Late Permian to Tertiary dynamics of the Polish Trough. Terra Nostra, 97/11: 104-109
- Poprawa P., Grotek I., Wagner M. & Matyja H. (2002), Phanerozoic thermal history of the Trans-European Suture Zone in Poland – recent stage of research in the project PAP. Przeglad Geologiczny, 50(12): 1219-1220 (in Polish)
- Van Wees J.-D., Stephenson R.A., Ziegler P.A., Bayer U., McCann T., Dadlez R., Gaupp R., Narkiewicz M., Bitzer F. & Scheck M. (2000), On the origin of the Southern Permian Basin, Central Europe. Marine and Petroleum Geology, 17(1): 43-59
- Ziegler P. (1990), Geological Atlas of Western and Central Europe. Shell Intern. Petrol. Maatschappij BV, 239 pp.

AUTOMATED INVERSE MODELLING OF THE THERMO-TECTONIC EVOLUTION OF THE NW VØRING BASIN: MINERAL PHASE TRANSITIONS AS POSSIBLE MECHANISM FOR PALEOCENE UPLIFT 3-23

Stefan M. Schmalholz(*), Daniel W. Schmid(*), Yuri Yu. Podladchikov(*), Rob Hunsdale(**)

(*) Physics of Geological Processes, University of Oslo, PO Box 1048 Blindern, Norway
(**) Statoil ASA, 4035 Stavanger, Norway

NOTE: Pictures have not yet been included, since we have to wait for the final permission from Statoil to publish them.

Summary

We present reconstructions of the thermo-tectonic evolution of a stratigraphic section located in the NW Vøring basin, offshore Western Norway. Reconstructions were performed using a numerical forward

model which is coupled to an automated inverse algorithm. The forward model is based on kinematic thinning/stretching and the inverse algorithm automatically determines the optimal set of thinning/stretching factors that fit the observed stratigraphy best. The inverse algorithm was constrained to allow for thinning only in predefined time intervals to test various geological extension scenarios. A characteristic feature of the NW Vøring basin is regional uplift during the Paleocene (65 to 55 MyrsBP). Our reconstructions show that incorporating mineral phase transitions into the forward model enables to generate the geologically constrained uplift during the Paleocene and the following subsidence. Importantly, mineral phase transitions cause both uplift and the following subsidence, which is larger than the uplift, without considerable thinning or heating during the Paleocene. Without mineral phase transitions much higher heat input is necessary to fit both the geological constraints on uplift and subsidence. Thermal history reconstructions considering mineral phase transitions for the NW Vøring basin generate different heat flow histories than reconstructions without mineral phase transitions.

Abstract text

Extensional sedimentary basins in general, and especially rifted continental margins, are the world's largest repositories of hydrocarbon. Hydrocarbon generation and maturation are most sensitive to temperature, and thermal history reconstructions of sedimentary basins are essential for evaluating petroleum prospects. Furthermore, thermal history reconstructions provide important insight into the geodynamic process of lithospheric extension.

Here, we perform thermal history reconstructions for the NW Vøring basin. Reconstructions are performed through reproducing the basin's present day stratigraphy with a mathematical forward model (here TECMOD). The model is based on pure shear kinematics [*McKenzie*, 1978; *Royden and Keen*, 1980] [*Kooi et al.*, 1992] and a set of thinning/stretching factors controls the velocity field during extension. During the reconstruction, these thinning factors are modified iteratively so that the misfit between the observed (or real) stratigraphy and the modelled stratigraphy is minimized [*Podladchikov et al.*, 2002; *Poplavskii et al.*, 2001; *Robinson et al.*, 1995; *Van Wees et al.*, 1996; *White*, 1993; *White and Bellingham*, 2002]. The modification of the thinning factors is performed automatically. The set of thinning factors minimizing the misfit between real and modelled stratigraphy is termed the optimal set. The thermal evolution calculated with the optimal set is then considered as a possible thermal history reconstruction.

The applied forward model allows for depth-dependent stretching [*Royden and Keen*, 1980] and multiple rifting events of finite duration [*Jarvis and McKenzie*, 1980; *Reemst and Cloetingh*, 2000]. The model further includes the effects of flexural isostasy and depth of necking [*Braun and Beaumont*, 1989; *Kooi et al.*, 1992; *Watts et al.*, 1982; *Weissel and Karner*, 1989]. The velocity field derived from both pure shear kinematics and the flexure of the lithosphere is used to advect the temperature field. Thermal diffusion and radiogenic heat production are further included. Radiogenic heat production decreases exponentially with depth within the crust and is constant within the sediments. Water and sediments are incorporated in the thermal solver to include the effects of sediment blanketing [*Debremaecker*, 1983; *Lucazeau and Ledouaran*, 1985]. Sediment deposition is controlled by a specified water depth, which can vary in space and time. The deposited sediments are compacted using a compaction law with exponentially decreasing porosity.

We apply two methods to calculate density changes, which affect the differential, or dead, load in the flexure equation. The first method calculates density changes due to temperature variations only using a reference density and a thermal expansion factor [*McKenzie*, 1978]. The second method assumes a specific chemical composition for a certain model unit (e.g., granodiorite represents the crust), and calculates density values for given temperatures and pressures. The pressure at a certain depth is calculated by integrating the 1D density field above that depth with considering the pressure step caused by the flexural rigidity of the lithosphere. Density calculations are computed from thermodynamic data with a free-energy minimization program [*Connolly and Petrini*, 2002; *Petrini et al.*, 2001]. The applied chemical compositions for the crust and lithospheric mantle are taken from Petrini et al. 2001.

Automated inversion (or reconstruction) of extensional basin formation can be treated as a constrained optimisation problem [*Nocedal and Wright*, 1999]. The function to be minimized is the misfit between observed and modelled stratigraphic data and constraints are imposed due to geological data (e.g.,

extension is active in certain time intervals only). The inversion consists in the iterative search for the optimal set of δ, β and palaeo-water depth values, which yield the best fit between the observed and modelled stratigraphies. The optimal set of δ, β and palaeo-water depth values minimizes the chosen goal function, which is the misfit between the observed and modelled present-day depths of stratigraphic horizons. The goal function contains the misfits between every observed and modelled stratigraphic horizon for a chosen number of points on a cross section, which makes the minimization procedure equally sensitive for all observed data [*Poplavskii et al.*, 2001; *White and Bellingham*, 2002]. The first iterative forward run requires an initial guess for the δ, β and palaeo-water depth values. The initial guess for the stretching factors is based on simple analytical solutions for isostasy and thermal subsidence. After every forward run the misfit between the observed and modelled depth of stratigraphic horizons is determined. This misfit is used to modify the existing values of the δ and β factors and the palaeo-water depth. The update rules for modifying the δ and β factors and palaeo-water depths are weighted (i.e. weighted goal function approach) to increase convergence and stability of the inverse algorithm.

Several reconstructions of the thermo-tectonic evolution of a stratigraphic section from the NW Vøring basin have been performed with the above described methodology. One of the main difficulties encountered during the reconstructions are incorporating given geological constrains for the left part of the section. For example, at around 55 MyrsBP flood basalts have been deposited at the surface (zero water depth) and there are no clear evidences for considerable extension in the upper crust and in the sediments at this time [*Ren et al.*, 2003]. Furthermore, around 2km of subsidence occurred in the left part of the section between Paleocene and present day. Paleocene uplift is constrained by geological observations and is also required within the reconstruction, because prior to basalt deposition there is around 500m to 1000m of water depth above the sedimentary sequence. However, there is no clear mechanism explaining the Paleocene uplift and the following subsidence. Underplating is a possible mechanism for uplift, but cannot reproduce the 2km of subsidence following the uplift. Strong thermal upwelling (high β factor) will create uplift and following subsidence, but the depth of the sedimentary horizons should be approximately the same before and after the thermal event, if the lithosphere was in thermal equilibrium before Paleocene time. Therefore, thermal upwelling modelled by high β factors will not create considerable more subsidence than uplift, but the uplift is of the order of 500m whereas the following subsidence is around 2000m. We show that mineral phase transitions are a possible mechanism for the Paleocene uplift. In our reconstruction the lithosphere is not fully thermally equilibrated at around 55 MyrsBP and a thinning factor of 1.5 for the lithospheric mantle (δ=1, no crustal thinning!) is sufficient to trigger thermally mineral phase transitions which cause an uplift due to an effective density decrease within the lithospheric mantle. After the uplift, thermal cooling and retrograde mineral phase transitions are able to generate the 2km of subsidence between 55 MyrsBP and present day.

Our reconstructions show that mineral phase transitions can have considerable impact on the subsidence history. Furthermore, thermal history reconstructions performed with mineral phase transitions can provide considerable different thermal histories than reconstructions without mineral phase transitions.

REFERENCES

- Braun, J., and C. Beaumont, A physical explanation of the relation between flank uplifts and the breakup unconformity at rifted continental margins, Geology, 17 (8), 760-764, 1989.
- Connolly, J.A.D., and K. Petrini, An automated strategy for calculation of phase diagram sections and retrieval of rock properties as a function of physical conditions, Journal of Metamorphic Geology, 20 (7), 697-708, 2002.
- Debremaecker, J.C., Temperature, Subsidence, and Hydrocarbon Maturation in Extensional Basins - a Finite-Element Model, Aapg Bulletin-American Association of Petroleum Geologists, 67 (9), 1410-1414, 1983.
- Jarvis, G.T., and D.P. McKenzie, Sedimentary basin formation with finite extension rates, Earth and Planetary Science Letters, 48, 42-52, 1980.
- Kooi, H., S. Cloetingh, and J. Burrus, Lithospheric necking and regional isostasy at extensional basins, 1, Subsidence and gravity modelling with an application to the Gulf of Lions Margin (SE France), Journal of Geophysical Research, 97 (B12), 17553-17572, 1992.
- Lucazeau, F., and S. Ledouaran, The Blanketing Effect of Sediments in Basins Formed by Extension - a Numerical-Model - Application to the Gulf of Lion and Viking Graben, Earth and Planetary Science Letters, 74 (1), 92-102, 1985.
- McKenzie, D., Some remarks on the development of sedimentary basins, Earth and Planetary Science Letters, 40, 25-32, 1978.
- Nocedal, J., and S.J. Wright, Numerical optimization, Springer, New York, 1999.
- Petrini, K., J.A.D. Connolly, and Y.Y. Podladchikov, A coupled petrological-tectonic model for sedimentary basin evolution: the

influence of metamorphic reactions on basin subsidence, Terra Nova, 13 (5), 354-359, 2001.
- Podladchikov, Y.Y., S.M. Schmalholz, and D.W. Schmid, Inverse modelling of sedimentary basins, in Progress in industrial mathematics at ECMI 2000, edited by M. Anile, V. Capasso, and A. Graco, pp. 625-629, Springer Verlag, Berlin, 2002.
- Poplavskii, K.N., Y.Y. Podladchikov, and R.A. Stephenson, Two-dimensional inverse modeling of sedimentary basin subsidence, Journal of Geophysical Research-Solid Earth, 106 (B4), 6657-6671, 2001.
- Reemst, P., and S. Cloetingh, Polyphase rift evolution of the Voring margin (mid-Norway): Constraints from forward tectonostratigraphic modeling, Tectonics, 19 (2), 225-240, 2000.
- Ren, S., J.I. Faleide, O. Eldholm, J. Skogseid, and F. Gradstein, Late Cretaceous-Paleocene tectonic development of the NW Vøring Basin, Marine and Petroleum Geology, 20, 177-206, 2003.
- Robinson, A., G. Spadini, S. Cloetingh, and J. Rudat, Stratigraphic Evolution of the Black-Sea - Inferences From Basin Modeling, Marine and Petroleum Geology, 12 (8), 821-835, 1995.
- Royden, L., and C.E. Keen, Rifting process and thermal evolution of the continental margin of eastern Canada determined from subsidence curves, Earth and Planetary Science Letters, 51, 343-361, 1980.
- Van Wees, J.D., R.A. Stephenson, S.M. Stovba, and V.A. Shymanovskyi, Tectonic variation in the Dniepr-Donets Basin from automated modelling of backstripped subsidence curves, Tectonophysics, 268, 257-280, 1996.
- Watts, A.B., G.D. Karner, and M.S. Steckler, Lithosphere flexure and the evolution of sedimentary basins, Philosophical Transactions of the Royal Society of London, 305, 249-281, 1982.
- Weissel, J.K., and G.D. Karner, Flexural uplift of rift flanks due to mechanical unloading of the lithosphere during extension, Journal of Geophysical Research, 94, 13919-13950, 1989.
- White, N., Recovery of Strain-Rate Variation from Inversion of Subsidence Data, Nature, 366 (6454), 449-452, 1993.
- White, N., and P. Bellingham, A two-dimensional inverse model for extensional sedimentary basins 1. Theory, J. Geophys. Res., 107 (B10), 10.1029/2001JB000173, 2002.

3D ANALOGUE MODELLING OF BASIN INVERSION: THE EFFECT OF DISTRIBUTED WRENCHING OR TRANSPRESSION ON PRE-EXISTING GRABENS

3-24

Guido Schreurs

Institute of Geological Sciences, University of Bern, CH-3012 Bern, Switzerland; schreurs@geo.unibe.ch

Summary

3D analogue model experiments were performed to investigate basin inversion and involved a first phase of distributed extension followed by a second phase of either distributed wrenching or transpression. The experiments show that there is only limited basin inversion. The initial fault pattern during the second phase of deformation depends mainly on the obliquity of convergence. At low angles of convergence, strike-slip faults form initially, whereas at higher angles of convergence thrust faults dominate. The location of thrust faults is strongly controlled by the pre-existing basin geometry. Thrust faults root at the base of the graben where lateral changes in rheology are highest. They partially reactivate the lower part of graben-bounding faults and continue into the footwall of the graben. The location of early strike-slip faults seems to be less controlled by basal rheological changes. With increasing strain, local stress modifications occur governed mainly by earlier formed strike-slip faults. These stress modifications induce local reactivation of pre-existing normal faults and thus local basin inversion.

Introduction

Cooper et al. (1989) noted that the requirements for inversion are twofold (1) "development of a basin actively controlled by faults such that a synrift or passive infill stratigraphic sequence can be recognised; (2) "a change in the regional stress system resulting in the extensive re-use of the pre-existing fault (system), with the uplift affecting the hanging wall rather than the footwall". Seismic studies, field work, analogue and numerical modelling experiments have documented a wide range of geometries produced in basin inversion (e.g., Cooper & Williams, 1989; Buchanan & McClay, 1991; Coward, 1994; Buchanan & Buchanan, 1995; Nalpas et al., 1995; Buiter & Pfiffner, 2003). However, most of these studies are restricted to 2D and the geometries of inversion related structures in 3D are relatively poorly described and often not fully understood. Here, we present results of 3D analogue models investigating basin inversion. Each experiment involved two successive phases of

deformation. A first phase of extension was followed by a second phase of either wrenching or transpression. In contrast to most previous studies on basin inversion, neither rigid footwall nor basal velocity discontinuity were present in our models. Instead, deformation was distributed at the base of the model during both phases of deformation.

Modelling materials

In our experiments we used viscous silicone (polydimethylsiloxane, PDMS) and dry granular materials (quartz sand, corundum sand and glass powder) with a low cohesion. Ring-shear test results indicate that the granular materials have angles of internal friction similar to those determined experimentally for competent upper crustal rocks. Both brittle crust and granular materials are characterised by an elastic frictional-plastic material behaviour with an initial strain hardening phase preceding failure that is followed by a transitional phase of strain softening until stable sliding (Lohrmann et al., 2003; Ellis et al., 2004). PDMS has a Newtonian viscosity of 5 x 10^4 Pa·s at room temperature and at strain rates below 3 x 10^3 s^{-1} (Weijermars, 1986), and is considered to be a good analogue material to simulate the viscous rheology of materials such as salt or rocks in the lower crust.

Experimental set-up and procedure

The experimental apparatus used to model basin inversion is illustrated schematically in Fig. 1 and includes two base plates, one of which could be displaced past the other by a geared motor drive. The two base plates were overlain by an alternation of plexiglass and foam bars. Before constructing the model, the assemblage of plexiglass and foam bars was shortened 4 cm by displacement of the longitudinal sidewalls. The brittle-viscous model was then build on top. A 1 cm thick layer of viscous PDMS was placed at the base and was overlain by 3 alternating layers of granular materials each 1 cm thick. The long dimension of each model was 70 cm and transverse confinement of the model was provided by rubber sheets. Extension was produced by movement of both longitudinal sidewalls. During extension the foam bars "decompressed" and deformation was distributed at the base of the model. The presence of the basal viscous layer prevented localization of deformation above discontinuities presented by adjacent plexiglass and foam bars. At regular intervals granular material was sieved into the developing grabens to simulate syn-rift sedimentation. After 3 cm of extension the experiment was halted and an additional 1 cm thick layer of granular material was sieved on top to produce a post-rift sequence. The second phase of deformation involved either distributed wrenching or transpression. In the case of distributed wrenching, one of the two base plates was moved past the other and the overlying plexiglass and foam bars slipped past one another and the initial rectangular configuration changed into a parallelogram, inducing distributed wrenching in the overlying brittle-viscous model. In case of distributed transpression, wrenching was combined with transverse shortening induced by displacement of one longitudinal sidewall. Models were analysed by X-ray computed tomography (CT), a non-destructive method that allows a complete analysis of the internal geometry of analogue models.

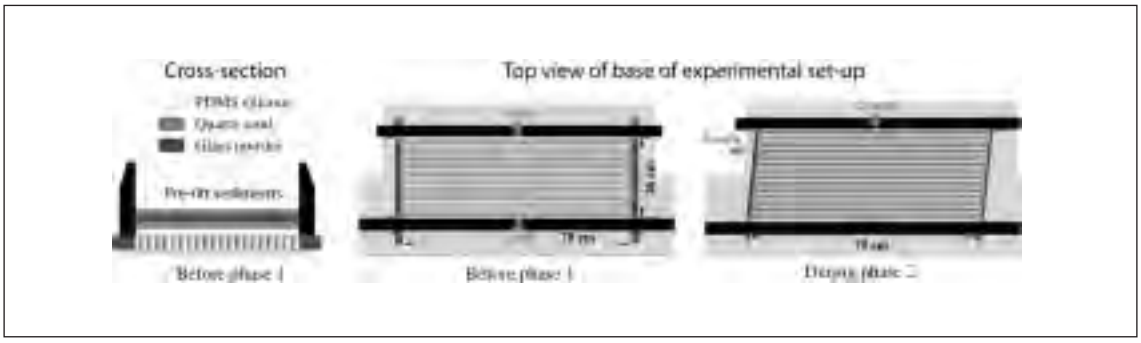

Fig.1. Schematic diagrams illustrating experimental set-up. The cross-section shows the alternation of vertical plexiglass and foam bars overlain by viscous silicone and granular materials. Top views shows the base of the experimental set-up for a model undergoing a phase of extension followed by a phase of transpression.

Experimental results

Table 1 lists the experimental parameters for four experiments. In all experiments the extensional phase was orthogonal to the longitudinal sidewalls whose bulk displacement was limited to 3 cm. Grabens formed during the extensional phase whose overall strike was parallel to the longitudinal wall. The dip of normal faults was about 60-67°. During the second phase of deformation the angle of convergence (i.e., angle between displacement vector and longitudinal sidewall) was varied from one experiment to the next.

	Exp. 1377	Exp. 1378	Exp. 1376	Exp. 1379
Phase 1: Distributed Extension				
Initial width	26 cm	26 cm	26 cm	26 cm
Divergent movement of each longitudinal sidewall	1 cm/h	0.75 cm/h	1 cm/h	0.75 cm/h
Syn-rift sedimentation at different stages of extension; after:	1.5, 2.3 and 3.0 cm	1.5, 2.3 and 3.0 cm	1.5 cm and 3.0 cm	1.5 cm and 3.0 cm
Thickness of post-rift sedimentation	1.0 cm	1.0 cm	1.0 cm	1.0 cm
Width before phase 2	29 cm	29 cm	29 cm	29 cm
Phase 2: Distributed Wrenching/ Transpression				
Obliquity of convergence (α)	0°	14°	27°	45°
Movement of base plate	4 cm/h	4 cm/h	4 cm/h	2 cm/h
Total displacement of base plate	8 cm	10 cm	7 cm	3.2 cm
Convergent movement of longitudinal sidewall	0 cm/h	1 cm/h	2 cm/h	2 cm/h
Total transverse shortening of model at end of phase 2	0 cm	2.5 cm	3.5 cm	3.2 cm
Final width of model	29 cm	26.5 cm	25.5 cm	25.8 cm

Table 1. Experimental parameters

Exp. 1377: Extension followed by wrenching (angle of obliquity during phase 2: α = 0°)

During the initial stages of dextral bulk wrenching, en echelon dextral strike-slip faults (Riedel shears) developed in the brittle part of the model. Their surface strike ranged between 17° and 23° with respect to the longitudinal wall. Domains with a slight vertical relief (push-up zones) appeared in the area comprised between two left-stepping strike-slip faults. As individual strike-slip faults propagated along strike, they overlapped with adjacent left-stepping strike-slip faults, and the propagating fault segments acquired gentler dips. Strike-slip faults merged at depth with pre-existing normal faults resulting locally in tulip structures as seen in cross-section with fault dips steepening upward in the post-rift sequence. Coalescence of en echelon strike-slip faults and graben-bounding normal faults resulted in major, anastomosing fault zones that strike subparallel to the longitudinal wall (Fig. 2).

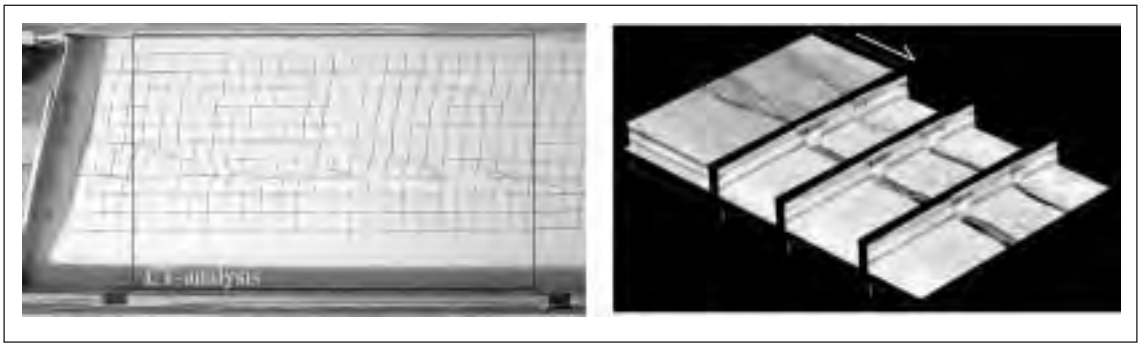

Fig. 2. Structures in experiment 1377: (a) Surface view during distributed dextral wrenching, after 7 cm of displacement of base plate; width of model is 29 cm. (b) 3D perspective block diagram of deformation stage shown in (a) with horizontal sections through post-rift sequence (left-hand side) and at depth (right-hand side), and three cross-sections. Note tulip structures in cross-sections.

Exp. 1378: Extension followed by transpression (α = 14°)

As in the previous experiment, dextral strike-slip faults formed during the early phases of distributed transpression However, their surface strike was now at larger values, ranging between 30 and 35°. The faults were arranged in a left-stepping en echelon pattern and mostly cut across the pre-existing basin. With increasing transpression, push-up zones appeared between two left-stepping strike-slip faults. As these faults propagated along strike, their surface strike and their dip decreased slightly in the area of overlap. Locally these faults coalesced at depth with graben-bounding normal faults (Fig. 3).

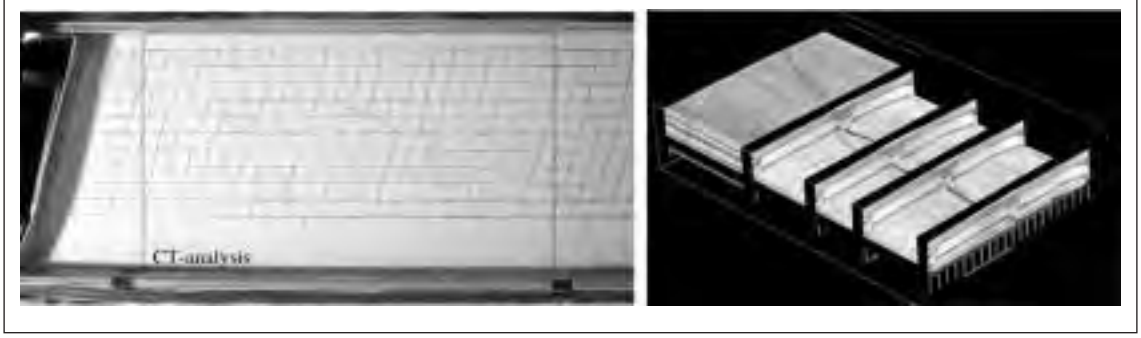

Fig. 3. Structures in experiment 1378: (a) Surface view during distributed dextral transpression, after 7 cm of displacement of base plate and 1.75 cm of shortening of upper longitudinal wall; width of model shown is 27.25 cm. (b) 3D perspective block diagram of deformation stage shown in (a) with horizontal sections through post-rift sequence (left-hand side) and at depth (right-hand side), and four cross-sections. Three frontal cross-sections show how a subvertical strike-slip fault cuts across the pre-existing graben.

Exp. 1376: Extension followed by transpression (α = 27°)

In contrast to the previous experiment, distributed transpression was initially taken up by the development of thrust faults. Strike-slip faults appeared slightly later than the thrust faults and their surface strike was 37°-40°. This fault pattern suggests partitioning of fault displacement during the early stages of transpression. Thrusts rooted at the base of the model where there was an important lateral rheological change from viscous to granular material. Major thrusts partially reactivated the lower part of graben-bounding faults that dip away from the mobile wall. They continued into the footwall of the graben and cut across the post-rift sequence. With increasing transpression, thrusts became dextral oblique-slip reverse fault. Graben-bounding faults dipping towards the mobile longitudinal wall were partially reactivated. As these faults propagated into the post-rift sequence their dip decreased. Strike-slip faults coalesced at depth with graben-bounding faults (Fig. 4).

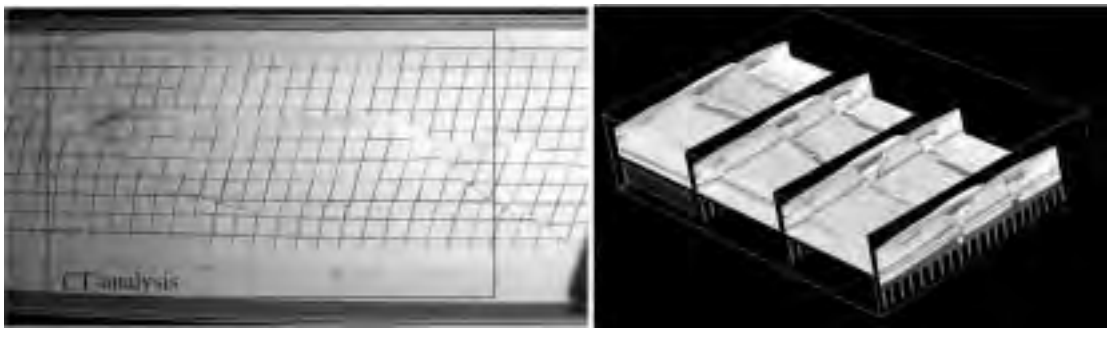

Fig. 4. Structures in experiment 1376: (a) Surface view during distributed dextral transpression, after 7 cm of displacement of base plate and 3.5 cm of shortening of upper longitudinal wall; width of model shown is 25.5 cm. (b) 3D perspective block diagram of deformation stage shown in (a) with horizontal sections and cross-sections. Note the major footwall short-cut thrust that roots at the top of the silicone. Strike-slip faults in frontal cross-section coalesce with graben-bounding normal fault.

Exp. 1379: Extension followed by transpression (α = 45°)

Distributed transpression was taken up entirely by thrust faulting and strike-slip faults were absent. The main thrust rooted at the base of the model and propagated upward into the footwall of the graben and into the post-rift sequence without changing its dip angle. With increasing transpression reverse slip along the forward thrust became oblique (Fig. 5).

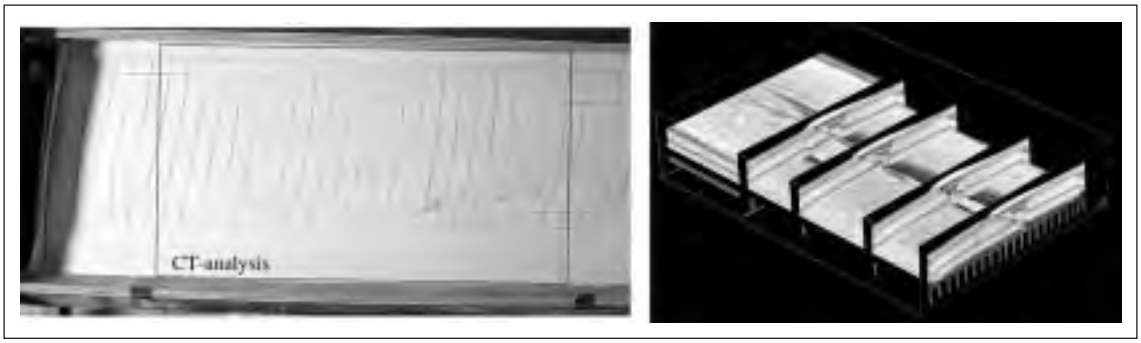

Fig. 5. Structures in experiment 1379: (a) Surface view during distributed dextral transpression, after 3 cm of displacement of base plate and 3 cm of shortening of upper longitudinal wall; width of model shown is 26 cm. (b) 3D perspective block diagram of deformation stage shown in (a) with horizontal sections and cross-sections. Note the major footwall short-cut thrust that roots at the base of the main graben and displaces the basin in its hanging-wall.

Conclusions

In the experiments shown here, there is only limited basin inversion (i.e., limited re-use of pre-existing basin-related faults). The initial fault pattern that evolves during the second phase of deformation depends mainly on the obliquity of convergence. At low angles of convergence, strike-slip faults form initially, whereas at higher angles of convergence thrust faults dominate. With increasing strain, these faults acquire a component of oblique slip. The orientations of early formed strike-slip faults are similar to those observed in wrenching and transpression experiments without pre-existing extensional structures (Schreurs & Colletta, 1998; Schreurs, 2003). This indicates that the orientations of early strike-slip faults are mainly governed by far-field stresses and are less controlled by the pre-existing graben geometry. Lateral changes in rheology occur at the base of the graben at the end of the extensional phase and strongly localize thrust faults that form during transpression. In case strike-slip faults form during wrenching or transpression, their location seems to be less controlled by the pre-existing basin geometry. Basin inversion occurs locally during advanced stages of wrenching or transpression and is mainly the result of local stress modifications governed by early formed faults.

REFERENCES

- Buchanan, J.G. & Buchanan, P.G., (1995), Basin Inversion, Geological Society Special Publications, 88.
- Buchanan, J.G. & McClay, K., (1991), Sandbox experiments of inverted listric and planar fault systems. Tectonophysics, 188, 97-115.
- Buiter, S. & Pfiffner, O.A., (2003), Numerical models of the inversion of half-graben basins, Tectonics, 22(5), 1057, doi:10.1029/2002TC001417.
- Cooper, M.A. & Williams, G.D., (1989), Inversion Tectonics. Geological Society Special Publications, 44.
- Coward, M.P., (1994), Inversion Tectonics. In: Hancock, P.L. (ed.) Continental Deformation. Pergamon Press, 280-304.
- Ellis, S., Schreurs, G. & Panien, M., (2004), Comparisons between analogue and numerical models of thrust wedge development. J. of Struct. Geology, in press.
- Lohrmann, J., Kokowski, N., Adam, J. & Oncken, O., (2003), The impact of analogue material properties on the geometry, kinematics, and dynamics of convergent sand wedges. J. of Struct. Geology, 25, 1691-1711.
- Schreurs, G. & Colletta, B., (1998), analogue modelling of faulting in zones of continental transpression and transtension. In: Holdsworth, R.E., Strachan, R.A. & Dewey, J.F. (eds). Continental Transpressional and Transtensional Tectonics. Geological Society Special Publications, 135, 59-79.
- Schreurs, G., (2003), Fault development and interaction in distributed strike-slip shear zones: an experimental approach. In: Storti, F., Holdworth, R.E. & Salvini, F. (eds). Intraplate Strike-Slip Deformation Belts. Geological Society Special Publications, 210, 35-52.
- Weijermars, R., (1986), Flow behaviour and physical chemistry of bouncing putties and related polymers in view of tectonic laboratory applications. Tectonophysics, 124, 325-358.

QUEEN CHARLOTTE BASIN - HYDROCARBON MODELING 3-25

T.K. Schümann(*), K.M.M. Rohr(**), M.J. Whiticar(***)

(*) School of Earth and Ocean Sciences, University of Victoria, PO Box 3055 STN CSC, Victoria, British Columbia, Canada V8W 3P6, phone: +001 250 721 6177, fax: +001 250 721 6200, email: ts@uvic.ca

(**) Rohr Geophysics, 719 Birch Rd., North Saanich, B.C., Canada V8L 5S1

(***) School of Earth and Ocean Sciences, University of Victoria, PO Box 3055 STN CSC, Victoria, British Columbia, Canada

Summary

Modeling the thermal history of individual sedimentary basins in Hecate Strait, Queen Charlotte Basin, offshore British Columbia, Canada accounts for elevated heat flow related to an Oligocene / Miocene extensional period, correlated to widely distributed volcanic rocks. It leads to an estimation for plate thickness in good agreement to seismicity and heat flow data. Hydrocarbon generation from potential oil prone source rocks within the pre-rift Jurassic Kunga / Maude formations and the Cretaceous Queen Charlotte Group, and gas prone source rocks within the post-rift Tertiary Skonun Formation is computed. The latter is predicted predicted to be much lower than previously estimated.

Introduction

The Queen Charlotte Basin (QCB) north of Vancouver Island is bound by the Queen Charlotte Fault (QCF) in the west, which separates the Pacific from the North American plate, and the Coast Mountains in the east (Figure 1). From north to south, Dixon Entrance, Hecate Strait, and Queen Charlotte Sound have experienced slightly different sedimentary and tectonic evolution. A network of strike-slip sub-basins in Hecate Strait and Queen Charlotte Sound contains up to 6 km of syn- and post-rift sedimentary infill and constitutes one of Canada's hydrocarbon frontier basins. The QCB is different from many other sedimentary basins in that the underlying crust is mafic (Woodsworth, 1988) and the lithosphere is thin (Spence and Asudeh, 1994). Thus the high observed heat flow can not be derived from the crust, but must relate to the rise lower boundary of the lithosphere (1350° C isotherm) during Tertiary rifting.

Fig.1 - Location map of the area under study. Approximately 1000 km of reflection seismic lines have been recorded by the Geological Survey of Canada (Rohr and Dietrich, 1992)). This study focuses on line 88-05 (bold) and offshore well Sockeye B-10 (Shell Canada). Queen Charlotte Fault (QCF), Queen Charlotte Islands (QCI), and Vancouver Island (VI) are marked.

Data

Multi-channel seismic reflection data is used in combination with geochemical information derived from eight offshore wells drilled by Shell Canada in 1968. Hydrocarbons have been encountered in one of the offshore wells (Sockeye B-10, see Figure 1) and in several onshore oil seeps on the Queen Charlotte Islands. Thermally mature Lower Jurassic organic-rich shales occur on the Queen Charlotte Islands and the northern tip of Vancouver Island. For the basin modeling source rocks of the Jurassic and Cretaceous formations were defined as mainly marine and source rocks from the Miocene were considered to be terrestrial (Haggart 1991, Bustin 1997).

Methods

Along seismic reflection line 88-05 (Rohr and Dietrich, 1992), which spans Hecate Strait and covers the location of the Sockeye B-10 (Figure 1) a 2D section was modeled using Temis2D™ (Beicip-Franlab, France) petroleum systems modeling software (Figure 2). The geometry of the crust and the amount of stretching (ß-factor) along the profile was defined based on the works of Spence and Asudeh (1994) and Dehler et al. (1997) in combination with the interpretation of the seismic reflection data so that the crust is differentially thinned along the profile (Figure 2b). Basaltic composition and physical properties were applied to crustal layers following the interpretations of Spence and Asudeh (1994) who found high seismic velocities which correspond to mafic rocks in the crust under Hecate Strait. This is consistent with mapped rocks of Wrangellia (Woodsworth, 1988), a regionally extensive mafic terrane. As radiogenic heat production is very low in the region we use an average value of 0.9 $\mu W/m^3$ (Dehler et al., 1997).

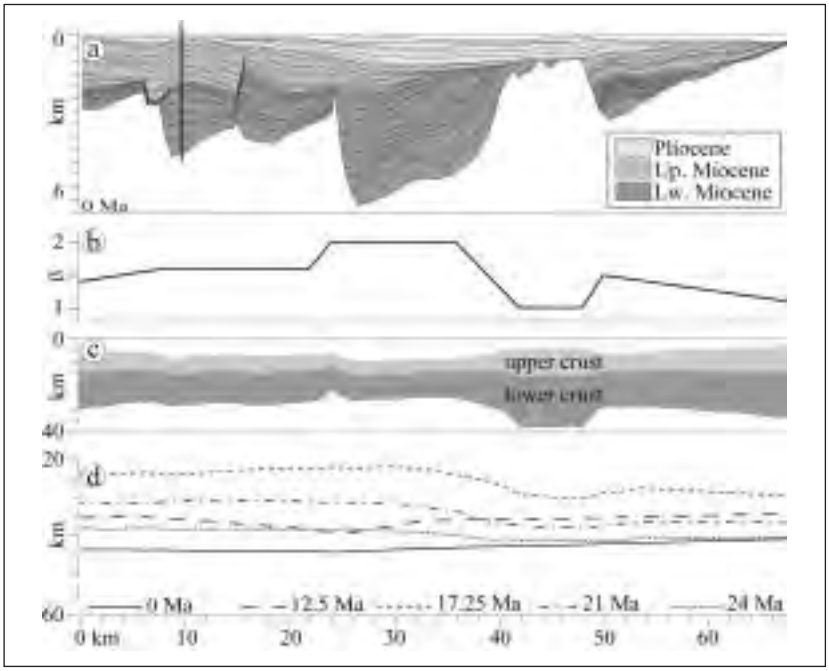

Fig.2 - (a) Depth converted line-interpretation of seismic reflection line 88-05 across Hecate Strait. (b) Interpreted lithospheric stretching factor ß. (c) Crustal thickness calculated for today. (d) Calculated rift related uplift of the 1350°C isotherm defining the lower boundary of the lithosphere.

Our petroleum systems model incorporates variable tectonic evolution and subsidence of individual sub-basins, which show variable sediment distribution, compaction and erosion, as well as thermal history. The thermal evolution and recent rifting history is taken into account to calculate maturity of hydrocarbons. Calibration of thermal evolution has been performed by matching available formation temperatures and heat flow values (Lewis et al., 1991) as well as vitrinite reflectance measurements on well samples (Bustin, 1997).

Results

Reflection seismic line 88-05 imaged multiple sub-basins (Figure 2a) which are bound on their west sides by main extensional faults. After the primary phase of extensional faulting, general subsidence

occurred along with uplift on several of the extensional faults. The greatest amount of recent uplift appears to have focused in western Hecate Strait. Sediment thickness ranges from less than 1 km over a basement high to more than 6 km in the deepest central basin (Figure 2a). Calculated crustal thickness based on an initial lithospheric thickness of 125 km according to Dehler et al. (1997) ranges from 26-30 km along the line (Figure 2c), which agrees with values of ca. 28 km from interpretations of refraction data in central Hecate Strait under this line (Spence and Asudeh, 1994).
Since this model predicts vitrinite reflectance not in accordance with well data a thinner initial plate thickness (35 km) had to be used to reach a good fit to the data. This value is in good agreement with estimates based on seismicity (Bird, 1997) and heat flow data (Lewis et al., 1991), which are 35-40 km under northern Hecate Strait (Rohr et al., 2000). Figure 2d illustrates the calculated rise of the 1350°C isotherm for multiple timesteps and the heat flow evolution predicted for the base of the sediments is given in Figure 3.

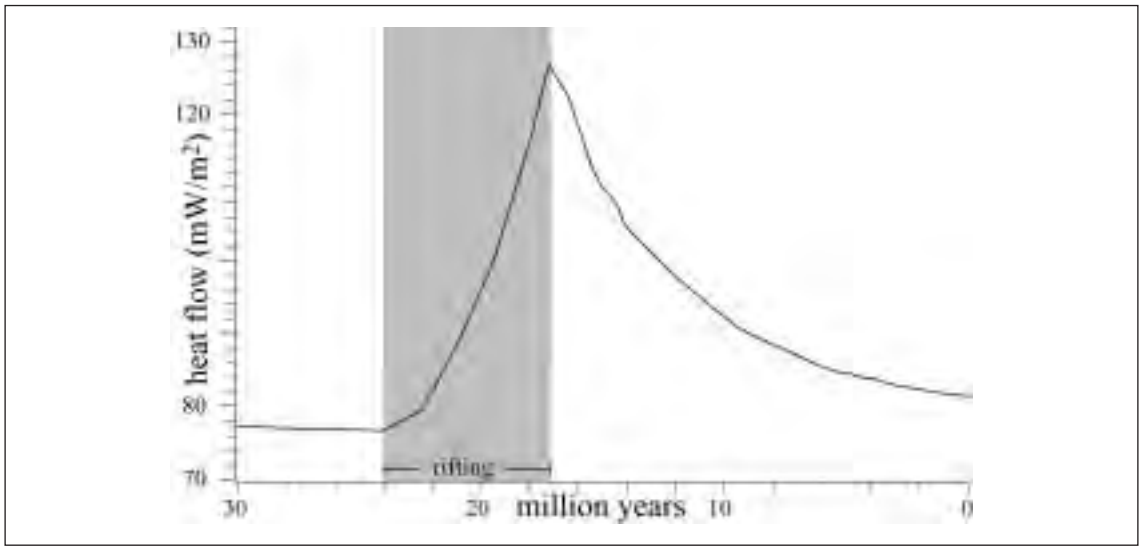

Fig. 3 - Heat flow evolution at the location of the Sockeye B-10 well predicted for the base of the sediments.

This model gave a good correlation to temperatures measured in the well (Figure 4a), vitrinite reflectance (%R_o) measured on samples from the well (Figure 4b), and heat flow data (Lewis et al., 1991).

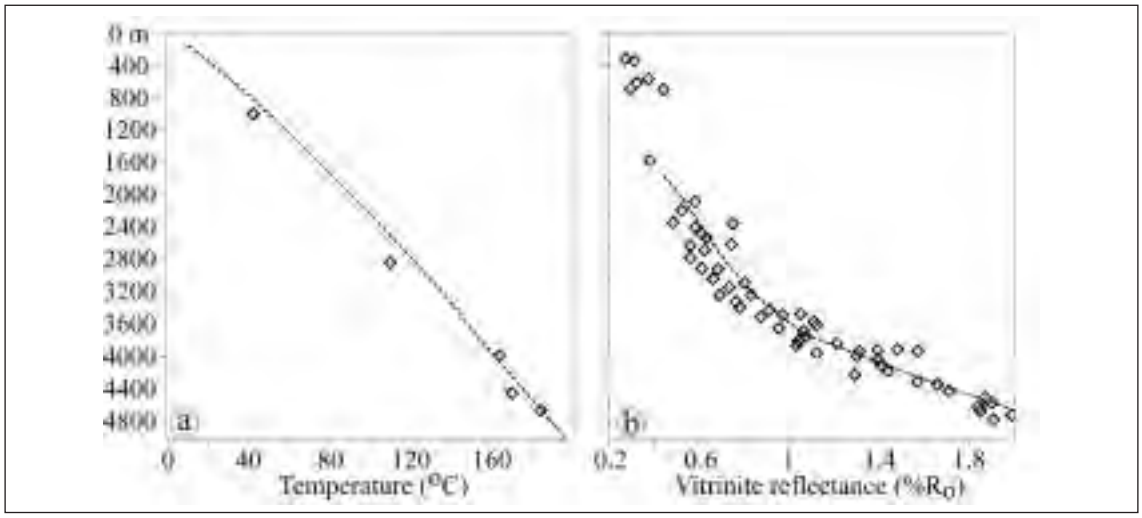

Fig. 4 - Calibration of formation temperature (°C) and vitrinite reflectance (%R_o).

Conclusion

Basin modeling based on the assumption of a thin plate model provides a good fit to vitrinite reflectance measurements and excellent fit to temperature and heat flow measurements in the Sockeye B-10 well. Estimated hydrocarbon generation from terrestrial source rocks within the Tertiary Skonun Formation are less optimistic than previously published, while marine source rocks within the Cretaceous and the Jurassic sequences are predicted to have generated hydrocarbons since Middle Miocene and Late Mesozoic, respectively.

REFERENCES

- Bustin, R.M. (1997). Petroleum source rocks, organic maturation and thermal history of the Queen Charlotte Basin, British Columbia. Bulletin of Canadian Petroleum Geology, v. 45(3), p. 255-278.
- Dehler, S.A., Keen, C.E. and Rohr, K.M.M. (1997). Tectonic and thermal evolution of Queen Charlotte Basin: lithospheric deformation and subsidence models. Basin Research, v. 9, p. 243-261.
- Haggart, J.W. (1991). A synthesis of Cretaceous stratigraphy, Queen Charlotte Islands, British Columbia. In: Evolution and Hydrocarbon Potential of the Queen Charlotte Basin, British Columbia. G.J. Woodsworth (ed.). Geological Survey of Canada, Paper 90-10, p. 253-277.
- Lewis, T.J., Bentowski, W.H., and Wright, J.A. (1991). Thermal state of the Queen Charlotte Basin, British Columbia: warm. In Evolution and Hydrocarbon Potential of the Queen Charlotte Basin, British Columbia. G.J. Woodsworth (ed.). Geological Survey of Canada, Paper 90-10, p. 489-506.
- Rohr, K.M.M. and Dietrich, J.R. (1992). Strike-slip tectonics and development of the Tertiary Queen Charlotte Basin, offshore western Canada: evidence from seismic reflection data. Basin Research, v. 4, p. 1-19.
- Rohr, K. M. M., Scheidhauer, M., and Trehu, M. (2000). Transpression between two warm mafic plates: The Queen Charlotte Fault revisited. Journal of Geophysical Research, v. 105, p 8,147-8,172.
- Spence, G.D. and Asudeh, I. (1994). Seismic velocity structure of the Queen Charlotte Basin beneath Hecate Strait. Canadian Journal of Earth Sciences, v.30, p.787-805.
- Woodsworth, G.J. (1988). Karmutsen Formation and the east boundary of Wrangellia, Queen Charlotte Basin, British Columbia. In: Current Research Part E, Geological Survey of Canada, Paper 88-1E, p. 209-212.

THE RIFT-LIKE MORPHOLOGY OF THE DEAD SEA TRANSFORM 3-26

J. Smit(*,**), J.P. Brun(**) and S. Cloetingh(*)

(*) Department of Tectonics, Faculty of Earth and Life Sciences, Vrije University,De Boelelaan 1085, 1081 HV Amsterdam, The Netherlands

(**) Géosciences Rennes, Université de Rennes1, campus de Beaulieu, Bât. 15, 35042 Rennes cédex, France

Summary

The Dead Sea Transform forms along its southern half a flat valley bordered by normal faults. This rift valley-like morphology has been attributed to a change in kinematics of the Arabian plate with respect to the Sinai sub-plate that resulted in the addition of a small extensional component to the overall strike-slip movement. We here present laboratory experiments that were designed to test this kinematic hypothesis and to identify the mechanical conditions necessary for a transform fault to evolve into a rift-like structure. Experiments indicate that a lower crustal decoupling between upper crust and mantle is required.

Introduction

The Dead Sea Transform forms the Western border of the Arabian plate separating it from the Sinai sub-plate. It connects the extensional domain of the Red Sea-Gulf of Suez in the South to the Taurus-Zagros compressional zone to the north (Quennell, 1958; Wilson 1965; Freund, 1965). Along the Southern half of the transform, from the Gulf of Aqaba in the South to the Hula basin in the North, a total of 105 km of left-lateral displacement has been identified (Quennell, 1958; Freund, 1965; Freund et al., 1970). Motion along the transform initiated about 13-15 Ma ago and still continues.

The Southern segment forms a 5 to 20 km wide flat valley that in places is bounded by steeply dipping

normal faults. It contains a number of deep basins like the Gulf of Aqaba, the Dead Sea and the Sea of Galilee. The rift valley-like morphology has led to the interpretation of the DST as a continental rift system like the East African Rift and the Red Sea Rift. Garfunkel (1981) presented the DST as a transform plate boundary bounded by steeply dipping normal faults that are responsible for its rift-valley morphology. From field observations along the southern part of the Dead Sea Transform (DST) and investigations on the Red Sea it has been suggested that the Arabian plate moves northward along the DST by a rotation along an Euler pole (Fig. 1) that for the last 4 Ma years is located at 33N23E (Garfunkel, 1981, Le Pichon and Gaulier, 1988). On the basis of these investigations it has also been suggested that this Euler pole was located about 5 more to the west during the first episode of movement. This change in motion of the Arabian plate coincides with the initiation of the main subsidence in the Dead Sea Basin and the Gulf of Aqaba.
We present a series of laboratory experiments to study the effects of a change in plate kinematics as is proposed for the DST. Interpretation of experimental results and comparison to the Dead Sea transform focuses on structural memory and formation of the rift valley-like morphology. A structural-morphological interpretation of the southern segment of the DST was carried out with the use of a DEM and satellite images of the area as well as structural and geophysical data.

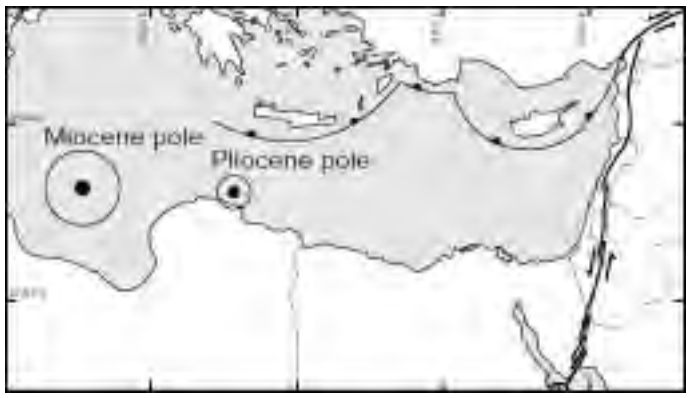

a.

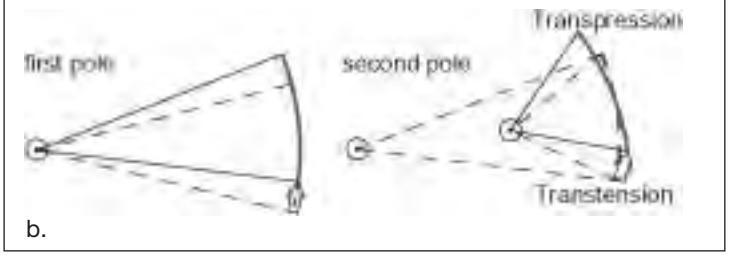

b.

Fig 1. a. Plate tectonic setting of Dead Sea Transform, b. kinematics of a change in the pole of rotation

Laboratory experiments

Deformation is generated by the displacement of a thin plastic plate at the base of the model. This plastic plate has a curved boundary that corresponds to the segment of a circle with a radius of 165 cm. Rotation around a pole formed by the centre of this circle gives a pure strike-slip motion during stage 1. At the beginning of phase 2, the rotational pole is approached towards the plate to a distance of 120 cm, thus adding a transtensional/ transpressional component to the strike slip movement of phase 1.
Models consist of a 7 mm thick basal ductile layer of Newtonian silicone putty with a viscosity ~ 6 10^4 Pas, covered by a 28 mm thick brittle layer made of sand with a mean density ~ 1550 kgm^{-3}, negligible cohesion and a coefficient of internal friction ~ 0.58. These two layers represent the ductile lower crust and the upper brittle crust, respectively. Three ductile strengths have been tested by

varying strain rate (from 6.6 x 10^{-4} to 2,6 x 10^{-3} s^{-1}). The model dimensions and the amounts of displacement are calibrated to the particular example of the DST. The model ratio for length is 10^{-6} (1cm in the model represents 10 km in nature).
After about 1.5 cm of displacement, Riedel fractures occur (Fig), that with continued deformation are linked by faults that are more parallel to the direction of displacement. From this moment, the tips of the Riedel fractures fall outside the active fault zone and become inactive. At the end of phase 1 (Fig. 2), after 6.5 cm of displacement, most of the motion is accommodated along two border faults that define the limits of a deformation corridor. Outside this corridor, the largest Riedels can still be recognized, most clearly on the western side of the fault zone (inner arc side).

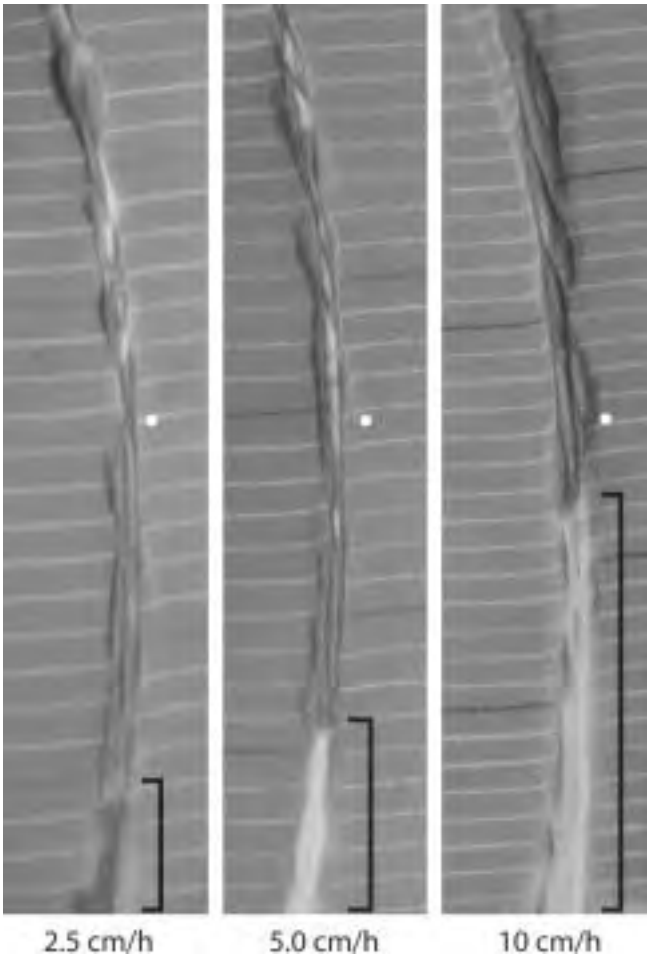

Fig. 2. Effect of varying brittle-ductile coupling, by means of velocity, on final structures and morphology. White dots indicate intersection of transtensional and transpressional domains, black bars indicate zone of negative topography in extensional domain.

The change in the pole of rotation at the onset of phase 2 adds a small component of extension to one half of the experiment and compression to the other half, a maximum of 4 mm on 40 mm of strike-slip movement during phase 2. Where extension and compression meet, pure strike-slip takes place during the entire deformation (white dots on Fig 2), at this position the width of the deformation corridor doesn't change notably during phase 2. The transtensional stress regime results in fast subsidence in the corridor. Vertical movements are concentrated on the two border faults that formed during phase 1. Subsidence is concentrated on a single steep fault along the eastern margin of the corridor, while subsidence along the western margin is much more diffuse. This causes the asymmetry of the basin as cross-sections show, with the deepest part along the eastern side
Although no erosion is applied to the models, most of the positive topography that formed during phase 1 disappears in the transtensional domain during phase 2. In the southernmost part, an asymmetric basin develops that, with ongoing transtension, propagates northward.
Structural style of experiments deformed at different displacement rates doesn't show much variation. Variations do occur in the amount and lateral extend of uplift and subsidence. At the end of phase two, experiments can be divided in three structural-morphological zones, compressional, (intermediate) neutral and extensional. Compressional and extensional zones migrate towards the centre during the second, oblique phase of movement. This inward migration is velocity (brittle-ductile coupling) dependant; it becomes more important with increasing velocity, leading to a decrease in the width of

the intermediate zone. In the model with the highest displacement rate (10cm/h), this intermediate zone has almost disappeared after the 40 mm of displacement of phase 2. The extensional area of negative topography occupies the entire transtensional domain.

Conclusions

The experimental results confirm that the invoked change in plate kinematics is responsible for the formation of the morphological rift valley of the southern segment of the Dead Sea Transform. But the experiments also provide explanations for a number of features of the Dead Sea Transform, including the rift valley-like morphology of its southern segment and its northward decrease in width. Comparison of the DST with the models exemplifies a number of common features. First of all, the difference between the sharp and regular border fault on the East side of the transform and the irregular Western side. This suggests the heritage of Riedel fractures, structures that formed early in the formation of the transform during phase 1 and that are rapidly abandoned outside the corridor zone. Model cross-sections show the asymmetry of the rift-like structure and demonstrate the decoupling role of the lower ductile crust during its development.

REFERENCES

- Freund, R., 1965, A model of the structural development of Israel and adjacent areas since upper Cretaceous times: Geological Magazine, v. 102, p. 189-205.
- Freund, R., Garfunkel, Z., Zak, I., Goldberg, M., Weissbrod, T., and Derin, B., 1970, A Discussion on the Structure and Evolution of the Red Sea and the Nature of the Red Sea: Philosophical Transactions for the Royal Society of London. Series A,, 267, 107-127.
- Garfunkel, Z., 1981. Internal structure of the Dead Sea leaky transform (rift) in relation to plate kinematics. Tectonophysics, 80(1-4): 81-108.
- Hatcher, R.D., Jr., Zietz, I., Regan, R.D., and Abu-Ajamieh, M., 1981, Sinistral strike-slip motion on the Dead Sea Rift; confirmation from new magnetic data: Geology (Boulder), v. 9, p. 458-462.
- Le Pichon, X. and Gaulier, J.M., 1988. The rotation of Arabia and the Levant fault system. Tectonophysics, 153(1-4): 271-294.
- Quennell, A.M., 1958, The structural and geomorphic evolution of the Dead Sea rift: Quarterly Journal of the Geological Society of London, v. 114, p. 1-24.
- Wilson, J.T., 1965, A new class of faults and their bearing on continental drift: Nature (London), v. 207, p. 343-347.

CRUSTAL ARCHITECTURE AND DEPTH-DEPENDENT LITHOSPHERE STRETCHING OF THE NORTHERN VØRING AND LOFOTEN SEGMENTS OF THE NORWEGIAN MARGIN: ALONG STRIKE VARIATION ACROSS THE BIVROST TRANSFER SYSTEM 3-27

F. Tsikalas(*), N.J. Kusznir(**), J.I. Faleide(*)

(*) Department of Geosciences, University of Oslo, P.O. Box 1047 Blindern, N-0316 Oslo, Norway (filippos.tsikalas@geo.uio.no, j.i.faleide@geo.uio.no)

(**) Department of Earth Sciences, University of Liverpool, Liverpool, L69 3BX, UK (n.kusznir@liverpool.ac.uk)

Summary

The mid-Norway margin in NE Atlantic with its increasingly extensive database provides a natural laboratory to exemplify the integrated approach between observations and structural and stratigraphic modelling iteration in order to study continental breakup and fundamental volcanic rifted margin processes in time and space. In particular, recent subsidence analysis studies on the northern Vøring and Lofoten margin segments combined with all available seismic reflection and refraction data, and potential field modelling, clearly reveal distinct differences in crustal and lithospheric architecture between the two segments. The same integrated analysis suggests that the Bivrost Transfer System (including the continental transfer zone and the oceanic fracture zone) separating the two margin segments has acted as a first-order, across-margin tectono-magmatic boundary, greatly influencing the pre-, syn- and post-breakup margin development.

Crustal Architecture

The Norwegian margin is part of the NW European margin which has a prolonged history of intermittent extension and basin formation, from post-Caledonian orogenic backsliding and collapse in Devonian times (e.g. Doré *et al.* 1999), to post-early Eocene passive margin development governed by the widening and deepening of the Norwegian-Greenland Sea (e.g. Eldholm *et al.* 2002).

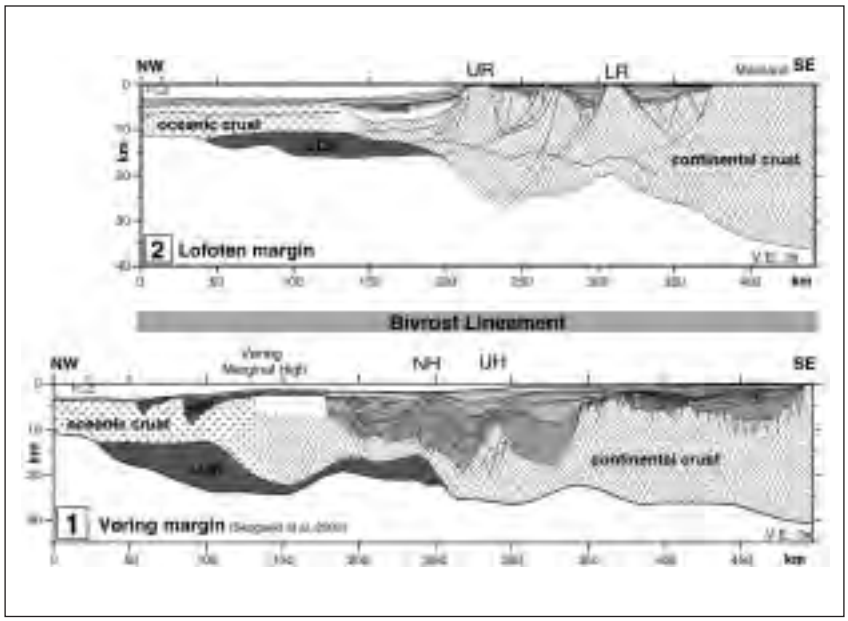

Fig. 1. Representative transects for Vøring and Lofoten margin segments. LCB, 7+ km/s lower crustal body; SDR, seaward dipping reflector sequences. Profile locations and other annotations in Fig. 4.

An extensive geophysical and geological database exists off mid-Norway, including a regional grid of deep wide-angle seismic data (OBS and ESP), deep and conventional multichannel seismic reflection profiles (MCS), potential field data, heat flow measurements, and scientific and commercial boreholes. Recent studies utilizing this database have refined the structural and stratigraphic framework landward of the continent-ocean boundary (COB) on the Vøring (e.g. Gernigon *et al.* 2003; Ren *et al.* 2003) and Lofoten-Vesterålen margins (Tsikalas *et al.* 2001). In particular, the dense seismic refraction coverage provides better resolution on the middle- and lower-crustal architecture demonstrating the progressive lateral focus of several post-Caledonian rift events towards the line of eventual opening (Fig. 1). It is also revealed that the structural margin configuration mainly evolved in response to the Late Jurassic-earliest Cretaceous rift episode, and exhibit structural and stratigraphic relations that indicate an Aptian-?Albian rift phase. The subsequent Late Cretaceous-Paleocene rifting, with onset in Campanian time, is characterised by prominent low-angle detachment structures. Complete lithospheric breakup was achieved near the Paleocene-Eocene transition and was accompanied by extensive magmatic activity (Fig. 1). After breakup, the passive margin evolved in response to subsidence and sediment loading during widening and deepening of the Norwegian-Greenland Sea. We observe a pulse of rapid progradation from the mainland in Oligocene, or alternatively late Middle Miocene, time and mid-Cenozoic intra-basinal doming in response to a regional compressive regime. The margin setting was changed in Late Pliocene when the Northern Hemisphere Glaciation led to rapid progradation forming a huge, regional depocentre near the shelf edge along the entire margin.

Depth Dependent Lithosphere Stretching

Recent analysis of pre- and post-breakup subsidence has been carried out on the southern Lofoten and northern Vøring segments using reverse post-rift subsidence modelling, consisting of flexural backstripping and reverse post-breakup thermal modelling (Kusznir *et al.* 2004). The analysis has shown depth dependent stretching of continental margin lithosphere in which lithosphere stretching and thinning at continental breakup at ~55 Ma greatly exceeds that of the upper crust within 100 km

landward of COB (Figs. 2 and 3). Depth dependent lithosphere stretching at rifted margins has been observed elsewhere for both volcanic and non-volcanic margins (Davis & Kusznir 2004). For the northern Vøring margin, lithosphere â stretching-factors of 2.5 are required at ~55 Ma to restore the Top Lava (top inner lava flow) and Top Paleocene reflectors to presumed sub-aerial depositional environments. In contrast, upper crustal faulting for the rifting immediately preceding breakup in Paleocene and Late Cretaceous has β stretching-factors <1.1. These observations are consistent with earlier work by Roberts *et al.* (1997). For the southern Lofoten margin, using a breakup lithosphere â factor approaching infinity west of the Utrost Ridge (Fig. 1) still produces a residual water depth of ~1500 m (Fig. 2). The latter may be explained by an additional post-breakup Eocene subsidence phase (Kusznir *et al.* 2004). Alternatively, increasing evidence of lateral variations in the seismic character of extrusives along the northern Vøring and Lofoten segments offer indications for extrusive volcanism not only in a subaerial (or at sea-level) environment, but also possibly into a shallow sub-marine environment (e.g. Berndt *et al.* 2001). The latter may reduce, but not eliminate, the remaining residual water depth after tectono-stratigraphic restoration.

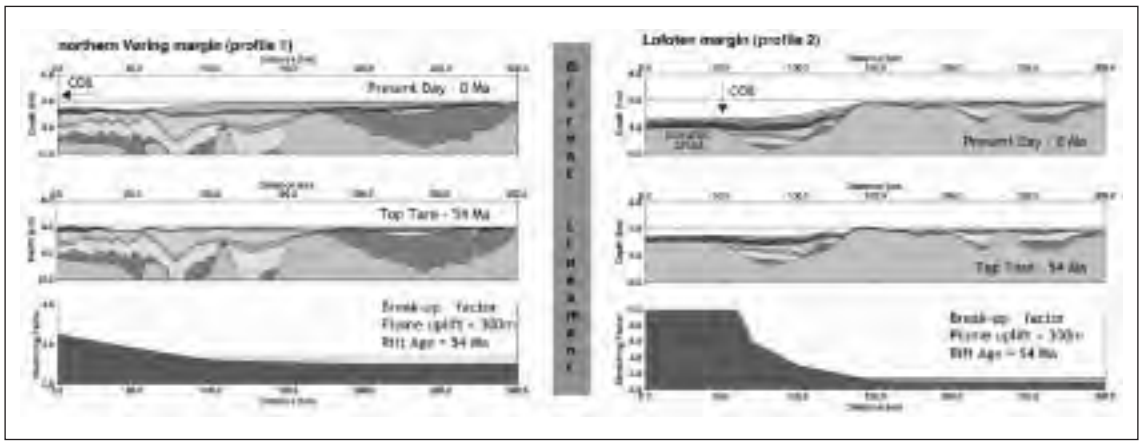

Fig. 2. Restored transect for the northern Vøring and southern Lofoten margin segments produced by 2D flexural backstripping and reverse post-rift modelling (Kusznir et al. 2004). Top Tare=Top Paleocene. COB, continent-ocean boundary. Profile locations in Fig. 4. Note the different vertical scale for the two stretching-factor profiles.

In both margin segments, a Paleocene plume dynamic uplift of 300 m is incorporated in the modelling. Furthermore, the modelling incorporates earlier major pre-breakup rift events, with corresponding β stretching-factors, that represent the residual thermal subsidence of earlier rift events. In particular, a β stretching-factor of 1.3 was included for the prominent Late Jurassic-Early Cretaceous rift episode and <1.1 for the rifting immediately preceding breakup in Paleocene and Late Cretaceous. More detailed further work will also take into consideration the Aptian-?Albian (mid-Cretaceous) rift phase as evidenced by several recent studies in Vøring (e.g. Ren *et al.* 2003) and Lofoten-Vesterålen (Tsikalas *et al.* 2001) margins, as well as at the conjugate equivalents onshore (e.g. Whitham *et al.* 1999) and offshore (Tsikalas *et al.* 2004) E/NE Greenland. Concerning the Late Cretaceous-Paleocene extension on the northern Vøring and Lofoten margins, Tsikalas *et al.* (2004) have showed that although the extent of the mapped deformation reaches minimum widths along the Lofoten-Vesterålen margin, along its conjugate counterpart off NE Greenland it reaches widths of ~100-150 km. Based on updated plate reconstructions (Fig. 4) (Tsikalas *et al.* 2002) the Late Cretaceous-Palaeocene rift may have reached a total cross-margin width of 200-250 km and thus contributing to a slightly higher β stretching-factor for the upper crust. However even allowing for this, the stretching and thinning of the lithosphere, as deduced from post-breakup thermal subsidence, greatly exceeds that achieved by faulting in the upper crust at and prior to breakup (Fig. 3). Furthermore, iteration of modelling and data interpretation from the extensive database increases the resolution on the timing and distribution of particularly the oldest Late Paleozoic-Early Mesozoic rift structures that are not well defined. In this way, better constrained stretching factors for all pre-breakup rift phases are defined for the entire rift system covering the conjugate margins.

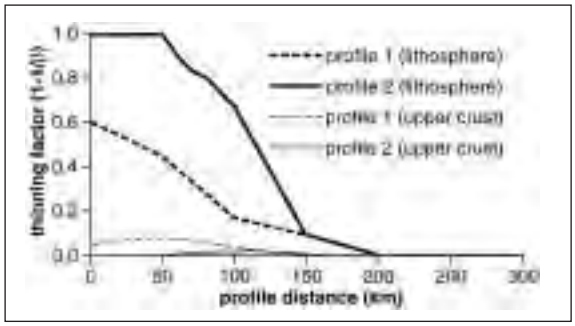

Fig. 3. Thinning factors (1-1/β) at breakup for whole lithosphere and upper crust for the northern Vøring (profile 1) and southern Lofoten (profile 2) margin segments. Profile locations in Fig. 4.

The presence of lithosphere depth dependent stretching and the absence of significant Paleocene and Late Cretaceous upper crustal extension imply that depth dependent stretching of the southern Lofoten and northern Vøring margins occured during sea-floor spreading initiation or early sea floor spreading rather than during pre-breakup intra-continental rifting (Davis & Kusznir 2004; Kusznir *et al.* 2004). Moreover, refinement of the continent-ocean boundary, seafloor spreading anomalies, and the location of oceanic fracture zones along the conjugate margins (Tsikalas *et al.* 2002) provide improved geometrical and azimuthal constraints on early opening plate reconstructions (Fig. 4). Reconstructions of potential field images are also used to support and extend structural trends. Improved early reconstructions contribute to a better understanding of the coupling between volcanism and early sea floor spreading.

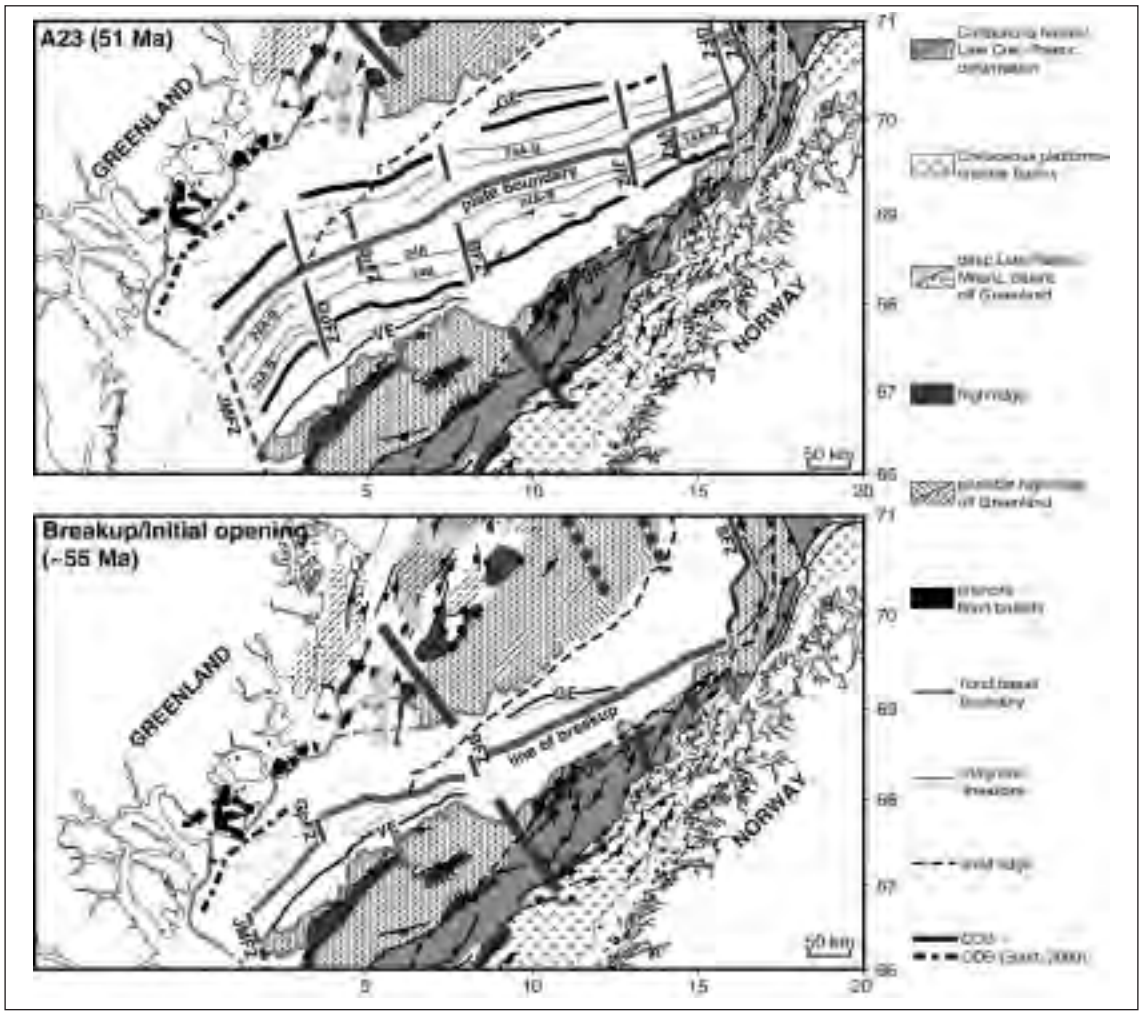

Fig. 4. Plate reconstructions at Chron 23n.2n (51 Ma) and opening (~55 Ma). JMFZ, GpFZ, SrFZ, BFZ, JFZ, VFZ, GFZ, SFZ, Jan Mayen, Gleipne, Surt, Bivrost, Jennegga, Vesterålen, Greenland, and Senja fracture zones, respectively; VE, GE, Vøring and Greenland escarpments, respectively; NH, UH, RH, JH, Nyk, Utgard, Røst, and Jennegga highs, respectively.

Bivrost Transfer System: a Primary Tectono-magmatic Feature

The Norwegian margin (taking also into consideration its conjugate East Greenland margin) (Fig. 4) exhibits distinct along-strike segmentation. The Jan Mayen and Senja fracture zones and their landward prolongations represent first-order features. In between, we identify several second- and third-order features (Fig. 4). Of these, the Bivrost transfer system is the most prominent. Off Norway, it separates two different physiographic provinces, i.e. the Vøring and Lofoten-Vesterålen margins. Structural studies, analysis of potential field images on the conjugate margins, and plate reconstructions to early Tertiary opening suggest a landward prolongation of the Bivrost Fracture Zone on both margins. The prolongations appear as low-relief Late Jurassic-Early Cretaceous accommodation zones, reactivated during Late Cretaceous-Paleocene rifting. We recognize a difference in trend, and possibly in polarity, of the relative motion between the older transfer zone and the younger fracture zone. The more northerly sinistral relative motion along the fracture zone suggests two different stress regimes, however the older feature may have determined the initial location of the fracture zone. Pre-opening structural spatial relations may imply sinistral offsets also along the continental prolongations. Furthermore, we observe a northward decrease in thickness and volume of the high-velocity lower crust, interpreted as related to magmatic underplating, across the Bivrost Fracture Zone. Other changes north of the fracture zone include: breakup lavas over most of the continental slope, a reduction in the intensity of sill intrusions, and a change in style of the seaward dipping seismic reflector images to less prominent and shallower features without the typical, deep wedge-like pattern observed to the south.

Although there is a decrease in breakup magmatism with distance from the plume (Eldholm & Grue 1994) both the melt potential and melt distribution has to be considered with reference to the pre-breakup structural configuration between Greenland and Norway. Here, the lithosphere experienced considerable Late Jurassic-Early Cretaceous extension and subsequent major Cretaceous basin formation. The renewed Late Cretaceous rifting further thinned the lithosphere providing conditions for large scale regional magmatism when the plume-related partial melts were captured by the pre-existing lithospheric relief. In a regional sense, however, the continental reconstruction (Fig. 4) shows that the line of breakup is notably oblique to the Cretaceous basin trend resulting in breakup in different locations with respect to pre-existing rift systems on either side of the Bivrost transfer system. In fact, the actual breakup may occur in a variety of locations within a rift system, depending on the tectono-magmatic crustal configuration and the corresponding rheologies (e.g. Boutilier & Keen 1999).

We interpret breakup occurring in different crustal configurations: in the south along the western flank of the deep Cretaceous Vøring Basin, and in the north along a deep-rooted detachment fault in relatively thick crust on the eastern basin flank (Figs. 1 and 2). The massive breakup magmatism caused uplift of the central rift zone, construction of the extensive marginal highs, and thickening of the lower crust, thereby reducing significantly the post-opening subsidence of these margin segments (e.g. White *et al.* 1995). In contrast, less magma was produced north of the Bivrost transfer system making the Lofoten-Vesterålen margin more susceptible to initial post-opening subsidence. Indeed, the narrow lava-covered, and progressively northward steepening, continental slope suggests rapid initial post-opening margin subsidence to bathyal depths (Tsikalas *et al.* 2001). The observations are in agreement with the distinct behaviour of the two margin segments during depth dependent lithosphere stretching. In total, both observations and modelling suggest that the Bivrost transfer system is a primary tectono-magmatic boundary, greatly influencing the pre-, syn- and post-breakup margin development in both crustal and lithospheric scales.

REFERENCES

- Berndt et al. (2001), Journal of the Geological Society, London, 158, 413-426.
- Boutilier & Keen (1999), Journal Geophysical Research, 104, 7389-7403.
- Davis & Kusznir (2004), Proc. NSF Rifted Margins Theoretical Institute, Columbia Univ. Press, 92-136.
- Doré et al. (1999), Petr. Geol. of NW Europe: Proceedings of the 5th Conference, Geol. Soc., London, 41-61.

• Eldholm & Grue (1994), Journal Geophysical Research, 99, 2955-2968.
• Eldholm et al. (2002), Geological Society, London, Special Publication, 197, 39-68.
• Gernigon et al. (2003), Journal of the Geological Society, London, 160, 197-208.
• Kusznir et al. (2004), NW Europe and Global Perspectives: Proc. 6th Conference, Geol. Soc., London, in press.
• Ren et al. (2003), Marine and Petroleum Geology, 20, 177-206.
• Roberts et al. (1997), Journal of the Geological Society, London, 154, 551-550.
• Skogseid et al. (2000), Geological Society, London, Special Publication, 167, 295-326.
• Tsikalas et al. (2001), Marine and Petroleum Geology, 18, 807-832.
• Tsikalas et al. (2002), Marine Geophysical researches, 23, 247-270.
• Tsikalas et al. (2004), NW Europe and Global Perspectives: Proc. 6th Conference, Geol. Soc., London, in press.
• White et al. (1995), Journal of the Geological Society, London, 152, 1039-1045.
• Whitham et al. (1999), Petr. Geol. of NW Europe: Proc. of the 5th Conference, Geol. Soc., London, 325-336.

REINTERPRETING A CLASSIC MODEL OF SALT-DIAPIR GROWTH USING PHYSICAL MODELLING AND CONCEPTUAL REASONING

3-28

Bruno C. Vendeville

Université des Sciences et Technologies de Lille I, U.F.R. des Sciences de la Terre, Cité Scientifique - Batiment SN5, UMR Processus et Bilans des Domaines Sédimentaires, 59655 Villeneuve d'Ascq cedex, France

Summary

We use physical modeling and mechanical reasoning to reinterpret the classic evolutionary model for salt diapirs (Trusheim, 1960) to develop a conceptual model in which salt movement is intimately linked to thin-skinned tectonics and associated lateral movement of the overburden.

Introduction

In a benchmark article published in 1960, F. Trusheim set the foundation for interpreting kinematic evolution of salt structures using the specific patterns of lateral thickening or thinning of adjacent sediment strata. Because Trusheim's conceptual model assumed that diapirs rise according to a mechanism of Rayleigh-Taylor instabilities, his evolutionary model suggested (1) that the overburden movement was essentially vertical and (2) that salt would inescapably rise if a density inversion was present. Since Trusheim's time, it has been demonstrated that typical overburden rocks and sediments do not behave like low-strength viscous fluid, as is required for Rayleigh-Taylor instabilities (Weijermars et al., 1993). Instead, overburden rocks are brittle and far stronger than rock salt. As a corollary of this observation, Vendeville and Jackson (1992a) showed than thin-skinned tectonics, which implies significant horizontal or lateral displacement of the overburden, are often necessary triggers controlling diapir initiation, growth, or collapse. Accordingly, despite Trusheim's remarkable observations, some aspects of his evolutionary model need to be updated in light of the new concepts in salt tectonics. This article presents an alternative interpretation of Trusheim's observations in the light of the newer, tectonically-driven model for salt movement.

Trusheim's Original Model

Trusheim summarized their main characteristics of salt diapirs using a series of synthetic cross sections (Fig. 1), in which there were three types of depocenters (*I*, *II* and *III*), each having its own characteristic pattern of lateral thickness changes.

Strata in the lowest group (*I* in Fig. 1), deposited during the early stages of salt movement, thin toward the salt high (*Primary Peripheral Sink)* because the center of the depocenter subsided faster than its flanks. Strata in the middle group (*II* in Fig. 1), deposited during the middle stages of salt movement, are thinnest in the center of the depocenter and thicken toward the diapir (*Secondary Peripheral Sink)*

because by then, the center of the depocenter was no longer subsiding, whereas the depocenter's flanks subsided. Strata in the upper group (*III* in Fig. 1), deposited during the latest stages of salt movement, thin only above the crest of the salt diapir and have constant thickness elsewhere (only the crest of the salt diapir rose).

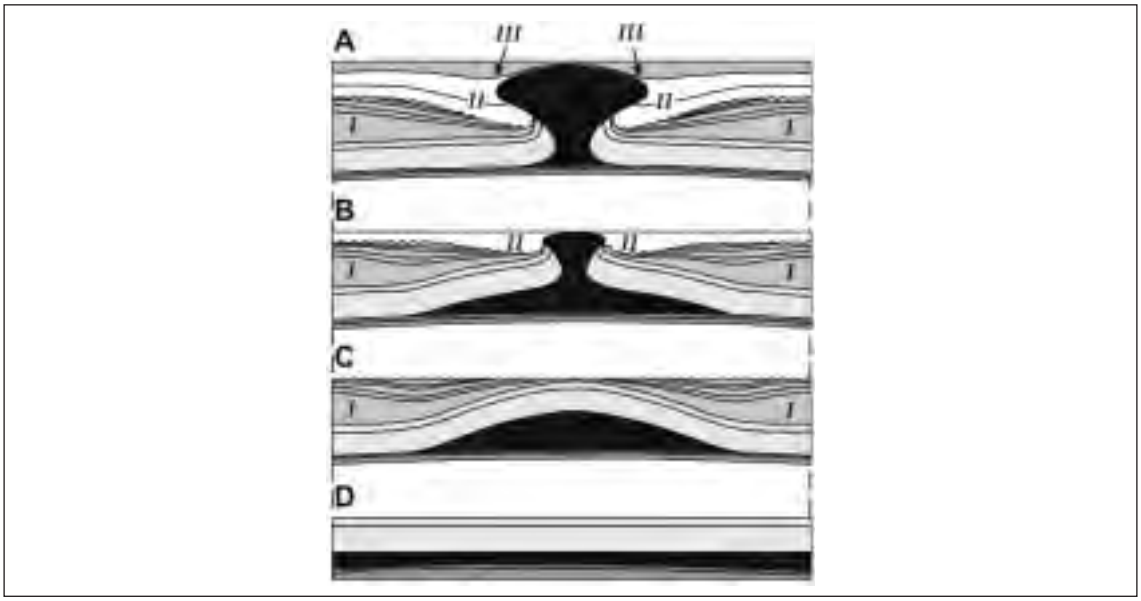

Figure 1: Restoration of a schematic cross section of a diapir and adjacent depocenters (Trusheim, 1960). A. Present-day (post-diapir stage) showing strata in the tertiary peripheral sink (III) thinning above the diapir crest. B. Diapir stage showing strata in the secondary peripheral sink (II) thickening toward the diapir. C. Pillow stage showing strata in the primary peripheral sink (I) thinning toward the diapir. D. Initial stage before salt movement.

Because of the striking geometric similarities between Trusheim's observations and results from physical models of Rayleigh-Taylor instabilities by Nettleton (1934), Trusheim concluded that the three types of peripheral sinks corresponded to the three evolutionary growth stages of Rayleigh-Taylor instabilities (illustrated in Figure 1). First, during the *Pillow Stage* (Fig. 1C), a wide, dome-shaped salt body rises spontaneously while adjacent primary peripheral sinks form. Second, during the *Diapir Stage* (Fig. 1B), the wide base of the diapir narrows, and the flanks of the adjacent depocenters subside, forming secondary peripheral sinks. Third, during the *Post-Diapir Stage* (Fig. 1A), the diapir pinches off and continues to rise, deforming only the overburden located above the diapir crest (tertiary peripheral sinks). It is important to emphasize that this evolutionary model assumes that (1) salt rise is a spontaneous process resulting solely from buoyancy forces and (2) there is no change in the cross-section length (i.e., neither regional extension nor shortening: Fig. 1).

Alternative Interpretations of the Pillow Stage

One process that can form pillow-like structures is regional, thin-skinned shortening. Shortening creates buckle-fold anticlines that rise above the regional datum even in the absence of density contrast between salt and overburden, while the adjacent synclines, like primary peripheral sinks, accumulate thicker sediments in their center. Buckle folding does not lead to much thinning of the roof of anticlines, which, therefore, seldom evolve into diapirs. A second process leading to pillow-like structures is thin-skinned extension (Vendeville and Jackson, 1992a), during which normal faulting of the overburden allows the underlying salt to rise reactively even in the absence of density inversion (Figure 2D and C). The grabens and their underlying reactive diapirs are raised above the regional datum while the adjacent overburden blocks subside and are flexed synformally, resulting in a geometry similar to that of Trusheim's salt pillows. This alternative interpretation explains why, as Trusheim himself noted, some diapirs show no signs of having passed through a pillow stage during their early evolution: such diapirs may have been triggered by a phase of thin-skinned extension that

occurred after sediments were already too thick—hence too rigid to allow for significant flexure of the overburden blocks.

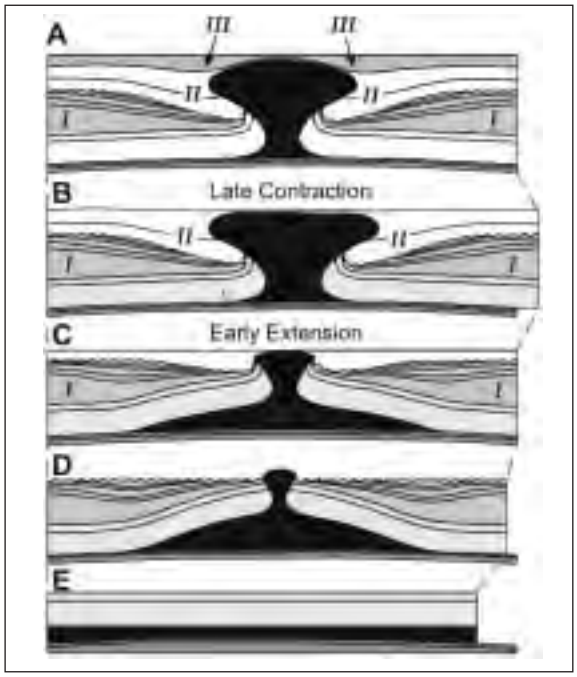

Figure 2 – Schematic cross-section restoration illustrating how successive tectonic events can contribute to the development of peripheral sinks. Early extension triggers reactive diapirism and formation of primary peripheral sinks. B; Late extension forces the flanks of the depocenters to subside, forming a secondary peripheral sinks. A: Late contraction rejuvenates the diapir, forming tertiary peripheral sinks above its crest.

Alternative Interpretation of the Diapir Stage

During the diapir stage (Figs. 1B and 2B), the base of the depocenter stops subsiding while its flanks subside, squeezing the underlying wedge of salt to feed the diapir. As observed by Trusheim, many diapirs have adjacent depocenter flanks that never subsided. There appears to be a correlation between the depocenter's ability to deform and (2) the tectonic setting: along salt-bearing, passive margins, the flanks of most depocenters located where late thin-skinned extension occurred (in the upper slope) have subsided, whereas those located in the lower slope typically have not. As shown by Vendeville and Jackson (1992b) late thin-skinned extension occurring after grounding of the depocenters causes subsidence of diapirs and unfolding of the flanks of adjacent depocenters, whose geometry becomes that of a secondary peripheral sink.

Alternative Interpretation of the Post-Diapir Stage

During the postdiapir stage (Figs. 1A and 2A), the diapir rises even though the adjacent depocenters and their flanks do not subside. During that stage, the depleted source layer is no longer capable of supplying additional salt to feed the rising diapirs. As for the other two stages, Trusheim noticed that, although some diapirs exhibit tertiary peripheral sinks, many diapirs do not. There are two alternative processes. First, modest amounts of late diapiric rise can be caused by differential compaction, owing to continued sediment aggradation during the postdiapir stage. However, the amount of relative rise remains small. Another, more powerful process, thin-skinned shortening, can lead to large, genuine late diapiric rise after source-layer depletion (Fig. 2A). Because rock salt is uncompressible and much weaker than the adjacent overburden rocks, thin-skinned shortening is preferentially accommodated by squeezing of the diapirs, which therefore continue to rise and deform their roofs (Vendeville and Nilsen, 1995; Vendeville and Rowan, 2002). Diapir rise driven by late contraction does not require additional salt supply because narrowing of the diapir compensates for its vertical rise. Eventually, late shortening can entirely pinch off the diapir stem, resulting in the classic inverted teardrop geometry common to many salt diapirs. Finally, this interpretation explains why some diapirs have kept rising whereas others have not. Diapirs located in tectonically quiet areas simply stopped rising after source layer depletion and remained dormant. Diapirs subjected to one or more pulses of late tectonic shortening were episodically rejuvenated.

Conclusions

Trusheim's evolutionary model was based on actual observations interpreted in the light of a conceptual model (Rayleigh-Taylor instabilities) that is not applicable to salt structures. This resulted in discrepancies between some of the observations and some of the model's predictions. The theory of Rayleigh-Taylor instabilities predicts that, once initiated, the salt body rises inescapably and continuously until the source layer is entirely depleted. On the other hand, Trusheim's own

observations indicate that most diapirs have undergone distinct episodes of growth and quiescence. This behavior cannot be explained by the continuous rise of buoyancy-driven Rayleigh-Taylor instabilities. Our analysis emphasizes the influence of regional tectonics, a process that often occurs by pulses and is not regionally widespread. Assuming that regional extension or shortening may have influenced or controlled salt-diapir evolution may help provide an explanation to this episodic history and differences between salt structures within a salt basin. Some salt structures may have undergone extension or shortening that allowed then to continue to rise, whereas others remained dormant because they were not subjected to regional tectonics. Whereas Trusheim proposed that diapiric rise is an autonomous and spontaneous process independent of regional tectonic events, our analysis demonstrates the importance of early or late regional extension and shortening in driving salt-diapir evolution.

REFERENCES

- Nettleton, L.L., 1934, Fluid mechanics of salt domes: American Association of Petroleum Geologists Bulletin, v. 27, p. 51-63.
- Trusheim, F., 1960, Mechanism of salt migration in northern Germany: Association of Petroleum Geologists Bulletin, v. 44, p. 1519-1540.
- Vendeville, B.C., and M.P.A. Jackson, 1992a, The rise of diapirs during thin-skinned extension: Marine and Petroleum Geology, v. 9, p. 331-353.
- Vendeville, B.C., and M.P.A. Jackson, 1992b, The fall of diapirs during thin-skinned extension: Marine and Petroleum Geology, v. 9, p. 354-371.
- Vendeville, B.C., and K.T. Nilsen, 1995, Episodic growth of salt diapirs driven by horizontal shortening, in C.J. Travis, B.C. Vendeville, Holly Harrison, F.J. Peel, M.R. Hudec, and B.F. Perkins, eds., Salt, Sediment, and Hydrocarbons: Society of Economic Paleontologists and Mineralogists, Gulf Coast Section, 16th Annual Research Conference Program and Extended Abstracts, p. 285-295.
- Vendeville, B.C. and M.G. Rowan, 2002, 3-D kinematics of minibasins and salt ridges remobilized by late contraction: physical models and seismic examples (southeast Mississippi Canyon, Gulf of Mexico) (abs.): American Association of Petroleum Geologists Annual Meeting Official Program, v. 11, p. 182.
- Weijermars, R., M.P.A. Jackson, and B.C. Vendeville, 1993, Rheological and tectonic modelling of salt provinces: Tectonophysics, v. 217, p. 143-174.

STRAIN PARTITIONING DURING CRUSTAL EXTENSION 3-29

C. Wijns [(1)], K. Gessner [(1)], R. Weinberg [(2)], L. Moresi [(2)]

(1) CSIRO Exploration and Mining, PO Box 1130, Bentley, WA 6102, Australia
(2) School of Geosciences, Monash University, VIC 3800, Australia

Summary

Pre-existing structures and weaknesses are often thought to control the behaviour of continental crust under extension. While such features do play a role, numerical modelling shows that the mechanical stratification of the crust can also dominate the mode of extension. A weak lower crust that flows easily leads to stretching being strongly localised onto relatively few normal fault zones. Each fault accommodates large displacements, eventually dissecting the upper crust and resulting in exhumation of the lower crust, as in the metamorphic core complexes of the North American Cordillera and the Aegean Sea region. A weak lower crust also favours symmetric exhumation of the metamorphic core, while a stronger lower crust will promote asymmetric exhumation.

Introduction

Continental lithosphere may be highly extended without entirely rifting to a new ocean basin. For example, total Cenozoic strain estimates (beta factors) of up to 2 have been proposed for parts of the Basin and Range in the western U.S.A., which has not been rifted (e.g., Jones et al., 1992). Stretching of the crust in this case may be accommodated by two contrasting phenomena: distributed, closely spaced, and limited-slip normal faulting over a large area (e.g., North Sea basin, Fossen and Roernes, 1996), or localised, large-strain normal faulting that often results in the complete dissection of the upper crust and exhumation of the lower crust. Large offset normal faults that juxtapose exhumed

high-grade metamorphic rocks against near-surface rocks are the hallmarks of a metamorphic core complex (MCC) (e.g., Wernicke and Axen, 1988; Lister and Davis, 1989). An MCC may form because of major lateral discontinuities in the strength of the crust that focus stresses and localise extension, either in the form of pre-existing faults in the upper crust (e.g., Wernicke and Axen, 1988), or rheologically weak zones, such as partial melts, in the lower crust (e.g., Brun et al., 1994). However, in the absence of significant lateral heterogeneities, vertical contrasts in rheology dictate whether extension will result in the distributed faulting or MCC mode. Thus the tectonic behaviour is a result of the combined ability of both lateral and vertical rheological structure to focus stresses in the brittle upper crust. Our numerical modelling concentrates on the relative strength of the lower crust in controlling the formation of an MCC and the strain partitioning in the final architecture.

Models

We use a two-dimensional Lagrangian integration point finite element code (Moresi et al., 2002) to explore the different behaviours of the crust during extension. The algorithm solves the governing equations of momentum, mass, and heat conservation. The particle-in-cell continuum approach allows simulations to develop very large strains while still tracking strain history accurately for the constitutive law. The initial geometry of the model consists of a brittle upper crust over a ductile lower crust (Figure 1a). Some simulations include a lower layer of strong, viscous, upper mantle (Figure 1c). A Byerlee (1968) plastic yield law approximates brittle behaviour below a critical temperature which governs the transition to purely viscous flow in the lower crust (Figure 1b). All walls of the closed bounding box are free-slip, top and bottom boundaries are maintained at constant temperatures, and vertical walls have zero heat flux. Extension proceeds by applying a uniform velocity to the right-hand boundary, equivalent to 100% strain in 5 Ma. This boundary velocity is low enough to not create tensional stresses, so gravity is in effect driving the deformation.

We use rock cohesion co=16 MPa, and the universal friction coefficient cp of 0.6 - 0.85 determined by Byerlee (1968) for dry samples is reduced to 0.44 by assuming an average hydrostatic pore pressure in our models. This translates into a maximum shear strength of about 250 MPa at the brittle to ductile transition. Strain weakening is included through an empirical power law function that decreases with plastic strain, such that a maximum of 80% strain weakening occurs after an accumulated plastic strain of 0.5. These values reflect evidence that major faults undergo significant weakening (Lachenbruch and Sass, 1992).

The boundary between upper and lower crust initially coincides with the brittle to ductile transition temperature at 300-350 C (e.g., Brace and Kohlstedt, 1980). With increasing extension, the lower crust may be exhumed into the brittle field and, through cooling, behave mechanically as the upper crust does. The second model, investigating MCC formation with a pre-existing fault, uses a lower crust with a temperature-independent visco-plastic rheology, and the lower crust remains ductile unless its yield stress is reached.

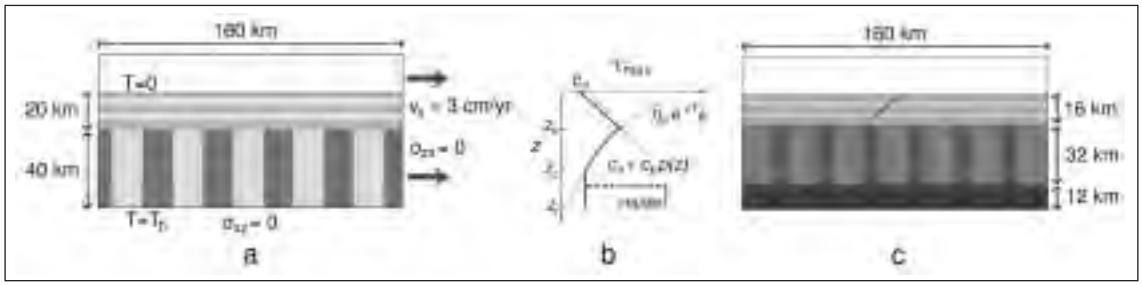

Figure 1: (a) Initial geometry and boundary conditions. Stripes in the upper and lower crust are marker materials for visualising deformation. (b) Representative maximum shear stress sigma_max with depth z through the crust for a given strain rate. Neglecting localised strain weakening, strength increases with pressure p from co at the surface to a maximum value at the base zu of the brittle upper crust, at which point the yield curve intersects the viscous, temperature (T) dependent flow law. The constants eta_o and c are chosen so that the viscosity eta varies at most by two orders of magnitude across the lower crust. In order to avoid an extremely low viscosity, eta > eta(zc). Where included, the upper mantle is highly viscous. (c) Model incorporating a bottom layer of strong upper mantle and a pre-existing fault to control the initiation of localisation in the upper crust. Boundary conditions are as in (a).

Extension modes

In all of the following simulations, bands of high localised plastic strain represent fault zones. Accumulated plastic strain in the brittle crust is indicated by darkened material, and the degree of shading is a measure of strain magnitude.

The two contrasting modes of crustal extension are illustrated in Figure 2. When the system is characterised by a relatively high viscosity lower crust (5x10^21 Pa.s or higher with this geometry and strain rate, measured in the weak zone below zc), the result is distributed faulting (Figure 2(i)). The upper crust develops many closely spaced steep faults, each of which accomodates limited strain, and the interface between upper and lower crust remains relatively flat. Even with more than 80% extension (beta > 1.8), the upper crust is never dissected. New steep faults form after older faults have accomodated minor shear strain, breaking the upper crust into numerous small blocks.

In the absence of any macroscopic heterogeneity in the lower crust to localise stresses, a uniformly weak lower crust (5x10^20 Pa.s or lower) is sufficient to trigger an MCC mode of extension (Figure 2(ii)). The lower crust is first exhumed at beta = 1.6, accomodated by only a few normal fault zones. Displacement is large within each fault zone, which, through weakening, remains active even after rotating to a shallow dip. The lower crust flows easily to isostatically compensate for localised thinning of the upper crust, which enhances block rotation and continued strain on low-angle faults. The rising lower crust enters the brittle domain, but cooling is slow enough, relative to exhumation, that brittle deformation does not penetrate to great depth. The propagation of faults from the upper crust into the exhuming lower crust allows continued strain along the original structures, until they become very gently dipping or even flat-lying detachment surfaces. There is evidence in the vertical lower crust markers that these faults are spatially connected to diffuse high shear zones that extend to the base of the entire crust, as traced in Figure 2(ii)c.

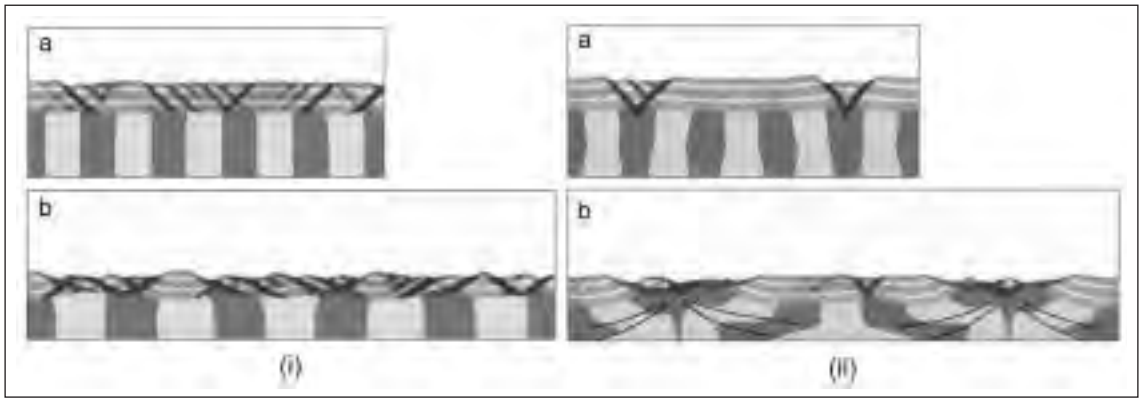

Figure 2: Evolution of (i) distributed faulting mode (strong lower crust) and (ii) MCC mode (weak lower crust) at a total extension of (a) 24% (1.2 Ma), and (b) 82% (4.1 Ma). Dark bands in the upper crust indicate accumulated plastic strain, or fault zones. Large offset faults are connected to diffuse high shear zones in the ductile region, indicated with pairs of solid lines in (ii)(c).

Exhumation patterns

Two important questions with regard to metamorphic core complexes are how ductile deformation in the footwall and brittle faulting in the hanging wall mechanically interact, and what causes the observed variations in thermal and structural architecture of the exhumed footwall (e.g., Foster and John, 1999; Miller et al., 1999). Some footwalls may be exhumed at high temperatures, such as in the Snake Range, U.S.A., where there is evidence of intrusion or partial melting during the extensional deformation (Miller et al., 1999). In other examples, both the hanging wall and the footwall have been deformed in the brittle field (Lister and Davis, 1989; Foster and John, 1999). The simulations in Figure 3 compare the interaction of detachment faulting and lower crustal flow for strong and weak lower crust, where the MCC is triggered by a fault in the upper crust (Figure 1c). The cool and strong lower crust (Figure 3(i)) has a viscosity of 1.25x10^21 Pa.s, and the hot and weak lower crust (Figure 3(ii)) has a viscosity of 1.25x10^20 Pa.s. In the strong case, a very localised plastic shear zone extends

from the initial brittle fault into the lower crust below the hanging wall, and over time exhumes increasingly deeper material, creating an overall asymmetric footwall area (Figure 3(i)c). The resulting metamorphic architecture is therefore also asymmetric. In the low-viscosity case, a symmetric pattern of diffuse, ductile shear zones evolves beneath both the hanging wall and the footwall (Figure 3(ii)c), resulting in a symmetric architecture for the exhumed core.

Discussion

The magnitude of lateral stress transfer from the unfaulted lower crust to the upper crust is key to the mode of extension, where the mode is specifically controlled by the number of active fault zones. A relatively strong lower crust provides greater traction at the base of the upper crust, which results in the yield stress being reached at shorter spacings between faults. The existence of few fault zones in the presence of a weak lower crust is simultaneously linked to the ability of crustal blocks to rotate because of the mobility of the lower crust, leading to MCC formation. Within this mode, the greater traction from a stronger lower crust is also responsible for increased ductile thinning of the upper crust relative to the very weak case (Figure 3).

The lower crust in our models is sufficiently thick and ductile that it effectively decouples the crust from the upper mantle. The strong upper mantle remains flat, as it flows less quickly than the lower crust in response to any unloading. This case is implicit in the two-layer model, explicit in the model with an upper mantle layer, and corresponds to the observations of a flat Moho boundary under, for example, areas of high extension in Arizona (Hauser et al., 1987).

The geometric origin of low-angle detachment faults remains controversial. According to Scott and Lister (1992), for example, structural field relations favour initiation and activation at a shallow dip. Others propose initial high-angle faults that subsequently rotate to shallow dip (Wernicke and Axen, 1988). In all of our simulations, initially high-angle normal faults form as planar features that evolve to shallower angles because of lower crustal flow, or isostatic compensation, during unloading of the footwall. These results do not contradict the hypothesis that detachment faults are formed at low angle. There is simply no condition present for an initial stress field rotated from the vertical, and new faults form at 35 degrees to sigma_1. However, the results do illustrate and support the hypothesis that initial high-angle faults can rotate to low angle and develop into shallow detachment faults that continue to slip due to significant weakening.

The variation in structural and thermal architecture of exhumed metamorphic cores can be explained by the dependency of crustal-scale strain patterns on the strength of the lower crust. Metamorphic

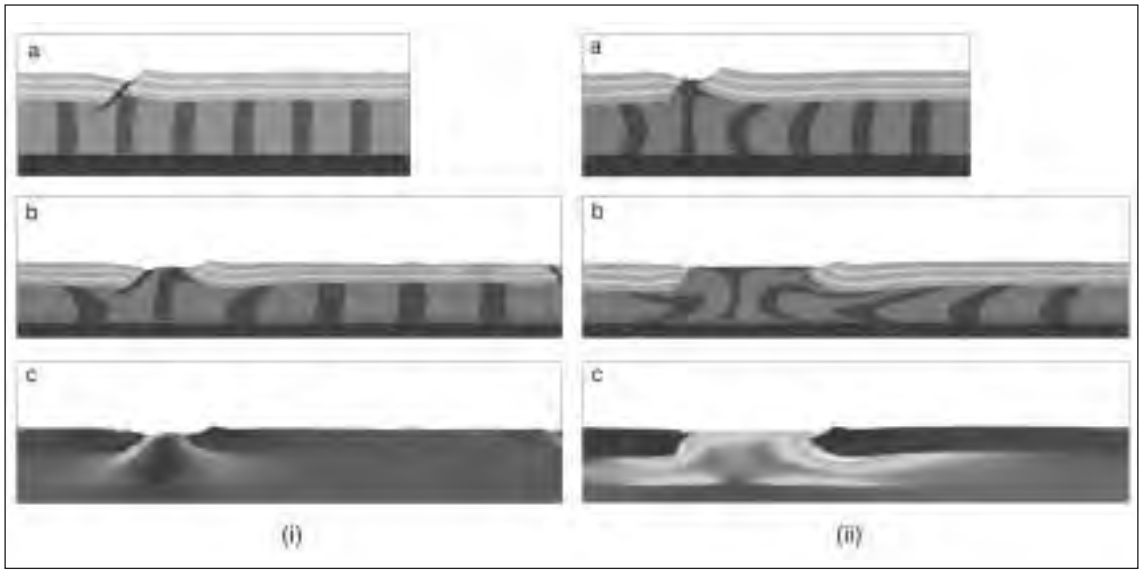

Figure 3: Evolution of an MCC from a pre-existing fault in the upper crust. (i) Strong (cool) lower crust and (ii) weak (hot) lower crust at a total extension of (a) 20% (1.0 Ma), and (b) 67% (3.4 Ma). (c) Final ductile strain distributions, from lowest (dark) to highest strain (white).

domes are predicted to form as a result of secondary detachments in the case of weak (e.g., partially melted or intruded) footwall areas. Compared to upper crustal MCCs, mid-crustal metamorphic domes such as those found in the Canadian Cordillera (Carr, 1995) generally lack the drastic footwall rotation of the former. While the metamorphic field gradient may be thinned, mid-crustal extensional shear zones generally display a concordant structural grain across structure. In our model this occurs because the footwall of the initial detachment has already rotated to an isostatically and geometrically stable position, enabling the secondary detachment to operate at shallow angles to the rheological layering.

REFERENCES

- Brace, W., Kohlstedt, D., 1980. Limits on lithospheric stress imposed by laboratory experiments, Journal of Geophysical Research, 85, 6248-6252.
- Brun, J.-P., Sokoutis, D., van den Driessche, J., 1994. Analogue modelling of detachment fault systems and core complexes, Geology, 22, 319-322.
- Byerlee, J., 1968. Brittle-ductile transition in rocks, Journal of Geophysical Research, 73, 4741-4750.
- Carr, S., 1995. The southern Omineca Belt, British Columbia: new perspectives from the Lithoprobe Geoscience Program, Canadian Journal of Earth Sciences, 32, 1720-1739.
- Fossen, H., Roernes, A., 1996. Properties of fault populations in the Gullfaks Field, northern North Sea, Journal of Structural Geology, 18, 179-190.
- Foster, D. A., John, B. E., 1999. Quantifying tectonic exhumation in an extensional orogen with thermochronology; examples from the southern Basin and Range Province, In: Ring, U., Brandon, M., Lister, G., Willett, S. (Eds.), Exhumation Processes: Normal Faulting, Ductile Flow and Erosion. Geological Soc., London, 343-364.
- Hauser, E., Gephart, T., Latham, T., Bown, L., Kaufman, S., Oliver, J., Lucchitta, I., 1987. COCORP Arizona transect: Strong crustal reflection data, Geological Society of America Bulletin, 99, 833-844.
- Jones, C., Wernicke, B., Farmer, G., Walker, J., Coleman, D., McKenna, L., Perry, F., 1992. Variations across and along a major continental rift: An interdisciplinary study of the Basin and Range province, western USA, Tectonophysics, 213, 57-96.
- Lachenbruch, A., Sass, J., 1992. Heat flow from Cajon Pass, fault strength, and tectonic implications, Journal of Geophysical Research, 97, 4995-5015.
- Lister, G., Davis, G., 1989. The origin of metamorphic core complexes and detachment faults formed during Tertiary continental extension in the northern Colorado River region, U.S.A., Journal of Geophysical Research, 11, 65-94.
- Miller, E., Dumitru, T., Brown, R., Gans, P., 1999. Rapid Miocene slip on the Snake Range - Deep Creek Range fault system, east-central Nevada, Geological Society of America Bulletin, 111, 886-905.
- Moresi, L., Dufour, F., Muhlhaus, H.-B., 2002. Mantle convection modeling with viscoelastic/brittle lithosphere: Numerical methodology and plate tectonic modeling, Pure and Applied Geophysics, 159, 2335-2356.
- Scott, R., Lister, G., 1992. Detachment faults; evidence for a low-angle origin, Geology, 20, 833-836.
- Wernicke, B., Axen, G., 1988. On the role of isostasy in the evolution of normal fault systems, Geology, 16, 848-851.

GEOMETRIC AND EXPERIMENTAL MODELS OF EXTENSIONAL FAULT-BEND FOLDS

3-30

Martha Oliver Withjack, Roy W. Schlische

Department of Geological Sciences, Rutgers University, Piscataway, NJ, 08854, USA

Summary

We have compared the results of geometric and experimental models that simulate fault-bend folding in the hanging walls of non-planar normal faults. The models show how the shape of the normal fault, the displacement on the normal fault, and the rates of footwall deposition and/or erosion influence the hanging-wall geometries through time.

Abstract

The geometric models ranged from simple models of listric normal faults with continuous hanging-wall deposition to complex models of normal faults with ramps and flats and footwall deposition and/or erosion. The inclined shear angle (i.e., the angle between the horizontal and the shear direction) was 70° toward the fault in all models. Withjack and Peterson (1993) describe the modeling technique. In the experimental models, a 4-cm-thick layer of either wet clay or dry sand covered a flat metal base

consisting of overlapping plates or precut blocks. Movement of the plates or blocks produced a listric normal fault in the overlying clay or sand layer. We added growth layers after every centimeter of displacement. Withjack and Callaway (2000) describe the properties of the wet clay and dry sand.
In models with a listric normal fault that dips at depth, all hanging-wall beds are below the level of their footwall counterparts (Fig. 1). Near the fault, pre-growth beds dip toward the fault, and growth beds dip and thicken toward the fault with a subtle wedge-shaped geometry. In the clay model, growth beds thin directly above the upward-propagating listric normal fault (Fig. 1b). Antithetic faults develop in the experimental models (Fig. 1a, 1b). The geometric models show that the limit of hanging-wall folding depends on the fault shape and the rates of footwall deposition or erosion (Fig. 1c).
In models with a listric normal fault that flattens at depth, pre-growth beds thin and dip toward the fault near the fault (Fig. 2). Far from the fault, hanging-wall beds rise to the level of their footwall counterparts. Shallow growth beds have a pronounced wedge-shaped geometry (i.e., they dip and substantially thicken toward the fault). Deep, older growth beds also dip toward the fault, but their wedge-shaped geometry is subtle or absent. Thus, deep, older growth beds can resemble pre-growth beds, especially if footwall erosion occurs during faulting (Fig. 2d). Deformation (i.e., inclined shear in the geometric models, small-scale normal faulting in the experimental models) thins the pre-growth beds and deeper growth beds near the fault.
In models with a normal fault with a ramp-flat-ramp geometry, growth beds near the fault dip and thicken toward the fault (Fig. 3a). Far from the fault, in a separate zone of deposition, growth beds are flat lying. Shallow pre-growth beds form an anticline above the fault flat. As fault displacement increases, a panel of steeply dipping growth beds forms near the fault. Growth beds far from the fault are flat lying. A dipping unconformity, resembling a fault, separates the two growth packages. Similar geometries develop with footwall deposition and erosion (Figs. 3b, 3c). The hanging-wall geometries predicted by the geometric and experimental models closely resemble those observed on seismic data from the Gulf of Mexico (Figs. 2e, 3d).

REFERENCES

- Withjack and Peterson, 1993, AAPG Bulletin, 77, 1860-1873.
- Withjack and Callaway, 2000, AAPG Bulletin, 84, 627-651.

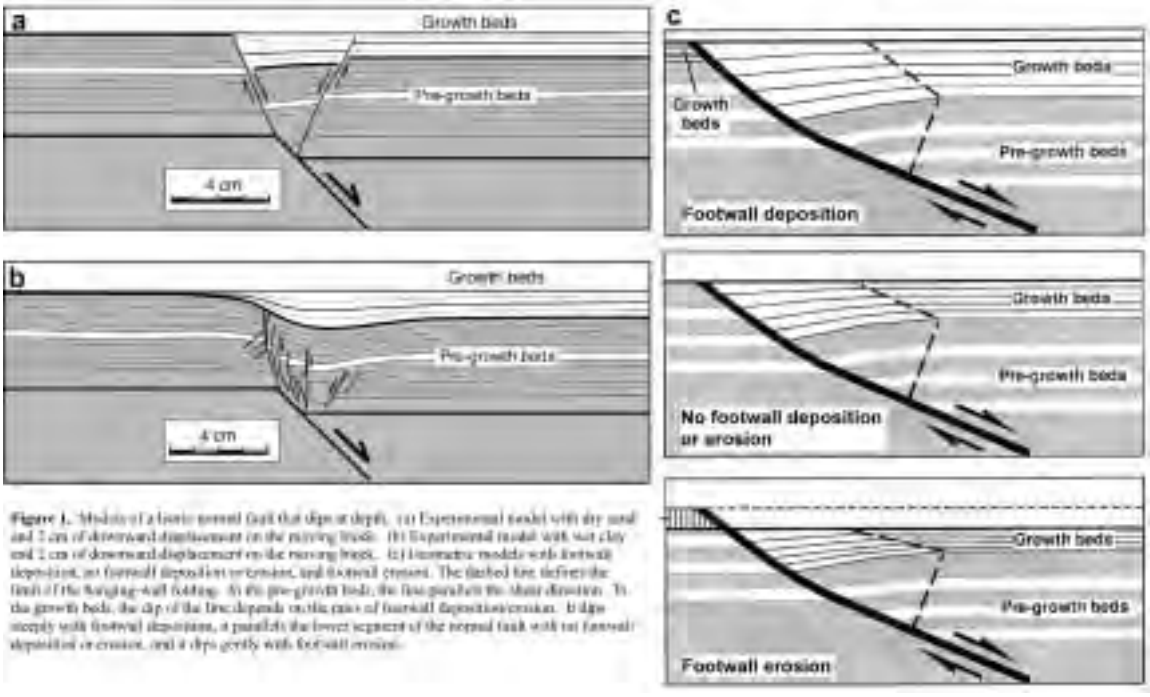

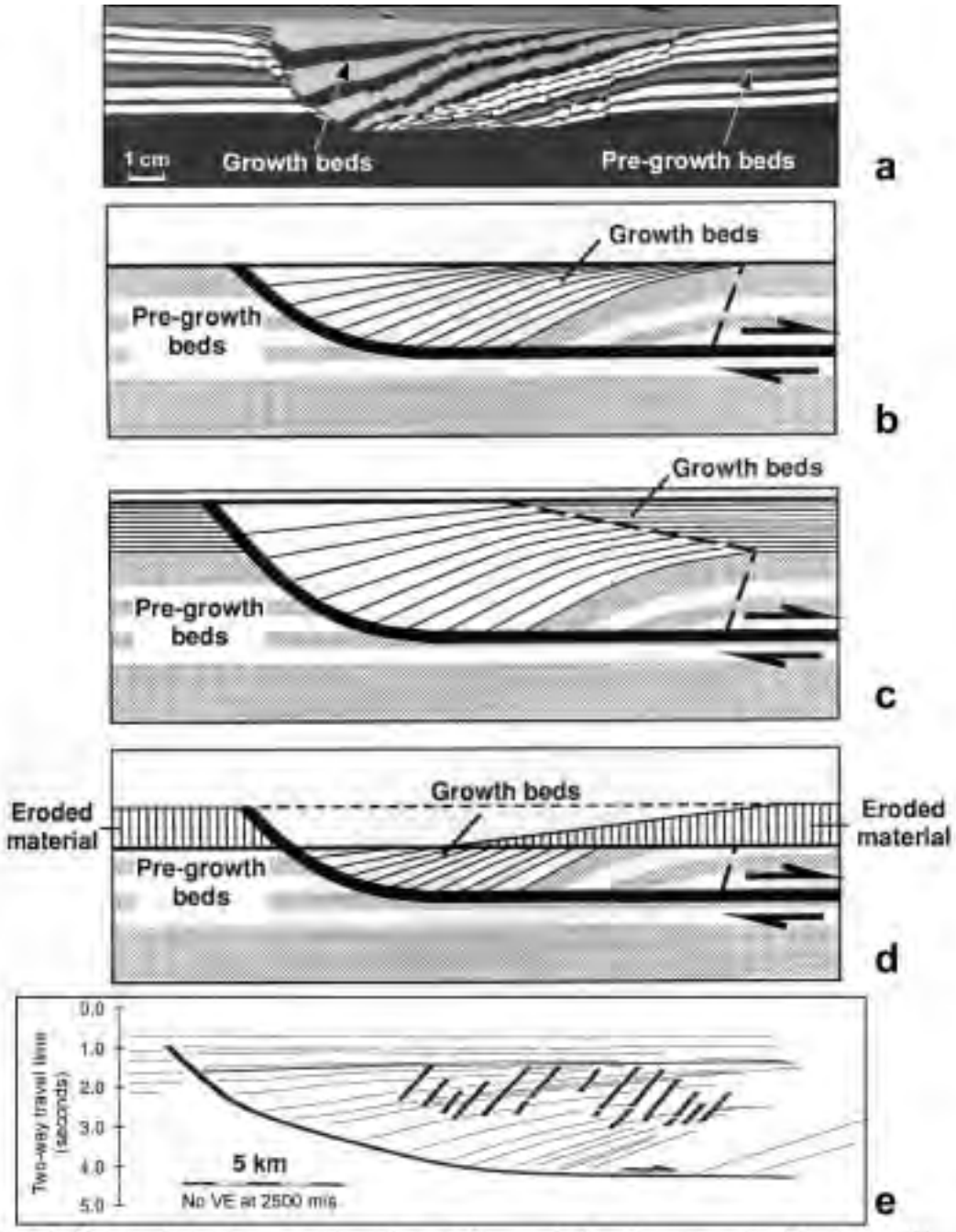

Figure 2. Models and natural example of listric faults that flatten at depth. (a) Experimental model with 8 cm of displacement. No footwall deposition or erosion. (b) Geometric model with 10 units of displacement. No footwall deposition or erosion. (c) Geometric model with 10 units of displacement and footwall deposition. (d) Geometric model with 10 units of displacement and footwall erosion. The dashed line in the geometric models defines the limit of hanging-wall folding. (e) Interpreted line drawing of seismic line from the Gulf of Mexico. Note the fault-bend fold in the hanging wall of the listric fault. Small-scale antithetic normal faults dipping about 60° accommodate some of the hanging-wall deformation. Shallow growth beds exhibit pronounced wedge geometry, whereas deep, older growth beds have a subtle wedge geometry, as in the geometric models and experimental model.

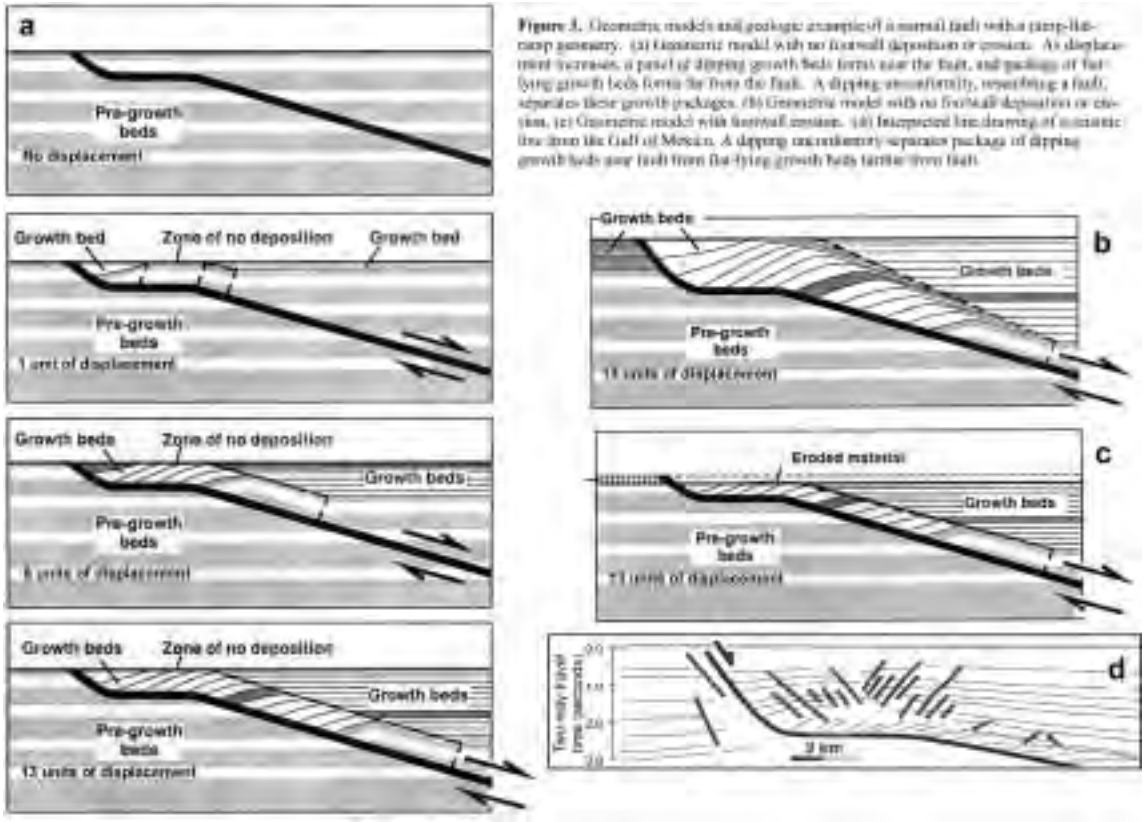

Figure 3. Geometric models and geologic examples of a normal fault with a ramp-flat-ramp geometry. (a) Geometric model with no footwall deposition or erosion. As displacement increases, a panel of dipping growth beds forms near the fault, and package of flat-lying growth beds forms far from the fault. A dipping unconformity, resembling a fault, separates these growth packages. (b) Geometric model with no footwall deposition or erosion. (c) Geometric model with footwall erosion. (d) Interpreted line drawing of a seismic line from the Gulf of Mexico. A dipping unconformity separates package of dipping growth beds near fault from flat-lying growth beds farther from fault.

Session 4

FRACTURES, FAULTS AND FLUID FLOW

FAULTS, FRACTURES AND FLUID FLOW IN SEDIMENTARY BASINS 4-01

Knut Bjørlykke
Department of Geoscience, University of Oslo

Prediction of the properties of faults and fractures depends on the distribution of effective stresses and on the properties of the rock matrix at the time of deformation. It is therefore important to understand the changes in physical properties due to sediment compaction (diagenesis) during burial.
Compaction of sediments in sedimentary basins involves very complex mechanical and chemical processes. Modelling sediment compaction and fluid flow requires that we can identify and quantify the rate limiting processes. The compaction process causes a reduction in fluid content (porosity) and an increase in density.
In subsiding sedimentary basins mechanical compaction will normally occur under increasing effective stress and the sediments are then normally consolidated and ductile (Bjørlykke and Høeg 1996, Bjørlykke 1999).
Sandstones are prior to carbonate or quartz cementation ductile and shearing will result in denser grain packing or grain crushing. As a result the fault plane will always be less permeable than the adjacent rock matrix can not be conduits for fluid flow. Also in the case of poorly cemented clays shearing will result in reduced permeability.
The precipitation of cement, mostly carbonate and quartz will cause an increase in rock strength and are over-consolidation in a mechanil sense resulting in brittle properties. (Fig 1)

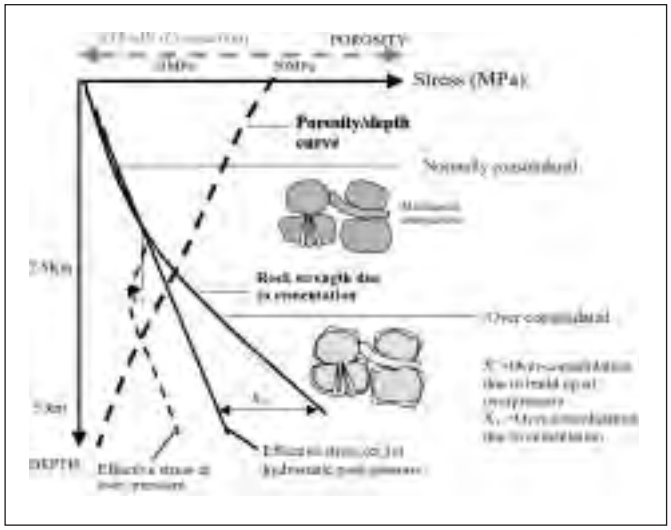

Fig 1. Changes in stress and rock properties of a sediment layer as a function of increasing burial. At hydrostatic pore pressure the effective stress will increase as a function of depth, but sediments may become "over consolidated" (X_2) due to cementation at shallow depth by carbonate and at greater depth (>70-100°C) by quartz cement. When a layer subsides into an over pressured zone the effective stress may be reduced compared to the stress the layer experienced at shallower depth causing over consolidation (X_1).

Modelling of fluid flow

In a sedimentary basin water will always be the continuous phase on a large scale and control the overall fluid potential. The pressure in the hydrocarbon phase will be controlled by the thickness of the hydrocarbon columns and the difference in pressure is balanced against the water pressure by the capillary forces.
The flow of water can be modelled using the simple Darcy equation:

$$F = k \cdot \nabla P/\mu$$

The fluid flux (F) can however in most cases not be modelled from these parameters because the pressure gradients (∇P) and the distribution of permeability (k) is not known. The viscosity (μ) of the fluids are better constrained. To predict the fluid flow in a sedimentary basin the three dimensional permeability distribution must be known over large distances. The flow in permeable sandstones in the deeper parts of a sedimentary basin depends to a little degree on the permeability of the sandstone, but on the minimum permeability along a pathway all the way to the surface. The distribution of pressure is also very difficult to predict.

The modelling of fluid flow in sedimentary basins thus requires that we have mapped the basin to such a degree that modelling would not be required or become circular.
The main constrains of fluid flow in sedimentary basins is the source of fluids. Both the meteoric water flowing into the basin and the water flux released by compaction can be quantified or at least constrained.
The compaction driven flux is a direct function of the reduction in porosity in the underlying sediments and the water released by mineral reactions.

The effect of faults on fluid flow in sedimentary basins.

A clear distinction must be made between flow perpendicular to faults in sandstones and flow along faults. Faults in sandstone reservoirs may be important barriers for fluid flow and the permeability across the fault is controlled both by the mechanical shearing and diagenetic reactions.
Shear deformation in uncemented sand depends on the normal stress and on the composition and size of the grains. This can be tested experimentally and for quartz rich sand significant grain crushing start at 5-10 MPa for coarse to medium grained sand while fine grained sand require normal stresses exceeding 10MPa corresponding to at least 1km of overburden for significant grain crushing to occur. (Kjeldstad 2002).
Shears stress produces a dense, interlocking grain fabric which causes reduced permeability even before grain crushing. Because of strain hardening the zone of shear deformation will tend to shift resulting in a broad zone of shear deformation without a well defined shear plane.
This type of shear deformation in clean sand is not likely to introduce clay smear.
Diagenetic reactions particularly quartz cementation causes a reduction in porosity and permeability as a function of time and temperature during burial and this process can be modelled (Fisher et al 2003, Walderhaug 1996). The porosity in the shear zone at the onset of quartz cementation is however one of the most critical factor determining the final porosity and permeability.
If the shearing occurs after the precipitation of clay coating, grain crushing will expose fresh quartz surfaces and cause higher rates of quartz cementation in the fault plane.
When shearing occurs before the precipitation of chlorite and illite there will be little quartz cementation also in the shear zones but the permeability is relatively low due to dense grain packing. Small amounts of clay present in the sand like mica and kaolinite will be concentrated along the fault plane and may later develop into stylolites which have a strong effect on the permeability and the capillary entry pressure.
The effective permeability of shear zones in clean sand is difficult to predict because the fault zone is broad and diffuse, containing numerous discontinuous shear zones.

Fluid flow along faults and fractures- leakage of faults

In most cases faults and fractures are barriers to fluid flow rather than conduits. When sediments are normally consolidated and ductile the fault plane will be characterized by sheared and densely packed fault gauge in clayey sediments or densely packed and/or crushed sand in coarser sediments. The permeability of the fault plane is then nearly always lower than the undeformed rocks and they are therefore not conduits for fluid flow.
Faulting in well cemented rocks may cause brittle deformation and brecciation. The permeability after shearing in cemented brittle rocks depends on the degree of dilation during shearing which depends on the normal stress during shearing, the shear strength of the rock and the relief of the shear plane. In metamorphic and igneous rock the dilation may be rather significant, producing a fault zone with high permeability. In metamorphic rocks nearly all the porosity are in the fractures and changes in the aperture of faults and fractures provide a mechanism for seismic pumping as described by Sibson (1981). In sedimentary basins, however, most of the fluids are stored in the pores even in well cemented sandstones and the effects of fractures are very different.
Extensional faulting due to rifting are often associated with uplift and erosion. This will stop mechanical compaction because of the reduced effective stress and reduce the rate of chemical compaction due to quartz cementation. It will therefore be little or no compaction driven fluid flow to fill the fractures and under-pressure may cause a draw down of meteoric water from above.

Open faults and fractures are rarely filled with cement precipitated due to advective water flow. Quartz cementation require very high fluid fluxes and temperatures about (70-100°C) and calcite will dissolve when upwards flowing water is cooled. (Bjørlykke and Egeberg 1993).
Fractures are most likely to be filled by crystal growth sourced by diffusion from the adjacent rocks (Egeberg and Saigal 1991).

Reactivation of faults

Faults may become reactivated when subjected to renewed stress provided that the fault planes have a lower shear strength than the undeformed rocks.
In metamorphic and well cemented sedimentary rocks faulting produce a plane of weakness (reduced shear strength) and when subjected to repeat shear stresses the shearing tend to follow existing shear planes. This is referred to as fault reactivation. In some sediments, notably clean sand, shear zones (shearbands) will produce strain hardening which will cause the shear zone to shift. These faults can not be reactivated. Clay rich sediments may develop a clay smear which results in strain softening and these may therefore be reactivated. During burial, however, the shear strength of the sediments may change very much due to increasing compaction and also due to diagenetic changes. Recrystallization of clay such as illitization of smectite and precipitation of quartz along the fault plane can cause an increase in the shear strength of the fault gauge so that it becomes stronger than the matrix. Carbonate cementation along the fault plane may also increase the shear strength.
Glacial loading have been proposed to cause leakage in reservoirs in the Northern North Sea (Grollimund and Zoback 2003). In their model they assume a brittle upper crust of 20 km and do not include the sediments of the North Sea Basin which to a large extent have ductile properties. The resulting distribution of shear stresses is therefore uncertain. Seismic data show no evidence of late faulting above the studied Visund Field or reactivation of the upper Jurassic faults above the reservoirs.
Even if these rocks should be subjected to high differential stresses the faults would probably not be reactivated because they would be stronger than the rock matrix. Higher up in the sequence Eocene and Oligocene is dominated by smectite rich mudstones (Thyberg et al 1999). These are relatively soft and ductile and could serve as a detachment plane decoupling horizontal stresses from the overlying sequence.

Cap rock integrity

Cap rock may leak due to intergranular flow when the capillary entry pressure for the hydrocarbons is exceed or by fracturing. Shales are normally impermeable for oil and fracturing are therefore required.
Fracturing occurs when the pore pressure exceeds the least principle stress. In subsiding sedimentary basins this is normally the horizontal stress (σ_h).
The requirement for hydrofracturing is that $P > \sigma_h + \tau$
The tensional strength (τ) is assumed to be small compared to σ_h .
The thickness of the hydrocarbon column determines the pressure difference between the hydrocarbon phase and the water phase but this difference is taken up by the capillary pressure. If the capillary entry pressure of the cap rock is not exceeded the thickness of the HC column has little effect on the risk for leakage by hydrofracturing.
High overpressures occur most commonly in pressure compartments with limited lateral drainage. If the pore pressure approach the fracture pressure the strength of the cap rock can not prevent fracturing. The compaction driven water flux in siliceous sediments is at temperatures above about 80-100°C primarily driven by temperatures (Walderhaug 1996). The underlying sediments will therefore continue to compact and provide water flux even if the effective stress is reduced.

Conclusion

The properties of faults and fractures with respect to fluid flow must be predicted based on rock and soil mechanical principles and on chemical processes including mineral precipitation and dissolution. During continued subsidence and compaction in sedimentary basins faults are rarely conduits for fluid

flow. When fracture pressure is reached, leakage will occur by hydro-fracturing independent of the faults. During uplift and extension there is little compaction driven fluid flow on fractures.

REFERENCES

- Bjørlykke, K & Egeberg, K. 1993. Quartz cementation in sedimentary basins. AAPG. Bull. 77, 1538 - 1548.
- Bjørlykke, K. & Høeg, K. 1997. Effects of burial diagenesis on stresses, compaction and fluid flow in sedimentary basins. Marine and Petroleum Geology.14, 267 - 276.
- Bjørlykke, K. 1999. An overview of factors controlling rates of compaction and fluid flow in sedimentary basins. In: Jamtveit, B and Meakin, P.(eds) Growth, Dissolution and Pattern Formation in Geosystems. p 381- 404.
- Chuhan, F. A., Kjeldstad, A. Bjørlykke, K. & Høeg, K. 2003. Experimental compression of loose sands simulating porosity reduction in petroleum reservoirs during burial. Canadian Geotechnical Journal. 40, 995-1011.
- Egeberg, P.K. & Saigal, G. 1991. North-Sea chalk diagenesis – cementation of chalks and healing of
- Fractures. Chemical Geology. 92, 339-354.
- Fisher, Q. J., Casey, M., Harris &Knipe, R.J. 2003. Fluid – flow properties of faults in sandstones: The importance of temperature history. Geology, 31, 965-968.
- Fisher, Q. J. & Knipe, R.J. 2001. The permeability of faults within siliciclastic petroleum reservoirs of the North Sea and Norwegian Continental Shelf. Marine and Petroleum Geology. 18, 1063-1081.
- Grollimund, B. and Zoback, M D. 2003. Impact of glacially induced stress changes on fault-seal integrity offshore Norway. AAPG Bull. 87, 493-506.
- Kjeldstad, A, 2002. Compaction and shear deformation in sedimentary basins. PhD Thesis. University of Oslo.
- Thyberg, B.I., Jordt, H., Bjørlykke, K. & Faleide, J.I. 2000. Relationships between sequence stratigraphy, mineralogy and geochemistry in Cenozoic sediments of the northern North Sea. In: Nøttvedt, A et al (eds) Dynamics of the Norwegian Margin, Geological Society. London. Special Publications 167,245-272.
- Sibson,R.H. 1981. Fluid flow accompanying faulting. Field evidence and models, In: Simpson, D.W. and Richards, P.G. (eds) Earthquake prediction: An international review: American Geophysical Union Maurice Ewing Series, v. 4, 593-603.
- Walderhaug, O. 1996. Kinetic modelling of quartz cementation and porosity loss in deeply buried sandstone reservoirs: AAPG Bull. 80, 731-745.
- Wong, T.-F. David.C. & Zhu,W. 1997. The transition from brittle faulting to cataclastic flow in porous sandstones. Mechanical deformation: Journal of Geophysical Research.102, 3009-3025.

ANALOGUE MODELLING OF MULTIPLE GRANITIC INTRUSIONS DURING STRIKE-SLIP FAULTING 4-02

G. Corti (*), G. Moratti (**), F. Sani (*)

(*) Dipartimento di Scienze della Terra, Università degli Studi di Firenze, Via La Pira, 4 – 50121 Firenze (Italy)

(**) CNR-IGG, Sezione di Firenze, La Pira, 4 – 50121 Firenze (Italy)

Summary

In this work we present a series of analogue models investigating the process of multiple granite intrusions at upper crustal levels during strike-slip faulting. We focus on the relations between magma emplacement and deformation by analysing on one side how multiple plutons influence the deformation pattern, on the other side how the resulting fault pattern influences the pluton emplacement. Sand is used to model a sedimentary cover in nature, whereas a mixture of silicone and oleic acid is used to model high viscosity granitic magmas. Experimental results show that intrusions have an important effect on deformation. Particularly, increasing the number of intrusions the number of faults in the models increases and the mean (tip to tip) fault length decreases. Whereas faults in models with no intrusions are characterised by a horizontal component of movement, the majority of faults in models with syn-deformation intrusions display a significant vertical component of displacement. Thus, transpression faults form to accomodate uprasing of the low-viscosity fluid. The experiments support previous modelling and observations from natural cases in that strike-slip deformation results in tipically asymmetric plutons, whose shape is strongly controlled by structural features.

Abstract text

Emplacement of granitic bodies along crustal-scale strike-slip faults has been documented in many regions worldwide. Many plutons emplaced at rather shallow crustal levels and they shape has been

suggested to be strongly controlled by structural features. Such a control has been documented in previous experimental models (Roman-Berdiel et al., 1997) investigating granite intrusion in a rheologically multilayered upper crust. These models illustrated the importance on intrusion shape of several parameters such as the brittle-ductile layering (e.g., depth and thickness of ductile layers), the position of the feeding pipes, the volume of injected magma. The experiments showed that the structural pattern has a major influence on the intrusion shape, resulting in tipically asymmetric sigmoidal- or lozenge-shaped plutons with a long axis tracking the local principal stretching direction.

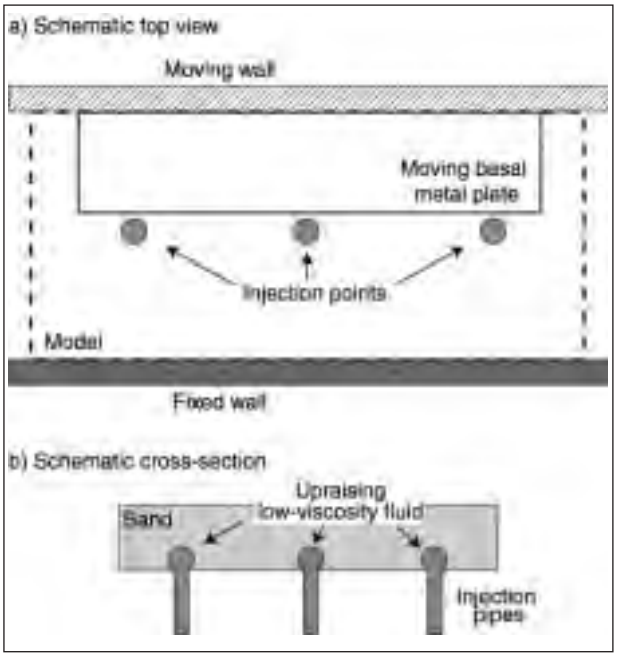

Fig. 1 - Experimental set-up

Our work aims to implement these previous models by investigating the process of multiple granite intrusions at upper crustal levels during strike-slip faulting. We focus on the relations between magma emplacement and deformation. In particular, we analyse on one side how multiple plutons influence the deformation pattern, on the other side how the resulting fault pattern influences the pluton emplacement.
Experiments were performed at the Tectonic Modelling Lab of CNR-IGG settled at the Earth Sciences Dept. of Florence University (Italy). Granite intrusions were modelled by injecting a low-viscosity Newtonian fluid (a mixture of Silicone and Oleic Acid) into a 5 cm thick sand pack, simulating the uppermost part of the brittle crust (mainly a sedimentary cover) in nature (Fig.1). During injection, half of the sand pack was moved horizontally with respect to the other half in order to create a strike-slip regime of deformation. Movement was obtained by lateral displacement of a basal metal plate driven by an electric motor (Fig. 1).
Three different experiments are presented. One experiment (model ME 01) considered strike-slip deformation with no magma intrusion; two other experiments investigated emplacement of magma from one (model ME 02) or three (model ME 03) injecting points. In order to compare the results, during each different experiment, the injection rate, the volume of injected material, the thickness of the brittle material, the deformation rate and the amount of lateral displacement were kept constant.

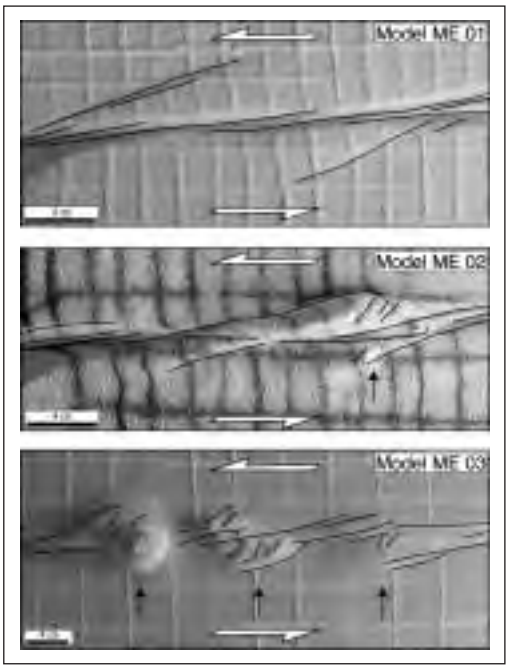

Fig. 2 - Final top view photo of the three different experiments discussed. Black lines represent faults; black arrows indicate the position of the injection points; big white arrows indicate the relative displacement. The elliptical pink body in model ME 03 is a piercing intrusion.

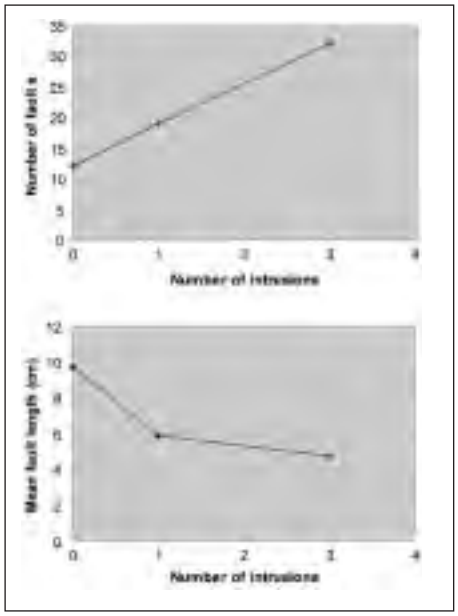

Fig. 3 - Graphs showing the variation of the fault number and length in relation to the intrusions number.

Experimental results show that intrusions have an important effect on deformation. In model ME 01 the structural pattern is rather simple and characterised by few R-shears (developing at the onset of deformation) and a main deformed zone accommodating most of the deformation. In models ME 02 and ME 03, the movement is accommodated by a more complex fault pattern, with a wider main deformed zone and an increasing number of T-fractures. Thus, the structural complexity increases increasing the number of intrusions (Fig. 2). This is related to the strong strain localisation due to the presence of the magmatic bodies. Particularly, increasing the number of intrusions the number of faults in the models increases and the mean (tip to tip) fault length decreases (Fig. 3). In addition, whereas faults in model ME 01 are solely characterised by a horizontal component of movement, the majority of faults in models ME 02 and ME 03 display a significant vertical component of displacement. Thus, transpression faults form to accomodate uprasing of the low-viscosity fluid.
The experiments support previous modelling and observations from natural cases in that strike-slip deformation results in tipically asymmetric plutons, whose shape is strongly controlled by structural features.

REFERENCES

• Román-Berdiel, T., Gapais, D., Brun, J.-P., 1997. American Journal of Science, 297, 651-678.

ROTATIONAL BEHAVIOUR OF MULTIPLE FAULTS IN SIMPLE SHEAR 4-03

Ulrike Exner*, Neil S. Mancktelow
Geologisches Institut ETH Zürich, Sonneggstrasse 5, CH-8092 Zürich
**ulrike.exner@erdw.ethz.ch*

Analogue experiments were performed to investigate the rotational behaviour and deformation around "brittle" faults (i.e. slip surfaces) in a linear viscous material under simple shear boundary conditions. Previous analogue and numerical studies have shown that, for single faults, characteristic deformation geometries are produced in initially straight marker lines parallel to the shear zone boundary ("flanking structures", Passchier 2001). In simple shear, these geometries are constrained by the initial orientation of the fault with respect to the shear zone boundary. Six different fields of instantaneously developing structures can be distinguished, whereas finite geometries are strongly dependent on the total amount of shear strain. Offset and deflection of marker lines can be used to distinguish between the various structures, and can thus provide a tool to interpret fault-related folds in natural shear zones (Grasemann et al. 2003).
Nevertheless, observations from several natural shear zones suggest that not only single faults, but often several parallel or conjugate fault planes are subjected to progressive shear. Further deformation of such complex fault structures results in distinctive fault patterns, which have been modelled in a series of analogue experiments. Not only the initial orientation of the faults, but also their initial length

and relative position were modified in order to reproduce the geometries that were observed in the natural shear zones.

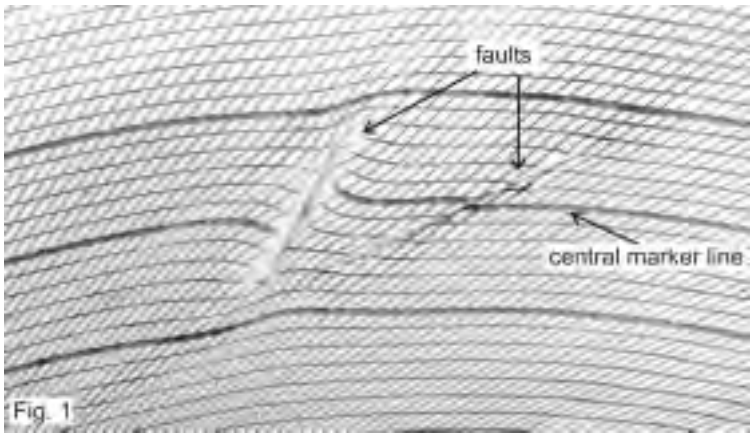

Fig. 1

Initially conjugate faults seem to be an especially common feature in rocks subjected to deformation at the brittle-ductile transition. Fig. 1 displays an analogue experiment of two faults initially conjugate at an angle of 60°. As a result of the different initial angles to the shear zone boundary, the two faults develop different deflection and offset of the central marker lines. In this case, continuous offset along the faults results in a wedge-shaped structure, which is also internally deformed. As the two faults with different orientations to the shear zone boundary rotate with different velocities, they finally combine to form a single, broader "fault zone" that accommodates further strain.

The analogue experiments may provide explanations for complex natural fold examples related to multiple faults and may also allow the shear sense to be inferred and the finite strain to be estimated.

REFERENCES

• Grasemann, B., Stüwe, K., Vannay, J.-C., 2003. Sense and non-sense of shear in flanking structures. Journal of Structural Geology 25, 19-34
• Passchier, C.W., 2001. Flanking Structures. Journal of Structural Geology 23, 951-962

DRAG ALONG A SINGLE FAULT 4-04

B. Grasemann(*), S. Martel(**), C. Passchier(***)

(*) Department of Geological Sciences, University of Vienna, Austria
(**) Department of Geology & Geophysics, University of Hawaii, USA
(***) Department of Geosciences, University of Mainz, Germany

Summary

By means of stress functions, we modelled the displacement of marker horizons along a single mode II fault in order to understand under what conditions normal and reverse fault drag develops. Slip along the fault generates a complex heterogeneous perturbation displacement field essentially resembling semi circles with increasing displacement magnitudes towards the centre of the fault. Contractional and extensional faults may develop, both with normal and reverse drag, depending on the angle between the markers and the fault plane: At low angles normal drag and at high angles reverse drag develop. Comparison of the model results with published models reveal that the characteristics of normal and reverse fault drag are insensitive on scale and rheology of the faulted rocks.

Abstract text

Fault drag usually describes the deflection of markers adjacent to a fault. Although some earlier descriptions on fault drag do exist (e.g. Margerie and Heim (1888); Suess, 1901) modern structural geology textbooks generally refer to Hamblin (1965) for the definition fault drag: The curvature of markers convex in the direction of shear (i.e. consistent with the sense of displacement on the fault) is called normal drag (Fig. 1). On the other hand, observations of reverse drag indicate concave deflection of markers (i.e. inconsistent with the sense of displacement on the fault).

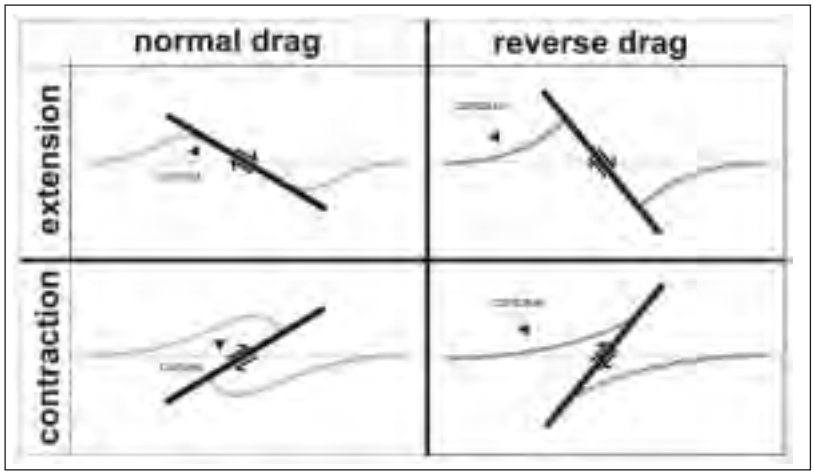

Fig. 1

In order to explain the counter intuitive geometry of reverse fault drag by progressive deformation several models have been proposed, for example, elastic and isostatic rebound, diapirism, sagging and differential compaction (Hamblin, 1965 and references cited therein). While Reches & Eidelman (1995) demonstrated by means of numerical modelling that drag effects may even change along a single fault from reverse in the centre to normal at the termination of the fault, Grasemann et al. (2003) demonstrated that at low angles between the fault and a central marker line normal drag forms but if the central marker lines meets the fault at higher angles, reverse drag develops. Surprisingly, the model results suggest that the type of fault drag is independent on the kinematic vorticity number of the far field deformation, but no explanation has yet been given.

In order to test parameters, which control the formation of fault drag we calculate the displacement along mode II fault using Westergaard stress functions (Westergaard, 1939) and largely follow the procedures described by Martel (1997). The model fault is located along the x-axis from x=-1 to x=1 and accommodates variable displacements, confined to the x, y – plane, ranging from a maximum in the centre of the fault to zero at the tip-line as a result of an imposed regional stress field (Fig. 2). The vector field in Figure 2 shows the displacement field near a mode II fault using *a* Poisson's ration of 0.3 and a ratio of the driving stress and the modulus of rigidity of 1:100.

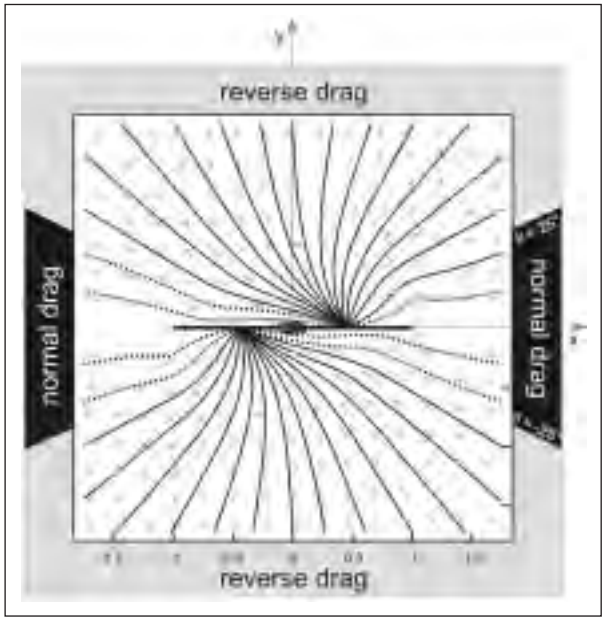

Fig. 2

The heterogeneous monoclinic displacement field in Figure 2 essentially resembles "opposing circulation cells" with increasing displacement magnitudes towards the centre of the fault. Beyond some distance from the fault the magnitude of the displacements becomes insignificant. In order to highlight the effects of the displacement field on fault drag, Figure 2 shows deformed marker lines meeting the fault in the centre at different angles before slip occurred along the fault. Marker lines meeting the fault at higher angles are dominated by the influence of the x-component of the displacement field resulting in reverse fault drag (solid lines). At lower angles, however, where x-component is less significant, the deformation of the marker lines is mainly a function of the y-component of the displacement field and therefore results in a normal fault drag (dashed lines). The analytical results of the stress functions confirm the instantaneous solutions of mechanical finite element models (Grasemann et al. 2003), suggesting that the drag of a central marker line is mainly dependent on the orientation between the marker line and the fault but insensitive of the kinematic vorticity number of the background strain.

REFERENCES

• de Margerie, E. and Heim, A. (1888), Verlag von J. Wurster & Comp., Zürich, 154 pp.
• Grasemann, B. et al. (2003), Journal of Structural Geology, 25, 19-34.
• Hamblin, W.K. (1965), Geological Society of America Bulletin, 76, 1145-1164.
• Martel, S.J. (1997), Journal of Structural Geology, 19, 835-847.
• Reches, Z. and Eidelman, A. (1995), Tectonophysics, 247, 145-156.
• Suess, E. (1901), Tempsky, F. - Freytag, G., Prag and Wien, 508 pp.
• Westergaard, H.M. (1939), Journal of Applied Mechanics, 66, 107-125.

ANALOGUE MODELLING OF STRUCTURES DEVELOPED ABOVE SINGLE AND MULTIPLE MANTLE PLUMES: APPLICATIONS TO BRITTLE CRUSTAL DEFORMATION ON EARTH AND VENUS

4-05

L. Harris(*), D. Byrne(**), S. Wetherley(†), J. Beeson(ˆ)

(*) Institut national de la recherche scientifique – Eau, Terre et Environnement, C.P. 7500, Sainte-Foy G1V 4C7, Québec, Canada (lyal_harris@inrs-ete.uquebec.ca.)
(**) Geoinformatics Exploration Australia Pty Ltd, 57 Havelock St., West Perth, WA 6005, Australia
(†) 113 Coogee St Mt Hawthorn, WA 6016, Australia
(ˆ) Placer (Granny Smith) Pty. Ltd., P.O. Box 33, Laverton, WA 6440, Australia

Summary

A pilot experimental modelling program was undertaken to study fault patterns associated with singular and multiple up-welling mantle plumes. The effects of plumes created using localised heat sources in a tank of honey (representing asthenosphere) is studied on overlying ductile silicone and brittle castor sugar layers representing a simplified, two-layered lithosphere. Concentric extension above plumes dominates the experiments, producing faults, graben and horsts in the brittle layer. Junctions with three to six radiating arms are produced depending on plume configuration both above and offset from plume heads suggesting caution in the interpretation of ancient plume positions based on fault patterns. Where there are two or more plumes, graben ± intervening horsts extend from above one plume to above the neighbouring plume. No triple or other multiple junctions develop when three plumes are aligned in a dogleg configuration. The silicone layer isostatically uplifts beneath graben and thins most at graben junctions. Volcano-like structures are locally developed above plumes.
Due to the absence of plate tectonics and limited surface erosion, Venus is thought to provide an excellent example of plume-related faulting and volcanism. Conflicting models exist for the formation of many brittle structures interpreted from Radar imagery of the surface of Venus and for the role of mantle plumes in their formation. Model results provide insights into the possible relationships between faulting and fracturing on Venus and the location of mantle plume centres. Alternative mechanisms of formation to those based on a single up-welling mantle plume are proposed.

Analogue modelling

Model materials simulate a simplified strength profile. Dow Corning 3179 dilatant compound (a silicone putty with density of 1.14 g/cm^3) was used to represent ductile lithosphere. This layer has unconstrained margins and floats and isostatically rebounds upon a basal layer of honey in a Perspex tank. A 10-mm thick layer of white castor sugar sprinkled onto the silicone putty layer is used to represent brittle crust. The edges of the silicone layer rise isostatically, thus constraining the sugar. Castor sugar was used in our models because of its low density (0.89 g/cm^3) and fine grain size which enhances the formation of minor faults and allows fine details to be observed. Vertical cylindrical heating coils (constructed of nichrome wire producing 47.2 watts of power) were positioned in the base of the tank. Tests without the presence of overlying layers showed development of a mushroom-shaped plume centred directly above a single heating coil and slight doming of the surface. Where several heating coils were used, discrete plumes centred over heating coils abut each other. In plan view there appears to be a "wall" or boundary of no mixing between adjacent plume heads. As the flow behaviour of silicone putty is temperature dependent, it deforms more readily with time above the impinging hot plume head mimicking the expected ductility increase of the lower lithosphere in nature above mantle plumes.

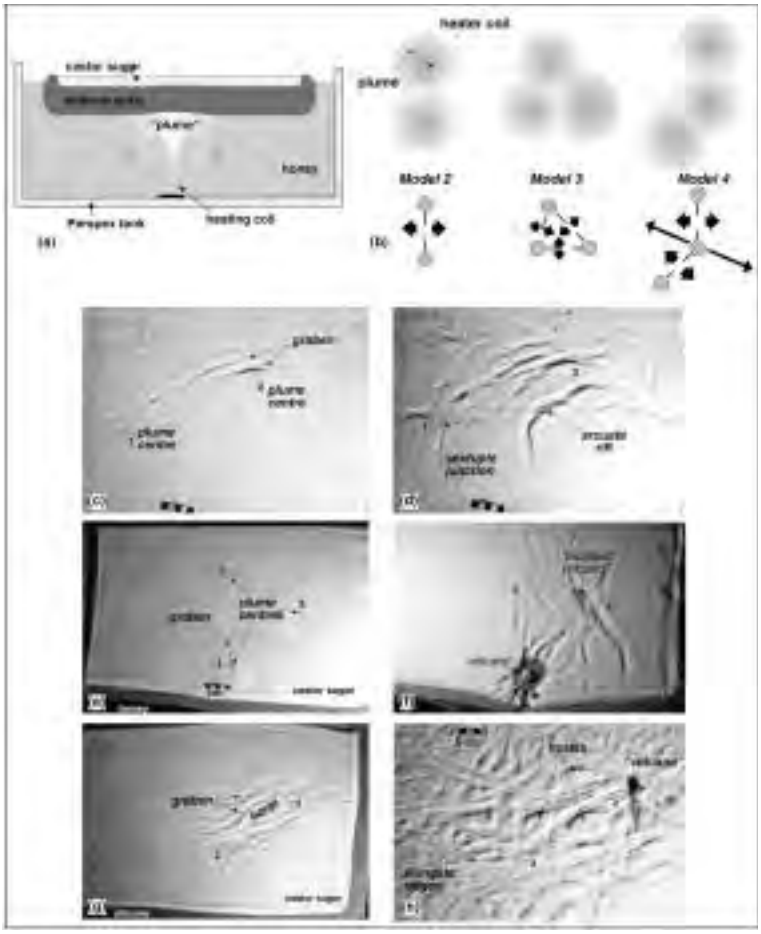

Figure 1. (a) Model construction. (b) Arrangement of heater coils and schematic form of plume heads for three models of multiple plume interactions. (c) to (h) Two stages in the development of each model of multiple plume interaction showing fault patterns and their relationship to plume centres. (c) & (d) Model 2 = two heater coils. (e) & (f) Model 3 = triangular arrangement of three heater coils. (g) – (h) Model 3 = dogleg arrangement of three heater coils.

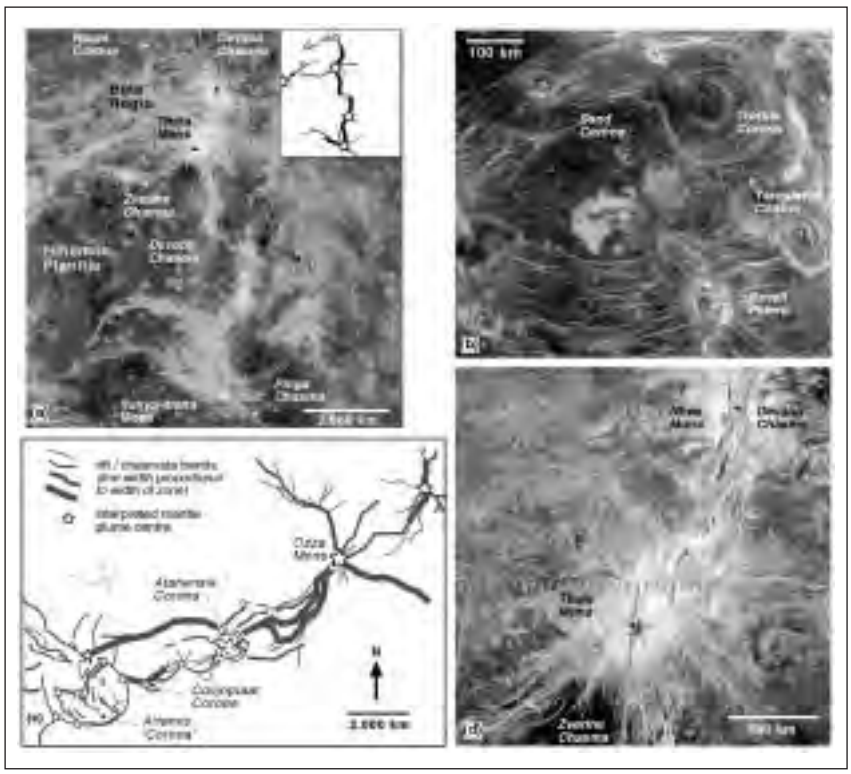

Figure 2. Magellan radar images of Venus and interpretation showing the suggested positions of plume centres between which extensional faults and graben have developed. Note the pattern of linked novae (such as Ozza Mons) and coronae and 'corona-like' features and multiple radiating chasmata (i.e. rifts). The geometry of chasmata resembles that of faults in analogue models.

Applications of models to the interpretation of upper-crustal faulting on Earth

Triple, quadruple, and even sextuple or more radiating graben are developed in models. Graben represent zones of localised horizontal extension of the brittle upper sugar layer and thinning and uplift of the underlying silicone. Graben intersections are sites of high extensional strain resulting in greatest thinning of the ductile silicone layer and local development of volcano-like structures. Whilst "honey volcanoes" (outpouring of honey in areas of thinned silicone) only occur directly over the centre of the underlying plume, some graben intersections (triple to sextuple junctions) developed in the intermediate to late stages of experiments do not occur over the main plume centre. If similar structures were to form in nature, the radiating nature of faults and/or dykes may erroneously be attributed to the presence of a mantle plume beneath the intersection. Horsts developed between graben remain mostly undeformed during the remainder of the experiment. Where there are two plumes, deformation is initially concentrated in a corridor between them, and may consist of either one or two closely spaced graben separated by a narrow horst. The resultant extension is perpendicular to a line connecting the two plumes. Where there are three plumes arranged in a dogleg configuration, deformation is initially concentrated in a corridor linking the plumes and no clear triple or other multiple junctions develop. Experimental results therefore provide potential normal fault and fracture geometries developed between plumes in different configurations prior to continental break-up. Late stages of models may show fault patterns developed early in the Earth's history that may have controlled outpourings of komatiite lava flows and localised plume-related mineralisation.

Applications of models to the interpretation of structures on Venus

Venus provides an excellent example of deformation due to vertical, plume-related tectonics without the influence of regional stresses due to plate tectonic processes. Venus lacks an asthenosphere and is thought to have a more ductile crust and upper mantle, with less of a rheological contrast between lithosphere and underlying mantle than on Earth. Radar imagery from Veneras 15 and 16 and especially the 1990-1994 Magellan mission provide details of fault, fracture and fold geometries, volcanoes, lava flows and impact craters on the Venusian surface. Prominent radiating fracture systems from central volcanic peaks are called novae. Complex circular to elliptical volcano-tectonic features that may also display radiating structures are called coronae. Their diameter varies from 60 to 2600 km. Coronae are characterised by an elevated interior, an annular graben and/or ridges 10 to 150 km across and radiating fractures and/or graben. Coronae may have associated volcanic features, such as small volcanic domes and lava flows and may be cut by regional extensional fractures and/or graben. Rifts, graben and fractures within and radiating from coronae may control dyke intrusion on Venus and have been compared to dyke swarms on Earth. Deep, fault-bounded rifts on Venus are called chasmata. Linear Chasmata radiate from or link novae and coronae and are thought to be similar to rift valleys on Earth. Annular chasmata develop due to radial extension about coronae. Tesserae (or tessera terrains) on Venus are defined as being characterised by intersecting sets of lineaments, high relief and surface roughness. Some tesserae comprise closely spaced faults or extension fractures, whereas other tesserae consist of intersecting sets of normal faults and extension fractures at variable angles to each other.

Elongate horsts, bounded by flat-bottomed, steep sided graben, formed in the early stages of several models resemble some plateaux and coronae on Venus. Triple, quadruple, sextuple and other multiple rift junctions resemble radiating faults and chasmata about novae and coronae. Such structures develop both above and away from plume centres, suggesting that large primary mantle plumes may not underlie all such features on Venus. Broad areas with single or intersecting sets of closely spaced extensional faults and fractures formed in late stages of models resemble ribbon and star terrain in tesserae on Venus. Their close spacing in models suggests that previous estimates of the thickness of brittle crust on Venus based on fracture spacing may have been underestimated by up to 50%.

Acknowledgements

Pancontinental Mining NL and the Australian Research Council funded experiments that were undertaken when the authors were at the Tectonics Special Research Centre, The University of Western Australia.

NUMERICAL MODELING OF PROGRESSIVE EVOLUTION OF FLANKING STRUCTURES

4-06

Thomas Kocher*, Neil Mancktelow

Geological Institute ETH Zürich – Sonneggstrasse 5, 8092 Zürich, Switzerland
**kocher@erdw.ethz.ch*

A planar discontinuity (e.g. a fracture) in a homogeneous flow field will perturb the flow in the vicinity of the discontinuity. The perturbation causes local inhomogeneous deformation, which can be seen in the deflection of passive marker lines away from their far field orientation. These deflections of marker lines are called flanking structures (Passchier 2001) and their geometry is a function of the initial fracture orientation, the marker line orientation, and the flow field.
Using a finite element code developed in-house for 2-D viscous incompressible materials, the deformation around an embedded planar fault was investigated for different initial geometries. The code allows experiments to be conducted up to high shear strains of $\gamma > 10$. The structures that developed instantaneously correspond well with the results of Grasemann and Stüwe (2001) and Grasemann et al. (2003), but the current model can now study the development to high finite strains. High strain experiments were conducted varying both the flow field parameters and the geometrical setup. The perturbation strain around a fracture at low angles to the shear plane in a flow field with a transpressive pure shear component produces a shearband-like geometry of the marker lines in the vicinity of the fracture (Fig. 1). These structures are pseudo-stable, since the fracture rotates only very slowly. This means that shear bands have no true stable orientation, because they still rotate slowly toward the fabric attractor. They can therefore only be preserved up to moderate amounts of strain.

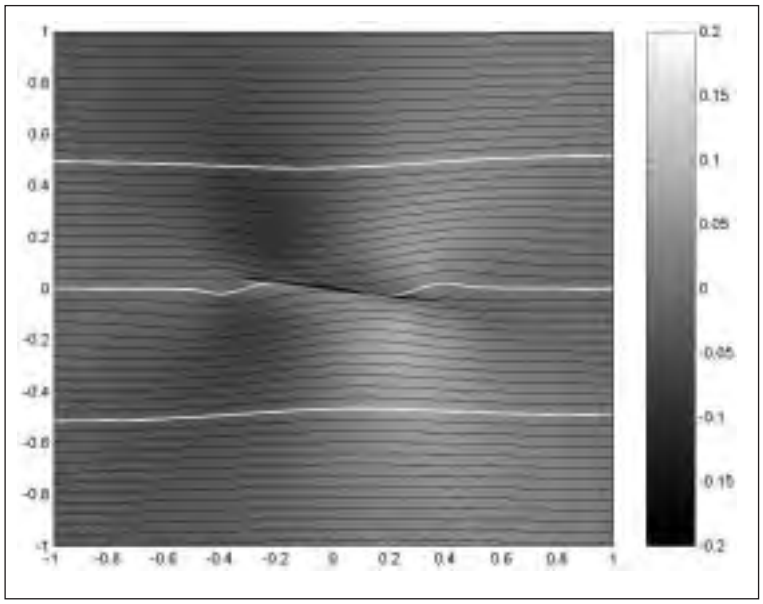

Fig. 1: Shearband-like geometry of marker lines around a fault in linear viscous material. The shearband is preserved only up to moderate strains. The grayscale plots the dimensionless vertical perturbation velocity. Transpressive dextral flow field, vorticity number Wk = 0.87; effective shear strain = 3.

The potential use of flanking structures as a source of quantitative information on the flow kinematics has also been investigated. A program was developed that allows reverse modeling of natural flanking structures to determine both the initial orientation of the fracture and the far flow field. The application of this program to a number of flanking structures in the same outcrop is potentially a way to estimate flow parameters at the time of formation of the structures.

REFERENCES

• Grasemann, B. Stüwe, K., (2001). Journal of Structural Geology 23, 715-724
• Grasemann, B., Stüwe, K., Vannay, J.-C. (2003). Journal of Structural Geology 25, 19-34.
• Passchier, C.W. (2001). Journal of Structural Geology 23, 951-962

OBSERVATIONS AND DISCRETE ELEMENT MODELING OF FORCE TRANSMISSION AND SHEAR BAND FORMATION IN DEFORMED CONGLOMERATES (JIU-JIU FON, TAIWAN)

4-07

Alfredo Taboada (*), Kuo-Jen Chang (*), Jacques Malavieille (*), Farhang Radjaï (**)

(*) Laboratoire de Dynamique de la Lithosphère, UMR CNRS/UMII 5573, cc 60, Université Montpellier II, 34095 Montpellier cedex 5, France.

(**) Laboratoire de Mécanique et Genie Civil, Université Montpellier II, 34095 Montpellier cedex 5, France.

The Jiu-Jiu-Fon massif is located in the hanging wall of the Che-Lung-Pu thrust, which was activated during the 1999 Chi-Chi earthquake in Taiwan, and it exposes a thick layer of Pleistocene conglomerates showing evidences of strong tectonic deformation.

The conglomerate layer is composed of rounded rock fragments with varying sizes (polydisperse size distribution). The mean diameter of cobbles and boulders ranges roughly between 5-50 cm. The packing of particles may be considered as very dense, and the remaining pores in between the cobbles are filled with a fine element matrix composed of clay and sand. Fractured pebbles observed within large diffuse zones characterize tectonic deformation, among others. Fractures exhibit a radial pattern and propagate from points of stress concentration located along the surface of the cobbles. These points are identified as the contact points between contiguous particles, ensuring the transmission of normal and shear forces within the conglomerate layer. Most of the fractures were formed by tensile forces, which are oriented perpendicularly to the tectonic compressional forces applied at the contacts. Although the conglomerate being poorly indurated and cemented, recristallisation of minerals along the fractures suggest that tectonic deformation occurred during the early stages of consolidation of the deposit, before the cementation of the matrix was achieved. This observation suggests that a frictional non-cohesive contact law may describe the mechanical interaction between particles. Fractured pebbles often occur along continuous chains of deformed particles. Stress transmission is heterogeneous within the particle set, and chains of particles showing strong contact forces are readily identified. The direction of compression between two contiguous pebbles may change depending on the location and orientation of contact points. Contrastingly, we also observed non-deformed pebbles in contact with highly fractured elements. Low deformation indicates that the stress level in these particles was probably much lower than the mean tectonic stress.

Strain localization along narrow shear bands (10 to 50 cm) was also observed along active fault traces, which cut through the conglomerate massif. Shear bands are characterized by intense fracturation and fragmentation of pebbles, along a zone of fault breccia showing crushed rock and small angular fragments of cobbles. The contact between the cohesive conglomerate layer and the shear zone is very sharp, suggesting that the shear strength along the fault zone is much lower than in the surrounding conglomerates. Strain weakening may be linked to the absence of cohesion within the shear zone, and to the fragmentation of pebbles. The decrease in the mean size of particles along the shear zone may lead to a decrease in the macroscopic shear strength, which depends on the relative size of asperities (rock fragments).

Our observations concerning both diffuse and localized deformations in conglomerates, are analyzed by means of a discrete element method (contact dynamics). This method allows to calculate the contact forces and the shear band geometry, linked to the compressional deformation of a polydisperse layer of particles. Several characteristics of the stress and strain pattern observed in the field are studied by means of the mechanical model:

a) The heterogeneous stress field at particle scale (chains of strong forces, weak force network, variation in orientation of mean stress directions).

b) The width of shear bands as a function of the contact law between particles (friction and/or cohesion).

c) The influence of heterogeneous zones composed of smaller particles on the macroscopic shear strength.

PARALLEL-DIPPING FAULT ARRAYS AND THE GEOMETRY OF CONTINENTAL RIFTING 4-08

Thorsten J. Nagel, W. Roger Buck

Lamont-Doherty Earth Observatory of Columbia University, Palisades, NY 10964, USA

Extension of the continental crust often produces arrays of faults dipping in the same direction over large regions. Until recently the only way to simulate the development of fault systems was with physical models and one goal of such models has been to reproduce and understand sets of parallel dipping normal faults (e.g. Brun et al. 1994, Mandl 1987). We used an advanced Finite Difference Technique to study the formation and mechanics of such faults arrays.

Numerical experiments with a floating lower boundary consistently show arrangement of normal faults in Horsts-and-Grabens if deformation is distributed. We produced parallel-dipping faults only, when we used a three-layer model with a weak layer sandwiched between a strong brittle layer on top and a lower boundary that did not deform in the vertical direction. We show a series of simple experiments with a setup typical for physical experiments using sand as a brittle material (Fig.1; e.g. Brun et al. 1994): The brittle layer rests on top of a weak material. The lower boundary and the right side of the model move to the left, whereas the right boundary is fixed in the horizontal direction. Because the lower and left boundary form a fixed frame, offset accommodated along normal faults in the upper layer is transferred to the right side of the model within the weak layer. Hence, this setup forces a right lateral shear flow in the weak material. In most experiments, normal faulting initiates at the right side of the model. With progressive extension, an array of parallel faults may propagate from this site into the model (depending on material-properties and precise setup.).

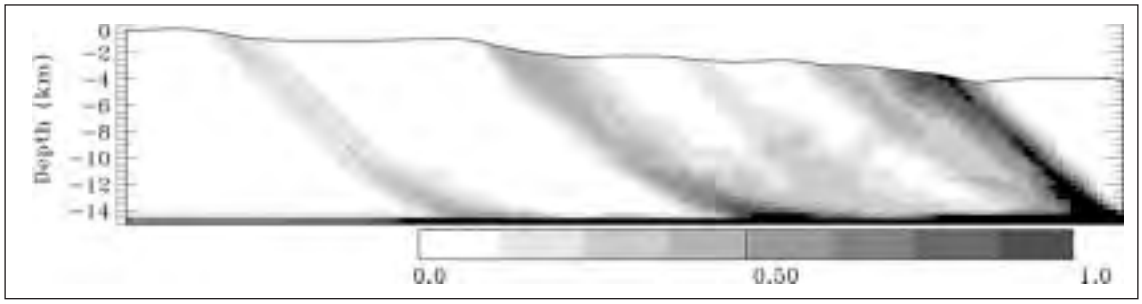

Fig.1: Strain produced in numerical experiments modeling a brittle layer (10 km thick) on top of a weak layer (5 km thick). In Fig. 1 and Fig. 2 the lower layer is modeled as a purely plastic material (a Bingham fluid with 10 MPa yield stress and zero viscosity).

The classic explanation for such parallel normal faulting is, that apart from the purely extensional stress field, an additional horizontal shear stress has to be superimposed on the system. This shear stress would deflect stress orientations and make one set of normal faults kinematically favorable (Brun et al. 1994, Mandl 1987, Melosh & Williams 1989). In the used setup this additional shear stress is produced by the forced right-lateral shear flow in the weak layer (Fig. 1). We propose a new idea, that the resistance of the weak layer to vertical motions of the brittle layer is an essential factor for the formation of parallel-dipping normal faults.

Using a linear viscous material as a weak layer results in well-developed parallel faults only within a relatively small parameter window (with layer-thicknesses, viscosity, strain rate, and fault weakening parameters as variables and with this particular kinematic boundary conditions). A high viscous lower layer (>1e21 Ps) does not allow for distributed collapse in the brittle layer and leads to localized deformation at the right side of the model. A low viscosity layer (<1E20 Ps) completely decouples the brittle layer from the rigid lower boundary. Therefore, extension often occurs in a Horst-and Graben-geometry or may even be localized, if the weak material can easily flow towards the site of deformation. The parameter-window is considerably larger, if (i) the viscous material has a yield, i.e. a Bingham-material is used (Fig.1) or (ii) the viscosity of the weak layer diminishes with strain.

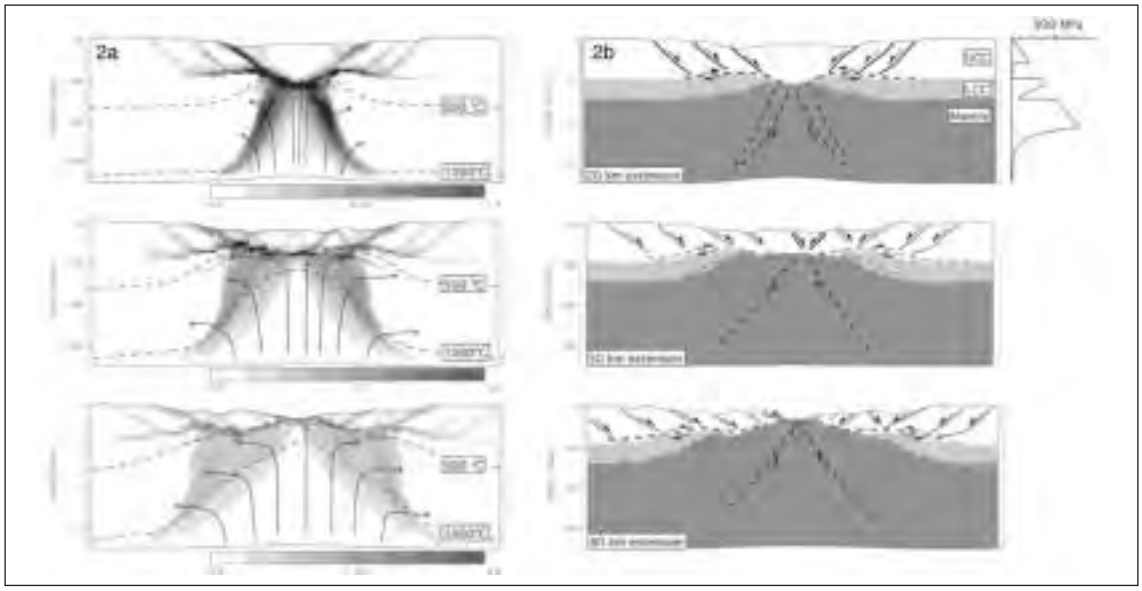

Fig.2: Rifting-model after 25, 60, and 100 km of extension. Upper crust follows Mohr-Coulomb-criterion in the upper 12 km and is purely plastic below. Lower crust and mantle follow thermally activated power-laws for diabase and olivine. 2a: Code denotes total strain (viscous and brittle). Dashed lines indicate 500ºC and 1000ºC isotherm respectively. Arrows indicate flow paths in the mantle. 2b: Upper crust, lower crust, and mantle during deformation. Labels and codes are same as in Fig. 1. Black lines indicate active, grey lines abandoned high strain zones. Solid lines mark brittle, dashed lines ductile deformation. Thick dashed line highlights high strain zone in the weak mid-crustal layer.

Based on these results we developed more complex models describing continental rifting and breakup. Our models reproduce the three major characteristics of magma-poor rifted margins, such as the Iberian Margin or the Apulian Margin, now exposed in the Alps (Fig.2). These characteristics are: (i) Upper crust rests directly on top of exhumed mantle on both sides of the rift. Significant amounts of lower crust only appear a few tens of kilometers away from the tip of the continent. (ii) The upper crust is defined by an oceanward dipping fault array and tilted blocks. (iii) A prominent sub-horizontal ductile high strain zone with top-to-the-ocean shear sense, the s-reflector, is present at the base of the upper crust.

Our models have a particular horizontal and vertical stratification. We assume a middle crust, that is considerable weaker than the lower crust. The lower crust is relatively strong and therefore mechanically coupled to the upper mantle. The calculation also starts with a predefined thermal anomaly in the rift center that represents a horizontal weakness in the lower lithosphere.

Extension of the deeper lithosphere occurs through localized necking at the site of the thermal perturbation. The partly decoupled upper crust collapses over the weak middle crust into the opening rift center (Fig. 2-20 km) and comes directly on top of exhumed mantle. During this stage of rifting the weak middle crust acts as a subhorizontal top-to-the rift-center shear zone. In a later stage, the mid-crustal shear zone is abandoned and deformation in entirely localized in the rift center (Fig. 2-50 km). New steep normal faults exhume the mid-crustal shear zone to the surface. In the final stage (Fig. 2-80 km) the mantle is exposed at the surface and further extension is extremely localized in the rift-center leaving behind a tectonically quiet margin.

Recent petrographic studies (Münterer et al. 2000) have shown, that the lower crust of the Apulian margin was (i) compositionally different than the typical upper crust and (ii) relatively cold and therefore strong at the onset of rifting. A thermal anomaly may not be present at the onset of rifting. However, once deformation localizes, a thermal perturbation at this site starts growing and a run-away-effect initiates. Extensional structures associated with early continental rifting are commonly distributed over tens to hundreds of kilometers parallel to the extension direction. The parallel-dipping fault array typically associated with strong thinning of the continental crust within the last 50 km of

the margin may reflect a transition from non-localized to localized deformation in the deeper lithosphere. The mentioned observations have been used to infer asymmetric rifting at these margins (e.g. Manatschal & Bernoulli 1999). Our model is symmetric at a lithospheric scale. The parallel-dipping fault array on top of mantle rocks represent a collapse structure found on both sides of the rift center (Brun & Beslier 1996).

REFERENCES

- Brun, J.-P., Sokoutis, D., & Van den Driessche, J., Analogue modelling of detachment fault systems, Geology, 22, 319-322, 1994.
- Brun, J. P., Beslier, M. O., Mantle exhumation at passive margins, Earth Planet. Sci. Lett. 142, 162-173, 1996.
- Manatschal, G., & Bernoulli, D., Architecture and tectonic evolution of nonvolcanic margins: presentday Galicia and ancient Adria, Tectonics, 18, 1099-1199, 1999.
- Mandl, G., Tectonic deformation by rotating parallel faults – the bookshelf mechanism, Tectonophysics, 141, 277-319, 1987.
- Melosh, H.J., & Williams, C.A., Mechanics of Graben formation in crustal rocks – a finite element analysis, J Geophys Res, 94, 13961-13973, 1989.
- Münterer, O., Hermann, J. & Trommsdorff, V., Cooling history and exhumation of lower-crustal granulite and upper mantle (Malenco, eastern central Alps). J. Petrol., 41, 175-200, 2000.

FRACTURES DEVELOPMENT IN SANDBOX MODELS 4-09

A. Ravaglia, S. Seno

Dipartimento di Scienze della Terra – Università di Pavia, via Ferrata 1 – 27100 PAVIA Italy

Summary

Fractures development is an interesting issue to study by means of laboratory analogue models. Here we attempt to simulate fracturing in sandbox experiments of compressional non-cylindrical structures, analysing the influence of the basal friction. Type 2 fractures (Stearns, 1967) developed in the cylindrical areas of the model, irrespectively of the basal friction. A wrench system formed in the non-cylindrical areas, with different characteristics related to the basal frictions.

Introduction

Fracture and faults are structural heterogeneities/discontinuities that affects brittle rock units. Fractures formed in association with folds may be the results of the regional stress field or of the local stresses generated as a result of folding. In sedimentary rocks, fractures nomenclature depends on the orientation of local structures, most commonly the fold axis. Stearns (1967) pointed out the folded sediments may have four fracture sets (types). Each set may consist of up to three fractures: an extension fracture and conjugate shear fractures. Conjugate shears form so that the acute angle between the shears faces $\sigma 1$. Each of the sets has no particular name; however, the extension fractures may be referred to as either cross joint (i.e. that group of joints perpendicular to the fold axis) or a strike joint (i.e. that group of joints parallel to the fold axis). Fractures origin and development is the object of a number of studies. Several works have aimed in the prediction of fractures orientation, distribution and density by means of numerical simulations, by using fault-bend, fault-propagation folding theory or curvature analysis (Narr, 1991; Lisle, 1994; Fisher and Wilkerson, 2000 among others). Not many works have attempted to simulate and analysed the development of fracturing in laboratory analogue models; recently, Mansfield and Cartwright (2001) studied growth and evolution of faults/fractures by means of extensional clay models. In particular, they analysed the lateral growth and displacement of extensional faults and their linking attitudes.

In this work, we attempted to simulate and analyse the pattern of fractures that develops in a sandbox analogue model. Usually, the small dimensions of fractures do not allow their generation in scaled sand models. We tested two different stratigraphies shortened in a box with rigid obstacles and indenters. The initial constraints are designed to produce non-cylindrical structures.

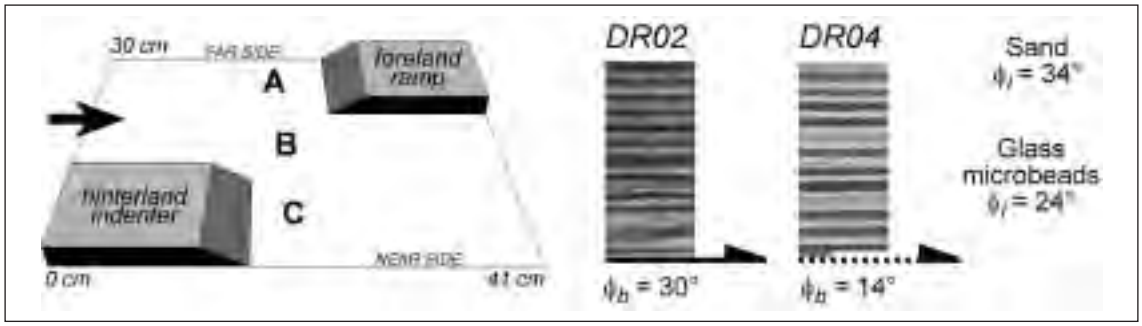

Fig. 1 – Sketch of the experimental rig and the two synthetic stratigraphies used in the modelling. Physical parameters of the analogue materials are indicated. Different domains are labelled A, B and C. ϕ_i= angle of internal friction. ϕ_b= angle of basal friction.

Experimental set up

In the modelling apparatus (Fig. 1), we placed a rigid footwall ramp in the foreland far side of the box; in the hinterland and near side of the box, a similar ramp was attached at the backstop, and moved as an indenter. Both ramp and indenter were 2.5 cm thick and 10 cm wide. As such, three distinctive domains along dip have been partitioned. Every model was 5 cm high, 41 cm long and 30 cm wide. We used two granular materials as rocks analogue: dry cohesionless quartz sand of different colours with a grain size of 100-300 μm, an internal friction angle of about ϕ_i= 33° (μ = 0.65) and a bulk density of 1.44 g/cm^3; and glass microbeads with a grain size of 300-400 μm, a bulk density of 1.6 g/cm^3 and an internal friction angle of ϕ_i= 24° (μ = 0.45). In the experiment DR02, a homogeneous stratigraphy made of sand only rested upon the basal detachment, having a basal friction angle ϕ_b=30°, while in the experiment DR04 we placed a glass microbead layer at the base of the stratigraphy, having a basal friction angle ϕ_b= 14°. We sieved a fine-grained brittle material (powder like) over the surface of the models. Because of its fine grain size, such material is able to reproduce (and easily visualize) small dimension structures, such as extensional and shear joints, without meddle in the deformation mechanism. The black squared grid on the surface of the models was 2 cm. The outline both of the hinterland indenter and of the foreland ramp has been drawn on each map. The shortening was from the left to the right. The final shortening was around 28%.

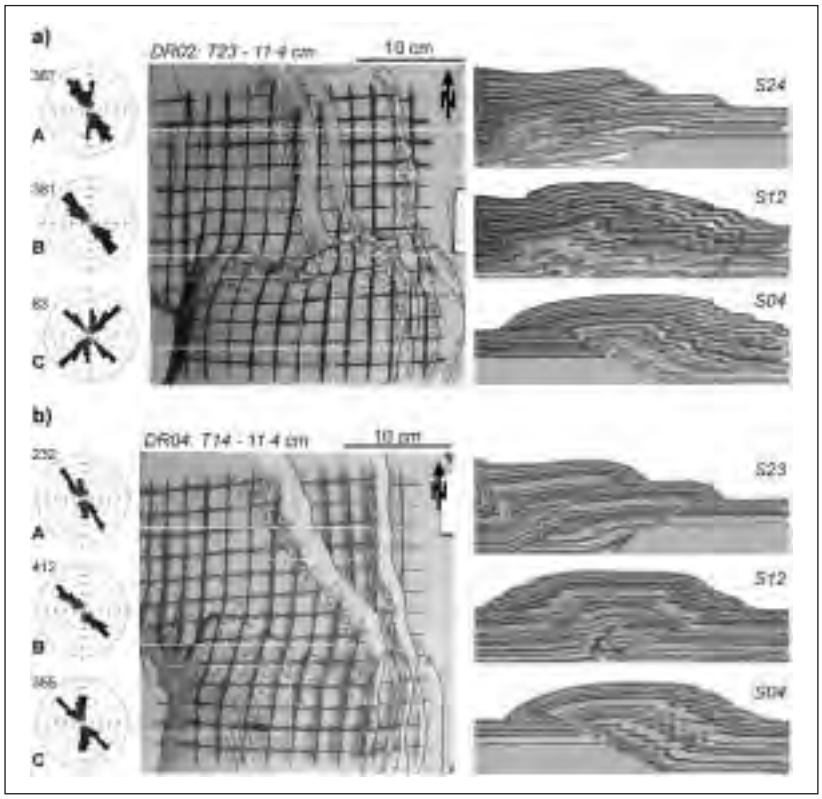

Fig. 2 - Final map views of each experiment, with the interpreted pattern of fractures and three cross sections cut in different domains. The rose diagrams on the left represent the counting and azimuth directions of fractures in each of the three domains. (a) Model DR02, high basal friction; (b) model DR04, low basal friction.

Results

Here we intend to only describe the pattern of fracture developed, omitting faults and folds interpretation.

In the high basal friction model DR02 (Fig. 2a) two lateral and almost cylindrical domains (A and C) are connected by a more complex transfer zone domain (B). In the lateral domains, at least three sets of fractures have been recognized. An extensional set on fold forelimbs, sub-parallel to thrust fronts or with slight deviations. Where thrust fronts are curved because of the side effect, the extensional set deviates as well. Two less developed sets of fractures, interpreted as shear fractures, are oblique with respect to thrust fronts, and strike 25°-30° and 140°-150°.

In the central domain B, a very complex transfer zone developed. Here, extensional, shear and hybrid fractures simultaneously occurred. A well-developed dextral shear zone took place across the border with C domain. Such wrench zone has a clear uplift and results in a high topography. The shear zone is around 6.3 cm wide and characterized by shear fractures and tension gashes. In particular, the following sets can be distinguished: synthetic R has a dextral shear and strikes 113° on average. The trace lengths are from 1.3 to 8 cm and the measured displacement is from 0.17 to 0.55 cm. In cross section (Fig. 2a, S12) they seem to be 2.3 cm high. They are seven, at least. Tension gashes, TG, are greatly developed. They strike 142° on average, they are arranged en échelon and confined within the R system. Fractures show clear apertures, from 0.03 to 0.14 cm, but do not display shear movement, also because of their little size. A P system is slightly formed and striking 90°. In the indenter C domain, fractures are less developed but are arranged similarly to the A domain.

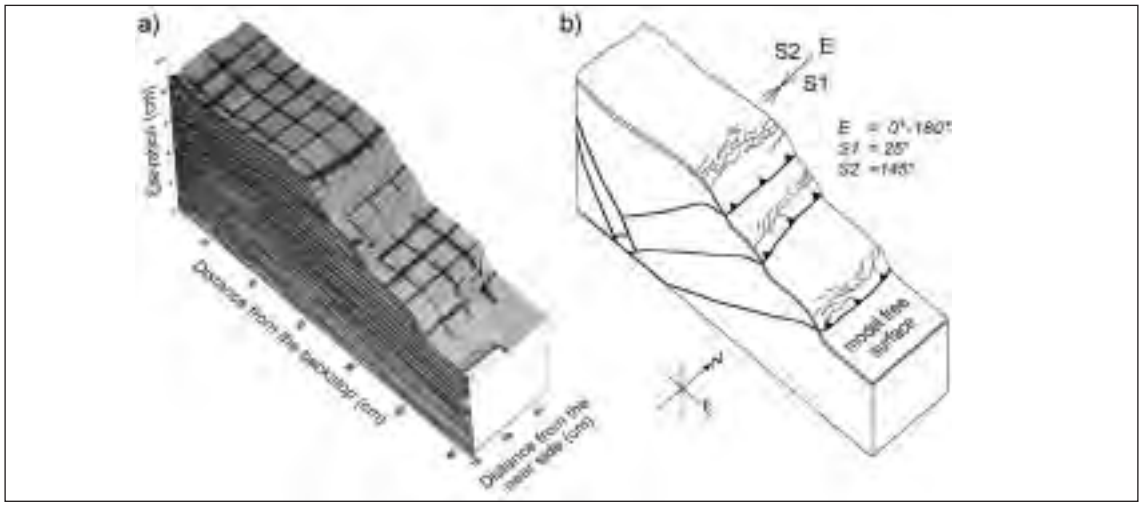

Fig. 3 - Fold-related fractures developed in model DR02, between domains A and B. (a) Block diagram of a portion of the model; (b) Line drawing of the fold-related Type 2 fractures (E + S1 + S2) developed on the short thrust forelimbs. Type 2 fractures are elongated and parallel to the fold hinges. E: extensional fracture; S: shear fracture. Azimuth is indicated.

In the low basal friction model DR04 (Fig. 2b), most of the fractures in the A domain are of the same set of previous model and are oriented parallel to the thrust fronts. The predominant sets of fractures in the B domain strike NW. The R system developed at 120°, with scattered direction. A poorly developed dextral shear zone formed across the border with C domain. In the C domain, a great deal of extensional joints formed across the internal limb of the fold, but globally the similar sets of the A domain.

Discussion

In both cylindrical domains (A and C), fold-related fractures seem to occur (Fig. 3). As an example, in model DR02, three sets of fracture developed in domain A; an extensional set parallel to fold hinges and two shear sets that form at about 25° to the extensional set. Indeed, shear fractures are not clearly interpretable. All three sets are interpreted as Type 2 fractures of Stearns. Type 2 fractures occur in

natural fold and have their σ2 perpendicular to the bedding surface. The three sets developed in a swarm of small fractures. A close inspection reveals that what appear as a single discontinuity in reality are short segments of all the three sets connected one another.
The system of fractures developed in the transfer zone in every model is easily amenable to a Riedel system formed in a dextral brittle shear zone (Fig. 2a). In the high basal friction model DR02 (Fig 4), such system is more developed. R synthetic shear are the longest features and clearly defined. Extensional fractures developed within the R system. Few P shear also occur. In low basal friction model, the wrench system is far less developed (Fig. 2b); the disturbed area is wider than in the previous model. The dextral shear is ascribed to the opposite relative movement between the fore thrusts in the A (and partially B domains) and the backthrust growing over the rigid indenter in the C domain (Fig. 2). Such along strike differential movement displayed distinctive degrees of deformation in each experiment.

Fig. 4 - Fault-related fractures developed in model DR02 (a), between domains B and C. Black squared grid is 2 cm. (b) Line drawing of interpreted fractures. (c) Sketch of the interpreted Riedel system, showing a dextral shear with an azimuth of 100°. TF: thrust fault; R: synthetic shear; P: low angle synthetic shear; TG: tension gashes.

Limitations

Because of the reduced fractures scale and due to the modelling technique, many limitations need to be considered. From a genetic perspective, in our models fractures are of tectonic origin (Nelson, 1985). According to such classification, in the lateral domains only fold-related fractures developed, whereas in the transfer zone central domain both fault- and fold-related fractures formed. Concerning fold-related fractures, only Stearns' Type 2 sets of fractures seem to develop. Because of the homogeneous stratigraphy adopted, no interlayer slip occurred in the models. As a consequence, Type 1 and Type 3 (generated mainly by interlayer slip) are absent.
Moreover, we do not reproduce stylolite or compaction bands. We do not replicate contractional, regional and surface-related fractures (Nelson, 1985). Because of the absence of any fluid flowing in the models, all fractures developed have no kind of mineralization. Only spot information can be locally gained concerning the fractures vertical dimension and their possible extension at "depth". No correlation can be defined between the layers thickness under deformation and the fractures occurrence across the model volume.

Conclusions

Despite the great simplifications and the technical limitations, interesting indications resulted from this experimental study. The comparison amongst the experiments shows that: in the transfer zone, mechanical stratigraphy plays a fundamental role in controlling deformation partitioning. The high basal friction accounted for a narrower transfer zone with a well-developed Riedel brittle shear zone. A dextral brittle shear zone always occurred in the transfer zone close to the border between B and C domains. Type 2 fractures developed in fold forelimb of the cylindrical domains and are related to the small curvatures of the surfaces. The greatest number of fractures always formed in the transfer zone domain B. Shear fractures occurred almost everywhere, but are widely distributed in the transfer zone domain B.

REFERENCES

• Fischer M.P. and Wilkerson M.S.; 2000: Predicting the orientation of joints from fold shape: results of pseudo-three dimensional modeling and curvature analysis. Geol., 28, 15-18.

- Lisle R.J.; 1994: Detection of zones of abnormal strains in structures using Gaussian curvature analysis. Am. Ass. Petrol. Geol. Bull., 78, 1811-1819.
- Mansfield C. and Cartwright J.; 2001: Fault growth by linkage: observation and implications from analogue models. J. Struct. Geol., 23, 745-763.
- Narr W.; 1991: Fracture density in the deep subsurface: techniques with applications to Point Arguello oil field. Am. Ass. Petrol. Geol. Bull., 75, 1300-1323.
- Nelson R.A.; 1985: Geological analysis of naturally fractured reservoirs. Houston, Gulf Publishing, 320 pp.
- Stearns D.W.; 1967: Certain aspects of fracture in naturally deformed rocks. In: Riecker, R.E. (Ed.), Rock Mechanics Seminar. US Air Force Cambridge Research Laboratories, contribution AD 669375, pp. 97-118.

A SCALING ANALYSIS OF THE LOCALIZATION PROCESSES IN BRITTLE-DUCTILE EXPERIMENTS

4-10

S. Schueller, P. Davy

Géosciences Rennes, UMR 6118/CNRS, Université de Rennes 1, France
sylvie.schueller@univ-rennes1.fr

Summary

In this paper, we aim at analyzing fault mechanisms that eventually lead to large-scale localization in brittle-ductile systems. The work is motivated both by bringing new highlights on the basic physics of such complex multi-scale phenomenon, and by having a better understanding of lithosphere deformation in continental collision. The experiments were built with the classical sand/silicone/honey sandwich horizontally shortened with two free lateral boundaries. Deformation results in the development of two main conjugate shear zones whose stress regime (compressional, wrenching or extensional) depends on the gravity balance between the sand/silicone sandwich and the confining honey. The eventual fault and deformation patterns are primarily dependent on a dimensionless ratio Γ, which quantifies the strength ratio between brittle and ductile layers. Γ is a function of the compression velocity, silicone viscosity, layer thicknesses and densities. Γ was found to well quantify the main transition between a pure ductile regime where no large fault develops, to a pure-brittle regime where localization takes place in a few very large faults. In between ($0.5<\Gamma<10$), faults organize in a complex multi-scale pattern that progressively leads to large-scale localization in two main conjugate shear bands densely fractured.

A fine analysis of the deformation field was achieved to precise the very nature of the localization process. Thanks to high-resolution measures of displacement, a scaling analysis of the average deformation intensity was performed to highlight the coalescence of locally deformed zone into a large-scale structure. This analysis reveals two additional modes of localization in the intermediate brittle regime ($0.5<\Gamma<10$), which differs in the scaling of the mean deformation intensity at small scales: a "ductile-but-localizing" regime where the deformation intensity becomes scale-independent at small scales, and a "brittle" regime where the deformation intensity increases continuously when decreasing scale. The latter regime directly addresses the issue of the homogenization of local heterogeneities since the basic notion of mean deformation is not univocally defined. In the former regime, the viscosity of the underlying ductile layer introduces a correlation length scale below which strain heterogeneities are smoothed. Localization occurs from structures whose size is large enough to become insensitive to viscosity effects. The large-scale localization rate is a function of Γ.

Introduction

Understanding how faults participate to large-scale localization is a classical but still active issue of lithosphere mechanics. From a mechanical point of view, the importance of faulting in the deformation process of "large-scale" mechanical systems, remains open [*Davy et al.*, 1995]. Indeed, the coexistence of strongly contrasting deformation micro-mechanisms, from brittle solids to non-Newtonian ductile fluids, the role of gravity, and the process of heat transfer, leave the question of large-scale behavior open, and beyond the scope of even the most sophisticated modeling. For instance, it remains unclear whether such a complex mechanical system can localize deformation at the largest scale in the continental lithosphere while it does at the local scale.

In this paper, we aim particularly at defining the basic deformation modes, i.e. the fundamental relationship between the local scale (faults) and the large-scale localization. This scaling issue is also motivated by the acknowledgement that geological fault networks appear to have a fractal organization and power-law length distribution, two scaling properties that reveal multiscale interactions between faults that attempt to grow.
We present sandbox experiments that have been designed to model geological deformation. These experiments used the ability of dry granular sand to localize the deformation in very narrow shear bands, a phenomenon that was extensively studied as an example of mechanical bifurcation. The shear zone patterns resemble natural fault zones, and share with them similar statistical properties.

Experimental method

Model set-up

The experiments are built with the classical sand/silicone/honey sandwich (cf. fig. 1) that is supposed to contain the prevailing mechanical properties for the continental lithosphere, that is the brittle/ductile layering, and the contribution of gravity forces to the stress balance. The upper brittle crust is modeled by a dry sand layer, which behaves as a cohesionless Coulomb material. The ductile lithosphere layers are replaced by a Newtonian silicone. A honey bath provides the underlying isostatic pressure as the asthenosphere does for the continental lithosphere. Details of the experimental technique including governing equations, rheological parameters and lithosphere analogy can be found in [*Davy and Cobbold*, 1991]. These lithosphere-like experiments are submitted to a uni-axial compression with two friction-free borders. Deformation basically results in the formation of two conjugate shear bands (cf. fig.1) that deform both sand and silicone layers.

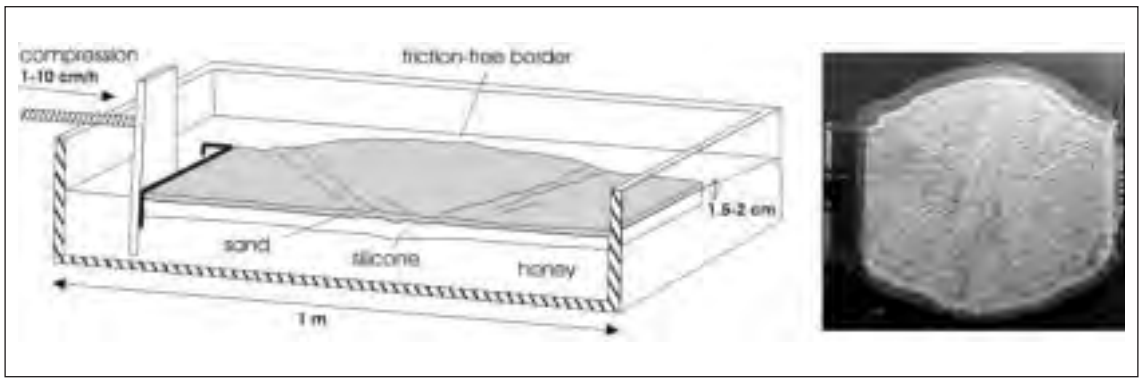

Figure 1: Half experimental set-up and top view of an experiment after 25% shortening.

A large number of experiments were performed by changing the size of the initial cake (length, width and layer thickness), the boundary conditions (compression velocity, shape of the indenter, number of friction free borders), and the mechanical parameters (density, silicone viscosity). About 80 experiments of that kind have been made for 15 years in the tectonic laboratory of the university of Rennes, with a large range of resulting deformation. This unique set of experiments is described in [*Schueller and Davy*, in prep].

Measurements

To analyze in detail the deformation, top view pictures were taken every 0.1% of bulk deformation. Incremental displacement fields are then calculated for a shortening of 0.5% by using a commercial software for advanced deformation measurement. It detects the local displacements of markers by a correlation analysis of pairs of digital images. We can obtain a data point density of approximately 4 per cm^2 and the accuracy on displacement is less than 0.3 mm. Strain intensity (second invariant of the stress tensor), rotation or area variation fields are calculated from these displacement fields. The figure 2 presents incremental strain intensity fields at different stages.

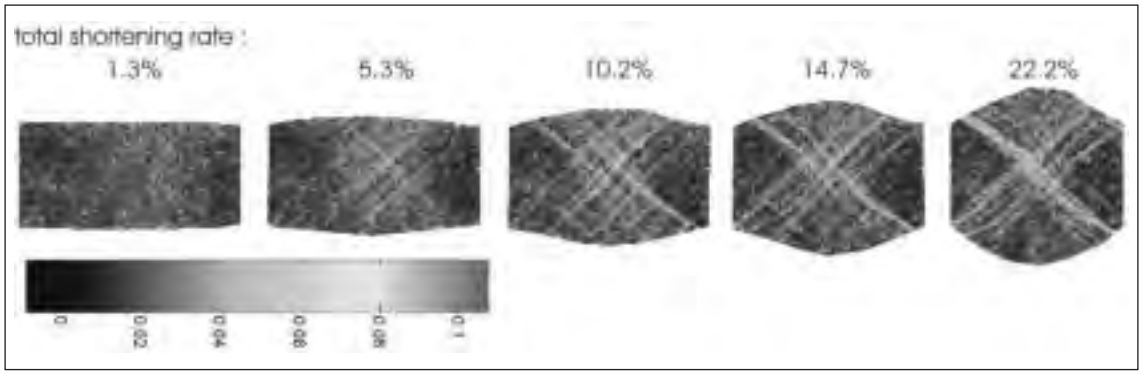

Figure 2: Evolution of the incremental strain intensity field according to the total shortening rate.

The observed modes of deformation

The experiment presented in figures 1 and 2 is an example of the variety of resulting deformation that was obtained when varying rheological parameters. The complete set of about 80 experiments is described in another paper still in preparation [*Schueller and Davy*, in prep]. We could classify all the experiments according to two dimensionless parameters: the brittle/ductile ratio Γ [*Bonnet,* 1997] and the Argand number Ar [*England and McKenzie,* 1982]. Ar is the ratio between gravity and the total material strength. It fixes the deformation regime that is the predominant existence of compressive or extensive structures. In systems with large gravity forces (i.e. light crust), extensive structures are prevailing. On the contrary, small gravity forces favor the existence of compressive structures in associations with the strike-slip faults. Γ expresses the strength ratio between brittle and ductile layers. It controls the nature of localization. For experiments whose rheology is almost entirely brittle, deformation is strongly localized in a few large faults. On the contrary, if ductile layers are mechanically prevailing, deformation is diffuse with no large fault.
An interesting result is that these two effects are nearly independent, meaning that the localization process is not or only slightly affected by gravity forces. The transition between non-localization and localization is obtained when Γ is around 0.5 whatever Ar.

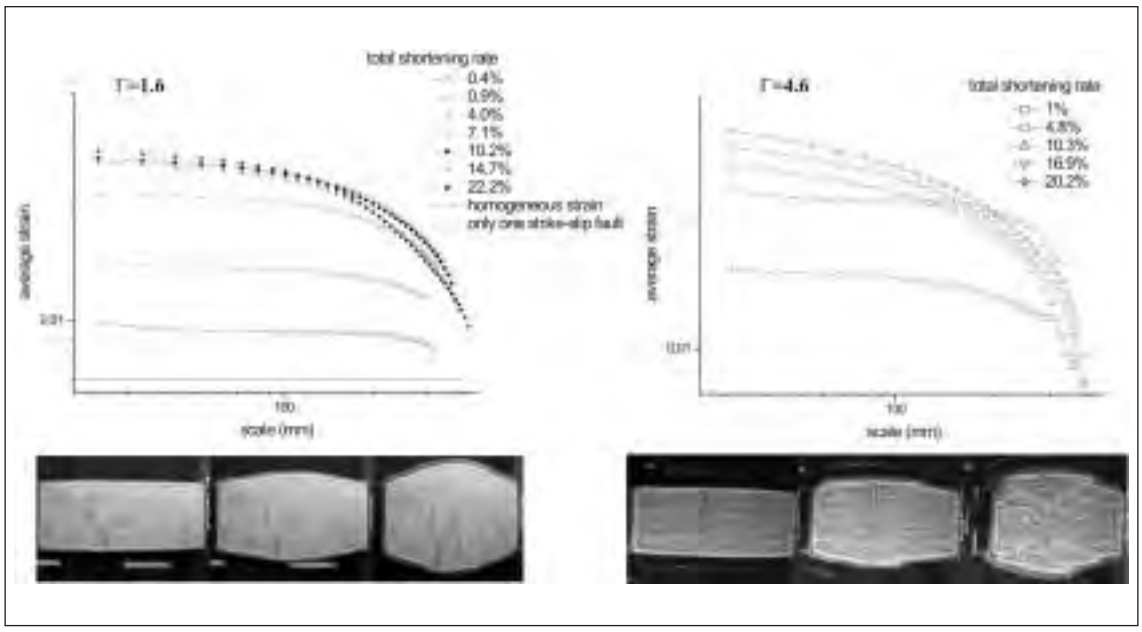

Figure 3: Evolution of the average strain with scale for different shortening rate (left: Γ=1.6, right: Γ= 4.6). Below: top views of the experiments for a total shortening rate of 1, 10 and 20%.

Scaling analysis of the deformation field

By analyzing the spatial correlation of strain field, we aim at defining correlation lengths and/or upscaling exponents that could be fundamental characteristics of strain field. Here we define "strain" as the equivalent strain tensor that would fit the measured displacement gradients over a certain scale. This classical definition emphasizes that strain is a scale-dependent measure, and that it can be used as a measure of the displacement correlation over a certain scale. In fact, we use the strain intensity, i.e. the second invariant of the stain tensor, as a scalar measure for defining the correlation function. To analyze scaling effects, we calculated the average strain intensity at different scales over the central part of experiment.

Experiments with small brittle/ductile strength ratio (Γ<3)

Figure 3 (left) presents the results for the experiment presented in fig. 1 and characterized by Ar~1.1 and Γ~1.6. This result is representative of all experiments for Γ<3. Lines with symbols correspond to the evolution of average strain with increasing scale at various shortening rate, the solid line would represent the experiment in which the strain applied at the boundaries is homogeneously distributed all over the experiment area and the doted line represents the case where all the strain is localized on a single strike-slip fault (displacement along the fault corresponds to the incremental displacement of the indenter).

At large scales, all the curves join in a unique curve where the average strain depends exponentially on scale. The characteristic length scale of this exponential function corresponds to the actual deformed size of the system. At small scales, the average deformation tends to a scale-independent value ε^*, which is significantly larger than the applied deformation. ε^* can be considered as the actual deformation; it defines a typical size for the actual deformation area, L^*, which the ratio between the incremental boundary displacement and ε^*. During localization, L^* decreases (ε^* increases) at a rate that depends on the brittle/ductile ratio Γ; the larger Γ is, the faster this decrease of L^* with applied deformation is (cf. fig. 4). The decrease of L^* quantifies the deformation localization; the dependency on Γ emphasizes the mechanical control exerted by the ductile layer on localization. At large shortening, ε^* reaches a plateau rendering the end of the localization process. The fact that the plateau value is about independent of the brittle-ductile ratio Γ emphasizes a control of the final stage by the boundary conditions rather than by rheology.

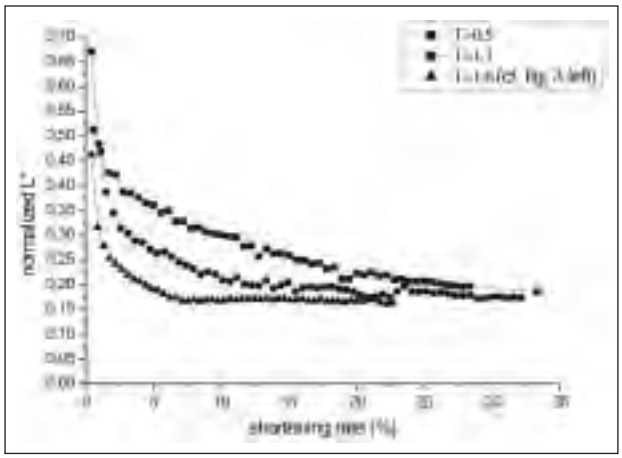

Figure 4: Evolution of the typical size L* (normalized by the initial length of the model) according to the total shortening rate, for experiments with different Γ.

Experiments with large brittle/ductile strength ratio (Γ>3)

When Γ is larger than 3, deformation eventually localizes in a few large faults. We have not performed yet a lot of experiments of that kind, but the preliminary results show that the localization process differs significantly from the one described in the previous paragraph. Indeed the mean deformation intensity is continuously varying when decreasing scale, at least down to the resolution scale of this study (cf. fig. 3 right). This characteristic implies that the mean deformation cannot be univocally defined, because strain fluctuations exist at all scales without any limit. The decrease of the deformation intensity with scale quantifies the upscaling of these strain fluctuations. Even if we do not have enough data to fully characterize the up scaling process, it seems that the average strain scales as a power law with an exponent of about – 0.12. This would correspond to the long-range fractal correlations that are observed on fault networks [*Bonnet et al.*, 2001] and calculated from numerically breaking assemblages of beams or springs [*Herrmann and Roux*, 1990]. We find again

that the average deformation fits an exponential law at large scales, which still emphasizes the strong control by boundary conditions.

Conclusion

A fine analysis of the deformation field was achieved on sand-silicone experiments to precise the very nature of the localization process. Thanks to high-resolution measures of displacement, a scaling analysis of the average deformation intensity was performed, that highlights the coalescence of locally deformed zone into a large-scale structure. This analysis completes the work by *Davy et al.* [1995], which describes the conditions of the transition between localizing and non-localizing experiments. The present study specifies the nature of the localization process, and reveals two fundamental regimes which differ in the scaling of the mean deformation intensity at small scales: a "ductile-but-localizing" regime where the deformation intensity becomes scale-independent at small scales, and a "brittle" regime where the deformation intensity increases continuously when decreasing scale. In the former regime, the localization rate is controlled by the brittle-ductile coupling: the larger the viscous forces are, the slower the localization is, with respect to applied shortening. In the latter regime, the basic notion of mean deformation is not univocally defined because of the observed scaling, which directly addresses the issue of the homogenization of local heterogeneities.

REFERENCES

- Bonnet (1997), Mémoires de Géosciences n°83, 183 p.
- Bonnet et al. (2001), Reviews of geophysics, 39,3, 347-383.
- Davy and Cobbold (1991), Tectonophysics, 188, 1-25.
- Davy et al. (1995), Journal of Geophysical Research, 100, B4, 6281-6294.
- England and McKenzie (1982), Geophysical Journal of the Royal Astronomical Society, 70, 295-321.
- Hermann and Roux (1990), Statistical models for the fracture of disordered media, In: Stanley and Guyon, Random material and processes, 353 p.

INCORPORATION OF FAULT ZONES AS VOLUMES IN RESERVOIR MODELS 4-11

J. Tveranger, T. Skar, A. Braathen

Centre of Integrated Petroleum Research, University of Bergen, Allegt. 41, 5007 Bergen, Norway

Summary

The conventional way of representing faults in reservoir models is as displacements of the model grid along planes. The impact of fault features on fluid flow in simulation models is normally only included in the shape of transmissibility multipliers attached to these planes. These modifiers are derived either from history matching of wells or by using specialized *ad hoc* applications (HAVANA, TransGen, FaultMult etc.). In other words, faults and fault features in reservoir models are described in an oversimplified way considering the fact that the impact of faults is not limited to discrete planes but affects whole volumes of the host rock. The objective of this paper is to describe an approach that allows faults to be modelled as finite volumes. The main advantages of treating faults as volumes are (1) the 3D distribution of rocks with tectonically modified petrophysical properties can be captured, (2) intra-fault fluid flow can be incorporated, and 3) it will allow more precise volumetric estimates of in-place hydrocarbon volumes in faulted reservoirs. Preliminary modelling results show that the tectonically induced permeability anisotropy within the central fault core and damage zones strongly controls the flow path within the fault zone illustrating the importance of modelling fault zones as 3D volumes.

Abstract text

Over the last ten years, three-dimensional modelling has become the standard way of compiling, synthesizing, presenting and manipulating geological, geophysical and engineering data. It has proven an invaluable tool for arriving at a better understanding of reservoir dynamics and the effect of

sedimentary architectures and property distributions on flow. Traditionally these tools emphasize the impact of sedimentological features over structural ones for two reasons: 1) most geologists involved in reservoir modelling were sedimentologists and 2) reservoir simulators are not designed to incorporate faults. Although the capabilities of modelling programs have improved significantly over the years, tectonic features are still modelled in a very simplified way: as planes and curved surfaces offsetting the modelled grids.

The need for capturing effects caused by tectonic deformation, i.e. changed petrophysical properties of host rock lithologies was recognized in the petroleum industry, and a number of specialized applications for modelling fault properties and fault transmissibility multipliers were developed in the early 90's. However, these tools and fault seal calculations derived from them are not an integral part of the standard workflow. In practice, most reservoir engineers still claim their right to 'guesstimate' the transmissibility multipliers – based on history matching rather than deriving them from geological data.

The concepts and technical solutions chosen for these ad-hoc applications were restricted by already established modelling conventions, such as the practice of representing faults as planes in modelling grids. These tools are able to capture effects caused by fault offset along a plane and assigning transmissibility values across fault planes as a function of parameters such as fault throw and host rock lithology. However, most existing specialized fault modelling tools and the reservoir modelling software they are linked to fail to capture the fact that faults zones represent three dimensional rock bodies where the petrophysical properties of a volume of host rock has been changed as a function of strain. It follows that current 3D modelling techniques and tools fail to incorporate the full impact of tectonic deformation of host-rock petrophysical properties and thus its effect on fluid flow in faulted reservoirs.

There are a number of important fault zone features that are not properly captured in existing simulation models. One example is two-phase flow properties. It is the combination of the cumulative thickness of the fault rock, pore size, pore-wetting fluid, and the interfacial tension between fluids that will determine the flow rates within the fault zone (Sverdrup et al. 2003). Whether or not hydrocarbons can move across a fault structure is also strongly dependent on the pressure gradient across the complete structure and not only the pressure difference on each side of the structure (Hesthammer et al. 2002). This picture is complicated by variations in strain distribution as faults typically overlap both vertically and horizontally (relay structures). What appears from a seismic section as a single fault structure will typically comprise several faults with more complicated geometries and tectonically induced petrophysical heterogeneities (Hesthammer and Fossen 2000).

Considering the fact that most petroleum reservoirs include faults with a proven, but in most cases poorly understood, influence on fluid flow, we consider the present way of including tectonic features in reservoir modelling as inadequate to understand reservoir behavior. Presently there are no standard methods to generate grids that accommodate 3D fault rock volumes. However, recent studies performed by CIPR (Berg et al. 2004, Skar et al. submitted) using the in-house simulation tool ATHENA, show the feasibility of the concept. The work focuses on designing grids that can be used in existing modelling and simulation tools (i.e. IRAP-RMS and ECLIPSE, ATHENA) in order to facilitate stochastic modelling of fault properties and simulation testing of these without having to build new modelling tools.

The objective of this work is to assess the importance of fault features influencing the petrophysical properties of a tectonically deformed host rock volume. From the literature it is well known that a fault zone consist of a fault core and a damage zone that are characterized by distinctly different permeability structure (e.g. Caine et al. 1996, Rawling et al. 2001). A fundamental assumption is that a relationship between strain and changed petrophysical properties of the host rock exists. Compilation and systematization of existing data on fault rock properties, field studies and petrophysical lab analysis of rock samples is therefore essential in order to establish relationships between petrophysical properties (i.e. porosity and permeability) of un-deformed and deformed lithologies at various degree of strain. The goal is to quantify fault properties with emphasis on defining parameter ranges, spatial distributions and probability of occurrence of deformed fault rock volumes for a given set of boundary conditions (i.e. lithology, geometry, tectonic regime, timing of

fault and diagenesis). These definitions and quantifications will form the base for 3D geological modelling.
It is the aim of this paper to describe a more realistic way of representing faults and fault properties (Fig. 1); this will ultimately allow tectonically modified rock bodies to be modelled with the same kind of precision and flexibility as sedimentary architectures are modelled at present, and allow a better understanding of fluid- and gas-flow dynamics in faulted reservoirs.

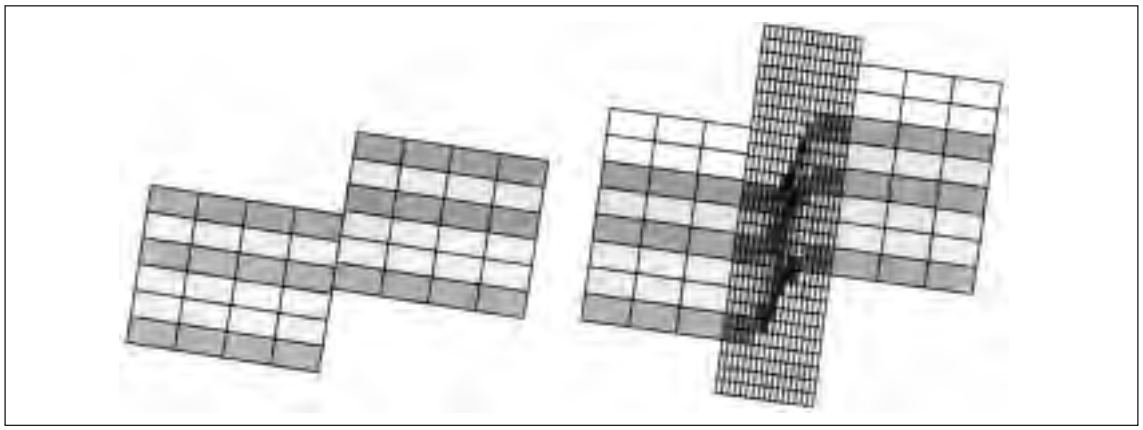

Figure 1. Simplified 2 D cross sections of 3D models illustrating the difference between conventional gridding of faults (left), where faults are only represented as planes off-setting the grid, and the gridding of a 'realistic' fault (right). The latter allows for the capture of any anisotropic petrophysical and geometrical change to the host rock caused by tectonic deformation and thus the ability to track fluid flow in three dimensions within the fault zone, and even flow out of the actural reservoir interval along the fault. The end result utilised in ECLIPSE may still be a grid of conventional type shown to the left, but with input parameters derived using a geological model with a modified grid.

REFERENCES

- Berg, S.S., Øian, E., Skar, T. and Gabrielsen, R.H. 2004: The architecture of faults and its consequence for fluid flow. Geologiska Föreningens i Stockholms Förhandlingar, 126, 61-62.
- Caine, J.S., Evans, J.P. and Forster, C.B. 1996: Fault zone architecture and permeability structure. Geology, 24, 1025-1028.
- Hesthammer, J., and Fossen, H. 2000: Uncertainties associated with fault sealing analysis. Petroleum Geoscience, 6, 37-45.
- Hesthammer, J., Bjørkum, P.A., and Watts, L.I. 2002: The effect of temperature on sealing capasity of faults in sandstone reservoirs. AAPG Bulletin, 86, 1733-1751.
- Rawling, G.C., Goodwin, L.B. and Wilson, J.L. 2001: Internal architecture, permeability structure, and hydrologic significance of contrasting fault-zone types. Geology, 29, 43-46.
- Skar, T., Berg, S.S., Braathen, A., Gabrielsen, R.H., Garrido, I. and Øian. E., submitted: Fluid flow in faults – modelling with the Athena simulator. EAGE Conference proceedings – Fault Seal and Top Seal, September 2003, Montpellier.
- Sverdrup, E., Helgesen, J. and Vold, J., 2003: Sealing properties of faults and their influence Water-alternating-gas (WAG) injection efficiency in the Snorre Field, northern North Sea. AAPG Bulletin, 87, 1437-1458.

STRUCTURAL ANALYSIS AND MODELING IN EXPLORATION AND PRODUCTION: AN OVERVIEW 4-12

John R. Tabor (*)

(*) Shell International Exploration and Production, Inc., Exploration and Technology Research and Applications, Houston, TX., USA.

Summary

Structural analysis is an essential component of the exploration and production (E+P) workflow. It has evolved from simple map-based trap analysis of the past into a rigorous and integrated model-based workflow encompassing a wide array of data sets, technologies and competencies (e.g. 3D volume interpretation and structural-framework modeling, fault seal and transmissibility analysis, 2D/3D

kinematic and finite-element restoration, and outcrop and core analysis and characterization of fractures).

Volume interpretation and structural-framework modeling integrate visualization, seismic interpretation, and fault-horizon modeling to construct a fault-horizon model of 3-D surfaces. During structural-framework modeling, 3-D models of fault networks, reservoir surfaces and reservoir-fault intersections (fault polygons) are generated during seismic interpretation. The structural validity and consistency inherent in these 3-D models greatly facilitates and streamlines the construction of geologic models, eliminating seismic reinterpretation and grid editing. Fault grids are created, preferably in batch-mode, and assembled into a fault framework within which stratigraphic horizons are modeled. Fault polygons (or horizon cutoffs) are generated, also preferably in batch-mode, at the fault-horizon intersections, in effect producing field-wide networks of 3-D fault-plane profiles. Structural complexity incorporated into the models is only constrained by the quality of the seismic data. The combination of 3-D fault-plane profiles, internally consistent horizons, and rigorously defined fault networks provides the geologic modeler with a structural "shell" that can subsequently be populated with facies models and reservoir properties for simulation. Structure maps are extracted from the models instead of assembling the models from various structure maps.

Fault seal and transmissibility analyses characterize the hydrocarbon sealing capacity and permeability of the faults in the model. Sealing capacity is important in exploration settings during which initial volumes are calculated, whereas fault transmissibility is important in development and production settings where cross-fault flows are calculated. Fault seal and transmissibility analyses require fault surfaces, fault-horizon intersections (i.e. fault polygons) and facies models to characterize juxtapositions, fault-gouge thickness and permeability. In general, fault seal capacity can be measured in two ways: 1) with respect to the amounts (i.e. heights) of seals (i.e. shales) juxtaposed against reservoirs (i.e. sands) across faults or 2) with respect to the capillarity of fault gouge necessary to hold back the buoyancy pressure exerted by a hydrocarbon column of a given height. Fault transmissibility analysis typically includes juxtaposition areas, fault-gouge thickness and permeability and in general measures the impact that faults have on fluid flow in a given reservoir over a specified time frame. Geologic models of reservoirs utilize both fault seal and transmissibility analysis during simulations in order to calculate both initial and recoverable volumes.

The most common use of restoration technology in the E+P workflow is to validate 2D, 3D and map-based seismic interpretation. However, restoration technology can be very useful in secondary migration analysis, geologic and basin modeling because it incorporates structural history and timing. In general, there are two types of restoration technology: 1) geometric/kinematic or 2) finite element. Geometric/kinematic restoration technology is most useful in validation of interpretation and characterization of structural history. Structural processes like flexural-slip or fault-propagation folding, which produce different geometries of folds, can be tested. Finite element restoration technology is most useful in characterization of 3D strain and incorporation of geomechanical properties into geologic models. This is very useful for the characterization of fractures and subseismic faults. In certain scenarios, fractures may be necessary to enhance production whereas small faults may act as permeability barriers and impede production. Predictions of fracture orientations and intensity based on 3D finite element restoration, linked to geomechanical modeling, and compared to outcrop and core facilitate development of unconventional reservoirs previously deemed uneconomic.

In the past the many structural analyses just described were viewed as a mixed bag of disparate technologies best applied by individual specialists. Currently, most of the deepwater or unconventional traps under consideration for exploration or development have work plans involving all of these analyses. Tight budgets and streamlined timelines require that one structural specialist applies all structural technologies in an integrated workflow. In the future, these structural technologies will be incorporated into one modeling platform.

A NEW MODEL FOR FAULT RELATED FOLDS: FLANKING STRUCTURES WITH LAYER PARALLEL SHORTENING

4-13

Gerhard Wiesmayr, Bernhard Grasemann

Institut für Geologische Wissenschaften, University of Vienna, A-1090 Vienna, Austria
E-mail: Gerhard.Wiesmayr@univie.ac.at
Bernhard.Grasemann@univie.ac.at

Abstract

We investigated the effects of fault related folding along a single fault that is pinned on both ends, upsection and down section. Using a numerical model we produced *flanking structures* (*Passchier, 2001*) under plane strain transtension for the whole range between simple shear, general shear and pure shear, with layer parallel shortening parallel and shear zone widening normal to the shear zone boundaries. Under these boundary conditions contractional flanking folds with thrusting kinematics are the favorite structures that will form. Comparison with natural examples reveals that contractional flanking structures occur from the outcrop scale within ductile shear zones up to the mesoscopic scale within fold and thrust belts. Flanking folds therefore can be compared with existing fault related fold models like fault bend folds, fault propagation folds, break thrust folds or wedge folds (Fig.1). The fundamental differences of our model to existing fault related fold models are: 1) The fault not necessarily maintains a stable orientation but may rotate during progressive development. 2) The drag can change from reverse to normal along the fault. 3) The displacement along the fault has its maximum in the centre of the fault and decreases in both directions, downsection and upsection towards fixed fault tips.

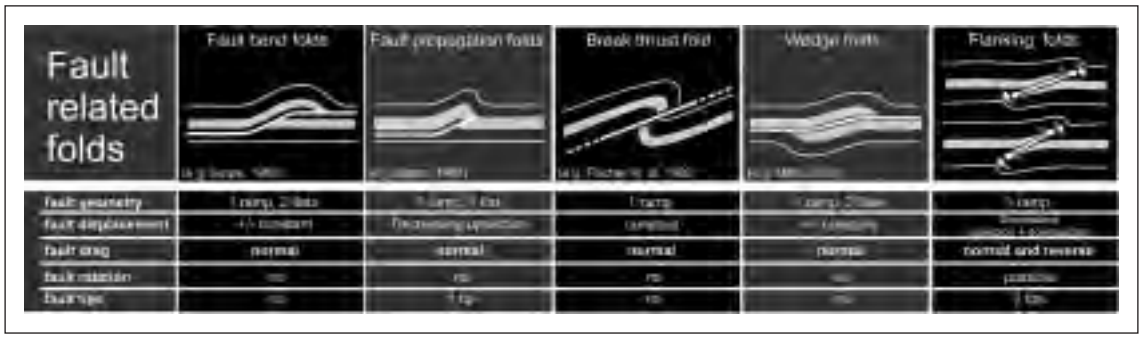

Fig. 1 - Comparison of the main characteristics of classical types of fault related folds with those flanking folds.

As flanking folds always cause footwall deformation, they provide an attractive explanation for the development of joined footwall synclines and hanging wall anticlines and should therefore be considered and re-investigated in the cross-section restoration procedures and structural interpretations, as we believe that footwall deformation has been underestimated and simplified in many fault related fold models.

REFERENCES

• Fischer, M.P., Woodward, N. B. & Mitchell, M. M. 1992. The kinematics of break-thrust folds. Journal of Structural Geology 14, 451-460.
• Mitra, G. 2002. Fold-accomodation faults. AAPG Bulletin 86, 671-693.
• Passchier, C.W. 2001. Flanking structures. Journal of Structural Geology 23, 951-962.
• Suppe, J. 1983. Geometry and kinematics of fault-bend folding. Amer. J. Sci. 283, 684-721.
• Suppe, J. 1985. Principles of Structural Geology. Prentice-Hall Inc. Englewood Cliffs, New Jersey.

Session 5

METHODS AND TECHNIQUES

3D MODEL OF THE LARDERELLO GEOTHERMAL AREA (NORTHERN APENNINES, ITALY) 5-01

R. Aquè, A. Brogi, A. Lazzarotto

Dipartimento di Scienze della Terra, Università di Siena, via Laterina, 8 – 53100 Siena, Italy

Summary

The 3D modeling techniques provide an excellent tool for the visualisation and validation of geological structures. We used these techniques to summarise the geological and geophysical knowledge of the Larderello geothermal field. The study area is located in southern Tuscany, inner Northern Apennines. The geological setting derives from the collision between African and European continental margins (Cretaceous-Early Miocene); since ?Early-Middle Miocene the inner Northern Apennines was affected by post-collisional extensional tectonics which produced thinning of the continental crust up to 22 km. Extension caused low-angle detachments which produced widespread boudinage of the continental crust and the elision of some tectonic units. These structures were followed by high-angle normal faults which caused the development of tectonic depressions infilled by Neogene continental and marine sediments.

Five regional tectono-stratigraphic elements have been recognised in the Larderello area. They are: Miocene-Quaternary continental and marine sediments (N), Ligurian l.s. Units (LU), Tuscan Nappe (TN), Monticiano-Roccastrada Unit (MRU) and Gneiss Complex (GU).

The large number of surface and subsurface data (mainly seismic reflection lines and deep wells) makes it possible to reconstruct with relative little uncertainty the 3D structural architecture of the Larderello geothermal area.

By using specific commercial software, we integrate geological and geophysical data and we obtain coherent layered models, volumes and grids, suitable for numerical models and flow simulators.

Abstract text

In the last two decades, the computer modeling techniques have been largely used for subsurface reconstruction of geology. Modern computer capabilities make it possible to produce complex 3D models containing and constrained by both geological and geophysical data. The resulting models should validate the interpretations and satisfy the multidisciplinary dataset, searching for the common objective: the geometry.

3D modeling and visualisation techniques were applied to the Larderello geothermal field for validate in 3D the geological interpretations and provide an insight of the main deep structural features of this area.

The tectonic setting of the Larderello area reflects the collisional (Cretaceous - Early Miocene) and extensional (Early Miocene-Present) processes of the Northern Apennines structural evolution. The extension produced the thinning of the tectonic pile previously stacked, and the development of post-orogenic basins (Tortonian-Middle Pliocene), bounded by high-angle normal faults which crosscut all the previous structures (Decandia et al., 1998; Carmignani et al., 2001).

On the whole, in the Larderello area three regional tectono-stratigraphic elements crop out (Fig. 1). These are, from top to bottom (Batini et al., 2003 and references therein):

1) Neogene and Quaternary deposits (N): Late Miocene - Pliocene and Quaternary, continental to marine sediments, filling up the extensional tectonic depressions which, in the geothermal areas, unconformably overlie the pre-Neogene substratum.
2) The Ligurian Complex l.s. (LU). This includes the Ligurian Units s.s. and the Sub-Ligurian Unit. The Ligurian Units are composed of remnants of the Jurassic oceanic basement and its pelagic sedimentary cover. The Sub-Ligurian Unit belongs to a palaeogeographic domain interposed between the Ligurian Domain and the Tuscan Domain. The Ligurian l.s. Complex was thrust eastward over the Tuscan Domain during the Latest Oligocene-Early Miocene.
3) The Tuscan Unit (Tuscan Nappe, TN). This is related to part of the Late Triassic – Early Miocene sedimentary cover of the Adria continental palaeomargin. The Tuscan Nappe was detached from its substratum along the Triassic evaporite level and was thrust over the outer palaeogeographic domains, during the Late Oligocene - Early Miocene contraction. It consist of an upper calcareous-silicoclastic (TN2) and a lower anidridic-dolomitic (TN1) sequences.

The substratum of the Larderello area is referred to as the Tuscan Metamorphic Complex. This is mainly known through drillings of the geothermal fields, some of these penetrating down to about 4.5 km. This Complex is composed of two metamorphic units: the upper Monticiano-Roccastrada Unit and the lower Gneiss Complex.

The Monticiano-Roccastrada Unit (MRU) consists of three groups:

- Verrucano Group (MRU3). It is made up of Carnian phyllites and metacarbonates, related to marine littoral facies, and by Middle-Early Triassic continental quartzites and quartz conglomerates. The Verrucano Group is embricated in duplex structures, often separated by Late Triassic evaporites and Early-Late Paleozoic phyllites and quartzites.
- Phyllite quartzite Group (MRU2). It mainly consists of Paleozoic phyillite and quartzite rocks, affected by the Alpine green-schist metamorphism which overprints a previous Hercynian blastesis. Levels of anhydritic-dolomites and basic metavolcanites in lenses can occur.
- Micaschist Group (MRU1). It includes Palaeozoic rocks (garnet-bearing micaschists and quartzites with amphibolite levels) affected by Alpine and Hercynian deformations. Particularly, the micaschists were affected by a syn-kinematic Hercynian metamorphism and by an Early Permian thermal event.

The Gneiss Complex (GU) consists of pre-Alpine polymetamorphic gneisses and paragneisses with intercalations of amphibolites and orthogneisses. In contrast to the Monticiano-Roccastrada Unit, the effects of the Alpine orogeny are not recorded in the Gneiss Complex. At different depths, deep boreholes encountered granitoids and felsic dykes (MG, 3.80-2.25 Ma) whose emplacement determined contact aureoles in the metamorphic host rocks. Moreover, hydrothermal mineralogical associations partially or totally fill the fractures affecting the Larderello metamorphic rocks.

We construct a regional model, about 240 km^2 wide and 4000 m deep, and several local models, up to 10 km^2 wide, highlighting respectively the overall geometric setting of the Larderello area and the main tectonic features characterising this area.

The initial dataset we used consists of several geological maps, about 100 deep (up to 3500 m) wells and 7 geological cross-sections, drawn in correspondence of relevant seismic reflection profiles. The CROP. 18 and CROP. 03 deep seismic surveys also provide good information for the model construction.

The modeling was performed by using specific commercial software, which allow referencing the dataset, producing balanced cross-sections and creating surfaces, volumes and 3D grids.

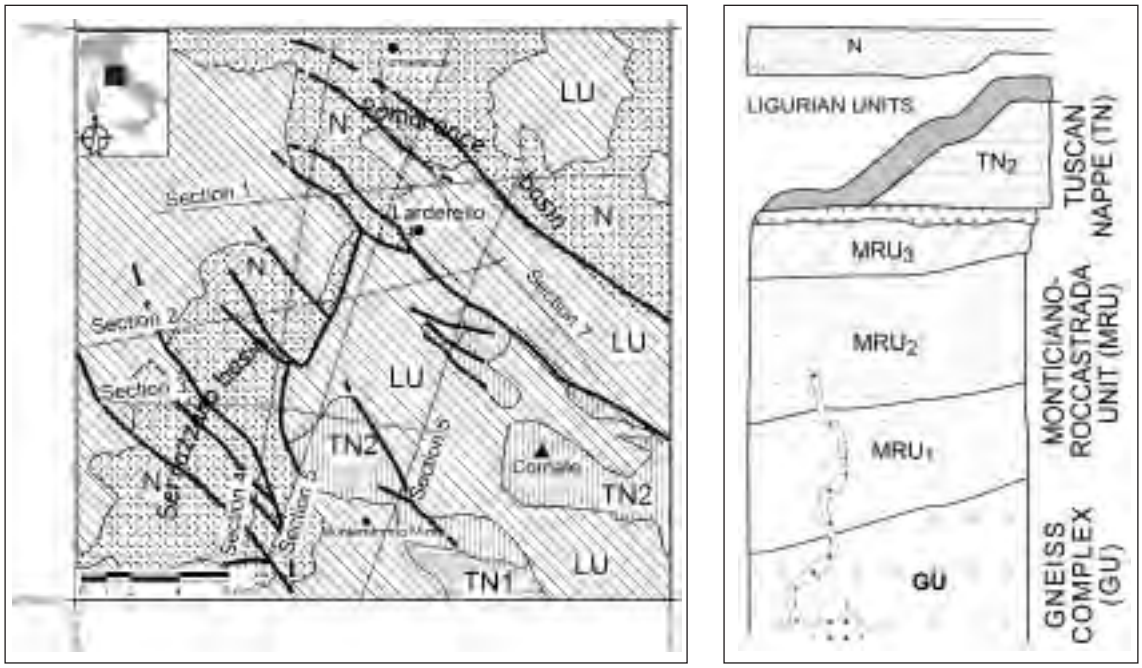

Fig. 1 - Geological sketch map and schematic stratigraphy of the study area.

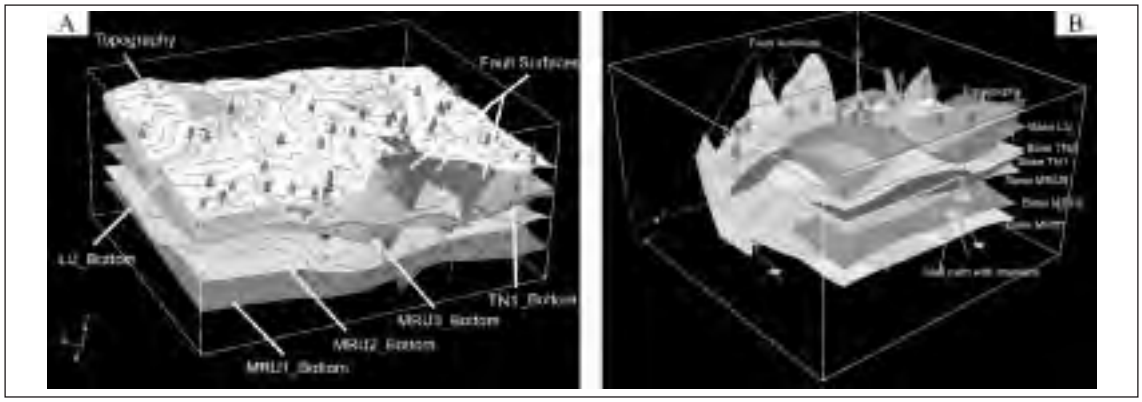

Fig. 2 - 2,5D layered model of the Larderello geothermal area; key surfaces represent the stratigraphic and structural boundaries of the main tectonic units; note the high angle Neogene normal faults crosscutting all the tectonic units. A) Regional model showing the overall geometry of the area. B) Local model of the southern part of the Larderello geothermal area.

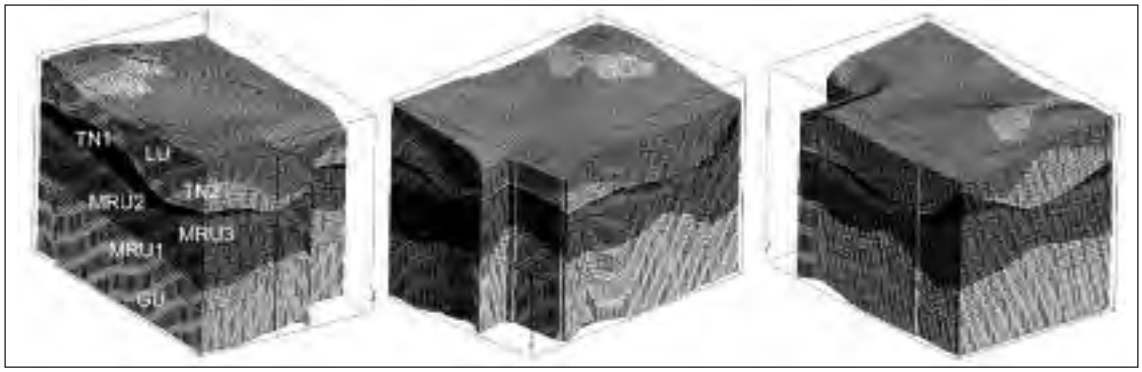

Fig. 3 - Different views of the obtained structured grids for the study area. Note the boudinage affecting the TN and UMR3 tectonic units.

The workflow for the model building is schematically as follows: a) digitising and referencing the raw data; b) drawing the 2D cross- sections; c) connecting cross-sections and well markers by common geological surfaces (faults, contacts, etc.); d) split up the 3D space to obtain the volume of the tectonic units; e) characterise the volumes with petrophysical properties and geophysical data. The characterisation of the model by using available geophysical and petrophysical data also provides new constraints for the structural and geometrical reconstruction of this area. Obviously, the model strongly depends on the data quality and its distribution, so that any data input imply iterative validation test for both the data and the model.

We obtained coherent layered models, volumes and grids, given in figures 2 and 3.

These data can be further used for reservoir characterisation, well planning and mining risk evaluation. Moreover, they can be easily exported in third software for numerical modeling (e.g. flow simulations, finite element analyses) or for comparison with (or setting-up of) analogue models.

The geometrical analysis of the model highlights the occurrence of megaboudins mainly consisting of the TN and UMR3 tectonic units, which are dissected by Neogene high-angle normal faults. Moreover, the models provide an insight of the extensional structure superimposition, volumetric computation for geothermal reservoirs and the distribution of analysed petrophysical properties.

We stress the role of the 3D modeling techniques as a tool for validation of geological and geophysical interpretations, to provide constrained dataset for further use in numerical models and to easily communicate the geology also to not geologists.

REFERENCES

- Batini F. et al. (2003), Episodes, 26, 239-244.
- Carmignani L. et al. (2001), in: Anatomy of an Orogen: the Apennines and adjacent Mediterranean Basins, Kluwier Academic publ., 197-214.
- Decandia F.A. et al. (1998), Mem. Soc. Geol. It., 52, 427-439.

NUMERICAL MODELING OF SOLID-MELT SYSTEMS DURING GRAIN GROWTH 5-02

J.K. Becker [1], P. Bons [2], D. Koehn [1], C. Passchier [1]

1 *University of Mainz, Dept. of Geology – Tectonophysic, Becherweg 21, 55099 Mainz, Germany*
2 *University of Tübingen, Institut für Geologie und Paläontologie, Sigwartstr. 10, 72076 Tübingen, Germany*

Summary

Numerical modeling of melt processes on the grain scale has strong advantages over high-temperature experiments or analogue modeling. These include, but are not limited to:

- no unknown or unconstrained material properties or physical/geochemical/geological laws can influence the simulation
- parameters can be changed easily and systematically
- statistical parameters can easily be calculated during the simulation
- all simulations are reproducible with the same results, if some parameters are changed the resulting change in the simulation must be due to the new values

The simulations of partially molten aggregates that were performed all underline the importance of the relative surface energies of solid-solid and solid-liquid boundaries. If the surface energies are adjusted so that a wetting angle of 10° is calculated, the melt pockets in the simulations tend to have outwardly convex boundaries. The boundaries straighten when the wetting angle is increased. If the surface energies are chosen so that the wetting angle is 60° or more, the boundaries of the melt pockets become increasingly concave. However, the wetting angle is not stable during the simulations but adjusts according to the fabric of the surrounding grains. If disequilibrium melt pockets form during the simulation, melt is redistributed and the wetting angle of melt pockets that loose (or gain) melt changes. These changes can temporarily be high, but tend to adjust towards the initial wetting angle when the disequilibrium melt pocket splits into two equilibrium melt pockets.

Introduction

The simulations on microstructural evolution in partially molten aggregates were performed using the Elle-package (Jessell et al., 2001). We introduce an Elle-module that can be used to simulate melt processes at the grain scale. In this module, only the known and/or assumed physical laws for the distribution of a liquid-phase within a solid matrix are used and, in contrast to e.g. HT-experiments, different parameters are easily controlled or changed.

The simulation software uses standard pictures (jpg, gif, etc.) as an input file and translates these into text files that can be read by the program. The Elle code uses a set of polygons (called “flynns”) that can, for example, represent grains in a thin section or an arbitrary designed (poly-) crystalline aggregate in two-dimensions. Flynns can have a number of attributes (such as physical or chemical properties etc.). Each flynn is bound by a number of vertices (called “nodes”). The nodes can have additional physical and/or chemical attributes such as surface energies. It is the movement of these nodes that changes the grain fabric over time.

A node is moved if the movement lowers the total free energy of the system according to:

$$\Delta X - F * m * \Delta t \qquad [1]$$

ΔX is the incremental displacement vector, F is the driving force vector, m is the mobility and Δt is the time increment. The magnitude of a displacement is thus proportional to the product of mobility and time increment. A change in mobility can be regarded as an effective change in Δt .

The wetting angle (θ) is calculated using the relative surface energy of solid-solid (γ_{ss}) and solid-liquid (γ_{s1}) boundaries:

$$2\cos\left(\frac{\theta}{2}\right) - \frac{\gamma_{ss}}{\gamma_{s1}} \qquad [2]$$

When $0° < \theta < 60°$, melt pockets have convex boundaries (Fig. 1a) and an interconnected network of channels along grain edges exists, even for an infinitesimally small amount of melt (Bulau et al., 1979). When $\theta = 60°$, a melt pocket has straight boundaries (see Fig. 1b) while with $\theta > 60°$ the melt pockets tend to have concave boundaries (see Fig. 1c) (Laporte et al., 1997).

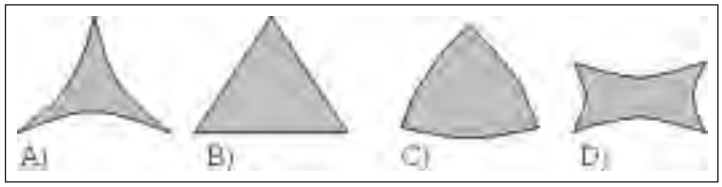

Fig. 1: Shapes of melt pockets at different wetting angles: a) $\theta = 10°$; b) $\theta = 60°$; c) $\theta < 60°$; d) disequilibrium melt pocket $\theta = 10°$.

Discussion

The simulations (Fig. 2) were performed to test the validity of the code and the equations used in the modeling software. The different simulations use the same starting grain fabric, only parameters such as the surface energies and the mobility of boundaries were changed.

Most of the melt pockets showed the expected behavior of minimizing their surface energy and hence the total energy of the system, by adjustment of the curvature of the melt pockets (convex for small wetting angles, concave for high wetting angles, Fig. 1). The shape of a melt pocket in equilibrium is triangular (Fig. 1a) for low wetting angles. The simulations have shown that the most important parameter is the relative surface energy and hence the wetting angle. If the surface energies in the simulations were chosen so that the wetting angle is high, the melt pockets tend to get straight or even concave boundaries before they quickly disappear, their melt being redistributed into large melt pockets. The large melt pockets are not triangular but resemble a distorted rectangle. The same holds true for melt pockets with a wetting angle of 60°. However, redistribution of melt into the larger melt pockets is much slower and the triangular shapes of melt pockets seems to be stable for a much longer period. Nevertheless, towards the end of the simulation all triangular melt pockets disappear and the melt is redistributed into the larger, rectangular shaped melt pockets.

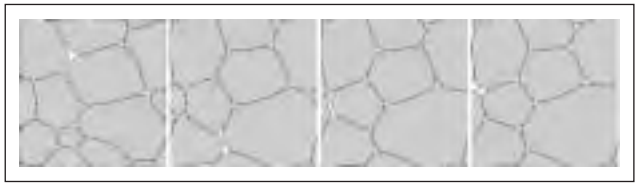

Fig. 2. Example of a simulation of a low wetting angle partial melt, calculated with ELLE. Shown are 4 stages during the simulation and the change in grain fabric as well as melt distribution (grains n gray, melt in white).

If the surface energies define a wetting angle of 10°, the triangular shaped melt pockets quickly adjust their ratio of circumference to area until they are stable. This includes a constant adjustment of the wetting angle at any given triple point because changes of the surrounding grains have to be accommodated. This change of the wetting angle also influences the mean curvature of boundaries between two triple points. The changes of the wetting angle can be quite large in case of melt being redistributed into rectangular shaped melt pockets (Fig. 1d). Only when the disequilibrium melt pocket splits into two equilibrium melt pockets (in this case triangular shapes) and melt is redistributed, the wetting angle is readjusted to approximately 10°. The same holds true for simulations with higher wetting angles. Therefore, the wetting angle (and the mean curvature of the melt pocket boundaries) during the simulations is not static but interactively adjusts to the loss or gain of melt and/or to the evolving shapes of the surrounding grains.

REFERENCES

- Bulau, J.R., Waff, H.S., and Tyburczy, J.A., 1979, Mechanical and thermodynamical constraints on fluid distribution in partial melts. J. Geophys. Res., 84, p. 6102-6108.
- Jessell, M., Bons, P., Evans, L., Barr, T., and Stüwe, K., 2001, Elle: the numerical simulation of metamorphic and deformation microstructures. Computers and Geoscience, 27, p. 17 – 30.
- Laporte, D., Rapaille, C., and Provost, A., 1997, Wetting angles, equilibrium melt geometry, and the permeability threshold of partially molten crustal protoliths. In: Granite: From segregation of melt to emplacement fabrics, ed: Bouchez, J.L., Kluwer Academic Publishers 1997.

GEOPHYSICAL CHARACTERIZATION OF AN OUTCROPPING CHANNEL COMPLEX 5-03

G. Benevelli, A. Valdisturlo, P. Rocchini, L. Fava, S. Angella
ENI E&P Division

Introduction

The use of oOutcrop analogues have been widely used for seismic modeling has been widely applied in the recent years in order to reconstruct the seismic image of well known geologic objects and in order to achieve a better understanding of the subsurface geologic settings. The key question in field-based seismic modeling regards which and how much geologic information we lose from detailed outcrop analysis to upscaled seismic profiles. A critical point concerns the different orders of resolution, which often prevents a clear comprehension of the degree of information loss, passing from onea data set to another (cores, well logs and seismic).

In subsurface studies, the integration ofbetween core analysis, petrophysical information from well logs and seismic data is the standard procedure for the geologic interpretation at a regional and a field scale. Well to seismic tie (based on synthetic seismograms generated from logs) represents the most commonune methodology to correlate core and log with seismic data. Log analysis and their classification (petroacoustic analysis) areare used to transfer the lithologic and sedimentological description within the seismic data.

Well log data have been used very rarely in forward seismic modeling of outcrop analogues (*e.g.*, Valdisturlo *et al*., 1996)), due to the difficulty of havingto have wells with a complete data set (cores and logs), which can be directly linked to measured field sections. For the Ainsa System (Eocene of the south-central Pyrenees), a classical example of a poorly efficient channelised turbiditey system (*e.g.*, Mutti and Ricci Lucchi, 1972; Mutti *et al*., 1985; Mutti and Normark, 1991; Clark, 1995; Pickering and Corregidor, 2000; Mutti *et al*., 2003), detailed field work (provided by Parma University), 2D seismic lines along the outcrop and, three wells with continuous coring and logging (acquired by ENI E&P Div.) are available. These data are used for the geophysical characterization of the "Ainsa 2 channel complex" (fig. 1a), trying to apply the methodologies of subsurface analysis methodologies.

This paper focuses on the upscaling procedure from the field and core sedimentological description, to well logs and finally to the seismic data, giving an at each step account of the information loss at each step. After we show the The results of the forward seismic modeling, based on the generation of the pseudo-log of the measured field section by the means of well logs, will then be illustrated.

Facies upscaling

Just hHow representative of the depositional features are actually well logs? And how does the resolution does decrease passing from a core data set to a well-log data set and to seismic data? In order to answer these critical questions, we construct an electrofacies model (*i.e.*, a facies model based on well logs), and compare it with the sedimentological profiles of the cores.

At first, a cluster analysis was performedrun on the most significant well logs (sonic, density and gamma ray) to identifyrecognize the most important lithological and petrophysical classes, and to obtain an electrofacies model. This model was then used to createconstruct a categorical data base linking well log values and electrofacies. Finally, this data base was usedemployed to perform automatic electrofacies estimation in the well, based on a discriminant analysis routine.

In order to correlate the sedimentological facies with the petrophysical values of well logs we subdivided the cored sections into discrete facies, obtaining a sedimentological facies log (fig. 1b). Then, the electrofacies were compared with the core facies for validation and to assess their mutual relationships (*i.e*., the association of sedimentological facies represented by a single electrofacies). These relationships are represented in the form of a matrix in which both the electrofacies and the sedimentological facies are ordered in the same way (from the most shaly to the most sandy). The matrix could be considered as a three-dimensional histogram illustrating the degree of correspondence of the two facies series. In this way, it is possible to define a degree of confidence in extending core information using electrofacies. In the case of thise present study, the matrix shows a

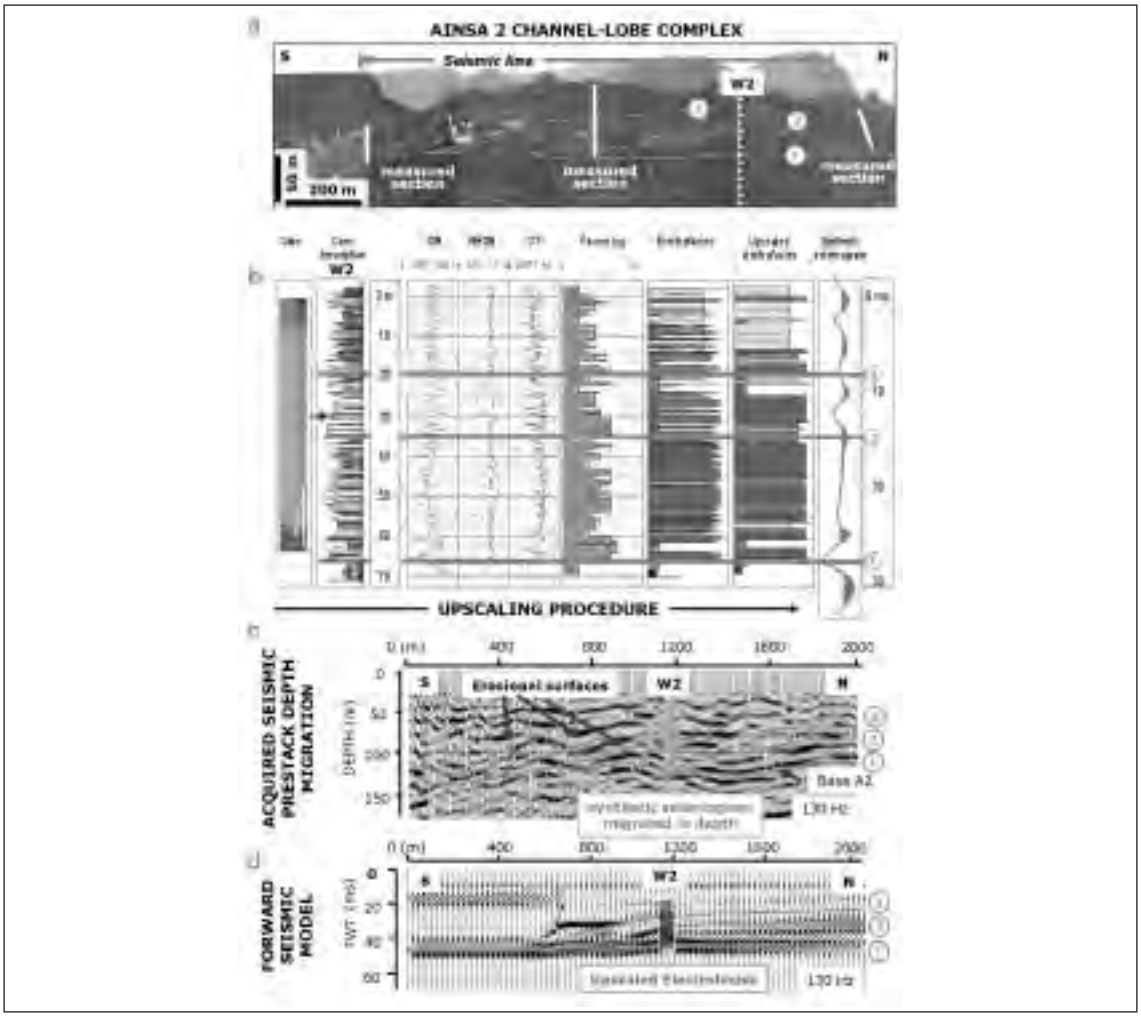

good correspondence between the single electrofacies and specific sedimentological facies associations characterized by homogeneous lithology.

The nextfurther step waswas to ascertain the correspondence between the electrofacies (which are a synthesis of sedimentological, lithologic and petrophysical properties) and the seismic signal. The electrofacies profiles were progressively upscaled up to reach a seismic scale (fig. 1b). This procedure is carried out gradually, in such a waymanner that the final upscaled profile is still representative of the original petrophysical properties. The upscaled electrofacies profile was validated by the comparison ofbetween the original well log data withand the synthetic logs obtained, assigning an average value of a petrophysical parameter (*e.g.*, sonic transit time) to each electrofacies. The tie of the upscaled electrofacies with the seismic lines allowed to characterization ofe the seismic signal by sedimentological, lithologic and petrophysical features and provided to support for seismic interpretation.

Forward seismic modeling

The fForward seismic modeling started with the measurement of field sections and the reconstruction of the stratigraphic cross-section of the "Ainsa 2 channel complex", also including comprehending also well 2. In order to generate an acoustic impedance section of the stratigraphic 2D model, the field sections were firstly converted into discrete facies curves (sedimentological log) using the same classification adopted for the wells. Then, a quantitative relational data base, associating sonic and density data recorded in wells and specific lithologic facies from core analysis, was used to construct pseudo-sonic and pseudo-density logs.

The results were tested by comparing the pseudo-logs constructed in the wells with both the recorded

logs and the direct velocity measurements on core plugs. The pseudo-logs obtained for the field sections were then underwentsubmitted to the automatic electrofacies analysis (based on the same electrofacies model used for the wells), thus obtaining pseudo-electrofacies directly comparable with the electrofacies profiles of the wells. Since no laboratory acoustic velocity measurements are available for outcrop sections, this procedure was used as an indirect tool to assess the reliability of the predicted pseudo-logs.
Using the seismic-modeling software, sonic and density logs and pseudo-logs were extrapolated within the interpreted layers of the cross-section, generating an acoustic impedance model. The fForward seismic modeling (Fig. 1d) starts with the ray tracing to calculateompute the depth section of reflectivity. We used in particular zero-offset, vertical incidence ray-tracing and compressional synthetic seismic source. Finally we convolved the reflectivity section with a zero-phase 130 Hz Ricker wavelet, the same wavelet of the acquired seismic data. The obtained forward modeling obtained was compared with the acquired seismic line processed using the with pre-stack depth migration methodology (fig. 1c).

Results

The acquired seismic line, tied with the well by the means of a synthetic seismogram, records the same reflector generated with the forward seismic model, based on upscaled electrofacies. This suggests that the acquired seismic data records an acoustic layering that can be described by means of through the upscaled electrofacies model (fig. 1d).
The applied upscaling procedure applied gives an account at each step of the real information content of our electrofacies profile and of correspondence the adherence with to the original sedimentological profile. Reversing the point of view, from the electrofacies profile we can establish in probabilistic terms the expected sedimentological facies association in a seismic interval. This integrated facies analysis represents a powerful tool to transfer detailed sedimentological information to the seismic data in forward modeling of outcrop analogues and in subsurface studies where only a few cores are available. The electrofacies analysis, linking sedimentological and seismic resolution, allows recognition of zing the degree of geological complexity recorded by the seismic.
This study is useful in exploration and production activities as it increases confidence in the geological interpretation of seismic data.

Acknowledgements

The authors would like to thank the many people of the ENI E&P Division that contributed to the analysis of the subsurface data and in particular M. Barnaba, M. Buia, M. Fervari, O. Meazza, F. Onorato, L. Tatarella and E. Visigalli. They are grateful to E. Mutti, G. Cavanna, J.J. Melick for the fundamental contribution in the field analysis of the Ainsa System and L. Papani for the detailed analysis of the cores. They also wish to thank D. Colombo (Geosystem s.r.l.) for acquisition and depth processing of the seismic data.

REFERENCES

- Clark J.D. (1995) - A detailed section across the Ainsa II channel complex, south-central Pyrenees, Spain. In: Pickering K.T., R.N. Hiscott, N.H. Kenyon, F. RicciLucchi e R.D.A. Smith (Eds), Atlas of Deep Water Environments: Architectural Style in Turbidite Systems, Chapman and Hall, London, 212-215.
- Mutti E. and F. Ricci Lucchi (1972) - Le torbiditi dell'Appennino Settentrionale: introduzione all'analisi di facies. Mem. Soc. Geol. It., 11, 161-199.
- Mutti E., E. Remacha, M. Sgavetti, J. Rosell, R. Valloni and M. Zamorano (1985) - Stratigraphy and facies characteristics of the Eocene Hecho Group turbidite systems, South Central Pyrenees. In: Mila M.D. e J. Rosell (Eds), Excursion Guidebook of the 6th European Regional Meeting of the International Association of Sedimentologists, Lerida, IAS, 521-576.
- Mutti E. and W.R Normark (1991) - An integrated approach to the study of turbidite systems. In: P. Weimer e M.H. Link (Eds), Seismic Facies and Sedimentary Processes of Modern and Ancient Submarine Fans, SpringerVerlag, New York, 75-106.
- Mutti E., R. Tinterri, G. Benevelli, S. Angella, D. di Biase and, G. Cavanna and A. Cotti (2003) – Deltaic, mixed and turbidite sedimentation of ancient foreland basins. Marine and Petroleum Geology, 20, 733-755.
- Pickering K.T. and J. Corregidor (2000) – 3D Reservoir-Scale Study of Eocene Confined Submarine Fans, South-Central Spanish Pyrenees. GCSSEPM Foundation 20th Annual Research Conference Deep-Water Reservoirs of the Word, Houston, December 3-6, 2000, 776-781.
- Valdisturlo A., M. Berra and R. Lotti (1996) – Seismic modelling from outcrop sections of a conglomeratic deep-sea fan complex (Gonfolite, Southern Alps, Lombardy). In: Wessely G. and Liebl W. (eds), Oil and Gas in Alpidic Thrustbelts and basins of Central and Eastern Europe, EAGE Special Publication N° 5, pp. 155-168.

HOW 3D IMPLICIT GEOMETRIC MODELLING HELPS TO UNDERSTAND GEOLOGY: EXPERIENCE FROM BRGM (FRANCE) 5-04

P. Calcagno(*), G. Courrioux(*), A. Guillen(*), C. Sue(**)

(*) BRGM – 3, avenue Claude Guillemin – 45060 Orléans cedex 2 – France
email: p.calcagno@brgm.fr

(**) IGUN - Université de Neuchâtel - Rue Emile-Argand 11, CP 2 - Switzerland
email: Christian.sue@unine.ch

Summary

3D geometric modelling is a powerful tool to better understand geology. It allows to check and validate the consistency of the separate 1D or 2D data. Building a 3D model is a way to share and communicate a common geological view of a studied area. 3D integrating methods such as gravimetry can be used to refine and validate the 3D model by comparing a measured field to the model contribution. Moreover, a consistent 3D geometric model is essential for post-process computations that need an accurate and consistent geometry of geological bodies.

An original methodology has been developed in BRGM (French Geological Survey) to interpolate at the same time geological contacts locations and dips of the formations. The model is calculated using a 3D potential field or multi-potential fields, depending on the geological context and complexity. This method also includes a geological pile containing the geological history of the studied area and the relationships between geological bodies. The geological pile drives automatic computation of intersections and volume reconstruction. Then, the geologist focuses on geological issues by easily testing different interpretations.

This methodology has been applied to various geological contexts. An Alpine case-study is presented on the Penninic front in the Briançon area. This crustal model allows to compute statistics on earthquakes locations in relation to the Penninic front geometry.

3D geometric modelling: a tool for geology

Geology has a strong geometric component. Thus, using 3-Dimensional geometric tools to interpret geology appears to be very powerful. Classical media for geological data and interpretation are 1D or 2D (boreholes, maps, cross-sections, etc.) Taking into account at the same time all available data of a given area allows to perform a global interpretation. Merging separate data in the same 3D space helps to identify and correct inconsistencies. Even if a given 2D interpretation on a cross-section appears suitable, its confrontation with the geological map or another secant cross-section may reveal geometric anomalies. The first contribution of 3D geometric modelling is the capability to highlight consistency issues.

When data have been checked and validated, geology is often only known on a few badly distributed locations, for instance a map, some cross-sections and boreholes. This is why a 3D model needs to be constructed to fill the gaps between data. Then, an interpolation method is used to infer the whole geological bodies geometry from spare data. The interpolation can be reinforced by extra 3D geological interpretation in areas where density of data is insufficient. Then, the modelling process and the model itself is shared by all the partners who have the same geometric vision of the geology. 3D geometric modelling allows to easily share and communicate a common view of the studied geology.

Moreover, 3D model can be refined and validated using 3D integrating data. For instance, by affecting a density to each geological modeled body, the gravimetric contribution of the 3D model is calculable and comparable to gravity measured on field. Then, discrepancies between computed and measured anomalies can be reduced by refining local interpretation and recalculating the model. In the same way, the final 3D model is the reference geometric data for post-processes such as hydrogeology, geohazards or mining computations. A 3D geometric model has to be built each time a calculation needs a consistent geometry of the geology.

The less the 3D modelling process is time-consuming, the more the method is helpful. It's much more important for geologists to focus on geological interpretation than on geometric building issues such as handmade intersections and volume reconstruction. An original interpolation method has been

developed in the BRGM (French Geological Survey) to take into account both the observed locations and dips of the geological interfaces. This method also includes the history and relationship between geological formations to automatically deal with intersections and volume reconstruction.

Interpolation method using 3D potential field

Geologists build maps and cross-sections to describe the geometry of a studied area. Those interpretations are often based on data coming from field observations, boreholes and seismic profiles. 3D modelling has to use those 1D and 2D data and interpretations. However, to construct the 3D model one need to fill the gaps between the data. Compared with other existing 3D solid modelling approaches (e. g. Boissonnat, 1988; Bertrand et al., 1992), a major original feature of this interpolation method is that the 3D description of the geological space is achieved through a potential field formulation in which geological boundaries are iso-potential surfaces and their dips are represented by gradients of the potential.

The potential field method (Lajaunie et al., 1997) allows to interpolate in the whole 3D space of the area. It considers the limits between geological bodies as isopotential surfaces. This method needs the position of the interfaces between geological bodies to be known at some place i.e. the ones given by boreholes, map and sections. It also requires orientation vectors that represent the tangential plane of isopotential surfaces and their polarity, in a geological language these are azimuths, dips and polarities of the geological structures measured on field. Dip measurements are not necessarily located on the geological interfaces. They can represent stratifications or foliations related to the contacts. Figure 1 shows this principle in 2 dimensions. When the potential field is calculated, the potential value is known for every point at 3D space. A range of potential values defines a geological body. On one hand, 3D points associated to the limits values belong to the interfaces. On the other hand, 3D points corresponding to values within the range are contained in the body.

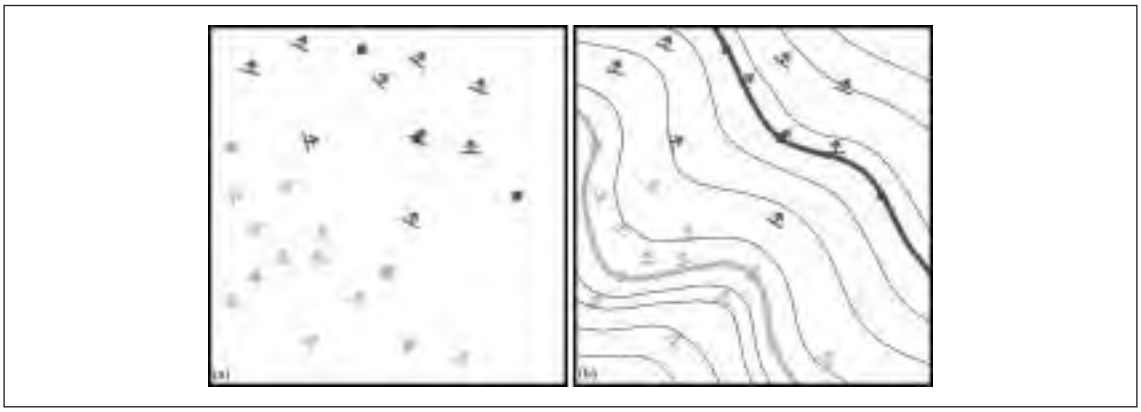

Figure 1. Principle in 2-Dimensions of the geostatistical interpolation using the potential field method. (a) A geological body observed by the locations of its contacts (squares points for one side, circles points for the other side) and dip measurements. (b) The geological body modelled by potential field method. Thick curves represent its limits. Thin curves represent foliations trajectories inside and outside the body. The isovalues honour both interface points and foliations attitude.

This interpolation method allows to build 3D model of sub-parallel geological interfaces. Nevertheless, generalisation to more complex geometry has been achieved.

Generalisation of the interpolation method with multiple potentials

According to their definition, isopotential surfaces can not be secant or have common points. Two adjacent interfaces contained in a given potential have a sub-parallel behaviour (Figure 1). Except in some sedimentary cases, a geological body is not present all over the studied area, it often settles and stops on (Onlap relation) or erodes (Erod relation) another. To perform these relations, one needs to associate each step of the geological history of the studied area to a potential field. Each potential field has a behaviour parameter (Erod or Onlap) which controls its relation with older geological bodies i.e. potential fields already interpolated (Figure 2).

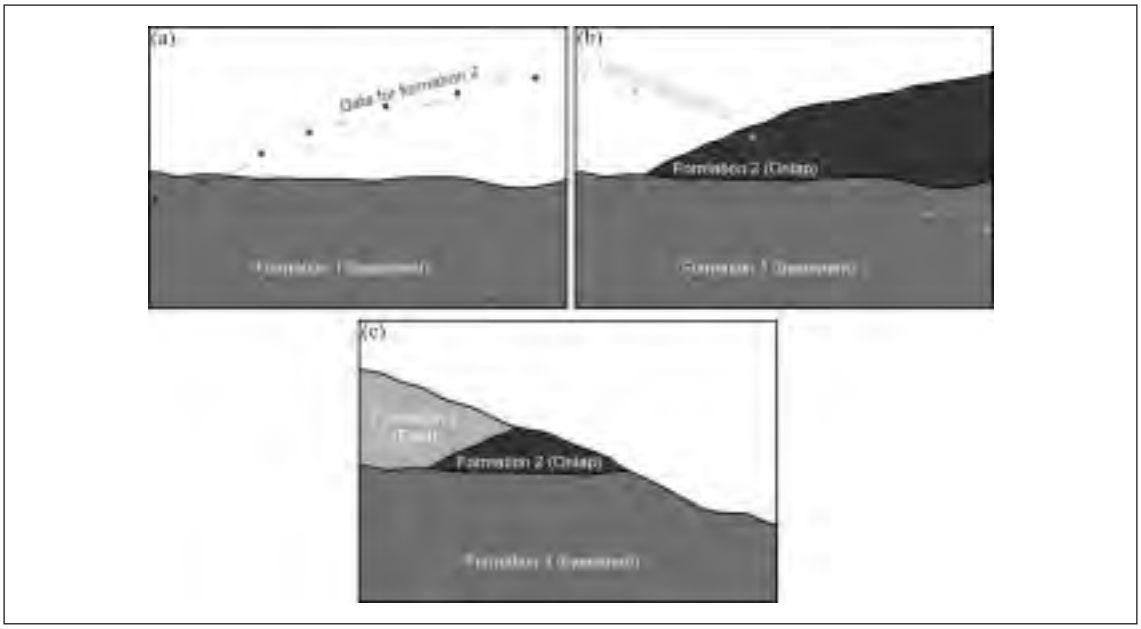

Figure 2. Multipotential fields allow Onlap and Erod relations between interfaces. (a) Interpolated formation 1 (basement). Data for potential field of formation 2 in black. (b) Formation 2 interpolated with Onlap relation. Data for potential field of formation 3 in light grey. (c) Formation 3 interpolated with Erod relation.

Let's call the chronological succession of the formations and their relationships the *geological pile*. Concerning Figure 2, each geological formation defines one potential field. The corresponding geological pile is, from the bottom to the top (i.e. from the first deposition to the last): Formation 1 (onlap), Formation 2 (onlap), Formation 3 (erod). As soon as the geological pile is defined, it contains all non-located geological history. Then, intersections between geological bodies are automatically governed by the geological pile. By using this tool, one can focus on geological interpretation without managing intersections purposes.
The methodology described above has been applied to various geological case-studies in different geological contexts such as basin, orogenic or urban geology (Putz et al., Calcagno et al., Courrioux et al.). A software, the "Geological Editor" has been developed in order to build 3D geometric models from maps, cross-sections, boreholes, etc. This software, providing a convivial Graphic User Interface, is used by geologists to test and refine their interpretations and finally to construct their 3D models. Import/export facilities allows to load data and to use 3D models for post-processes.

A case-study: The Briançon 3D model (French Alps)

A 3D-model of a key area of the southwestern Alps at the bounder between external and internal zones (Briançon region), has been constructed (Figure 3a). Six geological bodies have been modelled (internal and external basements, Briançonnais and Piemontais zones, exotic flyshs, and external sedimentary cover). 3D volumes of each geological body have been modelled using the structural map of the area projected on the Digital Elevation Model and 5 sections perpendicularly distributed along the Penninic Front. The model has been interpolated from the data by the potential fields method and represented by a marching-cube algorithm.
The 3D-model has then been used to plot the earthquakes of the GeoFrance3D database (Figure 3a). Thus, the relationships between crustal structures and present-day activity of the belt have been investigated. The bounder between external and internal zones corresponds to the so-called Crustal Penninic Front, which is a former Oligocene major thrust. Our model established that this former thrust represents globally the western limit of the seismic activity along the briançonnais seismic arc, currently undergoing extensional tectonics.
The Briançon study is fully described in Sue et al.

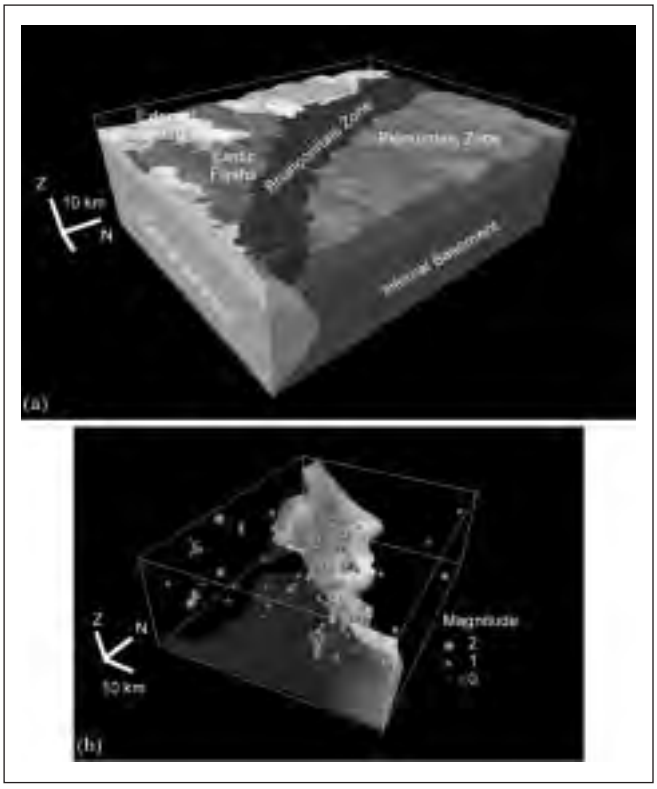

Figure 3: 3D Model of the Briançon zone. (a) View from S-E. (b) Crustal Penninic Front and earthquakes localisation. Each earthquake is presented by a sphere located at its epicentre with a radius proportional to the magnitude.

For further information, visit our site at http://3dweg.brgm.fr

REFERENCES

- Bertrand P. et al. (1992), Actes MICAD92 Paris 1, 59-74
- Boissonnat J.D. (1988), Computer Visualisation and Graphical Image Processing, 44, 1-29
- Calcagno P. et al. (2002), RST19, Nantes, p. 79 (abstract).
- Courrioux G. et al. (2001), Tectonophysics (331)1-2, 181-196
- Lajaunie Ch. et al. (1997), Mathematical Geology, 29(4), 571–584.
- Putz M. et al. (2004), GeoMod2004, this volume.
- Sue C. et al. (accepted), Tectonophysics

METHODS IN INTERPRETATIVE MODELLING OF STRUCTURALLY DEFORMED TERRANES: CASE STUDIES FROM THE LOWER PALAEOZOIC VOLCANIC TERRANE OF THE ENGLISH LAKE DISTRICT AND THE ORTHOTECTONIC TERRANE OF THE GRAMPIAN HIGHLANDS IN SCOTLAND

5-05

S.M. Clarke*, D. Millward*, A.G. Leslie*, P.W.G. Tanner**, C.L. Vye*

(*) British Geological Survey, Murchison House, West Mains Road, Edinburgh, EH9 3LA, United Kingdom

(**) Division of Geology, Gregory Building, University of Glasgow, Glasgow, G12 8QQ, United Kingdom

Summary

For many years, the British Geological Survey has constructed numerical, 3D, geological models by integrating wide-ranging forms of directly measured (primary), subsurface data (boreholes, surveyed mine plans etc.). These techniques have proved successful in areas of the UK where there is a wealth

of such data. However, there are many areas for which primary subsurface data are few. In these regions, the structure of the subsurface is represented by interpretations extrapolated from primary surface observations (cross-sections, contoured horizons etc.). Such *interpretative data* can be used to build a conceptual understanding of the geology and represent the structural architecture of the subsurface with reasonable confidence. However, in such cases the true depth, geometry and inter-relationships of subsurface horizons in 3D are often less well constrained.

We consider two regions of the UK where there is a wealth of primary surface data and a good conceptual understanding of the structural architecture, but no primary data relating to the subsurface. We use the English Lake District as a test-bed on which we develop modelling principles in an attempt to constrain the subsurface geometry of selected horizons. Careful comparison of the structural geometry of modelled horizons with surface structural data demonstrates that such a modelling approach can be used to constrain 3D interpretations in the absence of primary subsurface data. The validated methods are then applied to the Beinn Udlaidh region of the Scottish Highlands in an attempt to define and constrain both the subsurface and the subaerial geometry and position of a pair of kilometre-scale, recumbent folds. The fold shapes are delineated by the 3D outcrop patterns of three, distinctive, geological formations.

Central to our methods of modelling is the concept of *confidence*. Rigorous and tracked objective assessments of positional uncertainty in each of the contributing interpretative datasets allow conflicts between data to be resolved. This results in a 3D model that is a *weighted best-fit* solution dependent on confidence in input data and represents a significant improvement over a wholly subjective *average best-fit* result.

Interpretative modelling of the English Lake District

The completion recently of re-survey at 1:10k scale of the English Lake District has provided a wealth of primary data on the caldera-related, volcanic complex of the *Borrowdale Volcanic Group* (BVG). Its structural architecture is well understood from these data and using the developed interpretative modelling principles, the geometry and 3D relationships of units within the BVG can be constrained and the logical consistency of interpretations rigorously assessed.

The modelled area (fig. 1) represents the core of a large Ordovician (Caradoc), rhyolite caldera-volcano (Branney & Kokelaar, 1994). The complex arrangement of small faulted blocks, each with widely varying dip vectors, arose through piecemeal caldera collapse. Components of the extensive Lake District granitic batholith were emplaced beneath the caldera-system late in the volcanic episode. A broad, closed synclinal structure, termed the *Scafell Syncline* (fig. 1), resulted from Acadian (Early Devonian) compression of the stratified caldera-fill succession. The structural architecture can be well defined by structural form-line plots derived from surface data (fig. 1), but the true depth and geometry of given horizons both regionally within the BVG and within individual faulted blocks is less well understood.

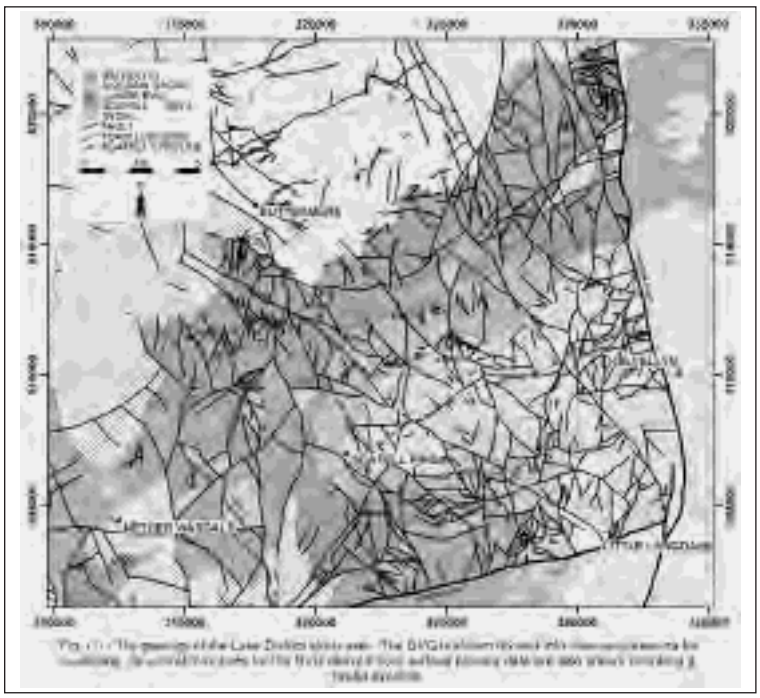

We project all available interpretative data including geological map data, cross-sections, geophysical interpreta-

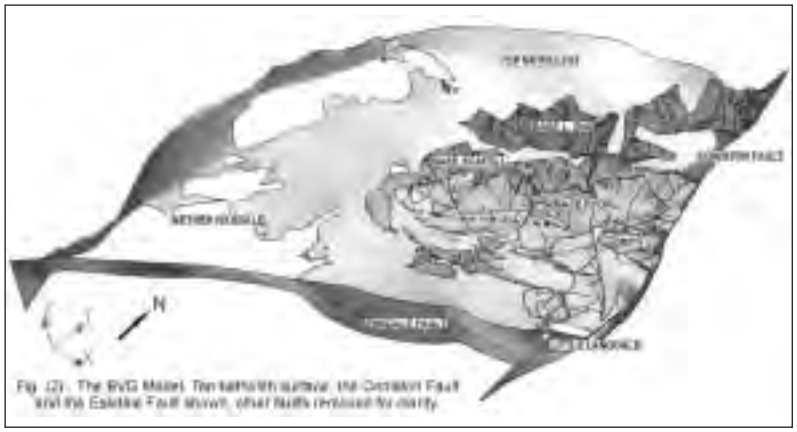

tions of the top batholith surface, facies architecture, fault deformation vectors and fault movement history, into 3D to develop a *structural framework* with which to constrain a 3D interpretation of the BVG.

The stratigraphy of the BVG is grouped to form *successions* (Millward, 2002) and three surfaces within the BVG are modelled: the base of the BVG, and the bases of the *Scafell* and the *Rydal* successions (fig. 1). The subsurface geometry and position of these surfaces are determined from interpreted structural geometries, constrained by outcrop lines and the 3D framework, and qualified by assessments of confidence in all elements. The 3D model is shown in figure (2)

Confidence in interpretative modelling

Diverse, but valid, interpretations of the subsurface arise from the importance attached to different component primary data and alternative geological concepts. A spatially coherent, structural framework requires assessments of *confidence* in contributing input data in order to resolve conflicts between interpretations.

In this case study, we have applied a semi-quantitative, objective assessment scheme to each interpretation in order to derive a *confidence plot* that incorporates many aspects of geological uncertainty (both quantitative and qualitative). The results of each assessment become part of the retained data for the model. Using this approach, the most likely spatial position of a BVG surface can be selected from differing datasets by interrogating the relative confidence scores. Additionally, the contribution to confidence (in the selected position of the BVG) given by supporting and refuting evidence can be assessed, using weighted sum and difference calculations, and propagated to the BVG surface.

Confidence scores are elicited for each unit area of every input interpretation, based on two criteria: *data quantity* and *interpretation quality* (Shrader-Frechette, 1993). In Figure (3) a confidence plot is given for the interpretation of the bedrock geological map as an illustrative example. For each square kilometre of the geological map the *quantity* of contributing primary data is assessed on the basis of *percentage of exposure* equated to five categories (*very-low* to *very-high*) with associated confidence scores (fig. 3). Similarly, a *quality* confidence score is determined for each square kilometre using a series of quality indicators, which include *theory, method, auditability, calibration, objectivity and data quality*, based on descriptive statements that define five categories with corresponding scores (Funtowicz & Ravetz, 1990). The quality score is then used to reduce the quantity score, using an exponential relationship, in order to derive an overall confidence score for each square kilometre (fig. 3).

Evaluation & discussion

Subsurface modelling with interpretative data is inherently difficult to evaluate given the lack of primary subsurface constraints. However, the structural *geometry* of interpreted subsurface horizons can be evaluated against primary surface structural data. The BVG model shows a close relationship between measured and modelled dip-azimuths. However, the correlation between measured and modelled dip-magnitudes is not so apparent. The model predicts that the Scafell Syncline has steeper limbs and a flatter hinge than has been interpreted from the surface data. Some of these differences are attributed to assumptions inherent in the evaluation methodology - the map-plane comparison of surface structural data with subsurface structural form assumes similar folding - although spatial

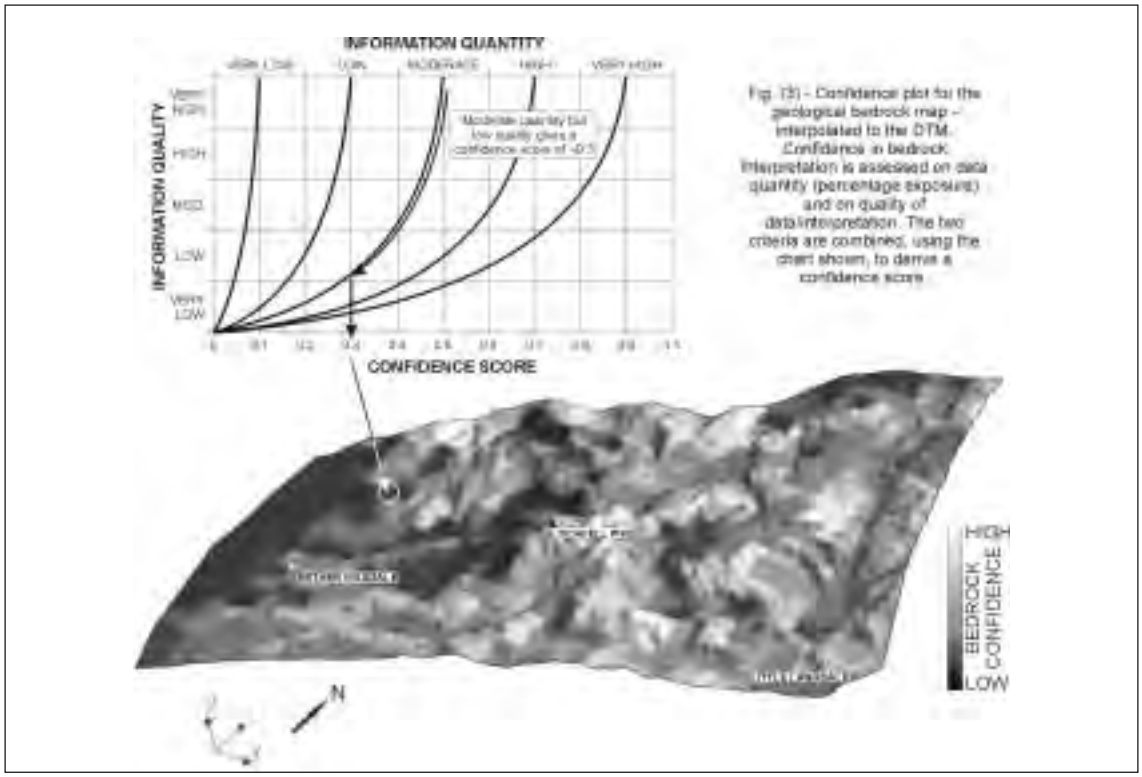

Fig. (3) - Confidence plot for the geological bedrock map – interpolated to the DTM. Confidence in bedrock interpretation is assessed on data quantity (percentage exposure) and on quality of data interpretation. The two criteria are combined, using the chart shown, to derive a confidence score.

comparisons that allow for a concentric folding style indicate that strong differences are still present. We may expect a low confidence level prediction for the BVG surfaces of the Scafell Syncline, given their poor correlation to surface structural data. However, the presence of a cross-section through this part of the model significantly increases confidence in the BVG surfaces. Cross-sections are constructed using topographical data, structural information and measured bed thicknesses with additions from data out of the plane of section. As a result, in folded terrains where both limbs crop out in the plane of the section (as here), the structural form of subsurface folds is quite highly constrained by cross-sectional interpretations. If the folds are not similar, cross-sectional interpretations of subsurface structural form (dip-magnitude distribution) have a higher confidence level than measured surface data (and form-line plots derived from them).

From complex faults to complex folds

3D modelling of the Lake District BVG has demonstrated the potential to construct models from interpretative data in a highly faulted area. In isoclinally folded terrains, the 3D structure is complicated by a number of issues additional to those explored above, most notably the presence of overturned folds. The orthotectonic Caledonian rocks of the Scottish Highlands provide an example where the protocols and modelling techniques refined in the English Lake District can be expanded in an attempt to model the Beinn Udlaidh Fold Complex of the Scottish Highlands. Recent detailed mapping of folded and faulted Dalradian lithostratigraphy (quartzites, psammites and semipelites) provides high confidence primary and interpretative data. Significant changes in depositional thicknesses combine with similar folding to produce uncertainty in subsurface geometry. The fold complex is exposed in mountainous terrain similar to the English Lake District and with similar problems of non-exposure and/or a thick covering of superficial deposits. Thus the model is based largely on a critical analysis of the surface outcrop, combined with structural measurements and a closely-spaced set of rigorous, detailed, intersecting, structural cross-sections. Topographical differences across the modelled area allow for some measure of "subsurface" penetration and so the degree of confidence in the cross-sections is also quite high. Initial attempts at building the model are encouraging.

Conclusions

Lake District modelling has shown that integrating wide-ranging interpretations of the subsurface with rigorous assessments of confidence can enhance and constrain 3D interpretations in areas with few primary subsurface data. The resultant model is a *weighted best-fit* to the data rather than an *average best-fit*. The former is a valid geological interpretation that takes account of relative strengths of the input data through assessments of confidence; the latter is a mathematical approximation lacking in geological insight. Given the varying nature of input interpretative data and their spatial density, the modelled surfaces show large variations in confidence, often over a range greater than that in an average surface modelled from primary data (Cave & Wood, 2002). Rigorous assessments of confidence are *essential* to the modelling process and must be propagated from input data to modelled surfaces. By applying the same approaches to confidence developed in the Lake District, it seems likely that well-constrained, 3D models of the overturned strata of the Beinn Udlaidh Fold Complex can be constructed.

Interpretative modelling can help to highlight the advantages, inaccuracies and errors in different methods of two-dimensional interpretation. Cross-sections can help to constrain subsurface geometry with high confidence levels in some structural domains but they can convey nothing about changes in geometry out of the plane of the section. Surface structural data and derived form-line plots (fig. 1) give an understanding of the regional structural form and can indicate regional changes in dip-azimuth (or strike) with a high degree of confidence. Changes in dip-magnitude in folded terrains cannot be predicted with such confidence as the modelling methodology inherently assumes similar folding.

REFERENCES

- Branney, M.J. & Kokelaar, B.P. 1994 Volcanotectonic faulting, soft-state deformation and rheomorphism of tuffs during development of a piecemeal caldera, English Lake District. Geological Society of America Bulletin. 106 507-530
- Cave, M.R. & Wood, B. 2002 Approaches to the measurement of uncertainty in geoscience data modelling. British Geological Survey Internal Report IR/02/068. British Geological Survey, Keyworth, Nottingham.
- Funtowicz, S.O. & Ravetz, J.R. 1990 Uncertainty & quality in science for policy. Kluwer Academic Publishers
- Millward, D. 2002 Early Palaeozoic magmatism in the English Lake District. Proceedings of the Yorkshire Geological Society. 54 65-93
- Shrader-Frechette, K.S. 1993 Burying uncertainty: Risk and the case against geological disposal of nuclear waste. University of California Press.

ON THE PROBLEM OF STRESS RECONSTRUCTION FROM DISCRETE ORIENTATIONS OF PRINCIPAL STRESSES

5-06

A.N Galybin(*), Sh.A. Mukhamediev(**)

(*) School of Civil and Resource Engineering, the University of Western Australia, WA, Australia
(**) Laboratory of Geomechanics, The Institute of Physics of the Earth, Moscow, Russia

Summary

This paper discusses different approaches to the problem of reconstruction of stress trajectories from discrete data on stress orientations. It is proposed to take into account rheology at the stage of reconstruction, which (in construct to conventional approaches based on interpolation) insures the consistency between stress trajectories and constitutive equations. Examples are presented for elastic regions.

Abstract text

There are two main approaches to the investigation of stresses in the lithosphere: analysis of observations (and special experiments, including direct in situ stress measurements) and mathematical modelling. Stress orientations represent the majority of available reliable data, they have been summarised and incorporated in the World Stress Map database, Reinecker et al. (2003). Since observations indicate that two of three principal stresses in the upper earth's crust are usually sub-

horizontal (Zoback et al., 1989), 2D elastic models are frequently employed for the determination of regional stress states in stable blocks of the lithosphere, Cloetingh and Wortel (1985, 1986) Coblentz, et al. (1995, 1998). In-situ measurements and stress indicators (e.g., focal mechanisms of earthquakes or borehole breakouts) provide real stress characteristics and possibility of monitoring, which are main advantages of the first approach. Its shortcomings can be identified as follows: not all stress components can be determined and output data are spatially discrete. Mathematical modelling based on conventional boundary value problems is capable to determine spatially and temporary continuous stress fields involving all stress components. However, simplifications and arbitrariness of assumptions, especially in posing boundary conditions, should be considered as disadvantages of this approach. This study intends to combine the advantages of the above-mentioned approaches

The aim of this study is the application of the concept of stress trajectories for the reconstruction of stresses from discrete data on stress orientations. This concept comes from photoelasticity, therefore one can adopt the following definition due to Frocht (1941): *stress trajectories* are curves the tangents to which represent the directions of one of the principal stresses at the points of tangency. In the case of plane regions, two mutually orthogonal families of stress trajectories can be drawn: they correspond to the directions of major (first family) and minor (second family) principal stresses. This study assumes that all data can be associated with one of these families, which significantly simplifies the problem of stress reconstruction. However, it is not a crucial restriction because this information is often available from different observations, e.g. breakouts are usually coaxial with minor (algebraically) principal stresses acting far from the borehole.

Let stress orientations be known at discrete points within a 2D region bounded by a closed contour. If density of data is sufficient to reconstruct stress trajectories, then typical approach in this case assumes interpolation by different methods. Examples are found in Hansen and Mount (1990), Lee and Angelier (1994) Bergerat and Anglier (1998) or Badawy and Horvath (1999). The major drawback of this approach is that the pattern of stress trajectories obtained by interpolation is not necessarily consistent with rheology introduced when one attempts to recover the complete stress tensor. Moreover, different interpolation techniques apparently lead to different rheologies; therefore, the choice of interpolation methods may be in conflict with physical meaning. In fact, as soon as the stress trajectories become known, the stress magnitudes can be found from the differential equations of equilibrium, DEE. It is evident from the DEE presented in the Lame-Maxell form

$$\frac{\partial T_1}{\partial s_1}+\frac{T_1-T_2}{r_2}=0,\quad \frac{\partial T_2}{\partial s_1}+\frac{T_1-T_2}{r_1}=0 \qquad (1)$$

Eqns (1) represent a complete system of partial differential equations for the determination of two unknown quantities (principal stresses T_1 and T_2) since the radii of curvature of the stress trajectories (r_1 and r_2) are known because the field of stress trajectories is known (s_1 and s_2 are the arc lengths along trajectories of the T_1- and T_2-families). This equation is of hyperbolic type; therefore, in order to find T_1 and T_2 uniquely, the boundary conditions have to be specified in accordance with the rules for partial differential equations (e.g. Cauchy's boundary value problem in which the boundary is not a characteristic of eqn (1)). It is important that no constitutive equations are required to determine the complete stress tensor. Therefore, the interpolation method used for compiling the continuous field of stress trajectories eventually replaces rheological models that could be considered for the region. It has been shown by Mukhamediev and Galybin (2003) that not every trajectory field is consistent with the given rheology. For instance, if trajectories are homogeneous near the boundaries of an elastic region then they have to be homogeneous through the entire region, otherwise this region is inelastic. The question regarding the determination of rheologies consistent with the given trajectories remain open, it requires thorough investigation. However, the rheology can be taken into account at the stage of interpolation. This means that solutions should be sought as linear combination of independent functions that automatically satisfy the system of DEE and rheology equations. This mathematical problem appears to be a minimisation problem in which calculated stress orientations provide the best fit to data. Solution of this problem is not unique: although stress trajectories can be found uniquely (with certain accuracy), stress magnitudes are determined with some degree of arbitrariness.

Let us illustrate this approach for elastic regions in which the constitutive equation (that can be derived from the Hooke's law and equations of compatibility by neglecting the body forces) assume the following form

$$\Delta(T_1 + T_2) = 0 \qquad (2)$$

where Δ is laplacian. Then general solution of the system of eqns (1) and (2) can be expressed in terms of two stress potentials $\Phi(z)$ and $\Psi(z)$ of complex variable z by the well-known formulas (Muskhelishvili, 1953)

$$\frac{T_1 + T_2}{2} = \Phi(z) + \overline{\Phi(z)}, \quad \frac{T_2 - T_1}{2} e^{-2i\theta} = \bar{z}\Phi'(z) + \Psi(z) \qquad (3)$$

Here it is assumed that $T_1 < T_2$, and the angle θ, representing principal direction, is positive if counted anticlockwise from the positive direction of the x-axis to the direction of T_1. Solution for complex potentials are sought in the form

$$\Psi(z) = \sum_{k=0}^{n} c_k R_k(z), \quad \Phi'(z) = \sum_{k=0}^{n-1} c_{k+n+1} R_k(z), \qquad (4)$$

where c_k are unknown coefficients and $R_k(z)$ are linearly independent holomorphic functions given inside the region. Let the number of data, N, be greater than the number of unknown coefficients (each complex one is counted as two real coefficients). Then the application when searching the best fit of calculated orientations to the data eventually leads to the following overdetermined system of linear algebraic equation

$$\mathrm{Im} \sum_{k=0}^{2n} e^{2i\theta_j} F_{kj} c_k = 0, \quad F_{kj} = \begin{cases} R_k(z_j), & k \le n \\ \bar{z}_j R_{k-n-1}(z_j), & k > n \end{cases}, \quad j = 1 \ldots N \quad (5)$$

Here θ_j represent data on stress orientation, symbol Im denotes extraction of the imaginary part of complex valued functions. This system is homogeneous, thus at least one extra condition is required in order to find its non-trivial solution. As it is evident, the multiplication of eqn (5) by any real constant does not violate this system, which means that any solution can be normalised by a real constant. This constant can be chosen from the condition that the average of the function $(T_2\text{-}T_1)/2$ over the domain is unity. Then the extra equation assumes the form

$$\mathrm{Im} \sum_{j=1}^{N} \sum_{k=0}^{2n} e^{2i\theta_j} F_{kj} c_k = N \qquad (6)$$

Solutions of the system, coefficients c_k, are further found by the least squares method. After that, one can draw the unique field of T_1 -trajectories everywhere within domain by integrating the following ordinary differential equation

$$\frac{dz}{ds_1} = e^{\frac{-i}{2}\arg[\bar{z}\Phi'(z) + \Psi(z)]} \qquad (7)$$

Stress magnitudes cannot be identified uniquely. They have a multiplier, which can either be a real positive constant or (in the special case when θ is a harmonic function) of the form $a|z|^2+2\mathrm{Re}(bz)+c$, where a and c are real constants, b is a complex constant, symbol Re denotes the real part of complex value function.

Examples of both approaches are presented in Fig. 1. The stress trajectories are recovered from the synthetic data used by Hansen and Mount (1990). Further explanations are given in caption under Fig.1.

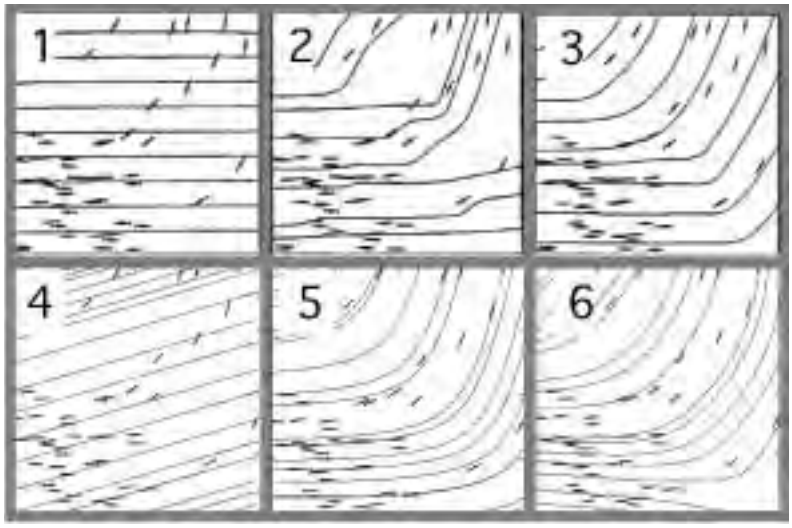

Figure 1. Continuous fields of stress trajectories obtained from synthetic data: 1-3 were recovered by Hansen and Mount (1990) by interpolation with the use of different weight functions; 4-6 have been recovered by the suggested technique for elastic regions for different number of approximating functions used in eqns (6) (1, 3, and 7 unknown coefficients correspondingly). The first row shows strong dependence on weights used in reconstruction; the authors acknowledged that the use of local weights provides better results of interpolation (plot 3). However, rheologies consistent with plots 2 and 3 remain unknown, while homogeneous trajectories in plot 1 are consistent with any rheology. On the other hand, plots 5 and 6 in the second row look very close, which demonstrates stability of reconstruction of stress trajectories performed under assumption that the region is elastic.

One important feature of the proposed approach should be pointed out: this approach allows for the determination of singular points in which stress trajectories are unidentified. These points are routinely observed in photoelasticity (so-called isotropic points) and they can be classified with respect to trajectory patterns that are realised near singular points. It is unclear if conventional interpolation methods can detect such points within the region without a-priory assumptions of their presence. The proposed approach overcomes this difficulty; singular points are associated with the roots of the second function in eqn (3) that can be easily found numerically as soon as coefficients *ck* are determined.

These points present interests for geophysics. In particular, they demonstrate what type of rotation of principal stress axis can be observed in different regions. Thus, Cloetingh and Wortel (1985, 1986) reported that the rotation of the stress orientations in the Australian continent is associated with its geographic location relatively close to the surrounding trench segments (along the northern boundary of the Indo-Australian plate) and with the lateral variation of the pull forces acting on the subsiding slabs. This result can directly be confirmed by the analysis of data available through the World Stress Map database, Reineckeret al.(2003). The results of recovery of the discontinuous field of stress trajectories within the Australia continent are presented in Fig. 2 for the case when $R_k(z)=z^k$ and n=4. They clearly demonstrate the presence of a singular point. Moreover, the analysis for n=2-10 revels that the location of this point does not strongly depend on the degree of polynomials used in the approximation. Other singular points found for different n are not stable, which suggests that their appearance is mainly explained by scattering (the best quality is estimated to have errors up to 15) and highly non-homogenous distribution of data. The fields of stress trajectories also vary with n but remain relatively stable for n<5, this indicates that thorough analysis is further required and results presented in Fig. 2 have not to be considered as final.

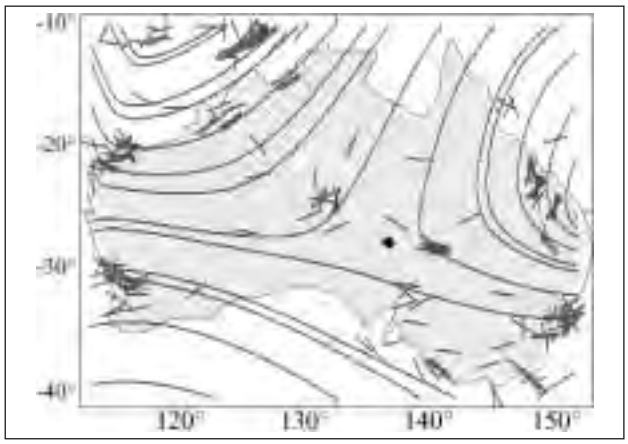

Figure 2. Stress trajectories in Australia: N = 269, n = 4, rhombus represents singular point

It should be noted that stresses within the Australian continent have been studied by finite element analysis (FEM), which presumes the specification of boundary conditions. This, however, is a major problem because different levels of stress magnitudes can be obtained even though the data are visually agree with calculated orientations of principal stresses. For example, the maximum magnitude of the compressive stresses obtained by Coblentz et al. (1995) is of order 25 MPa, while the results of Cloetingh and Wortel (1985, 1986) indicate that the level of the stress magnitudes for the same region is 100-200 MPa. The proposed approach eliminates this problem but requires the identification of an arbitrary multiplier from the data on in-situ stress measurement. Therefore in contrast to the FEM analysis no hypothesis is used for the determination of stresses and even the magnitudes of boundary stresses can be identify, which provides the estimation of forces in collision zones of plate boundaries.

REFERENCES

- Badawy, A. and Horvath, F., (1999), Tectonophysics, 304, 385–403
- Bergerat, F. and Anglier, J., (1998), Geodinamica Acta (Paris), 11, N2-3, 105-118
- Cloetingh, S. and Wortel, R., (1985), R. Geophys. Res. Lett., 12, 77-80
- Cloetingh, S. and Wortel, R., (1986), Tectonophysics, 132, 46-67
- Coblentz,D.D. et al., (1995), Earth Planet. Sci. Lett., 133, 299-309
- Coblentz,D.D et al., (1998), J. Geophys. Res., 103, 919-931.
- Frocht, M.M.,(1941), Photoelasticity, John Wiley & Sons, Inc. New York
- Hansen, K.M. and Mount, V.S. (1990), J. Geophys. Res., 95 (B), 1155-1165
- Lee, J.-C. and Angelier, J., (1994), Computers and Geosciences, 20, 161-191
- Mukhamediev, Sh A and Galybin, A.N (2004), Doklady Physics, in print
- Muskhelishvili, N.I. (1953) Some Basic Problems of the Mathematical Theory of Elasticity, Holland
- Reinecker, J. et al.(2003), The 2003 release of the World Stress Map, online at www.world-stress-map.org
- Zoback, M.L. et al. (1989), Nature, 341, 291-298

THERMAL-MECHANICAL PHYSICAL MODELLING: POTENTIALS, LIMITATIONS, PAST RESULTS AND FUTURE NEEDS

5-07

Djordje Grujic

Department of Earth Sciences, Dalhousie University, Halifax, N.S. B3J 3J5, Canada

Summary

In order to perform meaningful experiments of crustal and lithospheric processes thermal-mechanical processes have to be taken into account. Recent finite-element thermal-mechanical experiments have demonstrated the high sensitivity of crustal processes on both fine variations of mechanical parameters, and on the dynamics of surface processes. If the consistent scaling factors are respected, the mechanical properties of analogue materials and the construction limitations of the deformation rigs seriously limit the time- and length-scale of natural prototypes that can be modelled. Furthermore, the range of mechanical properties of the analogue materials excludes sensitivity tests in physical experiments, whereas the addition of dynamic surface processes offers insurmountable construction challenges. This discussion is illustrated by the example of modelling of a Himalayan-type orogen.

Abstract text

Advances in codes and in computing power of computers have led to significant progress in fully coupled thermal-mechanical numerical modelling (e.g. Beaumont et al., 2001). These and similar experiments demonstrate the high sensitivity of crustal- and lithospheric-scale tectonics on various parameters (Jamieson et al., 1998, 2002; Vanderhaeghe et al., 2003), which are linked either to thermal properties of earth materials or to their density. All these change over time-scales of 10s of millions of years. These processes are further complicated by internal heath production, and by phase changes (caused by e.g. partial melting or high-pressure metamorphism). In addition, coupling of tectonic and surface processes has been demonstrated both in field and trough numerical experiments. The

magnitude of influence of surface denudation (and sedimentation) on tectonics is mater of debate (e.g. Molnar, 2003). However, it is evident that surface processes follow strict and quite well established physical laws (Burbank and Anderson, 2000). The experiences from numerical experiments demonstrate that analogue models intended to improve our understanding of tectonics at crustal or lithosperic scale ought to respect these laws as well. "Round-cow" simplifications are needed in order to understand first order processes; however, some of the parameters have to be taken rigorously into account if a thermal-mechanical experiment were to provide geologically meaningful results.
Significant progress has been made in the recent years in techniques and instrumentation of analogue modelling that allows well-controlled and precise thermal-mechanical experiments to be performed (e.g. Chemenda et al., 2000; Rossetti et al., 2001; Wosnitza et al., 2001). Analyses of scaling (e.g. Davy and Cobbold, 1992; Cobbold and Jackson, 1992; Wosnitza et al., 2001) have shown that the consistent scaling factors can be achieved, which allows thermal-mechanical models of lithospheric processes to be attained. However, there are serious limitations to the power of this experimental technique:

(a) Scaling analyses and the physical experiments have ignored the time-scale of thermal-mechanical processes in crust and thus in the experiments.
(b) The range of physical properties of the available materials suitable to analogue modelling determines the parameter range of the experiments.
(c) For the reason above, sensitivity tests cannot be performed in the physical thermomechanical experiments;
(d) Although independent experiments on denudation processes have been performed (Bonett and Crave, 2003), it is technically impossible to incorporate them in the thermal mechanical experiments at much larger scale. Rule of thumb simulations of denudation and/or sedimentation performed in a number of physical experiments are not process driven but rather experimenter determined.

In thermal-mechanical experiments time t, length l and thermal diffusivity k are interdependent parameters and thus cannot be varied independently in a physical experiments because

$$S_t = \frac{S_l^2}{S_\kappa} \qquad (1)$$

where S is the scaling factor for the corresponding parameter. One order of magnitude change in S_l results in two orders of magnitude change of S_t for a constant S_κ (Fig. 1). Thermal diffusivity is a material property and cannot be varied in a given material. The best investigated analogue materials that have strongly temperature dependent viscosities (a prerequisite for thermal-mechanical physical experiments) are paraffin wax and colophony (a.k.a. gum rosin). The latter is very difficult to mould and, thus, has very limited potential to build precise models. The following discussion will therefore focus on paraffin wax only.
For silicates, κ is in the order of 10^{-6} m^2 s^{-1} (e.g. Ranalli, 1987), whereas for paraffin wax $\kappa \approx 8 \times 10^{-8}$ m^2 s^{-1} (Rossetti et. al., 1999). This results in scaling factor of S_κ 8 x 10^{-2} (vertical grey line in Fig. 1). For colophony the $\kappa \approx 6 \pm 3 \times 10^{-7}$ m^2 s^{-1} (Cobbold and Jackson, 1992), which results in scaling factor of $S_\kappa \approx 10^{-1}$. It would be more convenient for physical experiments if there were a material with one order of magnitude lover κ, which would result in one order magnitude smaller S_l or S_t (Fig.1). The paraffin wax has, however, very low thermal diffusivity; no material is known with κ one order of magnitude lower, and accordingly S_κ smaller by one order of magnitude. Orogenic processes have strain rates on the order of 10^{-14} s^{-1} (Pfiffner and Ramsay, 1982). If we decide to run an experiment at strain rate of 10^{-4}, the resulting scale factor for time is 10^{-10}. Using the equation (1) the scale factor for length is S_l 2.9 x 10^{-6} (horizontal grey line in fig. 1). Therefore, the initial paraffin wax model 1 m long corresponds to a length in nature of about 345 km. If the experiment is performed at strain rate of 10^{-5} s^{-1} the resulting scale factor for time is 10^{-9}, and the initial model of 1 m is reduced to ca. 112 km in the nature. In summary, because the S_κ is fixed for the given analogue material and the size of the experiment is determined by the size of the deformation rig, the change in experimental strain rate results in change in the size of the natural prototype to be modelled.

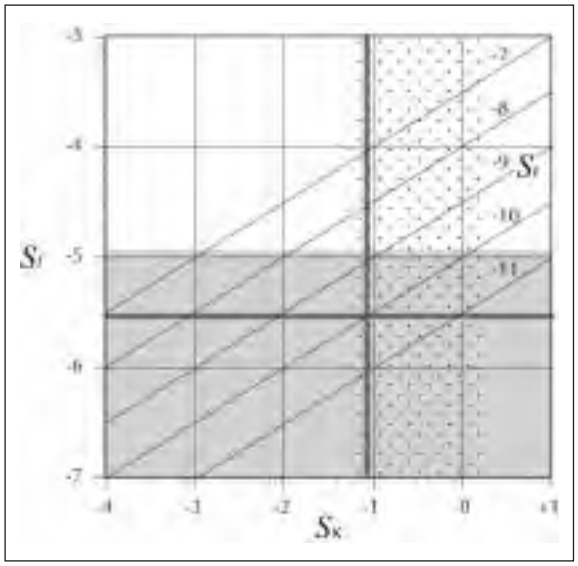

Figure 1. Graph of isolines of scaling factor for time plotted against scaling factors for length and thermal diffusivity. Numbers are the exponents for the corresponding scaling factor. Stippled field indicates the available range of S_k, and the grey field indicates the technically reasonable range of S_l.

The natural lengths stated above may be sufficient to present an orogen but are ca. order of magnitude too short to include plate convergence over the time-scale of a typical orogen. Finite-element thermo-mechanical modelling demonstrates that the initial stages of a collision have to be taken into account when modelling the latter stages of an orogen (e.g. Jamieson et al., 1998, 2002). Namely the tame scale for thermal equilibration of a subducted plate is ca. 20 Ma. To model a larger natural prototype the experiment ought to be run faster. The strain rate in the experiment cannot be changed arbitrarily, however, because of the parameters that relate deformation and the thermal diffusivity. The relevant dimensionless numbers that have to be taken into account are the Prandtl number and the Péclet number.

Prandtl Number is a dimensionless quantity, which is the ratio of kinematic viscosity ν ($m^2\ s^{-1}$) and thermal diffusivity κ ($m^2\ s^{-1}$). First describes how momentum diffuses, second how heat diffuses.

$$Pr \equiv \frac{\nu}{\kappa} \tag{2}$$

A fluid with a small *Pr* diffuses heat more rapidly than does momentum; the reverse is true for a fluid with a large value of *Pr*. Prandtl number characterizes the regime of convection; in order of increasing Prandtl number, modes of convection are as follows: (a) Rolls, (b) Three-dimensional steady pattern in which flow occurs in interlocking polygons, which are often hexagons or squares, (c) Irregularly shaped cells, (d) Narrow rising regions characterized by isothermal circulation, and (e) Turbulent convection in which no cells are present. This indicates that the corresponding scaling factor S_{Pr} should tend to 10^0 because if it were significantly larger or smaller convection regimes would be different in nature and the experiment. This is however not achievable. Prandtl number for mantle is on the order of magnitude $\approx 10^{24}$ (Ranalli, 1987). For paraffin wax it is in the order of 10^7 to 10^{12} as a function of temperature. As the dynamic viscosity changes with temperature so does the kinematic viscosity and with it the *Pr*.

The relative importance of convection (or advection) and conduction is expressed by the thermal Péclet number

$$Pe \equiv \frac{ul}{\kappa} \tag{3}$$

where *u* is the characteristic velocity (e.g. subduction rate), *l* is the characteristic length (e.g. thickness of a crustal or lithosperic layer) and κ is the thermal diffusivity. If *Pe* is much larger than unity, advection dominates; if *Pe* is much smaller than unity conduction dominates. Under ocean ridges *Pe* is about 30, for the mantle *Pe* is ca. 10^3 (Ranalli, 1987). The equation (3) can be rewritten as

$$Pe = \frac{1}{2} Re \times Pr \tag{4}$$

(Turcotte and Schubert, 2000; eq. 6-276), where *Pr* is the Prandtl number, and *Re* the Reynolds number (ratio of inertia and viscous forces). Two systems are therefore dynamically similar if they have the same *Re* and thermomechanically similar if they have the same *Re* and *Pr*. The values of *Pr*, *Pe* and *Re* for the mantle indicate that the convection is much more efficient than the conduction as an agent of heat transfer and inertia force are negligible (Ranalli, 1987). In tectonic sense the Péclet number controls the heating of the subducted material, or the cooling of the exhumed material (see e.g. Jamieson et al., 1998). Rapid denudation and exhumation remove surface material at high thermal Péclet number and the crustal material is advected upward with little cooling. That indicates that the surface processes (both denudation and sedimentation) have to be scaled properly. If they cannot be dynamically induced than they should be done by experimenter according to the rates predicted from numerical models. Therefore, for thermal-mechanical physical modelling concomitant numerical modelling should be performed. The importance of the thermal Péclet number indicates, in addition, that the upper crustal layer hast to be included in the lithosphere-scale physical models and that it has to have appropriate thermal properties too.

The technical challenges of rigorously scaling a thermal-mechanical physical model are presented on the example of the modelling of the Himalayas. The analysis considers that collisional orogen lasts 50 My, and that the amount of Indian continental lithosphere consumed in the Himalayas is up to 1500 km. Numerical models suggest that in order for orogen to evolve into today's configuration the tectonics during last 20-25 My had to be accompanied with surface denudation of up to 1 cm / yr over a zone ca. 100 km wide. Such high denudation rates are consistent with the actual observations in the nature (see Molnar, 2003 and references therein).

REFERENCES

- Beaumont, C., Jamieson, R.A., Nguyen, M.H. and Lee, B. (2001), Himalayan tectonics explained by extrusion of a low-viscosity crustal channel coupled to focused surface denudation. Nature 414, 738-742.
- Bonnet, S. and Crave, A. (2003), Landscape response to climate change: Insights from experimental modelling and implications for tectonic versus climatic uplift of topography. Geology, 31, 123-126.
- Burbank, D.W. and Anderson, R.S. (2000) Tectonic Geomorphology. Blackwell Scientific, Oxford, 270 p.
- Chemenda, A., Burg, J.-P., and Mattauer, M. (2000) Evolutionary model of the Himalaya-Tibet system: geopoem based on modelling, geological and geophysical data, Earth and Planetary Sciences Letters, 174, 397-409.
- Cobbold, P. R. and Jackson, M. P. A. (1992), Gum rosin (colophony): A suitable material for thermomechanical modelling of the lithosphere. Tectonophysics, 210, 255-271.
- Davy, P. and Cobbold, P. R. (1991) Experiments on shortening of a 4-layer model of the continental lithosphere. Tectonophysics, 188. 1-25.
- Jamieson, R. A., Beaumont, C. Fullsack, P. and Lee, B (1998), Barrovian regional metamorphism: wher's the heat? In: Treloar, P. J. and O'Brien P. J. (eds), What Drives Metamorphism and Metamorphic Reactions? Geological Society, London, Special Publications, 138, 23-51.
- Jamieson, R. A., Beaumont, C. Nguyen, M. H. and Lee, B (2002) Interaction of metamorphism, deformation and exhumation in large convergent orogens. Journal of Metamorphic Geology, 20, 9-24.
- Molnar, P. (2003) Nature, nurture and landscape. Nature, 426, 612-612.
- Ranalli, G. (1987), Rheology of the Earth. Allen & Unwin, Boston, 366.
- Rossetti, F., Faccenna, C., Ranalli, G., Funiciello, R. and Storti, F. (2001), Modelling of temperature dependent strength in orogenic wedges: First results from a new thermomechanical apparatus. In Tectonic Modelling: A Volume in Honour of Hans Ramberg, ed. H. A. Koyi, & N. S. Mancktelow, Geological Society of America Memoir 193, 253-259.
- Rossetti, F., Ranalli, G. and Faccenna, C. (1999), Rheological properties of paraffin as an analogue material for viscous crustal deformation. Journal of Structural Geology, 21, 413-417.
- Turcotte, D. L. and Schubert, G. (2002), Geodynamics. Second edition. Cambridge University Press, 456.
- Vanderhaeghe, O., Medvedev, S., Fullsack, P., Beaumont C. and Jamieson R. A. (2003) Evolution of orogenic wedges and continental plateaux: insights from crustal thermal–mechanical models overlying subducting mantle lithosphere. Geophysical Journal International 153, 27–51.
- Wosnitza, E. M., Grujic, D., Hofmann, R. and Behrmann, J. H. (2001), New apparatus for thermomechanical analogue modelling. In Tectonic Modelling: A Volume in Honour of Hans Ramberg, ed. H. A. Koyi, & N. S. Mancktelow, Geological Society of America Memoir 193, 245-251.

EULERIAN SPECTRAL/FINITE DIFFERENCE METHOD FOR LARGE DEFORMATION MODELLING OF VISCO-ELASTO-PLASTIC GEOMATERIALS

5-08

B.J.P Kaus(*), Y.Y. Podladchikov(*,**), D.W.Schmid(*,**)

(*) Geological Institute, ETH Zurich – Sonnegstrasse 5 – 8092 Zurich- Switzerland
(**) Physics of Geological Processes – University of Oslo – 0316 Oslo -Norway

Summary

Many problems that occur in geodynamics can be reduced to the solving of visco-elasto-plastic rheological equations. Many problems that occur in geodynamics can be reduced to the solving of visco-elasto-plastic rheological equations. Here a spectral/finite-difference method is described that can deal with these rheologies in an Eulerian framework. The method approximates derivatives in vertical direction by finite-differences and in horizontal direction(s) by a pseudospectral approach. Material boundaries are tracked by marker chains that are moved through a fixed grid and allow large deformations. It is demonstrated that the Gibbs effect is avoidable; the method is reliable up to large viscosity contrasts of $5x10^5$ and is able to resolve strongly localised solutions like shear bands.

Introduction

The ultimate goal of geoscientists is to understand the physical processes that formed and reworked the earth's tectonic plates and the underlying mantle. This is a difficult problem since the current state of earth is a result of billions of years of deformation and insight in the main driving mechanisms is at least indirect or approximate. In recent years numerical modelling has been proven useful here. Much of our understanding about mantle convection, for example, comes from numerical simulations that treat the mantle as a creeping highly viscous fluid. The lithospheric plates, on the other hand, are colder than the mantle and behave more like a viscoelastic, brittle solid. Numerical modelling of the deformation of these plates and their coupling to the mantle thus requires the solving of visco-elasto-plastic rheological equations. In addition it is important that a numerical method, developed for this purpose, is efficient, can handle large deformations, strong variations of material properties, free surface effects and non-linear rheologies. Previous workers utilized finite element methods (Huismans *et. al.* 2001), dynamic lagrangian remeshing methods (Braun and Sambridge 1994) and control-volume methods (Poliakov *et.al.* 1996) to deal with the problems described above. We follow a different approach and solve the governing equations by an Eulerian finite-difference/spectral method.

Mathematical model

For many geodynamic applications inertial effects are not important and the balance equations can be written as:

$$\begin{aligned} \frac{\partial \rho v_i}{\partial x_i} + \frac{\partial \rho}{\partial t} &= 0 \\ \frac{\partial \sigma_{ij}}{\partial x_j} &= \rho g_i \end{aligned} \qquad (1)$$

here v_i is velocity, σ_{ij} stress, ρ density, g gravitational acceleration and t is time.

A Maxwell viscoelastic rheology for stress- and strain-deviators is assumed (e.g. Schmalholz *et.al.* [4]):

$$\tilde{\dot{\varepsilon}}_{ij}^{ve} = \tilde{\dot{\varepsilon}}_{ij}^{v} + \tilde{\dot{\varepsilon}}_{ij}^{e} = \frac{1}{2\mu_{vis}}\tilde{\sigma}_{ij} + \frac{1}{2G}\frac{D\tilde{\sigma}_{ij}}{Dt} \qquad (2)$$

where $\tilde{\sigma}_{ij} = \sigma_{ij} + P$, $\tilde{\dot{\varepsilon}}_{ij} = \dot{\varepsilon}_{ij} - \bar{\dot{\varepsilon}}$, $\dot{\varepsilon}_{ij} = \frac{1}{2}\left(\frac{\partial v_i}{\partial x_j} + \frac{\partial v_j}{\partial x_i}\right)$, $P = -\frac{1}{3}tr\left(\sigma_{ij}\right)$, $\bar{\dot{\varepsilon}} = \frac{1}{3}tr\left(\dot{\varepsilon}_{ij}\right)$, G is the elastic shear modulus, μ_{vis} the shear viscosity (which might have a nonlinear stress- and temperature-dependence) and $\frac{D}{Dt}$ denotes the objective derivative of the stress tensor.
Rocks cannot sustain high stresses; they will fail plastically instead. Since in this case elastic strains are small it is adequate to make the additive strain rate decomposition, which states that:

$$\dot{\varepsilon}_{ij} = \dot{\varepsilon}^{ve}_{ij} + \dot{\varepsilon}^{p}_{ij} \tag{3}$$

The plastic strain rate can be calculated according to:

$$\dot{\varepsilon}^{p}_{ij} = \dot{\lambda}\frac{\partial Q}{\partial \sigma_{ij}} \tag{4}$$

where $\frac{\partial Q}{\partial \sigma_{ij}}$ is the direction of plastic flow and $\dot{\lambda}$ the plastic multiplier. The yield criterion can be expressed in Kuhn-Tucker form as

$$\dot{\lambda} \geq 0, F \leq 0, \dot{\lambda}F = 0 \tag{5}$$

For rocks under upper-crustal conditions, a Mohr-Coulomb yield function with non-associated flow rule is the minimum model. Spelled out for a 2D case it can be written as:

$$\begin{aligned} F &= \tau^* - \sigma^* \sin\left(\phi\right) - c\cos\left(\phi\right) \\ G &= \tau^* - \sigma^* \sin\left(\psi\right) \end{aligned} \tag{6}$$

where ϕ is the friction angle, ψ the dilation angle (in general smaller than ϕ), c the cohesion of the rocks, τ^* is the radius and σ^* the centre of the Mohr-circle.
By substituting Eqs. (3) and (4) into Eq. (2) we arrive at the rheological equation for a visco-elasto-plastic material:

$$\dot{\varepsilon}_{ij} - \dot{\varepsilon}^{p}_{ij} - \dot{\varepsilon}^{ve} = \tilde{\dot{\varepsilon}}^{ve}_{ij} = \frac{1}{2\mu_{vis}}\left(\sigma_{ij} + P\right) + \frac{1}{2G}\frac{D\left(\sigma_{ij} + P\right)}{Dt} \tag{7}$$

Numerical method

The system of equations, Eq. (1) and Eq. (7), is discretised using a finite difference/spectral approach. Differently to conventional approach leading to a 4th-order ordinary differential equation (e.g. Schmalholz *et.al.* 2001), our formulation results in two 2nd-order equations for two unknown functions. The balance equations are always satisfied analytically by choosing σ_{zz} and v_z as the primitive unknown functions. Moreover, the formulation makes the implementation of stress boundary-conditions straightforward. Variables are approximated by a Fourier series in the horizontal direction and by a finite-difference scheme in the vertical direction. The balance equations (Eqs. 1) can than be written for a 2D case as (see *e.g.* Trefethen 2001):

$$
\begin{aligned}
i\omega\hat{v}_x^l + \frac{\partial \hat{v}_z^l}{\partial z} &= \hat{\dot{\varepsilon}}^p + \hat{\dot{\varepsilon}}^{ve} \\
i\omega\hat{\sigma}_{xx}^k + \frac{\partial \hat{\sigma}_{xz}^k}{\partial z} &= 0 \\
i\omega\hat{\sigma}_{xz}^k + \frac{\partial \hat{\sigma}_{zz}^k}{\partial z} &= \hat{\rho}^k g
\end{aligned} \tag{8}
$$

for $k = 1..nk$ and $l = 1..nl$. Here hats denote the Fourier coefficients, $w = 2\pi k/L$ is the wave number, L the size of the domain in the horizontal direction, $i = \sqrt{-1}$ and nk, nl are the total number of harmonics in the spectral direction. From these equations expressions for $\hat{\sigma}_{xx}$ and $\hat{\sigma}_{xz}$ as a function of $\hat{\sigma}_{zz}$ can be written:

$$
\begin{aligned}
\hat{\sigma}_{xz}^k &= -\frac{1}{i\omega}\left(\frac{\partial \hat{\sigma}_{zz}^k}{\partial z} - \hat{\rho}^k g\right) \\
\hat{\sigma}_{xx}^k &= -\frac{1}{i\omega}\left(\frac{\partial \hat{\sigma}_{xz}^k}{\partial z}\right) = \frac{1}{i\omega}\left(\frac{\partial}{\partial z}\left(\frac{1}{i\omega}\left(\frac{\partial \hat{\sigma}_{zz}^k}{\partial z} - \hat{\rho}^k g\right)\right)\right)
\end{aligned} \tag{9}
$$

The same applies for $\hat{v}_x$ and $\hat{v}_z$:

$$
\hat{v}_x^l = -\frac{1}{i\omega}\left(\frac{\partial \hat{v}_z^l}{\partial z} - \left(\hat{\dot{\varepsilon}}^p + \hat{\dot{\varepsilon}}^{ve}\right)\right) \tag{10}
$$

The rheological equation (7) can be spelled out both for normal stresses and for shear stresses:

$$
\begin{aligned}
\left(\hat{\sigma}_{xx}^k - \hat{\sigma}_{zz}^k\right) = 2\hat{\mu}_{eff}^m &\left(\left(i\omega\hat{v}_x^l - \hat{\dot{\varepsilon}}_{xx}^p\right) - \left(\frac{\partial \hat{v}_z^l}{\partial z} - \hat{\dot{\varepsilon}}_{zz}^p\right)\right) + \\
&\hat{\eta}_{eff}^m\left(\hat{\overset{\nabla^{k,old}}{\sigma}}_{xx} - \hat{\overset{\nabla^{k,old}}{\sigma}}_{zz}\right) \\
\hat{\sigma}_{xz}^k = \hat{\mu}_{eff}^m &\left(\frac{\partial \hat{v}_x^l}{\partial z} + i\omega\hat{v}_z^l - \hat{\dot{\varepsilon}}_{xz}^p\right) + \hat{\eta}_{eff}^m\left(\hat{\overset{\nabla^{k,old}}{\sigma}}_{xz}\right)
\end{aligned} \tag{11}
$$

where $\mu_{eff} = \frac{1}{\frac{1}{\mu_{vis}} + \frac{1}{Gdt}}$ and $\eta_{eff} = \frac{1}{1 + \frac{Gdt}{\mu_{vis}}}$ are redefined effective viscosities (which become dependent on the timestep dt). ∇ denotes the objective Jaumann derivative of the stress component, which consists of an advective and a rotational part:

$$
\overset{\nabla^{old}}{\sigma}_{ij} = \left(v_i\frac{\partial \sigma_{ij}^{old}}{\partial x_i} + rotation(\sigma_{ij}^{old}\right) \tag{12}
$$

Advective terms are solved using a characteristics-based method (Malevsky and Yuen 1991) in order to minimize numerical diffusion, whereas the rotational terms are modelled using standard rotational formulas (*e.g.* Turcotte and Schubert 1981) that collapse into the Jaumann corotational derivative in the case of small rotations.

Two equations for the two unknowns $\hat{\sigma}_{zz}$ and $\hat{v}_x$ are obtained by combining eq. (9)-(12). Solving these equations is straightforward if the viscosity is constant or depth-dependent. If there are strong lateral gradients of effective viscosity, the algorithm finds the solution iteratively (Schmalholz *et. al.* 2001). The method converges even for large, sharply varying, viscosity contrasts of 5×10^5, without noteworthy Gibbs effect (see Figure 1a).

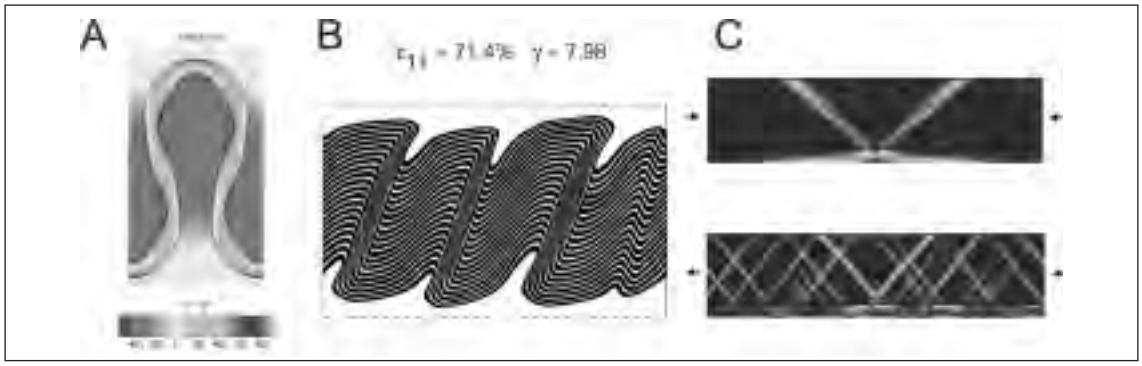

Figure 1. Numerical examples: A) Pressure distribution in a pure-shear fold with a viscosity contrast of $5x10^5$ (Schmalholz et. al. 2001). B) Multilayer sequence (viscosity contrast 1000) subjected to pure-and simple shear deformation (Schmid 2002). C) 2nd invariant of the strainrate tensor, during pure shear compression (upper picture) or extension (lower picture) of a Mohr-Coulomb brittle material with ϕ= 30° and ψ=0°, floating on top of a viscous substratum.

The current formulation makes it straightforward to implement no-slip or free-slip boundary-conditions. In addition, the implementation of stress-free boundary-conditions or any condition involving normal stresses does not require 3rd derivatives. A free surface boundary condition is difficult to incorporate in Eulerian fixed grid numerical codes such as the one described here. Therefore we approximate the free surface by putting a layer of low viscosity in the upper part of the numerical box.

Boundaries between materials with a sharp variation of properties are described by marker-chains that are moved through a fixed computational grid by an implicit time step algorithm (see Figure 1b for an example of simple-shear folding). Fourier coefficients of effective viscosity and density fields are calculated directly from the marker-chain. An advantage of such a marker-chain method over particle-based methods is that much less points are needed to describe a material like a fold. In the case that more slowly varying properties like temperature have to be advected, a characteristics-based method is employed.

Plastic yielding occurs if stresses are higher than the yield envelop (i.e. $F>0$ in equation (6)). If this is detected, stresses are pointwise returned to the yield envelop in the direction of the plastic flow (equation 4). Combining a Mohr-Coulomb yield envelop with a Mohr-Coulomb plastic flow potential results in shear bands with angles that are in-between the Roscoe angle (45-Ψ/2) and the Coulomb-angle (45-ϕ/2), which is in agreement with theoretical predictions (e.g. Vermeer 1990)

Conclusions

The Eulerian spectral/finite difference method is a promising tool for modeling geodynamic problems, since it can deal with large deformations. An algorithm such as the one described in this paper reduces a 2D or a 3D problem to the subsequent solving of 1D equations (see e.g. Schmalholz *et. al.* 2001 and Kaus and Podladchikov 2000), which is efficient even in the case with strongly varying material properties. Examples (Figure 1) illustrate the capability of the method to deal with large deformations, strongly varying material properties and non-associated Mohr-Coulomb plasticity.

REFERENCES

- Huismans et. al. (2001), Journal of Geophysical Research. 106, B6, 11271-11292.
- Braun ans Sambridge (1994), EPSL, 124, 211-220.
- Poliakov et. al (1996), Geological Society Special Publication, 100, 291-302.
- Schmalholz et.al. (2001), Geophysical Journal International, 145, 188-208.
- Turcotte and Schubert (1981), Geodynamics.
- Kaus and Podladchikov (2000), Geophysical Research Letters, 28(6), 1095-1098.
- Malevsky and Yuen (1991), Physics of Fluids, A3(9), 2105-2115.
- Trefethen (2001), Spectral Methods in MATLAB, SIAM.
- Schmid (2002), PhD-Thesis, ETH Zurich.
- Vermeer (1990), Geotechnique, 40(2), 223-236.

SNARK + UNDERWORLD: TOWARDS A GENERAL COMPUTATIONAL TOOL FOR GEODYNAMIC MODELLING

5-09

D.A. May(*), L. Moresi(*), Steve Quenette ($), Bill Appelbe ($)

(*) School of Mathematical Sciences, Monash University, Clayton Victoria, 3800, Australia.

($) Victorian Partnership for Advanced Computing, 110 Victoria St, Carlton S., Victoria, 3053, Australia

Summary

General computational tools which are specifically designed for geological modelling do not currently exist. The absence of such numerical packages is attributed to the fact that most geological problems evolve under extremely large strains in accordance to a complex, non-linear interaction between the geometrical structure and the rheology of the system (Moresi, Dufour, et al [2003]) We aim to ameliorate this problem by combining a well designed computational framework with a flexible Lagrangian integration point finite element based numerical scheme. A description of the philosophy behind the computational framework, the numerical method and some simulation results involving basin formation through faulting will be presented.

Modelling code requirements

We wish to create a suite of software applications which naturally deal with the coupled thermal-mechanical system of crust, lithosphere, and convecting mantle. Two problems immediately present themselves: (1) how to produce a mathematical / numerical formulation which is sufficiently general to handle viscoelastic, brittle deformation and faulting in the cool, shallow lithosphere, and extremely high strain, non-linear, temperature, pressure, and grain-size dependent viscous flow at depth (2) how to provide this formulation in a software application or library which is usable by a range of people from the specialist numerical modeller through to the end user.

The need for computational frameworks

Numerical codes within the geoscience community are typically highly specialised pieces of software. The main problem with many such stand-alone scientific codes is that they are difficult to modify and extend to new problems outside the domain for which they were originally designed. This is generally a result of inadequate software design.

To resolve this problem we utilise a software "framework" — defined to mean "an environment for the development of codes which are both extensible and interoperable". Since the computational requirements of end users is continually expanding with the expansion of computing power, the underlying framework is implicitly designed to be make use of shared memory and distributed memory environments. The framework allows developers to build applications that are scalable, extensible and interoperable. We utilise the open source framework StGermain which is currently under development by the Victorian Partnership for Advanced Computing (VPAC: Geoscience portal [2003]).

Utilising the StGermain framework, two higher level abstractions (Snark and Underworld) have been developed. Snark (Moresi, May, et al [2003]) essentially contains the Lagrangian integration point abstraction whilst Underworld contains the rheological abstractions. The details of each of each of these higher level abstractions is described in the following sections.

Snark - Finite elements with Lagrangian integration points

A wide variety of geological processes can be modelled from a fluid dynamical point of view. The choice of a fluid dynamical representation of the problem leads to a formulation which deals very effectively with the extreme strains associated with mantle convection where the stress / strain history is usually assumed to be unimportant. In the shallow lithosphere, however, the effects of viscoelasticity, brittle / plastic deformation with strain softening, and grain size dependent, non-linear viscous flow require a method which can track the stress / strain history of individual particles of fluid. For this we also need some form of Lagrangian material tracking.

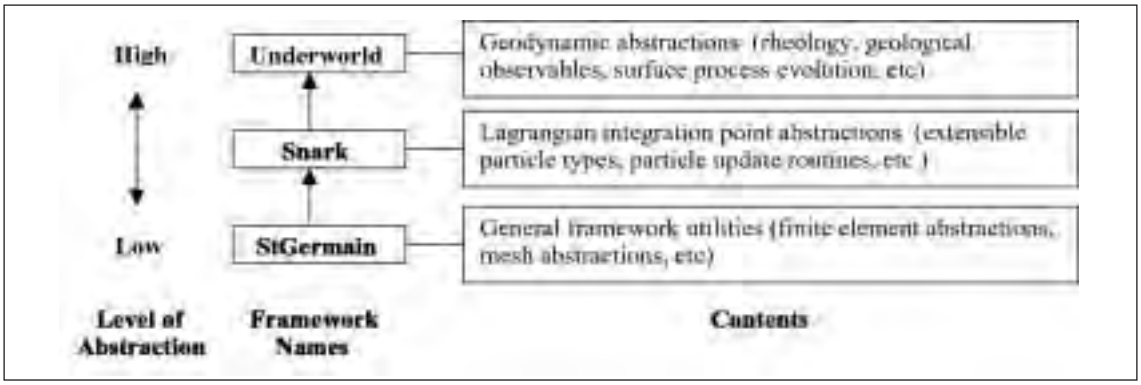

Figure 1: Visual representation of the framework hierarchy utilised and the basic contents of each.

The equations describing incompressible Stokes flow (1a-1b) serve as the continium representation which we use within our numerical scheme. The conservation equation for momentum in the creeping flow regime is given by;

$$\tau_{ij,j} - p_{,i} = f_i \tag{1a}$$

subject to the continuity requirement,

$$u_{i,i} = 0 \tag{1b}$$

Here **u** is the velocity, p is the pressure, **f** is a body forcing term and τ is the stress tensor. The exact form of the stress tensor τ is subject to the physics to be modelled. The nature of the stress tensor will be elaborated upon in the following section.

The finite element scheme with Lagrangian integration points consists of an ensemble of Lagrangian points embedded within an Eulerian mesh. Material properties are discretised using the Lagrangian points whilst the mesh is used to discretise the velocity and pressure fields which are solved using a standard mixed finite element formulation. The material points are advected using the velocity field interpolated from the mesh. Coupling between the finite element mesh and material points is achieved through the quadrature scheme used to approximate the integrals obtained from the weak form of the governing equations.

The discrete representation of the momentum and continuity equations are formed using a standard mixed finite element formulation. This requires us to obtain the weak form of the governing p.d.e. by multiplying (1a) with the test function N_i and (1b) by Q. Integrating over the volume Ω and applying Gauss' theorem yields

$$\begin{aligned} &\int_\Omega \tau_{ij,j} N_{i,j} d\Omega - \int_\Omega p N_{i,i} d\Omega = \int_\Omega f_i N_i d\Omega + \int_\Gamma \bar{t}_i N_i d\Gamma \\ &\int_\Omega u Q_{,i} d\Omega = 0 \end{aligned} \tag{2}$$

Now if we subdivide the volume into n_e elements and approximate the velocity and pressure by

$$\mathbf{u} = \sum_j N_j \mathbf{u}_j, \quad p = \sum_j Q_j p_j$$

where N_i and Q_j are the shape functions used to approximate the velocity and pressure spaces respectively and j is the node index. Then the discrete form of the Stokes problem can be written as

$$\begin{pmatrix} K & G \\ G^T & 0 \end{pmatrix} \begin{pmatrix} \mathbf{u} \\ \mathbf{p} \end{pmatrix} = \begin{pmatrix} \mathbf{f} \\ \mathbf{0} \end{pmatrix} \tag{3}$$

where K is the discrete stress tensor, G is the discrete gradient operator and **u** and **p** are represent the vectors of nodal unknowns for velocity and pressure respectively.

The entries within the stiffness matrix K consist of integrating some quantity, say ϕ over the element domain Ω^e. These integrals can be approximated numerically via a suitable quadrature scheme in which the integral is replaced with the summation over n_p integration points,

$$\int_{\Omega^e} \phi(\mathbf{x}) d\Omega^e - \sum_{p}^{n_p} w_p \phi(\mathbf{x}_p) = R$$

where $\mathbf{x}_p$ is the location of the integration point and w_p is the integration weight associated with point p. In standard finite elements, Gaussian quadrature is typically chosen. With this approach, the coordinates of the quadrature points and their weights are chosen to minimise the residual R. In the Lagrangian integration point scheme, we assume the integration points are the same as the material points used to discretise the material properties. The implication of this assumption is that material properties can easily be tracked using the proposed scheme and naturally couple to the finite element solution process through the quadrature scheme. However since the material points motion is governed by the velocity field, we have lost the ability to select the positions **and** the weights in our quadrature scheme in order to minimise R. Only the weights remain as a free parameter. This problem can be minimised since only a finite number of constraints need to be satisfied with a given order shape function to ensure optimal convergence rates (Hughes [1987]).

Underworld – Rheology for crustal deformation

As an example of the use of a Lagrangian integration point method for crustal deformation modelling, we briefly describe an unusual formulation which satisfies the Mohr-Coulomb failure model within a viscous mathematical model. This formulation is based on the idea that the material first deforms at high stress by frictional sliding on an ideally oriented slip surface. This provides a constraint on the maximum shear stress supported by the material, and the orientation of the slipping direction. On a given plane,

$$\tau_{\text{shear}} \leq \mu \sigma_{\text{normal}} + \text{cohesion} \qquad (4)$$

The Mohr-Coulomb failure model assumes that a fault which develops when an intact material yields occurs at the minimum possible stress for which (4) can be satisfied. In a material with incipient faults of all possible angles the ones which can slide at the minimum stress are oriented at $\pm\theta$ to the maximum (here: most compressive) principle stress direction, where

$$\tan(2\theta) = \frac{1}{\mu} \qquad (5)$$

The slip vector lies in the slip plane in the direction of the minimum principal stress. The two possible failure planes ($\pm\theta$) are entirely equivalent when failure occurs in an intact material.
Following Mühlhaus et al [2002], we define an anisotropic viscous material as a correction to an isotropic viscous part $2\eta D'_{ij}$ of the model by means of the Λ_{ijkl} tensor

$$\sigma_{ij} = 2\eta D'_{ij} - 2(\eta - \eta_S)\Lambda_{ijlm} D'_{lm} - p\delta_{ij} \qquad (6)$$

where a prime designates the deviator of the respective quantity, η_S is a second viscosity, and

$$\Lambda_{ijkl} = \frac{1}{2}(n_i n_k \delta_{lj} + n_j n_k \delta_{il} + n_i n_l \delta_{kj} + n_j n_l \delta_{ik}) - 2 n_i n_j n_k n_l \qquad (7)$$

is the anisotropy tensor. In (6) and (7) the vector $\boldsymbol{n}$ is the unit normal of the failure surface given initially by (5). The evolution of the director of the layers is described by

$$\dot{n}_i = W_{ij}^n n_j, \quad (8)$$

where

$$W_{ij}^n = W_{ij} - (D_{ki}\lambda_{kj} - D_{kj}\lambda_{ki}) \text{ and } \lambda_{ij} = n_i n_j. \quad (9)$$

The velocity gradient is given by $\boldsymbol{L} = \boldsymbol{D} + \boldsymbol{W}$ where $\boldsymbol{D}$ is the stretching tensor and $\boldsymbol{W}$ the spin tensor. The superscriped n distinguishes the spin $\boldsymbol{W}^n$ of the director $\boldsymbol{n}$ (the unit normal vector of the deformed layer surfaces) from the spin $\boldsymbol{W}$ of an infinitesimal volume element dV of the continuum.
For a given stress field, the most favorable failure directions are obtained from (5) for each Lagrangian integration point. If the shear stress exceeds the failure criterion, the second viscosity, η_S is set to

$$\eta_s \leftarrow \eta \frac{\mu\sigma_{\text{normal}} + \text{cohesion}}{\tau_{\text{shear}}} \quad (10)$$

which ensures that the stress is returned to the yield surface at this point \textit{assuming no consequent change in the stress field}. This process must then be repeated for all integration points, the stress recalculated, and the whole procedure iterated until changes in the stress field are small.
We need to be able to consider the possibility that the failure of a point is governed by whether the point has failed previously, and that the orientation of previous failure can influence the current failure mode. This means that each integration point should record both a scalar measure of the extent of failure and the preferred orientation of failure
In iterations after any failure has occurred at an integration point, the previous failure plane is tested to see if it will yield — allowing for any accumulated weakening of the yield criterion. In the examples shown, we assume that the plane which has the lowest η_{s} is the one which will fail first.

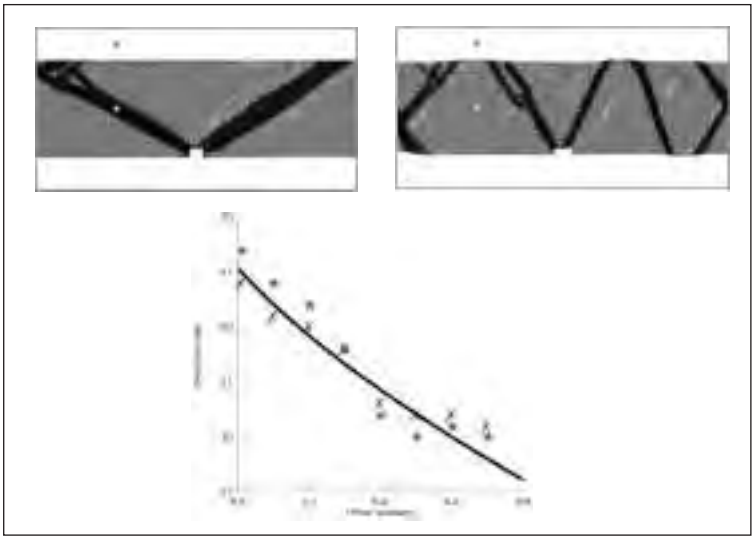

Figure 2 – A simple "benchmark" showing the angle to the vertical / horizontal of shear band formation in the notched beam test after 2% extension / compression for a range of the friction coefficient. The solid line is the microscopic failure angle

REFERENCES

- Hughes T.J.R., (1987), "The finite element method", Prentice-Hall, New Jersey.
- Moresi L., Dufour F. & Mühlhaus H.-B. (2003), "A Lagrangian integration point finite element method for large deformation modeling of viscoelastic geomaterials", Journal of Computational Physics, 184, 476-497.
- Moresi L., May D., Freeman J. and Appelbe B., (2003), "Mantle convection modeling with viscoelastic/brittle lithosphere: Numerical and computational methodology", Computational Science - Iccs 2003, Pt Iii, Proceedings, 2659, 781-787.
- Mühlhaus H.-B., Cada M. and Moresi L., (2003), "Anisotropic convection model for the earth's mantle", Computational Science - Iccs 2003, Pt Iii, Proceedings, 2659, 788-797.
- Mühlhaus H.-B., Dufour F., Moresi L. and Hobbs B., (2002), "A director theory for viscoelastic folding instabilities in multilayered rock", Int. J. Solids Structures, 39, 3675-3691.
- VPAC: Geoscience portal, (2003), http://www.vpac.org/VDT/Geoscience

DETECTION AND QUANTIFICATION OF DEEP GROUNDWATER FLOW USING 3-D GEOTHERMAL MODELLING 5-10

W. Rühaak(*), V. Rath (**), H. Deetjen(*), F. Höhne(**), A. Hartmann(**), A. Zschocke(*), R. Schellschmidt(*), C. Clauser (**)

(*) Leibniz Institute for Applied Geosciences (GGA), Stilleweg 2, D-30449 Hanover, Germany
(**) Applied Geophysics, RWTH Aachen University

Summary

Temperature in the Earth's upper crust is dominated by conductive heat transport. However, advection of heat associated with groundwater flow can alter the purely conductive regime significantly. We present a method which exploits this fact to quantify groundwater flow from precise subsurface temperature measurements.
We propose to detect areas disturbed by advection from computed temperature residuals, i.e. differences between temperatures measured in boreholes and calculated from a three-dimensional conductive model. The transient effect of paleoclimate is taken into account by subtracting its present signal from the measured data. If all processes are correctly considered, the calculated residuals represent the advective influence on the thermal regime. In order to obtain a quantitative estimate of groundwater flow, it is necessary to model the hydraulic flow regime. For this purpose we extended a 3-D conductive model into a fully coupled hydrothermal simulation. The model is calibrated using both the measured heads and the temperature residuals, which ideally should nearly vanish.
We demonstrate the potential of the method based on data from the German part of the Western Molasse Basin (northern Alpine foreland basin). Preliminary results show the potential of the method to detect advective temperature anomalies qualitatively. Obtaining quantitative estimates is a topic of current research.

Abstract text

Flow velocity and discharge rate of groundwater are of major interest in many geoscientific applications. However, it is particularly difficult to estimate these quantities in deep aquifers with normally little information. Groundwater flow can change the temperature field in the Earth's upper crust significantly. This fact is used to identify areas where the thermal regime is disturbed by water flow (e.g. Vasseur and Demongodin, 1995). We compared temperature-data (corrected for the diffusion of paleoclimate) from an extensive database of the GGA-Institute with results from a 3-D conductive simulation. The differences between these two data sets reflect well the assumed nature of the flow regime.

Development of a 3-D heat-transport model

A conductive 3-D reference model was set up in order to calculate residual temperatures. The study area is situated northeast of Lake Constance in southwest Germany. The depth range of interest extends from 500m to 1200m below the surface.
Setting up a model for computer simulations requires (1) defining a geologically consistent structural model, with a resolution on the order of the scale of the phenomena studied and (2) deriving a conceptual model from the structural model which transforms stratigraphic and lithological information into physical properties. The "true" real geological structures are simplified during this process so that the resulting model is a physically and geologically meaningful approximation.

The structural model (Fig. 1), used for the heat flow calculation, is based on simplified geological information obtained from a drilling database. In some cases it was necessary to include further information from geologic maps and seismic explorations. The model area is part of a sedimentary basin containing mostly Tertiary sediments from the Alpine orogeny. The basin is wedge-shaped with a moderate dip towards SSE. In order to reduce artefacts the entire model is rotated in this direction (20° NE).

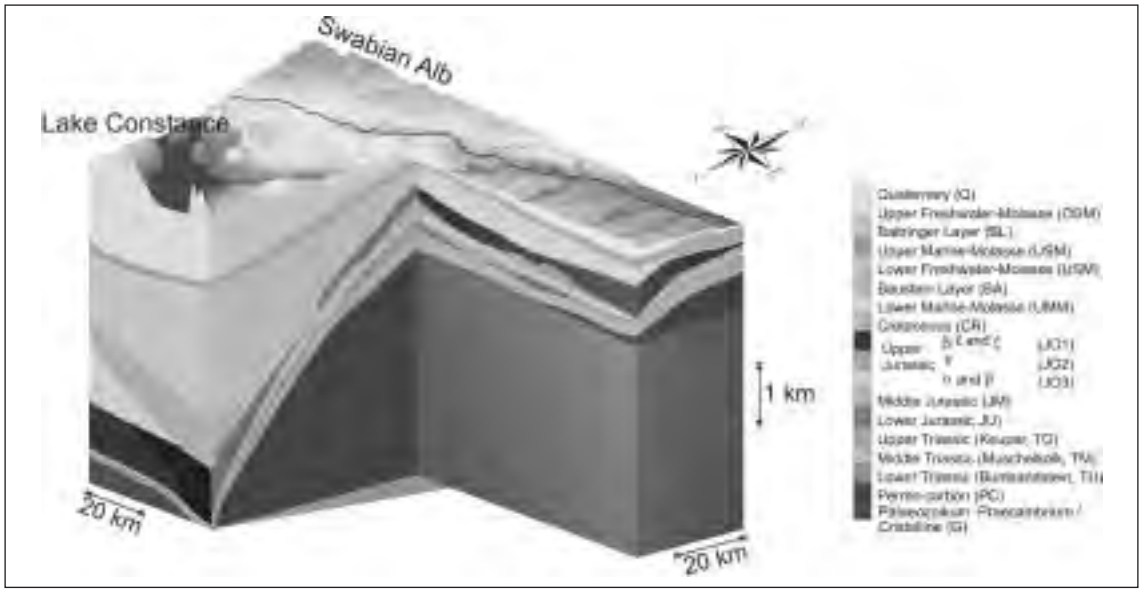

Fig.1: 3-D view of the structural model.

The numerical model

Simulation of flow and heat transport requires the solution of the following set of equations:
The steady-state nonlinear heat conduction equation:

$$\nabla \cdot (\boldsymbol{\lambda} \nabla T) = 0 \tag{1}$$

Modifying this equation in order to account for the effect of advective transport yields the steady-state heat transport equation:

$$\nabla \cdot (\boldsymbol{\lambda} \nabla T - \rho_f c_f T \mathbf{v}) + H = 0 \tag{2}$$

Specific discharge **v** is obtained from the flow equation:

$$\nabla \cdot \left(\frac{\rho_f g \mathbf{k}}{\mu} \cdot (\nabla h_0 + \rho_r \nabla z) \right) + W = 0 \tag{3}$$

Here $\boldsymbol{\lambda}$ is thermal conductivity, T temperature, ρ density, z the vertical coordinate taken positive upward, h_0 hydraulic head at reference temperature T_0, dynamic viscosity, g gravity, and H and W denote heat and fluid sources or sinks. Subscript f denote fluid properties, $\rho_r = (\rho(T, P)-\rho_0)/\rho_0$ is relative density.
Both equations were solved in three dimensions using the finite difference code SHEMAT (Clauser, 2003). The thermal conductivity is considered isotropic, and the temperature dependence of the rock thermal conductivity is implemented according to an empirical expression from Zoth and Hänel (1988).
The model extends 130 km x 95 km in the horizontal with horizontal and vertical grid sizes of 1 km (130 x 95 cells) and 25 m (280 cells), respectively. To study the influence of the grid resolution on the simulation results we also ran a model with half the grid size. This is of particular interest in cases where we included vertical fault zones.
Specific heat flow (lower boundary condition) is estimated to 86 mW m^{-2} for the total model area (in case of temperatures corrected for paleoclimate). Values for thermal properties were taken from different sources, mainly from measurements on cores from two drilling-sites, performed in the laboratories at GGA and RWTH. Additional data were taken from literature.

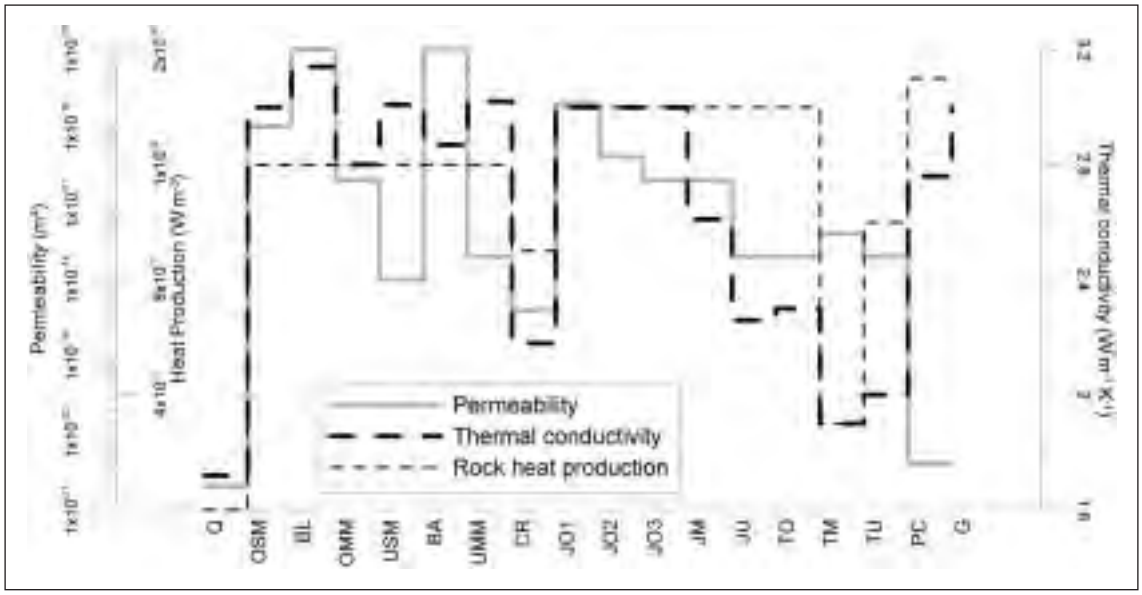

Fig.2: Permeability, thermal conductivity and rock heat production rate used in the model: Permeability in the Upper Freshwater-Molasse and in all upper Jurassic layers varies with position. For abbreviations see Fig. 1.

These data were assigned to the 18 stratigraphic basic units of the structural model. The model was then calibrated by varying these values within reasonable bounds. These best fitting values are shown in Fig. 2. The mean ground surface temperature (upper boundary condition) was determined using a linear regression of the borehole temperatures corrected for paleoclimate which was then interpolated on the surface.

GGA in Hanover has been maintaining and updating a temperature data base for Germany since 1977 (Pribnow and Schellschmidt, 2000). Most of the data are bottom hole temperatures (BHT). There are other types of subsurface measurements and also many undisturbed continuous logs. We used for this study: 596 BHT values, 453 re-sampled values from undisturbed continuous logs, 3081 values from 15 continuous logs re-sampled to 5 m interval (Fig. 3), and 162 other temperature measurements (mainly drill stem tests).

Results

The temperature residuals were calculated by subtracting the simulated temperatures from the measured paleoclimate-corrected temperatures. To avoid artefacts, no interpolation of the measured temperatures was used. To analyse this result we developed a 3-D inverse-distance weighting program that allows interpolating the residual temperatures with respect to the different qualities of the input data (Fig. 3).

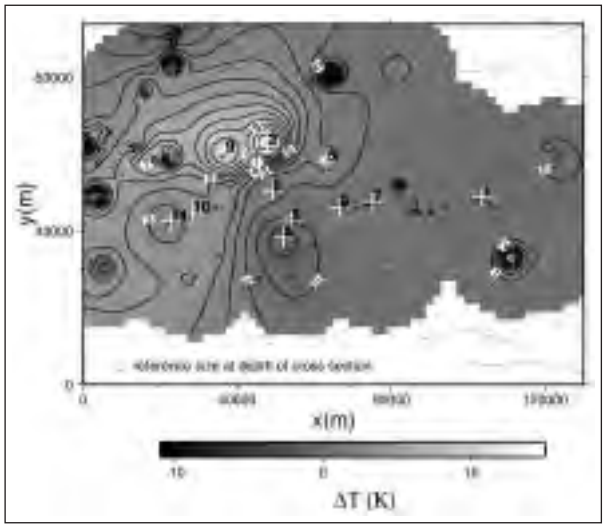

Fig. 3: Correlation between the calculated temperature residuals (measured minus simulated temperature) and major faults. The horizontal cross-section is 200 m below sea level which is approximately 700 to 800 m below surface. The numbered crosses mark the 15 log locations and the circles the points with other temperature data. The size of a circle is proportional to the vertical distance from this layer.

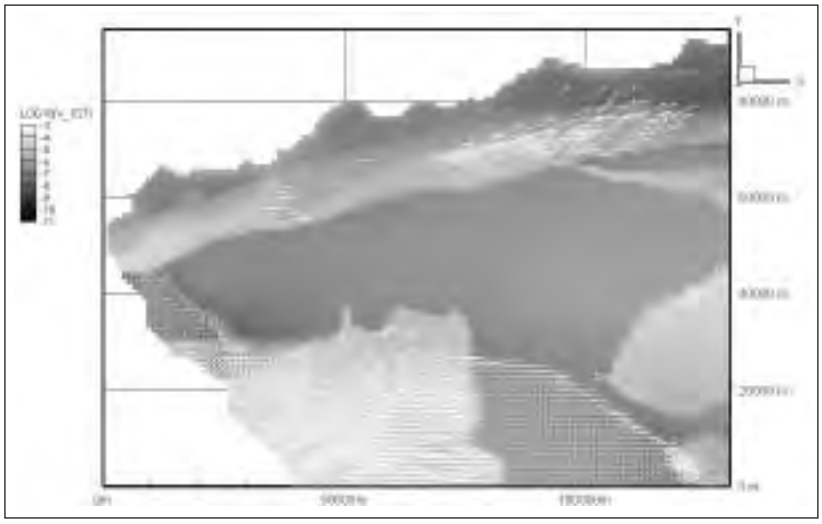

Fig.4: Another horizontal cross-section at 200 m below sea level showing first results of the modelled flow field. Decadic logarithmic scaling (base 10) is used for magnitude of the specific discharge in m/a, so that -3.5 corresponds to 0.03 m d^{-1} and -5 to 0.007 m d^{-1}.

The largest temperature residuals in Fig. 2 show an obvious agreement with the position of the well-known large Fronhofen fault zone in the western Molasse-basin (x = 46500 m, y = 61000 m). Other faults also display temperature anomalies, although in a smaller measure. This result is in line with the usually high permeability along such fault systems. Further, aspect, slope and position of the residual temperature field match reasonably well with those of the sedimentary layers and of the karstic aquifer in the north-west (Swabian-Alb). Further this anomaly lies at the position where the horizontal cross-section crosses the upper Jurassic karst aquifer.

The fully coupled heat-transport model was parameterized with head data taken from different maps. The most important parameter for this steady-state model is the permeability which is estimated and regionalized using information available in the literature and some rare data. We modelled a number of different scenarios with different lateral boundary conditions (no flow or fixed head) and with or without high permeability faults zones. The model could be calibrated to a satisfying degree, using measured heads.

One preliminary result of the fully coupled heat transport model is that for the flow-regime thermal-convection can have an important influence. Free convection can take place if the Rayleigh number Ra for flow in porous media

$$Ra = \frac{\rho g \beta k D \Delta T}{\mu a} \cos\theta \qquad (4)$$

is larger than a critical value Ra_c (Bachu, 1999), where β is the thermal expansion coefficient of water, a is thermal diffusivity of the saturated porous medium, ΔT is the temperature difference over a vertical distance D, θ is the angle of the aquifer with the horizontal, all values were assumed for $\beta = 10^{-3}$ K^{-1} and $\mu = 0.5 \times 10^{-3}$ N s m^{-2}. We will evaluate the influence of potential free convection using estimated Raleigh-maps, suggested by Pestov (2000). But the incomplete knowledge of the conditions in the deep underground (> 3000 m below the surface) is still a major problem.

The only flow-model able to reflect the measured thermal field in a satisfying manner has high-permeability vertical faults. All other models do not show a thermal anomaly at the correct positions. This leads to the hypothesis that the observed temperature anomalies are a combined result of a high-permeablity karst aquifer crossing high-permeablity vertical faults.

Discussion

Although detection of advectively disturbed regions is possible, a quantitative interpretation still poses some problems such as:

- different structures, such as high-permeability vertical faults and high-permeability aquifers will produce nearly the same anomaly;

- irregularities like fractures and faults can interrupt the aquifer and change the entire flow regime (Bethke, 1989);
- some of the flow patterns are difficult to understand, for instance because of the Jurassic limestone karst aquifer;
- although there is lots of data, there are still gaps, for instance regarding the deep groundwater head or the regional distribution of the permeability in the aquifer.

In spite of the difficulties, the method presented here can be used to quantify groundwater flow and discharge in situations where other methods fail (Fig. 4).

www.rwth-aachen.de/geop/Ww/geothermik/geothermik.htm

REFERENCES

- Bachu, S. (1999), Regional-Scale Geothermal and Hydrodynamic regimes in the Alberta basin: a synthesis, in Förster, A. and Merriam, D.F. (ed.), Geothermics in Basin Analysis, pp. 81-98, Kluwer, New York.
- Bethke, C.M. (1989), Modeling subsurface flow in a sedimentary basin, Geologische Rundschau, 78/1, p. 129-154.
- Clauser, C. (ed.) (2003), Numerical Simulation of Reactive Flow in Hot Aquifers, SHEMAT and Processing SHEMAT, Springer, Berlin.
- Pestov, I. (2000), Thermal Convection in the Great Artesian Basin, Australia, Water Res. Management, 14, p. 391-403.
- Pribnow, D. and Schellschmidt, R., (2000), Thermal tracking of flow, GRL 27, 1957-1960.
- Vasseur, G. and Demongodin, L., (1995), Convective and conductive heat transfer in sedimentary basins, Basin Res., 7, pp. 67-79.
- Zoth, G. and Hänel, R., (1988), Appendix. In: Hänel, R., Rybach, L. Stegena, L. (eds.), Handbook of terrestrial heat flow density determination, Kluwer, Dordrecht, pp. 447-468.

METHODOLOGY FOR AUTOMATIC BUILDING OF STRUCTURED GEOLOGICAL MODELS

5-11

Sébastien Schneider [1], Michel Perrin [2], Nicolas Guiard [3], Jean-François Rainaud [1],Pascal Lienhardt [3], Yves Bertrand [3]

1 Institut Français du Pétrole, DISMA, 1-4 Avenue de Bois-Préau, F-92852 Rueil-Malmaison Cedex {sebastien.schneider, j-francois.rainaud}@ifp.fr

2 Ecole des Mines de Paris, CGI, 60 Bd St. Michel, F-75272 Paris Cedex 06 - perrin@cge.ensmp.fr

3 Université de Poitiers, IRCOM-SIC, Bat. SP2MI, Téléport 2, Bd Marie et Pierre Curie, BP 30179, F-86960 Futuroscope Cedex - {guiard, lienhardt, bertrand}@sic.sp2mi.univ-poitiers.fr

1 Introduction

Present-day trends for earth modeling concern the possibility of achieving model building and management in distributed multi-agent environments. The result of the modeling must then be a "shared earth model" (SEM) i.e. an assemblage of elementary objects linked by definite geometrical/topological relationships [Mal02] able to be reused, revised or upgraded by any user over the network. Moreover, the relationships between the objects present in the model may either be described as such ("data-driven"approach) or deduced from the business (geological) properties of the objects themselves Brandel01]. The present paper refers to this latter "knowledge-driven" approach.
We intend to demonstrate that it is possible to perform significant improvements to 3D geological modeling by taking advantage of the specific structure, which underlies consistent geological assemblages (geological knowledge). By using adequate data structures for describing and managing macro and micro-topologies (Generalized-Maps [Lie94]), it is possible to automatically build and update consistent geological Earth models by taking into account step by step the geological interpretation i.e. the existing geological relationships between objects defined by the user. In consequence, it is possible to automatically build from one set of geometrical data, various models resting on different geological interpretations and possibly presenting significant topological differences. This opens the way to an easy revision of any model by any user over the net.

2. Theoretical and practical background

2.1 Geological syntax and Geological Evolution Scheme (GES)

Previous work [Per98] has shown that, in order to be geologically consistent, 3D models should be built in accordance with a few rules, which define a ***geological syntax***.

We will assume that the surfaces present in a 3D model are of two types:
- *polarized* surfaces (POL) corresponding to limits of sedimentary formations or of intrusive granites; their two sides are geologically different: one faces older formations and the other faces younger formations;
- *non polarized* tectonic surfaces (TEC) which correspond to geological discontinuities, faults for instance, whose two faces are geologically equivalent, both facing older formations.

We will also consider as fundamental rules the facts that each surface, either POL or TEC, has ***one*** well-determined age and that, when two surfaces intersect, one of them is necessarily interrupted by the other.

Space-time relationships between intersecting geological surfaces can be of two types:
- *on lap*: when the older surface is a POL (on lap surface), it interrupts the younger surfaces;
- *unconformity*: the younger surface (unconformable surface) interrupts the older surface (1).

Taking into account the age relationships between surfaces, we have defined a graph called a ***Geological Evolution Scheme*** (GES) whose nodes are individual POL or TEC surfaces. Each surface comprises two faces, which are given CONC/DISC attributes in accordance with the above defined rules: the CONC attribute stands for a side that may be interrupted and the DISC attribute for a side that may be interrupting.

The GES nodes are put in vertical order in accordance with their relative age (bottom = old, top = young) and linked by various types of arcs corresponding either to chronological relationships (A is older/younger than B)or to spatial relationships (fault A stops on /interrupts fault B) [BPR+01] (cf. Fig. 4 in section 3.3).

2.2 Topological data model: Generalized Maps

The 3D models, which must be performed, should be true topologically consistent "volumic models". This requires the use of a topological data model, which partitions an object into topological cells of different dimensions (vertices, edges, faces and volumes), and specifies their mutual relations. The data model that we have used is known as Generalized Maps and is fully described in [Lie94].

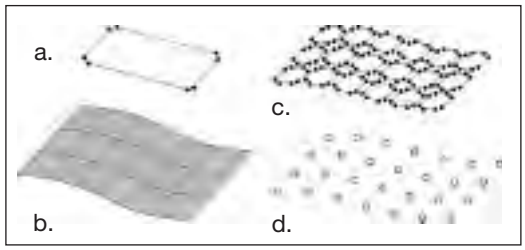

Figure 1. a) Macro-topological description, b) the corresponding embedding (the parametric surface itself). c) Micro-topological description, d) the corresponding embedding (a cloud of points corresponding to the u, v nodes).

In order to describe a model, a G-Map should be *embedded* in a definite geometry. This is done by associating each geometrical element of a given dimension with a specific cell of the G-Map: for instance, in the 3D models considered here, surfaces are associated with cells of the *face* type, curves with cells of *edge* type and points with cells of the *vertex* type. The G-Map structure can be applied to describe a **macro-topology** i.e. the topological relationships existing between the various edges, faces, volumes of a 3D model described by a set of surfaces of any type (parametric, triangulated, meshed etc.). This macro-topological description has been used in previous works concerning automatic model building [BPR+01], [Sch02] and [HH92] (Fig. 1a and 1b). In the case of a model consisting of triangulated or meshed surfaces, the G-Map structure can also be applied to describe the relationships between the various elementary edges and triangular or polyhedral surfaces (**micro-topology**) (Fig. 1c and 1d). Such micro-topological description will be used in the present work.

Moreover, in the case of geological models, the classical G-Map structure must be extended to take into account specific geological relationships such as those, which connect the different parts of a geological surface interrupted by a fault. This is done by using specific *beta* ties [Sch02].

3. Model building

The allover methodology proposed here supposes that the model building is operated in three successive phases:

1. A preprocessing, which builds the fault networks if needed;
2. A main phase, which determines the intersections to be operated through an iterative reading of the GES and then operates these intersections;

3. A post-processing stage for removing the artifacts created during the global building process.
The two first stages are operated by using a co-refinement algorithm that will be presented in section 3.1, This supposes, however, the previous determination of the various input data to be used by the algorithm i.e. a set of surfaces and a Geological Evolution Scheme.
Initial surfaces are assumed to be continuous, unstructured and geometrically independent from one another, possible intersections between them being ignored.
The GES must be built by the user previously to the model building itself. For this, the user must define the relative age order of the various geological surfaces and define the geological properties POL or TEC of each of them and, in the case of a POL surface, decide upon the CONC or DISC attributes to be put to the two faces. The user must also specify the links between the various geological surfaces and the various files describing their geometry. An independent user interface is presently being built, which will allow to define the links and properties of the various geological surfaces, and to insert them in a GES that will automatically be built step by step [BHB03]. We also study the possibility of realizing a supervised GES Builder, which will enable the user to deduce a GES from a set of interpreted cross-sections in a semi-automatic way.

3.1 Co-refinement algorithm for surface intersection processing

The method presented here assumes that the various surfaces are described by triangulations. Each newly introduced surface is co-refined with all the surfaces already present in the model. This co-refinement consists in computing the intersections between the various triangulated surfaces and in updating the underlying micro-topological model. This is operated by means of an optimized algorithm developed by Nicolas Guiard at University of Poitiers and Ecole des Mines de Paris. This algorithm uses a propagation approach and has thus a complexity of *0(n)*, with respect to the number of surfaces present in the model.

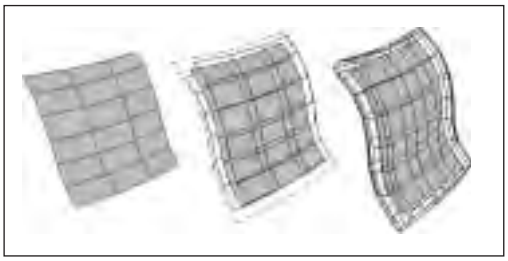

Figure 2. The pillow volume related to surface S is constructed by building at a given distance d form S two parallel surfaces S1 and S2, by extending S to a contour C' drawn at distance d from the contour C limiting S and by closing the pillow along C'.

In the case of a fault surface, a *"pillow volume "* is built around the surface itself (Fig. 2), in order to cope with the incertitude which may affect the intersections between the fault and the surfaces that it interrupts [Sch02]. In the case of a pillow volume, the co-refinement is operated both with the external pillow surface and with the original planar fault surface.

3.2 Pre-processing stage: building of fault networks

When the model to be built not only comprises individual faults, but one or several fault networks, the model building procedure must process them before all other surfaces by going through the following steps:

- building of a pillow volume around each fault of the network;
- co-refinement of all the pillow volumes corresponding to one definite network;
- removal of the parts of the pillow volumes, which do not belong to the model; the parts to be removed are determined by examining in the GES, which faults stop on another.

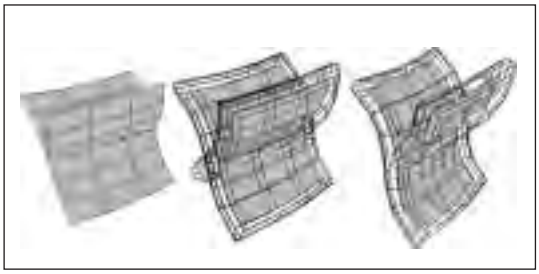

Figure 3. Example of a pillow structure built around a fault network.

The result of the above operations is a volumic fault network consisting in an assemblage of pillow structures inside which individual planar faults are kept just as in the case of individual pillows (Fig. 3). The volumic fault networks that have been built are then introduced into the model and treated in accordance with the procedure described in the next section and in the same way as individual faults.

3.3 GES iteration to determine the intersections to be operated

The partial order relationship established between the various geological surfaces by means of the GES is used to build a consistent model step by step. The basic rule is that an older geological event cannot modify a younger one. In consequence, the various geological surfaces must be introduced one after the other in reverse chronological order, beginning by the youngest one. Each geological surface is introduced by co-refining it with all the younger surfaces already present in the model.

In the GES shown on figure 4, the surfaces are introduced in the model beginning by surface B and finishing with surface S2. The fault network Φ is built in the pre-processing stage as explained previously and introduced into the model like a unique geological event.

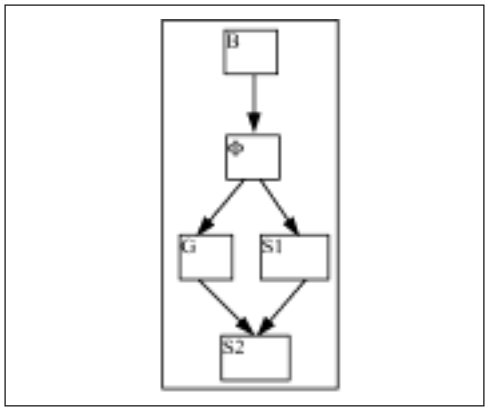

Figure 4: Example of a GES with B corresponding to the younger geological event and S2 corresponding to the older one. Φ corresponds to a fault network.

3.4 Post-processing stage

Once all the surfaces have been inserted, we obtain a model with incertitude volumes around each fault. However, we want to obtain a model that will only comprise horizons and faults represented by actual surfaces.

For this, the previously obtained model must be simplified by removing the incertitude pillow volumes. However, this operation reveals holes on the various surfaces interrupted by faults corresponding to the parts of these surfaces that were deleted when building the pillows. These holes are filled by extending the surface of the horizons up to the faults. For this, we add a set of polyhedric faces, perpendicular to the average normals of the vertices belonging to the border of the holes.

4. Results

Figures 5 and 6 show results corresponding to a model comprising horizons, elementary faults and a simple fault network. Figure 5 corresponds to a wireframe view of the micro-topology used to define the geological model at the issue of the building process. Figure 6 is a block-colored view on which one can identify the various geological blocks present in the model. The computing time for the automatic building process of this model is around 2 minutes on an Intel Pentium 4.

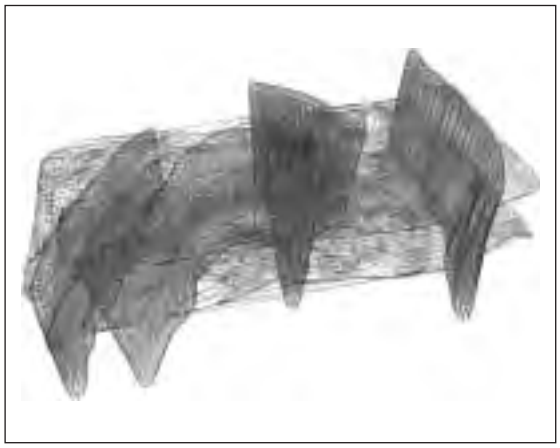

Figure 5. View of the final model built using the micro-topological approach.

Figure 6. Geology: final model.

5. Conclusion

We have presented here the prototype of a geological pilot apt to be coupled to all common geological modelers. This pilot enables the automatic building of a 3D geological model starting from elementary unsegmented surfaces. The methodology is innovative since it rests on an explicit description of the geological interpretation operated through the GES. It also takes advantage of an adequate data structure for managing the topological relationships (G-map structure) and of an efficient method for intersecting and segmenting the various surfaces (co-refinement).
The result is a topologically and geologically consistent model, which can easily be revised in case of changes of the data and/or of the interpretation made by the user. Improvements are already being studied that will make this tool an efficient auxiliary for exploration geologists by enabling them to operate the building and updating of voluminous 3D geological models entirely by themselves possibly in distributed environments.

REFERENCES

- [BHB03] S. Brandel, M. Haefele, D. Bechmann, A geological application in immersive virtual environments, VRIC 2003 5th Virtual Reality International Conference, Laval, France, 13-18 May 2003.
- [BPR+01] S. Brandel, M. Perrin, J.-F. Rainaud and S. Schneider, Geological Interpretation makes earth models easier to build, EAGE 63rd Conference, Extended Abstracts, 1: F-28, Amsterdam, The Netherlands, June 2001.
- [HH92] Y. Halbwachs and O. Hjelle, Generalized Maps in Geological Modeling: Object-Oriented Design of Topological Kernels, Advances in Software Tools for Scientific Computing, 10(1): 339-356, 2000.
- [Lie94] P. Lienhardt, N-dimensional Generalized Combinatorial Maps and Cellular Quasi-Manifolds, Journal of Computational Geometry and Applications, 4(3): 275-324, 1994.
- [Mal02] J.-L. Mallet, Geomodeling, Oxford University Press, 2002.
- [Per98] M. Perrin, Geological consistency: an opportunity for safe surface assembly and quick model exploration, 3D Modeling of Natural Objects, A Challenge for the 2000's, 3(4-5), Nancy, France, June 1998.
- [Sch02] S. Schneider, Pilotage automatique de la construction de modèles géologiques surfaciques, PhD of Jean Monnet University and Ecole des Mines de St Etienne, 2002.

PREDICTIVITY AND CALIBRATION IN GEOLOGIC MODELING: REVIEW OF CURRENT METHODS AND OUTLOOK 5-12

J. Wendebourg

Shell International Exploration and Production, Postbus 60, 2280 GB Den Haag, The Netherlands

Abstract

This paper gives a review of currently used methods to determine and reduce uncertainties of predictions of geological forward models. This is particularly important in industry where reliable predictions are important economically and reduced uncertainties are critical. Uncertainties require a probabilistic representation of outcomes but most geological models are deterministic forward models. Various methods exist to convert single-valued answers into a probabilistic form including Monte Carlo procedures based on advanced random sampling methods, experimental design and Bayesian inversion as well as combinations thereof. One of the most challenging aspects is the inclusion of constraints, either in the form of hard data or soft geologic concepts, the purpose of which is to reduce the variance of the outcome distribution or at least to polarize it as to facilitate the decision process. Methods are selected according to the modelling problem. Large areas with only a few data points have high uncertainties and therefore assumption testing is more important than close calibration, resulting in predicted trends, ideally indicating the impact of further data acquisition. On the other end, data mature areas that enjoy many constraints (well data, high resolution correlations, experimental data etc) need close calibration and predictions can be made locally, ideally with a much reduced uncertainty. Examples from Petroleum Systems Modelling will be given.

AUTHOR INDEX

The code after the name indicates the session and the place in the book.